Journal of Engineering for Gas Turbines and Power

Published Quarterly by ASME

VOLUME 126 • NUMBER 4 • OCTOBER 2004

Transactions of the ASME, Journal of Engineering for Gas Turbines and Power (ISSN 0742-4795) is published quarterly (Jan., April, July, Oct.) by The American Society of Mechanical Engineers, Three Park Avenue, New York, NY 10016. Periodicals postage paid at New York, NY and additional mailing offices. POSTMASTER: Send address changes to Transactions of the ASME, Journal of Engineering for Gas Turbines and Power, c/o THE AMERICAN SOCIETY OF MECHANICAL ENGINEERS, 22 Law Drive, Box 2300, Fairfield, NJ 07007-2300.
CHANGES OF ADDRESS must be received at Society headquarters seven weeks before they are to be effective. Please send old label and new address.
STATEMENT from By-Laws. The Society shall not be responsible for statements or opinions advanced in papers or ... printed in its publications (B7.1, par. 3).

INDEXED by Applied Mechanics Reviews and Engineering Information, Inc. Canadian Goods & Services Tax Registration #126148048

TECHNICAL PAPERS

(**Contents continued on inside back cover**)

This journal is printed on acid-free paper, which exceeds the ANSI Z39.48-1992 specification for permanence of paper and library materials. ♾™
♲ 85% recycled content, including 10% post-consumer fibers.

Journal of Engineering for Gas Turbines and Power **OCTOBER 2004**

Volume 126, Number 4

BOOK REVIEW

ANNOUNCEMENTS AND SPECIAL NOTES

(**Contents continued**)

Journal of Engineering for Gas Turbines and Power **OCTOBER 2004**

Volume 126, Number 4

The ASME Journal of Engineering for Gas Turbines and Power is abstracted and indexed in the following:

AESIS (Australia's Geoscience, Minerals, & Petroleum Database), Applied Science & Technology Index, Aquatic Sciences and Fisheries Abstracts, Civil Engineering Abstracts, Compendex (The electronic equivalent of Engineering Index), Computer & Information Systems Abstracts, Corrosion Abstracts, Current Contents, Engineered Materials Abstracts, Engineering Index, Enviroline (The electronic equivalent of Environment Abstracts), Environment Abstracts, Environmental Science and Pollution Management, Fluidex, INSPEC, Mechanical & Transportation Engineering Abstracts, Mechanical Engineering Abstracts, METADEX (The electronic equivalent of Metals Abstracts and Alloys Index), Pollution Abstracts, Referativnyi Zhurnal, Science Citation Index, SciSearch (The electronic equivalent of Science Citation Index), Shock and Vibration Digest

Determination of Chemical Kinetic Parameters of Surrogate Solid Wastes

D. Jinno

Ashwani K. Gupta[1]
e-mail: akgupta@eng.umd.edu

The Combustion Laboratory,
Department of Mechanical Engineering,
University of Maryland,
College Park, MD 20742

K. Yoshikawa
Department of Environmental Science and Technology,
Interdisciplinary Graduate School of Science and Engineering,
Tokyo Institute of Technology,
Yokohama, Japan

Results on the thermal decomposition behavior of several important components in solid wastes are presented under controlled chemical and thermal environments. Thermogravimetry (TGA) tests were conducted on the decomposition of cellulose, polyethylene, polypropylene, polystyrene and polyvinyl chloride in inert (nitrogen), and oxidative (air) atmospheres. Inert condition tests were performed at heating rates of 5, 10, 30, and 50°C/min while the oxidative condition tests were performed at one heating rate of 5°C/min. Differential scanning calorimetry (DSC) was also used to measure the heat flow into and out of the sample during thermal decomposition of the material. The TGA results on the mass evolution of the materials studied as a function of temperature showed that the cellulose contained a small amount of moisture whereas no moisture was found in the other materials examined. The DSC curve showed the heat flow into and out of the sample during the process of pyrolysis and oxidative pyrolysis. The temperature dependence and mass loss characteristics of materials were used to evaluate the Arrhenius kinetic parameters. The surrounding chemical environment, heating rate, and material composition and properties affect the overall decomposition rates under defined conditions. The composition of these materials was found to have a significant effect on the thermal decomposition behavior. Experimental results show that decomposition process shifts to higher temperatures at higher heating rates as a result of the competing effects of heat and mass transfer to the material. The results on the Arrhenius chemical kinetic parameters and heat of pyrolysis obtained from the thermal decomposition of the sample materials showed that different components in the waste have considerably different features. The thermal decomposition temperature, heat evolved and the kinetics parameters are significantly different various waste components examined. The amount of thermal energy required to destruct a waste material is only a small faction of the energy evolved from the material. These results assist in the design and development of advanced thermal destruction systems. [DOI: 10.1115/1.1772407]

Introduction

Environmentally benign, effective and permanent methods for the disposal of wastes continue to be on the high priority list worldwide especially in the developed countries. The two distinct reasons for this are (i) reduction in the number of available sites for direct landfill and (ii) emission of hazardous chemicals from disposition of wastes. As for the direct landfill, for example, the United States generates over one trillion, [1,2], pounds of solid waste every year (about 4 pounds per person per day) and even with extensive waste minimization plans, this amount is projected to increase at a rate of about 1% annually, [1–3]. The waste consists of 7%–9% by weight or 25%–30% by volume plastics, [4]. The use of plastics has dramatically increased during the last couple of decades and problem of disposing them has become progressively acute. In addition the United States produced over 4 million tons of polypropylene and 2.5 million tons of polystyrene annually, [5]. The solid wastes generated in the UK and Japan is respectively about 3.3 and 2.2 lb/person/day. The development of measuring technique has revealed the presence of newer and harmful chemicals (some in a very small quantity) from chemical wastes. The biologists have warned a risk on some of the chemicals not only for the typical pollutants, such as, NO_x, SO_2, HCl, CO, CO_2, unburned hydrocarbons but also the new chemicals called endocrine disruptors (Bisphenol A, PCB, DDT, dioxin, etc.), [6,7]. Several waste disposal options used to date includes: direct landfill, storage in surface impoundments, physical/chemical stabilization and direct incineration. Although all of these solutions seen viable, none is without problems. Of all the treatment technologies thermal destruction offers distinct advantage over the other methods since it provides maximum volume reduction (typically 80% of the original waste), its effectiveness to plastic, energy recovery (waste has about 5500Btu/lb calorific value) and the byproducts can be used in several ways, such as, building and road bed construction material, [4,8,9]. The byproducts are also nonleachable. The volume reduction can be further enhanced by proper separation and removal of the metals, glass and other materials from the waste. However, the disadvantages are that the technology must be environmentally benign and accepted by the public since the by-products from their application can be health hazardous and detrimental to our environment, [4,9,10].

The current practice for the disposal of municipal solid waste (MSW) is landfilling (83%), incineration (6%), and recycling (11%), [2,3]. The most common disposal of MSW is therefore landfilling, [4,9]. This is because it is relatively inexpensive as compared to other methods. It is to be noted that direct landfilling is becoming less acceptable worldwide. In Japan now the landfill option is no longer acceptable. This method of disposal creates the problem of odor in addition to the emission of methane, carbon dioxide, and other toxic gases. The leachate generated from the landfill site contaminates the soil and ground water. Special interest on the emission of air toxic organic pollutants and trace metals, from incinerators came after the risk assessment findings towards human life, [11,12]. The concerns on pollutants emission,

[1]To whom correspondence should be addressed.

Contributed by the Fuels and Combustion Division of THE AMERICAN SOCIETY OF MECHANICAL ENGINEERS for publication in the ASME JOURNAL OF ENGINEERING FOR GAS TURBINES AND POWER. Manuscript received by the F&C Division Mar. 2002; final revision received Mar. 2004. Associate Editor: S. R. Gollahalli.

which are produced as byproducts from the direct result of the combustion, are common to all combustion processes.

In order to obtain comprehensive understanding of the thermal destruction behavior of different kinds of wastes, the focus should be on understanding the basic behavior that occurs during their thermal decomposition. This then requires an understanding of how the various parameters, such as temperature, heating rate, and chemical composition influence thermal decomposition. How much is the energy required if the waste material were to be transformed into clean gas phase and nonleachable solid residue for building and construction material. This information can then be used for the design and technology development of advanced thermal destruction (incineration) systems.

Thermogravimetric analysis (TGA) has been used to study the pyrolysis of various waste materials. Raman et al. [13] used this method to study the devolatilization of biomass at two heating rates of 5 and 80°C/min. William and Besler [14] investigated the thermal decomposition of municipal solid waste at temperature of up to 560°C using TGA. In general TGA analysis, [15,16], was conducted under low heating rate (below 5°C/min) to avoid any error and because kinetic parameters definition was made at a fixed temperature. Some decomposition experiments, [17–19], using Curie point reactor were conducted under fixed temperature but these experiments were conducted under very quick heating rates of over 9000°C/sec. When one thinks about real decomposition in a reactor, it will occur at intermediate heating rates that lie between usual TGA conditions and Curie point reactor. In this study we provide chemical kinetic information on the thermal destruction of surrogate solid waste materials (cellulose, polyethylene, polypropylene, polystyrene, and polyvinyl chloride) at different heating rates (5°C/min to 50°C/min) under conditions of both pyrolysis and oxidative pyrolysis.

Experimental Procedure

Simultaneous thermogravimetry (TGA) analysis and differential scanning calorimetry (DSC) tests have been conducted to examine the thermal decomposition of cellulose, polyethylene, polypropylene, polystyrene, and polyvinyl chloride in inert (nitrogen) and oxidative (air) environments. The tests were performed using differential scanning calorimetry, DSC, and thermgravimetry, TGA analyzers that allowed simultaneous measurements of heat flow in and out of the sample and weight loss as a function of time or temperature in the thermal environment from ambient up to 1500°C. In this study the samples were subjected to temperature ramps in an inert gas (nitrogen) or an oxidative gas (air) in the temperature range of 25°C to 1000°C. Nitrogen and air at a flow rate of 40 ml/min was used as the inert and oxidative atmosphere, respectively. The heating rate was varied as 5, 10, 30, or 50°C/min. The results presented here are for only 5°C/min. The role of gas flow rate is significant in terms of heat transfer mechanisms (radiation, convection) from the hot gases to the material. In particular under oxidative conditions it is the energy source of oxidative reaction (with air). Platinum pans of about 4-mm diameter were utilized for the tests. The material sample sizes were in the range of 5 to 7 mg. The surrogate materials examined here were: cellulose, polyethylene, polypropylene, polystyrene, and polyvinyl chloride.

The mass evolution of these samples was determined as a function of temperature. The fractional reaction, defined as $\alpha=(m_0-m)/(m_0-m_f)$ (reaction progress), [20], where T_0 the reaction initial temperature and T_f the end temperature of the reaction, have been determined from the plot of T versus dm/dt. TGA has been extensively used to determine the devolatilization characteristics and kinetic parameters, [21,22]. It is to be noted that these ideal conditions as well as some simplifying assumptions, [20,23], made here may not necessarily correspond to the actual thermochemical decomposition of the materials in an incineration or a thermal destruction system. Despite these issues the data provides useful comparison of reaction parameters, such as, temperature and heating rate. In this study we have used two different methods to determine the Arrhenius kinetic parameters. Very broadly one can determine the Arrhenius kinetic parameter from the TGA curve with constant heating rate using two different methods. One method uses only one curve while the other uses several curves with different heating rate. In general using several heating rate provide better value than that obtained using only one curve. However, by using one curve method alone one can see the difference between different heating rate curves.

Calculations

Determination of the Arrhenius Parameters (From One Curve). The Arrhenius parameters, [20,23–25], for the thermal decomposition of the samples were determined assuming a first-order chemical reaction ($n=1$). The rate constant is defined as

$$k(T)=A\times\exp\left(-\frac{E}{RT}\right) \tag{1}$$

where

A = pre-exponential factor, min^{-1}
E = activation energy, kJ/mole
R = universal gas constant, kJ/mole K
T = temperature, K
t = time, s

Equation (1) defines the temperature dependence of the specific rate constant. A second equation that relates the reaction progress to time through the rate constant is also required.

$$\frac{d\alpha}{dt}=A\times\exp\left(-\frac{E}{RT}\right)\times(1-\alpha) \tag{2}$$

$$\int\frac{d\alpha}{1-\alpha}=A\times\int\exp\left(-\frac{E}{RT}\right)dt \tag{3}$$

$$\frac{dT}{dt}=\text{heating rate},\quad \beta. \tag{4}$$

Integrating yields

$$-\ln(1-\alpha)=\frac{A}{\beta}\times\int\exp\left(-\frac{E}{RT}\right)dT \tag{5}$$

where

α = reaction progress
β = heating rate, °C/min.

In Eq. (5), the right-hand side has no exact solution and several approximate solutions to this equation have been used to determine the order of reaction, activation energy, and pre-exponential factor.

$$-\ln(1-\alpha)\cong\frac{A}{\beta}\times\frac{RT^2}{E}\times\exp\left(-\frac{E}{RT}\right) \tag{6}$$

Taking the natural Logarithm of the above equation yields

$$\ln(-\ln(1-\alpha))=\ln\frac{ART^2}{\beta E}-\frac{E}{RT}. \tag{7}$$

The value of E and $\ln(A)$ was evaluated from the slope and intercept of function $\ln(-\ln(1-\alpha))$ versus $1/T$, [20,23]. The data to construct this plot are taken from the TGA curve (see Fig. 1). In this paper we have used $\alpha=0.5$.

Determination of the Arrhenius Parameters (From Several Curves). Taking the natural logarithm of Eq. (2) yields

$$\ln\left(\frac{d\alpha}{dt}\right)=\ln(A\times(1-\alpha))-\frac{E}{RT} \tag{8}$$

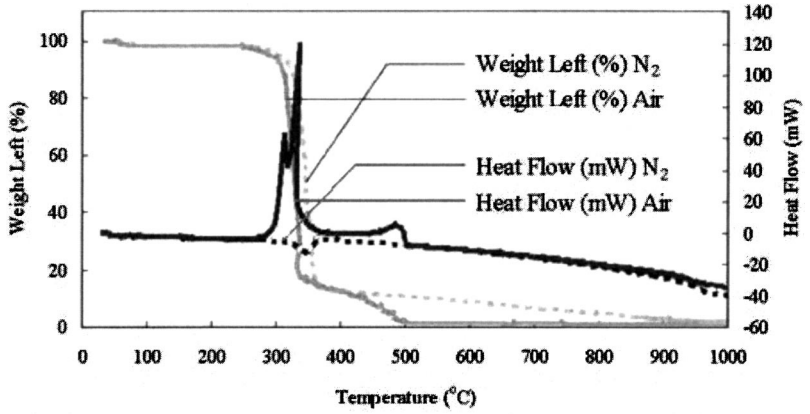

Fig. 1 Decomposition of cellulose

$$\ln\left(\beta\frac{d\alpha}{dT}\right)=\ln(A\times(1-\alpha))-\frac{E}{RT}. \tag{9}$$

By deciding on the value of α (taken as 0.5 here) and taking a plot of $\ln(d\alpha/dt)$ versus T^1 provides the value of activation energy, E.

Determination of the Heat of Pyrolysis. The value of heat of pyrolysis, [20], (see Fig. 2) was calculated from Eqs. (10) and (11).

$$h=\frac{T_2-T_1}{\beta}\times\frac{1}{m_i}\times\int_{T_1}^{T_2}P_{(T)}dT \tag{10}$$

$$h=\frac{1}{m_i}\times\int_{t_1}^{t_2}P_{(t)}dt \tag{11}$$

where

h = heat of pyrolysis
m_1 = initial mass
$P_{(t)}$ = heat flow
T = temperature
t = time
β = heating rate

Calculation of Required Amount of Oxygen for Complete Combustion.

Cellulose: $(C_6H_{10}O_5)+6O_2\rightarrow 6CO_2+5H_2O$

Polypropylene: $\{CH_2CH(CH_3)\}+4.5O_2\rightarrow 3CO_2+3H_2O$

Polystyrene: $\{CH_2CH(C_6H_5)\}+10O_2\rightarrow 8CO_2+4H_2O$

The required amount of air is calculated from

$$W_r=M_{w(\text{unit})}/m_s\times Cr/0.2\times 22{,}400 \tag{12}$$

where

W_r = required amount of air
$M_{w(\text{unit})}$ = Unit molecular weight of substance
m_s = Sample mass
Cr = Coefficient of oxygen in perfect combustion reaction
0.21 = oxygen fraction in air
22,400 ml = 1 mol.

Results and Discussion

The results obtained from the Thermogravimetric analysis (TGA) and differential scanning calorimetry (DSC) on the five different samples is shown in Figs. 1–5 for a heating rate of 5°C/min. They show the mass evolution and heat flow into and out from the sample versus temperature. The results under inert conditions (see, for example, TGA curve for N_2 case in Fig. 1) suggest that the decomposition occurs in a single-stage reaction while the results from oxidative condition (see TGA curve for air case in Fig. 1) suggest that the decomposition occurs in multi-stage. For oxidative condition the first stage is attributed to release of volatiles while the second stage is attributed to combustion of char. TGA results on cellulose show the presence of small amounts of moisture in the material under both inert and oxidative conditions. The DSC results of cellulose show endothermic behavior in inert conditions (see DSC curve for N_2 case in Fig. 1) and exothermic behavior in oxidative conditions (see DSC curve

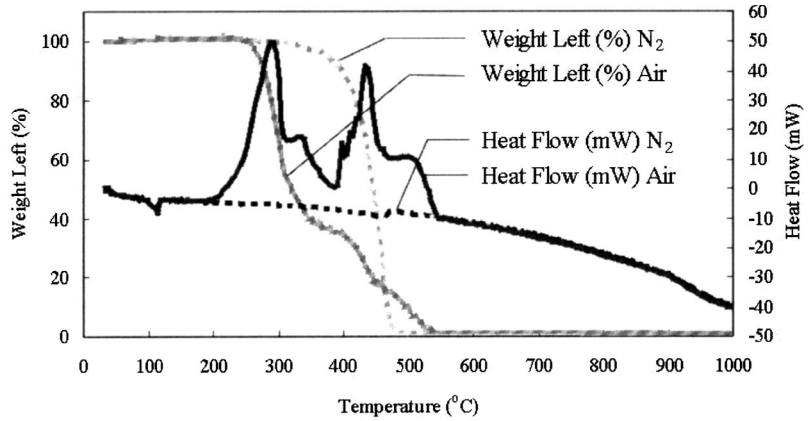

Fig. 2 Decomposition polyethylene

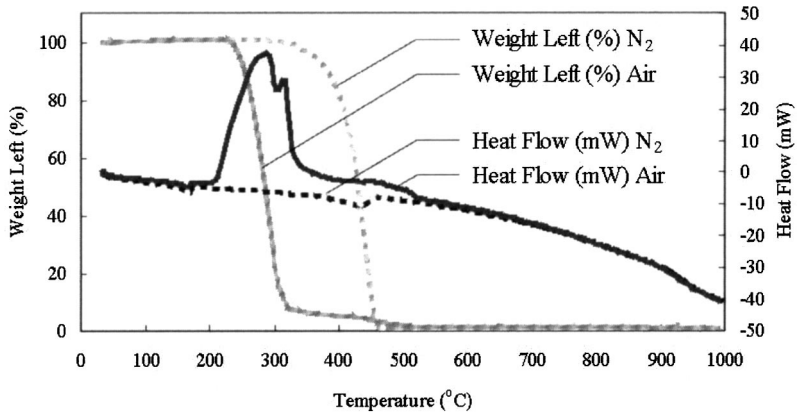

Fig. 3 Decomposition of polypropylene

for air case in Fig. 1). In addition the DSC results under oxidative condition suggest that the decomposition occurs in a multistage. They also show that the amount of thermal energy required destructing the material in most cases less is than 5% of the energy evolved from the material. The temperature of half decomposition is the temperature at which weight loss is 50%. The results for polyvinyl chloride, the initial decomposition of compound in N_2 is due to the detachment of chlorine from the compound at 290°C (first part of the decomposition) while the decomposition of the remaining compound has a half decomposition temperature of 451°C. In the case of decomposition in air the weight loss occurs in almost two stages with first part being the detachment of chlorine from the compound and the second part being from the thermal decomposition of remaining compound. Due to the widely different behavior of polyvinyl chloride, the half decomposition temperature is taken at 50% weight loss point for the two respective slopes.

The TGA results on polyethylene and polypropylene show that they have small amount of impurities in them (see TGA curves in Figs. 2 and 3). The destruction under oxidative conditions begins to occur at lower temperatures as compared to inert conditions. However, complete destruction of these compounds is at higher temperatures under oxidative conditions than inert conditions. This may be due to the inability of the surrounding gas composition to inhibit transportation of heat to the material under oxidative conditions. The DSC results on polyethylene and polypropylene show that at first they undergo fusion prior to decomposition. However, in inert conditions they show endothermic behavior while in oxidative condition they show an exothermic behavior (see DSC curves in Figs. 2 and 3). The TGA results for polystyrene show no evidence of any impurities in the material. At high heating rate under oxidative condition the thermal decomposition does not follow the usual smooth decay (see the TGA curves in Fig. 4). The DSC results suggest that polystyrene does not undergo melting prior to its decomposition and that in inert conditions the results suggest decomposition in a single stage with endothermic heat of pyrolysis (see DSC curves in Fig. 4). Therefore, in oxidative conditions the decomposition behavior varies between lower heating rate and higher heating rate. At lower heating rate it has large amount of exothermic heat of pyrolysis. The amount of energy required for material decomposition is highest among the materials examined and also relative to the heat evolved.

Cellulose contained approximately 2% moisture and approximately 2–3% fixed carbon by weight. At the end of the TGA tests, in excess of 98% weight loss was achieved. Initially cellulose has no fixed carbon. The change of carbon to fixed carbon depends on decomposition condition. Some of the carbons in cellulose undergo structural change to form fixed carbon during decomposition. The remaining residue represents mainly the impurities present in the original sample. In contrast for polyethylene, polypropylene, and polystyrene almost complete weight loss was achieved at the end of the TGA tests. For polyvinyl chloride under oxidative condition almost complete weight loss was achieved at the end the TGA tests (1000°C) while only about 95% weight loss was achieved under inert condition, see Fig. 5.

All samples, besides the polyvinyl chloride, examined here show that under oxidative conditions the samples decompose in a single stage except for the initial drying process at the beginning

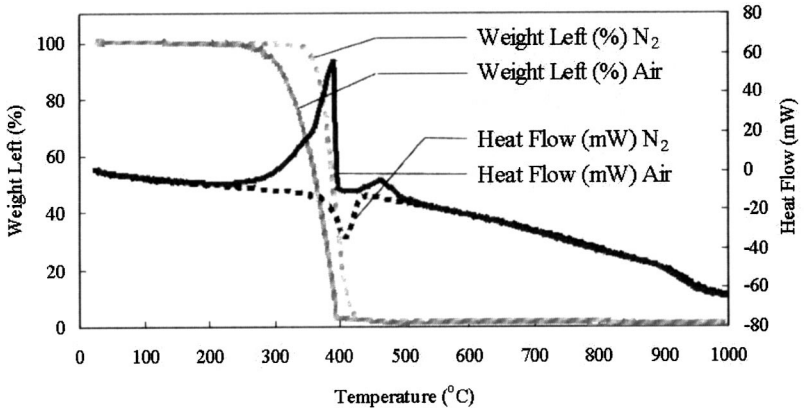

Fig. 4 Decomposition of polystyrene

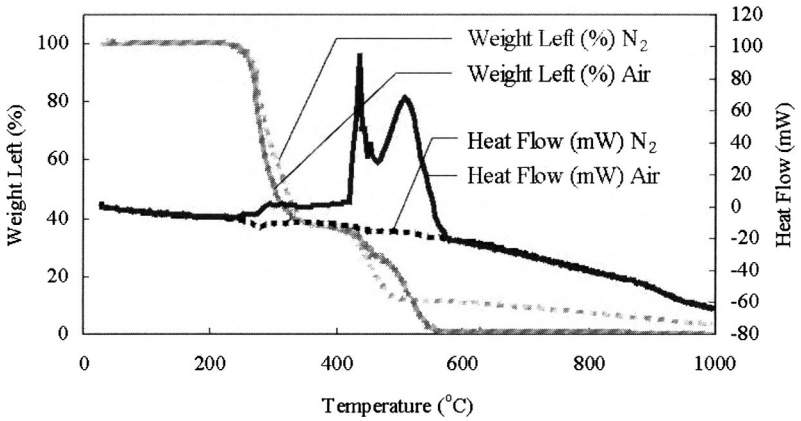

Fig. 5 Decomposition of polyvinyl chloride

of the test (up to about 110°C for cellulose). The subsequent weight loss in TGA curve for cellulose is due to the volatiles release during the pyrolysis. The two-stage destruction for polyvinyl chloride shown in Fig. 5 reveals the initial detachment of chlorine followed by destruction of the remaining carbon chain compound.

The use of TGA was made in order to obtain information on the overall kinetics of the decomposition for the surrogate waste materials. The decomposition behavior for the cellulose is shown in Fig. 1 while for the polypropylene and polystyrene it is shown in Figs. 3 and 4, respectively. These results provide the function $\ln(-\ln(1-\alpha))$ versus $1/T$ from which the Arrhenius parameters A (pre-exponential factor) and E (activation energy) can be evaluated from the graphically determined slope and intercept of the function $\ln(-\ln(1-\alpha))$ versus $1/T$. The results of $\ln(-\ln(1-\alpha))$ versus $1/T$ are shown in Fig. 6. The calculated results for $\mathrm{Ln}(A)$, E and temperature at which 50% of material is decomposed (called half decomposition temperature) are given in Tables 1–5. The half decomposition temperature is therefore the temperature at which half of the material weight loss occurs as inferred from the TGA results. In Table 5 it is to be noted that polyvinyl chloride possess a two staged reaction; first reaction process reveals detachment of chlorine from the compound while and second stage reaction suggests decomposition of main carbon chain. The amount of weight loss shows this to be the case since the amount of weight loss for the first stage is approximately equal to the weight of hydrochloric acid. Therefore, Table 5 has two sets of values for each condition. The upper five rows are for the detachment of chlorine while the bottom five rows are for the decomposition of remaining chain. The results for cellulose and polystyrene show that the activation energy E decreases with increase of temperature (heat ramp rate). However, for polypropylene under inert conditions the results show an increase of activation energy E with an increase of heat ramp rate. The thermal decomposition temperature increases with increase in the ramp rate. In any case the amount of heat of pyrolysis is relatively large under oxidative

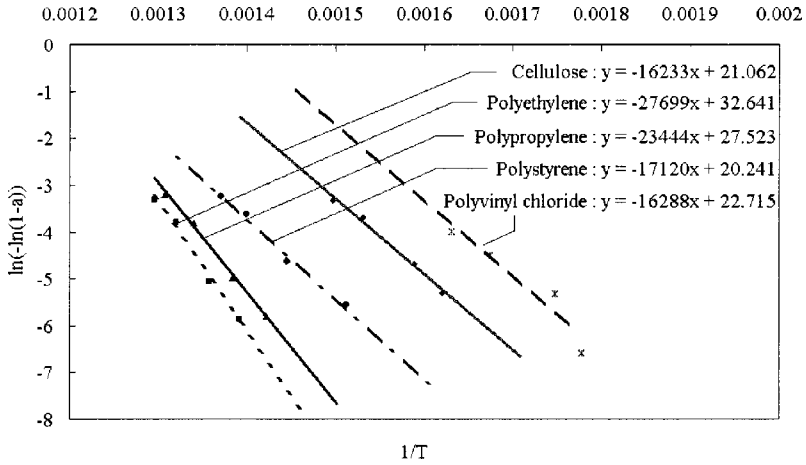

Fig. 6 Plot of $\ln(-\ln(1-\alpha))$ versus $1/T$

Table 1 Arrhenius parameters and maximum decomposition temperature for cellulose in nitrogen and air

	Heating Rate (°C/min)	Sample Weight (mg)	E (kJ/mole)	$\ln(A)$	Half Decomposition Temperature (°C)
Nitrogen	5	5.080	317	54.0	344
Nitrogen	10	5.657	322	54.2	357
Nitrogen	30	6.367	270	43.6	380
Nitrogen	50	6.122	246	38.5	395
Air	5	5.277	277	47.6	325

Table 2 Arrhenius parameter and maximum decomposition temperature for polyethylene in nitrogen and air

	Heating Rate (°C/min)	Sample Weight (mg)	E (kJ/mole)	ln(A)	Half Decomposition Temperature (°C)
Nitrogen	5	5.434	203	25.2	446
Nitrogen	10	6.407	236	30.6	464
Nitrogen	30	4.922	284	38.5	484
Nitrogen	50	5.027	326	44.8	499
Air	5	5.118	181	29.7	298

condition as compared to the inert condition. The temperature dependence of heat of pyrolysis depends on the material properties. Furthermore, for all the materials besides polystyrene, the amount of heat flow into the material to decompose the material is very small as compared to the heat evolved. Typically only about 5% of the energy contained in a material is required to decompose the material. This is important since one can decompose the waste into gas stream and then burn the gas in an environmentally benign form. Results for the heat of pyrolysis (obtained from Eqs. (10) and (11)), beginning of pyrolysis temperature and temperature for maximum decomposition rate are given in Tables 6–10. The heat of pyrolysis depends on the differences in the chemical structure of the material. The weight loss due to the volatiles released during pyrolysis exhibits itself as endothermic, which goes though a well-defined minimum. They correspond to the respective volatile loss that evolves from the materials (cellulose, polyethylene, polypropylene, polystyrene, or polyvinyl chloride). The temperature of maximum decomposition can be seen by comparing the results obtained from TGA with DSC results, see Figs. 1–5. The rate-controlling step (reaction rate) in pyrolysis depends upon temperature, composition of the material and its physical size. The products yield, composition and their calorific value are highly dependent upon the material composition, heating rate, surrounding chemical environment in which the destruction process takes place, and ultimate temperature of the material.

The information presented here allows one to determine how much heat is required (or can be obtained) during the thermal decomposition of wastes. In the experiments, where the atmosphere was maintained inert throughout, no further weight loss was observed as seen by the constant DSC data.

Conclusions

The results provided here show that thermogravimetry and differential scanning calorimetry analysis provide insightful information on the thermal decomposition characteristics of different surrogate materials in well-controlled thermal and chemical environment. The temperature dependence weight loss character-

Table 3 Arrhenius parameters and maximum decomposition temperature for polypropylene in nitrogen and air

	Heating Rate (°C/min)	Sample Weight (mg)	E (kJ/mole)	ln(A)	Half Decomposition Temperature (°C)
Nitrogen	5	5.369	205	26.4	430
Nitrogen	10	5.2022	247	33.3	449
Nitrogen	30	5.429	276	37.9	473
Nitrogen	50	5.248	317	43.8	491
Air	5	5.189	127	18.8	281

Table 4 Arrhenius parameter and maximum decomposition temperature for polystyrene in nitrogen and air

	Heating Rate (°C/min)	Sample Weight (mg)	E (kJ/mole)	ln(A)	Half Decomposition Temperature (°C)
Nitrogen	5	5.662	240	35.3	388
Nitrogen	10	5.525	333	50.4	420
Nitrogen	30	5.194	329	49.0	442
Nitrogen	50	5.744	317	46.2	457
Air	5	5.419	110	11.7	362

Table 5 Arrhenius parameter and maximum decomposition temperature for polyvinyl chloride in nitrogen and air

	Heating Rate (°C/min)	Sample Weight (mg)	E (kJ/mole)	ln(A)	Half Decomposition Temperature (°C)
		Detachment of chlorine (first peak in TGA)			
Nitrogen	5	5.506	94	11.1	290
Nitrogen	10	5.416	166	27.2	299
Nitrogen	30	5.803	126	18.2	324
Nitrogen	50	5.479	135	19.9	340
Air	5	5.357	180	30.8	279
		Decomposition of remaining compound (second peak in TGA)			
Nitrogen	5		213	26.7	451
Nitrogen	10		205	25.3	465
Nitrogen	30		197	24.3	483
Nitrogen	50		194	23.7	498
Air	5		152	14.6	501

Table 6 Influence of heating rate on heat of pyrolysis and maximum decomposition temperature for cellulose decomposition in nitrogen

Heating Rate (°C/min)	Heat of Pyrolysis (J/g)	Beginning of Pyrolysis Temperature (°C)	Temperature for Maximum Decomposition Rate (°C)
5	584	314	345
10	566	337	360
30	508	350	383
50	495	362	396

istics of materials can be obtained from the thermogravimetry analysis. This information provided the desired Arrhenius kinetic parameters and therefore the decomposition rates under defined conditions of temperature, surrounding chemical environment, heating rate, and material chemical composition. The differential scanning calorimetry provides information on the amount of energy needed to thermally destruct the solid waste and the amount of energy evolved during subsequent combustion of the gaseous byproducts. The amount of energy required to destruct the material is only a very small fraction of the energy contained in the material. The kinetics parameters have been determined for cellulose, polystyrene, polyethylene, polypropylene, and polyvinyl chloride. This information assists one to understand the basic thermal decomposition of the surrogate materials from which information on the real waste materials can be determined under characteristic operating conditions. It also helps one to mix different components in the wastes in better proportions to achieve efficient destruction.

The kinetic parameters of thermal decomposition were determined for the different samples as a function of the heating rates. The heating rate, surrounding environment, material composition, and temperature affects the thermal decomposition of materials. The rate-controlling step (reaction rate) in pyrolysis is the material and its physical size and ratio between the sample material and the surrounding chemical gas. The amount of energy required to ther-

Table 7 Influence of heating rate on heat of pyrolysis and maximum decomposition temperature for polyethylene decomposition in nitrogen

Heating Rate (°C/min)	Heat of Pyrolysis (J/g)	Beginning of Pyrolysis Temperature (°C)	Temperature for Maximum Decomposition Rate (°C)
5	254	332	455
10	354	417	470
30	358	424	491
50	351	448	500

Table 8 Influence of heating rate on heat of pyrolysis and maximum decomposition temperature for polypropylene decomposition in nitrogen

Heating Rate (°C/min)	Heat of Pyrolysis (J/g)	Beginning of Pyrolysis Temperature (°C)	Temperature for Maximum Decomposition Rate (°C)
5	423	340	439
10	452	350	458
30	469	361	483
50	911	369	496

Table 9 Influence of heating rate on heat of pyrolysis and maximum decomposition temperature for polystyrene decomposition in nitrogen

Heating Rate (°C/min)	Heat of Pyrolysis (J/g)	Beginning of Pyrolysis Temperature (°C)	Temperature for Maximum Decomposition Rate (°C)
5	1,499	362	412
10	1,491	373	424
30	1,430	395	451
50	1,392	405	466

Table 10 Influence of heating rate on heat of pyrolysis and maximum decomposition temperature for polyvinyl chloride decomposition in nitrogen

Heating Rate (°C/min)	Heat of Pyrolysis (J/g)	Beginning of Pyrolysis Temperature (°C)	Temperature for Maximum Decomposition Rate (°C)
5	757	232	281
10	736	232	298
30	695	253	321
50	727	259	335

mally destruct the material is very small as compared to the amount of energy evolved from the waste materials.

The information presented here helps to characterize and understand the thermal decomposition characteristics of waste materials. The information also assists in identifying materials of similar or different characteristics and also for the design and development of advanced thermal destruction systems.

Acknowledgments

This work was supported by the Japan Science and Technology Corporation (JST) and is gratefully acknowledged. JST also provided support to one of the authors (Daisuke Jinno) during his stay at the University of Maryland where this research was conducted. The support provided by the University of Maryland is gratefully acknowledged

References

[1] Gupta, A. K., Ilanchezhian, E., and Keating, E. L., 1996, ''Thermal Destruction Behavior of Plastic and Non-Plastic Wastes in a Laboratory Scale Facility,'' ASME J. Energy Resour. Technol., **118**, pp. 269–276.

[2] Oppelt, O. C., 1993, ''Hazardous Waste Critical Review,'' Air Waste **43**(Jan.), pp. 25–73.

[3] Gupta, A. K., Ilanchezian, E., and Keating, E. L., 1994, ''Thermal Destruction Behavior of Plastics,'' *Proc. ASME Computers and Information in Engineering (CIE) Conference*, Minneapolis, MN, Sept. 11–14, ASME, New York, pp. 25–73.

[4] Allen, D. T., and Behmanesh, N., 1992, ''Non-hazardous Waste Generation,'' Hazard. Waste Hazard. Mater., **9**(1), pp. 91–96.

[5] McMurry, J., 1992, *Organic Chemistry*, 3rd Ed., Brooks/Cole (Publishers), Stanford, CA; also Japanese translation version, Tokyo Kagaku Dojin Ltd, Tokyo, Japan, 1992, p. 1230.

[6] WHO Consultation, 1998, ''Assessment of the Health Risk of Dioxins: Re-evaluation of the Tolerable Daily Intake (TDI),'' May, Geneva, Switzerland, pp. 25–29, See details from the electronic link at: http://www.who.int/pcs/docs/dioxin-exec-sum/exe-sum-final.html.

[7] EPA Report, 1997, ''Special Report on Environmental Endocrine Disruption: an Effects Assessment and Analysis,'' EPA/630/R-96/012, Feb., see details from the electronic link at: http://www.epa.gov/ORD/WebPubs/endocrine/endocrine.pdf.

[8] Chopra, H., 1993, ''High Temperature Controlled Destruction of Surrogate Solid Wastes,'' M.S. thesis, Department of Mechanical Engineering, University of Maryland.

[9] Chopra, H., Gupta, A. K., Keating, E. L., and White, E. B., 1992, ''Thermal Destruction of Solid Wastes,'' *Proc. 27th Intersociety Energy Conversion Engineering Conference* (IECEC), **1**, pp. 377–381.

[10] Domalski, E. S., Jobe, T. L., and Miline, T. A., 1987, *Thermodynamic Data for Biomass Materials and Waste Components*, ASME, New York.

[11] Gupta, A. K., and Lilley, D. G., 2003, ''Thermal Destruction of Wastes and Plastics,'' *Plastics and the Environment*, John Wiley and Sons, New York, pp. 629–696.

[12] Tillman, D. A., 1991, *The Combustion of Solid Fuels and Wastes*, Academic Press, San Diego, CA.

[13] Raman, P., Walawender, W. P., Fan, L. T., and Howell, J. A., 1981, ''Thermogravimetric Analysis of Biomass: Devolatilization Studies on Feedlot Manure,'' Indust. Eng. Chem. Proc., American Chemical Society, **20**(4), pp. 630–636.

[14] Williams, P. T., and Besler, S., 1992, ''The Pyrolysis of Municipal Solid Waste,'' J. Inst. Energy, pp. 192–200.

[15] Hatakeyama, H., Hirose, S., Nakamura, K., and Hatakeyama, T., 1993, *Cellulosics: Chemical, Biochemical and Material Aspects*, Ellis Horwood, Chicester, UK, p. 281.

[16] Tanaka, H., 1992, ''The Kinetic Analysis of Inorganic Solid-state Reactions,'' Netsu Sokutei, **19**(1), Tokyo, Japan, pp. 32–39.

[17] Symanski, H., 1960, ''A Technique for Pyrolyzing or Vaporizing Samples for Gas Chromatographic Analysis,'' Nature (London), **188**(4748), pp. 403–404.

[18] Simon, W., and Giacabbo, H., 1965, *Chemie Ingenieur Technik*, Wiley-VCH, Berlin, Germany, **37**, pp. 709–718.

[19] Simon, W., Kriemler, P., Voellmin, J. A., and Steiner, H., 1967, J. Gas Chromatography, **5**, pp. 77–81.

[20] Gupta, A. K., and Muller, P., 1999, ''Pyrolysis of Paper and Cardboard in Inert and Oxidative Environments,'' J. Propul. Power, **15**(2), March–April, pp. 187–194.

[21] Agrawal, R. K., 1987, ''Compositional Analysis by Thermogravimetry,'' American Society for Testing and Materials, ASTM-STP997, Symposium on Compositional Analysis by Thermogravimetry, Philadelphia, PA, March 16–17.

[22] Boateng, A. A., Walawender, W. P., and Fan, L. T., 1990, *Biomass for Energy and Industry*, Elsevier Applied Science, London, UK.

[23] Gupta, A. K., 2000, ''Thermal Destruction of Cellulose and Surrogate Solid Wastes,'' J. Propul. Power, **16**(4), July–August, pp. 615–622.

[24] Missoum, A., Gupta, A. K., and Chen, J., 1997, ''Global Kinetics of the Thermal Decomposition of Waste Materials,'' Proc. 1997 ASME Computers and Information in Engineering (CIE) Conference, Sept. 14–17, Paper No. DETC 97/CIE-4433.

[25] Jain, A. K., Sharma, S. K., and Singh, D., 1996, ''Reaction Kinetics of Paddy Husk Thermal Decomposition,'' IECEC Conference, Washington, DC, Aug. 11–16, Paper No. 96486.

Application of Genetic Algorithms in the Engine Technology Selection Process

Bryce Roth

Chirag Patel

School of Aerospace Engineering,
Georgia Institute of Technology,
Atlanta, GA 30332-0150

The objective of this paper is to demonstrate the application of genetic algorithms to the engine technology selection process. The "technology identification, evaluation, and selection" method is discussed in conjunction with genetic algorithm optimization as a technique to quickly evaluate the impact of various technologies and select the subset with the highest potential payoff. Techniques used to model various aspects of engine technologies are described, with emphasis on technology constraints and their impact on the combinatorial optimization of technologies. Challenges include objective function formulation and development of models to deal with incompatibilities among different technologies. Typical results are presented for an 80-technology optimization using various visualization techniques to assist in easy interpretation of genetic algorithm results. Finally, several ideas for future development of these methods are briefly explored.
[DOI: 10.1115/1.1772404]

Introduction

The process of selecting technologies for implementation into new engine designs is a challenging exercise in multi-objective combinatorial optimization. Engine technology selection is a rather difficult class of problem to solve for several reasons. First, the technologies are always selected on the basis of their impact on a variety of objectives rather than a single objective. Hence the technology solution is always a compromise between conflicting objectives. Second, the *curse of dimensionality* (i.e., the geometric increase of solution space with each additional option) makes an exhaustive combinatorial search impractical for problems involving more than 20–30 technology options. Third, technologies can interact with each other and with the system in a variety of complex ways, all of which must be accounted for in the technology evaluation model if the results are to be useful.

Fortunately, research has shown that genetic algorithm optimization, combined with "technology identification, evaluation, and selection" (TIES) methods are ideally suited for this type of technology combinatorial optimization problem. TIES provides the framework for creation of a generic model to evaluate the impact of technologies in terms of system level figures of merit (FoMs). A genetic algorithm is then wrapped around this model to find and evaluate the best possible set of technology combinations. This paper gives a brief overview of the TIES method with emphasis on how technology constraints impact the solution space. The preferred genetic algorithm implementation is discussed and applied to a typical engine technology selection problem involving 80 engine technologies. Finally, several avenues for improving the usefulness of this method are discussed.

Technology Identification, Evaluation, and Selection Method

TIES is a comprehensive and structured method intended to assist designers in the technology selection process by enabling rapid and accurate evaluation of technologies applied in complex engineering systems. The general technology evaluation method is applicable to any complex system, and much of the basic theory is described extensively by Kirby and Mavris [1–3]. TIES has proven to be exceptionally adept at evaluating the impact of engine technologies, the details of which were described extensively by Roth, German, and Mavris [4]. As the literature describing the fundamental theory of TIES is already extensive, this paper will only present a brief overview sufficient to give the reader an understanding of the basic concepts. Further details are available in the previously cited references.

The fundamental premise of the TIES method lies in the idea that the system-level impact of most technologies can be quantified in terms of changes in a few key parameters known as technology metrics (or K factors). If the most important K factors for a given system can be identified and functionally related to the overall system performance, then one can obtain a fast and accurate estimate on the impact of a given technology by simply quantifying the impact of technology in terms of changes in the K factors. The chief advantage of quantifying the technology in terms of metrics is that once the relationships between the technology metrics and the system level FoMs has been created, the impact of any technology can be easily and quickly evaluated *without the need to create an explicit model of a specific technology*.

The heart of the TIES method is the technology impact forecasting (TIF) environment. TIF is the model used to relate K factors to system performance. For instance, a TIF for a turbofan engine analysis might have the form

design range=f(ΔOPR, ΔT41, . . . , ΔEng Wt, ΔFan η, . . .),

6 K nmi fuel burn=f(ΔOPR, ΔT41, . . . , ΔEng Wt, ΔFan η, . . .),

etc.

In this case, the K factors are change in overall cycle pressure ratio (ΔOPR), change in turbine inlet temperature (ΔT41), change in engine weight (ΔEng Wt), change in fan efficiency (ΔFan η), etc. These deltas are the key measures of technology capability that impact the respective system-level (i.e., aircraft) performance. The performance FoMs in this example are aircraft design range and fuel burn for a 6000 nmi mission. Note that it is presumed that all deltas are measured relative to a prescribed baseline engine and aircraft combination.

Technology Impact Matrix. Once a TIF environment is created, any number of technologies can be evaluated by simply quantifying how each changes the K factors. In effect, the entire technology impact is compressed into a single vector of K factors. The technology vectors for an arbitrary set of "*n*" technologies

Contributed by the International Gas Turbine Institute (IGTI) of THE AMERICAN SOCIETY OF MECHANICAL ENGINEERS for publication in the ASME JOURNAL OF ENGINEERING FOR GAS TURBINES AND POWER. Paper presented at the International Gas Turbine and Aeroengine Congress and Exhibition, Atlanta, GA, June 16–19, 2003, Paper No. 2003-GT-38482. Manuscript received by IGTI, Oct. 2002, final revision, Mar. 2003. Associate Editor: H. R. Simmons.

Table 1 Technology impact matrix

Tech. #	k- factors			
	1	2	3	4
1	7	2.71	0.72	0.75
2	9	0	-0.02	0.6
3	5	0	0	0.3
4	1	1.06	0	0.95
5	6	0.22	0	0.25

can be assembled into an n by k matrix, where k is the number of K factors and n represents the number of technologies. This is known as a technology impact matrix (TIM), an example of which is shown in Table 1. Each row in Table 1 contains the impact vector for a single technology while each column corresponds to a single K factor. These technology benefits and penalties are usually established via expert questionnaire, physics based modeling, or literature reviews.

TIF Formulation via Response Surface. The TIF environment can be manifested in a variety of forms ranging from an amalgamation of linked codes to a simple series of response surface equations. The key requirement is that the TIF functionally relate K factors to system performance FoMs. However, for problems involving many technologies (more than 15–20), it becomes increasingly imperative to have a compact and computationally inexpensive TIF formulation.

This can be achieved by creating a metamodel representation for the performance FoMs as a function of the K factors. Response surface equations (RSEs) are commonly used for this purpose and yield accurate results for most problems. The RSEs are created by running a series of cases on a sophisticated code (or linked series of codes) and analyzing the data to obtain a best fit regression equation. The upper and lower bounds on the regression equation can be obtained directly from the TIM itself. The sum of the benefits for each column in the TIM gives an upper bound to K factors, while the sum of the degradations yields a lower bound. This ensures that the metamodel ranges are defined such that the technologies cannot violate the RSE bounds.

Simple (Boolean) Technology Interactions. There are a variety of technology interactions that can exist between the technologies, with the specific nature of these interactions typically being problem-dependent. The most common technology interdependencies encountered are Boolean relationships as shown in Fig. 1. The simplest and most likely relationship between two technologies is for them to be completely independent of each other. Next is the one way enabling where the first technology is a prerequisite for the use of the other. Two additional possibilities are mutually inclusive and mutually exclusive (incompatible) technology pairs.

Technology incompatibilities can be captured in a compatibility matrix. Since incompatibilities between pairs of technologies are symmetric, all possible incompatibility pairs in a set of n technologies can be captured entirely in the super diagonal elements of the $n \times n$ compatibility matrix:

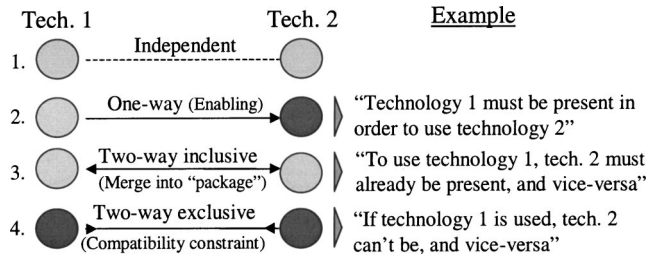

Fig. 1 Logical constraints on technologies (from Ref. [4])

Table 2 Typical technology constraint matrix

	T1	T2	T3	T4	T5	. . .
T1	0	1	0	-1	0	
T2	0	0	0	0	0	
T3	-1	0	0	0	1	
T4	0	0	0	0	0	
T5	0	0	0	0	0	
⋮						⋱

$$C = \begin{bmatrix} - & c_{12} & c_{13} & \cdots & c_{1n} \\ - & - & c_{23} & & \\ \vdots & & - & \cdot & \vdots \\ & & & - & c_{n-1,n} \\ - & & \cdots & - & - \end{bmatrix}. \quad (1)$$

Enabling relationships are asymmetric and must therefore be captured using the entire $n \times n$ matrix (excluding the diagonal elements):

$$E = \begin{bmatrix} - & e_{12} & e_{13} & \cdots & e_{1n} \\ e_{21} & - & e_{23} & & \\ e_{31} & e_{32} & - & \cdot & \vdots \\ \vdots & & & - & e_{n-1,n} \\ e_{n1} & & \cdots & e_{n,n-1} & - \end{bmatrix}. \quad (2)$$

Two-way inclusive technology relationships need not be captured in a matrix, and are instead modeled by merging the technologies into a single "package" that is either "on" or "off."

A simplification of the constraint model embodied in Eqs. (1) and (2) can be obtained by noting that a given pair of technologies cannot be simultaneously enabling *and* incompatible. Therefore, the compatibility and enabling matrices are guaranteed not to have overlapping elements and can be merged together into a single constraint matrix. Different symbols can then be used to denote whether a pair of technologies have compatibility, enabling, or no relationship. This single constraint matrix approach has an additional benefit in that it eliminates the possibility of accidentally making a pair technologies simultaneously enabling and incompatible.

A typical constraint matrix used for modeling technology interactions in TIES environment is shown in Table 2. The constraint matrix is always an n by n matrix where "n" is number of technologies. A common scheme is to denote independent technologies by "0," mutually exclusive (incompatible) technologies by "1" and mutually inclusive (enabling) technologies by "−1."

The matrix exemplified in Table 2 embodies a generalized set of constraints imposed on the basic combinatorial selection problem. If the matrix of Table 2 is empty (that is, it is the zeros matrix), then the technology combinatorial optimization is completely unconstrained. In this case, there will be 2^n permissible technology combinations. As compatibility and enabling relationships are added to the constraint matrix, the number of permissible technology combinations is reduced considerably. This, in principle, leads to a simplification of the general combinatorial optimization process. In practice, this simplification is tangible only in extreme cases where there are so many constraints as to reduce the number of permissible combinations to a number that can be exhaustively evaluated. For those cases where there are an intermediate number of constraints, the benefit in reduction of permissible combinations is counteracted by the fragmentation of the permissible objective space.

To understand this point, consider the combinatorial space as if it were a grid of possible technology combinations wherein each technology combination can be mapped to a unique coordinate in this grid. If each technology's state is characterized by a 0 ("off")

Fig. 2 Technology combinatorial space

or 1 (''on'') then each coordinate in the grid is uniquely mapped to a bit string representing the collective technology macro-state of the system. If there are only a few constraints on the combinatorial space, one can go from any initial point in the grid to any final point by simple succession of bit flips. Further, the successions of intermediate steps are likely to be admissible technology combinations. This is not so if many constraints are present because the constraints act to fragment the combinatorial space. Consequently, it is not possible to go from any point in technology space to any other through simple bit flips without violating constraints at some intermediate step. Instead, multiple, simultaneous bit flips will likely be needed to navigate the combinatorial space without violating constraints. This in turn complicates the search process.

A visually intuitive analogy to this phenomenon is given in Fig. 2. Imagine that the grids shown in this figure correspond to the grid of possible technology combinations mentioned previously. Further imagine that each black square represents an inadmissible technology combination. Starting with a sparse constraint density on the far left, the combinatorial space becomes increasingly fragmented with the addition of each new constraint. At 30% density, large portions of the state space have already been partitioned apart by the black dots. At 70% density, the combinatorial space has so many constraints that it becomes dominated not by admissible combinations but by inadmissible combinations. Somewhere near 50% constraint density is a ''phase transition'' point that is the bounding point between the two extremes (Kauffman [5]). Beyond the phase transition point, the combinatorial problem becomes less a search *of* admissible combinations and more a search *for* admissible combinations.

Non-Simple Technology Interactions. In addition to the simple technology interactions previously described, a variety of more complex interactions can and do arise. A common example is a three way interaction involving Boolean relationships among three technologies. This is illustrated in Fig. 3 for three imaginary technologies. If the technologies are independent, there are eight admissible combinations. However, if technology 1 enables 2, 2 enables 3, but 3 is incompatible with 1, then the resultant number of admissible combinations is reduced to three. In general, it is not easy to precisely count the number of admissible combinations. One can readily devise even more complex scenarios involving more than three technologies. This is a significant factor that complicates the constrained optimization of technology combinations. It is quite likely that some simplification of the constraint matrix could be secured through application of suitable methods, particularly those developed in the electronics industry (Karnaugh reduction maps, for instance), and this is an area for future investigation.

Non-Boolean interactions can also arise. It sometimes happens that one technology may have a reinforcing or degrading impact on another. For instance, the increase in turbine inlet temperature obtainable through application of new blade materials and new coatings may not be equal to the sum of the increases enabled by each technology individually. Such interactions are not modeled in the present formulation due to the complexity of doing so relative to the expected improvement in accuracy that might be obtained.

One likely approach to modeling this type of interaction would be to create a ''technology impact interaction matrix'' of size n by n by k where k is the number of K factors used in the TIES formulation. Each k index would contain the K factor corrections necessary to account for the impact of the first index on the second. The effort required to create and validate an n by n matrix is significant. Needless to say that the effort required to create an error-free n by n by k matrix is substantially greater. The probability of manually assembling such a matrix without making a mistake is disparagingly low. This approach will be much more practical when an algorithmic (automated) means of evaluating technology interactions becomes available.

Counting Technology States. The number and location of combinatorial constraints in the constraint matrix affects the complexity of the combinatorial selection problem. It is therefore of interest to examine in detail how the number of admissible combinations varies as a function of the number of technologies, along with the number (and placement) of the constraints. The minimum number of incompatibilities we can have in a system is zero and the number of permissible technology combinations corresponding to zero incompatibilities will be 2^n where n is the number of

Interaction Scenario	*Admissible Combinations*	*No. of States*	*Net Impact*
T1 (T2 T3)	All	8	None
T1 C C T2 C T3	000	1	All Technologies Deleted
T1 E E T2 E T3	111	1	All Technologies Merged
T1 E C T2 E T3	000 100 110	3	Technology No. 3 Deleted
T1 E C T2 C T3	000 100 110 001	4	Non-simple
T1 E E T2 C T3	000 100 110 101	4	Non-simple

Fig. 3 Three-way Boolean technology interactions

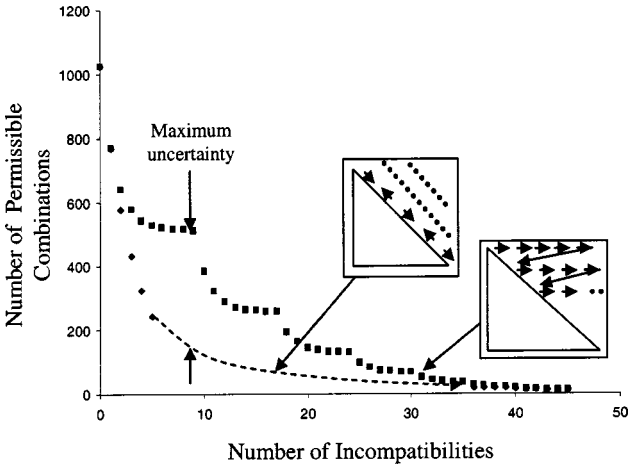

Fig. 4 Variation of permissible technology combinations with incompatibilities

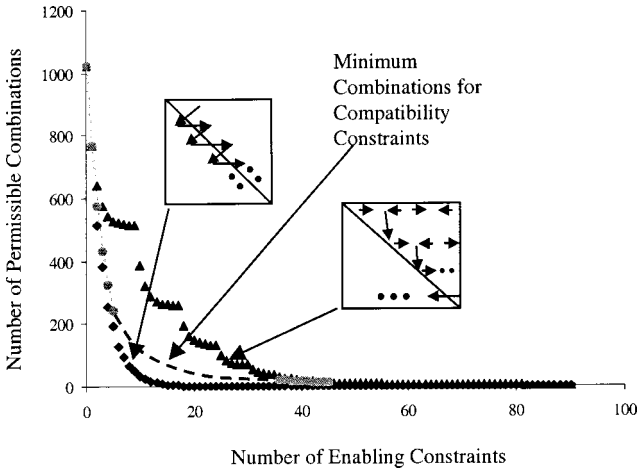

Fig. 5 Variation of permissible technology combinations with enabling constraints

technologies. The maximum number of incompatibilities possible is the combination of ''n'' items taken two at a time:

$$C_2^n = \frac{n}{2}(n-1). \tag{3}$$

This occurs when the super-diagonal matrix elements are fully populated. In this situation, only one technology can be used at a time. When this is the case, the number of technology options available is $n+1$ (n technologies are used one at a time plus the trivial case where no technologies are used). For any number of incompatibilities between 1 and C_2^n, the number of possible technology combinations not only depends on the number of incompatibilities but also on their relative position in the technology interaction matrix.

Figure 4 is a plot of the number of compatibility constraints versus the number of permissible technology combinations for a small combinatorial problem having only ten technologies. The bottom line corresponds to minimum possible number of admissible combinations while the upper line corresponds to the maximum possible number of combinations. Note that the upper line has the shape of an exponentially decaying series of exponential decays. Each small-scale section of the curve corresponds to an increasing number of constraints applied in the compatibility matrix according to the pattern indicated in the figure. The lower line is created by filling in alternating diagonal elements, starting with the largest super-diagonal and moving to the upper right corner.

As one might expect, the two curves converge at the extreme cases, these being the unconstrained and fully constrained cases. At intermediate constraint densities, there is a considerable difference between the upper and lower curves, with a maximum difference occurring when there are ten constraints present. Various arrangements of 10 compatibility constraints could yield systems with between 550 and 150 admissible technology combinations. One could think of this as being a point of maximal ''information entropy'' regarding the nature of the system, and systems with constraint densities in this range will generally be more difficult to optimize (Roth, Ender, and Mavris [6]).

Similar results are obtained when considering enabling technologies. The minimum number of enabling constraints is zero and the maximum is given by the permutation of n things taken two at a time:

$$P_2^n = n(n-1). \tag{4}$$

When there are no enabling constraints, the number of permissible technology combinations is 2^n. When the constraint matrix is fully populated by enabling constraints, the number of permissible technology combinations is 2 (either all or no technologies are selected). Figure 5 shows the variation of number of admissible states versus number of enabling constraints for the 10-technology example discussed previously. The upper curve is identical to that of Fig. 4 up to the 45th enabling constraint. Since enabling constraints are asymmetric, both the upper and lower portions of the matrix are populated, with the last 45 enabling constraints contributing little to the change in admissible states. The lower limit on enabling constraints is considerably less than that for compatibility constraints.

When incompatibilities and enabling relationships are simultaneously present, there are a variety of complex interactions among technologies that can arise. This makes it difficult to explicitly count the number of admissible technologies, let alone optimize the solution set. Fortunately, genetic algorithms are well suited to combinatorial optimization of technologies in the presence of large numbers of constraints.

Engine Technology Selection via Genetic Algorithm

Genetic algorithms (GAs) are a powerful means for global optimization of almost any function. They have been a topic of extensive research ([7–9]). Briefly, GAs work by creating an initially random pool of technology combinations and evaluating them in the technology impact model to yield estimates of how each technology combination impacts the performance of the whole system. These combinations are then compared to one another and the best combinations are kept in the pool and remaining are discarded. These best combinations are then used as parents to generate the next generation of population. This process is repeated for many generations until the population converges to a global optimum. The evolutionary bias imposed on the population ensures that the population set is driven towards the best technology combinations.

It happens that GAs, used in conjunction with the TIES formulation described previously, are well suited to solving the constrained combinatorial engine technology selection problem. The preferred approach (described in Ref. [4]) is to use a simple tournament-style genetic algorithm wherein each technology is assigned a bit in the GA bit string ''chromosome.'' The initial population is randomly selected with 50% probability of having a technology ''on'' in a given population member. Crossover is performed by splicing the genomes of two parents together at a randomly selected point, and mutation consists of a random bit flip occurring with specified probability of occurrence. Population size is kept constant throughout the process by comparing the fitness

values of any two randomly selected population members, deleting the weaker member and adding an extra copy of the more fit member.

Compatibility and Enabling Constraints. Compatibility and enabling constraints can be treated in one of two ways within the TIES/GA framework. One approach is rigid enforcement of constraints such that the GA is never allowed to create a combination that violates constraints. The preferred approach is to treat compatibility and enabling constraints as additional objectives to be minimized by the GA. Specifically, the number of compatibility and enabling constraint violations can easily be calculated for any arbitrary bit string, so it is simple to treat these functions as additional performance parameters to be minimized. The drawback to this approach is that the constraints are not guaranteed to be satisfied, but one can always force constraint satisfaction by increasing the relative weight of the compatibility and enabling terms in the objective function. The strength is that this approach is simple to implement and is not hindered by the complex technology interactions that can arise for highly constrained problems. Treatment of constraints is discussed extensively in Refs. [4] and [6].

Genetic Algorithm Objective Function. Genetic algorithms generally deal with a single objective function at a time. To optimize multiple objective functions using a genetic algorithm, some modifications must be made to the objective functions or to the formulation of a canonical GA. One way to handle multiple objectives is through formation of a single objective equation that combines all other objective functions, such as an overall evaluation criteria, with each individual criterion multiplied by a weighting factor. The drawback of this formulation is that there is a considerable increase in the run time because the code has to evaluate all the objectives for each and every member of the population. A more efficient formulation is to evaluate pairs of population members for only one objective function per pairwise tournament. The objective selected for any given tournament should be randomly selected, with the frequency of selection for each objective being determined by the objective weight. This is the preferred formulation used herein.

Robust Genetic Algorithm. As with most search and optimization techniques, genetic algorithms include a number of operational parameters whose values significantly alter the behavior of the algorithm for a given problem, sometimes in unpredictable ways. A canonical genetic algorithm typically requires user ''tuning'' of several key parameters: mutation rate, population size, and number of generations to be optimized. The particular settings chosen by the user can alter and/or make the optimal technology set vary between consecutive runs. As the objective is to find globally optimum engine technology solution sets, it is desirable to find means of removing these biases, or at least making them systematic. In the GA/TIES application, this is done by making the GA parameters adaptive to the study, i.e., the values of population size, number of generations, and probability of mutation are decided by the code itself without the need for user intervention.

There are numerous schemes described in subject literature on selection of GA optimization parameters, many of which undoubtedly offer substantial improvements in GA optimization accuracy. One approach that has proven effective is to automatically select mutation rate by scheduling it as a function of generation number. A typical variable mutation rate is given by Back and Schutz [10]:

$$p_t = \left\{ 2 + \frac{(i-2)}{(T-1)} t \right\}^{-1} \tag{5}$$

where

p_t=mutation rate for generation t
t=generation counter
T=maximum number of generations
i=current generation number.

This variable mutation schedule starts with an initially high probability of mutation and decreases rapidly with each generation in an exponential decay pattern. Variable mutation is highly effective in improving both solution accuracy and precision, [11].

Another desirable feature is to intelligently select the maximum number of generations to be optimized. Simple GA implementations are typically run for a user-specified number of generations, assuming it will converge at or before the prescribed number of generations is reached. It is difficult to estimate a priori the number of generations GA will take to converge, so the user must balance between too few generations resulting in incomplete convergence or too many generations resulting in wasted computational effort. This dilemma can be avoided through the implementation of a simple convergence criterion. For example, one can assume that the GA solution is converged when the number of *distinct* genotypes in the population is equal to or less than some prescribed fraction of the total population size (5% works well). For example if the total population size is 200, then the GA will stop when the number of distinct genotypes in the population of any *n*th generation is less than or equal to 10. One must still place an upper limit on the number of generations in case the GA can't converge for some reason. A maximum number of generations is also needed for use in Eq. (5).

Another parameter of interest is population size. It is very desirable to have the initial population uniformly distributed over the range of the design variables. This is because fragments of genes or schema representing the optimal design must be present in the initial pool in order to be used as building blocks for assembly of an optimal solution. If they are not initially present, the only other means by which they can be introduced is through mutation. It is therefore desirable to have a large enough population that a diversity of gene fragments are present to be used during crossover. On the other hand, inordinately large population sizes are computationally burdensome, especially in applications where function evaluations are expensive. A good rule of thumb for technology evaluation studies is to make the population size be three times the DNA string length. This allows the population size to change in proportion to the number of technologies under consideration and yields good results.

Typical GA-Optimized Technology Results

Implementation of the previously described schemes for GA parameters helps make the GA very robust and effective at finding optimal technology sets, even for very highly constrained problems. As an example, consider a fictitious problem consisting of 80 engine technologies. These technologies were created by simply making randomly generated technology impact and constraint matrices but are representative of real engine technology sets encountered in industrial practice. In this case, the TIM was randomly populated by nonzero values with a probability of 50% while the constraint matrix was populated with 20% incompatibilities and 10% enabling. The objective is to find the set of technologies from 80 given technologies that yields the optimum balance between minimizing two parameters: production cost score and mission fuel burn. In order to be a valid solution, the number of compatibility constraint violations must also be minimized, for a total of three objectives.

Once the TIM and constraint matrices are created, the next step is to create a suitably compact TIF. The TIF usually consists of one response surface per objective, each response surface typically being a function of the K factors. The K factors are selected based on their importance as technology metrics for turbofan engines and are intended to be sufficient to capture the impact of all technologies considered for the current problem. The TIM scores each of the 80 technologies in terms of deltas in the K factors as well as one additional parameter: relative production cost score. Relative production cost is a qualitative score: scores less than zero $(-1,-2,\ldots)$ indicate progressively less expensive technology relative to a current baseline, while scores greater than zero

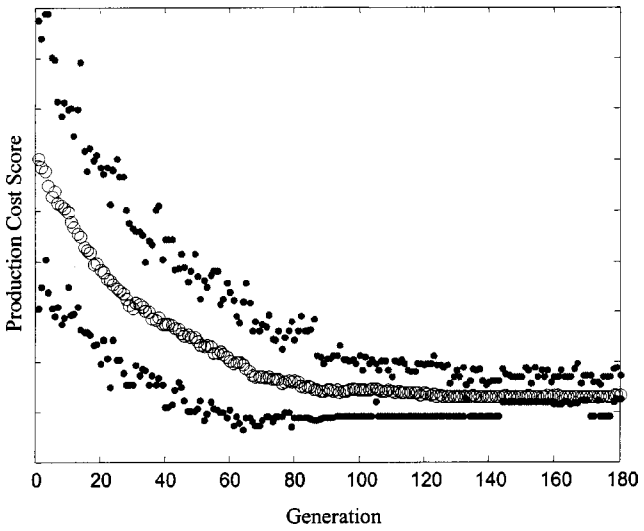

Fig. 6 Evolution of relative production cost score

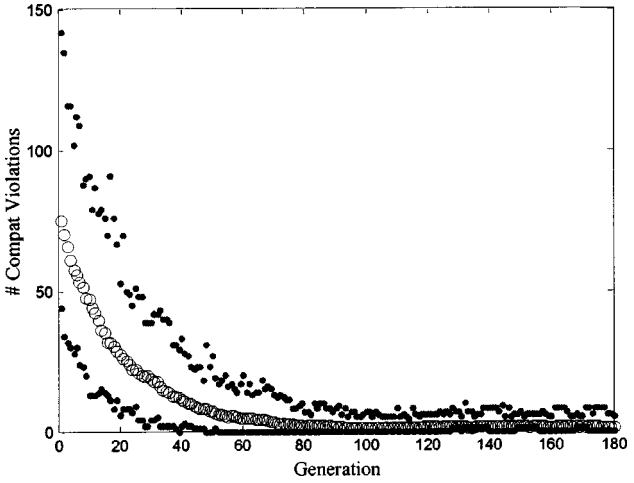

Fig. 8 Number of incompatibilities as a function of population generation

indicate progressively more manufacturing expense. This is an important point: it illustrates that the method outlined herein is capable of optimizing *qualitative* and *quantitative* data.

Convergence histories for a typical technology optimization run are shown in Figs. 6, 7 and 8. The GA objectives used for this example are 50% minimize compatibility conflicts, 25% minimize fuel burn, and 25% minimize production cost score. Solution of this scenario required 180 generations and took 7 minutes of PC runtime. The three groups of symbols on each plot represent the maximum, mean, and minimum of each score encountered in the population at each generation. The relative spread between the minimum and maximum for all three figures is relatively small, indicating that the solution is converged by the 180th generation. In Figs. 6 and 8, the average value starts relatively high and decreases gradually as undesirable technologies are removed from the population pool. It is interesting to note, however, that the population mean shown in Fig. 7 does not monotonically decay, but shows a minimum then goes slightly higher before finally converging. This is due to the presence of the compatibility constraint, which forces a slight increase in mission fuel burn in the interest of eliminating numerous compatibility conflicts. It is important to understand that the GA solution is represented by the final population average, *not* the population minimum. The minimum points are misleading because the genotype that gives rise to a minimum point in one objective is also the genotype giving rise to a maximum in the other objective(s).

Figure 8 shows that there are no compatibility constraint violations in the final technology solution set. This is due to the fact that the compatibility constraint was heavily weighted relative to the other objectives. This is a marked reduction in compatibility violations from the initial average of 75. While there are doubtless alternate technology combinations that reduce the value of fuel burn or production cost score, those sets do so only at the expense of employing incompatible pairs of technologies.

Figure 9 shows the frequency of occurrence of each technology in the final population. If the technology is uniformly present in the final population members, then it is assumed to be part of the optimal solution set. This occurs for 21 out of 80 technologies. Generally it is advisable to define a cutoff point above which if the technology exists in the final population then it is selected (''on''). In this case, technology is taken as being selected if it exists in more than 90% of the population members. If the technology is present in only 10% or less of the population then it is considered to be ''off.'' The technologies between 10% and 90% are intermediate technologies. No conclusive decision can be

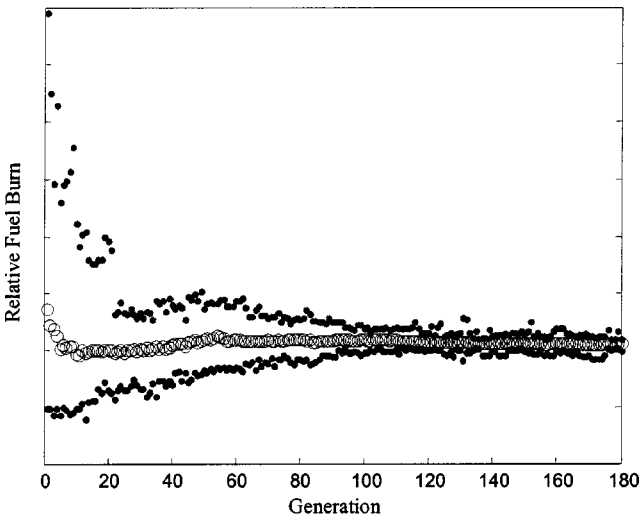

Fig. 7 Evolution of relative fuel burn

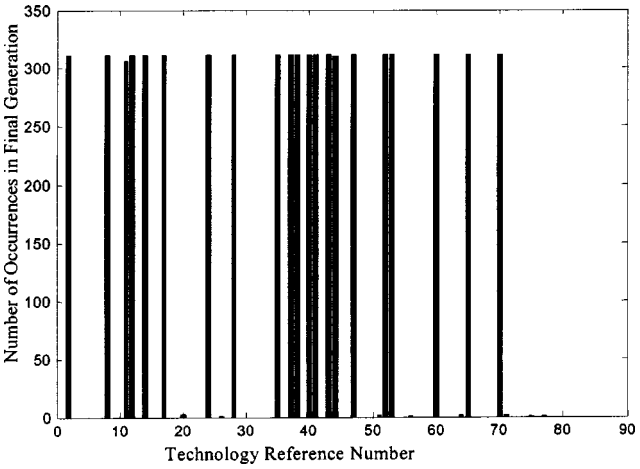

Fig. 9 Frequency of occurrence of each technology in final population

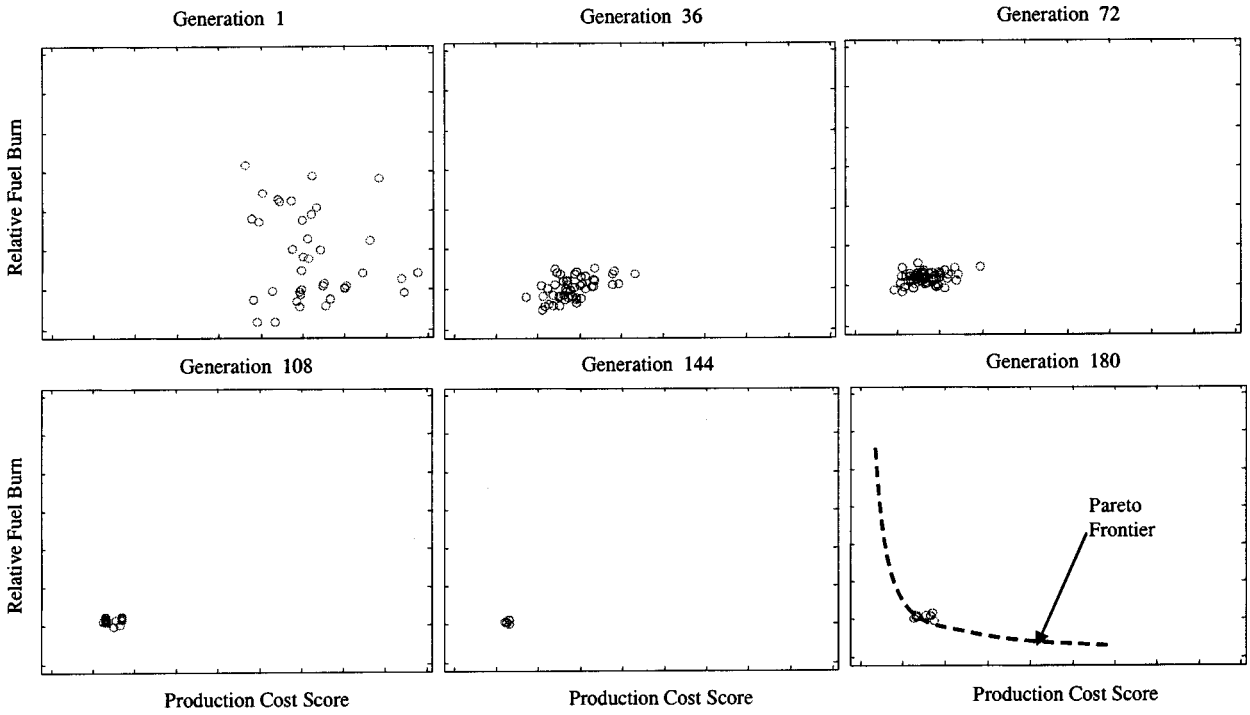

Fig. 10 Evolution of population through 180 generations

drawn regarding these technologies because their impact on the objective functions is so balanced as to have no net impact on population fitness.

One can obtain a better understanding of the convergence trajectory by cross-plotting objectives at several points during the optimization process. Figure 10 shows six plots of the population distribution at various stages of evolution from the initial generation through the final generation. The axis objectives are normalized fuel burn and production cost score. As seen from the first panel of Fig. 10, the initial population has a wide distribution of on the objective space. As the GA progresses (panels 2–5), undesirable technology sets are deleted and new, better technology combinations are added causing the values of both objectives to decrease. The initially wide dispersion of points collapses to a single tight cluster of points in the final panel. This is the optimum solution for the prescribed objective weights.

The final solution lies on the technology Pareto frontier. A technology Pareto frontier (Roth et al. [12]) is defined the locus of non-dominated optimum technology solutions on the objective functions cross-plot. A technology Pareto frontier is ''ghosted'' in the final panel to illustrate that the solution corresponds to a single point on the Pareto frontier. Each point on the frontier corresponds to a particular objective weighting. For this example, the weighting on both the objectives is same, hence the final solution moves on a generally diagonal trajectory toward the Pareto front. Note that since the combinatorial problem is discrete, the Pareto front is not continuous, but is instead composed of a finite set of nondominated solutions. Naturally, as the number of technologies under consideration grows, the Pareto frontier approaches the continuum model.

Areas for Future Research

As observed from the results shown in the previous section, the present application of GA and TIES gives a set of technology combinations that are optimized for user-prescribed weightings of the objectives. These technology sets constitute only a limited portion of the Pareto-front as shown in the last panel of Fig. 10. It is often desirable to understand how the optimal technology set changes with changes in the requirements (i.e., one would like to see the entire Pareto front). The present method can only do this through repeated optimization runs while parametrically varying objective weights—a time-consuming procedure. A niched-Pareto algorithm, as described by Horn et al. [13] and Fonseca [14], can obtain the entire Pareto front in one run and would be useful in this application.

A second area of research that could potentially yield greater insight into the fundamental nature of the technology optimization problem is to examine this constrained combinatorial problem from the standpoint of information theory. If the Shannon entropy of each possible constraint configuration were calculated, could it be analytically shown that the configuration with the greatest ''information entropy'' (see Fig. 4) be the situation that is most difficult to solve? Furthermore, could this knowledge be used to make some general observations on optimization of highly constrained combinatorial problems that would be useful in finding better solutions in the future?

A third possible avenue for future research is to consider the application of well-known Boolean algebra reduction methods as a possible means to simplify the technology combinatorial optimization in the presence of complex constraint interactions amongst technologies. An obvious starting point would be to consider the application of Karnaugh reduction maps to simplify the analysis of multi-way technology constraint interactions. It is very likely that the integrated circuit industry has developed a variety of highly advanced Boolean network reduction algorithms, some of which might find productive application to the present problem.

A final area that warrants further investigation is to determine how one might develop a practical model to account for intermediate interactions between technologies. This type of interaction was mentioned previously and can be thought of as a weak compatibility or enabling constraint. It is exemplified by the situation where the introduction of technology ''A'' causes a change in the K factors of technology ''B.'' Either ''B'' will be slightly helped or hindered by the presence of ''A'' but will not be entirely turned ''on'' or ''off'' as was the case in Boolean interactions. For example, the maximum allowable metal temperature for a turbine

blade might be a weak function of the type of thermal barrier coating used. It was suggested earlier that one possible approach is to model the technologies using an n by k by n TIM. However, the manual creation of such a three-dimensional TIM would be quite tedious and error-prone for any practical technology selection problem. A better approach is required to solve this problem.

Conclusions

This paper has shown that the TIES/GA is an effective method for solving high-dimensional, highly constrained, multi-objective technology combinatorial optimization problems. If implemented properly, the TIES methodology is accurate, fast, and suitable as a framework for conducting various technology studies, including conventional ''one-on/one-off'' engine technology evaluation methods as well as combinatorial optimization. The constraints among technologies, especially compatibility and enabling, complicate the optimization process considerably. The problem complexity appears to be correlated with constraint density, with intermediate numbers of mixed constraints being the most difficult to optimize. A technology constraint matrix is a good means to model Boolean constraints but more sophisticated models will likely be needed in the future. This research area is relatively new with abundant opportunities to develop new and innovative approaches to finding optimal engine technology solution sets yet remaining.

Acknowledgments

We gratefully acknowledge the support of the Office of Naval Research, the National Science Foundation under grant DMI97-34234, and GE Aircraft Engines.

References

[1] Kirby, M. R., and Mavris, D. N., 2001, ''A Technique for Selecting Emerging Technologies for a Fleet of Commercial Aircraft to Maximize R&D Investment,'' Paper No. SAE2001-01-3018.
[2] Mavris, D. N., Kirby, M. R., and Qiu, S., 1998, ''Technology Impact Forecasting for a High Speed Civil Transport,'' Paper No. SAE-985547.
[3] Kirby, M. R., 2001, ''A Method for Technology Identification, Evaluation and Selection in Conceptual and Preliminary Aircraft Design,'' Ph.D. thesis, Georgia Institute of Technology, Atlanta, GA.
[4] Roth, B., German, B. J., Mavris, D. N., and Macsotai, N., 2001, ''Adaptive Selection of Engine Technology Solution Sets From a Large Combinatorial Space,'' Paper No. AIAA2001-3208.
[5] Kauffman, S., 1995, *At Home in the Universe*, Oxford University Press, New York, p. 56.
[6] Roth, B. A., Ender, T., and Mavris, D. N., 2002, ''Technology Portfolio Assessments Using a Modified Genetic Algorithm Approach,'' Paper No. AIAA2002-5424.
[7] Goldberg, D. E., 1989, *Genetic Algorithms in Search, Optimization and Machine Learning*, Addison-Wesley, Reading, MA.
[8] Khuri, S., Back, Th., and Heitkotter, J., 1994, ''An Evolutionary Approach to Combinatorial Optimization Problems,'' *Proc. of the 22nd Annual ACM Computer Science Conference*, D. Cizmar, ed., ACM Press, New York, pp. 66–73.
[9] Muhlenbein, H., 1992, ''How Genetic Algorithms Really Work: I. Mutation and Hill Climbing,'' R. Manner and B. Manderick, eds., *Parallel Problem Solving From Nature*, **2**, Elsevier, Amsterdam, pp. 15–25.
[10] Back, Th., and Schutz, M., 1996, ''Intelligent Mutation Rate Control in Canonical Genetic Algorithms,'' *Foundations of Intelligent Systems, 9th International Symposium ISMIS '96* (Volume Lecture Notes in Artificial Intelligence 1079), Springer-Verlag, New York, pp. 158–167.
[11] Back, Th., 1992, ''The Interaction of Mutation Rate, Selection and Self Adaptation Within a Genetic Algorithm,'' *Parallel Problem Solving From Nature*, **2**, R. Manner and B. Manderick, eds., Elsevier, Amsterdam, pp. 85–94.
[12] Roth, B. A., Mavris, D. N., Graham, M. D., and Macsotai, N. I., 2002, ''Adaptive Selection of Pareto-Optimal Engine Technology Solution Sets,'' 23rd Congress of the International Aeronautical Sciences, Toronto, Sept. 8–13.
[13] Horn, J., Nafpliotis, N., and Goldberg, D. E., 1994, ''A Niched Pareto Genetic Algorithm for Multiobjective Optimization,'' *Proceedings of the First IEEE Conference of Evolutionary Computation*, Orlando, FL. IEEE, Piscataway, NJ.
[14] Fonseca, C. M., and Fleming, P. J., 1993, ''Genetic Algorithms for Multiobjective Optimization: Formulation, Discussion and Generalization,'' *Proceedings of the Fifth International Conference on Genetic Algorithms*, Morgan-Kauffman, San Mateo, CA.

Investigation of Turbulence Models Applied to Premixed Combustion Using a Level-Set Flamelet Library Approach

Ulf Engdar
e-mail: ulf.engdar@vok.lth.se
Department of Heat and Power Engineering,
Lund Institute of Technology,
P.O. Box 118,
221 00 Lund, Sweden

Per Nilsson
e-mail: per.e.nilsson@af.se
ÅF Energi & Miljo,
Box 222 26,
250 24 Helsingborg, Sweden

Jens Klingmann
e-mail: jens.klingmann.vok.lth.se
Department of Heat and Power Engineering,
Lund Institute of Technology,
P. O. Box 118,
221 00 Lund, Sweden

Most of the common modeling approaches to premixed combustion in engineering applications are either based on the assumption of infinitely fast chemistry or the flamelet assumption with simple chemistry. The level-set flamelet library approach (FLA) has shown great potential in predicting major species and heat release, as well as intermediate and minor species, where more simple models often fail. In this approach, the mean flame surface is tracked by a level-set equation. The flamelet libraries are generated by an external code, which employs a detailed chemical mechanism. However, a model for the turbulent flame speed is required, which, among other considerations, depends on the turbulence intensity, i.e., these models may show sensitivity to turbulence modeling. In this paper, the FLA model was implemented in the commercial CFD program Star-Cd, and applied to a lean premixed flame stabilized by a triangular prism (bluff body). The objective of this paper has been to investigate the impact on the mean flame position, and hence on the temperature and species distribution, using three different turbulent flame speed models in combination with four different turbulence models. The turbulence models investigated are: the standard k-ε model, a cubic nonlinear k-ε model, the standard k-ω model and the shear stress transport (SST) k-ω model. In general, the computed results agree well with experimental data for all computed cases, although the turbulence intensity is strongly underestimated at the downstream position. The use of the nonlinear k-ε model offers no advantage over the standard model, regardless of flame speed model. The k-ω based turbulence models predict the highest turbulence intensity with the shortest flame lengths as a consequence. The Müller flame speed model shows the least sensitivity to the choice of turbulence model. [DOI: 10.1115/1.1771687]

Introduction

A common way of achieving low emissions and high combustion efficiencies in gas turbines today is to use a lean premixed combustion system. Accurate predictions of these systems are crucial for further development and understanding of premixed combustion.

Most of the common modeling approaches to premixed turbulent combustion in engineering applications are either based on the assumption of infinitely fast chemistry, or the flamelet assumption with simple chemistry. These models are often capable of predicting the major species and the heat release. To predict intermediate and minor species such as carbon monoxide (CO) and nitric oxides (NO_x), a detailed chemical mechanism has to be included in the model. The level-set flamelet library approach (FLA) is a modeling concept for turbulent premixed combustion which is capable of predicting these species (as well as the other properties), [1,2].

To make fair judgments about the capability of a model, a relevant flame configuration with a detailed set of experimental data is required to validate the model. The FLA approach has been applied successfully to a bluff body stabilized flame configuration, [1]. However, this model uses a model for the turbulent flame speed and these are based more or less on the turbulence intensity. So far, all computations have been done with the standard k-ε model, [3], and it is well known that this model has its limitations, which are of relevance to combustion modeling.

A number of modifications of the standard k-ε model have been suggested, mainly to the source terms in the turbulence dissipation equation, [4]. Another way of expressing two-equation models is in terms of k-ω models, [5], which use the turbulence frequency ($\omega \sim \varepsilon/k$) variable instead of the turbulence dissipation. One way of improving the capability of capturing the effects of strong curvature and anisotropy better might be to use a non-linear relationship between the Reynolds stresses and the rates of strain. However, these non-linear models are often claimed to be more difficult to handle numerically.

The objective of this paper has been to study the impact on the mean flame position, and hence on the temperature and the major species distribution, of three different turbulent flame speed models in combination with four different turbulence models. The FLA model was implemented in the commercial CFD program Star-CD, through Fortran-based user-subroutines. This facilitates adoption of this model to other more complex flame configurations.

Other studies have been performed on this flame configuration. The standard k-ε with simple combustion models has been applied by Bai et al. [6] for example, and large eddy simulation (LES) has been used to study nonstationary effects by, e.g., Möller et al. [7]. A limited flamelet model which combines the G-equation approach and the coherent flame model for LES has been tested using this configuration, [8].

Contributed by the International Gas Turbine Institute (IGTI) of THE AMERICAN SOCIETY OF MECHANICAL ENGINEERS for publication in the ASME JOURNAL OF ENGINEERING FOR GAS TURBINES AND POWER. Paper presented at the International Gas Turbine and Aeroengine Congress and Exhibition, Atlanta, GA, June 16–19; 2003, Paper No. 2003-GT-38331. Manuscript received by IGTI, Oct. 2002, final revision, Mar. 2003. Associate Editor: H. R. Simmons.

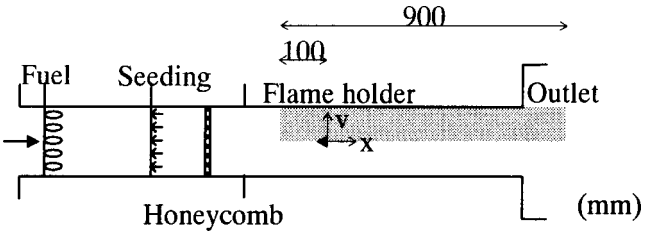

Fig. 1 A sketch of the experimental and computational domain (shadowed), [9]

Materials and Methods

The configuration analyzed is a turbulent lean premixed propane/air flame, where the flame is stabilized by a triangular prism-shaped flame holder. The flow field is what can be expected in a model aircraft afterburner. A sketch of the experimental domain and the computational domain is shown in Fig. 1. The breadth (y-direction) and the length (z-direction) of the prism are 40 mm and 240 mm, respectively. The width of the channel is 240 mm.

The computations were compared to measurements performed by Sjunnesson, et al. [9,10]. The species (CO_2, CO, NO_x, and UHC) were measured by gas analysis equipment, at $x=0.15$, 0.35, and 0.55 m. The temperature was computed from the measured species, assuming equilibrium chemistry. Laser Doppler anemometry (LDA) was used to measure the velocities and turbulence, at $x=-0.2$, -0.1, 0.015, 0.038, 0.061, 0.15, and 0.38 m. The experimental conditions investigated here were an airflow of 0.6 kg/s, an equivalence ratio of 0.6, an inlet temperature of 600 K and a pressure of 1 bar.

Governing Equations. The governing equations to be solved are the continuity and the momentum equations:

$$\frac{\partial \overline{\rho}\widetilde{u}_i}{\partial x_i}=0 \tag{1}$$

$$\frac{\partial}{\partial x_j}(\overline{\rho}\widetilde{u}_j\widetilde{u}_i)=-\frac{\partial \overline{p}}{\partial x_i}+\frac{\partial}{\partial x_j}(\overline{\tau}_{ij}-\overline{\rho u_i'' u_j''}). \tag{2}$$

Furthermore, transport equations for turbulence kinetic energy and turbulence dissipation (or turbulence frequency in the case of k-ω model) are solved. The G-equation and some additional equations related to the flamelet library approach are also solved for.

Turbulence Modeling. The following turbulence models are studied in this work:

- k-ε based two-equation models

1. The standard linear k-ε model, [3]
2. The nonlinear (cubic) k-ε model, [11]

- k-ω based two-equation models

3. The standard linear k-ω model, [5]
4. shear stress transport (SST) k-ω model, [12]

The first three models are well-known two-equation turbulence models. However, the SST k-ω model has been shown to be an attractive choice of two-equation models for swirling flows, [13], which is of considerable interest for real gas turbine combustors. The equations for the turbulence models used are listed at the end of this paper.

The Level-Set Flamelet Library Approach. The level-set flamelet library approach (described in detail in [14]) is based on viewing the turbulent flame surface as an ensemble of locally laminar flames, called flamelets.

The flamelet library is a table describing the inner structure of a laminar flamelet, e.g., species molar fraction and temperature as a function of position in the flamelet. The flamelet library is generated in separate code developed by Mauss [15]. Here, a freely propagating one-dimensional laminar flame is computed using a detailed chemical mechanism. This mechanism consists of 402 elementary reactions involving 50 species, and was developed by Peters [16].

In a turbulent flow field, the mean flame position is tracked by the Favre averaged level-set G-equation, where G is a nonreacting scalar. The level $\widetilde{G}=0$ defines the mean flame position and divides the flow field into two regions, where $\widetilde{G}<0$ and $\widetilde{G}>0$ represent the regions of unburnt and burnt state, respectively. The Favre-averaged G-equation is given by, [17]:

$$\frac{\partial \overline{\rho}\widetilde{G}}{\partial t}+\frac{\partial \overline{\rho}\widetilde{u}_i\widetilde{G}}{\partial x_i}=\overline{\rho}s_T\sqrt{\frac{\partial \widetilde{G}}{\partial x_i}\frac{\partial \widetilde{G}}{\partial x_i}}. \tag{3}$$

The turbulent flame speed, s_T, in Eq. (3) depends, among other factors, on the turbulence intensity, the turbulent Reynolds number and flame stretch [18]. There exist several different turbulent flame speed models, which include these properties to a greater or lesser extent. The flame speed models examined are Damköhler [19]:

$$s_T=s_L+u' \tag{4}$$

Peters [17]:

$$s_T=s_L\left[1-0.195\frac{\mathrm{Re}_T}{u'/s_L}+\sqrt{\left(0.195\frac{\mathrm{Re}_T}{u'/s_L}\right)^2+0.78\,\mathrm{Re}_T}-\frac{D_T\overline{\kappa}(\widetilde{G})}{s_L}\right] \tag{5}$$

Müller et al. [20]:

$$s_T=s_L+0.46u'+0.2\sqrt{s_L u'}-D_T\overline{\kappa}(\widetilde{G}). \tag{6}$$

The mean flame curvature, $\overline{\kappa}$, is defined as

$$\overline{\kappa}(\widetilde{G})=-\frac{\partial}{\partial x_i}\left(\left(\frac{\partial \widetilde{G}}{\partial x_j}\frac{\partial \widetilde{G}}{\partial x_j}\right)^{-1/2}\frac{\partial \widetilde{G}}{\partial x_i}\right). \tag{7}$$

The turbulent diffusivity is modeled as

$$D_T=\frac{\mu_T}{\overline{\rho}Sc_T}. \tag{8}$$

Equation (3) only defines the mean flame position, since the turbulent flame speed is not defined outside the flame. To extend the meaning of $\widetilde{G}$ to the entire flow field, $\widetilde{G}$ can be formulated as distance function, where $\widetilde{G}$ then defines the closest distance to the mean flame surface. This is accomplished by a re-initialization step [21], where the following constraint is enforced to the $\widetilde{G}$-field outside the mean flame position:

$$\sqrt{\frac{\partial \widetilde{G}}{\partial x_i}\frac{\partial \widetilde{G}}{\partial x_i}}=1. \tag{9}$$

A presumed Gaussian distribution, $\mathscr{P}$, of positions around the flame surface is used to average the locally laminar flamelet properties over the turbulent flame. The mean temperature field, the mean density field and the mean species molar fractions field are thus obtained by integration of the library over the Gaussian distribution. For example, at x_i, the mean molar fraction of θ is computed by

$$\overline{X}_\theta(x_i)=\int_{-\infty}^{+\infty}\mathscr{P}(G;\widetilde{G}(x_i),G''^2(x_i))X_\theta(G)dG. \tag{10}$$

Here, $X_\theta(G)$ is the flamelet library for θ as a function of the flamelet coordinate G. The variance of G, G''^2, describes how the

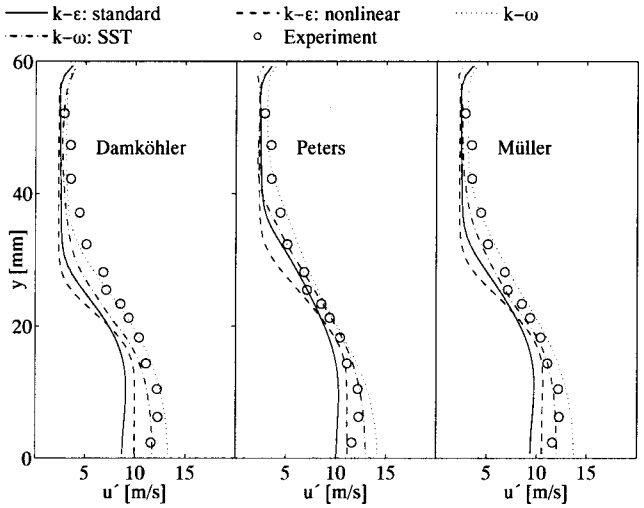

Fig. 2 Turbulence intensity profiles at $x=0.15$ m

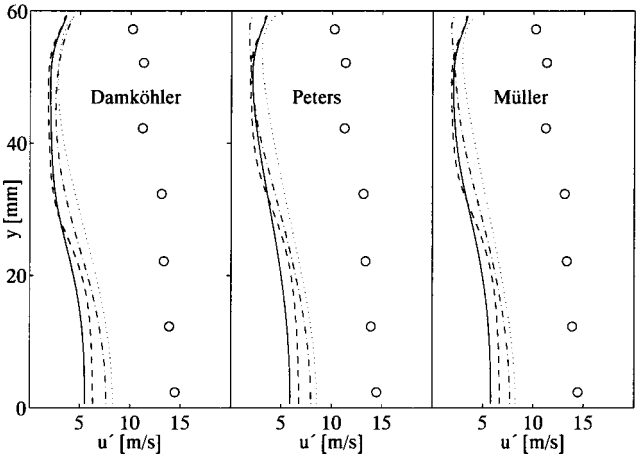

Fig. 3 Turbulence intensity profiles at $x=0.38$ m

laminar flamelet fluctuates around its mean position and it is a measure of the turbulent flame thickness. In this paper, the variance of G is estimated via experiments and is expressed as, [14]:

$$G''^2=(0.045x)^2. \tag{11}$$

It should be noted that in this implementation, the FLA model uses no energy equation or species transport equations. The effect of, for example, radiation would require a slightly different implementation: if the library supplies the heat of reactions instead of the temperature, a conservation equation for the energy must be solved. This could then be complemented with radiation models, for example.

Numerical Methods and Boundary Conditions. A two-dimensional grid was employed for all computations and the numerical method is based on the finite volume method, [22]. The convective terms in the transport equations were handled by a second-order scheme (MARS [23]) and the pressure-velocity coupling was solved by the PISO algorithm. An investigation of the grid dependence was carried out (grid used ≈20,000 cells).

As stated above, Star-Cd was used for all flow-field computations. However, a separate solver was developed for the reinitialization step (i.e., Eq. (9)) and the $\tilde{G}$-field was passed between Star-Cd and the solver at the end of every iteration. The laminar flame speed, s_L, was obtained from the chemistry code and was equal to 0.743 m/s.

Measurement data for the mean velocities and the turbulence kinetic energy were used to set up the inlet boundary condition. However, there is an uncertainty regarding the specification of the turbulence dissipation rate at the inlet. A frequently used assumption of turbulence energy equilibrium was employed to estimate ε, i.e., $\varepsilon=0.09^{0.75}k^{1.5}/0.07H$, [22], where H is the height of the channel. For the k-ω models, the turbulence frequency is given by Eq. (44).

At the outlet boundary condition, all gradients of the flow variables in the x-direction are set to zero. At solid walls, wall functions are used to avoid near-wall treatment, and symmetry boundary conditions were used in the z-direction and at $y=0$.

Results and Discussion

Figures 2 and 3 show the characteristic velocity fluctuation profiles for the flame speed models examined, at $x=0.15$ and 0.38 m. The computed flame positions are shown in Fig. 4. Figures 5 to 7 show the temperature profiles at $x=0.15$, 0.35 and 0.55 m. Figures 8 to 10 show the molar fraction of the O_2 profiles at the same positions as for the temperature. The legend to Fig. 2 applies to all figures. All the computations presented in this paper showed about the same convergence rate and approximately the same computational time. The computational time was roughly two to three times longer than using a standard k-ε turbulence model with the

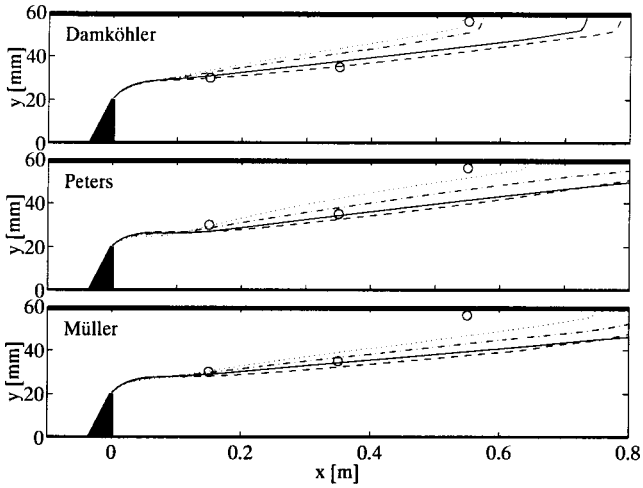

Fig. 4 Mean flame positions

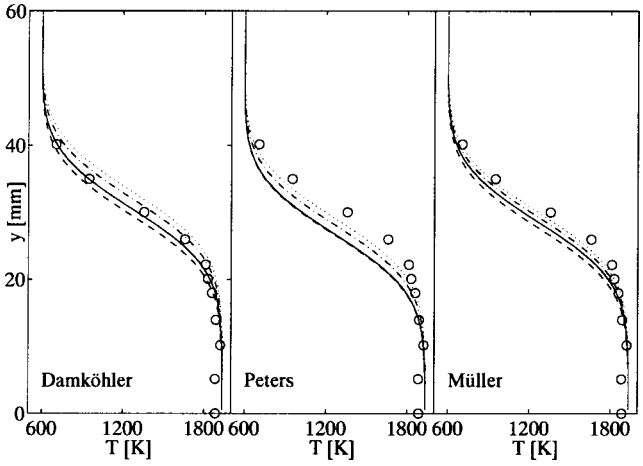

Fig. 5 Temperature profiles at $x=0.15$ m

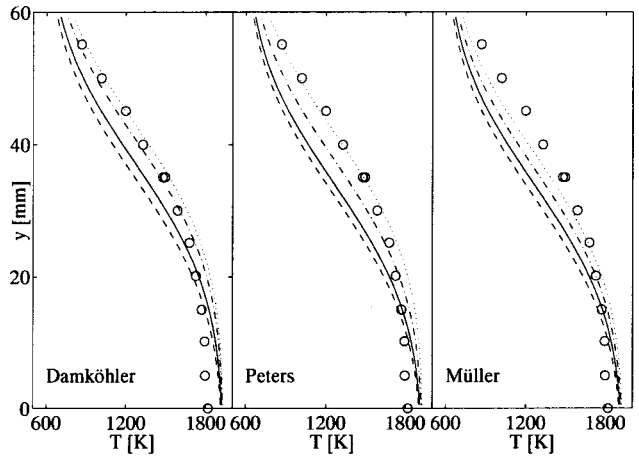

Fig. 6 Temperature profiles at $x=0.35$ m

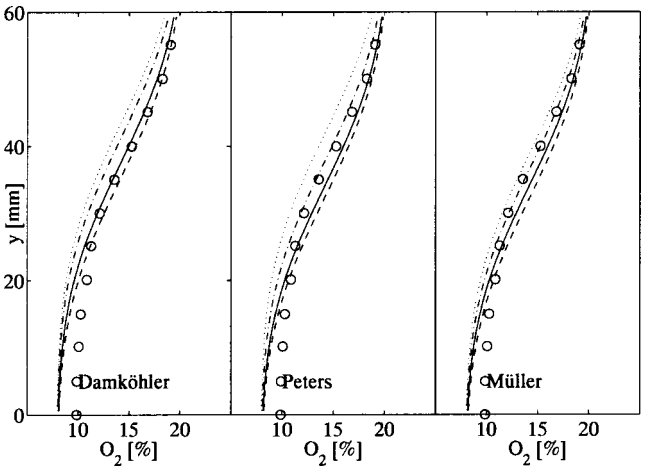

Fig. 9 O_2 mole fraction profiles at $x=0.35$ m

eddy dissipation concept model by Magnussen and Hjertager [24]. However, this FLA model presented is not optimized in terms of speed.

Modeling of the Turbulence Intensity. At the section 0.15 m downstream of flame holder, shown in Fig. 2, all cases have shown good agreement with the experimental data. However, the difference between the turbulence models increases slightly towards $y=0$. The SST k-ω model shows best agreement with the experimental data for the Peters and Müller flame speed models, but all models fail to predict the decrease in turbulence kinetic energy towards $y=0$. In general, the Damköhler model predicts values that are lower than those predicted by other flame speed models.

Further downstream, at the section $x=0.38$ m shown in Fig. 3, a strong decay in the turbulence intensity is predicted for all combinations of models, which does not agree with the experiments, where it increased instead. This is most likely due to the fact that the large-scale motion of the von Karman vortex cannot be resolved in a steady RANS computation, but it contributes strongly to the measured u'. In the LES computation of Möller et al. [7], for example, this large-scale motion is resolved and the discrepancy does not occur. This can be seen as being analogous to the precessing vortex core of a swirl-stabilized flame, which generally yields high values of u' at the centerline, if treated as a stationary turbulent flow. However, it is not likely that this periodic motion contributes to the mean turbulent flame speed much. In reciprocating engines, for example, there are large differences between turbulence levels obtained from ensemble averages and from cycle resolved measurements. These are the result of cycle-to-cycle variations, which introduce measured turbulence levels that are not accompanied by a corresponding increase in flame speed, [25]. However, the trend is similar to the upstream position, i.e., the k-ω based models predict higher values than the k-ε based models and the Damköhler model still predicts the lowest values.

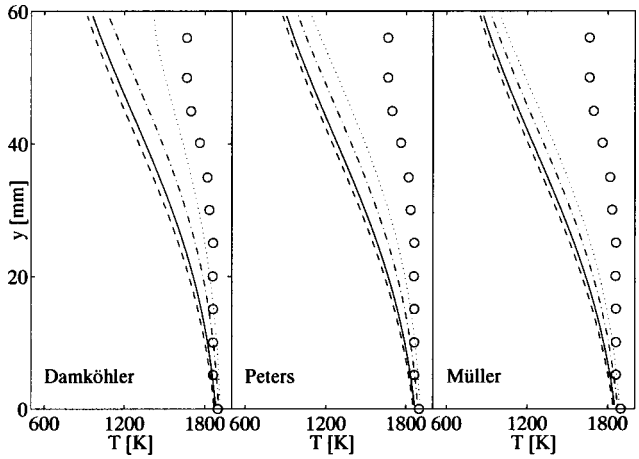

Fig. 7 Temperature profiles at $x=0.55$ m

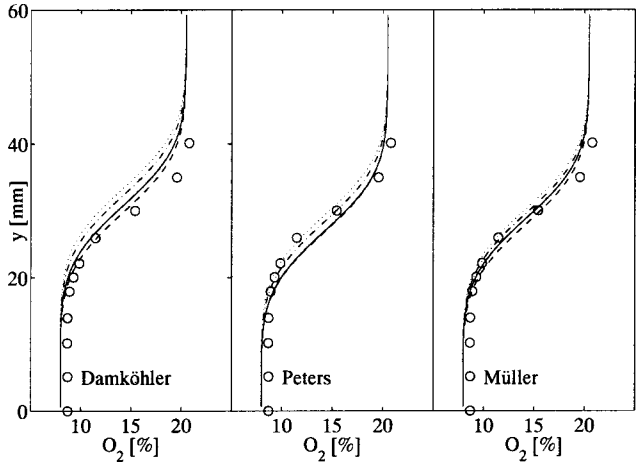

Fig. 8 O_2 mole fraction profiles at $x=0.15$ m

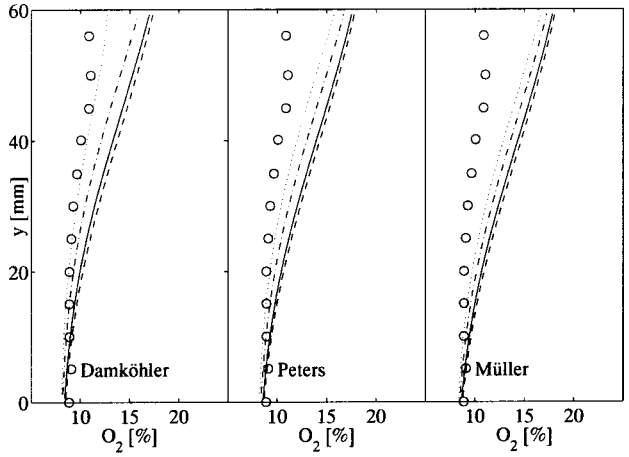

Fig. 10 O_2 mole fraction profiles at $x=0.55$ m

Modeling of the Flame Position. The experimental flame position is defined as being where the CO content reaches its maximum value. It should be noted that there are some uncertainties in the experimental flame position for the last section ($x=0.55$ m), because during the experiments, there were occasionally problems with flashback in the wall boundary layer, [14].

The mean flame position is shown in Fig. 4. In general, the flame positions are well predicted for all cases, at least at the two upstream positions. At the last section, only the Damköhler flame speed model with standard k-ω turbulence model reproduces the experimental flame position reasonably well. In general, the Damköhler flame speed model predicts shorter flame lengths than the other flame speed models do. The difference in the computed flame length between the turbulence models is considerably larger for this model than for the other flame speed models. This is due to the fact that this model has a higher dependency on the turbulence intensity than the other models. The lowest spread can be seen for the Müller flame speed model, which indicates that this model shows least sensitivity to turbulence intensity. This model also predicts the longest flame lengths, but the difference between the Peters and the Müller flame speed models for the k-ε based models is quite small. Even the mutual difference between these models is small for the Peters and the Müller flame speed models. The standard k-ω model predicts the lowest flame lengths for all flame speed models, followed by the SST k-ω model.

Modeling of Temperature and O_2 Molar Fractions. The temperature and O_2 molar fractions are strongly dependent on the mean flame position and the flamelet library. Therefore, a difference in the computed temperature profiles will also be reflected in the O_2 molar profiles.

The temperature profiles for the position closest to the flame holder, shown in Fig. 5, agree well with the experimental data for all combinations. However, the Peters and the Müller flame speed models under-predict the temperature slightly. As noticed for the mean flame positions, the Müller flame speed model shows the least spread in temperature between the turbulence models, and the Damköhler flame speed model shows the most spread. For all flame speed models, the standard k-ω model predicts the highest values. Similar results are obtained when predicting the O_2 molar fractions; see Fig. 8. In this case, however, the k-ω model predicts the lowest values instead of the highest.

At the section 0.35 m downstream of the flame holder, shown in Fig. 6, a similar trend is obtained as for the upstream position, i.e., the k-ω based models show best agreement with the experimental data and the highest values are computed with the standard k-ω model. However, as a consequence of the larger spread in the computed flame positions at this position as compared to the upstream position, the spread between the computed temperature profiles have increased. The best overall agreement is obtained with the Peters flame speed model and the standard k-ω model. The trends are also valid for the O_2 molar fractions shown in Fig. 9.

At the last section measured, shown in Fig. 7, the agreement with the experimental data is less satisfactory than for the upstream positions. This is most likely due to the fact that reproduction of the experimental flame positions is also poor at this position, except for the Damköhler flame speed model with the standard k-ω model. For this position as well as for the other positions, the Müller flame speed model shows the least spread between the computed temperature profiles and the greatest spread is shown by the Damköhler flame speed model. These trends are also valid for the O_2 molar fractions in Fig. 10.

Conclusions

In general, it can be stated that good agreement with the experimental data has been obtained from all combinations of flame speed and turbulence models, although the turbulence intensity is strongly under-predicted at the downstream position. This discrepancy between measured and computed values most likely comes from the RANS inability to capture the periodic fluctuations usually found in this kind of flow field. However, the fairly good computations of the flame position indicate that the periodic motion does not contribute significantly to flame propagation.

Of the four investigated turbulence models, the k-ω based models predict the highest turbulence intensity with the shortest flame lengths as a consequence. This is in agreement with the measurements. The use of the nonlinear k-ε model offers no advantage over the standard model, regardless of flame speed model.

The best agreement with the experimental data for the last section was obtained with the Damköhler flame speed model in combination with the standard k-ω turbulence model. However, some uncertainties exist in the experimental data at the most downstream point.

The Müller flame speed model showed least sensitivity to the turbulence intensity and the Damköhler flame speed model showed most.

Acknowledgments

Financial support from the Swedish National Energy Administration, within the framework of the research program ''Thermal processes for electric power production,'' is gratefully acknowledged.

Nomenclature

Scalars

- D = diffusivity (m^2/s^2)
- G = signed distance to flame surface (m)
- k = turbulence kinetic energy (m^2/s^2)
- p = pressure (N/m^2)
- Re = Reynolds number
- s = flame speed (m/s)
- Sc = Schmidt number
- T = temperature (K) or turbulence model time scale (s)
- u' = turbulence intensity (m/s)
- H = channel height (m)
- x = coordinate (m)
- X = mole fraction
- y = coordinate (m)
- y^* = distance from first node to wall (m)
- ε = turbulence dissipation (m^2/s^3)
- θ = arbitrary property
- κ = mean flame curvature (m^{-1})
- μ = dynamic viscosity
- ρ = density (kg/m^3)
- ω = turbulence frequency (s^{-1})

Vectors and Tensors

- S_{ij} = strain rate tensor (s^{-1})
- u_i = velocity vector (m/s)
- x_i = coordinate in a Cartesian coordinate system
- δ_{ij} = Kronecker delta
- τ_{ij} = stress tensor (N/m^2)
- Ω_{ij} = vorticity tensor (s^{-1})

Statistical Quantities

- $\overline{\theta}$ = Reynolds average
- $\tilde{\theta}$ = Favre average
- θ'' = Favre fluctuation
- $\not{p}$ = probability density function

Subscripts

- T = turbulent
- L = laminar
- θ = arbitrary property

Appendix

List of Turbulence Models

The k-ε Based Turbulence Models. All k-ε based models use the following transport equations for k and ε:

$$\frac{\partial}{\partial x_j}\left(\overline{\rho}\widetilde{u}_j k-\left(\mu+\frac{\mu_T}{\sigma_k}\right)\frac{\partial k}{\partial x_j}\right)=\mu_T P_k-\overline{\rho}\varepsilon \tag{12}$$

$$\frac{\partial}{\partial x_j}\left(\overline{\rho}\widetilde{u}_j \varepsilon-\left(\mu+\frac{\mu_T}{\sigma_\varepsilon}\right)\frac{\partial \varepsilon}{\partial x_j}\right)=C_{\varepsilon 1}\frac{\mu_T P_k}{T}-C_{\varepsilon 2}\frac{\overline{\rho}\varepsilon}{T}+C_{\varepsilon 3}\overline{\rho}\varepsilon\frac{\partial \widetilde{u}_i}{\partial x_i}. \tag{13}$$

Furthermore, these models compute the turbulent viscosity as

$$\mu_T=f_\mu C_\mu \overline{\rho} T \tag{14}$$

where

$$f_\mu=1.0, \quad T=\frac{k}{\varepsilon}. \tag{15}$$

The standard linear k-ε model. The following set of coefficients is used:

$$\sigma_k=1.0, \quad \sigma_\varepsilon=1.22, \quad C_{\varepsilon 1}=1.44, \quad C_{\varepsilon 2}=1.92, \quad C_{\varepsilon 3}=-0.33, \quad C_\mu=0.09 \tag{16}$$

$$P_k=S_{ij}\frac{\partial \widetilde{u}_i}{\partial x_j}-\frac{2}{3}\left(\frac{\partial \widetilde{u}_i}{\partial x_i}+\overline{\rho}k\right)\frac{\partial \widetilde{u}_i}{\partial x_i} \tag{17}$$

$$-\overline{\rho u_i'' u_j''}=2\mu_T S_{ij}-\frac{2}{3}\left(\mu_T\frac{\partial \widetilde{u}_k}{\partial x_k}+\overline{\rho}k\right)\delta_{ij}. \tag{18}$$

The cubic k-ε model. This nonlinear model uses a cubic relationship between the Reynolds stresses and the rate of strain, i.e.:

$$\begin{aligned}-\overline{\rho u_i'' u_j''}=&2\mu_T S_{ij}-\frac{2}{3}\left(\mu_T\frac{\partial \widetilde{u}_k}{\partial x_k}+\rho k\right)\delta_{ij}-4C_1\mu_T T\left(S_{ik}S_{kj}-\frac{1}{3}S_{kl}S_{kl}\delta_{ij}\right)-4C_2\mu_T T(\Omega_{ik}S_{kj}+\Omega_{jk}S_{ki})\\&-4C_3\mu_T T\left(\Omega_{ik}\Omega_{jk}-\frac{1}{3}\Omega_{kl}\Omega_{kl}\delta_{ij}\right)-8C_4\mu_T\frac{T}{\varepsilon}(\Omega_{ki}S_{lj}+\Omega_{kj}S_{li})S_{kl}\\&-8C_5\mu_T\frac{T}{\varepsilon}\left(S_{kl}S_{kl}-\frac{1}{3}\Omega_{kl}\Omega_{kl}\right)S_{ij}.\end{aligned} \tag{19}$$

The following set of coefficients is used:

$$\sigma_k=1.0, \quad \sigma_\varepsilon=1.22, \quad C_{\varepsilon 1}=1.44, \quad C_{\varepsilon 2}=1.92, \quad C_{\varepsilon 3}=-0.33 \tag{20}$$

$$P_k=\frac{-\overline{\rho u_i'' u_j''}}{\mu_T}\frac{\partial \widetilde{u}_i}{\partial x_j} \tag{21}$$

$$C_\mu=\frac{0.667}{1.25+S+0.9\Omega}, \quad C_1=\frac{0.75}{(1000+S^3)C_\mu} \tag{22}$$

$$C_2=\frac{3.75}{(1000+S^3)C_\mu}, \quad C_3=\frac{4.75}{(1000+S^3)C_\mu} \tag{23}$$

$$C_4=-10.0C_\mu^2, \quad C_5=-2.0C_\mu^2, \quad S=T\sqrt{2S_{ij}S_{ij}}, \quad \Omega=T\sqrt{2\Omega_{ij}\Omega_{ij}}. \tag{24}$$

The k-ω Based Turbulence Model. All k-ω based models use the following transport equations for k and ω.

$$\frac{\partial}{\partial x_j}\left(\overline{\rho}\widetilde{u}_j k-\left(\mu+\frac{\mu_T}{\sigma_k^\omega}\right)\frac{\partial k}{\partial x_j}\right)=P_k-\overline{\rho}\beta^* k\omega \tag{25}$$

$$\frac{\partial}{\partial x_j}\left(\overline{\rho}\widetilde{u}_j \omega-\left(\mu+\frac{\mu_T}{\sigma_\omega^\omega}\right)\frac{\partial \omega}{\partial x_j}\right)=\frac{\alpha P_k}{kT}-\frac{\overline{\rho}\beta\omega}{T}+\overline{\rho}S_\omega \tag{26}$$

where

$$P_k=S_{ij}\frac{\partial \widetilde{u}_i}{\partial x_j}, \quad T=\frac{1}{\omega} \tag{27}$$

$$-\overline{\rho u_i'' u_j''}=2\mu_T S_{ij}-\frac{2}{3}\left(\mu_T\frac{\partial \widetilde{u}_k}{\partial x_k}+\overline{\rho}k\right)\delta_{ij}. \tag{28}$$

The standard k-ω model. The following set of coefficients is used:

$$\alpha=\frac{13}{25}, \quad \beta=\beta_0 f_\beta, \quad \beta^*=\beta_0^* f_{\beta^*}, \quad \sigma_k^\omega=\sigma_\omega^\omega=2, \quad \beta_0=\frac{9}{125}, \quad S_\omega=0 \tag{29}$$

$$f_\beta=\frac{1+70\chi_\omega}{1+80\chi_\omega}, \quad \chi_\omega=\left|\frac{\Omega_{ij}\Omega_{jk}S_{ki}}{(\beta_0^*\omega)^3}\right|, \quad \beta_0^*=0.09 \tag{30}$$

$$f_{\beta^*}=\begin{cases}1, & \chi_k\leqslant 0\\ \dfrac{1+680\chi_k^2}{1+400\chi_k^2}, & \chi_k>0,\end{cases} \quad \chi_k=\frac{1}{\omega^3}\frac{\partial k}{\partial x_j}\frac{\partial \omega}{\partial x_j}. \tag{31}$$

The eddy viscosity is computed through

$$\mu_t=\overline{\rho}\frac{k}{\omega}. \tag{32}$$

The SST k-ω model. The SST k-ω model uses two sets of coefficients expressed in the following form:

$$C_\phi=F_1 C_{\phi 1}+(1-F_1)C_{\phi 2} \tag{33}$$

where

$$F_1=\tanh\left(\min\left[\max\left(\frac{\sqrt{k}}{0.09\omega y^*};\frac{500\nu}{y^{*2}\omega}\right);\frac{4\overline{\rho}k}{\sigma_{\omega 2}^\omega CD_{k\omega}y^{*2}}\right]^4\right) \tag{34}$$

$$CD_{k\omega}=\max\left(\frac{2\overline{\rho}}{\omega\sigma_{\omega 2}^\omega}\frac{\partial k}{\partial x_j}\frac{\partial \omega}{\partial x_j},10^{-20}\right). \tag{35}$$

The first set of coefficients is

$$\sigma_{k1}^\omega=1.176, \quad \sigma_{\omega 1}^\omega=2, \quad \beta_1=0.075, \quad \beta_1^*=0.09 \tag{36}$$

$$\alpha_1=\frac{\beta_1}{\beta_1^*}-\frac{1}{\sigma_{\omega 1}^\omega}\frac{\zeta^2}{\sqrt{\beta_1^*}}, \quad \zeta=0.41 \tag{37}$$

and the second is

$$\sigma_{k2}^\omega=1, \quad \sigma_{\omega 2}^\omega=1.176, \quad \beta_1=0.0828, \quad \beta_1^*=0.09 \tag{38}$$

$$\alpha_2=\frac{\beta_2}{\beta_2^*}-\frac{1}{\sigma_{\omega 2}^\omega}\frac{\zeta^2}{\sqrt{\beta_2^*}}, \quad \zeta=0.41 \tag{39}$$

$$S_\omega=2(1-F_1)\frac{1}{\sigma_{\omega 2}^\omega}\frac{1}{\omega}\frac{\partial \omega}{\partial x_j}\frac{\partial k}{\partial x_j}. \tag{40}$$

The eddy viscosity is computed by

$$\mu_T=\rho\frac{a_1 k}{\max(a_1\omega,\Omega^* F_2)} \tag{41}$$

where

$$a_1 = 0.31, \quad F_2 = \tanh\left(\left(\max\left(2\frac{\sqrt{k}}{0.09\omega y^*}, \frac{500\mu}{\overline{\rho} y^{*2}\omega}\right)\right)^2\right),$$

$$\Omega^* = \sqrt{\frac{1}{2}\Omega_{ij}\Omega_{ij}}. \tag{42}$$

For all models, the following expressions are valid:

$$S_{ij} = \frac{1}{2}\left(\frac{\partial \tilde{u}_i}{\partial x_j} + \frac{\partial \tilde{u}_j}{\partial x_i}\right), \quad \Omega_{ij} = \frac{1}{2}\left(\frac{\partial \tilde{u}_i}{\partial x_j} - \frac{\partial \tilde{u}_j}{\partial x_i}\right). \tag{43}$$

The relationship between ω and ε is given by

$$\omega = \frac{\varepsilon}{C_\mu k}. \tag{44}$$

References

[1] Nilsson, P., and Bai, X. S., 2000, ''Level-Set Flamelet Library Approach for Premixed Turbulent Combustion,'' Exp. Therm. Fluid Sci., **21**, pp. 87–98.

[2] Herrmann, M., 2001, ''Numerical Simulation of Premixed Turbulent Combustion Based on a Level Set Flamelet Model,'' Ph.D. thesis, Rheinisch-Westfählishe Technische Hochschule.

[3] Launder, B. E., and Spalding, D. B., 1974, ''The Numerical Computation of Turbulent Flows,'' Comp. Meth. In Appl. Mech., **3**(2), pp. 269–289.

[4] Chen, Y.-S., and Kim, S.-W., 1987, ''Computation of Turbulent Flows Using an Extended k-e Turbulence Closure Model,'' NASA, CR-179204.

[5] Wilcox, D. C., 2000, ''Turbulence Modeling for CFD,'' 2nd Ed., DCW Industries, Inc.

[6] Bai, X. S., and Fuchs, L., 1994, ''Modelling of Turbulent Reacting Flows Past a Bluff Body: Assessment of Accuracy and Efficiency,'' Comput. Fluids, **23**(3), pp. 507–521.

[7] Möller, S. I., Lundgren, E., and Fureby, C., 1996, ''Large Eddy Simulation of Unsteady Combustion,'' *Proceedings of the Combustion Institute*, **26**, The Combustion Institute, Pittsburgh, PA, pp. 241–248.

[8] Duwig, C., 2002, ''A Flamelet Formulation for Large Eddy Simulation,'' Proc. 9th European Turbulence Conference.

[9] Sjunnesson, A., Olovsson, S., and Sjöblom, B., 1991, ''Validation Rig—A Tool for Flame Studies,'' Volvo Flygmotor Internal Report, VFA 9370-308.

[10] Sjunnesson, A., Nelsson, C., and Max, E., 1991, ''LDA Measurements of Velocities and Turbulence in a Bluff Body Stabilized Flame,'' Volvo Flygmotor Internal Report, VFA 9370-307.

[11] Lien, F. S., Chen, W. L., and Leschziner, M. A., 1996, ''Low-Reynolds-Number Eddy-Viscosity Modeling Based on Nonlinear Stress-Strain/Vorticty Relations,'' Proc. 3rd Symp. Engineering Turbulence Modelling and Measurements, Crete, Greece.

[12] Menter, F., 1993, ''Zonal Two Equation k-ω Turbulence Models for Aerodynamic Flows,'' AIAA Paper, 93-2906.

[13] Engdar, U., and Klingmann, J., 2002, ''Investigation of Two-Equation Turbulence Models Applied to a Confined Axis-Symmetric Swirling Flow,'' C. R. Kleijn and S. Kawano, *4th International Symposium on Computational Technologies for Fluid/Thermal/Chemical Systems With Industrial Applications*, C. R. Kleijn and S. Kawano, eds., ASME, New York, **PVP-Vol. 448-2**, pp. 199–206.

[14] Nilsson, P., 2001, ''A Level-Set Flamelet Library Model for Premixed Turbulent Combustion,'' Ph.D. thesis, Lund Institute of Technology.

[15] Mauss, F., 1998, ''Entwicklung eines kinetischen Modells der Russbildung mit Schneller Polymerisation,'' Ph.D. thesis, Rheinisch-Westfählishe Technische Hochschule.

[16] Peters, N., 1993, ''Flame Calculation With Reduced Mechanism—An Outline,'' *Reduced Mechanism for Applications in Combustion Systems* (Lecture Notes in Physics), N. Peters and B. Rogg, eds., Springer-Verlag, New York, **m-15**, pp. 3–14.

[17] Peters, N., 2000, *Turbulent Combustion*, Cambridge University Press, Cambridge, UK.

[18] Klingmann, J., and Johansson, B., 1998, ''Measurements of Turbulent Flame Speed and Integral Length Scales in a Lean Stationary Premixed Flame,'' SAE Paper 981050.

[19] Damköhler, G., 1940, ''Der Einfuss der Turbulenz auf die Flammengeschwindigkeit in Gasgemischen,'' Z. Elektrochem. Angew. Phys. Chem., **11**, pp. 601–652.

[20] Müller, C. M., Breitbach, H., and Peters, N., 1994, ''Partially Premixed Turbulent Flame Propagation in Jet Flames,'' *Proceedings of the Combustion Institute*, **25**, pp. 1099–1106.

[21] Sussman, M., Smereka, P., and Osher, S., 1994, ''A Level Set Approach for Computing Solutions to Incompressible Two-Phase Flow,'' J. Comput. Phys., **114**, pp. 146–159.

[22] Versteg, H. K., and Malalsekera, W., 1995, *An Introduction to Computational Fluid Dynamics*, Longman Group Ltd.

[23] Computational Dynamics Limited, 2001, *Methodology, Star-Cd version 3.15*, U.K.

[24] Magnussen, B. F., and Hjertager, B. H., 1976, ''On Mathematical of Turbulent Combustion With Special Emphasis on Soot Formation and Combustion,'' Proceedings of the Combustion Institute, **16**, pp. 719–729.

[25] Klingmann, J., and Johansson, B., 1999, ''Interaction Between Turbulence and Flame in a S.I. Engine and in a Stationary Burner,'' SAE Technical Paper 1999-01-0569.

A. J. Riley
Department of Engineering,
University of Cambridge,
Cambridge CB2 1PZ, UK

S. Park
Department of Mechanical Engineering,
Massachusetts Institute of Technology,
Cambridge, MA 02139

A. P. Dowling[1]
Department of Engineering,
University of Cambridge,
Cambridge CB2 1PZ, UK

S. Evesque
Lehrstuhl fuer Thermodynamik,
Technische Universitaet Muenchen,
Boltzmannstrasse 15,
85748 Garching, Germany

A. M. Annaswamy
Department of Mechanical Engineering,
Massachusetts Institute of Technology,
Cambridge, MA 02139

Advanced Closed-Loop Control on an Atmospheric Gaseous Lean-Premixed Combustor

Active control of pressure oscillations has been successfully applied to a lean premixed prevaporized (LPP) combustion rig operating at atmospheric conditions. The design of the rig is based on the primary stage of the Rolls-Royce RB211-DLE industrial gas turbine. Control was achieved by modulating the fuel flow rate in response to a measured pressure signal. The feedback control is an adaptive, model-based self-tuning regulator (STR), which only requires the total time delay between actuation and response to achieve control. The STR algorithm achieves a reduction of up to 30 dB on the primary instability frequency. This performance was an improvement of 5–15 dB over an empirical control strategy (simple time-delay controller) specifically tuned to the same operating point. Initial robustness studies have shown that the STR retains control for a 20% change in frequency and a 23% change in air mass flow rate. [DOI: 10.1115/1.1788685]

Introduction

The use of lean premixed prevaporized (LPP) combustion in industrial gas turbines is a well-known method of producing low levels of NO_x and CO emissions. Such systems eliminate local regions of high temperature within the flame that increase the level of NO_x output. However, the practical application of such systems is challenged by the presence of strong pressure oscillations in the combustor at lean equivalence ratios.

The mechanism producing such flow instabilities is an interaction between unsteady combustion and acoustic waves. Unsteady combustion produces acoustic waves, which reflect at the boundaries of the system to further perturb the flame. This generates even more unsteady combustion. According to Rayleigh [1], if the rate of heat addition and the acoustic waves are in phase, the heat addition amplifies the acoustic waves and self-excited oscillations can occur. In gas turbines this basic mechanism has been seen to occur in various forms, leading to ''buzz'' in afterburners and low-frequency ''rumble'' in aeroengine combustors at idle/subidle conditions (Bloxsidge, Dowling, and Langhorne [2], Zhu, Dowling, and Bray [3]).

LPP combustion in industrial gas turbines is very susceptible to the self-excited oscillations. Small pressure fluctuations can produce resultant fluctuations in the air flow entering the premix ducts. This in turn produces small changes in the flame equivalence ratio, which, near the lean limit, lead to appreciable variations in the combustor reaction rate (Richard and Janus [4]). Amplification occurs when these variations in the combustor reaction rate reinforce the pressure oscillations. This may result in significant damage to the combustor and hence limit the operational envelope of the gas turbine.

As emissions regulations become stricter for both industrial gas turbines and aeroengines, control methods to reduce these detrimental effects are currently required by engine manufacturers. It is still difficult to predict the occurrence of combustion instabilities at the development stage of an industrial combustor. When instabilities are found during testing, the solutions currently available will be either passive or active techniques.

Passive control techniques tend to be tuned to particular frequencies and require substantial development time. They can address the high-frequency combustor modes that occur in LPP systems. However, passive absorption is ineffective at low frequencies unless very large volume resonators are used, which increase the mass, volume, and cost of the combustion chamber. Aspects such as low maintenance and high durability make passive techniques an attractive proposal above about 300 Hz (see Putnam [5] for a general discussion).

Active control techniques have a greater potential for more effective control across a range of running conditions, but there are a number of practical issues that still need to be resolved. Active feedback control uses a quantity that characterizes the instability as the input signal for a feedback loop: pressure perturbations and the fluctuating light emission from the combustion zone are commonly used input signals; however, these both have the disadvantage of introducing a long time delay to the control loop. Currently pressure transducers are more robust and easier to locate in a combustor, not requiring line-of-sight to the flame. In the future, a measurement of either velocity or equivalence ratio in the premix ducts would make the control task simpler. The feedback signal is processed by a controller and then sent to an actuator. The role of the actuator is to influence the acoustics and/or the combustion process in order to alter the energetics of the interaction between acoustic waves and combustion, hence damping out oscillations.

The application of feedback control was initially conducted using loudspeakers and fluctuating valves to modulate the air flow (see McManus, Poinsot, and Candel [6] for a review of this early work). However, this is not an easy task in full-scale applications and hence fuel modulation was found to be a more practical option. This was first applied to the problem of buzz in afterburners. Langhorne, Dowling, and Hooper [7] showed that only 3% modulation of the fuel, using a simple on–off valve, could lead to a

[1]Author whom all correspondence should be addressed.

Contributed by the International Gas Turbine Institute (IGTI) of THE AMERICAN SOCIETY OF MECHANICAL ENGINEERS for publication in the ASME JOURNAL OF ENGINEERING FOR GAS TURBINES AND POWER. Paper presented at the International Gas Turbine and Aeroengine Congress and Exhibition, Atlanta, GA, June 16–19; 2003, Paper No. 2003-GT-38418. Manuscript received by IGTI, Oct. 2002, final revision, Mar. 2003. Associate Editor: H. R. Simmons.

significant decrease in pressure levels for longitudinal disturbances in a simple premixed ducted flame. This was quickly followed by a full-scale demonstration of active control on the afterburner of a RB199 aeroengine (Moran, Steele, and Dowling [8]). The recent problems in industrial turbines lend themselves to a similar approach in terms of active control and also do not have the obvious restrictions of weight and safety that come with aeroengine technology.

Solenoid valves have been used in more recent studies to modulate the fuel since they have the potential to take advantage of linear control theory. Seume et al. [9] have reported the application of control to a Siemens heavy-duty gas turbine, using modulation of the pilot fuel supply as the actuator. Hibshman et al. [10] have also demonstrated control at full-scale, on a section of a liquid-fuelled lean premixed combustor. However, the limited bandwidth of solenoid valves means that they have only been applied to low frequency instabilities ($<$400 Hz). In addition, solenoid valves also have issues over durability and integrity that could lead to maintenance problems over the life cycle of an industrial gas turbine. Magnetorestrictive valves have the potential to overcome bandwidth limitations, so long as the authority of the valve can be maintained at higher frequencies (Neumeier and Zinn [11]).

The design of the control algorithm perhaps presents the biggest challenge to active control. The controller needs to be effective across all regimes of plant operation and must not go unstable, causing damage to the plant. Simple time delay controllers, forcing heat release out of phase to unstable pressure oscillations, have been successfully applied to full-scale rigs (Seume et al. [9], Hibshman et al. [10]). However, without knowledge of the open-loop transfer function, such a controller needs to be tuned in order to obtain the correct phase for each operating condition. In addition, new modes of instability have been amplified as the controller gain is increased (Langhorne, Dowling, and Hooper [7], Hibshman et al. [10]).

Other control techniques that have been applied to combustion problems include the least mean square (LMS) filter (Billoud et al. [12]) and an adaptive application of Rayleigh's criterion (Neumeier and Zinn [11]). LMS applications have had mixed results and have a number of unresolved issues, perhaps their greatest disadvantage is that there are no theorems to guarantee global stability. The adaptive Rayleigh technique addresses the fact that the dominant frequency can shift during out of phase forcing by determining the unstable frequency in real time. However, this controller still requires information from an open loop transfer function to obtain effective control.

The self-tuning regulator (STR) is an adaptive controller that can track changes in unstable frequencies and modify the control parameters appropriately. It does not require any prior knowledge of the transfer function for the system, except for the overall time delay between actuation and response (see Evesque, Dowling, and Annaswamy [13] for a detailed description). The end goal of the STR controller is to have an algorithm that can achieve robust control over a variety of combustors and operating conditions with very little prior knowledge of the system.

This paper presents results for the STR algorithm applied to a simplified atmospheric combustor rig, which is based on the Rolls-Royce RB211-DLE industrial gas turbine. Initially a short resume of the controller theory is given. The characteristics of the rig are then described, including the experimental setup, instrumentation, and the self-excited oscillations. The actuation system includes details of the high-speed valve, the effects of open-loop forcing and how the controller inputs were determined. This is followed by results for the STR algorithm including comparisons with a fixed time-delay controller, and finally a discussion and conclusions.

Background Theory

The STR design is based on a one-dimensional open-loop actuated combustion model, which is characterized by the transfer function

$$W(s)=\frac{P_{\mathrm{ref}}(s)}{V_c(s)}=W_0(s)e^{-s\tau_{\mathrm{tot}}}, \tag{1}$$

where $V_c(s)$ is the voltage sent to the actuator, $P_{\mathrm{ref}}(s)$ is the fluctuating pressure in the combustor, and τ_{tot} is the total time delay in the actuated system. Evesque, Dowling, and Annaswamy [13] show that an expression for $W_0(s)$, based on physical models of the flame dynamics, the actuator dynamics, and the acoustics of the combustor, can take a rational form (once a Padé approximation to the exponential terms has been applied) and hence

$$W(s)\cong k_0\frac{Z_0(s)}{R_0(s)}e^{-s\tau_{\mathrm{tot}}}, \tag{2}$$

where Z_0 and R_0 are two coprime (no common factors) and monic polynomials (the leading coefficient is unity). $W_0(s)$ is dominated by the properties of the actuator transfer function, which is assumed to have a low relative order ($\leqslant$2), positive gain, and no unstable zeros. The STR controller updates the control signal V_c as

$$V_c(t)=\mathbf{k}^T(t)\mathbf{d}(t)+\dot{\mathbf{k}}^T(t)\mathbf{d}_a(t), \tag{3}$$

$$\dot{\mathbf{k}}(t)=-\mathrm{sgn}(k_0)P_{\mathrm{ref}}\Gamma\mathbf{d}_a(t-\tau_{\mathrm{tot}}), \tag{4}$$

where $\mathbf{k}$ and $\mathbf{d}$ are the controller parameters and data vectors, respectively, defined as

$$\mathbf{k}(t)^T=(-k_1(t),-k_2(t),\lambda_n(t),\ldots,\lambda_1(t)), \tag{5}$$

$$\mathbf{d}(t)^T=(P_{\mathrm{ref}}(t),V(t),V_c(t-ndt),\ldots,V_c(t-dt)), \tag{6}$$

where $V(t)=[1/(s+z_c)][V_c(t)]$,[1] Γ is the diagonal matrix whose diagonal values, γ_1, γ_2, $\ldots$, γ_{n+2}, are the adaptation gains and $\mathbf{d}_a(t)=[1/(s+a)][\mathbf{d}(t)]$. In $\mathbf{k}$ and $\mathbf{d}$, k_1, k_2, and z_c represent the phase-lead components of a delay-free system as $V_c(t)=k_1[(s+z_c)/(s+z_c+k_2)][P_{\mathrm{ref}}(t)]$, the λ's are the Smith controller components to compensate the time delay of the system (Smith [14]), dt is the sampling time step and $ndt=\tau_{\mathrm{tot}}$.

It is shown in Evesque, Dowling, and Annaswamy [13] that the stability of the system is guaranteed with the adaptation law in Eq. (4) if the relative degree of $W_0(s)$ is less than or equal to 2 and $Z_0(s)$ (effectively the actuator transfer function) has all stable zeros.

The only knowledge that the STR requires of the transfer function, based on the assumptions above, is the total time delay between actuation and response. This is input into the control algorithm in terms of the sampling frequency and the number of Smith components. Other required inputs are the adaptation gains γ_1, γ_2, and γ_3 ($\gamma_3=\gamma_4\cdots\gamma_{n+2}$) and the characteristic constants, a and z_c.

Rig Characteristics

Rig Setup. The facility is a generic combustor designed to model the fuel injection/premix ducts of a Rolls-Royce RB211-DLE industrial gas turbine. The swirler unit is a scale model; however, the geometry of the plenum and combustor has been reduced to simple cylindrical pipes. This is because their influence on the instability can be easily quantified provided the experimental setup has well-defined acoustic boundary conditions. A schematic of the working section is shown in Fig. 1.

A metered and steady air flow is supplied to the plenum (128 mm ID) through a choked plate. This effectively decouples the air

[1] $R(s)[\cdots]$, where $R(s)$ is a rational function and the variable s denotes an operator of d/dt; thus $V(t)=[1/(s+z_c)][V_c(t)]$ means that $dV(t)/dt+z_cV(t)=V_c(t)$.

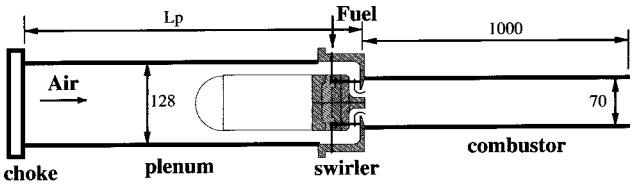

Fig. 1 Schematic of the rig downstream of the choke plate, showing the plenum/combustion chambers and the swirler unit (all dimensions in mm, diagram not to scale)

supply from pressure fluctuations in the working section, enabling air to be supplied at a constant mass flow rate (m_a) and providing a well-defined acoustic boundary condition. The maximum mass flow rate available is approximately 0.2 kg/s; however, the typical operating range is 0.03–0.08 kg/s. The downstream end of the plenum chamber incorporates an annular section prior to the swirler unit. The swirler exit is connected to a quartz tube (70 mm ID) along which combustion takes place. This provides ideal optical access to the flame region. The exit of the tube is open to atmospheric pressure and is not choked.

The fuel (ethylene, C_2H_4) and air are mixed using a Rolls-Royce DLE counterrotating, radial swirler unit, scaled to fit the existing facilities (approximately 54%). Once the airflow has passed into the annular section, it is split into two streams that flow through concentric channels. In the channels, blades are fixed to induce two counterrotating flows. The fuel is injected upstream into the annular channels through eight cylindrical bars each fitted with two exit holes of 1.0 mm diameter (see Fig. 2). A pressurized commercial cylinder is used to supply the fuel for the swirler unit. The fuel line comprises a pressure regulator, control valve, and turbine flow meter (see Fig. 4). Together with suitably located pressure transducers and thermocouples, the turbine flow meter is used to provide a mass flow reading. Fuel mass flow rates (m_f) are in the range 1.6–3.0 g/s in order to obtain equivalence ratios (ϕ) from 0.5 to 1.0 for the air mass flow rates used in these tests.

The airflow rate, the equivalence ratio, and the geometric configuration (including the fuel bars) are all used to define the operating points of the combustor rig.

Instrumentation. The feedback signal for the control algorithms is provided by a Kistler piezoelectric pressure transducer (type 601A) measuring combustor pressure 700 mm downstream of the swirler unit. The transducer is located in a side arm, 30 mm from the combustor wall. The semi-infinite line technique (Englund and Richards [15]) is used to provide adequate thermal isolation from the hot products of combustion, while also ensuring that the pressure signal at the transducer is not distorted by reflecting waves.

A photomultiplier, together with a uv filter, was used to look at the heat release rate of the flame. The uv narrow-band filter is centered at 310 nm in order to look at the radiation emitted from OH radicals. This has been shown to linearly track the heat release rate for premixed flames (Drederichsen and Gould [16]).

The two closed-loop control algorithms proceed in three steps: acquisition of the unsteady pressure signal, processing of the control signal by the control algorithm in real time, and then sending of the resulting signal to drive the DDV valve. The algorithms have been implemented on a 32-bit M62 digital signal processing (DSP) board, developed by Innovative Integration, based on the Texas Instruments TMS320C6201 processor.

Unsteady measurements of pressures, light, and valve displacements are recorded on a PC-based data acquisition system incorporating a 16-channel PCI-MIO-16XE-10 acquisition board from National Instruments. The signals are conditioned using an isolation amplifier and an eighth-order elliptic low-pass filter. The cutoff frequency is automatically set to one-third of the sampling rate (5 kHz). The sound pressure level (SPL) data presented are acquired over periods of up to 20 s and averaged over the maximum number of 1-s frames available.

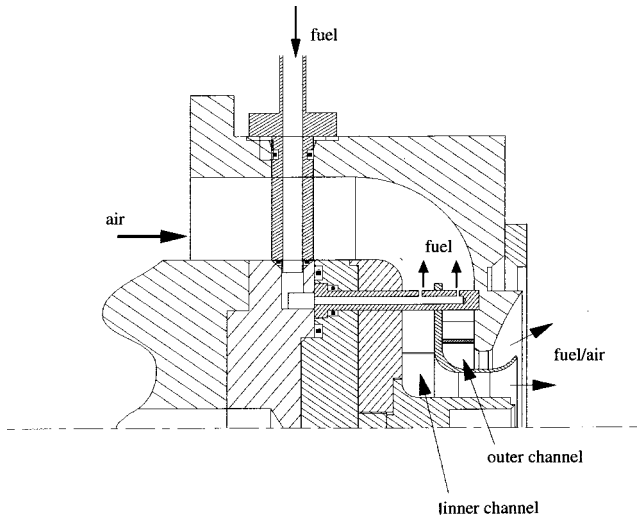

Fig. 2 Detailed schematic showing a cross section of the swirler unit and the orientation of the fuel injection bars

Self-Excited Oscillations. The instability characteristics of the rig have been investigated for a range of flow conditions and plenum and combustor lengths. Within the typical envelope of the operating parameters ($m_a = 0.03-0.08$ kg/s, $\phi = 0.5-1.0$), several intense combustion instabilities with multiple frequencies have been observed. Typical pressure spectra contain dominant peaks at one or two low frequencies (100–300 Hz) and an additional high-frequency peak (550–700 Hz). Previous work has shown that these frequencies relate approximately to half-wavelength modes of the plenum and to quarter-wavelength modes of the combustor. The reason for this is that the premix ducts have a much higher velocity than either the plenum or the combustor chambers, leading to a high-impedance boundary condition. Hence the plenum modes are approximately those for a duct with two high-impedance ends. Similarly, the combustor modes are approximately those for a duct with a high-impedance end and an open end.

In the current set of feedback control tests the experimental data has been obtained in the ranges $m_a = 0.03-0.05$ kg/s and $m_f = 1.6-2.5$ g/s, resulting in $\phi = 0.5-0.75$. For the geometric configuration shown in Fig. 1 ($L_p = 1.73$ m, $L_c = 1.0$ m) the rig exhibits a 207-Hz plenum mode instability. In order to obtain different unstable frequencies the plenum length was varied ($L_p = 1.46$, 1.73, 1.97 m). The pressure spectra for these cases all contain dominant low-frequency peaks (<300 Hz) with magnitudes of up to 165 dB that set an ideal challenge for active control (Fig. 3).

These dominant modes correspond to the second harmonic of the plenum (wavelength $= L_p$). The fundamental and the higher harmonics are also present. In addition, for the $L_p = 1.97$ m case there is a peak at 244 Hz that corresponds to the quarter-wavelength mode of the combustor tube. The appearance of the combustor modes is not as predictable as the plenum modes.

Actuation System

Valve Setup. Actuation for control was achieved using a high-frequency valve to modulate the fuel flow rate into the swirler and hence produce variations in equivalence ratio in the premix ducts. This leads to unsteady combustion with a significant time delay that needs to be accounted for in the control strategy. A pressure transducer located in the combustor section provides feedback for the control algorithms.

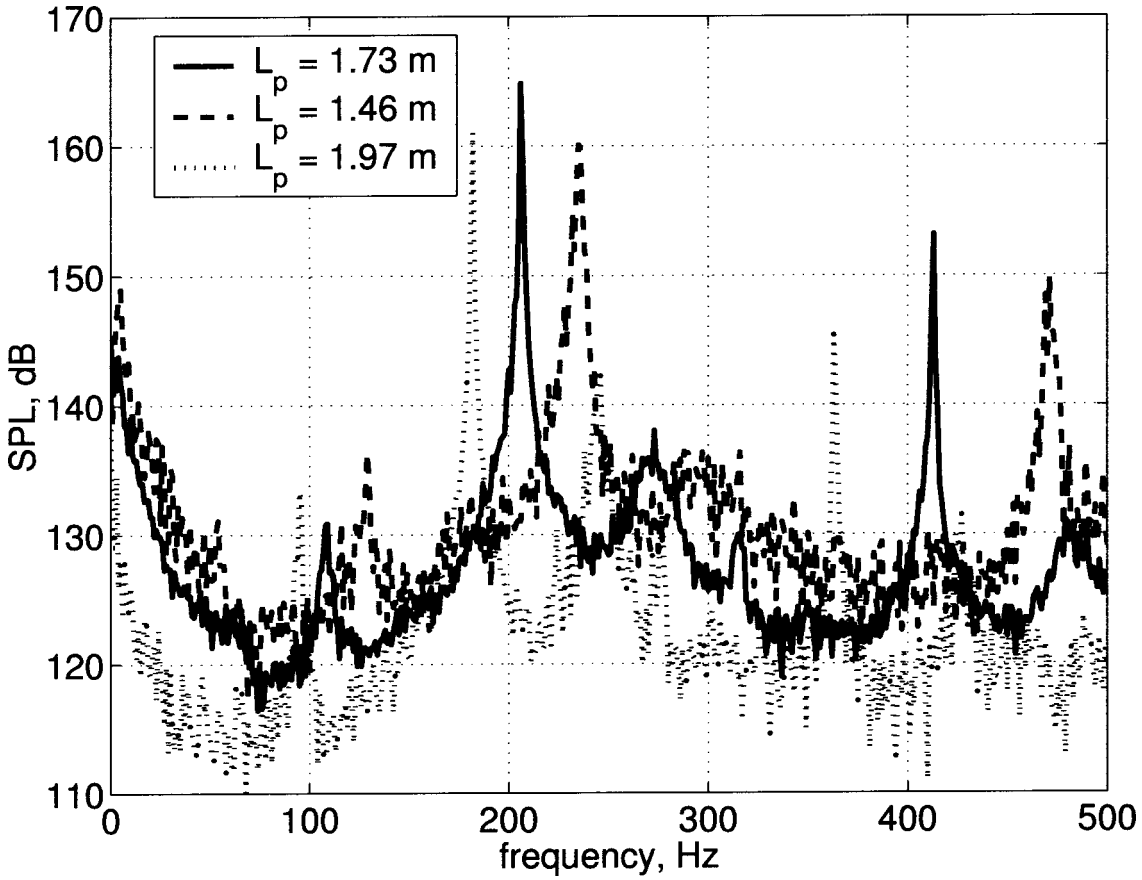

Fig. 3 Sound pressure level (SPL) spectrum of the self-excited combustion oscillations; $m_a = 0.04$ kg/s, $\phi = 0.7$

A direct drive valve (DDV) manufactured by Moog was used to modulate the fuel flow, as shown in the fuel system schematic (Fig. 4). The DDV uses a linear force motor where the stroke is proportional to the applied voltage. The spool in the DDV can be moved from the fully closed position (no flow through the valve, 0% open) to the fully opened position (maximum flow through the valve, 100% open) by increasing the applied voltage from 0 to 10 V. The large pressure drop across the regulator and the inertia of the flowmeter means that the mass flow rate is effectively constant upstream of the plenum, in spite of the high-frequency modulations downstream. The plenum provides mass storage, so that the fuel flow rate through the DDV can change as its open area is modulated. The pipe length between the DDV and the swirler unit was kept as short as possible in order to decrease the attenuation and time delay. The transfer function between the spool position and the input voltage shows uniform gain for frequencies below 350 Hz. The phase change throughout this frequency range is linear and indicates a time delay equal to 1.5 ms. However, the transfer function between the fuel flow rate and input voltage is of more direct relevance. This was investigated in a series of bench tests with different fuel bar exit areas. These tests showed that reducing the valve oscillation frequency and the pressure drop across the valve and increasing the fuel bar exit area were positive factors in achieving modulation of the fuel flow. Based on these results the total fuel bar exit area was chosen to be 12.6 mm^2 (eight cylindrical bars each fitted with two exit holes of 1.0 mm diameter).

Figure 5 shows the percentage increase obtained in the fuel jet velocity rms, with a decrease in valve frequency. The mean mass flow was kept constant at 1.62 g/s, corresponding to a $\phi = 0.6$ for a $m_a = 0.04$ kg/s (standard test case). The valve inlet voltage was oscillated harmonically at maximum amplitude around the 50% open position, i.e., from 0 to 10 V.

A similar increase in fuel jet velocity rms was found for a decrease in the mean mass flow through the valve, which corresponds to a reduction in pressure drop for a fixed exit area. However, the effect of a variation in the mean fuel mass flow was not as significant as the effect of the valve frequency, for the equiva-

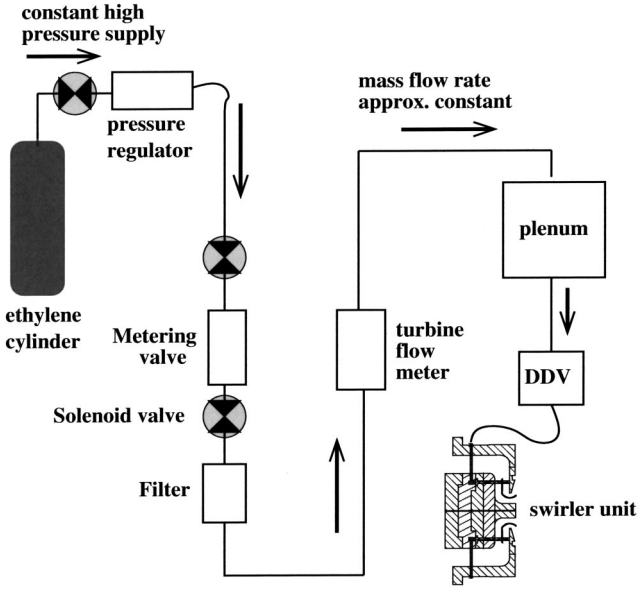

Fig. 4 Detailed schematic of the fuel system, together with the DDV and the plenum chamber

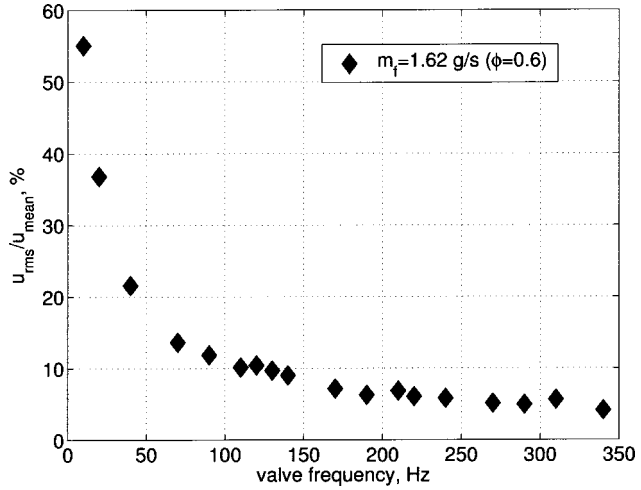

Fig. 5 Variation in the fuel jet velocity rms with valve frequency for maximum amplitude harmonic oscillations around 50% open position; $m_f = 1.62$ g/s ($\phi = 0.6$ for an air mass flow of $m_a = 0.04$ kg/s)

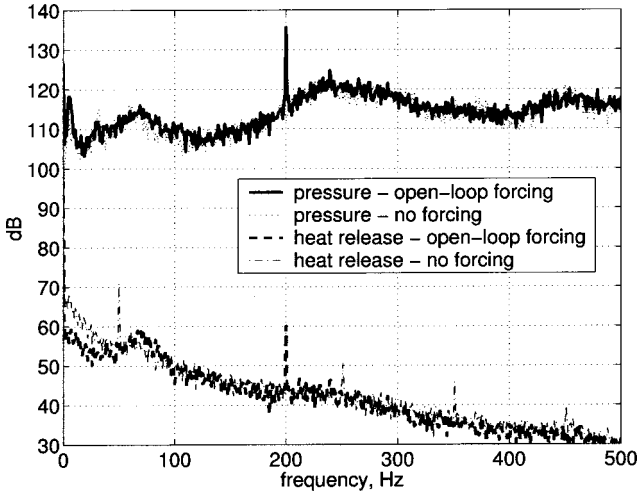

Fig. 6 The effect on the combustor pressure and the OH emission of forcing the fuel flow at 200 Hz; the valve driven harmonically at maximum amplitude, about 50% open position; $m_a = 0.04$ kg/s, $\phi = 0.60$, $L_p = 0.41$ m, $f_{DDV} = 200$ Hz

lence ratios and air mass flow rates used in these experiments. For the current set of tests ($m_a = 0.03–0.05$ kg/s and $\phi = 0.5–0.75$), the valve produces 5.0–10.0% rms fuel modulation in the valve frequency range 150–250 Hz.

Open-Loop Forcing. The response of the flame to the valve at a forcing frequency of 200 Hz is presented in Fig. 6, in terms of the combustor pressure and the unsteady heat release monitored through the OH radical light emission. In this test a much shorter plenum has been used increasing the fundamental resonance frequency of the chamber to above 400 Hz ($L_p = 0.41$ m). This results in no self-excited oscillations in the frequency range of interest and hence improves the signal-to-noise ratio in the open-loop tests. The effect of this change can be seen by comparing Figs. 3 and 6. Without forcing there are no narrow-band peaks in the pressure spectrum and the unsteady heat release decreases with frequency (the peak at 50 Hz is due to electrical noise). Forcing the DDV harmonically at maximum amplitude shows an increase of up to 17 dB above background noise throughout the valve frequency range 50–300 Hz.

Determination of τ_{tot}. The total time delay, τ_{tot}, is needed to determine the adaptation law in Eq. (4) and n in Eq. (5), respectively. This can be determined through open-loop forcing and investigating the transfer function $W(s) = P_{ref}/V_c$ at a range of frequencies through system-identification tests (Murugappan et al. [17]). At the desired operating condition a simple time-delay controller was applied, in order to minimize the self-excited oscillation. In addition to this a sine sweep of $V_c(t)$, with changing frequency from 40 to 430 Hz, was also supplied to the DDV valve. The resulting pressure data were postprocessed with a band-pass filter (80–230 Hz) to better capture dynamics around the unstable frequency. $W(s)$ was obtained using a linear autoregressive with external input (ARX) model-structure (Ljung [18]) and τ_{tot} was found to be 9.6 ms.

Initial tests with the STR were conducted using a system-identification reduced-order model to obtain optimal starting values for the control parameters. To obtain this another system identification was carried out using $V_c(t-\tau_{tot})$ and $P_{ref}(t)$ to yield an ARX model, which resulted in a $W(s)$ given by

$$W(s) = 0.8787 \frac{s^3 + 1071s^2 + 2.105e6s + 7.894e6}{s^4 + 24.75s^3 + 2.366e6s^2 + 3.312e7s + 1.169e12} \times e^{-0.0096s},$$

where $\mathrm{sgn}(k_0) = -1$ [see Eq. (2)]. This negative gain was an unexpected result. A system identification of the fuel supply system found that the transfer function contained three low-frequency poles. These produced a change in phase at the unstable frequency that could account for the negative gain. The additional dynamics in the fuel supply system were not addressed in the model (see the section entitled "Background Theory"). For the current tests the sign of k_0 was changed in the adaptation scheme [Eq. (4)].

We note that identifying $\mathrm{sgn}(k_0)$ and τ_{tot} simultaneously, rather than sequentially, will warrant the identification of a high-order system, which is prone to large numerical errors. It should also be noted that in the present setup, no other parameters of the transfer function $W(s)$ are required to design the adaptive controller except the values of $\mathrm{sgn}(k_0)$ and τ_{tot}.

In the current tests, the user inputs into the STR were a sampling rate of 2 kHz, $n = 19$, $a = z_c = 1000$, $\gamma_1 = \gamma_2 = 100{,}000$, and $\gamma_3 = 10$, unless otherwise stated. The reason of reduced sampling rate from 5 to 2 kHz is to minimize computation time for the λ's. This is due to the number of λ's, n, being inversely proportional to the sampling rate, dt, by $n = \tau_{tot}/dt$. The γ's are determined to have reasonable settling time and overshoot of control parameters. Depending on the speed of change of the combustion characteristics, desired settling time of the controller, and valve saturation, these values must be fine-tuned to get the optimal "transient" response. They do not, however, affect the steady-state performance.

Results

Nominal Case: $L_p = 1.73$ m. Initial tests of the STR controller produced reductions in noise that were 5–15 dB larger than those gained with the appropriately tuned fixed time-delay controller. However inspection of a typical time series indicates that control is lost intermittently, as shown in Fig. 7, which degraded the performance of the STR.

Analysis of the valve time series, just prior to the controller divergence, suggested that there was significant control action around 100 Hz growing rapidly in amplitude. A band-pass filter (120–500 Hz) was introduced between detection and the controller input to remove the low-frequency dynamics. The filter generated approximately a 20 deg phase lead at 200 Hz. In the range 170–300 Hz, the impact of the filter dynamics on the overall system was negligible. Figure 8 shows the resulting improvement in performance. The controller is turned on at 4.4 s and stabilization is achieved in about 3.6 s. The control parameters such as k_1

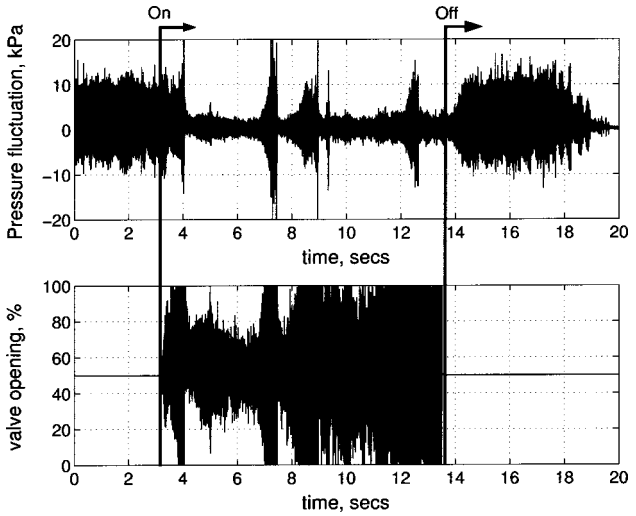

Fig. 7 Time series showing the low-frequency fluctuations present in the combustor when the STR controller is activated; m_a=0.04 kg/s, ϕ=0.65, τ_{tot}=9.6 ms, L_p=1.73 m, zero initial conditions for control parameters

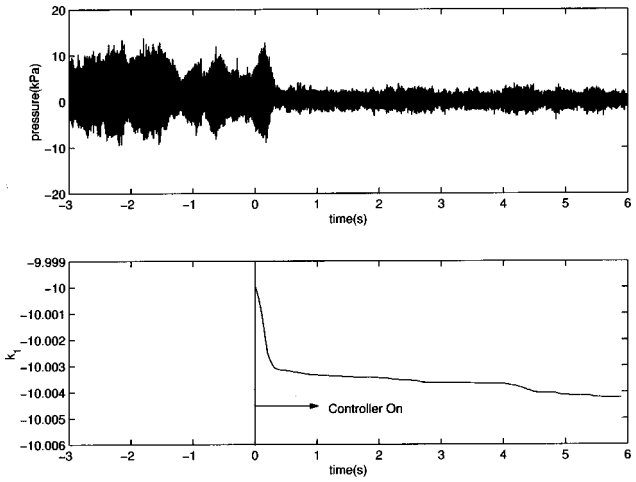

Fig. 9 Time series showing the improvement in the settling time of the STR controller when appropriate initial conditions are chosen; m_a=0.04 kg/s, ϕ=0.65, τ_{tot}=9.6 ms, L_p=1.73 m, initial conditions of $k_1=-10$, $k_2=10$

and k_2 start at zero and converge to a specific value, as shown for k_1 in Fig. 8. The zero initial conditions simply imply that the controller does not know the combustion dynamics initially and these values are automatically tuned by the STR to give optimal performance. However, it should be mentioned that the settling time for other test cases, under nominally the same operating conditions, can be large (up to 7 s). This was due to two reasons: (1) higher pressure oscillations (more than 10 kPa) made the valve saturate (already present to some degree in Fig. 8) and (2) zero initial conditions of the control parameters requires time for the controller to search for the optimal control parameters. When the pressure amplitude was smaller than 10 kPa and the initial conditions were chosen based on $W(s)$, the settling time could be reduced to less than 1 s as shown in Fig. 9. Figure 10 shows a typical pressure spectrum for the control on–off cases where there is a reduction of approximately 15 dB by the fixed time-delay controller and 30 dB for the STR controller at the 207-Hz instability. (Note: all pressure spectra presented are for prefiltered data). One of the reasons for the limited performance of the time-delay controller was due to a low-frequency mode, which can be seen in Fig. 10 and is similar to that seen in Fig. 7. In some cases, when this low-frequency mode was not present, the time-delay controller was able to reduce pressure oscillations up to 26 dB.

Robustness Studies. As mentioned previously, the STR controller can automatically tune its control parameters when the combustion dynamics change. In this section, we carry out extensive robustness studies with respect to changes in the resonant frequency, total time delays, changes in operating conditions, and initial conditions of control parameters.

Changes in the Resonant Frequency. The resonant frequency varies as the temperature of a combustor changes. Banaszuk, Zhang, and Jacobson [19] reported a 20% change in resonant frequency over a 9-s period during warming up of an experimental combustor. As a result, at a start up or during thrust change, the STR needs to be able to cope with possible changes in frequency. As explained in the section entitled "Self-Excited Oscillations,"

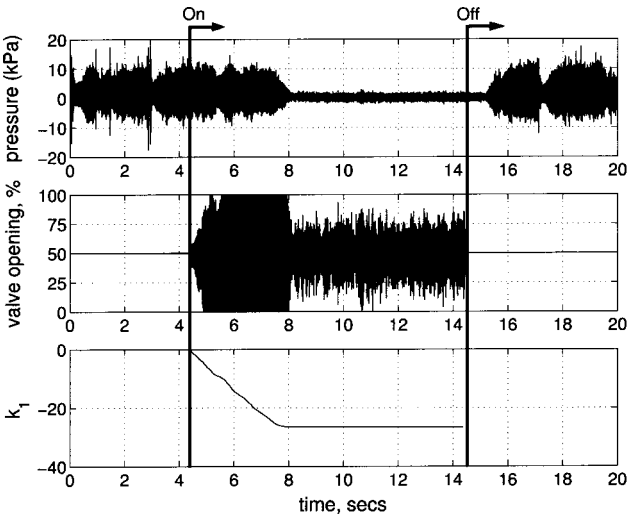

Fig. 8 Time series showing the improvement on the pressure fluctuations in the combustor gained by filtering the STR controller input; m_a=0.04 kg/s, ϕ=0.65, τ_{tot}=9.6 ms, L_p=1.73 m, controller input filter is 120–500 Hz

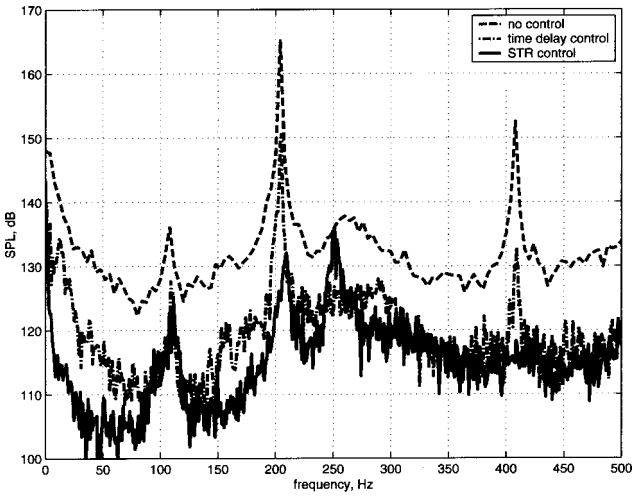

Fig. 10 SPL spectra showing the reduction in noise when the STR and the delay controllers are turned on; m_a=0.04 kg/s, ϕ=0.65, τ_{tot}=9.6 ms, L_p=1.73 m; controller input filter is 120–500 Hz

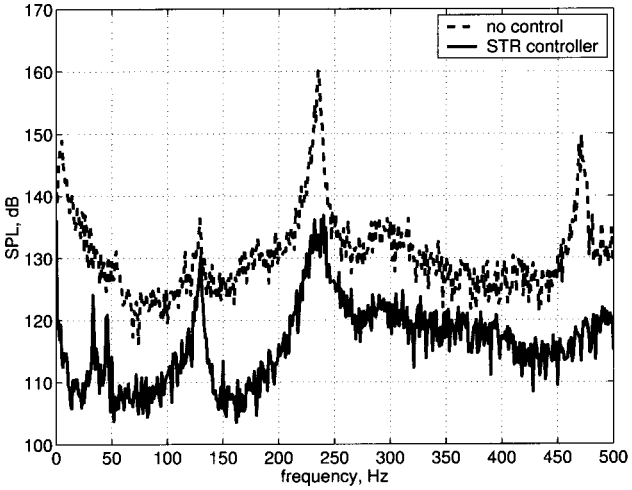

Fig. 11 SPL spectra showing the reduction in noise when the STR is turned on in the shorter plenum case; m_a=0.04 kg/s, ϕ=0.70, τ_{tot}=9.6 ms, L_p=1.46 m, controller input filter is 120–500 Hz

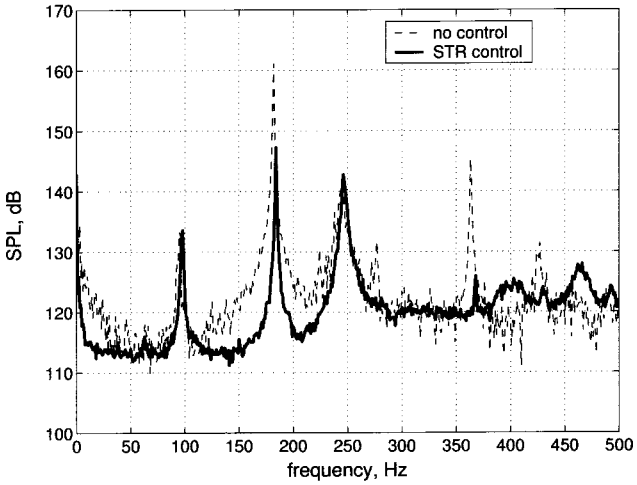

Fig. 12 SPL spectra showing the reduction in noise when the STR is turned on in the longer plenum case; m_a=0.04 kg/s, ϕ=0.65, τ_{tot}=9.6 ms, L_p=1.97 m, controller input filter is 120–500 Hz

the resonant frequency was varied by changing the plenum length L_p. Initially, L_p was changed from 1.73 to 1.46 m and both the time delay and the STR controllers were tested with input parameters predetermined in the nominal case (L_p=1.73 m). Note: the STR still had zero initial conditions for the control parameters. Figure 11 shows the pressure spectrum and as expected, the resonant frequency moved to 240 Hz. The STR controller produced a 28-dB reduction at the unstable frequency. It is worth noting that k_1 converges to positive values of approximately 25–30 for this case, whereas it converges to a negative value in the nominal case in Fig. 8. The simple time-delay controller, using time-delay/gain inputs determined in the nominal case, did not have any effect and has not been included in Fig. 11.

Next, L_p was increased to 1.97 m, and the delay and the STR controllers were tested with parameters predetermined in the nominal case. Once again the time-delay controller had no significant effect. Figure 12 shows the pressure spectrum for the no control and STR cases and interestingly, two modes at 180 and 244 Hz were observed in the no-control case. The latter is the quarter-wavelength mode for the combustor tube. The optimal k_1 values are different for these two modes and hence k_1 is found to oscillate as it tries to control first one and then the other mode (Fig. 13). Finally, k_1 converges to a value that is in between these two optimal values. (Note: average k_1 is negative in this case.) Large adaptation gains may generate overshoot during convergence, but this can be reduced using a smaller adaptation gain, γ_1. When the adaptation gain was halved to γ_1=50,000, k_1 showed less oscillatory behavior (Fig. 13) and the resulting pressure reduction was 15 dB (4 dB lower than that achieved with γ_1=100,000).

For both cases described above, the performance of the simple time-delay controller could be improved by optimizing the time-delay input. However, for L_p=1.46 m only a 7-dB reduction was achieved, compared with 28 dB for the STR. For L_p=1.97 m, a 22-dB reduction was achieved, compared with only 15 dB for the STR. In this case, though, there was also a 10-dB increase at the fundamental.

Variation in Total Time Delay. The impact of a change in the total time delay on the performance of the STR controller was also evaluated. Such a change can occur with a change in the flow rate or a change of the burning zone location. Instead of changing the operating conditions, the total time delay in the STR was changed by τ_Δ. Experimental results show that the STR still maintains control up to a maximum of τ_Δ=1.1 ms less than the τ_{tot} derived from the system identification. However, control was lost if τ_{tot} was increased beyond 9.6 ms. Please note that the algorithm is not currently capable of adapting to a variable τ_{tot}.

Changes in Flow Rate and Equivalence Ratio. The robustness of the STR controller was investigated with respect to changes in the mass flow rate of the air. The controller was turned on at the nominal case with an air flow rate of 0.04 kg/s, which was then decreased slowly by 23% (0.009 kg/s) over 100 s while keeping the equivalence ratio constant. Figure 14 shows that the controller was able to maintain control as the flow rate changes. After 100 s, once the controller was turned off, the pressure amplitude returned to previous levels, indicating that the final operating condition was also unstable. The air mass flow rate was also increased from 0.04 to 0.055 kg/s. However, at higher air flow rate, the combustion was stable. Also, the controller parameters remained constant due to low amplitude of pressure oscillations.

The rig exhibits an unstable mode at 207 Hz when m_a = 0.04 kg/s and ϕ=0.6–0.7, and ϕ=0.6 is very close to the flammability limit. The STR controller maintains control as ϕ is varied

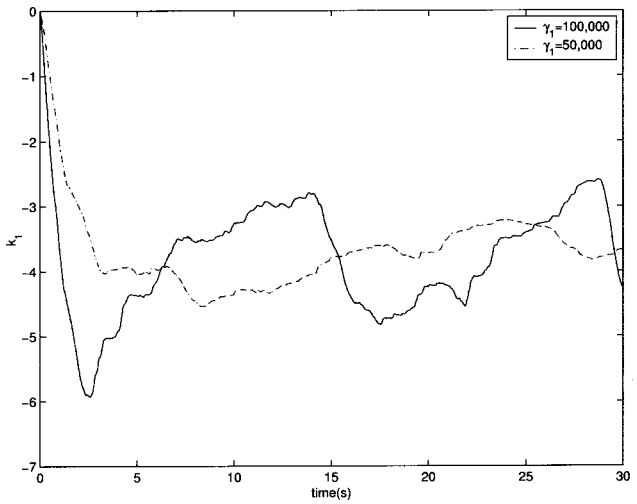

Fig. 13 Change of the controller parameter, k_1 in a longer plenum case with different adaptation gain γ_1; m_a=0.04 kg/s, ϕ=0.65, τ_{tot}=9.6 ms, L_p=1.97 m

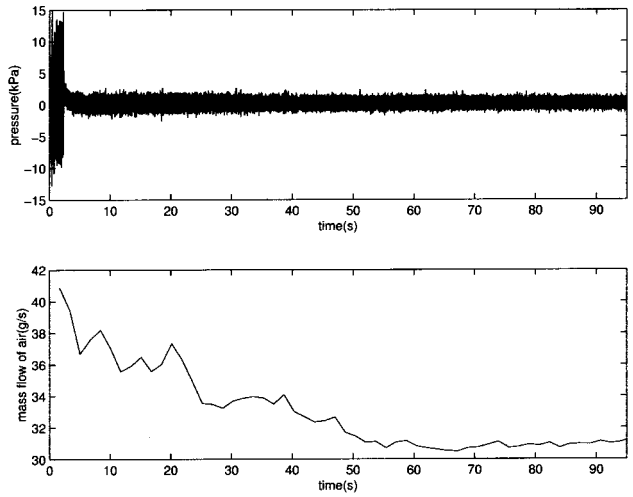

Fig. 14 Time series showing the effect of the STR controller with changes in the mass flow rate of air, while the equivalence ratio is kept constant; ϕ=0.7, L_p=1.73 m, controller input filter is 120–500 Hz

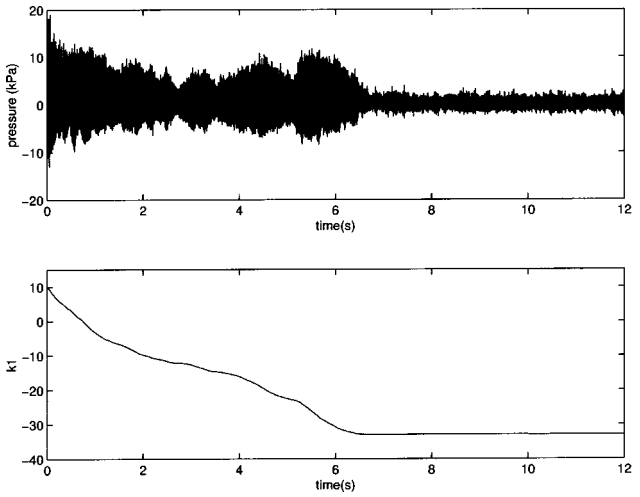

Fig. 15 Time series showing the effect of the STR controller with incorrect initial condition in the control parameter; m_a = 0.04 kg/s, ϕ=0.65, τ_{tot}=9.6 ms, L_p=1.73 m, controller input filter is 120–500 Hz

within this range. At ϕ larger than 0.75, a combustor tube mode above 600 Hz was excited. As a result, the STR can only be tested in the range ϕ=0.6–0.7 due to bandwidth limitation of the DDV valve and the flammability limit.

Initial Conditions of the Control Parameters. As mentioned earlier, carefully chosen initial conditions can reduce the settling time of the STR significantly. We can also test the sensitivity of the STR controller to the initial conditions of control parameters, by deliberately setting the control parameters far from the optimum values. The control gain, k_1, was set to +10 initially, which is opposite in sign to the optimal value. Figure 15 shows that the STR still converges to the optimal parameters and that it is robust with respect to the initial conditions of the control parameters. However, the settling time increased by an order of magnitude over that shown in Fig. 9, where the initial condition of k_1 is set close to the optimal value.

Discussion

Forced unsteady combustion has been successfully achieved by using a high-frequency valve to modulate the rate of fuel injection into a Rolls-Royce RB211-DLE swirler unit. The DDV valve can exert significant authority over the combustion system for frequencies in the range 50–300 Hz. This has allowed the application of feedback control algorithms to the system in an attempt to reduce the amplitude of certain unstable frequencies.

The STR adaptive controller has been designed to account for variations in the unstable frequency. It has a fixed structure, consisting of a phase-lead compensator and a Smith controller, and theoretically only requires the total time delay between actuation and response, since the control parameters are found adaptively. Tests on the current combustion rig, which has a significant time delay (9.6 ms), have shown that it can successfully reduce noise levels by an additional 5–15 dB compared to a tuned fixed time-delay controller pulsing the same amount of fuel (6.5%). Better performance of the STR controller in a nominal condition can be attributed as follows: (1) Since the closed loop is essentially a delay-free system due to the design of the STR, the transport delay does not interact with the inherent dynamics of the combustor. Hence, it is not likely to introduce secondary peaks. (2) Due to (1), larger gain is permitted, which results in larger pressure reduction at the unstable frequency without generating secondary peaks.

System identification of the rig, in order to test the assumptions of the modeling, has found that $\mathrm{sgn}(k_0)=-1$ [see Eq. (2)]. Although this does not affect the stability of the system, it does suggest that there are unmodeled dynamics in the system. The source of this unmodeled dynamics is found to be the fuel supply system. In terms of future applications of the STR, this would not be a detrimental result, since actuation systems are easily characterized without the need for combustion.

Robustness studies have been started to test the STR controller over a wide range of frequencies and operating conditions. The initial results have been encouraging. With changes in the resonant frequency of 20%, the STR controller was able to adjust its control parameters and produce a significant pressure reduction. Even with two unstable modes, the STR controller adjusted its parameters to compromise and produce a pressure reduction in both modes. The algorithm is not currently capable of adapting to a variable τ_{tot}, however 1.1-ms delay change was achievable. For air flow rate and equivalence ratio, 23% and 14% changes, respectively, were allowable.

Due to limited authority of the actuator and no prior knowledge of combustion dynamics (zero initial conditions of control parameters), the settling time could be large (up to 7 s). Also, when two unstable modes are present, large adaptation gain produced overshoot in control parameters. These suggest that adaptation gain and initial conditions of control parameters need to be selected carefully to make the STR controller better perform in the ''transient region.'' After the control parameters were converged, the performance of the controller was not changed with changes in the adaptation gain and the initial conditions.

The simple fixed time-delay controller, which was used as a benchmark for the STR, was designed to generate canceling pressures waves and hence stabilize the combustor, as predicted by the Rayleigh criterion. This led to a noise reduction of 15–26 dB at the primary instability frequency for L_p=1.73 m. However, this kind of controller is limited by the constant time delay employed, as demonstrated by the lack of success once the instability frequency was changed. Detailed knowledge of the phase of the system transfer function and the frequency of instability is needed to choose this time delay appropriately, since the value of the time delay must be continually adjusted as the operating conditions vary and the frequencies of instability change. The advantage of the STR is that theoretically it does not require such detailed information regarding the open-loop transfer function and the frequency of instability, needing only the total time delay of the

system, which is independent of frequency. In addition, the combustion dynamics do not interact with a delay in the system.

The hope for future applications of the STR on different rigs is that once the actuation system is characterized, the total time delay of the system can be estimated based on a knowledge of the convection and combustion properties of the rig. It has been demonstrated that the STR has a stability band of approximately 1 ms in the present setup, in terms of total time delay. If the convection time delay was shown to be the dominant factor over the combustion time delay (time delay once the fuel has arrived in the combustion zone), then a simple lookup table could be used whenever the operating conditions are changed.

Conclusions

- Closed-loop control of a generic LPP combustor has been achieved using a high-speed solenoid valve to modulate the rate of fuel injection into a scaled Rolls-Royce RB211-DLE swirler unit and hence force unsteady combustion.
- An STR control algorithm has outperformed a simple time-delay controller at a single operating point by 5–15 dB.
- The STR has been shown to maintain control at different unstable frequencies, and also while adapting to changing operating conditions, without any additional information input to the controller.
- Initial robustness studies have shown that the STR algorithm has the potential to act as a controller in an industrial environment, where limited system information and a range of frequencies/operating conditions are encountered.

Acknowledgments

The authors would like to gratefully acknowledge the support of Trinity College, Cambridge, the Cambridge European Trust, the European Union Brite Euram Programme Research Project ACIACOC (Project No. BE 97 4324), the Engineering and Physical Sciences Research Council ESR21 Programme, the National Science Foundation (Grant No. ECS 9713415), and the Office of Naval Research (Grant No. N00014-99-1-0448). P. Ford has helped extensively in running the rig.

Nomenclature

γ = STR adaptation gains
τ_Δ = Change in total time delay
τ_{tot} = Total time delay
ϕ = Equivalence ratio
ω = Angular frequency
λ = Smith controller component in the STR
a = Characteristic constant of first-order filter
DDV = Direct drive valve
dt = Sampling time step
f_{DDV} = Valve oscillation frequency
k_0 = Gain of the combustion transfer function
k_1 = STR gain parameter
k_2 = STR gain parameter
m_a = Air mass flow
m_f = Fuel mass flow
n = Number of the Smith controller component
L_p = Plenum length
L_c = Combustor length
P_{ref} = Combustor pressure
s = Laplace variable
SPL = Sound pressure level
STR = Self-tuning regulator
$R_0(s)$ = Poles of the combustion transfer function
t = Time
u_{mean} = Mean fuel jet velocity
u_{rms} = rms fuel jet velocity
V_c = DDV input voltage
$W(s)$ = Combustion transfer function
$W_0(s)$ = Combustion transfer function without delay
$Z_0(s)$ = Zeros of the combustion transfer function
z_c = Location of the zero of the phase-lead component in the STR

References

[1] Rayleigh, Lord, 1896, *The Theory of Sound*, Macmillan, London.
[2] Bloxsidge, G. J., Dowling, A. P., and Langhorne, P. J., 1988, "Reheat Buzz: An Acoustically Coupled Combustion Instability. Part 2. Theory," J. Fluid Mech., **193**, pp. 445–473.
[3] Zhu, M., Dowling, A. P., and Bray, K. N. C., 2000, "Forced Oscillations in Combustors With Spray Atomisers," ASME paper 2000-GT-108.
[4] Richard, G. A., and Janus, M. C., 1998, "Characterization of Oscillations During Premix Gas Turbine Combustion," ASME J. Eng. Gas Turbines Power, **120**, pp. 294–302.
[5] Putnam, A. A., 1971, *Combustion-Driven Oscillations in Industry*, Elsevier, New York.
[6] McManus, K. R., Poinsot, T., and Candel, S. M., 1993, "A Review of Active Control of Combustion Instabilities," Prog. Energy Combust. Sci., **19**, pp. 1–29.
[7] Langhorne, P. J., Dowling, A. P., and Hooper, N., 1990, "Practical Active Control Systems for Combustion Oscillations," J. Propul. Power, **6**, pp. 324–333.
[8] Moran, A. J., Steele, D., and Dowling, A. P., 2000, "Active Control and Its Applications," Paper (PSP) 2, RTO AVT Symposium on Active Control Technology for Enhanced Performance Operational Capabilities of Military Aircraft, Land Vehicles and Sea Vehicles, NATO Research and Technology Organization, Neuilly-sur-Seine, France, Paper No. RTO-MP-051.
[9] Seume, J. R., Vortmeyer, N., Krause, W., Hermann, J., Hantschk, C.-C., Zangl, P., Gleis, S., Vortmeyer, D., and Orthmann, A., 1998, "Application of Active Combustion Instability Control to a Heavy Duty Gas Turbine," ASME J. Eng. Gas Turbines Power, **120**, pp. 721–726.
[10] Hibshman, J. R., Cohen, J. M., Banaszuk, A., Anderson, T. J., and Alholm, H. A., 1999, "Active Control of Combustion Instability in Liquid-Fueled Sector Combustor," ASME 99-GT-215.
[11] Neumeier, Y., and Zinn, B. T., 1996, "Experimental Demonstration of Active Control of Combustion Instabilities Using Real-Time Modes Observation and Secondary Fuel Injection," Twenty-Sixth Symposium (International) on Combustion, The Combustion Institute, Pittsburgh, **2**, pp. 2811–2818.
[12] Billoud, G., Galland, M. A., Huynh Huu, C., and Candel, S., 1992, "Adaptive Active Control of Combustion Instabilities," Combust. Sci. Technol., **81**, pp. 257–283.
[13] Evesque, S., Dowling, A. P., and Annaswamy, A. M., 2000, "Adaptive Algorithms for Control of Combustion," Paper (PSP) 22, RTO AVT Symposium on Active Control Technology for Enhanced Performance Operational Capabilities of Military Aircraft, Land Vehicles and Sea Vehicles, NATO Research and Technology Organization, Neuilly-sur-Seine, France, Paper No. RTO-MP-051.
[14] Smith, O., 1959, "A Controller to Overcome Dead Time," ISA Trans., **6**, pp. 28–33.
[15] Englund, D. R., and Richards, W. B., 1984, "The Infinite Line Pressure Probe," *Proceedings of the 30th International Instrumentation Symposium*, Instrumentation Society of America, Research Triangle Park, NC, pp. 115–124.
[16] Drederichsen, J., and Gould, R. D., 1965, Combust. Flame, **2**, p. 25.
[17] Murugappan, S., Acharya, S., Allgood, D. C., Park, S., Annaswamy, A. M., and Ghoniem, A. F., 2003, "Optimal Control of a Swirl Stabilized Spray Combustor Using System Identification Approach," Combust. Sci. Technol., **175**, pp. 55–81.
[18] Ljung, L., 1999, *System Identification: Theory for the User*, 2nd ed., Prentice-Hall, Upper Saddle River, NJ.
[19] Banaszuk, A., Zhang, Y., and Jacobson, C. A., 2000, "Adaptive Control of Combustion Instability Using Extremum-Seeking," *Proceedings of American Control Conference*, American Automatic Control Council, Dayton, OH, **1**, pp. 416–422.

Experimental and Computational Study of Hybrid Diffusers for Gas Turbine Combustors

A. Duncan Walker
e-mail: A.D.Walker@lboro.ac.uk

Paul A. Denman

James J. McGuirk

Department of Aeronautical and Automotive Engineering,
Loughborough University,
Loughborough,
Leics LE11 3TU, UK

The increasing radial depth of modern combustors poses a particularly difficult aerodynamic challenge for the pre-diffuser. Conventional diffuser systems have a finite limit to the diffusion that can be achieved in a given length and it is, therefore, necessary for designers to consider more radical and unconventional diffuser configurations. This paper will report on one such unconventional diffuser; the hybrid diffuser which, under the action of bleed, has been shown to achieve high rates of diffusion in relatively short lengths. However, previous studies have not been conducted under representative conditions and have failed to provide a complete description of the relevant flow mechanisms making optimization difficult. Utilizing an isothermal representation of a modern gas turbine combustor an experimental investigation was undertaken to study the performance of a hybrid diffuser compared to that of a conventional, single-passage, dump diffuser system. The hybrid diffuser achieved a 53% increase in area ratio within the same axial length generating a 13% increase in the pre-diffuser static pressure recovery coefficient which, in turn, produced a 25% reduction in the combustor feed annulus total pressure loss coefficient. A computational investigation was also undertaken in order to investigate the governing flow mechanisms. A detailed examination of the flow field, including an analysis of the terms within the momentum equation, demonstrated that the controlling flow mechanisms were not simply a boundary layer bleed but involve a more complex interaction between the accelerating bleed flow and the diffusing mainstream flow. A greater understanding of these mechanisms enabled a more practical design of hybrid diffuser to be developed that not only simplified the geometry but also improved the quality of the bleed air making it more attractive for use in component cooling. [DOI: 10.1115/1.1772403]

Introduction

The International Civil Aviation Organization (ICAO) has, for many years, prescribed acceptable average levels for the emission of pollutants from aircraft gas turbines. In April 1998 the ICAO's Committee on Aviation Environmental Protection (CAEP) recommended further tightening of the legislation and it is likely that this will be enforced in 2004. Although these CAEP/4 recommendations will redefine limits for unburnt hydrocarbons, carbon monoxide and smoke, Lefebvre [1] states, that it is a reduction in the levels of nitrogen oxides (NO_x) which will provide the greatest challenge for aircraft gas turbines. It is questionable whether current single annular combustor technology will be able to achieve CAPE/4 targets for NO_x without the introduction of radically new combustor configurations. Figure 1 graphically illustrates the NO_x problem and suggests that future legislative requirements are only likely to be met by employing some form of staged combustion in which the fuel is selectively shared either between a pair of primary zones (optimized for low and high power operation), or by improving the mixing of fuel and air prior to combustor entry through pre-mixing/pre-vaporization. A typical radially staged combustor is shown in Fig. 2 and Lefebvre [1] reports that this type of configuration has been shown to achieve a 45% reduction in NO_x emissions when compared to a corresponding single annular combustor fitted in the same engine type.

In comparison with single annular designs, a disadvantage of radially staged combustors is the introduction of an excessively deep flametube. This necessitates a high degree of turning within the dump cavity which Carrotte and Barker [2] have demonstrated inevitably leads to increased aerodynamic losses between compressor exit and the flametube feed annuli. High total pressure losses are undesirable as they have an adverse effect on the feed to various flametube features and ultimately increase specific fuel consumption. Fishenden and Stevens [3] note that the main cause of this loss is the amount of flow turning and diffusion attempted within the dump cavity and that it is important to perform as much diffusion as possible within the pre-diffuser. Traditionally, conventional combustion systems have employed single-passage pre-diffusers followed by a dump diffuser but it is unlikely that this simple device will be able to achieve the high area ratios necessary to distribute the compressor efflux around deep flametubes without incurring high losses. However, one unconventional alternative which has been shown to achieve much higher rates of diffusion in a far shorter length than conventional single-passage dump pre-diffusers is the hybrid or bled diffuser.

This type of diffuser, as proposed by Adkins et al. [4], comprises a wide angle diffuser downstream of a sudden step expansion with flow separation prevented (or minimized) by the removal of a small portion of air via a pair of vortex chambers, as illustrated in Fig. 3. A more detailed review of previous work is presented by Walker [5] but the various studies all demonstrate that hybrid diffusers can indeed achieve much higher rates of diffusion than a single-passage conventional alternative. However, no completely satisfactory explanation of the flow mechanisms has been presented and, consequently, without an understanding of the role of the vortex chamber, the step/fence arrangement or the bleed gap geometry it has not been possible to optimize the hybrid diffuser for use in a gas turbine combustion system. This is important not only in aerodynamic terms, for maximizing performance, but also in engineering terms since features such as the

Contributed by the International Gas Turbine Institute (IGTI) of THE AMERICAN SOCIETY OF MECHANICAL ENGINEERS for publication in the ASME JOURNAL OF ENGINEERING FOR GAS TURBINES AND POWER. Paper presented at the International Gas Turbine and Aeroengine Congress and Exhibition, Atlanta, GA, June 16–19, 2003, Paper No. 2003-GT-38406. Manuscript received by IGTI, October 2002, final revision, March 2003. Associate Editor: H. R. Simmons.

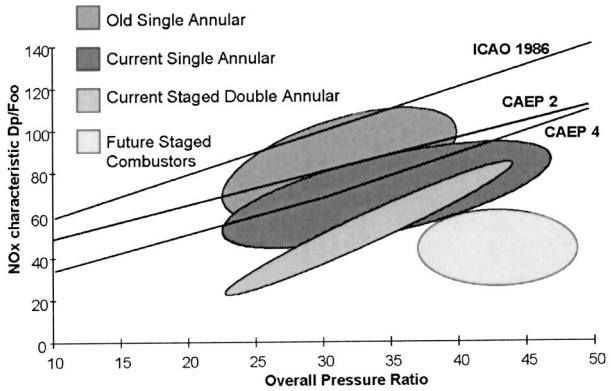

Fig. 1 Variation of NO_x characteristics with engine pressure ratio (Birch [15])

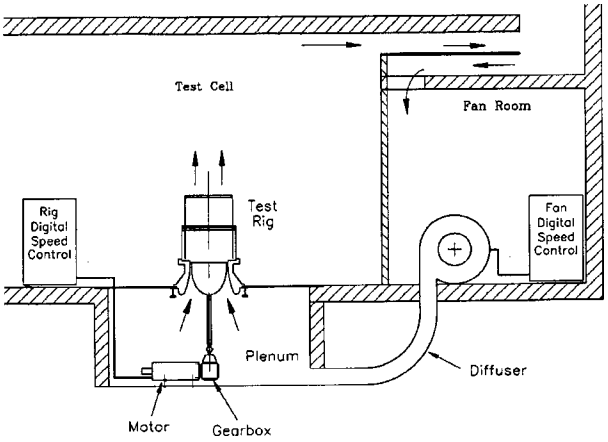

Fig. 4 Double annular combustor test facility

vortex chamber add complexity, length, and weight. Additionally, Adkins and Yost [6] recognized that within a modern gas turbine cycle, high pressure air is a valuable commodity and identified a potential to use the bleed air for turbine blade/disk cooling. However, without optimized bleed geometry it is not possible to assess whether the bleed air is of sufficient quality for this purpose. In the present paper, therefore, attention is focused on an experimental and computational study into the suitability of hybrid diffusers for use in modern, low emission, radially staged gas turbine combustion systems. An isothermal test facility containing a single-stage axial flow compressor is used to compare and contrast the performance of a datum, conventional, single-passage dump diffuser system with that of a hybrid diffuser in the presence of representative inlet conditions. The objective of the computational work was to provide an improved understanding of the flow mechanisms, specifically around the bleed off-takes, and hence enable optimization of the hybrid concept. A commercial CFD code, Fluent (V5.1), was used to predict the flow within a simplified, two-dimensional hybrid diffuser generically similar to that investigated experimentally.

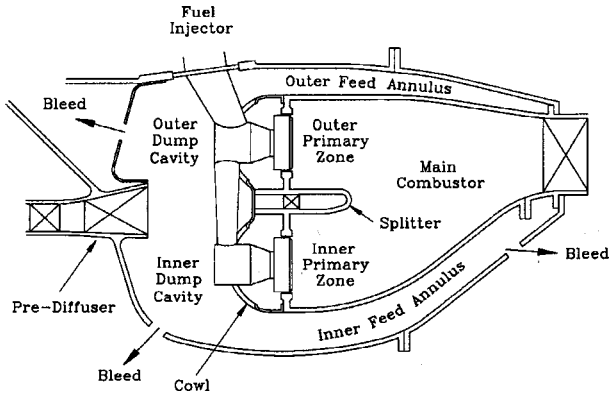

Fig. 2 A typical radially staged combustor

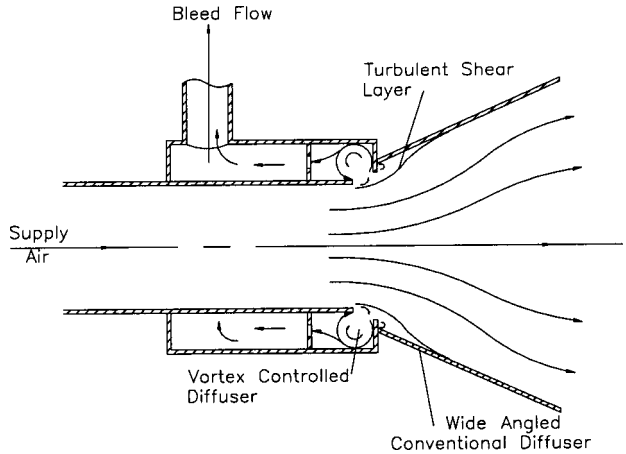

Fig. 3 The hybrid diffuser (Adkins et al. [4])

Experimental Arrangement

The Test Facility. The present investigation was performed using the test facility shown in Fig. 4, the development and operation of which is described in detail by Denman [7]. The facility comprises a large centrifugal fan, driven by a variable speed, 75 kW DC motor, and a rig sited in an adjacent test cell. Ambient air is drawn through filters into the fan room and delivered via a diffuser into an under-floor plenum chamber. The clean air is then passed through a honeycomb flow straightener and into the intake of a single-stage axial flow compressor. The latter is driven by an 80 kW variable speed DC motor through a spiral bevel gearbox and vertical propshaft. Figure 5 shows a cross section of the test rig containing a hybrid pre-diffuser located immediately downstream of the single-stage axial compressor. The latter includes an outlet guide vane (OGV) row typical of a modern aeroengine h.p. compressor stage. The test section, which is manufactured principally from plexiglas and aluminum, has a mean radius and annulus height at compressor exit of 316.75 mm and 30.5 mm, respectively.

The experimental investigations reported here have concentrated on the quality of the flow between compressor exit and entry to each of the combustor feed annuli. Consequently, it has not been necessary to include flametube air admission ports or wall cooling devices. As a result, the five flametube flows (inner, outer and splitter feed annuli, main and pilot combustors) remain separate until they have passed through the flow metering section shown in Fig. 5. The inner and outer bleed flows necessary for the successful operation of the hybrid pre-diffuser were controlled and monitored using a pair of infinitely variable throttles together with a suitably calibrated orifice. Using these flow metering devices, the distribution of air to each of the combustor features was set to within $\pm 0.1\%$ of the total air mass flow rate entering the test facility. Air was delivered to the test rig close to ambient temperature and pressure and the operating conditions of the axial flow compressor were chosen to provide an OGV Reynolds number well above the critical value. The operating conditions were monitored using three Furness FCO44 pressure transducers and a single K-type thermocouple to provide the inlet stagnation tem-

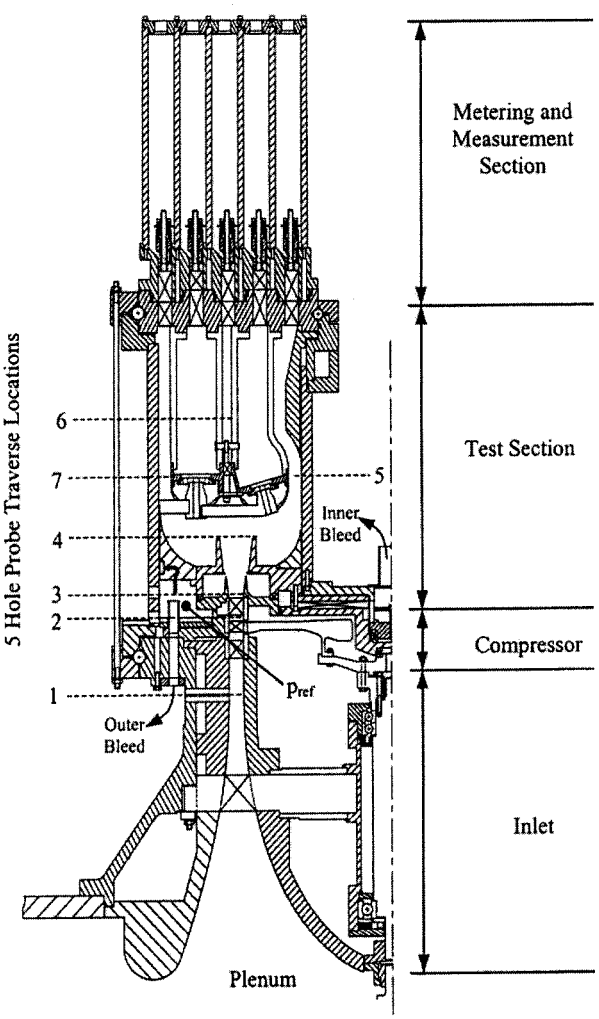

Fig. 5 Test rig cross section

perature (To_1). Two of the pressure transducers were used to record the inlet dynamic and gauge static pressures whilst the third provided a reference gauge pressure at a suitable location downstream of the rotor. Using these signals $N/\sqrt{To_1}$ and Va/U_{blade} were maintained to within $\pm 0.08\%$ and $\pm 0.18\%$, respectively, of their prescribed values for the duration of the experiment. For the measurements reported here, the compressor stage was operated at an $N/\sqrt{To_1}$ equivalent to an inlet Mach number of 0.15 and at a design flow coefficient (V_a/U_{blade}) of 0.403. The resulting Reynolds number based upon the OGV chord at mid-annulus height was close to 2.0×10^5 and the total air mass flow rate corrected to ICAO conditions was 3.8 kg s^{-1}.

The aerodynamic performance of each pre-diffuser was assessed using suitably calibrated miniature five-hole probes as described by Wray and Carrotte [8]. The probes were employed in the non-nulled mode to determine the local flow vector and total and static pressures. As indicated in Fig. 5, five-hole probe area traverses were conducted at rotor exit, OGV exit, pre-diffuser exit and at entry to the inner and outer feed annuli. The probes were traversed in the radial direction using a stepper motor powered linear guide attached to the external casings of the test section shown in Fig. 5. The resulting positional resolution in the radial direction was ± 0.025 mm. Circumferential traversing was achieved by rotating both casings about the test section using a DC servo to provide a positional accuracy better than $\pm 0.01°$. Pressure information from the splitter annulus between the two

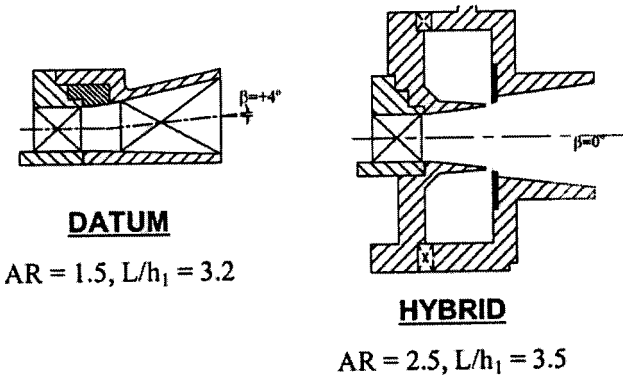

Fig. 6 Pre-diffuser geometry

combustors was recovered from a system of fixed pitot rakes and wall static tappings via a Furness FCO510 scanivalve.

Pre-Diffuser Geometry. The area ratios (AR) and non-dimensional lengths (L/h_1) associated with the conventional datum pre-diffuser and the alternative hybrid design are presented in Figs. 6 and 7. The aerodynamic loading is summarized in Fig. 8 where (AR-1) and L/h_1 are plotted relative to the "line of first stall" compiled by Sovran and Klomp [9] for diffusers in the absence of engine representative inlet conditions.

The datum pre-diffuser contains 22 radial struts located 0.8 OGV chord lengths downstream of the OGV exit plane and positioned midway between the fuel injectors. The alternative hybrid diffuser configuration, which is unstrutted, consists of a three-stage design comprising of a modest diffusing passage followed

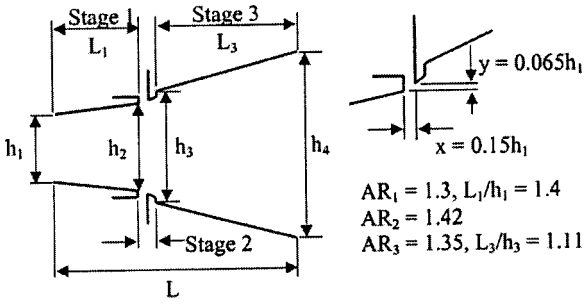

Fig. 7 Hybrid pre-diffuser geometry

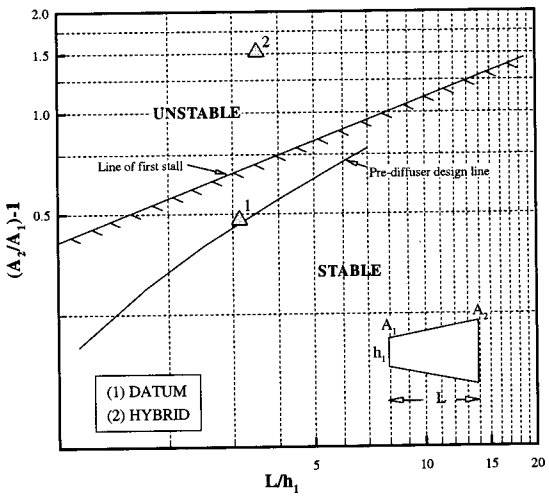

Fig. 8 Pre-diffuser loading chart

by a sudden step expansion and bleed before a final diffusing passage. The detailed design of the bleed off-take geometry was produced using the investigation of hybrid diffusers by Adkins and Yost [6]. A diffusing passage upstream of the step expansion was included firstly to allow some OGV wake mixing to occur prior to the bleed off-takes and, secondly, to enhance the quality of the bleed air by taking advantage of the modest pressure recovery within the primary passage.

Data Reduction and Errors. The aerodynamic performance of various diffuser geometries is usually assessed in terms of their resultant total pressure loss and static pressure recovery coefficients. The data presented here were derived from five-hole probe area traverses performed at the locations shown in Fig. 5. The individual pressures were recorded using Furness FCO44 pressure transducers and corrected to ICAO standard day conditions (i.e., 101,325 Pa and 288.15 K). At any measurement plane the air mass flow rate and bulk average velocity are defined using the following:

$$\dot{m} = \int \rho U dA = \rho \bar{U} A. \tag{1}$$

For the experiments described here, the resulting mass flow balance between, for example, OGV exit (3) and pre-diffuser exit (4) was within ±1% of the total air mass flow entering the test facility. Spatially averaged values of total and static pressure at each plane are derived using the mass-weighted technique (Klein [10]).

$$\tilde{P} = \frac{1}{\dot{m}} \int P d\dot{m} = \frac{1}{\rho U A} \int P \rho U dA \tag{2}$$

$$\tilde{p} = \frac{1}{\dot{m}} \int p d\dot{m} = \frac{1}{\rho U A} \int p \rho U dA \tag{3}$$

Changes in the spatially averaged pressures between for example OGV exit (3) and pre-diffuser exit (4) are expressed in terms of the mass-weighted total pressure loss (λ) and static pressure rise (Cp) coefficients as follows:

$$\lambda_{3-4} = \frac{\tilde{P}_3 - \tilde{P}_4}{\tilde{P}_3 - \tilde{p}_3} \quad Cp_{3-4} = \frac{\tilde{p}_4 - \tilde{p}_3}{\tilde{P}_3 - \tilde{p}_3}. \tag{4}$$

The mass-weighted pressures derived at each of the traverse planes shown in Fig. 5 were repeatable to within ±1 mm H_2O, a variation that amounted to less than ±0.5% of the dynamic pressure recorded at OGV exit. This resulted in a repeatability of the derived total pressure loss and static pressure rise coefficients relating to overall performance of better than ±0.005 of the values presented here.

Numerical Methodology

The computational approach adopted for the present work has been described fully in Walker [5], so only a brief summary is given here. The mathematical model was based on solution of the Reynolds-averaged Navier-Stokes equations using the standard high-Reynolds number two-equation *k*-model (Launder and Spalding [11]) with a conventional wall-function treatment. Some calculations were repeated using a Reynolds-stress transport model, and alternative (pressure-gradient sensitized) wall functions, but, in terms of the pressure loss behavior given highest priority here, little differences were observed, so only k-ε results are reported. It was, however, found important to ensure that the wall-nearest grid nodes were located in the fully turbulent zone ($y+ > 30$), otherwise nonphysical near-wall velocity profile shapes were observed, particularly in the stage 3 part of the pre-diffuser. (For further details on this, see Walker [5].)

Numerical solution of the governing flow equations was carried out via the commercial CFD code FLUENT (V5.1). The equations were discretized using a cell-centered finite-volume implicit scheme. Blended second-order-upwind/central differencing was used for convective flux evaluation. A SIMPLE-based pressure-correction formulation was combined with Rhie and Chow based pressure smoothing to avoid pressure/velocity oscillations on the colocated mesh (see Ferziger and Peric [12]). In order to generate boundary-conforming meshes for the non-Cartesian-shaped solution domains, the geometries were input into the PreBFC (from Fluent Inc.) mesh generator to create the required meshes (using algebraic grids only, with no elliptic pde smoothing). Details of the grid densities used are given below, with grid-independence tests available in Walker [5].

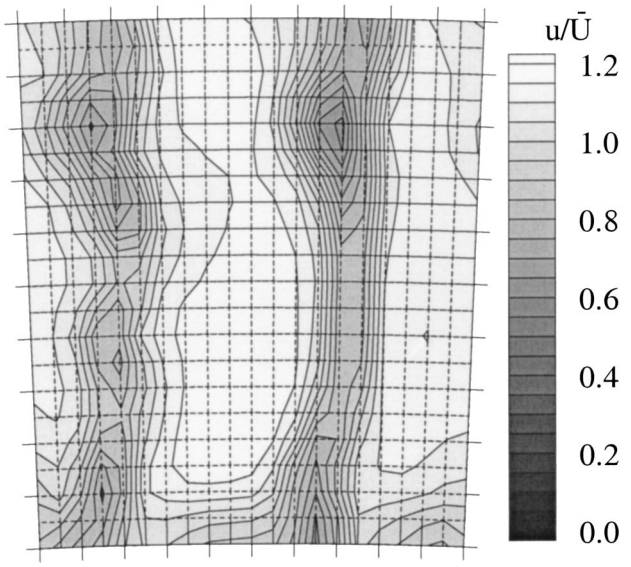

Fig. 9 Measured axial velocity contours at OGV exit

Inlet boundary conditions for CFD analysis should as far as possible be deduced directly from the measurements taken. It was also desirable to start the CFD calculations at OGV exit. Measured inlet axial velocity contours show significant effects of the OGV wakes and associated secondary flows; see, for example, Fig. 9.

Note that measurements have been made over two OGV blade spaces—the single-stage compressor in the rig contained half as many IGVs as OGVs, and this can still be detected at OGV exit. However, the main purpose of the CFD predictions to be described was a detailed examination of the bleed flow/pre-diffuser region. Thus OGV wakes were omitted, as these would further complicate the flow and perhaps conceal the governing mechanisms. Accordingly, it was felt that a two-dimensional planar geometric description of the pre-diffuser alone (no downstream combustor) would be sufficient (assuming radius effects small) and would allow rapid CFD explorations. In these two-dimensional calculations, the velocity field inlet conditions were therefore circumferentially averaged versions of the three-dimensional measurements. Clearly these would no longer capture any secondary flow at inlet, but it was felt important to simulate the boundary layer thickness. The inlet profile deduced from the three-dimensional data of Fig. 9 is shown in Fig. 10. Guesses had to be made for the turbulence conditions at OGV exit and these were fixed after preliminary sensitivity studies (little change in predictions was observed for reasonable variations in turbulence inlet values, see Walker [5]). The final values chosen were a 5% turbulence intensity and a length scale equal to the passage height.

Several geometric variants of a bled diffuser were studied. These variants were chosen to help identify the importance (or otherwise) of particular geometrical aspects of the vortex bled hybrid diffuser. These geometries are shown in Figs. 11 and 12. They represent: Fig. 11 a vortex-bled diffuser, Fig. 12(*a*) a duct-

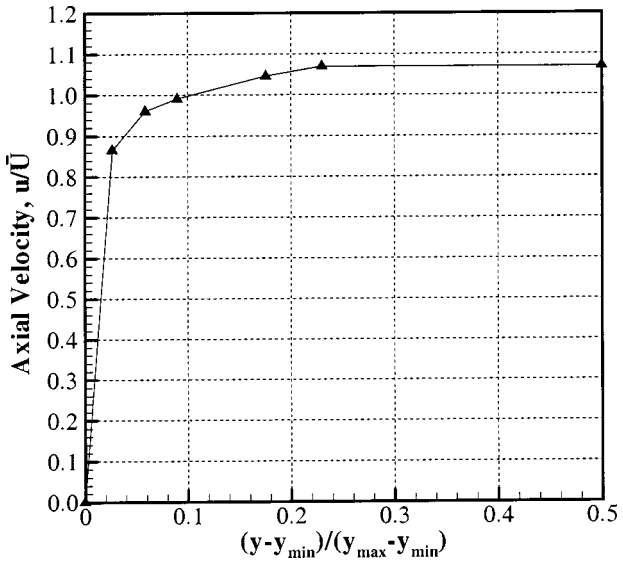

Fig. 10 Axial velocity profile at inlet

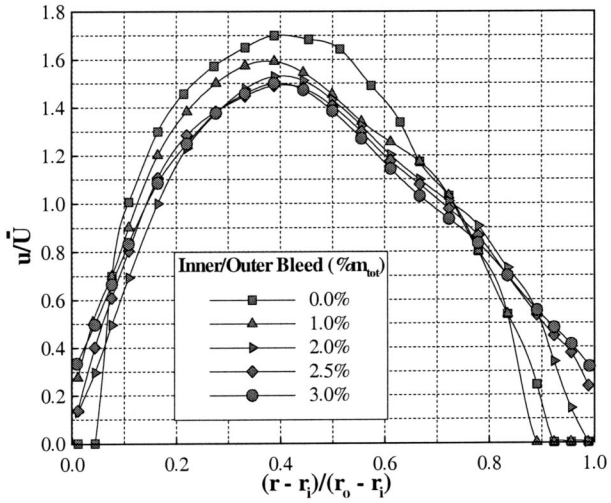

Fig. 13 Variation of hybrid diffuser pitch-averaged axial velocity profile with bleed

bled diffuser, (*b*) a diffuser with simple boundary layer bleed, (*c*) a diffuser similar to (*a*) but with the fence removed and the bleed duct entrance profiled. Note that all these diffusers possess the same inlet passage height (30.5 mm), the same overall area ratio (2.5) and the same nondimensional length (3.5).

Experimental Results

The mass-weighted static pressure rise and total pressure loss coefficients determined for both diffusers are presented in Table 1. The data are derived with respect to the rotor exit plane (2) and therefore include the aerodynamic performance of the OGV row. It is noted that the pressure rise obtained with the hybrid diffuser is substantially greater than with the conventional diffuser, although the pressure loss has also increased. However, even though λ_{2-4} has increased the dump loss will be reduced due to the lower dynamic pressure at pre-diffuser exit in the hybrid system. The performance coefficients for the hybrid pre-diffuser were recorded at a bleed rate equal to 3% of the total inlet mass flow bled through each vortex chamber. This represents the ''minimum bleed requirement,'' described by Adkins et al. [4], below which the diffuser exhibits a stall. Figure 13 shows the effect of increasing bleed on the pitch-averaged velocity profile at pre-diffuser exit and demonstrates that flow reattachment can be achieved above 2.5–3.0% bleed.

Normalized axial velocity contours recorded at pre-diffuser exit are presented in Figs. 14 and 15 for the datum and hybrid diffusers, respectively. These are plotted over a repeatable measurement sector, which for the datum diffuser represents a strut sector but for the unstrutted hybrid diffuser is reduced to a pair of OGV's. Figures 14 and 15 demonstrate that the OGV wakes persist to the exit plane and that the flow within each diffuser remains attached. Notably, as shown in Fig. 8, the hybrid diffuser operating point lies significantly beyond the ''line of first stall'' defined by Sovran and Klomp [9].

Pitch-averaged profiles of axial velocity measured within the combustor inner and outer feed annuli at traverse location (5) and (7) are presented in Fig. 16. Although the velocity profiles remain largely unaltered due to the dominance of the dump process, the increased diffusion afforded by the higher area ratio hybrid diffuser has significantly reduced the turning loss within the dump cavity and, as a result, the total pressure losses to the feed annuli are greatly improved. The mass-weighted total pressure loss coef-

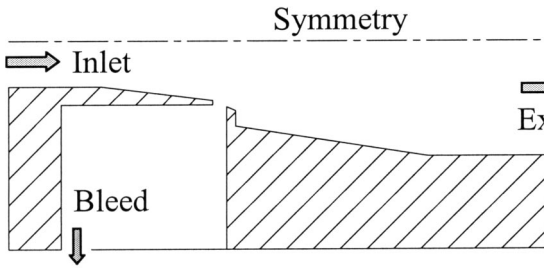

Fig. 11 Computational model of vortex-bled diffuser

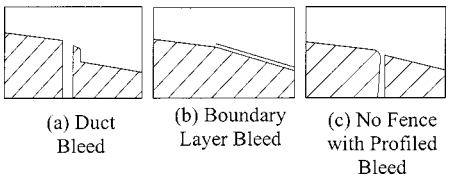

Fig. 12 Alternative bleed geometries

Table 1 Pre-diffuser performance data

Diffuser	Area Ratio	Cp_{2-4}	λ_{2-4}
Datum	1.48	0.63	0.16
Hybrid	2.50	0.71	0.20

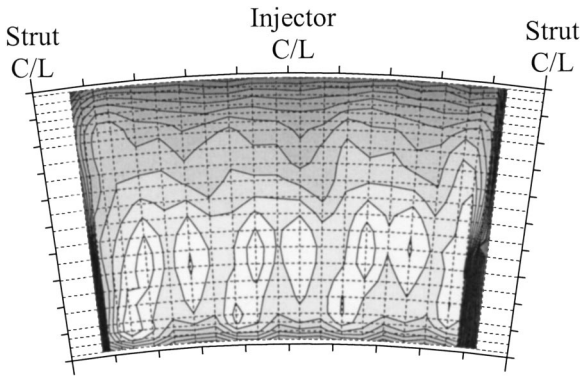

Fig. 14 Axial velocity contours at datum diffuser exit

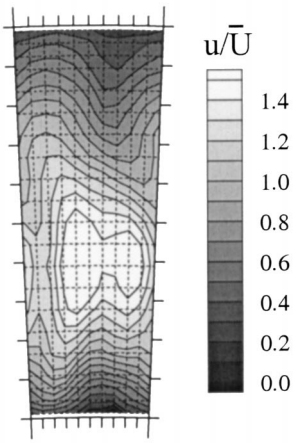

Fig. 15 Axial velocity contours at hybrid diffuser exit

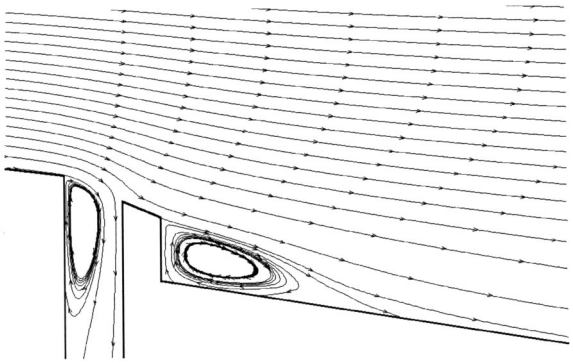

Fig. 17 Streamline plot, 3% bleed

ficients are presented in Table 2 and show that, on average, a 25% reduction has been achieved using the hybrid design. Moreover, Adenubi [13] suggests that total pressure losses to the combustor feed annuli should be no more than 30% of rotor exit dynamic pressure. Significantly, Table 2 shows that this can be achieved for the present combustor geometry using a hybrid diffuser.

With regard to the quality of the air bled from the hybrid diffuser, a mass-weighted total pressure loss coefficient was defined using

$$\lambda_{2-B}=\frac{\tilde{P}_2-\tilde{P}_{\mathrm{BLEED}}}{\tilde{q}_2} \tag{5}$$

where $\tilde{P}_{\mathrm{BLEED}}=p_{\mathrm{ref}}$, the total pressure of the air removed from the outer vortex cavity as shown in Fig. 5. The measured loss coefficient is high relative to the feed annuli and increased with bleed rate up to a value of 0.55 at 3% bleed. However, significant improvements can be made to the quality of this air by redesigning the way in which it is removed from the diffuser, thus making its use for turbine component cooling a more viable option.

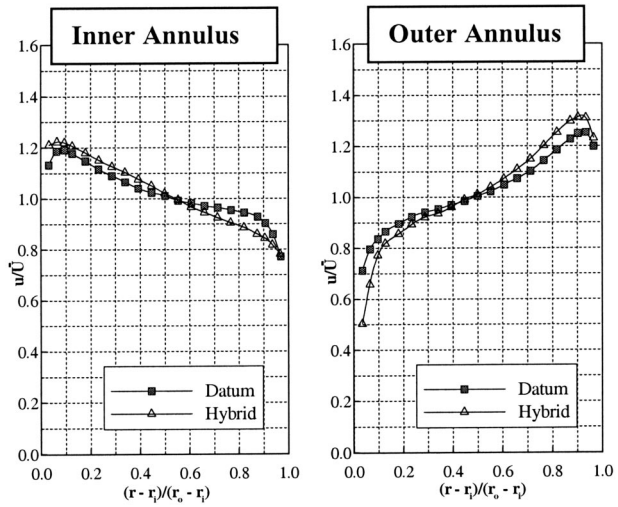

Fig. 16 Pitch-averaged axial velocity profiles at entry in the inner and outer feed annuli

Table 2 Loss coefficients to the feed annulus

Diffuser	λ_{2-5}	λ_{2-6}	λ_{2-7}
Datum	0.35	0.33	0.33
Hybrid	0.26	0.22	0.27

Computational Results

A grid of 300×100 (streamwise×transverse) cells was used; some calculations were repeated on a 600×200 mesh with less than 1% change in the predictions. An illustration of the flow pattern obtained for one of the two-dimensional diffusers (duct-bled, 3% bleed) is given in Fig. 17; the streamline pattern in the region of the bleed/fence/stage 3 diffuser is given particular emphasis in this figure. The presence of a separation zone inside the bleed duct, the curvature of the streamlines as the flow passes over the bleed location, and the separation downstream of the fence are all clearly visible and will be referred to in the discussion below.

Table 3 shows performance parameters predicted for the vortex-bled and duct-bled two-dimensional diffusers at four bleed flows. It is clear that no significant difference is obtained. The important conclusion to be inferred here is that it is the bleed mass flow that is the primary mechanism, rather than the use of a vortex chamber as a bleed geometry. This conclusion is in contrast to earlier studies (Adkins [4]) where the inclusion of a vortex chamber was seen as crucial. Given the added manufacturing complexity of a vortex-bleed compared to a simple duct-bleed, this conclusion is significant. The effect of the bleed flow in unstalling and then reducing the separation length in the stage 3 diffuser is quite marked. The minimum bleed flow required to unstall the diffuser was predicted to be 1.5% for the two-dimensional geometries with no OGV wakes at inlet. The superfluous nature of the vortex chamber was already observed in the experimental study described above and is further confirmed by these predictions.

There is a temptation to deduce from these results that perhaps the beneficial effects are all obtained by simple removal of the low momentum boundary layer fluid before entry to the adverse pressure gradients in the stage 3 diffuser. To investigate this, results comparing predictions from geometries Figs. 12(*a*) (duct-bled)

Table 3 Hybrid diffuser performance

	Bleed Rate ($\%\dot{m}_{\mathrm{tot}}$)	λ_{2-4}	Cp_{2-4}	X_R/L_3
Vortex-bled	0.0	0.139	0.647	stalled
	1.0	0.124	0.724	stalled
	2.0	0.118	0.764	0.33
	3.0	0.115	0.786	0.21
Duct-bled	0.0	0.140	0.649	stalled
	1.0	0.125	0.713	stalled
	2.0	0.121	0.756	0.33
	3.0	0.115	0.778	0.21

Table 4 Diffuser performance at 2.5% bleed

	λ_{2-4}	Cp_{2-4}	X_R/L_3
Duct-bled	0.116	0.774	0.25
B-l bled	0.116	0.785	stall @ 0.72

and 12(*b*) (boundary layer-bled) were compared at a single bleed rate of 2.5%. These performance results are given in Table 4.

Although the loss and pressure rise characteristics are very similar, the boundary-layer bled system has produced a flow that is unable to negotiate the stage 3 diffuser without separation, which, in spite of the good overall performance figures, is a poor design feature. The conclusion to be drawn here is that duct-bled (and vortex-bled) diffusers must operate with an additional and more complex mechanism than mere low momentum fluid removal. It is believed (and supporting evidence is produced below) that the additional mechanism is due to the streamline curvature introduced into the flow by the nonsimple boundary-layer type bleed systems. This streamline curvature gives rise to momentum transfer to the ''mainstream'' flow, i.e., the flow that just by-passes the bleed duct to become the near wall flow in the stage 3 diffuser. The momentum gain so achieved now enables the near-wall fluid to negotiate the stage 3 adverse pressure gradient, whereas it was unable to do so in the simple boundary-layer bled system.

One penalty of the duct-bled system is the loss associated with the separation regions in the duct itself and after the fence. To avoid these, the profiled duct/fenceless geometry of Fig. 12(*c*) was investigated. Table 5 shows that the overall performance has improved as expected compared to the standard duct-bled design. Figure 18 shows the flow pattern with this geometry and all flow separation regions have disappeared. This reduces loss and increases the pressure rise performance, but, just as importantly, the total pressure quality of the bleed flow air has improved substantially as shown in the last column in Table 5. This is of crucial significance for the introduction of a bled diffuser system into engine practice, since any bleed air must be of sufficiently high total pressure to be useable elsewhere in the engine, e.g., for turbine blade cooling. A further conclusion is that the fence feature of the vortex-bled system is also not of fundamental importance, again of significance for ease of manufacture.

A hypothesis has been introduced above, viz: the additional benefit of a bled diffuser system is achieved by optimizing the

Table 5 Diffuser performance at 2.5% bleed

	λ_{2-4}	Cp_{2-4}	X_R/L_3	λ_{2-B}
Vortex-bled	0.116	0.777	0.25	0.552
Duct-bled	0.116	0.774	0.25	0.494
Profiled duct-bled with no fence	0.109	0.795	0.0	0.384

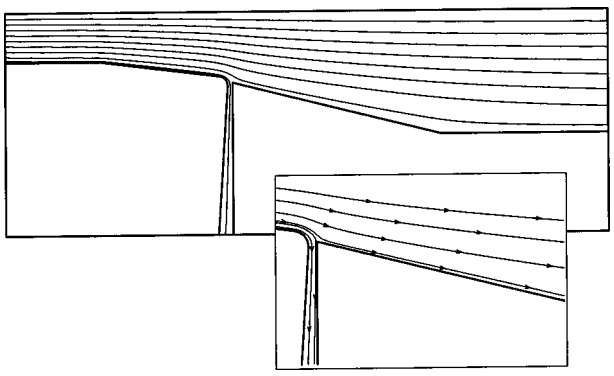

Fig. 18 Streamline plot, 2.5% bleed

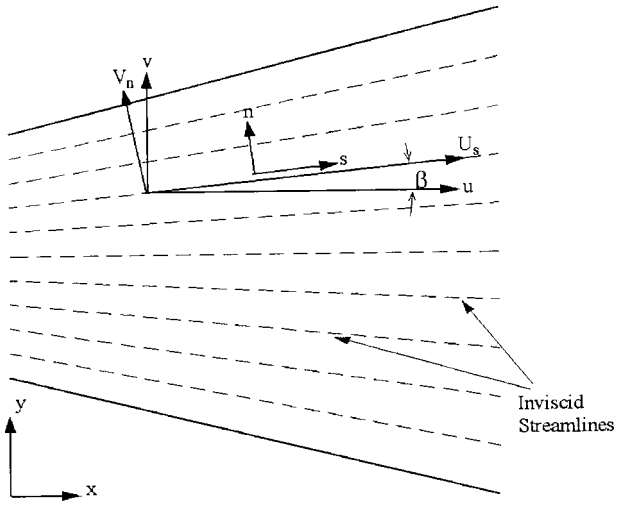

Fig. 19 Momentum analysis nomenclature

ability of the bleed-induced streamline curvature (and hence flow acceleration) to increase locally the streamwise momentum of the mainstream flow before this passes further down the diffuser. This hypothesis has been investigated by performing a momentum analysis of the CFD predictions for the profiled duct/no fence system at 2.5% bleed.

The momentum analysis is performed following the same ideas suggested by Barker and Carrotte [14] in their experiments on the passage of OGV wakes down diffusers. It is shown in [14] that it is necessary to perform the momentum analysis (of the actual turbulent flow) relative to the flow pattern that would be obtained for an inviscid fluid passing through the same diffuser geometry. The reason for this is that secondary flows play an important role in momentum transfer, but it is necessary to identify the secondary velocities *in excess* of those that would occur in an inviscid flow pattern (secondary flows occur in the inviscid flow but of course do not contribute to any useful momentum transfer). If the flow is analyzed relative to a frame of reference defined by the local inviscid streamlines, then the true role of secondary flows and stress gradients in distributing streamwise momentum can be revealed.

An inviscid-streamline coordinate frame can be identified by performing an inviscid analysis with the CFD code. The time-averaged streamwise momentum equation relative to this inviscid frame of reference may be written:

$$0 = -U_s\frac{\partial U_s}{\partial s} - V_n\frac{\partial U_s}{\partial n} - \frac{1}{\rho}\frac{\partial p}{\partial s} - \left[\frac{\partial \overline{u_s^2}}{\partial s} + \frac{\partial \overline{u_s v_n}}{\partial n}\right]. \tag{6}$$

In this equation (s,n) represents the inviscid-streamline-based frame of reference, which is assumed to be locally defined by a pair of orthogonal straight lines rotated (by an angle β) relative to the Cartesian (x,y) directions, see Fig. 19. The various terms in this equation may be computed by simple trigonometric transformations from the CFD predicted Cartesian velocity field. For example, the computed turbulent flow Cartesian velocity components at a point (U,V) can be resolved locally into the components parallel to and normal to the inviscid streamlines (U_s,V_n):

$$\begin{pmatrix} U_s \\ V_n \end{pmatrix} = \begin{pmatrix} \cos\beta & \sin\beta \\ -\sin\beta & \cos\beta \end{pmatrix} \begin{pmatrix} U \\ V \end{pmatrix}. \tag{7}$$

Similarly, all derivatives in Cartesian (x,y) space may be transformed into (s,n) space. Hence at each point in the flowfield, each term in the above equation may be evaluated (see Walker [5] for details). In this analysis, all terms must sum to zero (in a con-

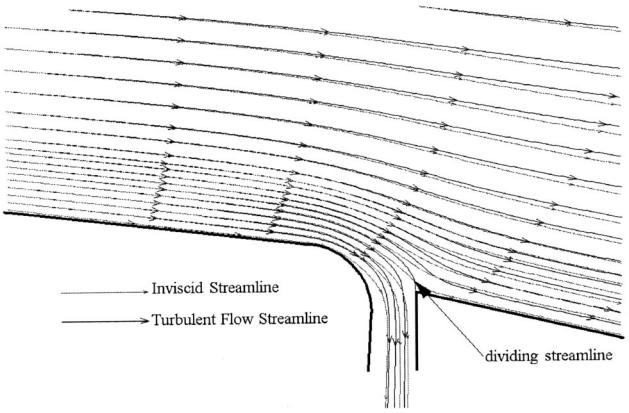

Fig. 20 Streamlines, 2.5% bleed

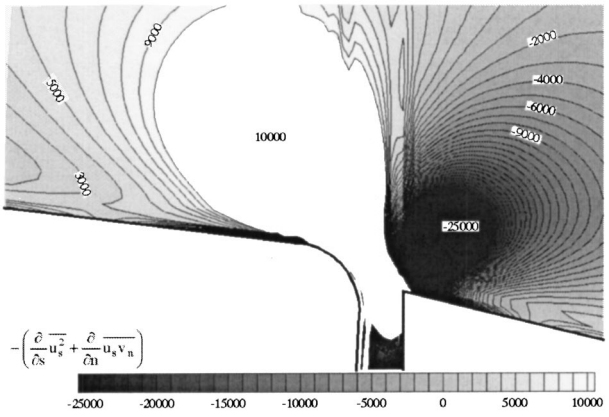

Fig. 22 Contours of $-((\partial/\partial)s\overline{u_s^2}+(\partial/\partial n)\overline{u_s v_n})$, 2.5% bleed

verged solution), so the turbulent stress terms have not been computed individually, but calculated as the ''closing term.''

Note that terms that are positive on the RHS of Eq. (6) represent a process contributing to a local *gain* of streamwise momentum, whereas a negative term represents a momentum *loss* process. This is easily illustrated by considering the effect of a favorable pressure gradient ($\partial p/\partial s$ negative) or an adverse pressure gradient ($\partial p/\partial s$ positive).

Figure 20 shows the streamlines (actual and inviscid) in the region of the bleed duct for the case considered. This picture illustrates clearly that the part of the mainstream flow that becomes the near-wall flow after the bleed experiences strong streamline curvature as it passes over the bleed. Similarly the bleed flow itself experiences strong streamline curvature.

After analyzing this flow pattern in the manner described, the terms in the momentum balance equation may be evaluated. Figure 21 for example shows the pressure gradient term. It is noticeable that this term is positive close to the wall in the region just upstream of the bleed duct front edge. This indicates a favorable pressure gradient tending to accelerate the flow. Figure 22 shows the contours of the turbulent stress term. There is a large region of the mainstream flow upstream of the bleed location (away from the wall) where the sign of this term indicates it is a source of streamwise momentum. Similarly, just downstream of the rear edge of the bleed duct, there is a large region of favorable pressure gradient, which will help the flow maintain its forward progress in the stage 3 diffuser. The interpretation of these observations is that the bleed flow is gaining streamwise momentum as it accelerates towards the bleed duct, but transferring some of this momentum by turbulent diffusion to the outer mainstream flow. This will help the flow when it enters the stage 3 diffuser, where it is further aided by the region of favorable pressure gradient. This analysis seems to support the interpretation of the flow mechanism suggested above.

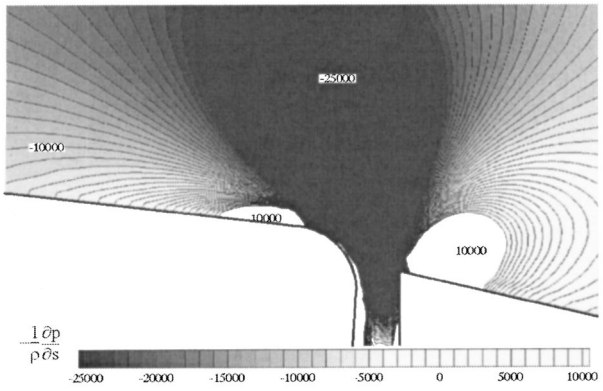

Fig. 21 Contours of $-1/\rho\ \partial p/\partial s$, 2.5% bleed

Conclusions

The experimental study has demonstrated the operation of a hybrid diffuser within an isothermal representation of a modern gas turbine combustion system. Compared to a conventional single-passage pre-diffuser the hybrid diffuser achieved a significant increase in area ratio within the same axial length. Moreover, the increased area ratio resulted in an improved diffuser static pressure recovery, reducing total pressure losses in the dump cavity and to the feed annuli. The required level of bleed was found to be similar to that used for turbine blade cooling and measurements suggested that the bleed air would be of sufficient quality for this purpose.

The computational investigation demonstrated that not only are the governing flow mechanisms more complex than a simple boundary layer bleed but also that the step, fence and vortex chamber are unnecessary features. An analysis of the CFD predictions revealed that the governing flow mechanisms involve a local streamwise momentum transfer from the accelerating bleed flow to the diffusing mainstream flow. Thus the additional benefit of a bled diffuser system is achieved by optimizing the ability of the bleed-induced streamline curvature (and hence flow acceleration) to increase locally the streamwise momentum of the mainstream flow before this passes further down the diffuser. An understanding of this has lead to a more practical design of bled diffuser which also improves the total pressure quality of the bleed flow leading to a design more suited for use in modern gas turbine combustors.

Acknowledgments

This work has been carried within the Rolls-Royce University Technology Center in Combustion Aerodynamics at Loughborough University. The authors would like to thank their colleagues within the UTC for many useful technical discussions.

Nomenclature

A = area
AR = area ratio
Cp = static pressure recovery coefficient
h_1 = pre-diffuser passage entry height
L = pre-diffuser passage length
$\dot{m}$ = mass flow rate

N = rotational speed
P = local mean total pressure
p = local mean static pressure
r = radius relative to engine center line
r_i = inner wall radius relative to engine center line
r_o = outer wall radius relative to engine center line
To_1 = Inlet total temperature
U_{blade} = mean blade speed
U = local mean velocity
Va = axial velocity
X_R = reattachment length
β = air angle between viscous and inviscid streamlines
η = diffuser effectiveness
λ = mass-weighted total pressure loss coefficient
ρ = density

Superscripts

$\sim$ = mass-weighted mean value
$-$ = area-weighted mean value (bulk average)

Subscripts

2 = rotor exit
3 = OGV exit
4 = pre-diffuser exit
5 = inner annulus
6 = outer annulus
B = bleed flow
s = tangential to inviscid streamline
n = normal to inviscid streamline

References

[1] Lefebvre, A. H., 1995, ''The Role of Fuel Preparation in Low-Emission Combustion,'' ASME J. Eng. Gas Turbines Power, **117**, pp. 617–654.
[2] Carrotte, J., and Barker, A. G., 1994, ''Annular Dump Diffuser Systems, Part II: The Combined Effect of Shortened Pre-Diffusers and Dump Gap Variation,'' Internal Report TT95R03, Dept. AAE, Loughborough University.
[3] Fishenden, C. R., and Stevens, S. J., 1977, ''Performance of Annular Combustor-Dump Diffuser,'' J. Aircr., **14**, pp. 60–67.
[4] Adkins, R. C., Matharu, D. S., and Yost, J. O., 1981, ''The Hybrid Diffuser,'' ASME J. Eng. Gas Turbines Power, **103**, pp. 229–236.
[5] Walker, A. D., 2002, ''Experimental and Computational Study of Hybrid Diffusers for Gas Turbine Combustors,'' Ph.D. thesis, Loughborough University.
[6] Adkins, R. C., and Yost, J. O., 1983, ''A Compact Diffuser System for Annular Combustors,'' ASME Paper 83-GT-43.
[7] Denman, P. A., 2002, ''Aerodynamic Evaluation of Double Annular Combustion Systems,'' ASME Paper GT-2002-30465.
[8] Wray, A. P., and Carrotte, J. F., 1993, ''The Development of a Large Annular Facility for Testing Gas Turbine Combustor Diffuser Systems,'' Paper No. AIAA-93-2546.
[9] Sovran, G., and Klomp, E. D., 1967, ''Experimentally Determined Optimum Geometries for Rectilinear Diffusers With Rectangular, Conical or Annular Cross-Section,'' *Fluid Mech. Of Internal Flow*, Elsevier, New York, pp. 270–319.
[10] Klein, A., 1995, ''Characteristics of Combustor Diffusers,'' Prog. Aerosp. Sci., **31**, pp. 171–271.
[11] Launder, B. E., and Spalding, D. B., 1974, ''The Numerical Computation of Turbulent Flows,'' Comput. Methods Appl. Mech. Eng., **3**, pp. 269–289.
[12] Ferziger, J. H., and Peric, M., 2001, *Computational Methods for Fluid Dynamics*, Springer-Verlag, Berlin.
[13] Adenubi, S. O., 1976, ''Performance and Flow Regime of Annular Diffusers With Axial Turbomachine Discharge Inlet Conditions,'' ASME J. Fluids Eng., **98**, pp. 236–243.
[14] Barker, A. G., and Carrotte, J. F., 2001, ''Influence of Compressor Exit Conditions on Combustor Annular Diffusers—Part II: Flow Redistribution,'' J. Propul. Power, **17**(3), pp. 687–694.
[15] Birch, N. T., 2000, ''2020 Vision: The Prospects for Large Civil Aircraft Propulsion,'' Aeronaut. J., **104**(1038), pp. 347–352.

Masahiro Kurosaki
Tadashi Morioka
Kosuke Ebina
Masatoshi Maruyama
Tomoshige Yasuda
Makoto Endoh

Research and Engineering Division,
Aero-Engine and Space Operations,
Ishikawajima-Harima Heavy Industries Co. Ltd.,
Mizuho-machi, Nishitama-gun,
Tokyo 190-1297, Japan

Fault Detection and Identification in an IM270 Gas Turbine Using Measurements for Engine Control

A unique fault detection and identification algorithm using measurements for engine control use is presented. The algorithm detects an engine fault and identifies the associated component, using a gas path analysis technique with a detailed nonlinear engine model. The algorithm is intended to detect steplike changes in component performance rather than gradual change of all components. Component performance deviation (efficiency and flow rate) is represented by a magnitude and a phase. The phase is selected to minimize the error of evaluation matrices. Then the magnitude is computed. By utilizing operational data of the IM270 engine, the compressor and the turbine performance deviation was quantitatively identified. [DOI: 10.1115/1.1787515]

1 Introduction

Recently, research and development of engine performance condition monitoring has become popular. This is motivated not only by economics but also by recent trends in energy conservation and environmental awareness. Currently there are many gas turbines in service without condition monitoring systems. In order to retrofit these engines with monitoring capabilities, it would be convenient to use the existing sensors on the engine. Most late-model gas turbines use an electronic control unit (ECU). Condition monitoring based on the ECU acquired data for engine control may have considerable benefit.

Advanced monitoring systems not only monitor total gas turbine performance deterioration but also identify individual component health. Monitoring component conditions requires pressure and temperature measurements at both the inlet and outlet of the component. Engine speed measurements are also required for rotating components. The ECU does not measure all required parameters. In order to overcome this difficulty, either an engine model or a linear sensitivity matrix relating measurements and performance parameters is needed. However, the number of measurements may not be sufficient to uniquely identify individual component condition. In this paper we propose a unique algorithm using ECU acquired measurements to address this problem. The algorithm can not only detect fault occurrence but also can identify the faulty component with low computational throughput.

Research and development of algorithms to estimate individual component condition was initiated by Urban [1] in the 1970s and followed by Doel [2]. Both programs used a weighted-least-squares approach and were improved to include the capability of identifying a single large-magnitude fault [3]. The development history and approach are well described in Ref. [4]. The weighted-least-squares technique requires a time-consuming optimization iteration when a nonlinear engine model is used in the process. Appropriate weighting factor selection for use in the performance index is crucial and requires significant experience. As a result it is difficult to apply this approach to newly developed engines. Stimulated by recent interest in engine condition monitoring, a variety of methods have been proposed including linear and nonlinear gas path analysis, multioperation point methods, use of neural networks, genetic algorithms, etc. Among them, Aretakis et al. [5] proposed a combinatorial approach to address the problem of having fewer measurements than parameters to be identified. The concept is that the average of the estimations of all of the possible combinations may be close to the actual values of each parameter.

In this study, we propose a unique algorithm that can detect an engine fault and identify the associated component with measurements acquired for engine control use.

The next section introduces the IM270 engine and the nonlinear engine model, which was used with the algorithm. This is followed by a description of the measurements and adjustable parameters. A linear dependency analysis of measurement deviation caused by different components is presented in Section 4. Section 5 describes the proposed fault detection and identification algorithm in detail. A numerical simulation, which quantifies the combined effects of the linear dependency and noise upon the detection and identification capability of the proposed algorithm, is discussed in Section 6. Finally, in Section 7, it is shown that with operational data the algorithm was able to detect an engine fault and quantitatively identify compressor and turbine performance deviations.

2 IM270 Engine and Engine Model

The proposed algorithm was developed specifically for the IM270 engine, although the concept is more general and can be applied to many other gas turbine engines. The IM270 with 2-MW output capacity consists of a two-stage centrifugal compressor,

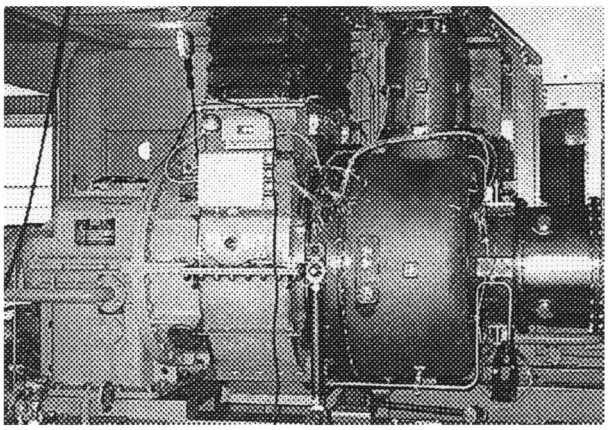

Fig. 1 IM270 gas turbine

Contributed by the International Gas Turbine Institute (IGTI) of THE AMERICAN SOCIETY OF MECHANICAL ENGINEERS for publication in the ASME JOURNAL OF ENGINEERING FOR GAS TURBINES AND POWER. Paper presented at the International Gas Turbine and Aeroengine Congress and Exhibition, Atlanta, GA, June 16–19, 2003, Paper No. 2003-GT-38378. Manuscript received by IGTI, October 2002, final revision, March 2003. Associate Editor: H. R. Simmons.

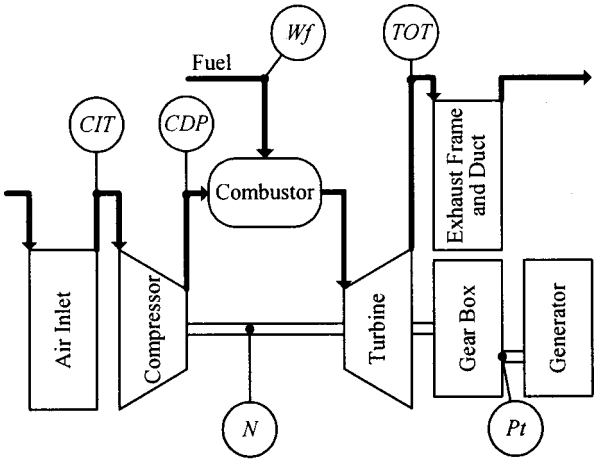

Fig. 2 Schematic of engine components and sensors

low NO_x combustor, and a three-stage axial turbine (see Figs. 1 and 2). The features of the IM270 engines are described in Refs. [6,7].

The algorithm is partly based on a nonlinear gas path analysis. A highly accurate engine model is required since several percent of engine component deviation must be identified. The engine model, based on Ref. [8], consists of a compressor, a combustor, and a turbine as shown in Fig. 3. The compressor and turbine characteristics are represented by performance maps. For thermodynamics calculations, specific heat at constant pressure is represented as polynomials, which are functions of temperature and fuel-air ratio. Given engine inlet temperature and pressure, power output, and engine speed, nonlinear equations that represent mass and energy conservation of the gas path as well as a power balance between compressor, generator, and turbine are solved by a Newton-Raphson method. To better match operational data, each performance map was adjusted using correction factors. Figure 4 shows that the measured values and the model output agree very well over a considerable range of power output.

3 Fault Detection and Identification

We devised a unique fault detection and identification algorithm for the IM270 engine that can not only detect occurrence of a fault but also can identify the faulty component by using measurements obtained for engine control. This study was motivated by the need to retrofit existing machines with condition monitoring functions without adding sensors.

The engine control unit (ECU) of the IM270 uses the following measurements for engine control: compressor inlet temperature (CIT), compressor discharge pressure (CDP), turbine discharge temperature (TOT), engine speed (N), engine power output (Pt), and fuel flow (W_f), as shown in Fig. 2. Compressor inlet pressure (CIP) is assumed to be equal to the ambient pressure minus a fixed inlet filter pressure loss. These measurements are common to modern gas turbines. Most engine control systems use fuel-air ratio control where CDP is used as a pseudoairflow parameter. It is well known that fuel-air ratio (W_f/CDP) has a high correlation with compressor stall margin. In order to ensure stable compressor operation, limiting W_f/CDP as a function of corrected speed is a reliable and common method. Moreover, when compressor stall/surge occurs, simultaneous CDP decrease results in a correspond-

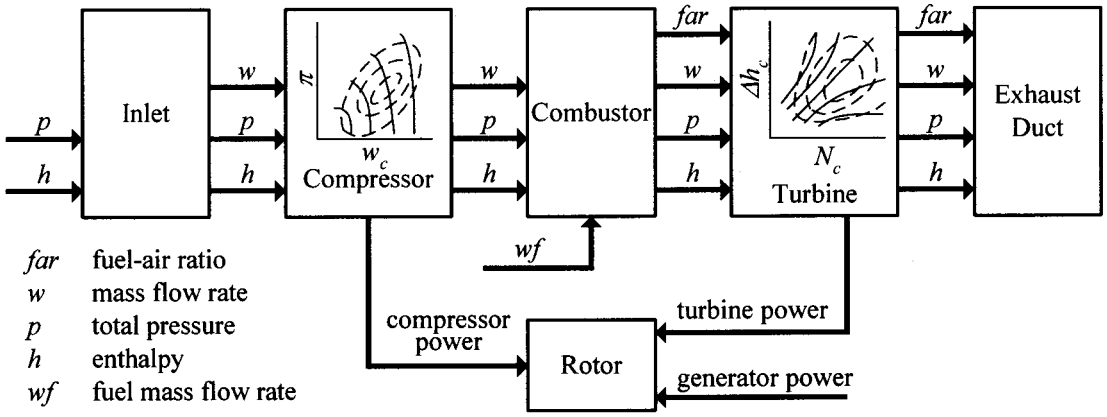

Fig. 3 Schematic of model components

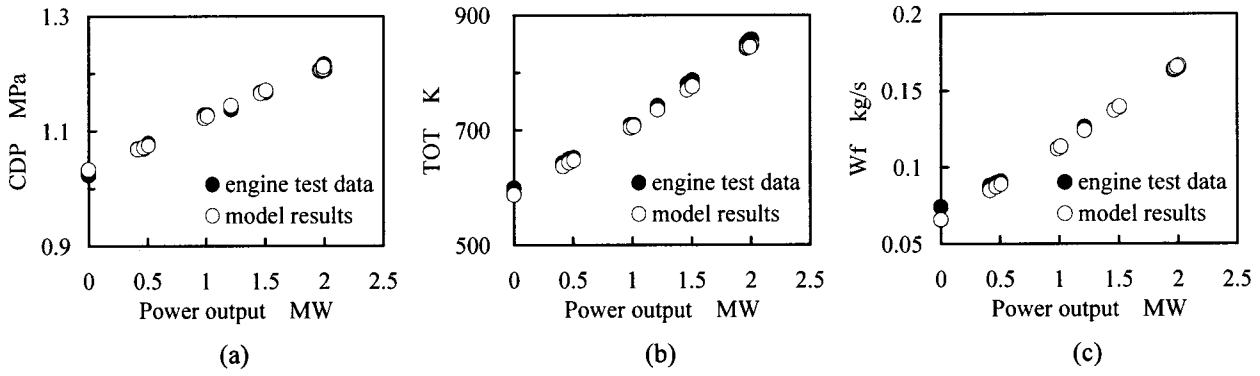

Fig. 4 Comparison of model results to engine test data: (*a*) compressor discharge pressure; (*b*) turbine outlet temperature; (*c*) fuel mass flow rate

ing fuel flow decrease preventing further damage. Turbine discharge temperature is clearly an important parameter not only for engine performance but also for engine safety.

The IM270 consists of a compressor, a combustor, and a turbine. The characteristics of the compressor and the turbine are described by corrected mass flow rate and efficiency. These are functions of reduced speed and pressure ratio. Combustor efficiency is also a major performance parameter for gas turbines. Therefore there are at least five parameters to be identified. The correction factors related to those parameters defined below are adjustable:

$$W_{Cc} = Cf_{wc} \times \text{function}_{\text{compressor flow rate}}(N_c, \pi_C)$$

$$\eta_C = Cf_{\eta c} \times \text{function}_{\text{compressor efficiency}}(N_c, \pi_C)$$

$$W_{Tc} = Cf_{wT} \times \text{function}_{\text{turbine flow rate}}(N_c, \pi_T)$$

$$\eta_T = Cf_{\eta T} \times \text{function}_{\text{turbine efficiency}}(N_c, \pi_T)$$

$$\eta_B = Cf_{\eta B} \times \eta_{B\ \text{nominal}}.$$

Given CIT, CIP, Pt, and N measurements, the engine model outputs CDP, TOT, and W_f. The differences between measured and computed CDP, TOT, and W_f are used to estimate component performance deviation. It is possible to eliminate the differences by adjusting the correction factors. However, by adjusting the five correction factors with only three measurements available, there are an infinite number of solutions. This situation is common for most of gas turbine engine condition monitoring tasks: namely, there are more adjustable parameters than available measurements, making algorithm development challenging.

In order to overcome this difficulty, throughout this study single component fault is assumed since simultaneous multiple faults are unlikely to occur. This assumption reduces the number of unknown parameters from 5 to at most 2.

4 Ability to Identify and Linear Dependency

When different combinations of parameter deviations cause identical measurement deviation, it is impossible to identify them separately. It is important to know a priori that the sensor system can identify the type of fault. The ability to identify any two faults can be determined by examining the linear dependency of the measurement deviation vectors caused by the parameter deviations. When the measurement deviation vectors are linearly dependent, it is impossible to distinguish them from each other. Taking the inner product checks the linear dependency of the vectors. When the inner product of the normalized vectors is 1, the two vectors are linearly dependent.

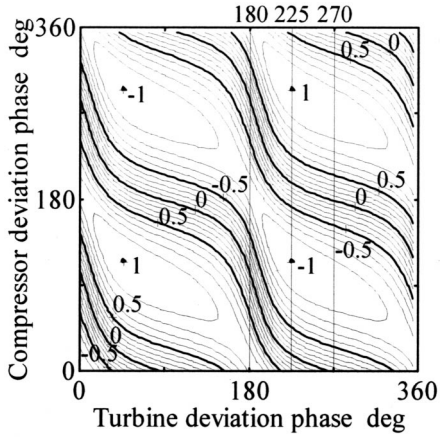

Fig. 5 Linear dependency of compressor fault and turbine fault

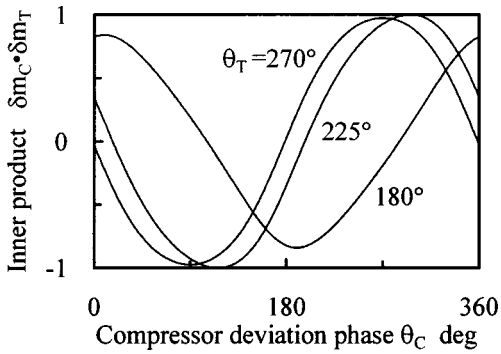

Fig. 6 Linear dependency of compressor fault for fixed turbine faults

When the parameter deviations are small, the relation between measurements and parameters are linear and written as follows:

$$\delta m = S \cdot \delta P, \tag{1a}$$

$$\delta m = \begin{pmatrix} \delta\text{CDP} \\ \delta\text{TOT} \\ \delta W_f \end{pmatrix}, \quad \delta P = \begin{pmatrix} \delta\eta_C \\ \delta W_C \\ \delta\eta_T \\ \delta W_T \\ \delta\eta_B \end{pmatrix}.$$

S is the sensitivity matrix and δ is the normalized deviation from the nominal value. The sensitivity matrix computed by the engine model at the design point with 2-MW output is shown below. Each parameter was changed by $\pm 1\%$ and 2%. The relations were reasonably linear,

$$S = \begin{pmatrix} -0.2796 & 0.7056 & -0.3969 & -0.7509 & -0.0059 \\ -0.5801 & -0.3827 & -0.8492 & 0.1188 & 0.0409 \\ -0.7286 & 0.0047 & -1.7379 & 0.4177 & -1.0055 \end{pmatrix}. \tag{1b}$$

In order to determine the ability to identify compressor and turbine faults with existing sensors, the normalized efficiency and flow rate deviation of them is represented by a magnitude and a phase as follows. Since the deviation magnitude does not affect the linear dependency check, the magnitude is set to unity,

$$\left.\begin{aligned} \delta\eta_C &= \sin\theta_C \\ \delta W_C &= \cos\theta_C \\ \delta P_C &= (\delta\eta_C \quad \delta W_C \quad 0 \quad 0 \quad 0)^T \end{aligned}\right\}, \tag{2}$$

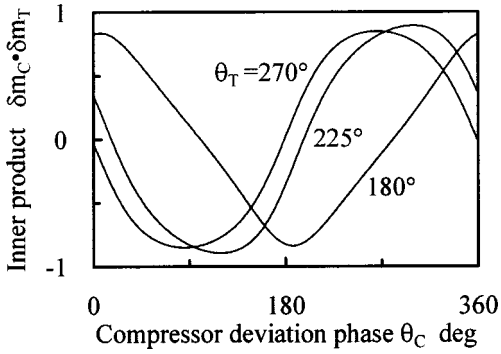

Fig. 7 Linear dependency of compressor fault with compressor discharge temperature

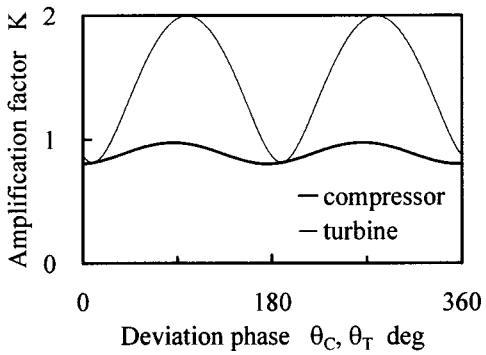

Fig. 8 Magnitude of measurement deviation due to compressor and turbine fault

$$\left.\begin{aligned}\delta\eta_T &= \sin\theta_T \\ \delta W_T &= \cos\theta_T \\ \delta P_T &= (0\ \ 0\ \ \delta\eta_T\ \ \delta W_T\ \ 0)^T\end{aligned}\right\}. \tag{3}$$

δP_C and δP_T are the parameter deviation vectors of the compressor and turbine, respectively.

By taking θ_C and θ_T from 0 to 2π, all combinations of compressor and turbine performance deviations can be examined. The measurement deviation vectors resulting from compressor and turbine deviations are expressed as follows:

$$\left.\begin{aligned}\delta m_C &= S\cdot\delta P_C \\ \delta m_T &= S\cdot\delta P_T\end{aligned}\right\}. \tag{4}$$

The linear dependency of the δm_C and δm_T provides information about the ability to identify compressor and turbine faults with the existing measurement system.

Figure 5 shows the linear dependency of the compressor and turbine performance deviations. There are regions where the inner product becomes nearly 1. Since it is impossible to distinguish compressor fault or turbine fault in these regions, other means such as physical reasoning are required. Figure 6 shows that the linear dependency varies with compressor deviation phase θ_C along the constant turbine deviation phase lines shown in Fig. 5. It is possible to theoretically distinguish between compressor and turbine fault when the inner product is not 1. However, there exists measurement noise that may degrade the quality of the signals. Noise effects on detection capability are discussed in a later section.

Figure 7 shows that when the compressor discharge temperature is known, regions of inner product equal to 1 are eliminated. This is a desirable condition for diagnostics since it is possible to determine the type of fault throughout the entire region; namely, all combinations of efficiency and flow rate deviation are distinguishable. In this paper, however, the capability of the fault detection and identification of the sensor system without the compressor discharge temperature measurement is explored.

Compressor and turbine faults are not linearly dependent with any combustor efficiency fault. Combustor flow rate faults and combustor pressure loss deviations were not studied in this paper.

Thus far, we have discussed the phase of the component performance deviation vector. In order to study fault detection ability, it is necessary to know the amplitude relations among performance and measurement deviation vectors and noise vectors. The amplification factor K is defined as follows:

$$|\delta m| = K|\delta P|, \tag{5}$$

where $|\delta m|$ and $|\delta P|$ are the magnitude of the measurement and parameter deviation vectors. As shown in Fig. 8, the amplification factor K of the compressor is nearly constant regardless of the value of the phase. On the other hand, K of the turbine varies with the phase. For turbine efficiency and flow capacity, K is about 2 and 1, respectively.

When the noise vector δn is perpendicular to the measurement deviation vector, the noise effect on the solution error is the largest. The inner product of the noise contaminated measurement deviation vector $\delta m+\delta n$ and the measurement deviation vector δm is approximately $1-\frac{1}{2}(|\delta n|/|\delta m|)^2$ when $|\delta n|/|\delta m| \ll 1$. For 20% of noise level-to-measurement deviation, the inner product is approximately 0.98.

5 Fault Detection and Identification Algorithm

If two adjustable parameters are fixed to their respective nominal values, the number of equations and unknown parameters are the same. Therefore three adjustable parameters are computed by nonlinear equation solving techniques such as the Newton-Raphson method. All ten possible combinations were computed. Four of them were found to be numerically unstable while the following six cases were stable (see Table 1).

Suppose that a compressor related fault occurs. The measurements may differ from the nominal values as follows:

$$\begin{pmatrix}\delta\text{CDP}\\ \delta\text{TOT}\\ \delta W_f\end{pmatrix} = \begin{pmatrix}s_{11} & s_{12}\\ s_{21} & s_{22}\\ s_{31} & s_{32}\end{pmatrix}\begin{pmatrix}\delta\eta_C\\ \delta W_C\end{pmatrix}. \tag{6}$$

In the case where η_C and W_C are fixed, the adjustable parameters are computed by

$$\begin{pmatrix}\delta\eta_T^*\\ \delta W_T^*\\ \delta\eta_B^*\end{pmatrix} = \begin{pmatrix}s_{13} & s_{14} & s_{15}\\ s_{23} & s_{24} & s_{25}\\ s_{33} & s_{34} & s_{35}\end{pmatrix}^{-1}\begin{pmatrix}s_{11} & s_{12}\\ s_{21} & s_{22}\\ s_{31} & s_{32}\end{pmatrix}\begin{pmatrix}\delta\eta_C\\ \delta W_C\end{pmatrix}. \tag{7}$$

From possible combinations, the following matrix is obtained. Each column vector consists of the corresponding adjustable parameters of each case:

$$M = ((\delta P_1^*),(\delta P_2^*),(\delta P_3^*),(\delta P_4^*),(\delta P_5^*),(\delta P_6^*)), \tag{8}$$

where $\delta P_4^* = (0\ 0\ \delta\eta_T^*\ \delta W_T^*\ \delta\eta_B^*)^T$, etc. These vectors are called pseudoparameter deviation vectors in order to distinguish them from the real parameter deviation vectors. The matrix is called a pseudoparameter deviation matrix.

When the engine performance deviates from the nominal values, the measurement values also deviate. Given the measurement deviation vectors, the engine model can compute the pseudoparameter deviation vectors $\delta P_{E\,i}^*$ and the pseudomatrix M_E. The average magnitude of the pseudoparameter deviation vectors can be used for fault detection purposes,

$$\zeta = \frac{1}{6}\sum_{i=1}^{6}|\delta P_{E\ i}^*|. \tag{9}$$

$|\delta P_{E\,i}^*|$ is the magnitude of ith pseudoparameter deviation vector.

The next step is to identify the faulty component. First, the compressor fault is assumed to be

Table 1 Numerically stable combinations of adjustable parameters

	η_C	W_C	η_T	W_T	η_B
Case 1	compute	compute	fix	compute	fix
Case 2	compute	compute	fix	fix	compute
Case 3	fix	compute	compute	compute	fix
Case 4	fix	fix	compute	compute	compute
Case 5	compute	fix	fix	compute	compute
Case 6	fix	compute	compute	fix	compute

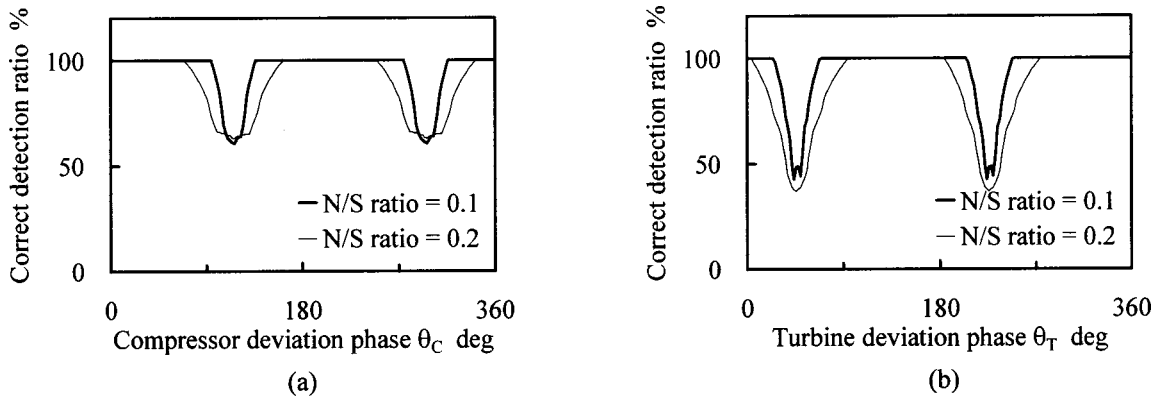

Fig. 9 Correct identification ratio: (*a*) ratio for compressor fault; (*b*) ratio for turbine fault

$$\left.\begin{aligned}\delta\eta_C &= R_C \sin\theta_C \\ \delta W_C &= R_C \cos\theta_C\end{aligned}\right\}. \tag{10}$$

Using the sensitivity matrix, the pseudoparameter deviation vectors $\delta P^*_{C\,i}$ and the pseudomatrix M_C are computed. Setting $R_C = 1$, the matrix M_C becomes a function of θ_C,

$$M_C = fn(\theta_C). \tag{11}$$

After normalizing each column vector of the matrix M_C and M_E, $\theta_{C\,\mathrm{fit}}$, which gives minimum error, is selected as the phase of the compressor fault and $(\delta P^*_{C\,\mathrm{fit}})_i$ is computed. R_C is computed as the ratio of the magnitudes of the column vectors,

$$R_C = \frac{1}{6}\sum_{i=1}^{6}\frac{|\delta P^*_{E\,i}|}{|(\delta P^*_{C\,\mathrm{fit}})_i|}. \tag{12}$$

Finally, the residual error is computed from the following:

$$\left.\begin{aligned}E_{C\,\mathrm{abs}} &= \sqrt{\frac{1}{6}\sum_{i=1}^{6}|\delta P^*_{E\,i} - (\delta P^*_{C\,\mathrm{fit}})_i|^2} \\ E_{C\,\mathrm{rel}} &= \frac{E_{C\,\mathrm{abs}}}{R_C}\end{aligned}\right\}. \tag{13}$$

Similarly, θ_T, R_T, and E_T for the turbine are computed. The faulty component is the one that gives smaller residual error.

The above-mentioned procedure is summarized as follows:

(a) Compute the pseudoparameter deviation vector $\delta P^*_{E\,i}$ and matrix M_E by using the detailed nonlinear engine model with measurements (Eq. (8)).

(b) Detect a fault by using the average magnitude of the pseudoparameter deviation vectors ζ (Eq. (9)).

(c) Assume a compressor fault as Eq. (10).

(d) Compute $\delta P^*_{C\,i}$ and M_C as a function of phase by using the sensitivity matrix S (Eq. (11)).

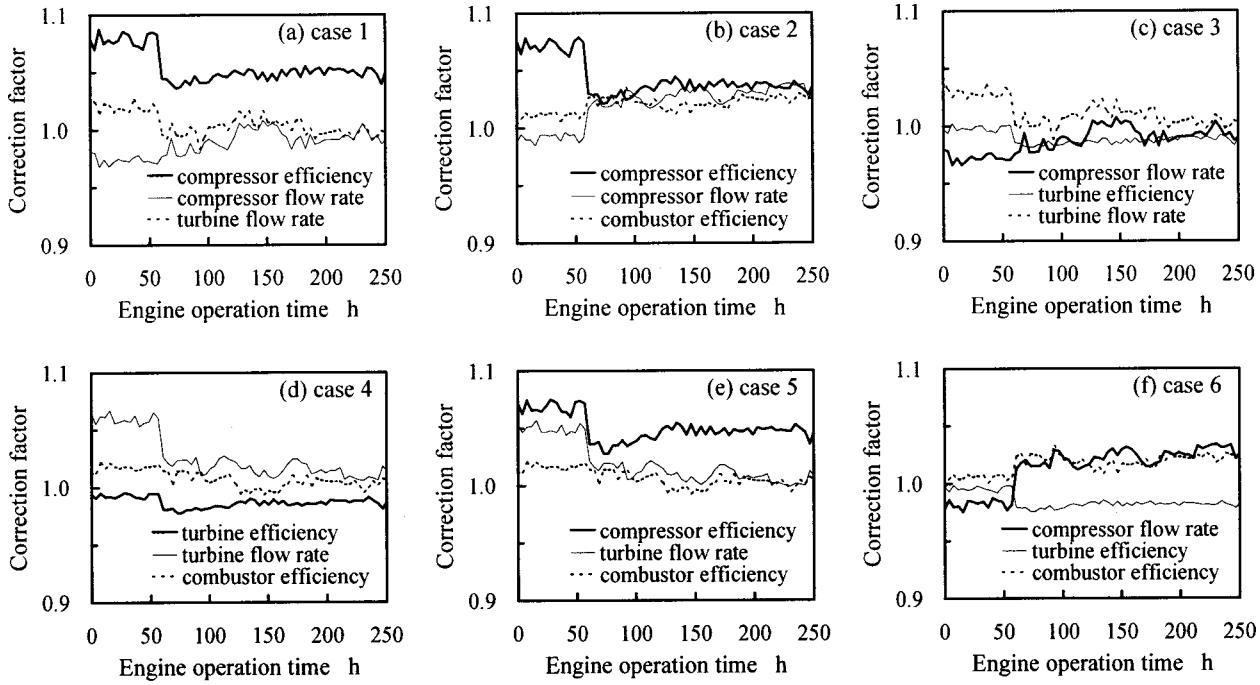

Fig. 10 Time history of correction factor deviation

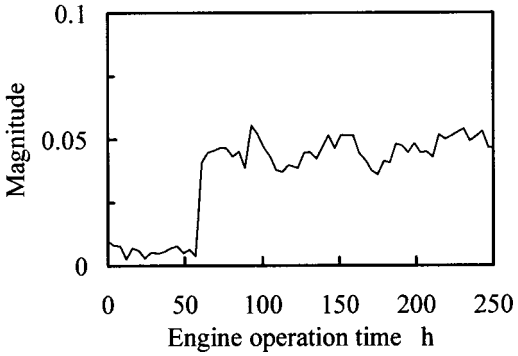

Fig. 11 Time history of average magnitude of pseudoparameter deviation vectors

(e) Find the phase $\theta_{C\,\mathrm{fit}}$ which gives minimum error of the normalized $\delta P^*_{E\,i}$ and $\delta P^*_{C\,i}$.

(f) Compute the magnitude R_C and the residual error E_C as Eqs. (12) and (13), respectively.

(g) Repeat the procedure from (c) through (f) for the turbine.

(h) Identify the faulty component by comparing the residual errors E_C and E_T.

6 Numerical Simulation

In order to evaluate the combined effects of linear dependency and noise on the correct identification ratio, a numerical simulation was conducted. As shown in Fig. 9 the correct identification ratio varies with the phase of the fault. At phases where the linear dependency is nearly unity the correct identification ratio falls to 50% as expected. The ratio also decreases as the noise magnitude level increases. The thick line and the thin line show 0.1 and 0.2 noise levels over parameter deviation ratio, respectively.

7 Application to Operational Data

The algorithm was applied to the actual IM270 operational data that were acquired by the ECU. Figure 10 shows the time history of the correction factor deviations computed by the engine model with the measurements.

Figure 11 shows the average magnitude of these pseudoparameter deviation vectors. A significant jump in magnitude from about 1% to 5% at time 61 h can be clearly seen. Figures 12(*a*) and (*b*) show the time history of the phase and magnitude of the compressor performance deviations, respectively. The fluctuating phase converges to a nearly constant 300 deg after the event. The magnitude jumps from nearly 1% to 4% and remains at that level after the event. The phase and magnitude correspond to −3.5% and +2% efficiency and flow rate deviations, respectively. Figure 12(*c*) shows a polar graph of the compressor performance deviation.

Figure 13 shows the turbine performance deviation. Similar observations are obtained. For the turbine, the magnitude and the phase were found to be 5% and 200 deg, respectively, which correspond to −1.7% and −4.7% efficiency and flow rate deviation, respectively.

Figure 14 shows the average relative and absolute error magnitude of the pseudoparameter deviation vectors for the compressor and the turbine, respectively. Both figures indicate that after the

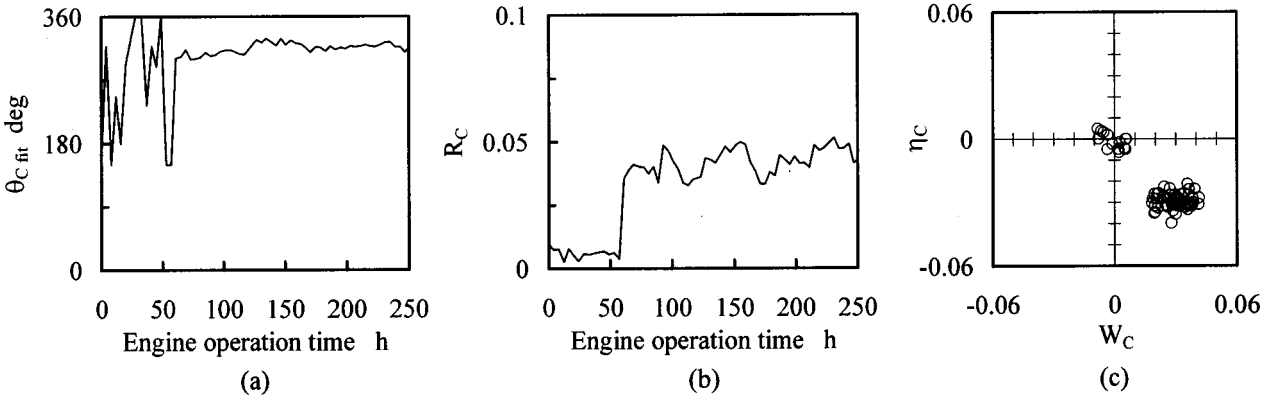

Fig. 12 Compressor fault detection: (*a*) time history of compressor fault phase; (*b*) time history of compressor fault magnitude; (*c*) polar diagram of compressor fault

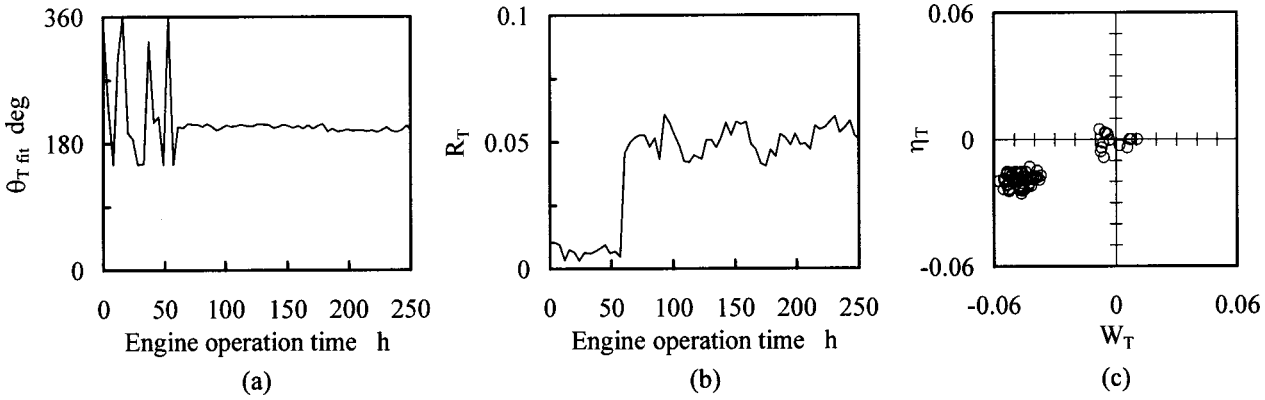

Fig. 13 Turbine fault detection: (*a*) time history of turbine fault phase; (*b*) time history of turbine fault magnitude; (*c*) polar diagram of turbine fault

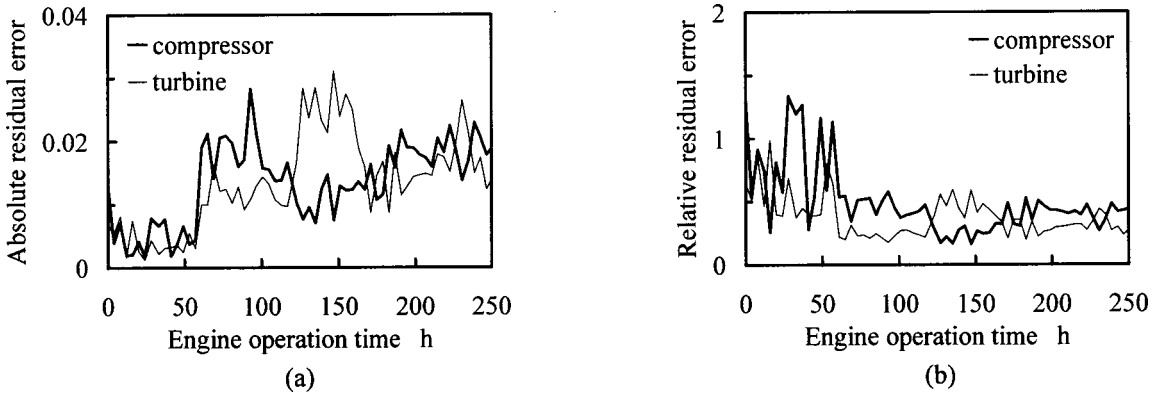

Fig. 14 Time history of identification error: (*a*) absolute identification error; (*b*) relative identification error

event, at time 61–123 h, the turbine error magnitude is smaller than that of the compressor. On the contrary, from time 123–191 h the turbine errors are greater than those of the compressor. The turbine error magnitude is again smaller after time 191 h. It is difficult to determine which component is responsible. This ambiguity stems from the linear dependency of the measurement deviation vectors (see Fig. 6). Turbine malfunction was found to be responsible for the event after the engine was disassembled and inspected.

8 Conclusions

The proposed fault detection and identification algorithm has the following features:

(i) Only measurements acquired for the engine control are used. No additional measurements are required.

(ii) The number of available measurements may be smaller than parameters to be identified.

(iii) Weighting factors that require significant experience are not necessary. It is easily applied to newly developed engines.

(iv) An accurate engine model and a sensitivity matrix about the operating point are required for correct fault detection and identification.

Given IM270 operational data, the algorithm was able to quantitatively identify the efficiency and the flow rate deviation of the compressor and the turbine, assuming a single component fault.

There remains some ambiguity regarding which component is responsible for the sudden performance deviation. It was shown that this was due to the high linear dependency of the measurement deviation vectors. Addition of a compressor discharge temperature sensor would improve detection and identification.

In this study only the efficiency deviation was considered for the combustor. It is straightforward to extend the algorithm to include the combustor flow rate or pressure loss deviation.

Acknowledgment

This study was funded by an in-house research fund.

Nomenclature

CDP = compressor discharge pressure
Cf_{WC} = compressor mass flow rate correction factor
Cf_{WT} = turbine mass flow rate correction factor
$Cf_{\eta B}$ = combustor efficiency correction factor
$Cf_{\eta C}$ = compressor efficiency correction factor
$Cf_{\eta T}$ = turbine efficiency correction factor
CIT = compressor inlet temperature
E = residual error magnitude of pseudoparameter deviation matrix
M = pseudoparameter deviation matrix
m = measurement vector
N = engine rotor speed
N_c = corrected engine rotor speed
P = parameter vector
R = magnitude of component fault
S = sensitivity matrix
TOT = turbine outlet temperature
W_C = compressor mass flow rate
W_{Cc} = corrected compressor mass flow rate
W_f = fuel mass flow rate
W_T = turbine mass flow rate
W_{Tc} = corrected turbine mass flow rate
δP^* = pseudoparameter deviation vector
δx = normalized deviation from nominal value $(=x-x_{\text{nominal}}/x_{\text{nominal}})$
η_B = combustor efficiency
η_C = compressor efficiency
η_T = turbine efficiency
π_C = compressor pressure ratio
π_T = turbine pressure ratio
θ = phase of component fault
ζ = average magnitude of pseudoparameter deviation vector

Sub- and Superscripts

C = compressor
E = engine model derived
T = turbine
$*$ = pseudoparameter vector or its element

References

[1] Urban, L. A., 1972, "Gas Path Analysis Applied to Turbine Engine Condition Monitoring," AIAA/SAE Paper 72–1082.
[2] Doel, D. L., 1994, "TEMPER—A Gas Path Analysis Tool for Commercial Jet Engines," ASME J. Eng. Gas Turbines Power, **116**, pp. 82–89.
[3] Volponi, A. J., 1982, "A Large Measurement Error Recovery Algorithm for Gas Turbine Module Performance Analysis," Hamilton Standard Report No. 3430.
[4] Doel, D. L., 2002, "Interpretation of Weighted-Least-Squares Gas Path Analysis Results," ASME Paper GT-2002-30025.
[5] Aretakis, N., Mathioudakis, K., and Stamatis, A., 2002, "Non-Linear Engine Component Fault Diagnosis From a Limited Number of Measurements Using a Combinatorial Approach," ASME Paper GT-2002-30031.
[6] Kobayashi, H., Tugumi, S., Yonezawa, Y., and Imamura, R., 1996, "2MW Class High Efficiency Gas Turbine IM270 for Co-Generation Plants," ASME Paper 96-GT-001.
[7] Yonezawa, Y., Imamura, R., and Kobayashi, H., 1998, "Development of 2MW Class Gas Turbine IM270 for Co-Generation Plants," Proc. 22th CIMAC.
[8] Sellers, J. F., and Daniele, C. J., 1975, "DYNGEN—A Program for Calculating Steady-State and Transient Performance of Turbojet and Turbofan Engines," NASA TN D-7901.

Herbert Jericha

Emil Göttlich

Wolfgang Sanz
e-mail: Wolfgang.sanz@tugraz.at

Franz Heitmeir

Institute for Thermal Turbomachinery and
Machine Dynamics,
Graz University of Technology,
Inffeldgasse 25,
A-8010 Graz, Austria

Design Optimization of the Graz Cycle Prototype Plant

Introduction of closed-cycle gas turbines with their capability of retaining combustion generated CO_2 can offer a valuable contribution to the Kyoto goal and to future power generation. The use of well-established gas turbine technology enhanced by recent research results enables designers even today to present proposals for prototype plants. Research and development work of TTM Institute of Graz University of Technology since the 1990s has lead to the Graz cycle, a zero-emission power cycle of highest efficiency and with most positive features. In this work the design for a prototype plant based on current technology as well as cutting-edge turbomachinery is presented. The object of such a plant shall be the demonstration of operational capabilities and shall lead to the planning and design of much larger units of highest reliability and thermal efficiency. [DOI: 10.1115/1.1762910]

Introduction

Optimization of a thermal power plant starts with the optimization of the cycle scheme, i.e., the thermodynamic relations of cycle media in the process of power production. Like in any heat engine it involves according to Carnot's rule introduction of fuel heat input at maximum possible temperature, compression and expansion at maximum compressor and turbine efficiency and release of non-convertible heat to ambient at minimum loss. The relations of media within the cycle have to be optimised regarding heat transfer, pressure loss, material cooling, in the many connections that have been invented and are in use today.

Turbomachinery design has to be optimised first of all in terms of flow efficiency, high temperature blade cooling methods, rotor speed and turbine-compressor driving connections in any case on the basis of sound rotor dynamics.

Surface heat exchangers such as steam generators, feed water heaters and condensers have to be carefully studied to minimize costs in general and to minimize requirements of high temperature metal for heat transfer surfaces and associated pressure losses.

Closed-cycle gas turbines of zero emission with the capability of capturing or retaining combustion generated CO_2 require novel cycle solutions. A general comparison between different solutions of CO_2 retaining plants is given very detailed in [1]. Among them was the so-called Graz cycle system, which has been presented by the authors in several papers at previous conferences (CIMAC, ASME, VDI, [2–6]). Any fossil fuel gas (preferable with low nitrogen content) is proposed to be combusted with oxygen so that mainly only the two combustion products CO_2 and H_2O are generated. Oxygen can be generated from air by air separation plants which are in use worldwide with great outputs in steel making industry and even in enhanced oil recovery.

Although the Graz cycle is suited for all kinds of fossil fuels, for natural gas fuel it seems reasonable to reform CH_4 to $CO + H_2$. Hydrogen can be separated and burned in an air-breathing gas turbine, a solution which reduces the oxygen requirements considerably, [7]. But in using oxygen blown coal gas as a fuel a Graz cycle plant is most effective in retaining CO_2 and in use of oxygen.

The thermodynamic details of a prototype Graz cycle plant of 92 MW power fired with oxygen blown coal fuel gas were presented to VDI in 2000 [5]. This cycle scheme shall be used here as the basis of turbomachinery optimization discussion. A general layout of all components, especially turbomachines, combustion chamber and burners, and general arrangement with gears and electric generators was presented at ASME IGTI conference 2002, [6].

The object of this paper is to present this kind of zero-emission cycle optimized for highest thermal cycle efficiency. The deliberations which have led to the cycle scheme as well as to the special design of blading and rotors are shown. This work specially concentrates on the high temperature turbine and its first transonic stage with the associated innovative steam cooling system.

Cycle Optimization

Figure 1 shows the principle flow scheme of the Graz cycle with the main components and will be used to explain the main characteristics of this zero-emission power cycle. Detailed cycle data for a 92 MW pilot plant, like mass flow, pressure, temperature, enthalpy, or cycle fluid composition as well as the details of the thermodynamic simulation performed with the commercial code IPSEpro by SIMTECH Comp. can be found in the Appendix (Fig. 13 from [6]).

Basically the Graz cycle consists of a high-temperature Brayton cycle (compressors C2, C3, combustion chamber, and HTT) and a low temperature Rankine cycle (LPT, condenser, HRSG, and HPT). In the layout presented a proposed fuel with a typical composition from an oxygen blown coal gasification plant is taken (fuel gas mole fractions: 0.1 CO_2, 0.4 CO, 0.5 H_2). The fuel together with the stoichiometric mass flow of oxygen is fed to the combustion chamber, which is operated at a pressure of 40 bar. Steam as well as CO_2 is supplied to cool the burners and the liner. A mixture of about three quarters of CO_2 and one quarter of steam leaves the combustion chamber at a mean temperature of 1400°C. The fluid is expanded to a pressure of 1 bar and 642°C in the HTT. The hot exhaust gas is used in the following HRSG to vaporize and superheat steam for the HPT. Then it is further expanded in the LPT to a condenser pressure of 0.25 bar. In the condenser the separation of CO_2 and H_2O takes place by water condensation. The water is preheated and in the HRSG vaporized and superheated. The steam is then delivered to the HPT with 180 bar and 567°C, after the expansion it is used to cool the burners. The CO_2 from the condenser is compressed to atmospheric pressure, the combustion CO_2 is then separated for further use or storage. The remaining CO_2 is compressed and fed to the combustion chamber to cool the liners.

The cycle arrangement of the Graz cycle offers several advantages: On one hand, it allows heat input at very high temperature, whereas on the other hand expansion takes place till to vacuum

Contributed by the International Gas Turbine Institute (IGTI) of THE AMERICAN SOCIETY OF MECHANICAL ENGINEERS for publication in the ASME JOURNAL OF ENGINEERING FOR GAS TURBINES AND POWER. Paper presented at the International Gas Turbine and Aeroengine Congress and Exhibition, Atlanta, GA, June 16–19, 2003, Paper No. 2003-GT-38120. Manuscript received by IGTI, October 2002, final revision, March 2003. Associate Editor: H. R. Simmons.

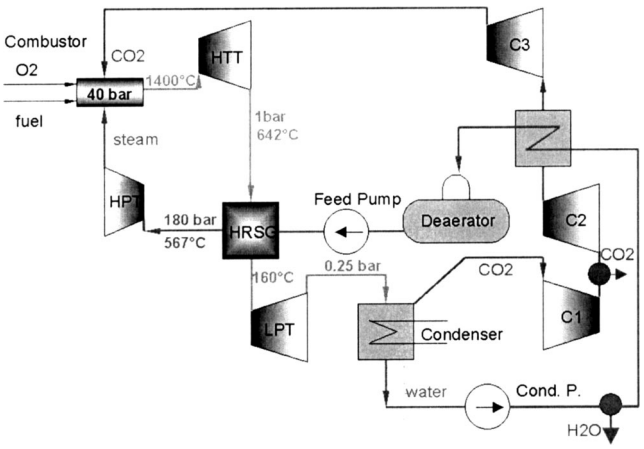

Fig. 1 Principle flow scheme of Graz cycle power plant

conditions, so that a high thermal efficiency according to Carnot can be achieved. The dual medium CO_2 and H_2O results also in very low compression work (see Appendix). With both medium components in use over the full temperature range, the cycle gives this beneficial effect since only the gas CO_2 requires turbo compressors (C1, C2, C3) whereas feed water can be pumped to form high pressure steam. High pressure steam can be expanded to generate additional power in the high pressure turbine HPT, before being united with the CO_2 flow in the combustion chamber. Further beneficial effects are the possibility to create burner vortices and to cool the hottest nozzles and blades of the HTT first stage, because the exhaust steam of the HPT is of suitable pressure and temperature and can be passed through the hollow blades in order to cool the blading. The effect of blade cooling is simulated by extracting steam after the HPT and its admixing to the cycle medium before and after the first stage of the HTT (see Appendix).

Assuming state-of-the-art turbomachinery efficiencies the thermodynamic simulation for a 92 MW pilot plant shows a total turbine power of 111 MW, 90 MW of it are supplied by the HTT (see Table 1). On the other side the total compression power mostly used for CO_2 compression is 18.8 MW. Considering component pressure losses as well as mechanical and electrical losses, an overall thermal cycle efficiency of 63.0% can be evaluated which is significantly beyond state-of-the-art combined cycle power plants of 60%. But considering the efforts for oxygen production (0.25 kWh/kg O_2) the efficiency is reduced to 57.5%, the effort for the oxygen compression from atmosphere to combustion pressure results in a net efficiency of 55%. This efficiency penalty compared to combined cycle plants has to be balanced by the savings from a future tax on CO_2.

Table 1 Main turbomachinery data and Graz cycle power balance [6]

Turbines: Total Turbine Power 111081 kW						
Turbine Name		HPT	HPT cool	HTT hp	HTT 1p	LPT
m	kg/s	21.36	3.0	88.48	91.48	91.48
V_{inlet}	m^3/s	0.4125	0.195	9.264	31.50	106.67
V_{exit}	m^3/s	1.387	0.590	30.65	226.05	331.71
P	kW	8544	837	39374	51595	10731
n	rpm	20000	20000	20000	12000	3000
z	-	1 rad+ 2axi	1 part. adm.	1	2	2
$D_{m,inlet}$	m	0.468	-	0.496	0.800	1.640
L_{inlet}	m	0.01	-	0.064	0.170	0.338
$D_{m,exit}$	m	0.227	-	0.510	0.880	1.640
L_{exit}	m	0.027	-	0.070	0.250	0.513
Compressors and Pumps: Total Compression Power 18830 kW						
Compressor Name		C1	C2	C3	Cond. Pump	Feed Pump
m	kg/s	66.33	52.48	51.15	25.16	21.36
V_{inlet}	m^3/s	150.83	39.13	10.60	0.0252	0.0233
V_{exit}	m^3/s	49.46	17.43	1.169	0.0252	0.022
P	kW	5498	3957	8953	12	410
n	rpm	3000	12000	20000	3000	3000
z	-	7	5	7+1 rad		
$D_{a,inlet}$	m	1.47	0.528	0.274		
L_{inlet}	m	0.304	0.137	0.068		
D_i/D_a	-	0.586	0.481	0.504		
M	rel.at tip	1.00	1.31	1.39		
$D_{a,exit}$	m	1.47	0.462	0.280		
L_{exit}	m	0.084	0.071	0.014		
Power balance:						
Net power:						92251 kW
Total combustion heat input:						143342 kW
Mechanical and generator efficiency:						0.98
Thermal cycle efficiency:						**63.0%**
O_2 generation by air separation (0.25 kWh/kg):						7940 kW
O_2 compression (atmosphere to burner):						3440 kW
Net cycle efficiency:						**55.0%**

Turbomachinery Optimization

Figure 2 shows a schematic arrangement of turbomachinery shafts as presented in [6]. Mass flow, power, speed, dimensions, and number of stages of the turbomachinery are given in Table 1.

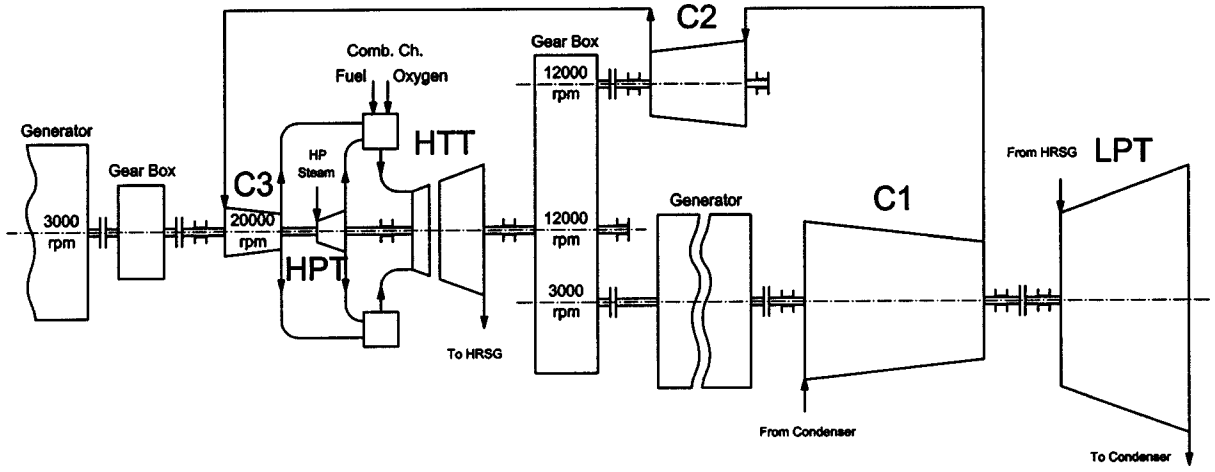

Fig. 2 Schematic arrangement of turbomachine shafts

The reader is asked to take note that a priori design optimization experience is introduced by this basic turbomachinery arrangement already. Design rules such as putting on a common shaft of turbines and driven compressors of similar optimal speed are observed as well as the rule to expand the hottest gas flow in a single annular channel without any buried bearings or casing crossovers.

From the logic of these connections and from the capabilities of the diverse components enabling them to fulfil their tasks most effectively an optimal situation is clearly visible, insofar as each specific task is made to function optional in itself. But anyhow the designer should keep in mind that care must be taken in introducing inventive features and not to contradict the rule of maximum simplicity.

In order to present a design optimization solution the design logic of three systems is discussed: the fuel oxygen burner and combustion chamber flow, the blading layout of the high temperature turbine HTT and its associated innovative steam cooling system ICS and finally the general arrangement of compressors, turbines, gear boxes, and electric generators of the prototype Graz cycle power plant.

Combustion Chamber. First the oxygen burner with stoichiometric combustion is treated. The system is being studied by several Japanese research institutions (CRIEPI, NEDO; HITACHI, MHI), recent research was done by [8]. The burners developed there are compared to the authors' proposal (see Fig. 3, H_2+O_2 burner design [2], CH_4+O_2 burner [8], oxygen blown fuel gas$+O_2$ [6]). As detailed in [6] the choice of burner design depends on the flame speed of fuel gas in oxygen. A fuel gas containing free hydrogen has a much higher flame speed, so no kind of premix appears possible.

Careful research is done to obtain optimal combustion efficiency and to avoid loss of reaction partners during the introduction of inert cooling flow into the burner zone, a measure necessary to avoid dissociation of molecules of reaction products in the hottest region of the flame. From previous work the authors' knowledge is that the effect of dissociation becomes important above 2000°C. Thus a complete combustion of the reaction partners is aimed at since dissociated molecules could be prone to be swept out of reaction zone by the surrounding inert cooling and cycle medium.

Figure 4 shows the cross section of combustion chamber and annular flame cage. The radial inflow with a strong swirl lengthens the reaction zone and gives a flatter turning angle for the HTT first stage nozzles.

Compressor Layout. Before discussing the high temperature turbine the compressors have to be deliberated since they more strictly define the speed requirements. After separation of the cycle media by condensation of water content compression of CO_2 is effected in axial turbo compressors C1 3000 rpm, C2 12,000 rpm and C3 20,000 rpm. The compressor C3 delivers pure CO_2 to the combustion chamber whereas compressors C1 and C2 contain a small amount of water which is finally condensed out during compression. The necessity of different speeds is given by the compressibility of CO_2 because the volume flow changes from 150 m^3/s at first compressor inlet to 1.17 m^3/s at last compressor outlet (see Table 1). The requirements for long first stage blades of C2 and C3 and a maximum admissible blade tip Mach number of 1.35, [9,10] lead to three different compressor speeds. This design allows to achieve at the same time a reasonable last stage blade length. Last stage of C3 is built as radial stage which allows to arrange a radial diffuser and scroll for efficient transfer to the combustion chamber.

High Temperature Turbine. The most advanced turbo machinery proposal is that of the high temperature gas turbine. Compared to an air-breathing gas turbine the cycle fluid has a gas constant R which is 11% smaller and a heat capacity c_p which is 23% larger. This results in nearly the same enthalpy drop for a given pressure ratio, but in higher temperatures, so that cooling is more important. The design features of the HTT make full use of the possibilities offered by the cycle. Even after part of the steam is mixed with the CO_2 flow in the combustion chamber already there is sufficient steam of low temperature and suitable pressure available to effect the cooling of the high temperature blading.

The high pressure ratio of 40:1 in the HTT together with the specific strong volume change of the media results in a very high ratio of outlet volume flow to inlet volume flow. So it is optimal to split the HTT in a first stage of 20,000 rpm directly connected to HPT and C3 thus giving also optimal speed for the last CO_2 axial

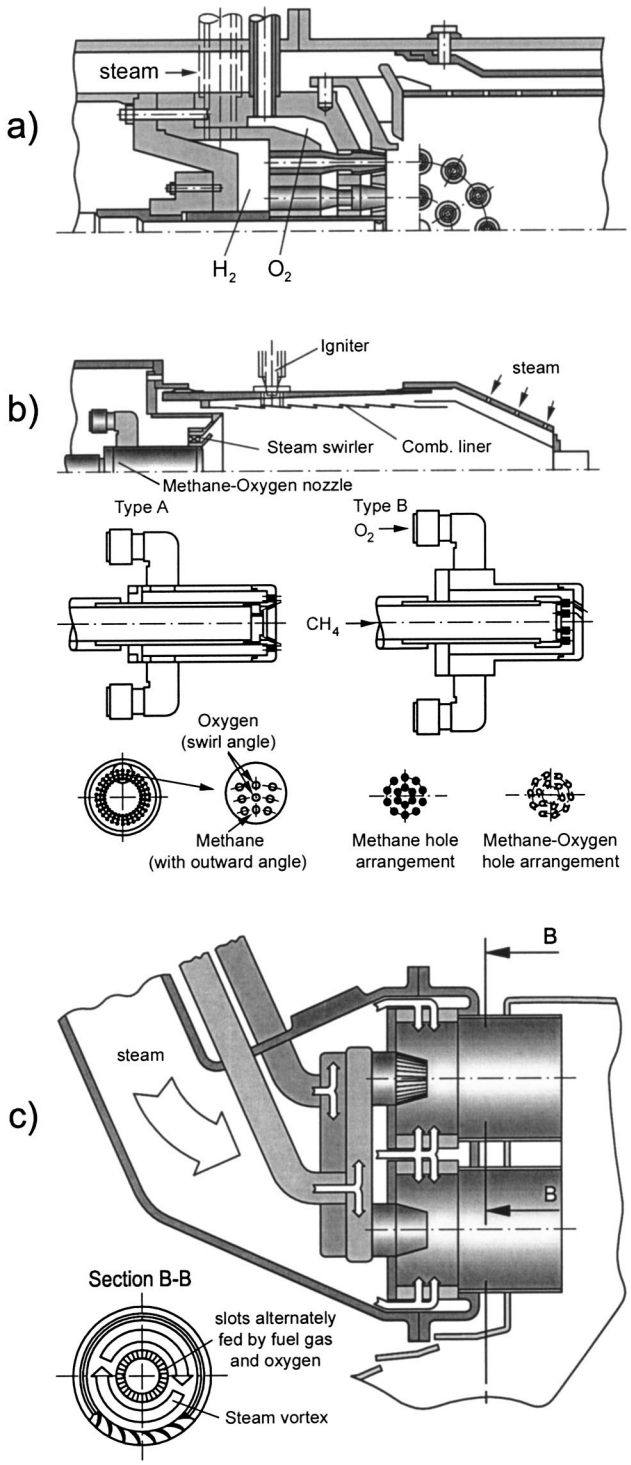

Fig. 3 Comparison of O_2 burner design solutions (*a*) H_2+O_2, (*b*) CH_4+O_2, (c) oxygen blown fuel gas$+O_2$

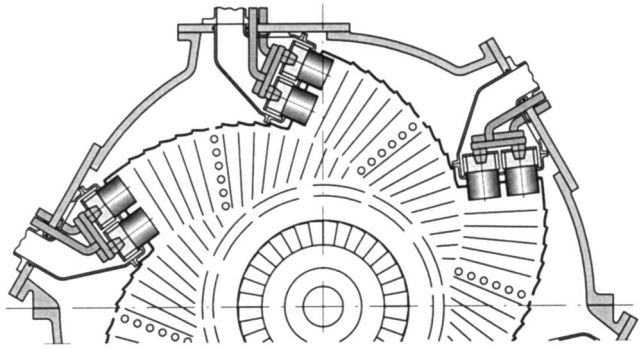

Fig. 4 Combustion chamber, O_2 burner and annular flame cage cross section at entry to HTT

compressor with a final radial stage (see Fig. 5). Two more stages also overhang on a common shaft with the main gear pinion with a side drive to C2 (this for physical arrangement reason only). This arrangement also allows a direct introduction of cooling steam from the HPT into the combustion chamber burners and into the HTT blade and disk cooling as described below (see Fig. 2 or 5).

As an example of design optimization the speed variation of the rotor of a standard gas turbine unit is shown in Fig. 6(*a*). Given is the enthalpy head and volume flow in and out of the three stage blading. The rotational speed is varied in the range of plus and minus 20% keeping the load factor ψ and degree of reaction constant at mean diameter. At higher speed a smaller mean diameter and thus higher blade lengths are obtained and accordingly a lower degree of reaction at the inner radius and a higher degree of reaction at the outer radius. On the other hand, lower speed at unchanged volume flow and enthalpy head leads to higher degree of reaction at the inner radius and lower degree of reaction at the outer radius.

Comparing the three cases shown in Fig. 6(*a*) at lower speed an improvement in blade isentropic flow efficiency (i.e., stage flow efficiency covering losses by friction on blade surfaces and side walls, tip leakage loss, etc., due to higher degree of reaction *R* at the root) can be expected but an increase in leakage loss (larger clearance and outer radius, shorter last blade). On the other hand an increase in speed lengthens the blade, decreases the rotor outer radius but at the inner radius leads to an unacceptable negative degree of reaction, an indication of possible hub and blade flow separation.

We observe a situation quite general in flow theory, that going close to separation gives some improvement in efficiency, but bears risks, so that a safe distance should be kept. So it can be concluded that for this turbine 5252 rpm is close to the optimal speed.

Figure 6(*b*) gives the comparable data of the Graz cycle HTT. The enthalpy head is still higher and the volume flow change is

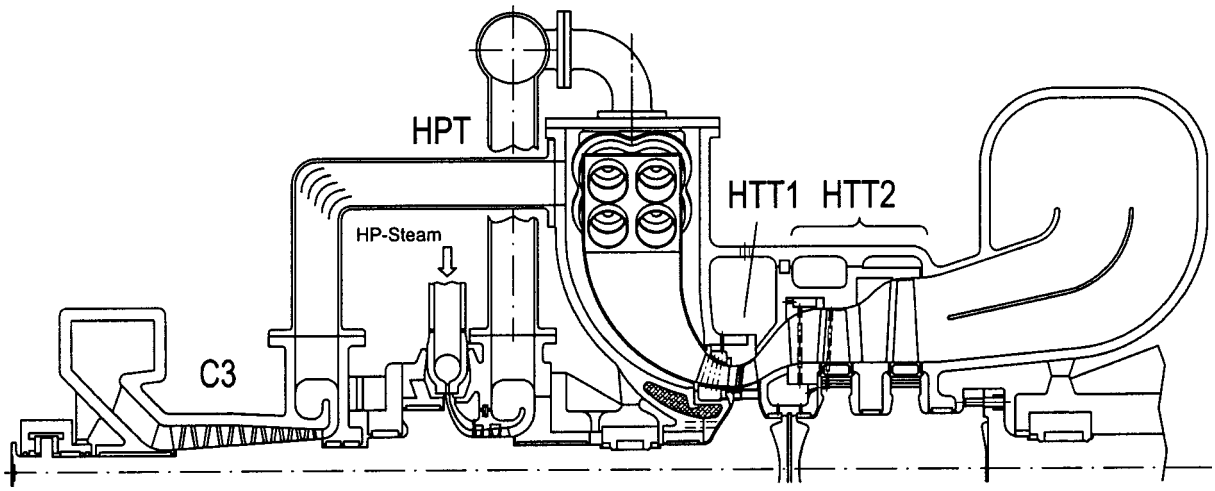

Fig. 5 High speed shaft, HTT and HPT driving C3 and power gear to el. generator Nr. 2

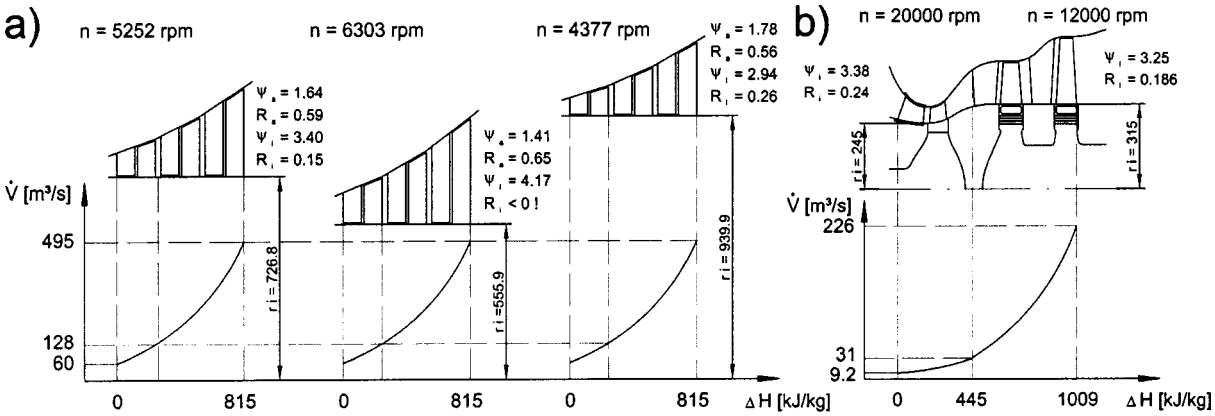

Fig. 6 (*a*) Standard gas turbine rotor speed optimization at given volume flow and enthalpy head; (*b*) HTT shaft built in two overhung disks (single and double) with optimal speed selected for compressor and gear drive

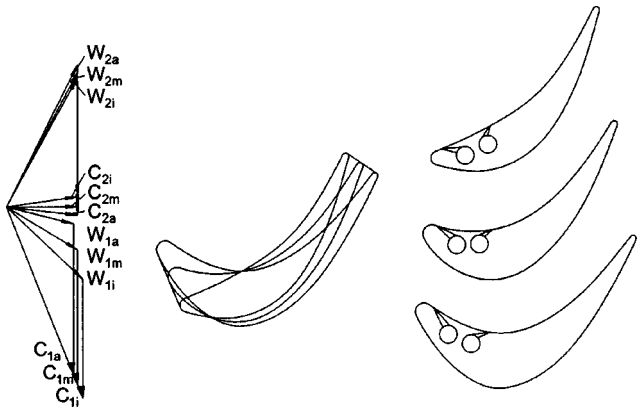

Fig. 7 HTT first-stage velocity triangles and blade profiles over blade height, for tip, mean and root section in curved annular blade channel

still more pronounced, so there is good reason to split into two shafts with the HTT first stage running much faster than the second and third stages.

The speeds are optimally suited to drive compressors and gear boxes for power transfer. The difference in diameter of stage one to stage two requires an annular flow connection and an inward curved channel from combustion chamber inlet via first stage outward to the larger radius of the second stage. This inward curved channel has the beneficial effect of reducing the otherwise high value of change of reaction of the first stage blade (see HTT first stage radial equilibrium of flow in the Appendix). A velocity triangle (see Fig. 7) obtained in this way shows the beneficial property of low twist and an almost straight trailing edge. The inlet edge follows a cone oblique to the blade radial axis and allows to keep the inlet edge radius almost constant. This facilitates manufacture of the high temperature material blade.

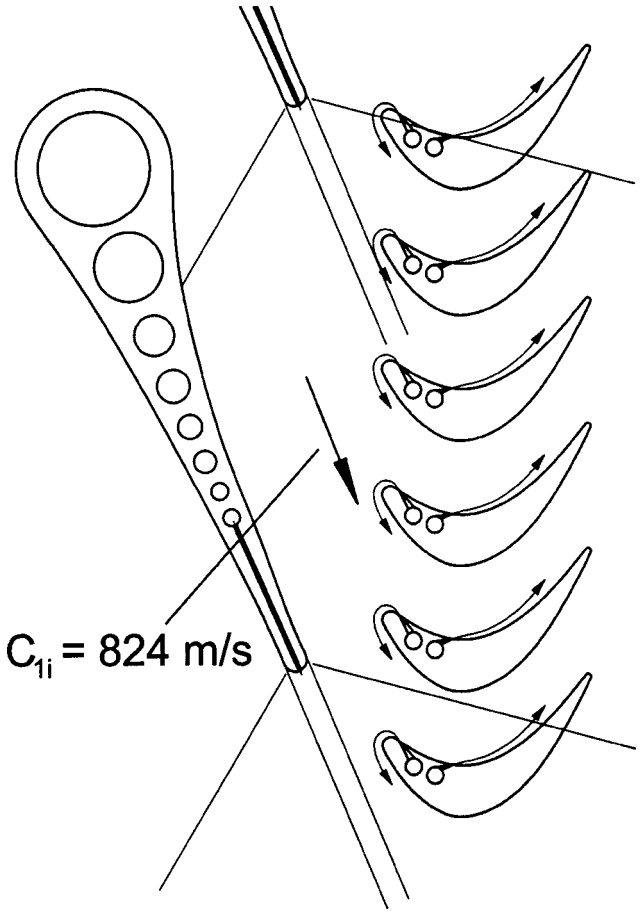

Fig. 8 HTT first-stage transonic expansion in nozzle profile near blade root and tail shocks of nozzle trailing edges reaching into blade profile inlet creating a high-frequency shock passing flow situation there

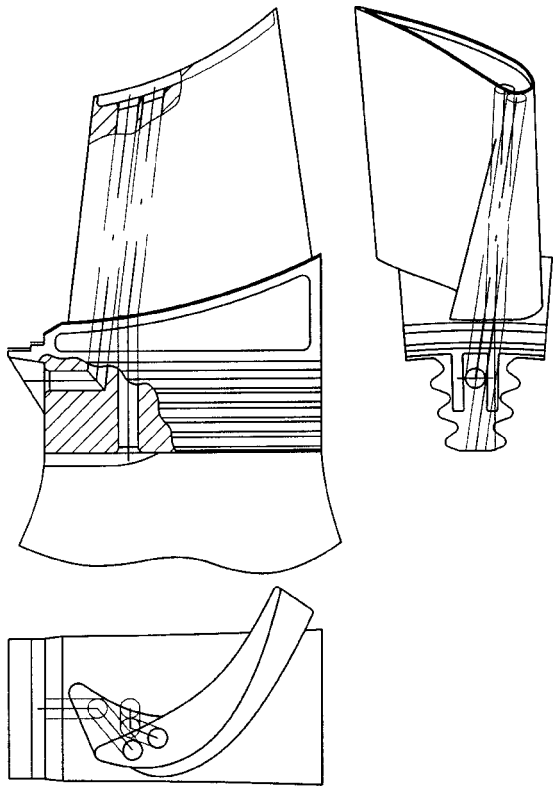

Fig. 9 HTT first-stage blade design drawing, steam cooling ICS slits and supply hole arrangement

HTT Cooling. The cooling is performed with an innovative cooling system ICS. The innovative feature is the use of the property of an underexpanded jet which means a jet from a choked convergent nozzle where the flow subsequently expands supersonically because the external pressure is below the critical value. This jet has the strong tendency to bend towards a convex surface like the leading edge of a turbine blade. So air or steam of high total pressure is ejected from slits of small height, partly against the main flow direction (see Figs. 7 and 8).

Experimental investigations showed that the ICS film is able to cover the thermally heavily loaded leading edge safely and is very resistant against the trailing edge shocks of the previous vanes, [11–15]. Applying the ICS no internal serpentine passages are required, only two almost radial holes near the center providing cooling steam for the slits are needed (ICS is patented to the authors, [12]). Slit inlets and supply holes can be manufactured on a blade cast in one piece by modern electro-erosive machining.

The high speed and centrifugal load involves high stress of the disk which has to be built as constant stress disk with a bell shaped radial thickness variation. This disk surface has to be and can be cooled on both sides all over to a temperature of 350°C where full cold stress properties can be maintained.

The cooling flow path in the first stage is shown in more detail in Figs. 9–11. Cooling flow introduction to HTT first stage nozzles and blades is done by introduction of 40 bar steam exhausted from the HPT into the outer annular cavity of the HTT first stage nozzle ring. From here steam flows radially inward

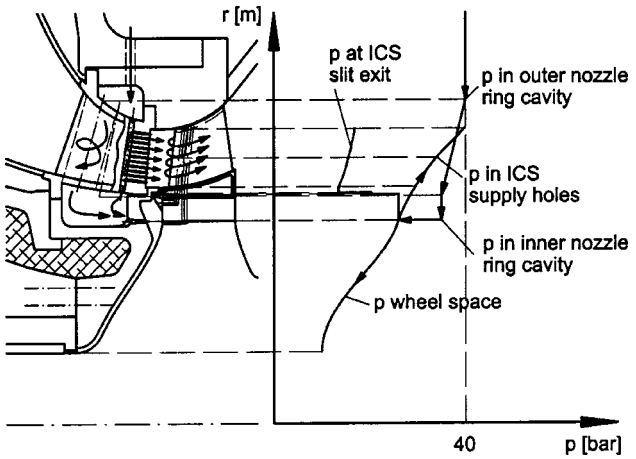

Fig. 10 HTT first-stage steam cooling flow; pressure distribution radial, through nozzle cooling holes inward, through tangential acceleration nozzles into wheel space and radially outwards in ICS supply holes is shown, transonic pressure ratio for ICS slits is secured

through circular holes, the large ones with swirl inducers into the inner cavity ring where the cooling steam is collected at conditions of 36 bar and 380°C. The last radial hole supplies ten axial holes of smallest diameter ejecting steam into the main flow thus effectively cooling the trailing edge (see Fig. 8).

From the inner nozzle ring cavity steam nozzles are fed accelerating the cooling flow into the wheel space in circumferential direction below the radius of blade root. Under an extension of the root plate the cooling steam enters first axially into the blade fir tree root part, then flows radially outward to supply the first row of slits of the innovative cooling system ICS (see Fig. 9). The second more central hole is supplied from a slot in the disk groove under the fir tree. This second radial hole feeds in the same manner the ICS slits pointing downwards on the blade pressure side.

In Fig. 10 the pressure distribution of steam flow inside HTT first stage nozzles, during expansion into the wheel space and supply to radial holes in the blades is shown proving that for all radii the necessary transonic pressure ratio is provided.

Cooling of HTT first stage disk low pressure side is done by introduction of further cooling steam into the annular space between first and second stage (see Fig. 11). Passing through the radial holes in the second stage nozzles, an ICS for the rotor as well as for two hydrostatic bearings on both first and second stage inner disks is supplied. These are intended to operate as seals for the steam flow and to act as mild dampers improving the rotor dynamics of both shafts involved. The second stage disk is provided with internal flow channels to lead the cooling flow to the fir tree roots of the blades cooled in a similar way with ICS slits.

At part-load and even during start up (auxiliary steam supply) the ICS steam supply is sufficient high to form transonic underexpanded cooling layers ensuring proper cooling function.

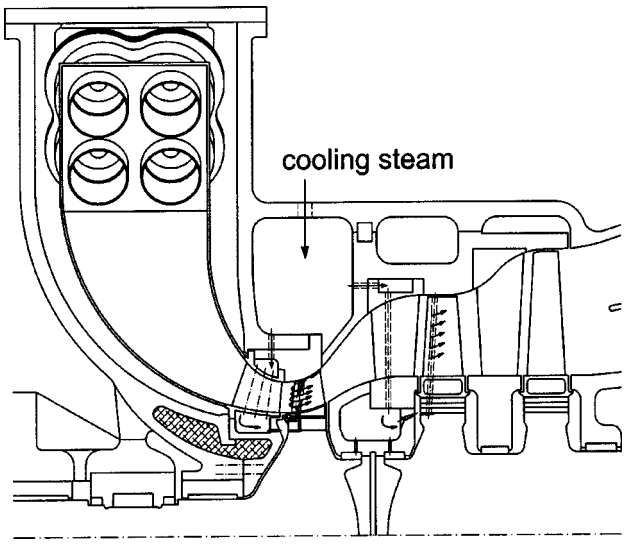

Fig. 11 HTT cooling flow in both rotors and intermediate shaft vibration damper

General Arrangement

As the last issue to be treated the most far reaching optimization deliberation is presented. According to the design decision of having the high temperature flow channel with minimum surface and minimum heat loss and also with minimum cooling flow supply the general arrangement of turbomachines is given (see Fig. 12). Two overhang disks of different speed provide the shortest possible high temperature annular flow channel. So power end drive has to be on opposite sides. At 20,000 rpm HPT and C3 can be optimally connected. At the 12,000 rpm side main power is delivered via gears to the main generator. On the other side of the generator C1 and low pressure turbine LPT are arranged.

The power produced by HTT first stage and HPT greatly surpasses the power demand of C3, so a second electric generator is necessary. The only alternative would have been an outside gear shaft connecting to the main gear box and the main generator. The electric shaft proposed here seems to be a superior solution since for much larger units the same type of arrangement can be kept. Since gears with a power of about 100 MW are in successful operation in standard gas turbine units, the output of this Graz cycle prototype unit could be doubled in a range to 200 MW.

Deliberations about the magnitude of cost of manufacture of such a plant in comparison to a standard combined cycle plant have already been made in [6] on the bases of the number of stages assuming that there is a very little variation of cost with size of blading. There it was shown that the total number of stages for a Graz cycle power plant is 28, compared to about 40 for a standard combined cycle power plant.

Conclusions

The Graz cycle, a novel type of closed-cycle gas turbine plant with the capability of retaining all the combustion generated CO_2

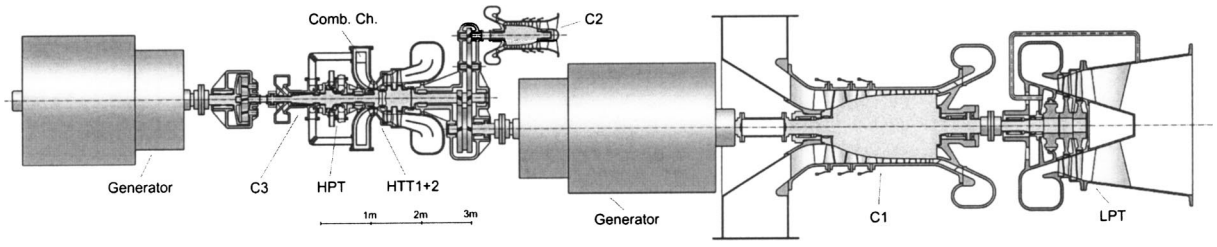

Fig. 12 General optimized arrangement of turbomachines for a 92 MW prototype unit

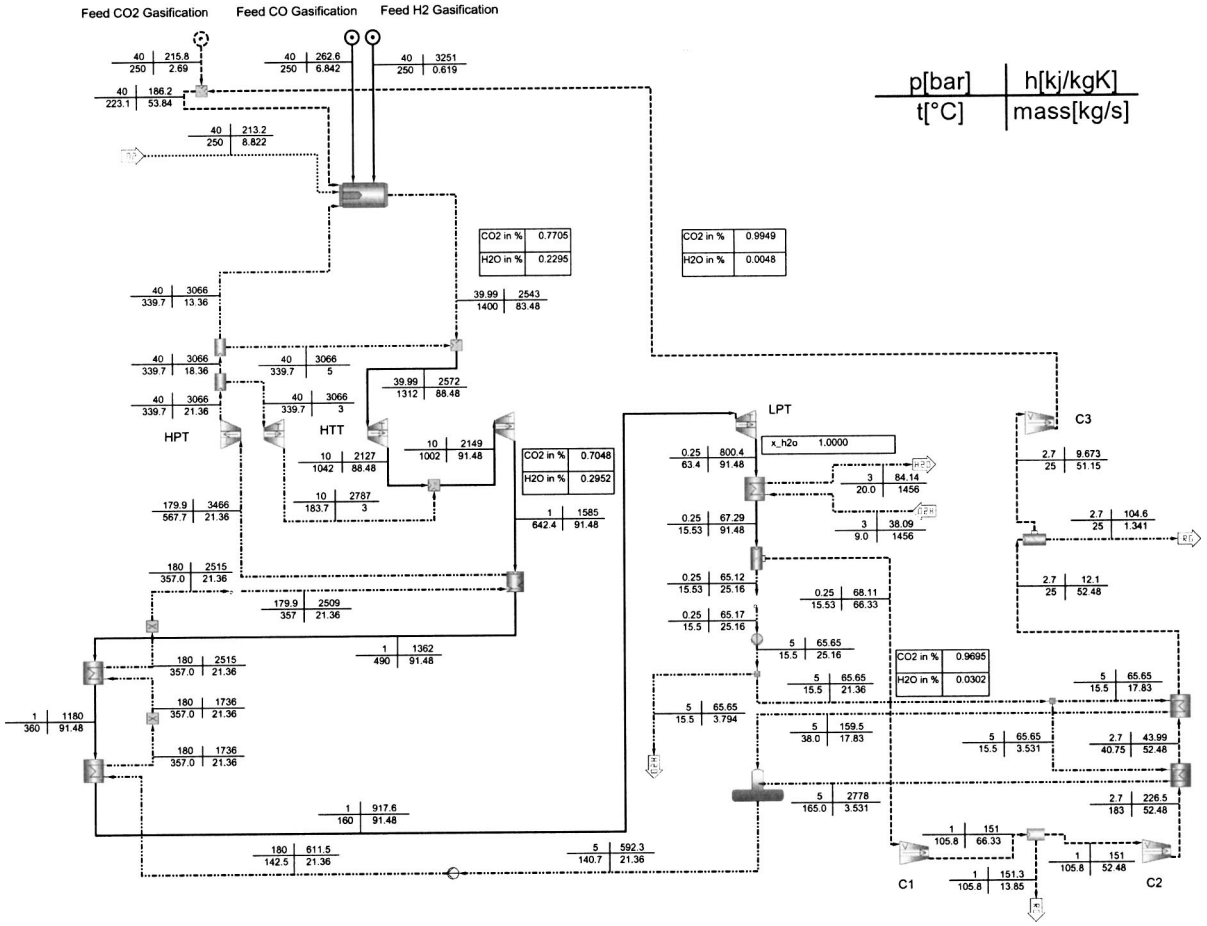

Fig. 13 Detailed thermodynamic cycle data of 92 MW Graz cycle plant, [12]

for further technical use, has been presented. It is based on the internal stoichiometric combustion of fossil fuels with oxygen and offers very high efficiency. The cycle uses only turbomachinery components. A general layout of all components has been performed for a pilot power plant to verify the feasibility of the components.

The deliberations of the design of the most difficult components, the combustion chamber and the HTT, as well as the general arrangement of the turbomachinery are discussed in detail. Especially for the HTT an innovative design is presented where the first stage has a higher speed than the succeeding two stages. An innovative cooling system for the rotor blades using steam is applied.

The next step is the investigation of the economics of such a zero emission power plant, which depends largely on the amount of a future CO_2 tax. But if it proves economically reasonable, a Graz cycle power plant could be put into operation within a few years based on the vast experience of successful gas turbine operation and research now well under way.

Acknowledgments

The thermodynamic cycle calculations presented were done using the program system IPSEpro developed by SIMTECH Comp. The support by the Austrian Science Foundation (FWF) and the Austrian Federal Ministry for Education, Science and Culture (BMBWK) within the grant Y57-TEC ''Non-intrusive Measurement of Turbulence in Turbomachinery'' (START program, J. Woisetschläger) is gratefully acknowledged.

Appendix

Please see Fig. 13.

HTT First Stage Radial Equilibrium of Flow. According to [16] the radial equilibrium of flow in the annular space between nozzle exit and blade entry can be calculated with Eq. (1) according to Fig. 14:

$$\underbrace{-\frac{c_u^2}{r}\cdot\cos\varepsilon}_{a}\underbrace{-\frac{c_y^2}{r_K}}_{b}=\underbrace{-\frac{1}{\rho}\cdot\frac{\partial p}{\partial x}}_{c}. \tag{1}$$

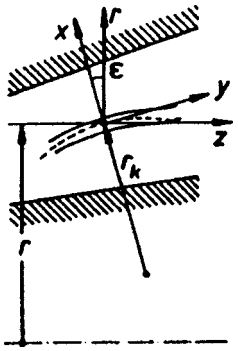

Fig. 14 Radial equilibrium

a=x-component of the centripetal acceleration evoked by the movement in circumferential direction

b=x-component of the centripetal acceleration evoked by the movement in meridional direction

c=x-component of the force evoked by the pressure distribution

With angle of deviation from axis ε zero and constant head at all radii the equation modifies to

$$-c_u \cdot \frac{\partial c_u}{\partial r} - c_z \cdot \frac{\partial c_z}{\partial r} = \frac{c_u^2}{r} + \frac{c_z^2}{r_K} = \frac{c_u^2}{r} + \frac{c_u^2 \cdot \tan^2 \alpha}{r_K}. \quad (2)$$

$$c_z = c_u \cdot \tan \alpha \quad (3)$$

With the assumption of constant nozzle angle α follows:

$$-\frac{\partial c_u}{c_u} \cdot (1 + \tan^2 \alpha) = \frac{\partial r}{r} \cdot \left(1 - \frac{r \cdot \tan^2 \alpha}{r_K}\right) \quad (4)$$

$$\int \frac{dc_u}{c_u} = -\cos^2 \alpha \cdot \int \frac{1}{r}\left(1 - \frac{r \cdot \tan^2 \alpha}{r_k}\right) dr. \quad (5)$$

Numerical integration:

$$\ln c_u = -\cos^2 \alpha \cdot \int f(r)dr \quad \text{with} \quad f(r) = f_0 + f_1 \cdot \Delta r + f_2 \cdot \Delta r^2, \quad \Delta r = r - r_m \quad \text{and} \quad dr = d(\Delta r) \quad \text{follows:}$$

$$\ln c_u = -\cos^2 \alpha \cdot \left(f_0 \cdot \Delta r + f_1 \cdot \frac{\Delta r^2}{2} + f_2 \cdot \frac{\Delta r^3}{3}\right). \quad (6)$$

Nomenclature

m = mass flow (kg/s)
M = Mach number
n = speed (rpm)
P = power (kW)
V = volume flow (m^3/s)
H = enthalpy (kJ/kg)
R = degree of reaction
r = radius (m)
D = diameter (m)
L = blade length (m)
z = number of stages (m)
u = circumferential velocity (m)
x, y, z = Cartesian coordinates (m)
p = pressure (bar)
c = velocity (m/s)
C = absolute velocity (m/s)
W = relative velocity (m/s)
ψ = load factor, $2\ \Delta H/u^2$
α = nozzle exit angle (°)
ε = inclination of stream line versus axis (°)

Subscripts

a = tip
m = mean
i = hub
r = radial
u = circumferential
x, y, z = components in x, y, z direction
K = curvature
1,2 = nozzle exit, rotor exit

Abbreviations

NEDO = New Energy Development Organization (Japan)
CRIEPI = Central Research Institute of Electric Power Industry (Japan)
TTM = Institute for Thermal Turbomachinery and Machine Dynamics—Graz University of Technology
HPT = high pressure turbine
HTT = high temperature turbine
LPT = low pressure turbine
C1, C2, C3 = compressor 1, 2, 3
ICS = innovative cooling system
HRSG = heat recovery steam generator

References

[1] Bolland, O., Kvamsdal, H., and Boden, J., 2001, "A Thermodynamic Comparison of the Oxy-Fuel Power Cycles Water-Cycle, Graz-Cycle and Matiant-Cycle," Proc. of the Intern. Conf. Power Generation and Sustainable Development, Liège, Belgium.

[2] Jericha, H., and Starzer, O., 1991, "Steam Cooled Hydrogen/Oxygen Combustion Chamber for the High-Temperature-Steam Cycle," CIMAC, Florence, Italy.

[3] Jericha, H., Sanz, W., Woisetschläger, J., and Fesharaki, M., 1995, "CO_2–Retention Capability of CH_4 /O_2—Fired Graz Cycle," CIMAC, Interlaken, Switzerland.

[4] Jericha, H., and Fesharaki, M., 1995, "The Graz Cycle–1500°C Max Temperature Potential H_2–O_2 Fired CO_2 Capture with CH_4–O_2 Firing," ASME Paper 95-CTP-79.

[5] Jericha, H., Lukasser, A., and Gatterbauer, W., 2000, "Der "Graz Cycle" für Industriekraftwerke gefeuert mit Brenngasen aus Kohle- und Schweröl-vergasung," VDI Berichte 1566, Essen, Germany (in German).

[6] Jericha, H., and Göttlich, E., 2002, "Conceptual Design for an Industrial Prototype Graz Cycle Power Plant," ASME Paper 2002-GT-30118.

[7] Moritsuka, H., 2001, "CO_2 Capture Using a Hydrogen Decomposed from Natural Gas Turbine," ASME Paper 2001-GT-0093.

[8] Inoue, H., Kobayashi, N., and Koganezawa, T., 2001, "Research and Development of Methane-Oxygen Combustor for Carbon Dioxide Recovery Closed-Cycle Gas Turbine," CIMAC, Hamburg, Germany.

[9] Benvenuti, E., 1997, "Design and Test of a New Axial Compressor for the Nuovo Pignone Heavy-Duty Gas Turbine," ASME J. Eng. Gas Turbines Power, **119**, pp. 633–639.

[10] Hennecke, D. K., 1997, "Transsonik-Verdichter-Technologien für stationäre Gasturbinen und Flugtriebwerke (in German)," *Festschrift zum Jubiläum 100 Jahre Turbomaschinen TU-Darmstadt*, TU-Darmstadt, Darmstadt, Germany.

[11] Woisetschläger, J., Jericha, H., Sanz, W., and Gollner, F., 1995, "Optical Investigation of Transonic Wall-Jet Film Cooling," ASME Paper 95-CTP-26.

[12] Jericha, H., Sanz, W., and Woisetschläger, J., 1997, "Hohle Gasturbinenschaufel und Verfahren zur Aussen-Film-Kühlung derselben," Austrian Patent No. 406160 (in German).

[13] Moser, S., Jericha, H., Woisetschläger, J., Gehrer, A., and Reinalter, W., 1998, "The Influence of Pressure Pulses to an Innovative Turbine Blade Film Cooling System," ASME Paper 98-GT-545.

[14] Moser, S., Ivanisin, M., Woisetschläger, J., and Jericha, H., 2000, "Novel Blade Cooling Engineering Solution," ASME Paper 2000-GT-242.

[15] Göttlich E., Lang H., Sanz W., and Woisetschläger J., 2002, "Experimental Investigation of an Innovative Cooling System (ICS) for High Temperature Transonic Turbine Stages," ASME Paper 2002-GT-30341.

[16] Traupel, W., 2001, *Thermische Turbomaschinen I*, 4th Ed., Springer, Berlin (in German).

Fuzzy Approaches for Searching Optimal Component Matching Point in Gas Turbine Performance Simulation

Changduk Kong
e-mail: cdgong@mail.chosun.ac.kr

Jayoung Ki
e-mail: setgods@hotmail.com

Myoungcheol Kang
e-mail: k0914@stmail.chosun.ac.kr

Department of Aerospace Engineering,
Chosun University,
#375 Seosuk-dong, Dong-gu,
Kwangju 501-759, Korea

In performance simulation of gas turbine, some iteration processes for searching the operating point, which should be matched through gas path components, would be needed. Therefore if the engine is very complicated, the efficiency of convergence is getting lower due to increasing the number of routines and iterations for matching procedure. Furthermore, there may be some problems in numerical calculation such as the tendency of divergence, instability, and increase of calculation time. In the traditional matching methods, after some variable parameters are initially assumed and then calculated, the calculation is iterated to converge within an appropriate error range by expressing the new variables with the previous calculation error function. Even though these traditional methods show comparatively reasonable results in performance simulation, there may be some unsatisfied results in particular cases. Moreover, in this case it can be more difficult in more precise calculation due to simplification by using various assumptions. Therefore in order to search the optimal matching point in performance simulation of gas turbine efficiently and quickly, the fuzzy approaches were applied. In performance simulation using the fuzzy logic, it was found that more effective engine operating points were found and calculation time was considerably reduced less than the traditional methods. Furthermore, MATLAB *was used to apply the fuzzy logic easily as well as to make user-friendly circumstance in performance analysis.* [DOI: 10.1115/1.1787511]

Introduction

Performance simulation is one of the most important research activities not only to minimize risk and cost in the development phase but also to monitor engine health in the operation phase.

Performance simulation programs have been developed by text based languages such as FORTRAN, PASCAL, etc. [1,2]. However, there is a growing tendency to transform into the Graphic User Interface (GUI) program recently [3]. Therefore the commercial program MATLAB, which can apply various numerical analysis techniques and add easily the control function, has been widely used as a new simulation language [4].

Generally, the gas turbine engine, which is operating in steady state, should follow the mass conservation law as well as the energy conservation law. In other words, the mass flow passed through the intake, the compressor, the compressor turbine, and the power turbine must be constant, and the work done by the compressor and the turbine connected with the same shaft must be the same.

Because each component performance operated in steady state must follow component performance characteristics, both the mass flow matching and the work matching between the related components should be performed on their component performance maps [5]. Therefore the steady-state performance analysis can be carried iteratively out by changing data read on the related component performance maps until satisfying the mass flow matching and the work matching after starting the calculation from the assumed arbitrary operating point. In order to find the component matching points effectively, the data assumption scheme for the next step calculation and the iteration scheme are very important.

Generally, a method in which the calculation is repeated using the beta-line values as an error function until converging within the proper error range is used. However, this method cannot converge sometimes within the assumed tolerance due to the calculation formulas for the beta line and the interpolation scheme. Therefore the programmer's experience can be relied upon.

Generally, the concentric iteration scheme and the simultaneous iteration schemes are widely used for matching [6]. The concentric iteration scheme is that each check for matching is linked to the most recent guess that has not already been checked. Because this method can proceed to the next check procedure after satisfying the previous check, the convergence characteristic is much better than other methods. However, it has disadvantages such as long calculation time due to the continuous iterative matching process and accumulation of the matching error in the matching process. The simultaneous iteration scheme is a widely used method that can be available to use due to the appearance of the fast digital computer. Because this scheme can perform the calculation with all guesses like real engine behavior and check simultaneously the matching at the end of the program, it can simulate very closely the real engine. However, because it has the relevancy with lots of iteration loops through the performance analysis at each operating point, there are some difficulties such as complication in calculation and divergence due to an improper selection of initial values [6].

In this study, steady-state performance simulation code for a turboprop engine which was programmed by FORTRAN language in the previous study [7] has been transformed into MATLAB code. Although MATLAB has great benefits to user in the programming aspect, it requires a much longer time to calculate the iterative loop than other high-level programming languages. For that reason, it is very difficult and inefficient to employ the existing itera-

Contributed by the International Gas Turbine Institute (IGTI) of THE AMERICAN SOCIETY OF MECHANICAL ENGINEERS for publication in the ASME JOURNAL OF ENGINEERING FOR GAS TURBINES AND POWER. Paper presented at the International Gas Turbine and Aeroengine Congress and Exhibition, Atlanta, GA, June 16–19; 2003, Paper No. 2003-GT-38148. Manuscript received by IGTI, Oct. 2002, final revision, Mar. 2003. Associate Editor: H. R. Simmons.

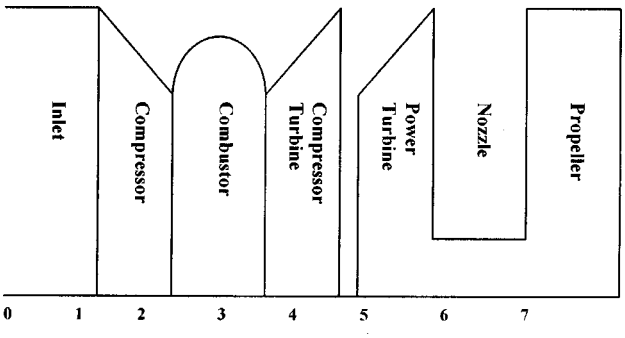

Fig. 1 Station no. and layout of the study engine

Table 1 Performance data by engine manufacturer

Variable	Values
Atmospheric condition	Sea Level Static Standard Condition
Mass flow rate (kg/s)	4.18
Fuel flow rate (kg/s)	0.0818
Shaft horse power (hp)	1150
SFC (kg/kw hr)	0.3432
Nozzle throat area (m^2)	0.058
Gas generator rotational speed (100% RPM)	37468
Propeller rotational speed (100% RPM)	2000

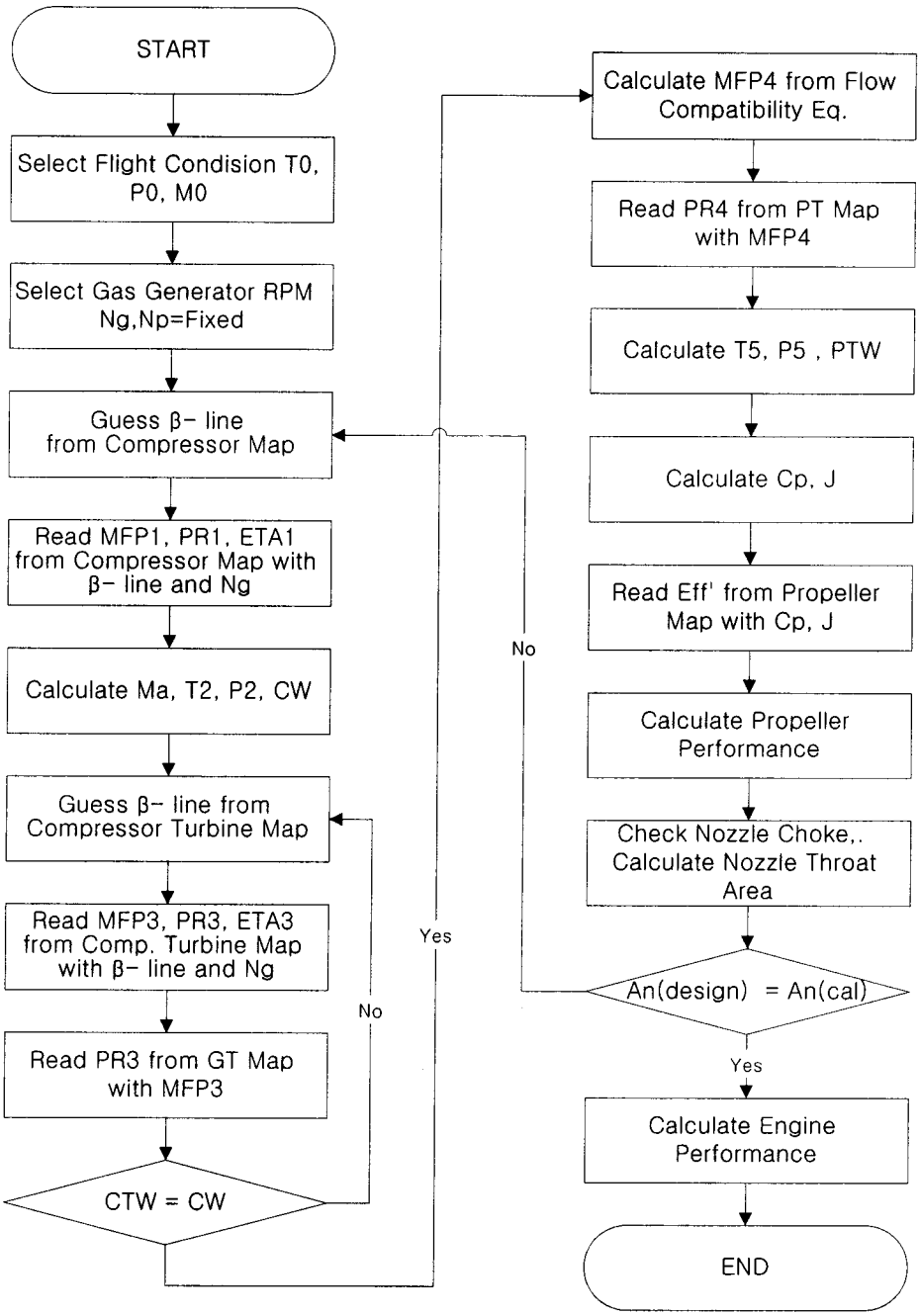

Fig. 2 Flowchart of FORTRAN program with traditional matching scheme

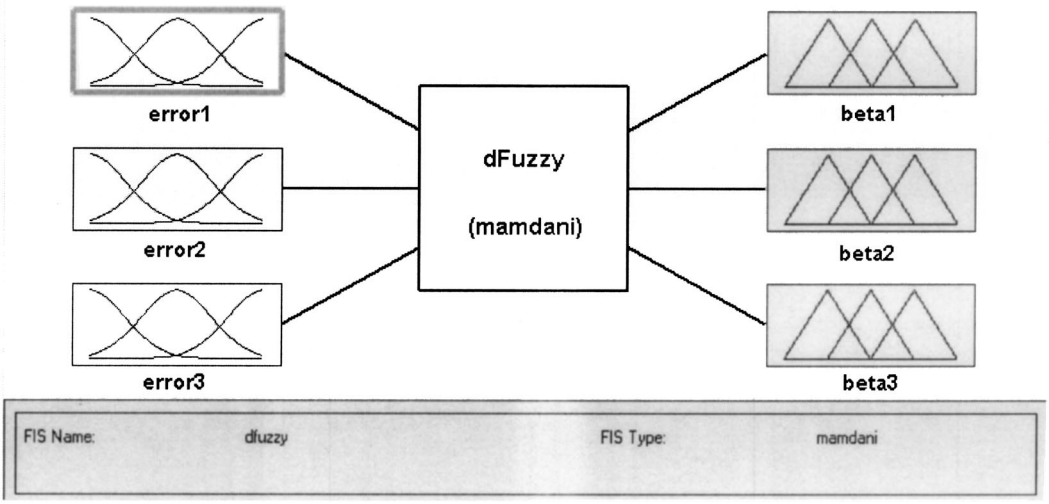

Fig. 3 Mamdani-type fuzzy inference system

Table 2 Applied fuzzy rules

1	IF (ERR1 is IMF1) AND (ERR2 is IMF1) AND (ERR3 is IMF1) THEN (BETA1 is OMF4), (BETA2 is OMF4), (BETA3 is OMF4)
2	IF (ERR1 is IMF1) AND (ERR2 is IMF3) AND (ERR3 is IMF5) THEN (BETA1 is OMF5), (BETA2 is OMF4), (BETA3 is OMF4)
3	IF (ERR1 is IMF7) AND (ERR2 is IMF5) AND (ERR3 is IMF4) THEN (BETA1 is OMF5), (BETA2 is OMF3), (BETA3 is OMF4)
4	IF (ERR1 is IMF2) AND (ERR2 is IMF4) AND (ERR3 is IMF5) THEN (BETA1 is OMF4), (BETA2 is OMF3), (BETA3 is OMF1)
5	IF (ERR1 is IMF4) AND (ERR2 is IMF4) AND (ERR3 is IMF4) THEN (BETA1 is OMF5), (BETA2 is OMF4), (BETA3 is OMF4)
:	:

Table 3 Comparison of major calculated parameters at the maximum take off (Ng=100% rmp) condition

Variable	M. D.	F. P.	Err.(%)	M. P.	Err.(%)
MA (kg/s)	4.18	4.1816	0.039	4.1818	0.044
MF (kg/s)	0.0818	0.0818	0.011	0.0817	-0.070
CPR	9.4	9.3944	-0.059	9.3944	-0.059
CET (K)	616.7	615.84	-0.140	616.31	-0.063
SHP (hp)	1150	1149.4	-0.055	1149.7	-0.025
SFC (kg/kwhr)	0.3432	0.3436	0.122	0.3432	0.012

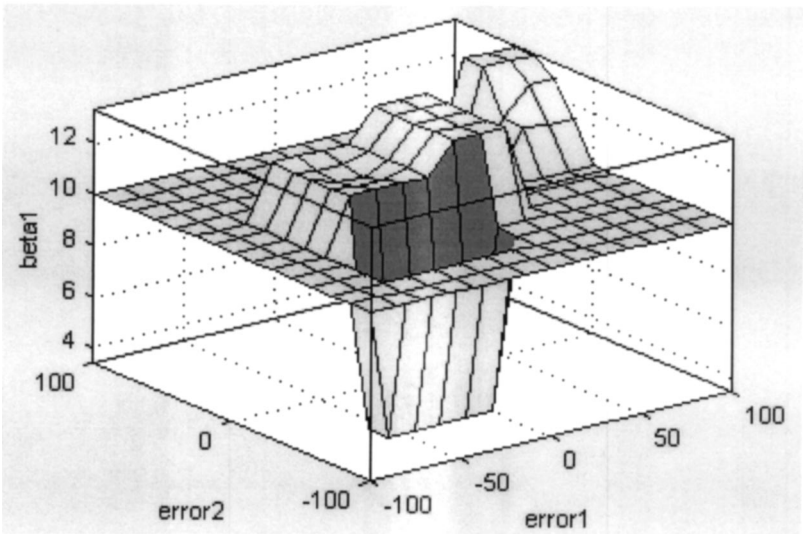

Fig. 4 Variation of BETA1 versus the variations of ERR1 and ERR2 by the fuzzy rule

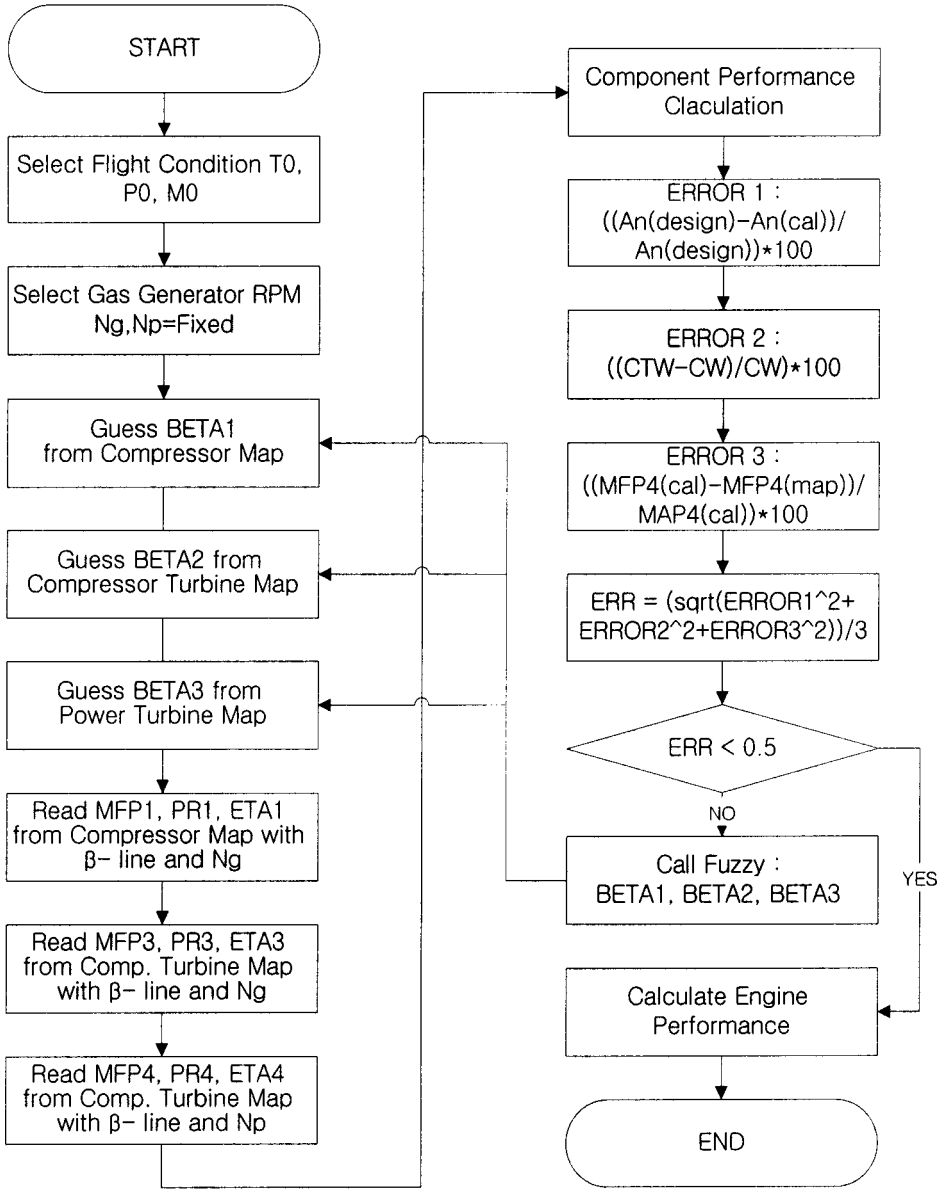

Fig. 5 Flowchart of matching algorithms with fuzzy logic

tion algorithm commonly used in text based language. Therefore the matching algorithms are newly proposed in this study, using fuzzy approaches to find the optimal matching point between the relevant components in the steady-state performance analysis of a turboprop engine.

Fuzzy logic can search effectively the running line on the component performance maps of the compressor, the compressor turbine, and power turbine by satisfying the mass and work compatibility in the gas generator and the mass compatibility between the gas generator and the power turbine.

In order to verify the newly proposed algorithm, the analysis results by applying the fuzzy logic were compared with them by the FORTRAN program using the traditional matching algorithm. Therefore there were comparisons of a convergence tendency between the newly proposed fuzzy approaches and the traditional matching algorithm. In this comparison, it was found that the MATLAB program using the fuzzy logic was faster than that of the FORTRAN program using the traditional matching algorithm. Furthermore, the performance analysis results of the newly proposed fuzzy logic algorithm were confirmed by the analysis error within 0.1%.

Engine Specification

The engine selected for analysis is the PT6A-62 free-turbine turboprop engine. The engine's shaft horsepower is 857.9 kW (1150 hp) at sea level, but is flat rated to reduce at around 708.7 kW (950 hp). The engine has a compressor with three axial stages and a single centrifugal stage, a reversed flow combustor, single stage compressor turbine with cooled NGV and blades and a two stage uncooled power turbine.

The selected propeller for PT6A-62 of the Korean basic trainer was the Hartzell HC-E4V-3Ex1/E9512CX model, which has four blades, a constant speed of 2000 rpm, featherable, and 95 in. in diameter [7].

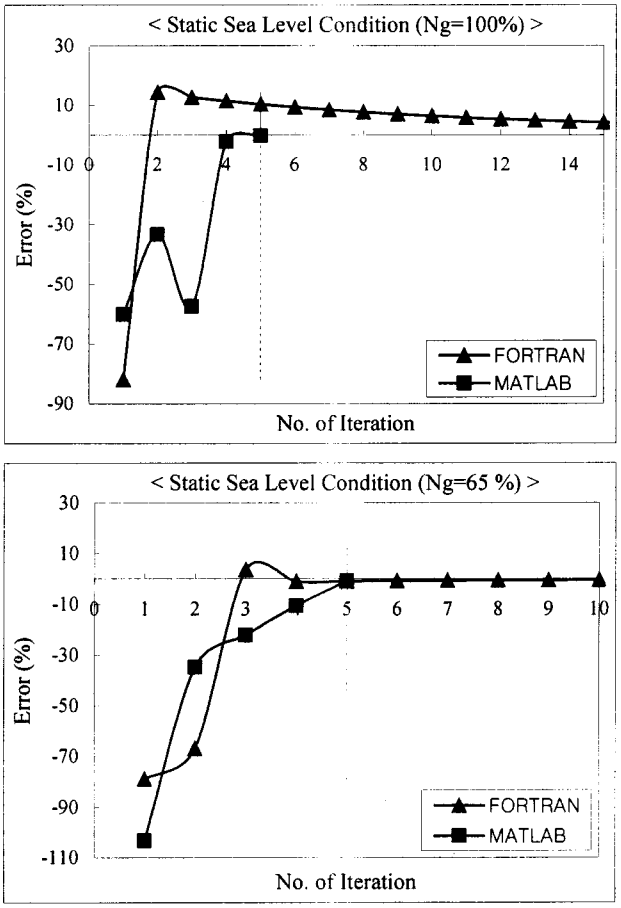

Fig. 6 Comparison of the number of iterations to check the convergence speed at the takeoff and idle conditions

The station number and layout for performance analysis of the study engine is shown in Fig. 1. Table 1 shows the performance data at maximum take-off condition, which were provided by the engine manufacturer [8].

Traditional Matching Algorithms

In the FORTRAN program using the traditional matching scheme, the performance map data for the component performance matching are transformed in the form of the look-up table with the beta lines, where each beta line has 20-point values per a rotational speed line. The performance analysis is iteratively performed until satisfying the allowable matching error by assuming a new beta line value from the error function derived from the initial guesses.

In the component performance maps, the operating point can be conveniently defined by the beta lines, then the mass flow, pressure ratio, and efficiency are fully defined by corrected rotational speed and beta value. The concentric iteration scheme is used, and the flow chart of the developed program code is shown in Fig. 2 [9]. However, if this matching algorithm is applied to the MATLAB

Table 4 Comparison of major calculated parameters at the idle (Ng =65%) condition

Variable	F. P.	M. P.	Err. (%)
MA (kg/s)	1.6166	1.6176	-0.062
MF (kg/s)	0.0163	0.0163	-0.000
CPR	2.8667	2.8676	-0.031
CET (K)	417.32	417.43	-0.026
SHP (hp)	64.744	66.617	-2.893
SFC (kg/kwhr)	1.2154	1.1829	2.674

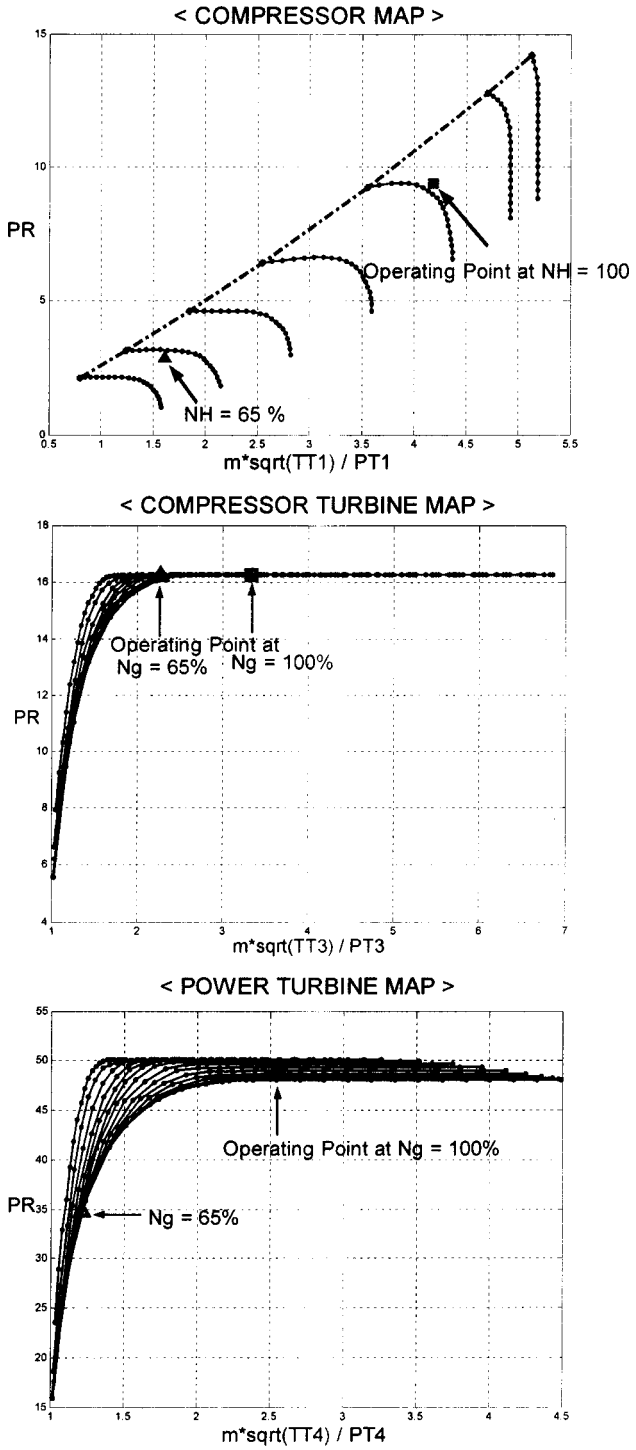

Fig. 7 Optimal matching point on component maps of compressor, compressor turbine and power turbine using fuzzy logic

simulation program, not only is the calculation process complicated but also there sometimes may be occurred divergence due to increase of calculation time. Therefore in order to solve the problem the fuzzy logic is newly proposed to find the optimal matching point.

Matching Algorithms Using Fuzzy Logic

Fuzzy logic is conceptually easy to understand and tolerant of imprecise data. Also fuzzy logic can model nonlinear functions with arbitrary complexity and it is based on natural language. Furthermore, it allows much greater flexibility in formulating system descriptions at the appropriate level of details. In fuzzy systems, the reverse situation prevails. The input and output variables are encoded in ''fuzzy'' representation, while their interrelationships take the form of well-defined if/then rules [10].

In this study, a matching method using fuzzy logic is newly proposed with the modified simultaneous iteration scheme. Fuzzy logic is applied by using the Fuzzy Toolbox provided by MATLAB [11].

Following Eqs. (1)–(3) we show the definitions of error calculations at each matching processes, such as the mass flow and work matching between the compressor and the compressor turbine, and the mass flow matching between the gas generator and the power turbine [6],

$$\mathrm{ERR1} = ((\mathrm{ANCAL} - \mathrm{ANDEG})/\mathrm{ANDEG}) \times 100, \quad (1)$$

$$\mathrm{ERR2} = ((\mathrm{CTW} - \mathrm{COW})/\mathrm{COW}) \times 100, \quad (2)$$

$$\mathrm{ERR3} = ((\mathrm{MFP4}_{\mathrm{CAL}} - \mathrm{MFP4}_{\mathrm{MAP}})/\mathrm{MFP4}_{\mathrm{MAP}}) \times 100. \quad (3)$$

Each error can be calculated by changing the beta values on the performance maps of the compressor, the compressor turbine, and the power turbine, and the calculation is repeatedly performed until converging to the error range defined by Eq. (4).

$$\mathrm{ERR} = \sqrt{(\mathrm{ERR1}^2 + \mathrm{ERR2}^2 + \mathrm{ERR3}^2)/3}. \quad (4)$$

For calculation of the beta values, the Mamdani-type fuzzy inference system is designed as shown in Fig. 3 [12].

The input parameters for fuzzification are matching errors ERR1, ERR2, and ERR3, and the output variables are the beta line values of compressor, compressor turbine, power turbine performance characteristics. The triangular-shaped membership function type is used for calculation, and some of the applied rules are shown in Table 2.

The IMF is divided into seven steps from -100 to 100 as an input membership function, and the OMF is similarly divided into seven steps from 0 to 20 as an output membership function.

The variation of BETA1 versus the variations of ERR1 and ERR2 by the fuzzy rule expressed in Table 2 is shown in Fig. 4.

The centroid calculation scheme, which returns the center of area under the curve, is applied for defuzzification. The matching program algorithm with the fuzzy logic is shown in Fig. 5.

Results of Performance Analysis

In order to verify the applied fuzzy logic, after performing the steady-state performance analysis at the maximum take-off condition (Ng=100% rpm) and the idle condition (Ng=65% rpm) with the sea level static standard atmosphere, the analysis results of the MATLAB program using fuzzy logic are compared with them of the FORTRAN program using the traditional matching scheme and engine manufacturer's data [12]. In comparison of major calculated parameters as shown in Tables 3 and 4, the analysis results using two schemes are well agreed with the engine manufacturer's data and the results of the FORTRAN program using the traditional matching scheme within 0.1% error.

Where, CPR is the compressor pressure ratio and the CET is the compressor exit temperature.

In case of comparisons of the number of iterations as shown in Fig. 6 to check the convergent speed, the analysis using fuzzy logic is much faster in convergence than that using the traditional matching scheme.

The optimal matching points on the component maps using fuzzy logic are marked as shown in Fig. 7.

Conclusion

The steady-state performance analysis program using MATLAB for a turboprop engine, PT6A-62, was developed, and then the analysis results by this program were compared with those results by the FORTRAN program using the traditional matching algorithm. In the developed MATLAB program, the fuzzy inference system was designed to search matching points between the components.

The applied fuzzy inference system was the Mamdani type, and the used membership function was the triangular shaped type. The input parameters for fuzzification are matching errors such as ERR1, ERR2, and ERR3, and the output variables are beta line data of compressor, compressor turbine, and power turbine performance characteristics by the fuzzy logic. The centroid calculation method was applied for defuzzification, and the fuzzy toolbox provided by MATLAB was used.

After performing the steady-state performance analysis by the MATLAB program using fuzzy logic at the take off condition and the idle condition with the sea level static standard atmosphere, the analysis results by this program were the compared with those results by the FORTRAN program using the traditional matching scheme. In comparison, it was found that the fuzzy logic converged much faster than the traditional matching scheme, and the results of performance calculation using the fuzzy logic well agree with engine manufacturer's data within 0.1%.

Because the relatively simple turboprop engine was used in this study, the further general fuzzy inference system, which can be applied to much more complicated gas turbines, for instance the complex turbofan engines, must be studied later.

Nomenclature

ANCAL = calculated nozzle area (m^2)
ANDEG = designed nozzle area (m^2)
BETA1 = beta-line value on compressor performance map
BETA2 = beta-line value on compressor turbine performance map
BETA3 = beta-line value on power turbine performance map
CET = compressor exit temperature (K)
COW = compressor work (kW)
CTW = compressor turbine work (Kw)
ERR1 = mass flow matching error for all components
ERR2 = work matching error between compressor and compressor turbine
ERR3 = mass flow matching error between gas generator and power turbine
ERR = total matching error
ETA = efficiency
F.P. = FORTRAN program using traditional matching algorithm
IMF = input membership function
MA = air mass flow rate (kg/sec)
M.D. = provided data by manufacturer
MF = fuel flow rate (kg/sec)
MFP = mass flow parameter
M.P. = MATLAB program using fuzzy matching algorithm
Ng = gas generator rotational speed (rpm)
Np = power Turbine rotational speed (rpm)
OMF = output membership function
PTW = power Turbine Work
PR = pressure Ratio
SFC = specific fuel consumption (kg/Kw h)
SHP = shaft horse power (hp)

References

[1] Sellers, J. F., and Daniele, C. J., 1975, ''DYNGEN-A Program for Calculating Steady-State and Transient Performance of Turbojet and Turbofan Engines,'' NASA TN D-7901.

[2] Palmer, J. R., and Yan, C. Z., 1985, ''TURBOTRANS—A Programming Language for the Performance Simulation of Arbitrary Gas Turbine Engines With Arbitrary Control Systems,'' International Journal of Turbo and Jet Engines: 19–28.

[3] Kurzke, J., 1998, ''Manual GASTURB 8.0 for Windows—A Program to Calculate Design and Off-Design Performance of Gas Turbines,'' technical report.

[4] Crosa, G. et al., 1998, ''Heavy-Duty Gas Turbine Plant Aerothermo Dynamic Simulation Using SIMULINK,'' ASME J. Turbomach., **120**, pp. 550–560.

[5] Cohen, H., Rogers, G. F. C., and Saravanamuttoo, H. I. H., 1996, *Gas Turbine Theory*, 4th Ed., Longman, London.

[6] Pilidis, P., 1996, ''Gas Turbine Performance,'' Cranfield Short Course Note, UK.

[7] Kong, C. D., 2000, ''Propulsion System Integration of Turboprop Aircraft for Basic Trainer,'' ASME Paper 00-GT-10.

[8] Na, J. J., 1996, ''A Study on PT6A-62 Engine Install Performance Analysis,'' Agency of Defense Development, Technical Report.

[9] Kong, C. D., and Ki, J. Y., 2001, ''Performance Simulation of Turboprop Engine for Basic Trainer,'' ASME Paper 00-GT-391.

[10] Tsoukalas, L. H., and Uhrig, R. E., 1997, ''Fuzzy and Neural Approaches in Engineering,'' Wiley, New York.

[11] Math Works, 2001, ''MATLAB User Guide Ver. 6.1,'' The Math Works, Inc., USA.

[12] Math Works, 2001, *Fuzzy Logic Toolbox User Guide Ver. 2.0*, The Math Works, Inc.

An Evaluation of the Effects of Water Injection on Compressor Performance

A. J. White

A. J. Meacock
e-mail: ajw36@cam.ac.uk

Hopkinson Laboratory,
Cambridge University Engineering Department,
Trumpington Street,
Cambridge CB2 1PZ, UK

The injection of water droplets into compressor inlet ducting is now commonly used as a means of boosting the output from industrial gas turbines. The chief mechanisms responsible for the increase in power are the reduction in compressor work per unit flow and the increase in mass flow rate, both of which are achieved by evaporative cooling upstream of and within the compressor. This paper examines the impact of such evaporative processes on compressor operation, focussing particular attention on cases with substantial overspray—i.e., for which significant evaporation takes place within the compressor itself, rather than in the inlet. A simple numerical method is described for the computation of wet compression processes, based on a combination of droplet evaporation and mean-line calculations. The method is applied to a "generic" compressor geometry in order to investigate the nature of the off-design behavior that results from evaporative cooling. Consideration is also given to the efficiency of the compression process, the implications for choking and stall, and the magnitude of the thermodynamic loss resulting from irreversible phase change. [DOI: 10.1115/1.1765125]

1 Introduction

Inlet fog boost (IFB) is now commonplace as means of boosting the power output from industrial gas turbines, with a variety of bolt-on kits commercially available. Typical water injection rates are about 1% of air mass flow, and the main benefit stems from lowering of the compressor inlet temperature. Research interest is now, however, turning toward cycles with considerably higher water injection rates than those used for IFB. Examples include the recuperated water injected (RWI) cycle, [1], and the so-called Tophat cycle for which particularly impressive performance figures are claimed, [2]. In such cycles, water injection serves to enhance power output and efficiency via a variety of mechanisms, including: (i) reduction of compressor work due to continuous evaporative intercooling, (ii) increased turbine mass flow, and (iii) increased turbine work per unit flow resulting from the high heat capacity of water vapor. Unlike traditional intercooling methods, evaporative intercooling increases cycle efficiency irrespective of whether an exhaust gas heat exchanger is employed, [3].

The current paper deals with the effect of water evaporation throughout compressor stages, examining the consequent off-design behavior and the potential reduction in compressor work input. This subject has received some attention in past literature, and in particular the paper by Hill [4] provides an excellent description of the wet compression process and includes an analysis of the shift in compressor characteristics due to coolant injection. Hill also made approximate calculations to show that droplets injected at the compressor inlet would soon be deposited onto blade surfaces or centrifuged to the casing. Consequently, he suggested, evaporation is limited by surface film area and is relatively unaffected by the initial droplet size. However, his work was undertaken at a time when realistically achievable droplet diameters were in the range 30–70 μm. More recently, Horlock [5] undertook a linearised analysis of water-injected compressors, with the particular aim of identifying departures from design of individual stages. This work will be discussed further in section 4.

Contributed by the International Gas Turbine Institute (IGTI) of THE AMERICAN SOCIETY OF MECHANICAL ENGINEERS for publication in the ASME JOURNAL OF ENGINEERING FOR GAS TURBINES AND POWER. Paper presented at the International Gas Turbine and Aeroengine Congress and Exhibition, Atlanta, GA, June 16–19, 2003, Paper No. 2003-GT-38237. Manuscript received by IGTI, October 2002, final revision, March 2003. Associate Editor: H. R. Simmons.

Zhluktov et al. [6] have also computed wet compressor characteristics, using a one-dimensional numerical method applied to an Allison 501-KB7 engine with ~1% inlet fog. Their calculations take account of a wealth of two-phase phenomena, including droplet centrifuging, film formation and film evaporation. By contrast, the present work is restricted to small droplets which follow the gas-phase velocity with negligible slip. The justification for this simpler approach is that the high evaporation rates which are the focus of the current investigation will only be achievable if the droplets are sufficiently small to remain entrained in the flow. (Furthermore, with high injection rates, the impact of larger droplets on blade surfaces would lead to severe erosion problems, and would exert a braking torque, thereby countering the benefits of evaporation.) For typical compressor conditions, preliminary calculations (using Gyarmathy's method, described in Young and Yau [7]) suggest that neglect of slip limits droplet diameters to approximately 5 μm. Recent developments in injector technology, particularly the use of superheated feed-water, [2], suggest that such fine sprays are achievable.

2 Ideal Wet Compression Work

As a guide to the benefits that might be achieved by water injection, it is instructive to compute the ''ideal'' wet compression work. The mechanism for work reduction is essentially the increase in density brought about by cooling, and the magnitude of this effect is readily evaluated from the relation

$$Tds_A = dh - v\,dp. \tag{1}$$

In this equation, s_A, h and v are mixture quantities per unit mass of dry air (e.g., $h = h_a + \omega h_v + f h_\ell$). The incremental change ds_A is the entropy increase due to ''aerodynamic'' effects alone; it does not include the contribution from irreversible phase change. (That this is so may be seen by setting ds_A to zero; the resulting equation describes inviscid, adiabatic flow which is only isentropic in the absence of phase change.) A truly reversible compression will only be accomplished if the air remains saturated, thereby maintaining thermodynamic equilibrium between the liquid and vapor. The saturated condition may be introduced into (1) via the Clausius-Clapeyron equation, as shown in Appendix A. Setting $ds_A = 0$ then gives

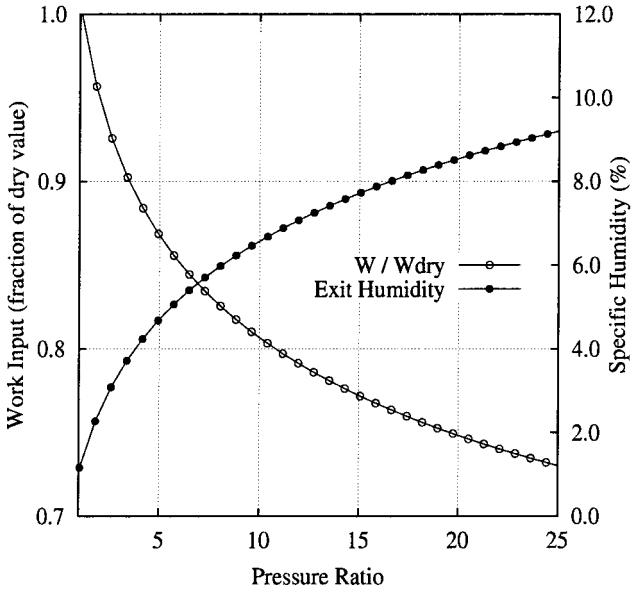

Fig. 1 Comparison of ideal wet and dry compression. $p_1 = 1$ bar, $T_1 = 288$ K, RH = 100%. (Note: work is per kg of compressor delivery air.)

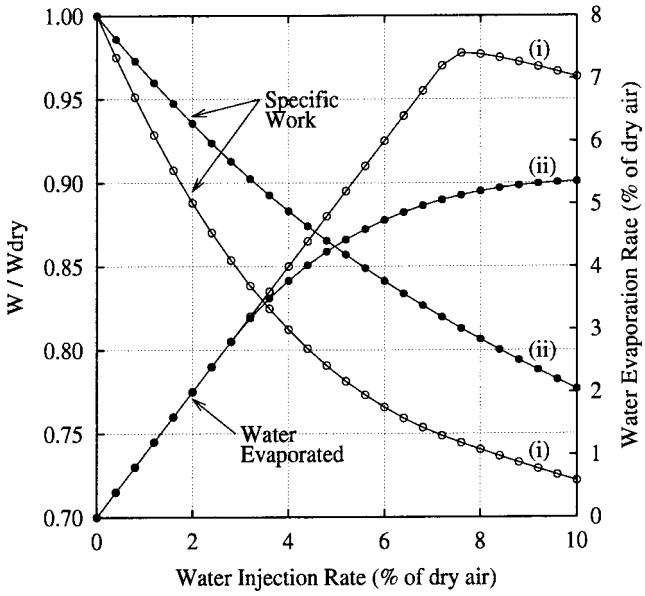

Fig. 2 Work input per unit flow and evaporation rate for a polytropic compression with $\eta_p = 90\%$ and $p_2/p_1 = 15$. Curve (i): $\dot{p}\tau = 0.8$, curve (ii): $\dot{p}\tau = 20$.

$$c_p^* \frac{dT}{T} = R^* \frac{dp}{p} \tag{2}$$

where c_p^* and R^* are the effective heat capacity and gas constant (see Appendix A). As noted in the Appendix, the effective isentropic index obtained by combining these quantities is approximately constant, and typically in the range 1.12–1.16.[1]

The ideal wet compression work, computed by numerical integration of (2), is shown in Fig. 1, plotted as a fraction of the (ideal) dry compression work. The figure also shows the specific humidity (i.e., mass of water per unit mass of dry air) of the delivery air. Thus, for example, for a compression ratio of 15, a 23% reduction in work input is achieved, requiring a water injection rate of approximately 6.5% (given by the final, less initial, specific humidities). Bearing in mind the high work ratios typical of industrial gas turbines, it is clear that such work reductions are worth pursuing. However, it is likely that the benefits suggested by Fig. 1 will be compromised by (i) irreversible phase change, and (ii) changes in aerodynamic performance due to water injection.

3 Nonequilibrium Polytropic Compression

Drop-wise evaporation is, of course, a rate process and cannot normally proceed at a pace sufficient to maintain saturated conditions. On the other hand, departures from ideal aerodynamic behavior result in a greater temperature rise through the compressor, allowing more water to evaporate. These two effects compete, and it is not clear a priori whether the percentage reduction in work input for a real compressor will be greater or less than that suggested by Fig. 1. These issues are addressed here by coupling a droplet evaporation model with simple polytropic compression calculations.

Irrespective of whether phase change is occurring, aerodynamic performance may be characterized by a polytropic efficiency, η_p, defined such that

$$dh = v\,dp/\eta_p . \tag{3}$$

[1]Zheng et al. [8], following Hill, derived a similar value for γ^* by specifying a value for the quantity, $d\omega/dT$.

(Of course, phase-change effects will generally change the value of η_p for a given compressor, as discussed in Section 4, but here it is maintained constant. This is tantamount to assuming the compressor has been redesigned for water-injection). Allowing for departures from equilibrium between the liquid and vapor, the increment dh may also be written

$$dh = (c_{pa} + \omega c_{pv})dT + (h_v - h_\ell)d\omega + f c_{p\ell} dT_\ell \tag{4}$$

where T_ℓ is the droplet temperature which, in general, differs from both the gas-phase and wet-bulb temperatures. Over a short time interval dt during which the pressure rises by dp, the quantities $d\omega$ and dT_ℓ can be determined from the droplet evaporation model outlined in Appendix B. The work input may thus be evaluated by numerical integration of (3) and (4) once the pressure-time variation, $p(t)$, and initial droplet size are specified.

The extent of departures from thermodynamic equilibrium will clearly depend on both the evaporation rate and the rate of compression. The relationship between these two rates is characterized by the dimensionless combination $\dot{p}\tau$, where τ is the droplet vaporization time (given in Appendix B), and $\dot{p}$ is the compression rate defined by

$$\dot{p} = \frac{1}{p}\frac{Dp}{Dt} \tag{5}$$

(D/Dt being the time derivative following a fluid particle). Assuming a constant value for $\dot{p}$ implies an exponential form for $p(t)$ which, although approximate, provides an acceptable distribution for within a compressor. (An average value of $\dot{p}$ may be used to characterize real machines.) Figure 2 shows the work input calculated on this basis as a function of water injection rate. The results are expressed as a fraction of the dry, polytropic compression work (per kg of delivery air) and are for $\eta_p = 90\%$ and a pressure ratio of 15. The different curves are for different values of the product $\dot{p}\tau$. (Note, however, that identical curves are produced by varying $\dot{p}$ but keeping $\dot{p}\tau$ constant, emphasising the importance of this parameter.) For a typical $\dot{p}$ of 200 s^{-1}, the open circles in the figure correspond to a droplet diameter of 2 μm, and the closed circles to 10 μm. Comparing with Fig. 1, it is evident that a similar percentage reduction in compressor work is only achieved if the droplets are very small, even if it is assumed that

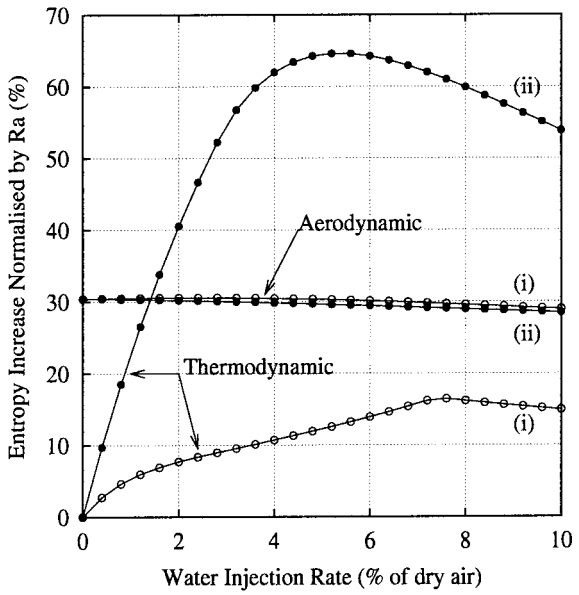

Fig. 3 Entropy increase, $\Delta S/R_a$, for the compression of Fig. 2

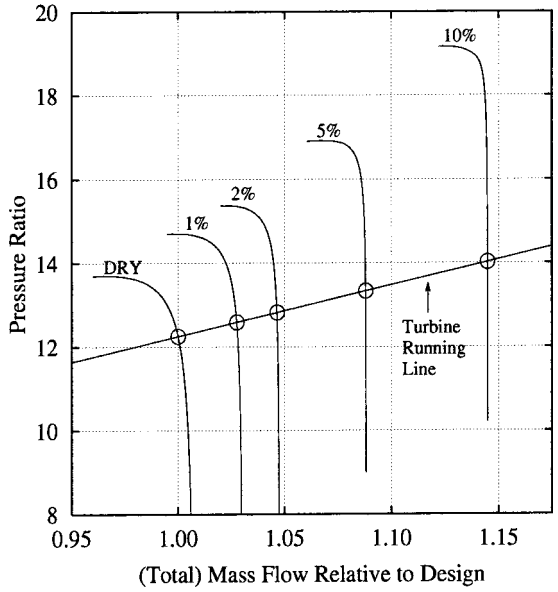

Fig. 4 Compressor characteristics for different water injection rates (Inlet conditions: T_o=288 K, P_o=1.0 bar, RH=100%, injected droplets are of 5 μm diameter and at 288 K)

the larger droplets follow the flow. (In practise, the curve for large droplets would not be achievable since substantial deposition would occur.)

Figure 2 also shows the amount of water evaporated during compression. Departures from the initial straight line (i.e., where evaporation rate equals injection rate) signify unevaporated droplets at the compressor exit. It is interesting to note that, for $\dot{p}\tau = 0.8$, the evaporation rate actually falls when the injection rate exceeds 7.5%. This is because, as the injection rate is increased, the rapid initial evaporation leads to lower subsequent temperatures (and higher relative humidities) and hence reduces the overall evaporation rate.

One aspect of wet compression that has received little attention in the literature is the thermodynamic entropy increase due to irreversible phase change. This may be determined either by calculating the mixture entropy and subtracting changes due to aerodynamic effects, or by computing the entropy production rate directly, as described by Young [9] (see also Appendix B). Figure 3 compares the ''aerodynamic'' and ''thermodynamic'' entropy increase for the polytropic compression of Fig. 2. (The two calculation methods gave almost identical results for the thermodynamic entropy rise. This is in fact a very stringent test of the numerical integration procedures and lends support to the validity of the results.) As expected, a much higher thermodynamic entropy increase occurs for the higher value of $\dot{p}\tau$, reflecting the greater departures from thermal equilibrium. It is striking that in the case of larger droplets (but still small by normal injection standards) the thermodynamic ''loss'' is comparable to aerodynamic losses even for injection rates of just 1%.

4 Compressor Mean-Line Calculations

For the polytropic compression described above, it has been assumed that the polytropic efficiency is unaffected by evaporation. Even small quantities of water, however, will cause significant departures from the design point which are likely to compromise aerodynamic performance. In this section the extent and nature of this off-design behavior is assessed by coupling compressor mean-line and droplet evaporation calculations.

The mean-line calculation method is standard, involving the Euler work equation and loss and deviation correlations. Thus, for example, the static enthalpy rise across a rotor blade may be written

$$\Delta h = \frac{1}{2}(1+\omega+f)\{V_{x1}^2(1+\tan^2\beta_1) - U_1^2 - V_{x2}^2(1+\tan^2\beta_2) + U_2^2\} \tag{6}$$

where subscripts 1 and 2 refer to upstream and downstream, respectively, and β is the relative flow angle. (The constant factor $(1+\omega+f)$ appears in (6) because the specific enthalpy, h, is per unit mass of *dry* air.) Aerodynamic performance is characterized by Markov blade loss coefficients, ζ, defined such that

$$T_1 \Delta s_A = \zeta \frac{1}{2} V_1^2. \tag{7}$$

Likewise, exit flow angles, β_2 (and α_2 for stators), are governed by empirical deviation models. Both loss and deviation depend chiefly on the blade incidence angles, and the models used here are based on correlations described by Wright and Miller [10]. (In the current calculations, the Mach number dependence has not been included, but in practice any loss and deviation model may easily be implemented.)

Coupling of the mean-line and evaporation calculations requires an iterative approach; in an initial dry step, the values of Δh and Δs_A given by the above equations may be unwrapped to furnish the pressure variation through the machine, $p(t)$. This, together with the aerodynamic entropy variation, $s_A(t)$, provides the ''input'' for the evaporative calculations via Eq. (1), in a manner similar to that described in Section 3. In subsequent iterations, the thermodynamic entropy rise, together with the values of ω, f and T_ℓ supplement the changes Δh and Δs_A enabling the pressure rise through each blade row to be computed. Typically, 10–20 iterations are required per blade row for convergence. Computation of an entire characteristic (with 50 condition points) requires approximately 20 seconds on a PC operating at 1.7 GHz.

Wet Compressor Characteristics. Figure 4 shows wet and dry characteristics computed for a ''generic'' 12-stage compressor, the geometry for which is given in Appendix C and Table 2. The figure also shows an approximate turbine running line, computed on the basis of choked nozzle flow, constant turbine inlet temperature, and constant rotational speed, thus yielding a straight line. (Note that the mass flow on the horizontal axis includes the mass of water.)

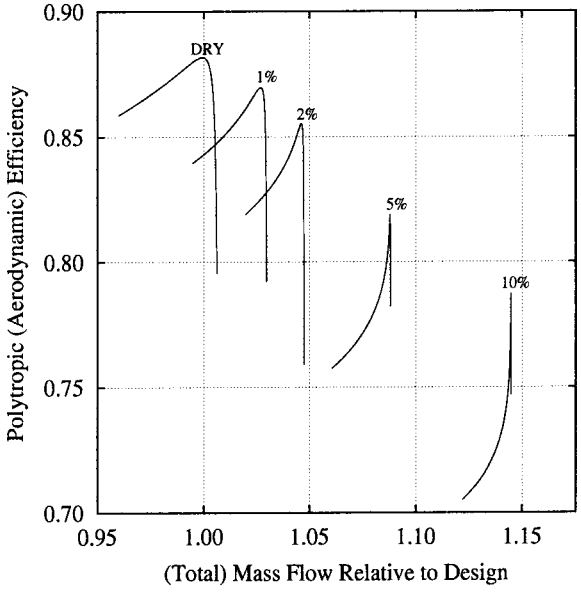

Fig. 5 Aerodynamic efficiency curves corresponding to Fig. 4

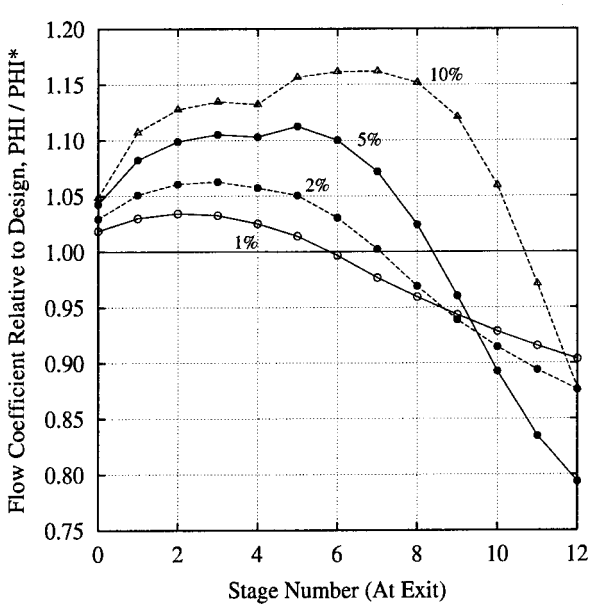

Fig. 6 Stage flow coefficients relative to their design value (ϕ/ϕ^*) for the compressor of Fig. 4. Each curve is plotted at the new operating point—i.e., the open circles of Fig. 4.

Although the precise shape of the characteristics will be a function of the compressor geometry, the loss and deviation models, and the droplet size (only a single size of 5 μm is considered here), the *general* effects of water injection are largely independent of such details and may be summarized as follows:

1. the characteristics shift progressively to a higher mass flow and pressure ratio,
2. the increment in mass flow is greater than the additional mass of water—i.e., the mass flow of dry air increases,
3. the characteristics become steeper and the operating range narrower,
4. the turbine running line shows the operating points moving to higher mass flow and pressure ratio, and approaching the choking limit.

The displacement of the characteristics may be explained by once again referring to Eq. (1). The range of operation of a given stage within the compressor is essentially determined by the flow coefficient, defined as $\phi = V_x/U$. For fixed values of this quantity, the loss, deviation and hence static enthalpy rise across the stage are (to a first approximation) largely fixed. Application of (1) then gives

$$\int_{\text{stage}} v\,dp \approx \text{const.} \tag{8}$$

At fixed ϕ, the lower value of v that accompanies evaporative cooling leads to increased mass flow (since $\dot{m}_a = \phi UA/v$) and, through (8), also provides an increased pressure rise, thereby giving the observed shift in the curves.

Changes in the pressure rise characteristics are accompanied by a degradation in aerodynamic performance, as shown in Fig. 5. The quantity plotted here is an ''equivalent'' polytropic efficiency, defined as

$$\eta_p' = \frac{1}{1 + \Delta s_A/(R_a \ln\{P_{o_2}/P_{o_1}\})} \tag{9}$$

where Δs_A is the (aerodynamic) specific entropy increase across the whole compressor. (This may be viewed as a means of normalizing the aerodynamic entropy increase in a fashion which accounts for variation in pressure ratio, and which yields exactly the polytropic efficiency for dry, semi-perfect gas compression.) The figure shows a marked reduction in aerodynamic efficiency as injection rate increases, and the efficiency peaks become much narrower. The reasons for this become clear upon studying the individual stage flow coefficients, relative to their design values, as shown in Fig. 6. The above-described increment in mass flow at the new operating conditions results in an unloading (i.e., higher flow coefficient) for the first stage. Consequently the pressure and density rise are less than their design values, thereby giving an initial increase in axial velocity and the observed rise in flow coefficient over the first few stages. Eventually, however, the effect of evaporative cooling takes over so that the density rises and the flow coefficient falls below the design value in the latter stages. This behavior occurs irrespective of the compressor geometry, and results in the early stages operating near choke and the rear stages near stall. Since nearly all stages operate off-design, the aerodynamic efficiency is impaired. Furthermore, these effects are exacerbated by small perturbations in mass flow, resulting in the narrow efficiency peaks of Fig. 5.

The linearized analysis presented by Horlock [5] appears at first to tell a different story to Fig. 6, with (for small injection rates) the flow coefficient increasing above its design value continuously throughout the machine. However, his calculations are for a fixed mass flow, and do not account for the change in operating point. (Repeating the current calculations at fixed mass flow show the same monotonic increase in ϕ/ϕ^*.) The Horlock approach is very valuable in determining trends in stage matching behavior, and there is clearly scope for extending it to deal with the change in operating point.

Actual Reduction in Compression Work. Degradation in compressor performance as result of off-design behavior inevitably compromises the benefits that accrue from water injection. This is highlighted by computing the fractional reduction in work input and comparing with that which could be achieved if the polytropic efficiency were maintained. Care must be taken in comparing the wet and dry work inputs since the shift in operating points to higher pressure ratios inevitably leads to an increased work requirement. A correction to account for this is made by computing the hypothetical dry compression work at the new pressure ratio while assuming the polytropic efficiency remains at its peak (dry) value. The results are presented in Table 1, from which it is clear that work reduction is substantially less than

Table 1 Comparison of work input for wet and dry compression

Water Injection Rate (%)	Operating Pressure Ratio	Work Input (kJ/kg)	Hypothetical (Dry) Work (kJ/kg)	Ratio Wet:Dry
0	12.25	360.8	360.8	1.00
1	12.59	355.1	366.5	0.97
2	12.82	350.9	370.3	0.95
5	13.33	343.6	378.6	0.91
10	14.02	338.8	389.6	0.87

suggested by the ideal or polytropic calculations of Section 2 and Section 3. For example, with a water injection rate of 5%, specific work is reduced by less than 10% compared to approximately 20% in Fig. 2. This is not to suggest that such injection rates are not worthwhile (overall GT output will still be significantly increased through the increment in mass flow and pressure ratio), but unless some redesign of the compressor is undertaken the advantages will be somewhat less than could otherwise be achieved.

Conclusions

Thermodynamic and aerodynamic aspects of wet compression have been investigated by simple numerical methods, applicable to very fine droplet sprays. It has been shown that the entropy production due to irreversible phase change is strongly dependent on droplet size, as expressed through the dimensionless combination $\dot{p}\tau$. Mean-line compressor calculations reveal that water-injection shifts the characteristics to higher mass flow and compression ratio, and these effects have been explained by simple aerothermodynamical reasoning. Individual compressor stages will, however, operate considerably off design, with front stages moving toward choke and rear stages toward stall. This has the effect of lowering the aerodynamic efficiency and narrowing the efficiency peak. The combination of thermodynamic losses and impaired aerodynamic efficiency result in the fractional work reduction due to evaporative intercooling being substantially less than that suggested by ideal wet compression calculation. On this basis it would seem reasonable that some redesign of the compressor would be necessary to achieve the full benefits that are possible with water-injected cycles.

Acknowledgment

The authors are grateful to Rolls-Royce plc. and the Engineering and Physical Sciences Research Council for their support.

Nomenclature

A = flow cross section (m^2)
c_p = specific heat capacity (J/kgK)
D_v = diffusion coefficient (m^2/s)
f = mass of liquid water per unit mass of dry air
h = specific enthalpy (J/kg)
J = vapor mass flux ($kg/(m^2s)$)
L = specific enthalpy of vaporisation for H_2O (J/kg)
M = molecular weight (kg/kmol)
n = number of droplets per kg of dry air (kg^{-1})
p = pressure (N/m^2)
$\dot{p}$ = compression rate (s^{-1})
Q = heat flux (W/m^2)
r = droplet radius (m)
R = specific gas constant (J/kg)
s = specific entropy (J/kgK)
T = temperature (K)
U, V = blade and flow velocities (m/s)
v = specific volume (per unit mass of dry air) (m^3/kg)
w_c = work input per unit flow (kJ/kg)
α, β = absolute and relative flow angle referred to axial (deg)
η_p, η_R = polytropic and (quasi) rational efficiency
λ = thermal conductivity (W/m^2K)
ρ = density (kg/m^3)
τ = droplet evaporation time (s)
τ_t = droplet temperature relaxation time (s)
ζ = Markov loss coefficient
ω = mass of water vapor per unit mass of dry air

Subscripts

a = dry air
A = aerodynamic (entropy increases)
ℓ = liquid water
s = saturated
T = thermodynamic (entropy increases)
v = water vapor
x = axial component

Appendix A

Isentropic Exponent for Wet Compression. Isentropic wet compression requires (a) that there is no entropy increase due aerodynamic effects, and hence from (1) that

$$dh = v\,dp, \tag{10}$$

and (b) that saturated, thermodynamic equilibrium is maintained, such that

$$\frac{p_v}{p} = \frac{\omega}{\omega + M_v/M_a} = \frac{p_s(T)}{p}, \tag{11}$$

(with T being the common temperature of the gas and liquid). Assuming semi-perfect gas relations, the specific volume and change in enthalpy may be written

$$v = (R_a + \omega R_v)\frac{T}{p} \tag{12}$$

$$dh = (c_{pa} + \omega c_{pv} + f c_{p\ell})dT + L\,d\omega. \tag{13}$$

The increment in specific humidity, $d\omega$, is obtained by differentiating the RHS of (11) and introducing the Clausius-Clapeyron equation in the form

$$\frac{dp_s}{p_s} \approx \frac{L}{R_v T}\frac{dT}{T}. \tag{14}$$

After some algebra this gives

$$d\omega = \omega\left(1 + \frac{M_a}{M_v}\omega\right)\left\{\frac{L}{R_v T}\frac{dT}{T} - \frac{dp}{p}\right\}. \tag{15}$$

Introducing this expression into (10), and incorporating (12) and (13), finally gives

$$c_p^* \frac{dT}{T} = R^* \frac{dp}{p} \tag{16}$$

where c_p^* and R^* are effective values for the specific heat capacity and gas constant, given by

$$c_p^* = c_{pa} + \omega c_{pv} + f c_{p\ell} + \left(1 + \frac{M_a}{M_v}\omega\right)\frac{\omega L^2}{R_v T^2}, \tag{17}$$

$$R^* = R_a + \omega R_v + \left(1 + \frac{M_a}{M_v}\omega\right)\frac{\omega L}{T}. \tag{18}$$

Together these define an effective value for the isentropic exponent, $\gamma^* = c_p^*/(c_p^* - R^*)$, which, although a function of the independent variables f and T, is approximately constant for typical compression conditions.

Appendix B

Evaporation Rate Model. The evaporation model employed in the present work is essentially that described by Spalding [11]. The analysis is standard but quite involved, and so is given here in outline only. For simplicity, droplets are assumed to be spherical and monodispersed; extension to deal with polydispersed sprays is, nonetheless, straightforward.

For droplets of radius r, the mass of liquid per unit mass of dry air is

$$f = \frac{4\pi}{3} r^2 n \rho_\ell , \tag{19}$$

where n is the number of droplets (per unit mass of dry air). The no-slip condition requires that n remains constant after injection. Thus,

$$\frac{D\omega}{Dt} = -\frac{Df}{Dt} = -4\pi\rho_\ell n r^2 \frac{Dr}{Dt}. \tag{20}$$

Following Spalding, the quasi-steady mass diffusion-convection equation for a spherical droplet yields[2]

$$\frac{Dr}{Dt} = -\frac{J}{\rho_\ell} = \frac{\rho D_v}{r} \ln\left(\frac{1+\omega}{1+\omega_\ell}\right) \tag{21}$$

where J is the vapor mass flux away from the droplet, ρ is the density of the (humid) air and D_v is the diffusion coefficient for water vapor in air. The vapor in contact with the droplet surface is assumed to be saturated, and hence its specific humidity, ω_ℓ, is a function of the liquid temperature, T_ℓ.

It is well established that droplets rapidly acquire the quasi-steady wet-bulb temperature, which is independent of radius. However, since the initial water injection temperature may differ significantly from the wet-bulb value, T_ℓ is determined here by the droplet energy balance,

$$\frac{DT_\ell}{Dt} = -\frac{3}{\rho_\ell c_{p\ell} r}(Q + LJ), \tag{22}$$

where Q is the heat flux away from the droplet. Based on quasi-steady heat and mass transfer, Spalding's analysis gives

$$Q = \frac{c_{pv} J (T - T_\ell)}{1 - \exp(J c_{pv} r/\lambda)}, \tag{23}$$

where λ is the thermal conductivity of (humid) air. (Note that the theory leading to (21) and (23) assumes that the droplet is immersed in a stationary gas-vapor mixture, and results in Nusselt and Sherwood numbers that are both approximately 2.)

Numerical integration of Eqs. (20)–(23) leads to problems of mathematical stiffness, since the initial temperature relaxation is very much faster than the evaporation process. These problems are circumvented here using a simple semi-analytical technique: by linearising the expressions for Q and J with respect to a small perturbation in T_ℓ, it is possible to express (22) in the form

$$\frac{DT_\ell}{Dt} = -\frac{T_\ell - T_{\text{ref}}}{\tau_t} \tag{24}$$

where τ_t is the droplet temperature relaxation time and T_{ref} is a reference temperature which lies close to the wet-bulb value. (The analysis leading to expressions for T_{ref} and τ_t is not included here due to space constraints.) T_{ref} and τ_t remain approximately constant over modestly large time-steps, so (24) may be integrated analytically, giving

$$T_{l2} = T_{\text{ref}} + (T_{l1} - T_{\text{ref}}) \exp(-\Delta t/\tau_t), \tag{25}$$

[2]The form of this equation is slightly different from that given by Spalding due to the use of specific humidity, ω, rather than vapor mass fraction.

subscripts 1 and 2 referring to the beginning and end, respectively, of the time-step Δt. In practice, T_{ref} and τ_t are calculated at each time step and average values used in (25).

Droplet Vaporization Time. As noted above, the timescale τ_t is very short so that droplets quickly acquire the wet-bulb temperature. Under constant gas-phase conditions, Eq. (21) may then be integrated to give the droplet vaporization time,

$$\tau = \frac{r^2}{2\rho D_v \ln\left(\frac{1+\omega_\ell}{1+\omega}\right)}. \tag{26}$$

Gas conditions, and hence τ, will of course vary greatly through a compressor. For the purpose of forming the dimensionless parameter $\dot{p}\tau$ used in Section 3, τ is evaluated on the basis of a dry inlet condition.

Thermodynamic Entropy Increase. The derivation of the entropy generation rate due to irreversible heat and mass transfer between phases requires careful attention to detail, and the reader is referred to Young [9] for a full account. The simplified result used here, applicable to non-nucleating flows with no velocity slip, is

$$\frac{Ds_T}{Dt} = -4\pi r^2 n \left\{ \frac{Q}{T_\ell}\left[\frac{T - T_\ell}{T}\right] + J\left[\frac{h_v - h_\ell}{T_\ell} - (s_v - s_\ell)\right]\right\} \tag{27}$$

where s_T refers to changes in entropy per unit mass of dry air.

Appendix C

Compressor Geometry. The results presented in Section 4 are for a "generic" single-shaft 12-stage compressor with a design pressure ratio of 12.25. The (fictitious) geometry is as follows:

Rotational speed:	5000 rpm
Design mass flow:	156.75 kg/s
Mean blade radius:	0.5 m
IGV exit angle:	15.0 deg
Stator inlet angles:	42.2 deg (stages 1, 12) 46.0 deg (stages 2–11)
Stator exit angles:	15.0 deg
Rotor inlet angles:	55.9 deg
Rotor exit angles:	40.0 deg (stages 1, 12) 35.4 deg (stages 2–11)
Axial chord:	40% blade height
Axial blade gaps:	25% axial chord

Table 2 Compressor area schedule

Stage:	1	2	3	4
Inlet area (m^2)	0.947	0.821	0.675	0.564
Stage:	5	6	7	8
Inlet area (m^2)	0.478	0.410	0.355	0.310
Stage:	9	10	11	12
Inlet area (m^2)	0.273	0.243	0.217	0.194

References

[1] Chiesa, P., Lozza, G., Macchi, E., and Consonni, S., 1994, "An Assessment of the Thermodynamic Performance of Mixed Gas-Steam Cycles—Part II: Water-Injected and Hat Cycles," ASME Paper No. 94-GT-424.

[2] Van Liere, J., "The Tophat Turbine Cycle," Modern Power Syst., Apr.

[3] Utamura, M., Takehara, I., and Karasawa, H., 1998, "MAT, A Novel Open Cycle Gas Turbine for Power Augmentation," Energy Convers. Manage., **39**(16–18), pp. 1631–1642.

[4] Hill, P., 1963, "Aerodynamic and Thermodynamic Effects of Coolant Injection on Axial Compressors," Aeronaut. Q., Nov., pp. 331–348.

[5] Horlock, J. H., 2001, "Compressor Performance With Water Injection," ASME Paper No. 2001-GT-343.

[6] Zhluktov, S., Bram, S., and De Ruyck, J., 2001, "Injection of Water Droplets in an Axial Compressor," *Proceedings of the Sixth World Conference on*

Experimental Heat Transfer, Fluid Mechanics, and Thermodynamics, Thessaloniki, Sept., **II**, 1415–1420.
[7] Young, J., and Yau, K., 1998, ''The Inertial Deposition of Fog Droplets on Steam Turbine Blades,'' ASME J. Trubomach., **110**, pp. 155–162.
[8] Zheng, Q., Sun, Y., Li, S., and Wang, Y., 2002, ''Thermodynamic Analysis of Wet Compression Process in the Compressor of a Gas Turbine,'' ASME Paper No. GT-2002-30590.
[9] Young, J., 1995, ''The Fundamental Equations of Gas-Droplet Multiphase Flow,'' Int. J. Multiphase Flow, (**21**)2, pp. 175–191.
[10] Wright, P., and Miller, D., 1991, ''An Improved Compressor Performance Prediction Model,'' Proc. Inst. Mech. Eng., pp. 69–82, Paper No. C423/028.
[11] Spalding, D., 1979, *Combustion and Mass Transfer*, Pergamon Press, New York, Chap. 3.

Hideyuki Uechi[1]
e-mail: hideyuki_uechi@mhi.co.jp

Shinji Kimijima[2]
e-mail: kimi@sic.shibaura-it.ac.jp

Nobuhide Kasagi
Professor,
e-mail: kasagi@thtlab.t.u-tokyo.ac.jp
Fellow ASME

Department of Mechanical Engineering,
The University of Tokyo,
Hongo 7-3-1, Bunkyo-ku,
113-8656 Tokyo, Japan

Cycle Analysis of Gas Turbine–Fuel Cell Cycle Hybrid Micro Generation System

Hybrid systems, which are based on a micro gas turbine (μGT) and a solid oxide fuel cell (SOFC), are expected to achieve much higher efficiency than traditional μGT's. In this paper, the effects of cycle design parameters on the performance and feasibility of a μGT-SOFC hybrid system of 30 kW power output are investigated. It is confirmed that the hybrid system is much superior to a recuperated gas turbine in terms of its power generation efficiency and aptitude for small distributed generation. General design strategy is found that less direct fuel input to a combustor as well as higher recuperator effectiveness leads to higher generation efficiency, while higher steam-carbon ratio moderates requirements for the material strength. The best possible conceptual design of a 30-kW μGT-SOFC hybrid system is shown to give power generation efficiency over 65% (lower heating value). [DOI: 10.1115/1.1787505]

1 Introduction

Small distributed generation systems, which make it possible to use the exhaust heat of power generation processes, are expected to achieve the higher efficiency of energy utilization. Currently, micro gas turbines (μGT's) under 100 kW are in practical use [1]. Even a smaller μGT of 5 kW has a perspective to be realized [2]. Moreover, μGT's have possibility to achieve such high efficiency as 40% with higher turbine inlet temperatures (TIT's) and recuperator effectiveness. It is, however, difficult to achieve much higher efficiency beyond 40% using a traditional μGT's, while μGT's combined with fuel cells, i.e., a solid oxide type (SOFC), are expected to attain extremely higher efficiency [3]. It is already shown that μGT-SOFC hybrid systems offer efficiency over 60% [4]. Current status of developing hybrids is reviewed [5], and the field demonstration of a 220-kW μGT-SOFC hybrid system has been reported [6]. In addition, various analyses, which are related to performance of combined systems involving fuel cells and gas/steam cycles, have been carried out to develop highly efficient systems [7]. Part-load performance analyses have also been investigated to find effective operation strategy of hybrids [8–10].

Although past studies mainly focused on systems over 100 kW, smaller systems [11,12] are necessary to meet the growth of energy demand in domestic sectors, and to encourage the broad use of the hybrid systems. It is probable that popularization can decrease costs of fuel cells. In this paper, a 30-kW μGT-SOFC hybrid system for small businesses and apartments is investigated. We show the effectiveness and features of hybrid systems through an exergy analysis. Cycle calculations are performed to clarify the effects of design parameters on the cycle performance and to find design strategy of μGT-SOFC hybrids. The conceptual design of a 30-kW μGT-SOFC hybrid system is also made to estimate the size and efficiency of the system in the best possible case.

2 System Configuration

Figure 1 shows the configurations of a μGT-SOFC hybrid system. This system is fed with methane at the atmospheric condition (15°C, 101.325 kPa). The air pressurized in the compressor and preheated in the recuperator is supplied into the cathode of the fuel cell. The cathode outlet air is utilized to burn the residual hydrogen, carbon oxide, and methane in the anode outlet gas. The combustible chemical species in the anode exhaust are very lean, hence we consider the additional methane injection into the combustor in order to stabilize the combustion. This extra fuel is not for increasing the turbine inlet temperature. The combustor outlet gas is expanded in the uncooled turbine and heats the compressor outlet air in the recuperator. The mixed gas including the fuel and a part of the anode exhaust is supplied into the reformer.

The numerical specifications in this figure are those of the typical design-point values described later. Several cycle-point temperatures are put in a high-risk range, e.g., the anode recirculation blower operates at the temperature over 800°C. The turbine inlet temperature is also extremely high for conventional metal components without cooling arrangement. These results are considered to be due to the SOFC operating temperature at 1000°C. The application of an intermediate temperature SOFC leads to that these cycle-point temperatures will be mitigated, whereas it is possible that the power generation efficiency decreases depending on the SOFC operating temperature. The feasibility of hybrid systems depends on the technological advancement of refractory alloy and improving the electrochemical performance of cell material.

3 Cycle Analysis Method

3.1 Modeling Approach. Thermodynamic cycle calculation of a recuperative gas turbine coupled with equilibrium analyses of a fuel cell is established to support system design. We consider mass and energy balance equations for energy conversion processes in all components. Temperatures, pressures, and compositions of working fluids at the inlet/outlet of each component are also considered. Component models are independent of their specific factors, i.e., structures of a compressor and turbine, cell geometry, a stack configuration, and a type of reformer. Theoretical expressions are adopted into the cycle analysis to account for general characteristics of components. However, empirical relationships developed in previously reported work are employed to estimate a voltage drop in a fuel cell.

For analyzing reaction in the reformer and the cell, reaction heat and equilibrium constants should be known. Reaction heat is obtained from the formation enthalpy in the JANAF table [13], except methane, of which coefficient is given in the literature [14].

[1]Presently at Mitsubishi Heavy Industries, Ltd., Takasago Research and Development Center, Arai-cho 2-1-1, Shinhama, Takasago-shi, Hyogo 676-8686, Japan.

[2]Presently at Shibaura Institute of Technology, Department of Machinery & Control Systems, Fukasuku 307, Minuma-ku, Saitama-shi, Saitama 337-8570, Japan.

Contributed by the Cycle Innovation Committee of THE AMERICAN SOCIETY OF MECHANICAL ENGINEERS for publication in the ASME JOURNAL OF ENGINEERING FOR GAS TURBINES AND POWER. Manuscript received by the Cycle Innovation Committee August 26, 2002; final revision received April 6, 2004. IGTI Chair: P. Pilides.

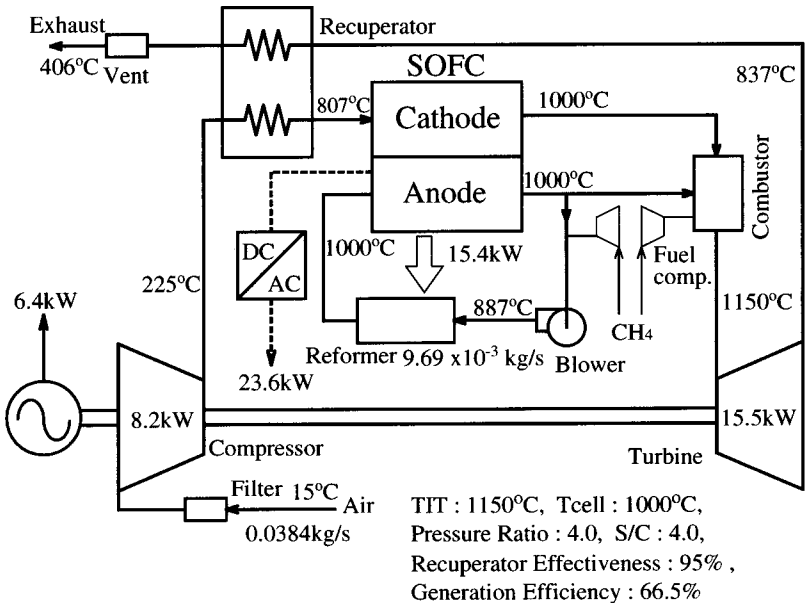

Fig. 1 Schematic diagrams of μGT-SOFC hybrid system

Equilibrium constants are obtained from differences of the Gibbs energy. The reaction heat and equilibrium constants are given as polynomial-fitting functions of temperatures.

3.2 Assumptions. In this paper, we will find out the future development goal of small-sized (<100 kW) hybrid system technology. The analysis results described in this paper are applicable to best possible hybrid systems, because the bold assumptions as shown below are introduced into the present cycle analysis. Under ordinary circumstances, these assumptions should be validated with experimental data of practical SOFC's and μGT's, whereas sufficient numbers of reference data to evaluate the present cycle analysis have not been published.

The values of the cycle parameters in the present analysis are shown in Table 1. Unless otherwise indicated, these conditions are assumed. The following assumptions are made to simplify the analysis:

(i) gases do not leak outside the system;
(ii) heat loss is negligibly small;
(iii) chemical reactions proceed to equilibrium states;
(iv) internal distributions of temperatures, gas composition, and pressure in each system component are uniform;
(v) steady-state operation is achieved;
(vi) heat required in the reformer is supplied from the cell;
(vii) the temperatures at the outlets of anode, cathode, and reformer are equal to the cell temperature;
(viii) in the combustor, the residual species from the anode and the injected methane are burnt completely.

3.3 Micro Gas Turbine. To evaluate characteristics of compression and expansion processes in the compressor and turbine, a standard method in the literature [15] is used. The combustor outlet temperature is first assumed, then the fuel consumption is determined by iterative calculations. The power output from the gas turbine is obtained by using the following equation:

$$W_{gt} = \eta_{gen}(\eta_{gt} W_t - W_c) - W_{gcgt}. \quad (1)$$

3.4 Reformer. In the reformer, hydrogen and carbon oxide are produced from methane and steam. Inside the reformer, the reactions bellow are considered:

$$\text{reforming:} \quad CH_4 + H_2O \rightarrow 3H_2 + CO, \quad (2)$$

$$\text{shifting:} \quad CO + H_2O \rightarrow H_2 + CO_2. \quad (3)$$

Reforming is endothermic reaction, where shifting is exothermic reaction. As a whole, the reaction in the reformer is endothermic. To allow methane and steam to react, the residual heat in the cell is transferred to the reformer.

Based on the partial pressures of the species in the reformer, the equilibrium constant of reforming K_{ref} and that of shifting K_{shf} are defined as follows:

Table 1 Standard cycle analysis conditions

Power Output (kW)	30
Cell Temperature T_{cell} (°C)	1000
Turbine Inlet Temperatue (°C)	>1000
Pressure Ratio (-)	4.0
Recuperator Temperature Effectiveness (%)	95
Compressor Adiabatic Efficiency (%)	73
Turbine Adiabatic Efficiency (%)	80
GT Mechanical Efficiency, η_{gt} (%)	95
Blower Adiabatic Efficiency (%)	70
Blower Mechanical Efficiency (%)	90
Gas Compressor Adiabatic Efficiency (%)	60
Gas Compressor Mechanical Efficiency (%)	90
Steam Carbon Ration S/C (-)	3.0
Current Density, J (A/m^2)	3000
H_2 Utilization Ratio, U_f (%)	80
Cathode Thickness, δ_{ea} (mm)	2
Anode Thickness, δ_{an} (mm)	0.1
Electrolyte Thickness, δ_{el} (mm)	0.02
SOFC Pressure Drop (%)	5
Reformer Pressure Drop (%)	4
Filter Pressure Drop (%)	0.5
Vent Pressure Drop (%)	0.5
Recuperator Pressure Drop (Air Side) (%)	3
Recuperator Pressure Drop (Exhaust Side) (%)	2
Atmospheric Temperature (°C)	15
Generator Efficiency, η_{gen} (%)	98
Inverter Efficiency, η_{DA} (%)	98

$$K_{ref}=(p_{H2}^3 p_{CO})/(p_{CH4}p_{H2O}), \quad (4)$$

$$K_{shf}=(p_{H2}p_{CO2})/(p_{CO}p_{H2O}). \quad (5)$$

We can obtain the mole numbers Δn_{ref} for reforming and Δn_{shf} for shifting by iterative calculation from K_{ref} and K_{shf}. Once the mole numbers to react are estimated, the reaction heat Q_{ref} can be calculated from the heat balance in the reformer.

Using the mole amount of steam in the recirculated anode exhaust gas $n_{an,H2O}$ and supplied methane n_{CH4}, the steam-carbon ratio (S/C) is defined as follows:

$$S/C=n_{an,H2O}/n_{CH4}. \quad (6)$$

3.5 Solid Oxide Fuel Cell. In a SOFC, the electric power is generated through the following processes:

$$\text{anode:} \quad H_2+O^{2-}\rightarrow H_2O+2e^-, \quad (7)$$

$$CO+O^{2-}\rightarrow CO_2+2e^-, \quad (8)$$

$$\text{cathode:} \quad O_2+4e^-\rightarrow 2O^{2-}. \quad (9)$$

The ideal voltage through the electrochemical oxidation of hydrogen is obtained as follows:

$$V_{H2}=-\frac{1}{2F}\Delta G_{H2}-\frac{RT}{2F}\ln\left(\frac{p_{an,H2O}}{p_{an,H2}\sqrt{p_{ca,O2}}}\right), \quad (10)$$

where ΔG_{H2} represents the change in the Gibbs energy before and after the reaction of hydrogen.

The amount of hydrogen to react is calculated by using the fuel utilization factor U_f, which is defined as follows:

$$U_f=\Delta n_{H2}/n_{an,H2}, \quad (11)$$

where Δn_{H2} is the hydrogen consumption in the anode and $n_{an,H2}$ is the amount of hydrogen supplied to the anode.

In a real cell, a net voltage is lower than an ideal one due to voltage drop caused by overpotentials, i.e., activation polarization, Ohmic loss, and concentration polarization. The activation polarization is estimated by the empirical expressions [16]. We apply the previously reported approximate expressions [17] to estimate the values of cell material resistivity. The concentration polarization is negligibly small if compared to other polarizations [9,16]. Considering the activation polarization and Ohmic loss, the net voltage is obtained as follows:

$$V_{net}=V_{H2}-V_{act}-J(\rho_{an}\delta_{an}+\rho_{ca}\delta_{ca}+\rho_{el}\delta_{el}). \quad (12)$$

At the design-point shown in Fig. 1, the ideal and net cell voltages are 0.863 and 0.704 V, respectively.

3.6 Fuel Cell Power Output. The current is obtained from the reacting amount of hydrogen and carbon oxide, and the fuel cell power output W'_{FC} is calculated from the current and the net voltage. We should take into account the power for the fuel cell auxiliaries. Then, the net output W_{FC} is obtained as follows:

$$W_{FC}=\eta_{DA}W'_{FC}-W_{gcfc}-W_{blow}. \quad (13)$$

3.7 Cell Energy Balance. From the total inlet enthalpy H_{in} and the reaction enthalpy ΔH_{cell}, the total cell exit enthalpy H_{out} is obtained as follows:

$$H_{out}=\{H_{in}+(-\Delta H_{cell})\}-(W'_{fc}+Q_{ref}). \quad (14)$$

Assuming that the anode and cathode outlet temperatures are equal, they are obtained from H_{out}. We can derive the fuel input to the fuel cell for a certain cell temperature condition by iterative calculation.

3.8 Generation Efficiency of Hybrid System. The power generation efficiency of the overall system is defined as follows:

$$\eta_{sys}=(W_{gt}+W_{FC})/\{(m_{gt}+m_{FC})\Delta H_{CH4}\}. \quad (15)$$

In this study, the generation efficiency is defined with the sum of the fuel cell and gas turbine heat input, which are estimated in terms of the lower heating value (LHV).

3.9 Comparison With Previously Reported Work. The advanced analysis results regarding the performance evaluation of the small-scale hybrid system, which consists of a pressurized SOFC and μGT, are reported [12]. We present the comparison between the present and previous results below.

Table 2 is the comparative chart of the present calculation and reported work [12]. In the previous results, the temperatures at the turbine inlet and the recuperator inlet, fall in moderate conditions. The pressure ratio is adequate with current turbocharger equipment. Hence, the previous results are considered to be more realistic estimation to develop the actual plant of the hybrid system based on the present technology. However, the power generation efficiency of the previous result is lower than that of the present result. The disagreement of the SOFC operating conditions, i.e., the cell temperature, pressure, current density, and fuel utilization factor, are principal reason for such differences. In this manner, it is found that the different assumptions make the difference with the previous results. However, the present analysis method is believed to be substantially proper to estimate the performance of hybrid systems.

4 Features of Gas Turbine–Fuel Cell Hybrid System

Gas turbine-fuel cell hybrid systems are expected to achieve efficiency over 60% (LHV). To clarify major reasons, we performed an exergy analysis. In this section, we focus on the performance of the μGT-SOFC hybrid system (Fig. 1).

Figure 2 shows a breakdown of exergy consumption in the μGT-SOFC hybrid system. To make clear the features of the hybrid system, we compare the results of the exergy calculations regarding a traditional recuperated gas turbine and an atmospheric SOFC in Fig. 2. Each exergy fraction is defined as the ratio of output or exergy loss to exergy of fuel input. Then, the exergy fraction of output is not equal to the generation efficiency.

The combustion loss of the hybrid system is lower than that of the recuperated gas turbine, because the electric power and heat are generated in the SOFC simultaneously. The exhaust and recuperator losses are also lower than those of the atmospheric SOFC. With the turbine, additional power is recovered effectively from the high-temperature exhaust gas. In the recuperator, smaller temperature difference between the exhaust gas and air makes the irreversibility of heat transfer smaller.

Generally, smaller power units offer lower generation efficiency. We performed cycle analyses for 30- and 300-kW hybrid systems and recuperated gas turbines in order to estimate the effects of power output size on the generation efficiency. In the cycle calculation, we assume that the compressor, turbine and mechanical efficiency depend on the system size. To give the component efficiency, it is also assumed that approximately one-fifth of the total output is gained by the gas turbine. As shown in Table 3, for the hybrid system, the difference in the heat input per 1 kW output between 30- and 300-kW systems is 0.07 kW, while that of the traditional recuperated gas turbines is 0.23 kW. It is evident that the generation efficiency of the hybrid system is less dependent on the power output size, so that the hybrid system is more suitable for small power generation use.

Generation efficiency of a gas turbine is generally decreased when intake air temperatures becomes higher. This characteristic is one of the disadvantages for power generation systems, because electric power demand increases in summer. We estimated the effects of atmospheric temperature on the generation efficiency. The cycle calculations for the compressor inlet temperatures of 15 and 30°C were performed for both the hybrid system and recuperated gas turbine. As shown in Table 4, for the hybrid system, the difference of the heat input per 1 kW output at 15 and 30°C is

Table 2 Comparison with previous work [12]

	Present analysis	Magistri et al.[12]
Total power output (kW)	30.0	36.0
SOFC power output (kW)	23.6	31.0
Gas turbine power output (kW)	6.4	5.0
Efficiency (%)	66.5	56.3
SOFC fuel utilization (%)	80.0	85.0
SOFC current density A/m^2	3000	3850
Compressor efficiency (%)	73.0	75.3
Turbine efficiency (%)	80.0	83.8
Pressure ratio (-)	4.0	2.7
Compressor inlet temp. (°C)	15	18
Compressor outlet temp. (°C)	225	161
Recuperator air side outlet temp. (°C)	807	643
Turbine inlet temp. (°C)	1150	898
Turbine oulet tenp. (°C)	837	680
Exhaust gas temp. (°C)	406	245
Recuperator air side pressure loss (%)	3.0	1.8
Recuperator combustion gas side pressure loss (%)	2.0	0

0.03 kW, while that of the recuperated gas turbine is 0.12 kW. The hybrid system deteriorates less in its efficiency during high-temperature seasons.

5 Strategy for Hybrid System Design

Some of the design parameters of a hybrid system are flexible, while the others cannot be changed widely. For example, the efficiency of the rotating components, i.e., a compressor and turbine, is strongly dependent on the power output size, whereas we can choose the pressure ratio rather freely. In the following subsection, the effects of the fuel cell operating temperature and TIT on the system performance are shown. Moreover, general strategy to decide the cycle parametric conditions, such as the recuperator temperature effectiveness, S/C ratio, pressure ratio, and TIT, is discussed.

5.1 Fuel Cell Operating Temperature and Turbine Inlet Temperature. While we investigate the effects of the fuel cell operating temperature and TIT, the other variables are fixed. The calculated results of the generation efficiency are shown in Fig. 3(*a*). It is clear that higher cell temperatures give higher efficiency. However, unlike a conventional gas turbine, the efficiency of the hybrid system decreases with increasing TIT at a fixed cell temperature. We should remember that higher cell temperatures imply higher cost and require longer time to start up because of avoiding the thermal shock caused by rapid temperature rise. In the following discussions, we fix the cell temperature at 1000°C, which is the limit for state-of-the-art technology of SOFC's.

Figure 3(*b*) shows the total heat input and the fuel cell heat input. The heat input to the combustor is obtained as the differ-

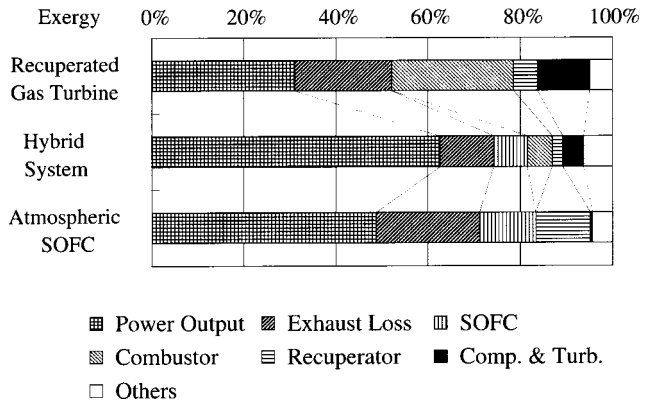

Fig. 2 Breakdown of exergy consumption in μGT-SOFC hybrid system

Table 3 Effect of power output capacity

	Recuperated GT		Hybrid System	
Total Output (kW)	30	300	30	300
Pressure Ratio (-)	5.0	6.0	5.0	
Compressor Adiabatic Efficiency (%)	75	79	73	76
Turbine Adiabatic Efficiency (%)	85	87	80	86
GT Mechanical Efficiency (%)	97	98	95	97
Turbine Inlet Temperature (°C)	1250			
Fuel Consumption for 1kW Output (kW)	2.65	2.42	1.54	1.47

Table 4 Effect of intake air temperature on design-point definition

	Recuperated GT		Hybrid System	
Total Output (kW)	30			
Compressor Inlet Temperature (°C)	15	30	15	30
Pressure Ratio (-)	5.0		5.0	
Compressor Adiabatic Efficiency (%)	75		73	
Turbine Adiabatic Efficiency (%)	85		80	
GT Mechanical Efficiency (%)	97		95	
Turbine Inlet Temperature (°C)	1250			
Fuel Consumption for 1kW Output (kW)	2.65	2.77	1.54	1.57

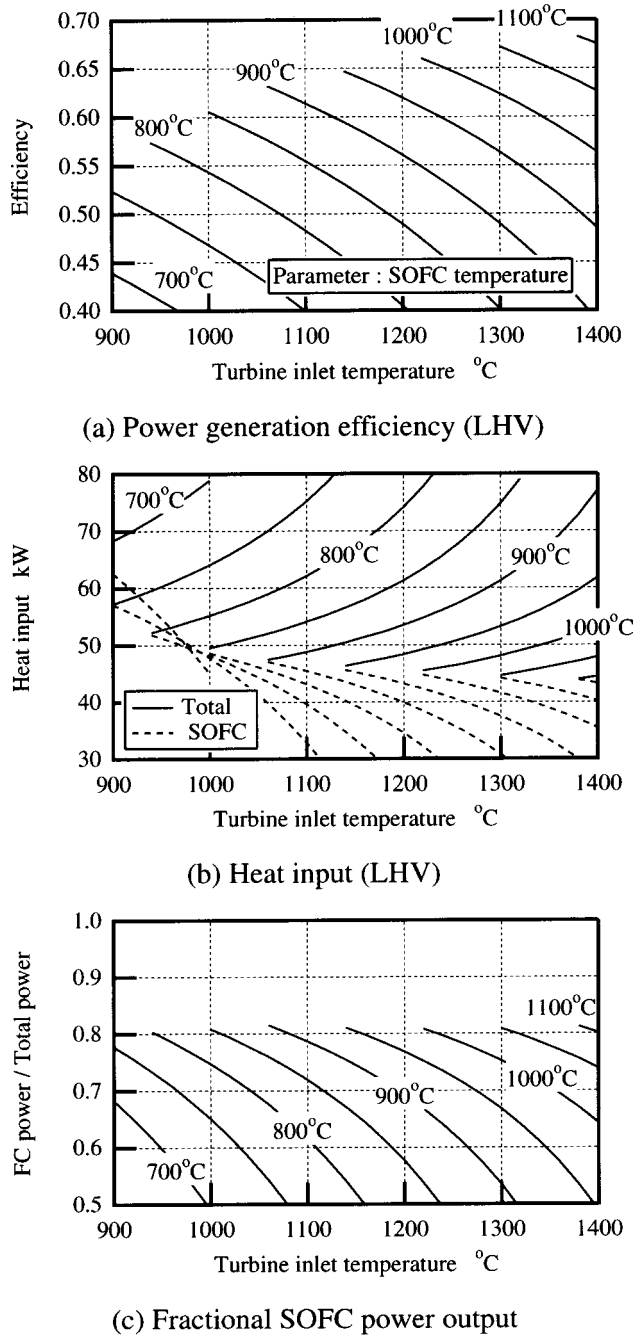

Fig. 3 Effects of SOFC operating temperature and TIT: (*a*) Power generation efficiency (LHV); (*b*) Heat input (LHV); (*c*) Fractional SOFC power output

ence between them. Large direct heat input to the combustor causes higher TIT's. However, it reduces the total generation efficiency, because the heat input to the fuel cell is utilized more effectively than that to the combustor. This result is supported by Fig. 3(*b*), in which a higher TIT or larger heat input to the combustor gives lower generation efficiency. It is also evident that there is a certain TIT for each cell temperature with zero heat input to the combustor. We cannot lower the TIT bellow the temperature that is equivalent to the zero heat input.

The ratio of the fuel cell output to the total output is shown in Fig. 3(*c*). Higher cell temperatures give higher fractional fuel cell power output, while higher TIT's give lower fuel cell fractions. At the lowest TIT for each cell temperature, the fuel cell fraction is approximately 80%. This value is slightly small against the value of 86% in the previously reported work [12], but the difference is considered to be insignificant.

5.2 Recuperator Temperature Effectiveness. We estimate the effects of the recuperator temperature effectiveness on the performance of the hybrids under the condition of the fixed current density and the constant fuel utilization. High recuperator effectiveness leads to high cathode inlet temperatures. Then, the fuel input to the fuel cell for a unit amount of air is reduced under a fixed cell temperature. This is confirmed by the decrease of the oxygen utilization in the SOFC (Fig. 4(*a*)). The small fuel input to the SOFC causes the decrease of the residual species such as hydrogen (Fig. 4(*b*)). The less residual gases lower the TIT, and thereby higher recuperator effectiveness causes reduction of the TIT for a fixed heat input to the combustor (Fig. 4(*c*)). The generation efficiency is increased together with increasing recuperator effectiveness, when the TIT is decreased, or the fuel input to the combustor is fixed (Fig. 4(*d*)). Although increasing recuperator effectiveness may result in the augmentation of both the size and cost, the performance improvement of a recuperator can also be led to for cost reduction and downsizing. As discussed in the following section, the size of the recuperator in the hybrid system is likely small as compared to the size of the SOFC reactor.

5.3 Steam-Carbon Ratio. Steam-carbon ratio is defined as the ratio of the mole fractions of steam and methane at the reformer inlet (Eq. (6)). The S/C ratio determines the mass flow rate of the anode recirculation. In the case of Fig. 1, the recirculation ratio to the anode exhaust is estimated at 0.63.

Increasing the S/C ratio with the other parameters fixed, the amount of the anode recirculation is increased. This results in the reduction of the energy input to the fuel cell at a fixed exhaust temperature. In the same manner, as the recuperator effectiveness is increased, higher S/C ratio causes lower TIT's (Fig. 5(*a*)). As shown in Fig. 5(*b*), the higher S/C ratio reduces the generation efficiency under the constant TIT. The reduction of the S/C ratio with the fixed fuel input to the combustor, the deterioration of the generation efficiency is not remarkable.

The turbine exit temperature can be decreased with the higher S/C ratio and the lower TIT (Fig. 5(*c*)). Increasing the S/C ratio, for instance, from 3.0 to 4.0, the minimal TIT decreases from 1210 to 1165°C. The turbine exit temperature is also lowered from 845 to 810°C. There is a maximum temperature for the use of metallic recuperators in the range between 850 and 900°C. Beyond this temperature, we should utilize ceramic recuperators with higher cost [2]. High S/C ratio may enable us to adopt metallic recuperators, and this is favorable even with some penalty in generation efficiency.

In addition, we should take the following issues into consideration for appropriate design-parameter setting. High S/C ratio operation accelerates the corrosion of the anode catalyst because of the high content of the steam in anode gas. Sufficient quantities of steam are essential to prevent carbon deposition on anodic electrodes.

5.4 Pressure Ratio. So far, it is clarified that high recuperator effectiveness is preferable and high S/C ratio moderates the requirement for thermal durability of component materials. In the following, the recuperator effectiveness and the S/C ratio are fixed at 95% [2] and 4.0, respectively.

Figure 6(*a*) shows the effect of the pressure ratio on the generation efficiency. The maximum efficiency is approximately 67% (LHV) at the pressure ratio of 4.5 without the direct heat input to the combustor. However, the variation of the maximum generation efficiency from the pressure ratio 2.5 to 6.0 is not remarkable. The higher pressure ratio reduces the turbine outlet and cathode inlet temperatures. The lower cathode inlet temperature causes the higher energy input to the fuel cell. Contrary to the effects of the recuperator effectiveness and S/C ratio, higher pressure ratio gives higher TIT's. We plot the heat input in Fig. 6(*b*) to determine the

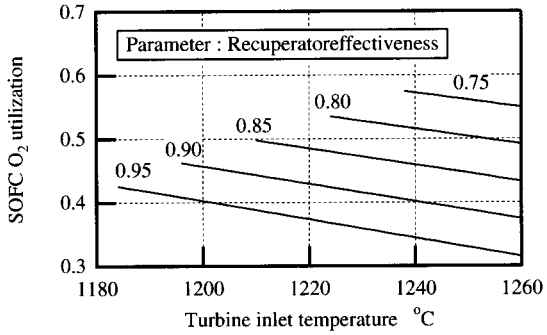

(a) Oxygen utilization in SOFC

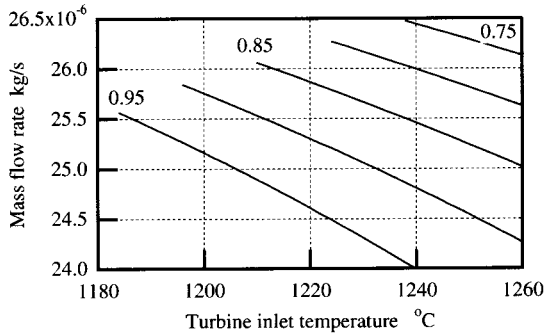

(b) Hydrogen mass flow rate input combustor

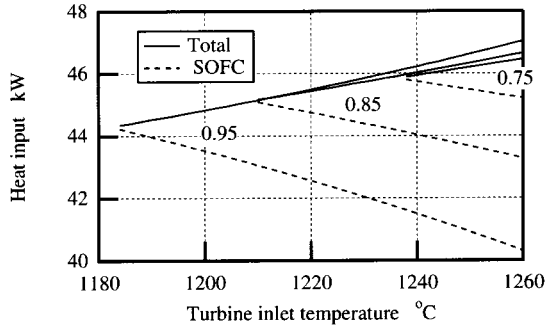

(c) Heat input (LHV)

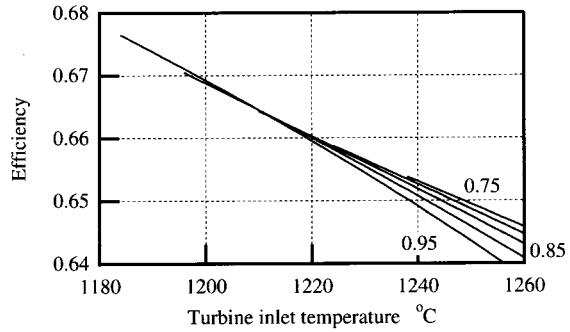

(d) Power generation efficiency (LHV)

Fig. 4 Effects of recuperator effectiveness: (*a*) Oxygen utilization in SOFC; (*b*) Hydrogen mass flow rate into combustor; (*c*) Heat input (LHV); (*d*) Power generation efficiency

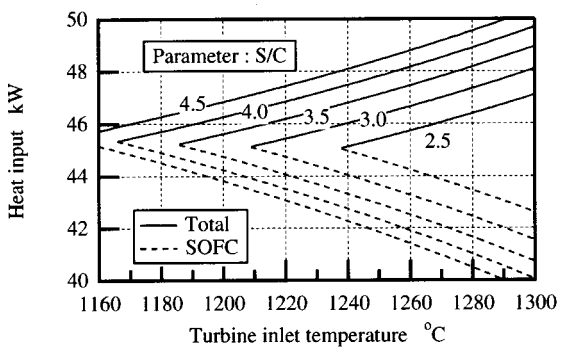

(a) Heat input (LHV)

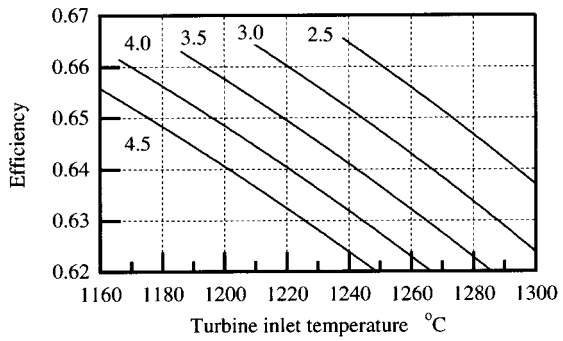

(b) Power generation efficiency (LHV)

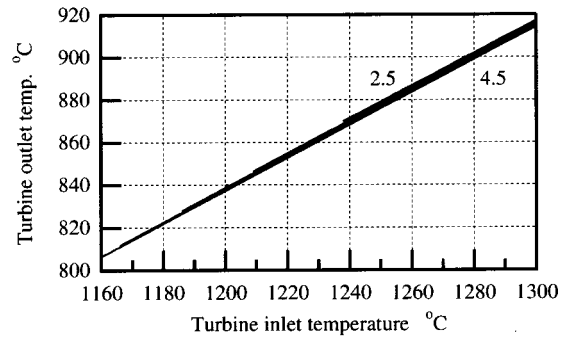

(c) Turbine outlet temeprature

Fig. 5 Effects of steam-carbon ratio: (*a*) Heat input (LHV); (*b*) Power generation efficiency; (*c*) Turbine outlet temperature

TIT. The smaller direct fuel input to the combustor is preferable, but we take the additional fuel input into consideration in the present analysis. This extra fuel is supplied for the combustion stabilization, since the concentration of the combustible mixture in the SOFC exhaust is very lean. Assuming that the heat input to the combustor is 1.5 kW, we can estimate TIT=1150°C in Fig. 6(*b*) for the pressure ratio of 4.0.

We should also account for the aspects of strength and high-temperature durability of materials. Lower turbine tip speeds are desirable to reduce turbine stresses. Low turbine outlet temperatures are also preferred because they enable us to utilize inexpensive materials for recuperators. As shown in Fig. 6(*d*), the turbine outlet temperature decreases as the pressure ratio increases, whereas the turbine tip speed increases simultaneously. Hence, we should compromise them to determine the design-point value of the pressure ratio. For the pressure ratio of 4.0 and TIT of 1150°C, the turbine tip speed is approximately 630 m/s and the turbine outlet temperature is 840°C. On the achievement of the ceramic gas turbine research project in Japan [18], these values should be technologically feasible in the foreseeable future.

6 Conceptual Design of μGT-SOFC Hybrid System

We performed a conceptual design of a 30-kW μGT-SOFC hybrid system for the best possible case. From the viewpoint of

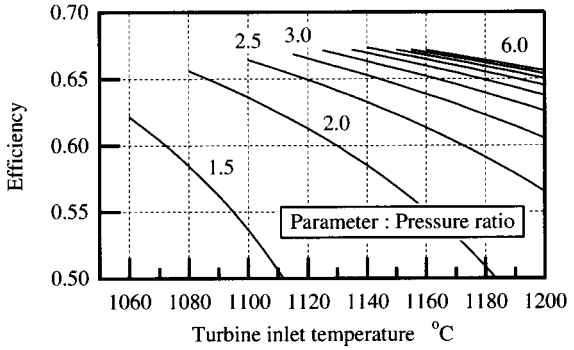

(a) Power generation efficiency (LHV)

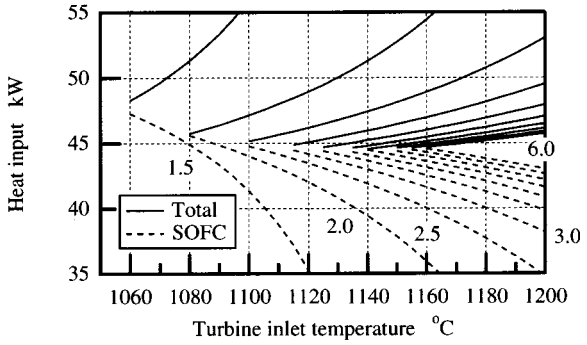

(b) Heat input (LHV)

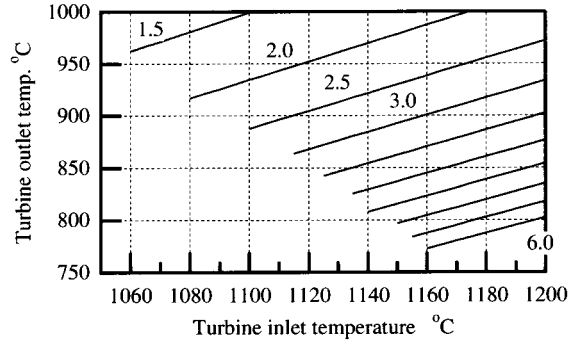

(c) Turbine outlet temperature

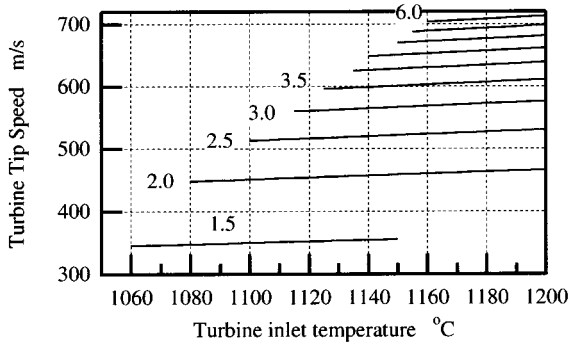

(d) Turbine tip speed

Fig. 6 Effects of pressure ratio: (*a*) Power generation efficiency (LHV); (*b*) Heat input (LHV); (*c*) Turbine outlet temperature; (*d*) Turbine tip speed

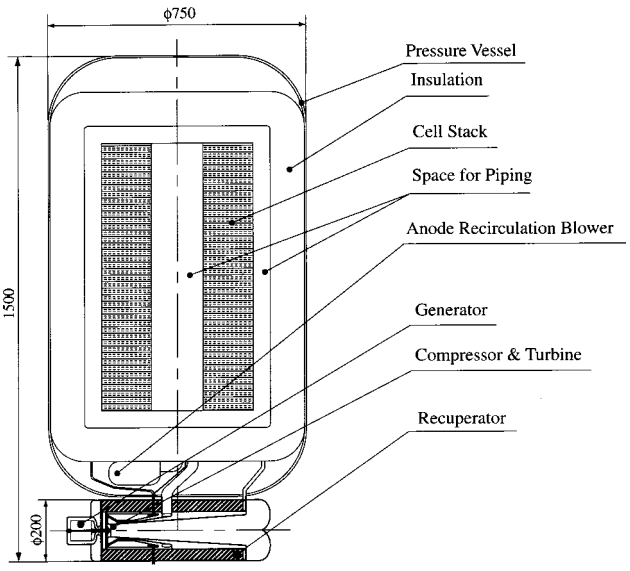

Fig. 7 Conceptual design of 30-kW μGT-SOFC hybrid system

production cost, metal components are recommended. The design-point conditions of the hybrid system should be fixed in consideration of thermal durability and mechanical strength of component materials. As mentioned above, based on the turbine tip speed (630 m/s) and the outlet gas temperature (840°C), we set the pressure ratio at 4.0, the TIT at 1150°C, the S/C ratio at 4.0.

A single-shaft arrangement using a centrifugal compressor and a radial-flow turbine is applied to the μGT. An electric generator is directly coupled with the compressor/turbine rotor. An annular-type combustor wraps around the rotor unit. The design processes for the compressor/turbine and combustor are based on the methods described in the literature [19]. A primary surface annular recuperator is suitable for a μGT in terms of its compactness. The recuperator temperature effectiveness is aimed at 0.95 as discussed in the previous section. In order to achieve such high performance, the substantial heat transfer area will be needed. Under the constraint of the allowable pressure loss shown in Table 1, the specifications of the gas flow channels, i.e., hydraulic diameter, flow length and the number of the flow paths, are determined to satisfy the targeted temperature effectiveness.

Regarding the SOFC, planar-type cells are applied and its surface area is estimated from the current and the targeted current density. The unit cell consists of an anode, a cathode, an electrolyte, and interconnectors. The thickness of the unit cell is estimated from an existing SOFC test model [20], of which thickness is 5 mm. A reformer part is set between the unit cells. The thickness of the reformer with support plate is assumed to be 3 mm. Consequently, the thickness of the single cell, i.e., a pair of the unit cell and the reformer, is estimated at 8 mm. The number of the single cell is determined from the total SOFC power generation capacity and the power output of the single cell. Hereby, the volume of the SOFC part of the hybrid system can be estimated.

Based on the procedures of component design as described above, we conduct the conceptual design of the 30-kW hybrid system shown in Fig. 7. The SOFC is put in the pressure vessel including heat shield material, and the μGT is set out of the SOFC reactor. The diameter and height of the system are estimated as about 750 and 1500 mm, respectively. The overall system size will be almost the same scale as a refrigerator for home use.

7 Conclusions

Cycle calculations of a 30kW μGT-SOFC hybrid system and its conceptual design have been carried out. The following conclusions are derived:

(i) The power generation efficiency of the μGT-SOFC hybrid system reaches 65% (LHV) for the best possible case.

(ii) Hybrid systems have higher efficiency than those of a recuperated gas turbine and atmospheric fuel cell, because the exergy losses of combustion and exhaust are made much smaller.

(iii) On design-point definition, unit capacity and ambient temperatures have smaller influence on hybrid systems than on recuperated gas turbines.

(iv) From the viewpoints of system efficiency and material durability, the additional fuel input to the combustor should be minimized.

(v) Higher recuperator effectiveness contributes to the improvement of system performance and moderates the requirements for material thermal durability.

(vi) Higher S/C ratio moderates the turbine inlet and outlet temperatures, although it causes a little decrease in power generation efficiency.

(vii) A certain pressure ratio gives the maximum generation efficiency, but its variation near the optimal point does not lead to a remarkable difference.

(viii) As a result of conceptual design, the diameter and height of a 30-kW μGT-SOFC hybrid system are estimated as about 750 and 1500 mm, respectively.

Acknowledgment

This work was supported through the research project on ''Micro Gas Turbine/Solid Oxide Fuel Cell Hybrid Cycles for Distributed Energy System'' by the Department of Core Research for Evolutional Science and Technology (CREST) of the Japan Science and Technology Agency (JST).

Nomenclature

Symbols

F = Faraday constant C/mol
G = Gibbs free energy J/kg
H = Enthalpy W
J = Current density A/m^2
K = Equilibrium constant
LHV = Lower heating value
m = Fuel mass flow rate kg/s
n = Mole number mol
p = Pressure normalized by standard atmopheric pressure
Q = Heat flow W
R = Gas constant J/mol K
T = Temperature K
U = Utilization factor
V = Voltage V
W = Power W
δ = Thickness m
ρ = Resistivity Ω m
η = Efficiency

Subscripts

act = Activation
an = Anode
blow = Blower
c = Compressor
ca = Cathode
cell = Cell
DA = Inverter
el = Electrolyte
f = Fuel
fc = Fuel cell
gcfc = Gas compressor (FC)
gcgt = Gas compressor (GT)
gen = Electrical generator
gt = Gas turbine
in = Inlet
net = Net value
out = Outlet
ref = Reforming
shf = Shifting
sys = Hybrid system
t = Turbine

References

[1] Craig, P., 1997, ''The Capstone Turbogenerator as an Alternative Power Source,'' SAE Paper No. 970292.
[2] Rodgers, C., 2000, ''25-5 kW Microturbine Design Aspects,'' ASME Paper No. 2000-GT-0626.
[3] White, D. J., 1999, ''Hybrid Gas Turbine and Fuel Cell Systems in Perspective Review,'' ASME Paper No. 99-GT-419.
[4] Massardo, A. F., and Lubelli, F., 2000, ''Internal Reforming Solid Oxide Fuel Cell-Gas Turbine Combined Cycles (IRSOFC-GT): Part A—Cell Model and Cycle Thermodynamic Analysis,'' ASME J. Eng. Gas Turbines Power, **122**, pp. 27–35.
[5] Layne, A., Williams, M., Samuelsen, S., and Holcombe, N., 2001, ''Hybrid Fuel Cell Heat Engines: Recent Efforts,'' ASME Paper No. 2001-GT-588.
[6] George, A. R., 2000, ''Status of Tubular SOFC Field Unit Demonstrations,'' J. Power Sources, **86**, pp. 134–139.
[7] Campanari, S., and Macchi, E., 2001, ''Comparative Analysis of Hybrid Cycles Based on Molten Carbonate and Solid Oxide Fuel Cells,'' ASME Paper No. 2001-GT-383.
[8] Campanari, S., 2000, ''Full Load and Part-Load Performance Prediction for Integrated SOFC and Microturbine Systems,'' ASME J. Eng. Gas Turbines Power, **122**, pp. 239–246.
[9] Costamagna, P., Magistri, L., and Massardo, A. F., 2001, ''Design and Part-Load Performance of a Hybrid System Based on a Solid Oxide Fuel Cell Reactor and a Micro Gas Turbine,'' J. Power Sources, **96**, pp. 352–368.
[10] Palsson, J., and Selimovic, 2001, ''Design and Off-Design Prediction of a Combined SOFC and Gas Turbine System,'' ASME Paper No. 2001-GT-379.
[11] Massardo, A. F., McDonald, C. F., and Korakianitis, T., 2002, ''Microturbine/Fuel Cell Coupling for High-Efficiency Electrical Power Generation,'' ASME J. Eng. Gas Turbines Power, **124**, pp. 110–116.
[12] Magistri, L., Massardo, A., Rodgers, C., and McDonald, C. F., 2001, ''A Hybrid System Based on a Personal Turbine (5 kW) and a SOFC Stack: A Flexible and High Efficiency Energy Concept for the Distributed Power Market,'' ASME Paper No. 2001-GT-92.
[13] Malcolm, W., 1989, ''NIST-JANAF Thermochemical Tables Fourth Edition,'' Part 1–Part 2, American Chemical Society and American Institute of Physics.
[14] Hougen, O. A., Watson, K. M., and Ragatz, R. A., 1959, *Chemical Process Principles Part II. Thermodynamics*, Appendix, New York.
[15] Matsunaga, N., Hoshino, T., and Nagashima, A., 1983, ''Critical Assessment of Thermophysical Properties Data of Combustion Gases for Calculating the Performance of Gas Turbine,'' IGTC Paper No. 83-TOKYO-IGTC-41.
[16] Nagata, S., Onda, K., Momma, A., Kasuga, Y., and Kato, K., 1993, ''Simulation of Temperature Dependence of SOFC and SOE,'' Bull. Electrotech. Lab. (Tokyo, Japan, 1970-2001), **57**(5-6), pp. 598–615 (in Japanese).
[17] Bessette, N. F., Wepfer, W. J., and Winnick, J., 1995, ''A Mathematical Model of a Solid Oxide Fuel Cell,'' J. Electrochem. Soc., **142**(11), pp. 3792–3800.
[18] Takehara, I., Tatsumi, T., and Ichikawa, Y., 2000, ''Summary of CGT302 Ceramic Gas Turbine Research and Development Program,'' ASME Paper No. 2000-GT-644.
[19] Wilson, D. G., and Korakianitis, T., 1998, *The Design of High Efficiency Turbomachinery and Gas Turbines*, Prentice-Hall, Englewood Cliffs, NJ.
[20] Sakaki, Y., Nakanishi, A., Hattori, M., Miyamoto, H., Aiki, H., and Takenobu, K., 2001, ''Development of MOLB Type SOFC,'' SOFC VII, Electrochemical Society Proceedings, Vol. 2001-16, pp. 72–77.

Performance Benefits Using Siemens Advanced Compressor Cleaning System

Christoph Pels Leusden
Siemens AG Power Generation,
Service Development,
Mülheim a.d.R., Germany

Christoph Sorgenfrey
Siemens AG Power Generation,
Marketing Modernisation and Upgrades Gas Turbine Power Plants,
Berlin, Germany

Lutz Dümmel
Kraftwerk Oberburg GmbH,
Obernburg, Germany

Extensive operational performance data from the Siemens Power Generation V64.3 unit in Obernburg, Germany (operated by Kraftwerk Obernburg GmbH) is evaluated. The unit was commissioned in 1996 and has been running continuously in base load operation with fuel gas to supply heat and power to a nearby chemical plant. In rare cases, fuel oil is used as a backup fuel. During the first major outage after approximately 25,000 equivalent operating hours (EOH), the Siemens PG Advanced Compressor Cleaning System (ACCS) was implemented at Obernburg. ACCS features separate nozzle systems for online and offline compressor cleaning accounting for different operating conditions. For online cleaning, the droplet size is optimized for the droplets to remain in the main air flow in order to minimize erosion effects while providing a homogeneous field over the whole air intake. With reduced rotational speed during offline compressor cleaning, erosion is less critical. Offline nozzles therefore provide higher mass flow and larger droplets in order to maximize cleaning performance for all compressor stages. ACCS, in its maximum automated version, features operation from the control room, online-washing at low ambient temperatures (officially released down to −15 °C without GT anti-icing) and minimum use of manpower. The ACCS system in Obernburg was operated according to the recommended online washing procedure. By June 2002, the V64.3 unit in Obernburg reached 50,000 EOH and the second major inspection was carried out. For this paper, operational data from the second inspection intervals (24,350–49,658 EOH) and from three performance tests with calibrated equipment are compared in order to evaluate the effectiveness of the advanced compressor cleaning system. Statistical evaluation of single-wash performance recovery and the evolution of long-term performance are presented. The effects of degradation and fouling are differentiated. It is shown that ACCS has a significant benefit for long-term engine performance. [DOI: 10.1115/1.1787512]

Introduction

With the growing interest in life cycle costs for heavy-duty gas turbines, equipment operators are investigating the tradeoff between performance improvements and associated maintenance costs. One of the key factors leading to performance losses during the plant operation is compressor fouling. This is the adherence of particles and small droplets to the blading surface. Also, the flow capacity and thereby, the pressure ratio of the unit are reduced. This leads to an overall loss in power output and efficiency of a gas turbine. Fouling causes increased surface roughness of compressor blading, thereby reducing its efficiency. In the literature, there have been estimates that fouling causes up to 85% of the accumulated performance loss during operation [1]. A cost estimate is given by Diakunchak [2]. In extreme cases, fouling may also result in surge problems. Despite the use of advanced filtering methods and filter maintenance, the ingestion of substances that can cause fouling cannot be completely suppressed. The fouling rate depends largely on the site location, surrounding environment, the layout of the air intake system, atmospheric parameters, and plant maintenance. While the first four factors cannot be influenced during the operation, the plant maintenance is the critical one for preventing extra costs resulting from degraded plant performance.

Various methods have been used in the past to clean fouled compressors. At times when heavy duty gas turbines did not yet possess highly sophisticated cooling schemes and coated compressor blades, cleaning was achieved by abrasion with the injection of solid compounds such as nutshells or rice husks. This had to be replaced by wet cleaning methods (water or solvent based) to protect modern coatings and to keep state of the art cooling systems from blockages. The most effective wet cleaning process is the crank soak or offline wash. For this, the unit has to be shut down and cooled off in order to assure that the cleaning agent is reaching all compressor stages and does not evaporate. The cleaning agent is injected into the compressor with the turbine turning at low speed. After a soaking time, the compressor is rinsed with water, which must be drained from the engine. Before the unit can be operated again commercially, it has to be dried. Thus offline washing reduces the availability of a unit.

With a growing number of gas turbines being used in combined cycle or combined heat and power applications, there was the need for the development of online washing systems with performance benefits comparable to offline systems but without required shut down times of the turbine. These systems are now state-of-the-art in modern heavy-duty gas turbines.

In this work, we analyze performance benefits of the Siemens Advanced Compressor Cleaning System (ACCS), which can be integrated as an upgrade product into all Siemens and Siemens Westinghouse gas turbine frames. For this, we have evaluated detailed operational performance data from one Siemens Power Generation V64.3 turbine where ACCS was implemented during the first major outage after 24,350 equivalent operating hours. In the following, we first describe special site conditions and features of ACCS and explain the data evaluation process. Presenting the results, we discuss the positive effects of ACCS taking into account other processes leading to performance degradation.

In literature, there has been comparable work describing the

Contributed by the International Gas Turbine Institute (IGTI) of THE AMERICAN SOCIETY OF MECHANICAL ENGINEERS for publication in the ASME JOURNAL OF ENGINEERING FOR GAS TURBINES AND POWER. Paper presented at the International Gas Turbine and Aeroengine Congress and Exhibition, Atlanta, GA, June 16–19, 2003, Paper No. 2003-GT-38184. Manuscript received by IGTI October 2002; final revision March 2003. Associate Editor: H. R. Simmons.

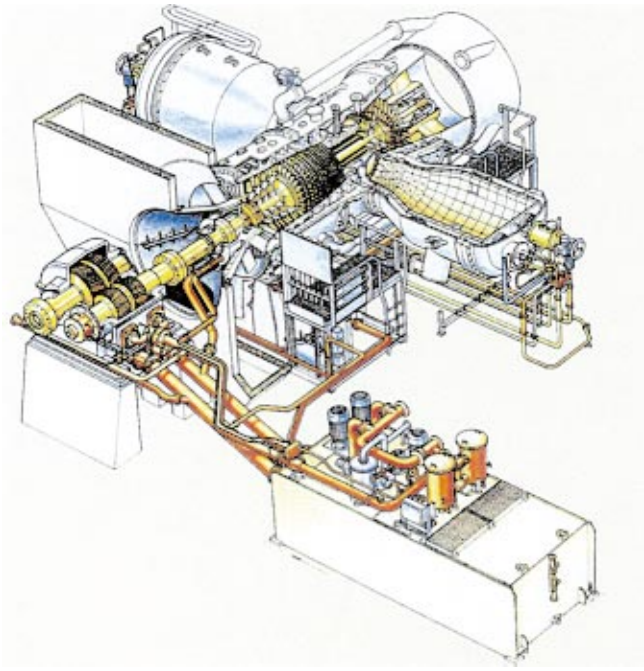

Fig. 1 Siemens AG Power Generation V64.3 unit

benefits of other cleaning systems [3–7]. It has to be underlined that fouling and, consequently, the compressor cleaning benefits are closely coupled to site specific conditions and cleaning intervals (especially of offline-cleaning). Therefore a direct comparison with measured benefits at other sites is not done in this work.

Site Conditions

For this work, performance data from the Siemens Power Generation V64.3 unit (see Fig. 1) that is operated in Obernburg, Germany, by Kraftwerk Obernburg GmbH is evaluated. The power plant is located within a chemical plant, which produces fibers for industrial and textile applications. Therefore it can be concluded that the site conditions are not particularly favorable for low fouling conditions. The nominal power output and efficiency of the unit are contained in Table 1 where these parameters are listed for three performance tests that were carried out in Obernburg with calibrated high-precision instrumentation. All data is from tests at stable base load operation with fuel gas in combined cycle mode and was corrected to ISO conditions (see Table 2). Generally, there is a strong interaction between ISO turbine inlet temperature (calculated according to Ref. [8]) and power output. In order to allow appropriate comparison of performance, power output is computed for constant turbine inlet temperature. The reference value of 1130 °C is the design value for V64.3 units.

V64.3-type turbines rotate at 90 Hz and use a gear box to shift the speed to the grid frequency. Other features and an extensive summary of operational experiences can be found in Ref. [9].

Table 1 Power output and efficiency measured with calibrated instrumentation and corrected to ISO reference conditions

Parameter	Unit	Test 1	Test 2	Test 3	Test 3 (corrected)
Date		Sept. 1996	Aug. 1999	June 2002	June 2002
EOH	H	2586	24,350	49,200	49,200
Gross power output	MW	62.5	63.4	60.9	61.6
Gross efficiency	%	35.3	35.7	35.2	35.4

Table 2 ISO conditions for the correction of measured performance data

Parameter	Unit	ISO conditions
Ambient temperature	°C	15
Ambient pressure	bars	1.013
Relative humidity	%	60
Fuel		methane
Pressure loss inlet/outlet	mbar	0/0
Power factor	1	0.8

Since its commissioning in 1996 the gas turbine has been running with fuel gas and in rare cases with fuel oil as a backup fuel. Because the plant has to provide constant heat and power to a nearby chemical factory, it is of great economical importance that the unit runs at baseload continuously. It is only shut down for forced and planned maintenance activities. Thus offline cleaning can only be carried out during those shut down periods which may occur only at large intervals (e.g., up to 12 months). Therefore the performance of online compressor cleaning is critical for this site. Until the outage for the first major inspection at 24,350 EOH in July 1999, the V64.3 unit at Obernburg was equipped with the Standard Siemens washing equipment.

During the 1999 major inspection, the entire compressor was hand washed and new turbine blading with new engine surface quality was implemented for the first three of the four-stage turbine. The success of the work carried out during the outage is reflected by the data in Table 1: the performance following the outage (test 2) clearly exceeded that of the acceptance test in 1996 (test 1).

Furthermore, the unit was equipped with the Advanced Compressor Cleaning System (ACCS). With the implementation of ACCS, the performance of the unit was monitored continuously until the second major outage in June 2002. With ACCS, the compressor was washed according to Siemens recommendations. This was one online wash per day. For one out of three (later changed to one out of two) washing sequences, the solvent-based detergent SIWASH was used. The remaining online washing sequences were done with demineralized water. Offline compressor cleaning was only performed when the plant was shut down for other imperative maintenance reasons.

In June 2002 the V64.3 at Obernburg reached the second major inspection with 49,658 equivalent operating hours (EOH). Before this inspection, a third performance test with high-precision equipment was carried out at 49,200 EOH. The results are also shown in Table 1 (test 3). It should be noted that the compressor could not be offline washed directly before that test due to operational reasons. The last offline wash took place approximately 1200 equivalent operating hours prior to test 3. In order to compare the performance to the other tests where the unit was offline cleaned directly before the test, we have corrected the parameters. This was done by multiplying the mean gradients for power and efficiency losses during operation without offline cleaning (derived in ''Results and Discussion'' section) with the number of operating hours between the last offline wash and the performance test 3. These corrected values are listed in the column which is denoted 3 (corrected) in Table 1.

Features of the Advanced Compressor Cleaning System

In order to support operators in reducing maintenance costs associated with regular compressor cleaning, ACCS offers a high level of automation. Semi-automatic or jet-pump skids enable automated online washing processes. Only the starting point for the cleaning has to be set manually. All operation parameters are software controlled by the PLC of the skid. In the fully automated version, parameters are calculated taking into account GT operation signals and outside temperature. Only a minimum use of

manpower is necessary, for example, to close drain valves on the GT during offline cleaning. Also, one ACCS supply package may serve up to five gas turbines.

A solvent based cleaner (SIWASH S) was developed for use against organic pollution, especially hydrocarbon particles (e.g., emissions from traffic, combustion particles) which were identified as contributing significantly to the fouling process. SIWASH S is specially designed for good online cleaning results where water based products fail. Even in areas with low industrial pollution, hydrocarbons create sticky layers on the blade surfaces, which also speeds up fouling with inorganic particles. For offline cleaning a water based cleaning agent (SIWASH W) is available in order to reduce costs of waste disposal.

ACCS has different nozzles for offline and online compressor cleaning. This is due to the difference in flow characteristics of a gas turbine intake during these operational modes.

For online cleaning special shaft nozzles with length depending on the intake housing depth are used to keep the droplets in the main air flow (prevent the droplets from recirculating in dead water regions). The nozzles are designed to provide a narrow spectrum of droplets with an optimum size for best cleaning properties. They are big enough not to evaporate before they reach the blades and to provide a mechanical cleaning effect on the blade surface. On the other hand, they are small enough to follow the streamlines into the compressor and not to damage the blades excessively by droplet erosion. A homogenous field of droplets during online operation is guaranteed by a high number of shaft nozzles in the GT intake and their optimised distribution. In contrast, offline nozzles provide a high mass flow of bigger droplets.

Conventional cleaning systems may not be operated at compressor inlet temperatures below $+6\,^{\circ}\mathrm{C}$ due to icing in the compressor. ACCS, with the semiautomatic supply skid tied to the gas turbine PLC, is released for online cleaning down to $-15\,^{\circ}\mathrm{C}$ (5 F) and offline cleaning down to $-10\,^{\circ}\mathrm{C}$ (14 F) without use of the gas turbine anti-icing system. Operation at such low temperatures is possible with the use of an antifreezing agent.

Other features of the system are:

- Washing parameters may be computed, displayed and optimized using a state of the art monitoring and diagnostic system (WIN-TS).
- The closed-loop supply system prevents operator staff from getting into contact with cleaning solution.
- ACCS lowers the costs associated with waste disposal of offline cleaning residuals.
- Implementation during a minor inspection is possible.

Currently, ACCS is in operation or commissioning in a total of 16 Siemens Power Generation V units of all major types (including V94.2, V64.3, V84.3A, and V94.3A). Cumulative operating experience reached, at the end of 2002, more than 200,000 GT operating hours without any major defect. There has been very positive customer feedback regarding the reliability and the performance of the system (efficiency improvement of up to $150\ \mathrm{kJ/kWh_{el.}}$).

Data Processing

For this analysis, one set of operational data for each 8-h work shift was recorded from the gas turbine diagnostic system in Obernburg. For each data set, the following performance parameters were computed:

- power output,
- efficiency,
- ISO turbine inlet temperature according to ISO standard 2314 [8],
- compressor air mass flow.

In order to compare the performance parameters recorded at different operating times, all values were corrected to the equivalent conditions. This included corrections to constant ISO turbine inlet temperature as well as constant ambient reference conditions, which are listed in Table 2. This was done with curves that were derived from a thermodynamic model for V64.3 units [10]. This model was developed using data from acceptance tests of several V64.3 units using high-precision measurement instrumentation.

In order to compute all of the above-mentioned parameters and to carry out the correction, each data set contains the following quantities:

- power output at generator terminals, speed and power factor,
- temperatures at compressor inlet, outlet and turbine exhaust,
- static pressure loss in the intake and exhaust ducts,
- pressure ratio,
- fuel volume flow, temperature, and pressure,
- ambient pressure and humidity.

Constant standard values were used for the gear box efficiency, cooling air consumption, and inlet and outlet parameters of the cooling air cooler.

The computation of most of the above-mentioned performance parameters is very sensitive to the total heat flux of the fuel mass flow. Uncertainty of this parameter results in errors that exceed those coming from other measured quantities. The heat flux is the product of fuel volume flow, its density, and lower heat value. While the fuel volume flow is a measured quantity, the lower heat value and the density can only be derived from the gas composition. Due to the absence of an online gaschromatograph in Obernburg, the composition could not be recorded in the diagnostic system. Therefore a constant average gas composition was used for a preliminary calculation of all performance parameters. Due to the sensitivity, the evaluation of the performance parameters contains a significant error if the real composition deviates from the assumed one. In order to avoid this error, the following adjustment method for the results of the preliminary computation was implemented:

The method is based upon the application of Stodola's law [11]:

$$\dot{m}_T \propto \frac{p_T}{\sqrt{T_T}}. \tag{1}$$

Therein, $\dot{m}_T$ denotes the mass flow through the turbine section, p_T and T_T the pressure and temperature at the turbine inlet. As mentioned above, the correction is done to equivalent reference conditions and constant turbine inlet temperature. Thereby, the mass flow is proportional to the pressure level at turbine inlet or, for further simplification, to the pressure ratio of the engine. With this reasoning, the measured pressure ratio was used to control the turbine air mass flow in the preliminary computation. If that air mass flow leaves a tolerance band of $+/-5\%$ of the expected air flow (derived from the pressure ratio applying Eq. (1), the heat flux (being the most sensitive input parameter) is adjusted. This process can be justified by the fact that the heat flux in the preliminary computation is partially an assumed quantity because the fuel gas composition is not known in detail.

If the air mass flow is within the above-mentioned tolerance band, no adjustment is made. No other measured parameters were modified. Following the final calculation, it is verified that the air mass flow is now within the tolerance band derived from the pressure ratio. All data presented in this work are results from the final calculation.

In the next section, we will base our analysis on the following performance parameters, the computation of which is explained below.

Mean Monthly Performance (P_m and η_m). The monthly mean for power output (P_m) and efficiency (η_m) was computed by averaging the measured values after correction to ISO conditions. When comparing results of different months, we used the performance level recorded in the first month of operation after the major outage at 24,350 EOH as a reference value for normalization. When an offline compressor cleaning took place during a month, the evaluation of P_m and η_m was split for the time before and after the offline wash.

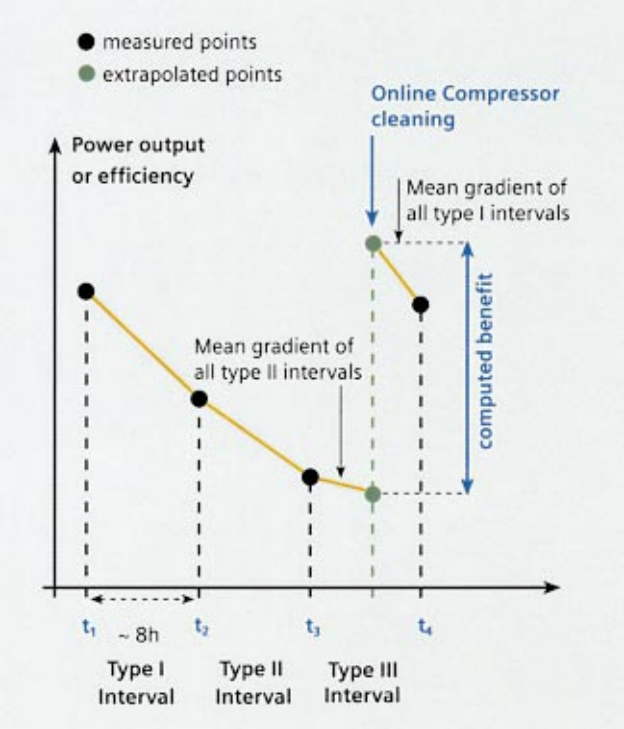

Fig. 2 Typical results for performance parameters for 24 h of operation. Evaluation of benefits for online-compressor cleaning.

Performance Gradient During Operation Without Compressor Wash (dP_{OP}/dt and $d\eta_{OP}/dt$). Figure 2 displays typical results for measured power output or efficiency after correction to ISO conditions (see Table 2) for four consecutive data recordings. Times between data recording were approximately 8 h and one online wash per day was performed. Therefore the operational interval containing a compressor wash was preceded by two intervals without wash, which are denoted type I and II intervals in Fig. 2. The performance gradient for operation without compressor wash can therefore be computed for those two intervals.

Performance Benefit of Online-Compressor Cleaning (ΔP_{ON} and $\Delta\eta_{ON}$). For the computation of these parameters, the mean values of dP_{OP}/dt and $d\eta_{OP}/dt$ for type I and II intervals were computed. As it is shown in Fig. 2, the mean gradients were used to extrapolate from the measured points before and after online compressor cleaning to the point in time when the cleaning took place. The benefit then results from the difference in performance at the time of cleaning. Because the individual data points that were derived from operational data possess a measurement error, the benefit computed with this method will also show a statistical distribution. We used the mean gradient here for the extrapolation instead of the measured gradient because the measured one is more sensitive to individual measurement errors. Therefore the procedure chosen here resulted in a lower uncertainty for the benefit of compressor cleaning.

When analysing performance data over long periods of operation, other mechanisms of degradation have to be taken into account. Potential main sources for degradaton are corrosion and erosion effects in the compressor and turbine parts, turbine fouling, foreign object damage, and thermal distortion [12,13]. Generally, these effects are not influenced by fouling and therefore remain constant when compressor washing is carried out. Thus the total degradation of a performance parameter is the sum of four types of losses as is shown schematically in Fig. 3:

- losses that can be recovered by an online wash (A),

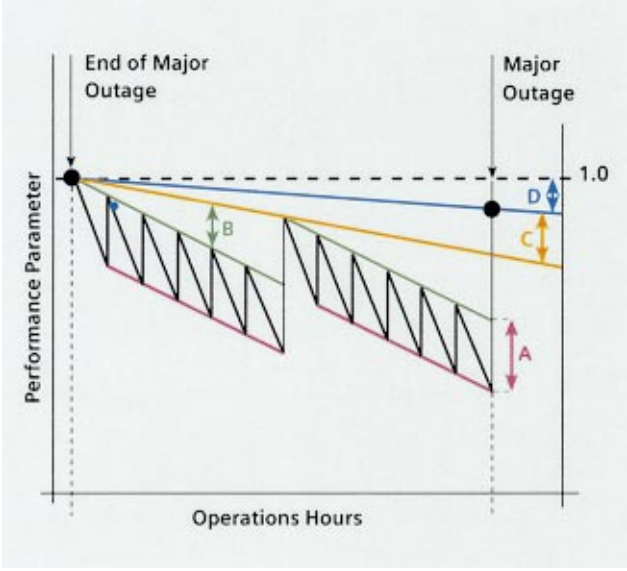

Fig. 3 Types of losses leading to overall performance degradation

- losses that can be recovered by an offline wash (B),
- losses that can be recovered during major inspection (C),
- and losses that cannot be recovered at all (D).

From that reasoning, one can easily see that all degradation mechanisms other than fouling lead to losses of type C and D. There may also be contributions of fouling to type C and D losses if fouling cannot be completely removed even with offline compressor cleaning. In this study, we concentrate on data that have been acquired within the second inspection interval of approximately 25,000 equivalent operating hours (EOH) for the V64.3 unit at Obernburg. Therefore the losses of type C and D are treated together for the most part.

Results and Discussion

Figure 4 shows the evolution of the monthly mean of power output P_m and efficiency η_m relative to their initial values, after the major inspection, as a function of equivalent operating hours. Both parameters show similar behavior with a distinct performance recovery due to offline compressor cleaning. In each of the seven intervals between offline washes, the performance decreases with a similar gradient. Some phenomena are of particular interest:

None of the offline washes leads to the initial performance level. However, even towards the end of the 25,000 EOH-inspection interval, offline compressor cleaning leads to a performance level that is comparable with the level reached with the first offline cleaning. This finding can be interpreted as follows. During the inspection, the entire compressor was hand cleaned leading to an optimal condition. This condition cannot be taken as representative for long-term operation of heavy-duty gas turbines. During the first weeks of operation, it can be assumed that there is onset of fouling in all compressor stages which causes the deterioration of the performance level. All of this initial fouling cannot be removed even with offline cleaning, because this cleaning method is not as effective as hand cleaning of all compressor stages. Therefore there are some contributions of fouling to losses of type C and D. This reasoning may also explain why performance test data from test 2 (recorded within the first 24 h after the inspection) was clearly better than test 1 (recorded 2586 EOH after first fire).

In order to distinguish the types of losses described in the previous section (compare Fig. 3), we used the performance levels directly following each offline wash in order to fit a line using

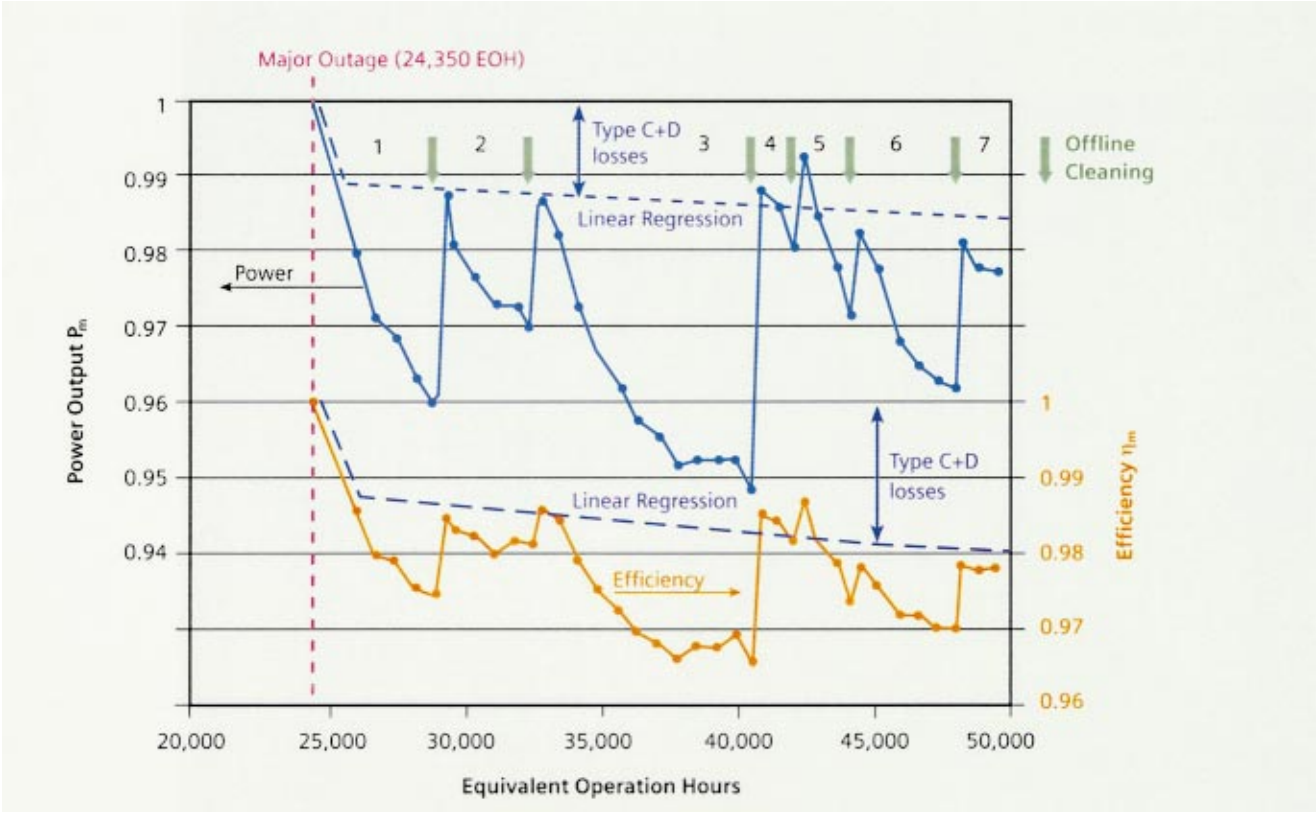

Fig. 4 Evaluation of mean monthly performance relative to initial performance after the first major outage

linear regression. These lines for power output and efficiency are also displayed in Fig. 4. The slopes of the regression lines are comparable for power output and efficiency (0.02%/1000 EOH and 0.03%/1000 EOH).

The third interval between offline washes is particularly long (7782 EOH). With increasing operating time after the last offline cleaning, the gradient both for power and efficiency decreases, indicating a saturation in the losses caused by fouling.

In order to characterize type-B losses, we have computed the average performance evolution of the seven intervals as a function of operating time after offline compressor cleaning. The values were calculated relative to the performance directly following the offline wash. Because the interval lengths are different, the mean values were computed for a varying amount of individual data points. The results for type-B losses are displayed in Fig. 5 for power output and Fig. 6 for efficiency. Within the first 3500 EOH after offline washing the slope remains relatively constant with 1% per 1000 EOH for power output and 0.5% per 1000 EOH for efficiency. Beyond 3500 EOH, the slope decreases significantly. Still, type-B losses exceed those of type C and D.

For the evaluation of performance benefits resulting from online compressor cleaning, we show the statistical results in the form of the probability density function for power output and efficiency in Figs. 7 and 8. The measured recovery by online cleaning was approximated by a normal distribution for both parameters with the mean value of 0.33% for power output and 0.27% for efficiency. These can be interpreted as mean values for type-A losses. Therefore they can be transferred into a parallel line in Figs. 5 and 6. It might be surprising that type-B losses largely exceed type-A losses. However, it has to be noted that regular online cleaning will lead to a smaller gradient for type-B losses.

This can be seen in Fig. 9 where we show performance gradients for intervals in which online compressor cleaning was not carried out. In the 25,000 EOH analyzed here, five of those intervals, lasting up to 11 days, were identified. The gradients of all intervals clearly exceed the average gradients for type-B losses. Therefore it can be concluded that regular online washing cannot prevent type-B performance losses but does minimize them.

It was explained above that the compressor could not be offline washed directly before performance test 3 (see Table 1) due to operational reasons. The last offline wash took place 1200 equiva-

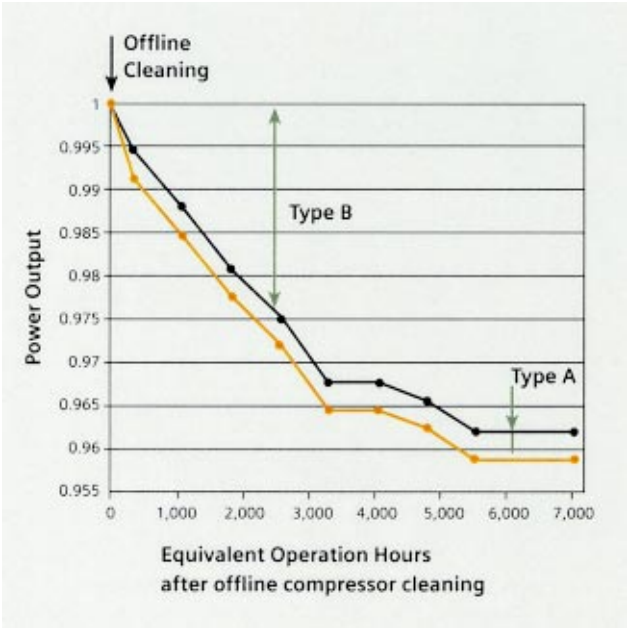

Fig. 5 Measured evolution of power output following offline compressor cleaning

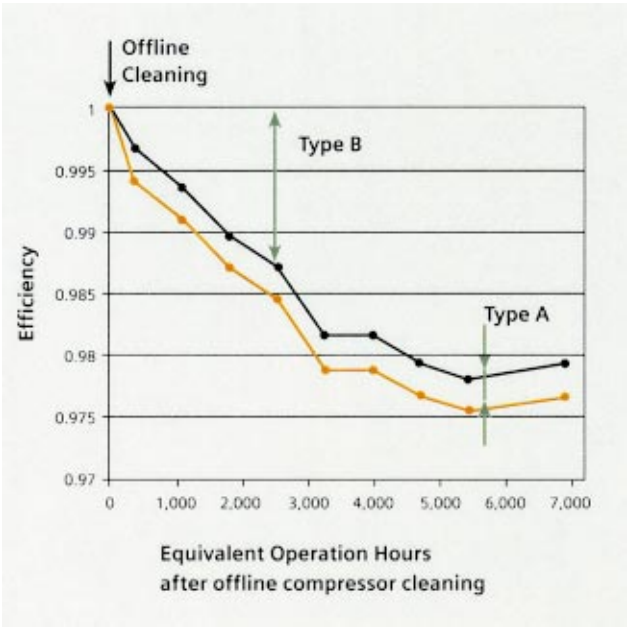

Fig. 6 Measured evolution of efficiency following offline-compressor cleaning

lent operating hours prior to that test. If the initial gradients for power and efficiency (compare Figs. 5 and 6) are taken into account, the values of test 3 can be corrected for an offline cleaned condition. The corrected values are listed in the column which is denoted test 3 (corrected) in Table 1. With this correction, there is a total loss in power output of 900 kW (1.4%) compared to the acceptance test (test 1). For efficiency, there are no losses after almost 50,000 EOH of operation. These values are remarkably low, underlining the positive impact of this state of the art cleaning system.

When tests 2 and 3 (corrected) are compared, the losses between major outages are 1800 kW (2.8%) for power output and 0.3% ($\Delta\eta/\eta$=0.8%) for efficiency. Again, it should be mentioned that test 2 values were above the acceptance test performance and were recorded with a fully hand cleaned compressor. This level cannot be considered as fully representative for long term commercial operation.

The test 2 and 3 values in Table 1 do not fully correspond to the curves in Fig. 4. This is due to the higher measurement errors of the plant instrumentation and the associated correction procedure.

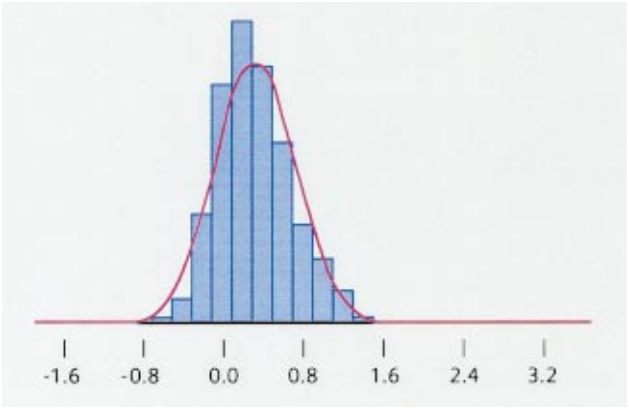

Fig. 7 Probability density function for power output benefits resulting from online-compressor cleaning

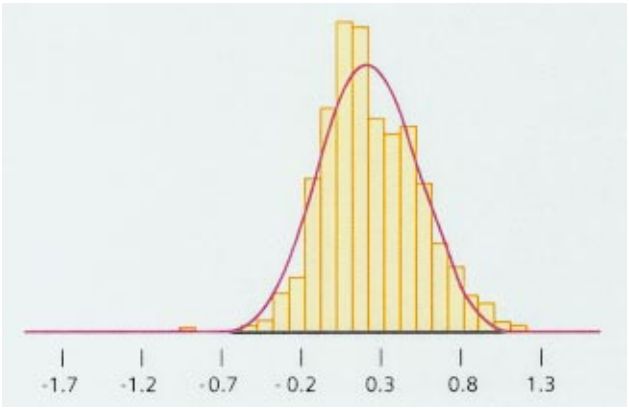

Fig. 8 Probability density function for efficiency benefits resulting from online-compressor cleaning

However, the results obtained from the plant instrumentation clearly show the characteristic behavior of the benefit resulting from on- and offline compressor cleaning.

Conclusion

In this work, we have analyzed operational performance data of a Siemens Power Generation V64.3 unit equipped with an Advanced Compressor Cleaning System (ACCS). With its high level of automation and optimized online cleaning characteristics, this system is designed to lower maintenance cost and to increase long-term performance and availability for heavy-duty gas turbines. Although online compressor cleaning cannot be as effective as offline cleaning because of the evaporation of the cleaning agent in the compressor, we have shown that online cleaning leads to a lower gradient of performance losses in the intervals between offline washes. Furthermore, the performance level that was reached after almost 50,000 EOH was remarkably high, underlining the positive impact of ACCS for the prevention of long-term performance degradation.

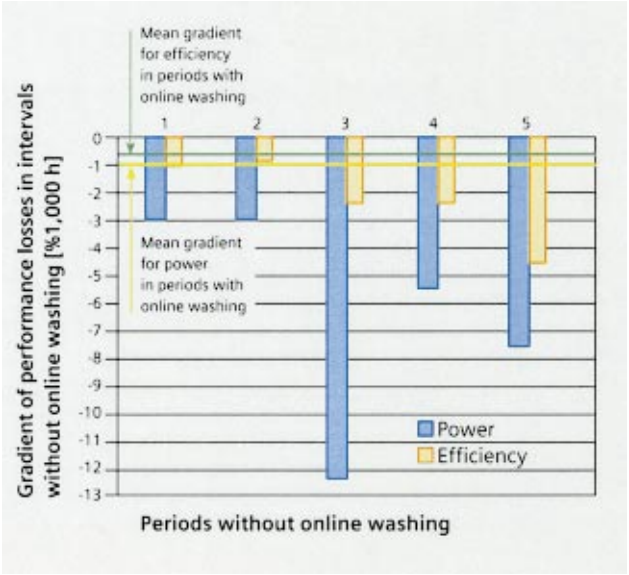

Fig. 9 Gradients of performance losses for intervals where online-washing was not carried out

Acknowledgment

We gratefully acknowledge the support of Jan-Dirk Beiler for the careful preparation and evaluation of the data and the diagrams.

Nomenclature

$\dot{m}$ = massflow
p = pressure
T = temperature
P = power output
η = efficiency

Indices:

T = turbine
m = monthly mean
ON = online cleaning
OP = operation

References

[1] Meher-Homji, C. B., 2000, ''Compressor Fouling . . . Causes and Solutions,'' Global Gas Turbine News, IGTI, **40**(3).
[2] Diakunchak, I. S., 1991, ''Performance Deterioration in Industrial Gas Turbines,'' ASME Paper 91-GT-228.
[3] Adams, J., and Schmitt-Wittrock, P., 1981, ''Optimierung der Reinigungsintervalle von Gasturbinenverdichtern,'' Brennst.-Warme-Kraft, **33**(1).
[4] Haub, G. L., and Hauhe, W. E., 1990, ''Field Evaluation of Online-Compressor Cleaning in Heavy Duty Industrial Gas Turbines,'' ASME-paper 1990-GT-107.
[5] de Jong, M. P., Laagland, G. H. M., and Zeijseink, A. G. L., 2000, ''Optimizing Compressor Cleaning,'' Power Gen.
[6] Stalder, J.-P., 1994, ''Compressor Washing Maintains Plant Performance and Reduces Cost of Energy Production,'' ASME Paper 1994-GT-436.
[7] Stalder, J.-P., 1998, ''Gas Turbine Compressor Washing State of the Art—Field Experiences,'' ASME Paper 1998-GT-420.
[8] ISO 2314, International Standard, ''Gas turbines—Acceptance Tests,'' 2nd edition, 1989.
[9] Umlauft, R., and Lipiak, G., 2000, ''Operating Experience and Potential After 10 Years of Siemens VX4.3 Gas Turbines,'' Power Gen.
[10] KREISPR, Siemens Internal Computer-Tool for Gas Turbine Thermodynamic Cycle Calculations, current version, 2002.
[11] Traupel, W., 1988, *Thermische Turbomaschinen*, 3rd edition, Springer-Verlag, Berlin.
[12] Kurz, R., and Brun, K., 2000, ''Degradation of Gas Turbine Systems,'' ASME Paper 2000-GT-345.
[13] Zwebek, A. I., and Pilidis, P., 2001, ''Degradation Effects on Combined Cycle Power Plants Performance, Part 1: Gas Turbine Cycle Component Degradation Effects,'' ASME paper 2001-GT-388.

A Thermodynamic Analysis of Different Options to Break 60% Electric Efficiency in Combined Cycle Power Plants

Paolo Chiesa
e-mail: paolo.chiesa@polimi.it

Ennio Macchi
e-mail: ennio.macchi@polimi.it

Dipartimento di Energetica,
Politecnico di Milano,
Piazza Leonardo da Vinci, 32,
20133 Milano, Italy

All major manufacturers of large size gas turbines are developing new techniques aimed at achieving net electric efficiency higher than 60% in combined cycle applications. An essential factor for this goal is the effective cooling of the hottest rows of the gas turbine. The present work investigates three different approaches to this problem: (i) the most conventional open-loop air cooling; (ii) the closed-loop steam cooling for vanes and rotor blades; (iii) the use of two independent closed-loop circuits: steam for stator vanes and air for rotor blades. Reference is made uniquely to large size, single shaft units and performance is estimated through an updated release of the thermodynamic code GS, developed at the Energy Department of Politecnico di Milano. A detailed presentation of the calculation method is given in the paper. Although many aspects (such as reliability, capital cost, environmental issues) which can affect gas turbine design were neglected, thermodynamic analysis showed that efficiency higher than 61% can be achieved in the frame of current, available technology. [DOI: 10.1115/1.1771684]

1 Introduction

All major manufacturers of large-size gas turbines are developing new strategies to realize combined cycles capable to exceed 60% electric efficiency. Since this ambitious efficiency target cannot be achieved with current material technology and conventional cooling techniques, novel and more effective cooling solutions for the hottest blade rows of the gas turbine, combined to more advanced gas cycle configurations and optimized interactions between gas and steam section are required. This work investigates the potential advantages brought about by the partial substitution of the conventional blade cooling approach, based on an extensive use of compressed air in open loop as cooling medium, by more advanced closed-loop cooling systems. The three solutions addressed in the paper are illustrated in Fig. 1: (a) open-loop air cooling (OL-AC), (b) closed-loop steam cooling (CL-SC) for vanes and rotor blades[1] and (c) closed-loop mixed air/steam cooling (CL-MC), made of two independent closed-loop cooling circuits: steam for stator and air for rotor blades.[2] The influence of sequential combustion, the path toward high efficiency proposed by an other leading manufacturer, [4], is also considered, in combination with open as well as closed-loop cooling systems.

Performance is estimated through an updated release of the thermodynamic code GS, developed at the Energy Department of Politecnico di Milano. The major improvement made in the present version is the detailed aero-thermodynamic design of the gas turbine stages, including the calculation of velocity triangles, the blading geometry, the cooling flow rates in each blade portion, etc. The rationale for this relevant modification of the code, that included a continuous cooling model in its original version, [5], is that, given the growing importance of cooling losses in modern advanced gas turbines, a realistic model for the detailed calculation of performance must address the cooling of each blade row separately, as pointed out in [6].

The paper is structured on four sections. The first section is devoted to a thorough description of the new calculation methodology adopted for modeling cooled gas turbine expansion and mainly deals with turbomachinery and heat transfer issues. The second section describes the calibration of factors that mainly influence the gas turbine performance (efficiency of turbomachines, parameters affecting heat transfer in blades) in order to make the code able to correctly predict the performance of power plants at the ''state of the art,'' as reported by major manufacturers. Reference is made uniquely to large-size single-shaft units. The third section presents the detailed results of simulations for five different cycle configurations considered, all based on the same turbine inlet temperature (TIT). For each of them, problems related to integration between gas and steam cycles are here examined. The last part compares the performance of the various cycles by means of a second-law analysis. Since all calculations are based on the same set of assumptions concerning component technology, this comparison allows clarifying the ''different quality'' of the thermodynamic processes taking place in the cycles considered and quantifying the true cycle efficiency gains related to closed-loop cooling and sequential combustion. Finally, the influence of TIT on cycle performance is discussed, showing that a further TIT increase up to 1500°C would be highly beneficial only for cycles not adopting sequential combustion.

2 Method of Calculation

2.1 The GS Code. The calculation model used to generate the results described has been originally developed in order to predict performance of gas turbine-based power plants but, thanks to its modular structure, it underwent substantial extensions which enabled it to analyze unconventional cycles whose complexity considerably exceeds the combined cycles here considered, [7,8]. Since the structure and the capabilities of the model have been extensively described elsewhere, [5,9], only the most significant features will be recalled here. The system to be calculated must be first modeled as a network of interconnected elements selected among 15 available components: compressor, combustor, gas tur-

Contributed by the International Gas Turbine Institute (IGTI) of THE AMERICAN SOCIETY OF MECHANICAL ENGINEERS for publication in the ASME JOURNAL OF ENGINEERING FOR GAS TURBINES AND POWER. Paper presented at the International Gas Turbine and Aeroengine Congress and Exhibition, Amsterdam, The Netherlands, June 3–6, 2002; Paper No. 2002-GT-30663. Manuscript received by IGTI, Dec. 2001, final revision, Mar. 2002. Associate Editor: E. Benvenuti.

[1]This option was selected by two large manufacturers in developing their ''H'' series, [1,2].

[2]This approach is proposed by an other manufacturer for its ''ATS'' engine, [3].

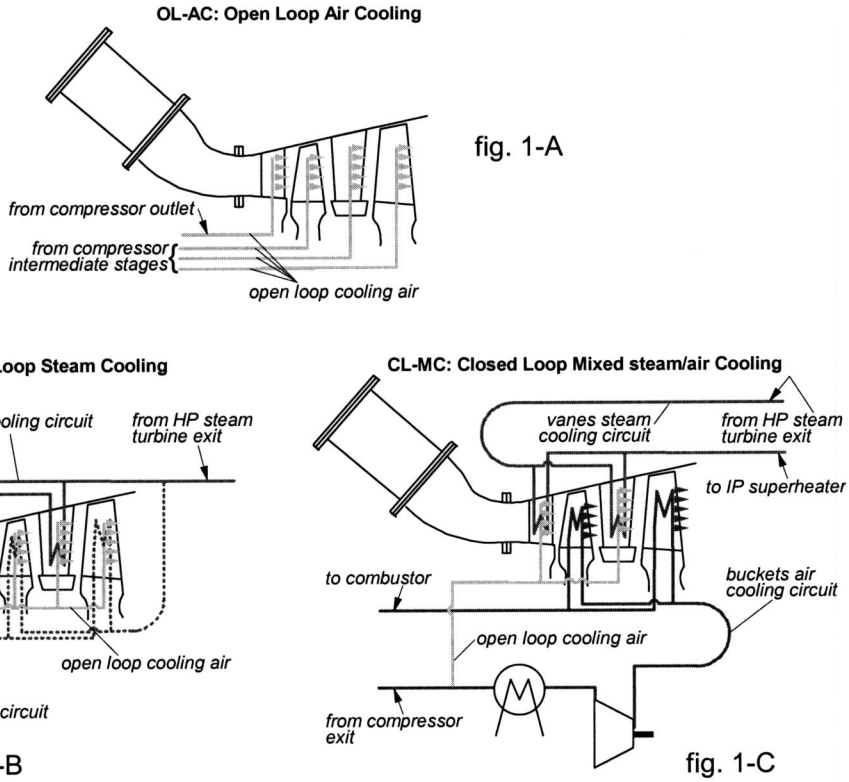

Fig. 1 The three blade cooling solutions investigated in this paper: (*a*) Cooling air is taken at proper compression stage and injected in the gas stream; for high TITs, it is necessary (and beneficial for cycle efficiency) to cool the air before turbine injection. The heat recovered is used in the bottoming steam cycle. (*b*) Most of the cooling in the first blade rows (stators and rotors) is performed by steam in a closed loop; steam enters the gas turbine at temperature above saturation and leaves the gas turbine superheated. Part of the blade cooling is still operated with open-loop air. (*c*) Vanes are steam cooled as in solution (*a*) while a closed-loop air circuit is adopted for rotor rows. An additional compressor is required to overcome head losses in the cooling passages. After cooling the turbine blades, air is reinjected into the combustor. A small fraction of this flow is used for open-loop cooling.

bine expander, splitter, mixer, heat exchanger, pump, heat recovery steam cycle, shaft (accounting for turbomachine spool interconnections as well as electric and auxiliary losses), saturator, air separation unit, chemical reactor, regenerative steam cycle, solid oxide and molten carbonate fuel cells. Only the first nine of them have been actually used to perform the simulations presented in this paper. During a calculation run, mass and energy balances are then calculated sequentially for each component applying the proper operating characteristics and the required additional constraints. After calculating all components, convergence is verified by comparing the conditions (pressure, enthalpy, mass flow rate, etc.) at all interconnections with those of the previous iteration. The iterative process ends when these variables converge toward stable values and all the constraints are satisfied.

Besides gas turbine expander, whose calculation model will be addressed in the following, components mainly affecting cycle performance are compressor and heat recovery steam cycle. Compressor is simply calculated applying the average polytropic efficiency $\overline{\eta}_{p,C}$ given by

$$\overline{\eta}_{p,C}=\frac{\int_{\mathrm{SP}_{in}}^{\mathrm{SP}_{out}}\eta_{p,C}(\mathrm{SP})\cdot d(\mathrm{SP})}{\mathrm{SP}_{out}-\mathrm{SP}_{in}} \tag{1}$$

where $\eta_{p,C}(\mathrm{SP})$ is a function that correlates stage efficiency to stage size parameter (SP) whose expression is

$$\eta_{p,C}=\eta_{\infty,C}\cdot\{1-0.071081\cdot[\log_{10}(\mathrm{SP})]^2\} \tag{2a}$$

$$\eta_{p,C}=\eta_{\infty,C}\quad \text{for } \mathrm{SP}>1. \tag{2b}$$

The calculation model of the heat recovery steam cycle can handle advanced three-pressure-level reheat steam generators usually utilized in modern large-size combined cycles. In these plants also a considerable number of flows is exchanged between gas turbine and steam cycle (besides the exhaust gases entering the HRSG): boiling feed water is used to heat up fuel before combustion, steam is generated or water heated by cooling air used to refrigerate hot blades, steam is reheated in closed-loop cooling circuit. In order to accurately consider these interactions, possibility to extract boiling feed water or steam from economizers, drums, superheaters and steam turbine has been implemented in the model. Steam turbine calculation is based on a stage-by-stage model described in [10], where total-to-total efficiency is predicted through appropriate correlations developed in [11]. Efficiency decay due to moisture appearance and flow splitting in the low-pressure turbine are accounted for.

2.2 One-Dimensional Aerodynamic Design of the Gas Turbine Stages. Schematization of the complex processes taking place in a real gas turbine is represented in Fig. 2, with reference to a four-stage machine. In each blade row, three main processes are considered: (i) the expansion of main stream, that, due to blade cooling and fluid-dynamic losses, is not adiabatic, nor frictionless; (ii) the continuous injection during the expansion of the film-cooling flows, that induces both temperature and velocity variation in the main stream; and (iii) the mixing of the convective cooling flow at the blade row exit. While in the first stages the cooling processes play a dominant role in the entropy evolution of

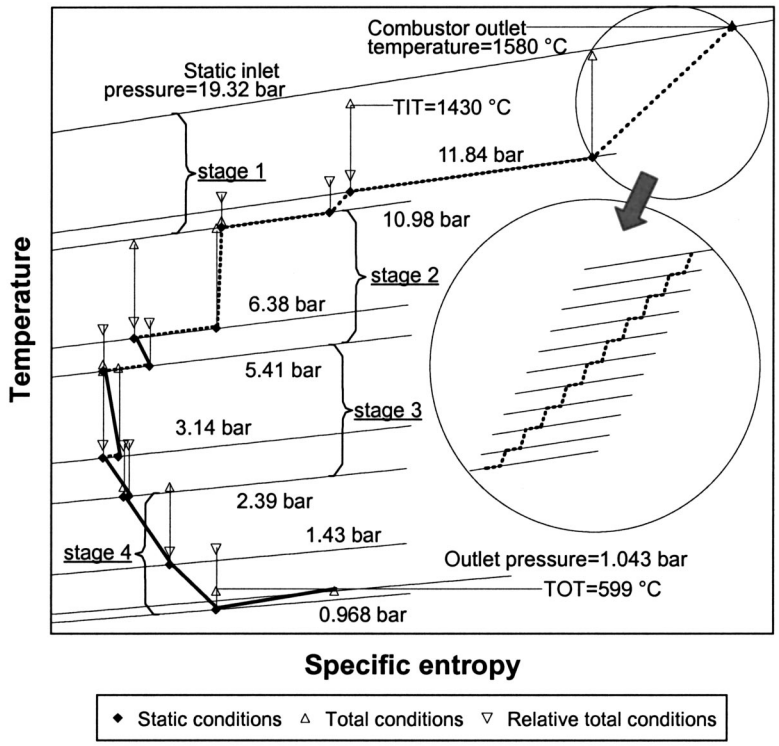

Fig. 2 The cooled expansion in a four stages "state-of-the-art" gas turbine represented in the temperature-specific entropy diagram. Data refer to the OL-AC turbine represented in Fig. 7. For each blade row, a line joins the static conditions at blade inlet (after convective cooling flow mixing) and outlet (before mixing of convective cooling flow). Dotted lines refer to transformations where the fluid composition varies, due to mixing of cooling air to the main gas stream, while solid lines refer to constant composition processes. After the last blade, a line connects the static conditions at turbine exit to total conditions at diffuser exit. The expansion in each cooled row is treated in ten steps, as shown (for a film-cooled row) in the enlargement.

the main stream fluid, in the final part of the expansion, when the blade temperature does not require cooling, the process becomes adiabatic and entropy increases. For sake of clarity, Fig. 2 represents the expansion in each blade row as a single process, but, as it will be discussed in a later section, each blade where cooling is present is actually divided into a large number (ten) of small steps, to obtain a better description of the processes involved.

2.2.1 Selection of the Blade Geometry Through an Iterative Procedure. Given the strict interdependence among fluid dynamic, thermodynamic, and heat transfer processes and the blade geometry, the method of calculation requires necessarily an iterative process. The starting point of the procedure is the one-dimensional design of the gas turbine stages. This step is necessary to establish all the aerodynamic, thermodynamic, and geometric characteristics of each blade row, that are required to calculate the cooling flows and the evolution of the cooled expansion. The iterative procedure adopted in the one-dimensional design can be summarized in the following points:

- The number of stages is assigned (either three or four in current heavy duty machines).
- Tentative initial values of the mean diameter $D_{m,1,s}$ and of the blade height $h_{1,s}$ (kept constant) for the first nozzle are assumed.
- The mean diameter D_m of each row increases linearly between the first and the last row at a rate set equal to 3.5% of $D_{m,1,s}$.
- The isentropic degree of reaction r^* at each stage is found by imposing a linear variation between 0.05 at the first stage and 0.4 at the last stage. Given r^*, the isentropic enthalpy drop of each stage is found by assuming the following relationship between k_{is} and r^*, [11]:

$$k_{is} = 4.70714 - 6.14286 \cdot r^*. \tag{3}$$

- The blade height at each row exit is found by assuming a hyperbolic relationship between axial velocity and pressure (with a tentative initial value of the axial velocity $V_{a,last,r}$ at turbine exit).
- The blade height at each row inlet is found by imposing a 5% overlap with respect to the previous blade exit.

An iterative procedure is applied, by varying the values $D_{m,1,s}$, $h_{1,s}$ and $V_{a,last,r}$ to obtain, respectively:

- the desired pressure at the turbine outlet,
- the required axial/peripheral velocity ratio $(2 \cdot v_{a,1,s}/\omega \cdot D_{1,s})$ at the first nozzle exit, and
- the specified axial Mach number $Ma_{a,last,r}$ at the last rotor exit.

An additional check is finally operated on the blade height/mean diameter ratio of the last rotor. If the stipulated procedure deter-

Table 1 Blade geometric data and cooling parameters

		1st nozzle	1st rotor	Down-stream stators	Down-stream rotors
Stagger angle	γ	40	15	25	15
Solidity (chord / pitch)		1.1	1.1	1.1	1.1
[Blade thickness] / Chord		0.11	0.1	0.1	0.1
[Blade wall thickness] / Chord	t_{blw}/c	0.0131	0.0179	0.0131	0.0179
[TBC thickness] / Chord	t_{TBC}/c	.00157	.00214	.00157	.00214
[Blade perimeter] / Chord	Φ	2.6	2.6	2.6	2.6
[Coolant passages cross-section] / Chord^2	α	0.095	0.08	0.085	0.08
Chord / [Channels hydraulic diameter]	c/d	40	27	27	27
Number of coolant passes	n	3	3	3	3
Enhancement heat factor at Re=50000	$E_{h,ref}$	1.0	1.8	1.0	1.0
Maximum metal temperature	$T_{bg,max}$	845	820[a]	815	790[a]
Pattern factor	λ	0.08	0.01	0.0[b]	0.0
Parameter f_1		0.0	0.0	0.05	0.0
Parameter f_2		0.057	0.052	0.057	0.052
Coolant channels interference coefficient	ψ	0.8	0.6	0.8	0.6

[a] for a 400 m/s reference peripheral speed [b] 0.02 for the 2nd stator only

mines a $(h/D_m)_{\text{last},r}$ exceeding the specified limit of 0.27, r^* for the first stage is increased to restore this constraint.[3]

The axial chord b of each row necessary to obtain the meridional flow path is computed from stage mean diameter and blade height through the expression:

$$b = f_1 \cdot h + f_2 \cdot D_m \tag{4}$$

where f_1 and f_2 are coefficients established according to gas turbine design practice (see Table 1). All other geometric variables affecting the heat transfer process are defined in Fig. 3 and their values assumed in the paper are listed in Table 1.

It should be noted that the above described procedure is carried out meanwhile the full cooling expansion model described below is applied. This implies that at each iteration all blade geometric characteristics required for blade cooling are computed, that the expansion in each blade row is divided in a large number (ten) steps and that all heat exchange and mixing processes are accounted for.

2.2.2 Stage Efficiency and Velocity Coefficients. Stage efficiency is a widely utilized concept in turbomachinery theory to estimate the quality of a turbine expansion. Following this philosophy, in our model the total-to-total efficiency of each stage $\eta_{TT,ad}$, referred to an adiabatic process without any coolant mixing, is computed according to the following correlation:

$$\eta_{TT,ad} = \eta_{\infty,T} \cdot \{1 - 0.02688 \cdot [\log_{10}(\mathrm{SP})]^2\} \cdot [1 - 0.125 \cdot (0.9 - \omega_s)^2] \tag{5a}$$

$$\eta_{TT,ad} = \eta_{\infty,T} \cdot [1 - 0.125 \cdot (0.9 - \omega_s)^2] \quad \text{for } SP > 1 \tag{5b}$$

where $\eta_{\infty,T}$ represents the efficiency of "state-of-the-art" turbine stages operating at optimum ω_s and large enough to avoid penalties related to dimensional effects (SP$\geqslant$1). Corrections for SP and ω_s account for stage efficiency penalties related to dimensional effects and not optimal specific speed, respectively, [11].

Nevertheless stage efficiency concept cannot be directly applied in our model since expansion is first divided between stator and rotor in order to determine velocity triangles, then each row is computed as a sequence of 10 small steps in order to properly evaluate blade cooling. To overcome this problem, a velocity coefficient φ is defined as the ratio between the actual and the isentropic velocity through a single step adiabatic expansion. To account for higher fluid-dynamic losses occurring in rows operating with larger flow deviations and less favorable pressure gradients,

[3] Increasing r^* for the first stage reduces the parameter k_{is} of all the stages except the last one. In order to restore the required overall enthalpy drop, value of $D_{m,1,s}$ is consequently increased. Since a linear increase in D_m is assumed for each row, it also takes to higher $D_{m,\text{last},r}$ and, provided that axial velocity is constant, to lower $(h/D_m)_{\text{last},r}$.

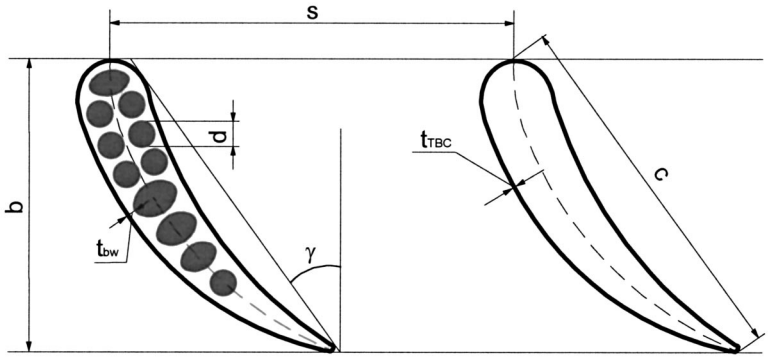

Fig. 3 Nomenclature of the turbine blade geometric parameters used in the paper

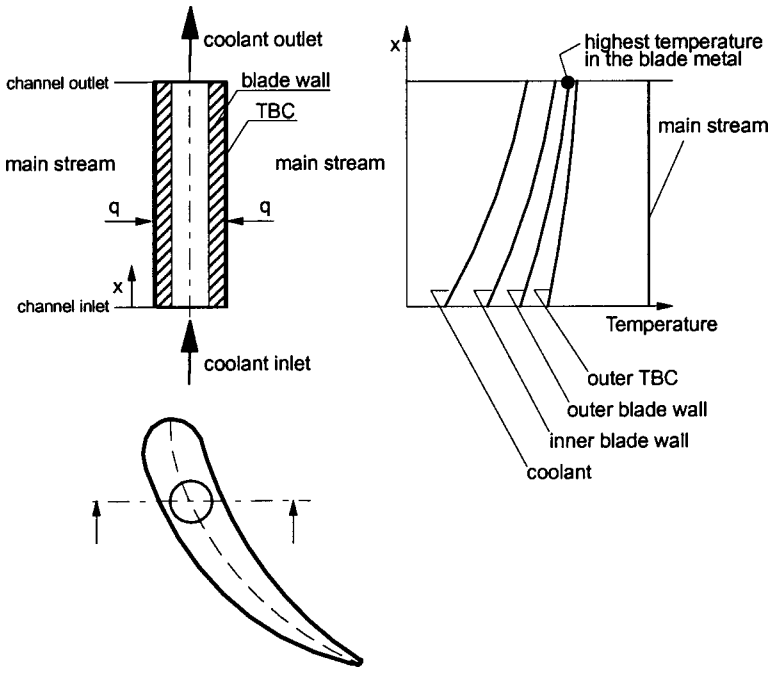

Fig. 4 Simplified blade cooling model

different values of φ are assumed for stators and rotors. Ratio between φ_r and φ_s (kept constant throughout the row) is set according to the following laws:

$$\varphi_r = 2 \cdot \varphi_s - 1 \quad \text{for stages with } r^* = 0 \tag{6a}$$

$$\varphi_r = \varphi_s \quad \text{for stages with } r^* = 0.5 \tag{6b}$$

while for intermediate r^* a linear interpolation between these values is assumed. Given the stage efficiency $\eta_{TT,ad}$, a root finding procedure is applied to obtain φ_s and φ_r that are finally used to account for fluid-dynamic losses in computing the actual expansion (see par. 2.3.3). Note that in cooled blades, the velocity changes in the main stream are also induced by the coolant injection. Proper conservation equations are used to account for these effects as explained below.

2.3 Main Schematization of Blade Cooling. The procedure adopted to calculate blade cooling is a revised version of the original methodology proposed by Consonni taking into account convection and film cooling. Although an exhaustive explanation of this methodology can be found in the literature, [5,12,13], it's worthwhile to give here a complete summary of the calculation method.

2.3.1 Convection Cooling. Although the actual blade geometry is much more complex than the simple duct considered in Fig. 4, it may help to illustrate the convective cooling model. Such a system behaves like a heat exchanger subject to the heat flux:

$$q_g = h_g \cdot (T_{gr} - T_{bg}). \tag{7}$$

Although h_g is strongly variable along the flow path, using its local value is not conceivable in a simplified model like this. It appears much more appropriate relying on a correlation providing the average heat transfer coefficient. For such a purpose the following correlation suggested by Louis [14] has been used:

$$\mathrm{St} = K\,\mathrm{Re}^{-0.37}\,\mathrm{Pr}^{-2/3} \tag{8}$$

where, according to the author, St is the mean Stanton number along the whole blade and both St and Re are referenced to the cascade exit velocity. Since the actual value of the parameter K is rather uncertain, [5], it was decided to include K in the variables considered for the final calibration.

Recovery temperature T_{gr} appearing in Eq. (7) is estimated through the correlation

$$T_{gr} = T_{\mathrm{stat}} + (T_{\mathrm{tot}} - T_{\mathrm{stat}})\mathrm{Pr}^{1/3} + \lambda \Delta T_{\mathrm{comb}} \tag{9}$$

where the last term accounts for the difference between peak and average temperature (ΔT_{comb} is the temperature rise in the combustor). It has been included since the cooling system is designed to withstand peak conditions rather than the average ones in order to ensure an adequate safety margin, [15]. The different values of λ (see Table 1) assumed for the successive rows reflect that

- temperature irregularities (caused by incomplete mixing of combustion gases) are much stronger in tangential than in radial direction but rotating blades do not experience the former because the residence time of their passes through the peak temperature zones is far from noticeably affecting the metal temperature due to their thermal inertia;
- temperature irregularities tend to disappear after the nozzle due to flow mixing and coolant injection.

For the system shown in Fig. 4 an energy conservation balance can be written:

$$m_g \cdot c_{p,g} \cdot \Delta T_g = m_{cl} \cdot c_{p,cl} \cdot (T_{cl,out} - T_{\mathrm{cl},in}) \tag{10}$$

and since ΔT_g is much lower than $(T_{cl,\mathrm{out}} - T_{cl,\mathrm{in}})$, the effectiveness of the heat exchanger can be calculated assuming that the hot thermal capacity is infinite so that:

$$\varepsilon = 1 - e^{-\mathrm{NTU}} \tag{11}$$

where effectiveness and number of thermal units are given, respectively, by

$$\varepsilon = (T_{cl,out} - T_{cl,in})/(T_{gr} - T_{cl,in}) \tag{12}$$

$$\mathrm{NTU} = US_c / m_{cl} \cdot c_{p,cl} \tag{13}$$

where U is the overall heat transfer coefficient that accounts also for heat conduction through the blade wall and TBC while S_c is

the surface of the cooling channel. The heat transfer coefficient on the coolant side is estimated through the Colburn equation:

$$\mathrm{St} = E_h 0.023\,\mathrm{Re}^{-0.2}\,\mathrm{Pr}^{-2/3} \tag{14}$$

where E_h is a heat transfer enhancement factor accounting for the presence of ribs and turbulence activators in the cooling channel.[4]

On the other hand, the equations expressing the heat flux balance across the blade wall can be written as follows:

$$\frac{h_g\cdot(T_{gr}-T_{bg})}{\frac{a_c}{1+a_t}} = \frac{k_{TBC}\cdot\Delta T_{TBC}}{t_{TBC}\frac{a_c}{1+a_t}} = \frac{k_{bl}\cdot\Delta T_{blw}}{t_{blw}\frac{a_c}{1+a_t}} = h_{cl}(T_{bcl}-T_{cl}) \tag{15}$$

where

$-T_{bg}-T_{bcl}=\Delta T_{\mathrm{TBC}}+\Delta T_{blw}$ is the temperature drop across TBC and blade wall,

$-a_t$ is the ratio between the shroud surface and the outer blade surface, and

$-a_c$ is the ratio between the cooling channel and outer blade heat area transfer given by $a_c=\psi 4\alpha/\Phi c/d$.

Combining the previous equations, it is possible to express the NTU parameter as a function of

- the geometric characteristics of the blade and the cooling system,
- the conductivity of the blade metal and TBC (if present),
- the heat transfer coefficients and the thermophysical properties of fluids on both the sides of the blade, and
- the mass flow rates of the coolant and the main stream.

Given blade geometry, materials and estimated fluid properties and heat transfer coefficients, temperature profiles reported in Fig. 4 can be calculated as a function of the coolant mass flow rate and the convection cooling problem is finally solved by determining the coolant mass flow rate that gives an acceptable blade temperature distribution. Since the highest temperature in the blade metal is reached at the end of the cooling channel (the black dot in Fig. 4), it is possible to ensure that the metal temperature (T_{bg}) can withstand the imposed thermal flux by imposing that maximum value $T_{bg,\max}$[5] is reached only on the coolant outlet section.

A performance measure of the convective cooling system described by this model can be drawn by the nondimensional parameter Z, [5], that is defined as a combination of various geometric and heat transfer parameters:

$$Z=\psi\cdot\alpha^{0.2}\cdot n^{0.8}\cdot E_h\cdot\left(\frac{c}{d}\right)^{1.2}. \tag{16}$$

The higher Z is, the lower the cooling flow required to maintain T_{bg} lower than $T_{bg,\max}$. Differently from the approach followed in [5] and [18], where Z is constant and identifies the cooling system efficiency of the whole expansion, in our model Z vary from row to row,[6] according to the different assumptions made about the stage geometry. It reflects that cooling circuits in the first rows are likely more sophisticated to cope with the higher thermal flows occurring at the beginning of the expansion.

Besides the flow required to cool blades and shrouds, the model considers an additional term accounting for disks, casings, struts, etc. Since a practical procedure for its estimation is unavailable to the authors, the additional cooling flows have been kept into account simply assuming their mass rate is a fraction (0.01) of the mainstream flow rate for each cooled stage. Rotor disk coolant is added to the blade cooling flow and simply follows the history of the latter.

2.3.2 Film Cooling. To simulate film cooling, a fraction r_{fc} of the coolant flow, after exchanging heat inside blades and shrouds, is ejected through a continuous slot covering the whole perimeter of the area wet by the gas. The remaining fraction $(1-r_{fc})$ is expelled at the blade tip or at the trailing edge. Considering the shielding effect provided by the coolant ejection, the heat flux to the blade now reduces to

$$q=h_g\cdot(T_{aw}-T_{bg}) \tag{17}$$

where the adiabatic wall temperature ($T_{aw}<T_{gr}$) is determined through a correlation proposed in [19]. Substituting Eq. (17) to Eq. (7) allows to solve the cooling problem with the same procedure previously adopted. Parameter r_{fc} should be regarded as a ''quality index'' of the film cooling technology since it includes the difference between the actual geometry (holes) and the continuous slot considered in the model which (for obvious mechanical reasons) is fictitious. Due to design and economical considerations, in heavy-duty engines film cooling is adopted only in the first rows. To account for this situation, parameter r_{fc} linearly decreases from the first nozzle to the first non-film-cooled blade row.

2.3.3 Cooled Expansion. In order to keep into account the variations that fluid experiences flowing through a row, calculation of each cooled row proceeds through a sequence of small steps as shown in Fig. 5. In each step the main stream is subject to an expansion (line A-B) whose pressure $(p_i-p_{i+i})/p_i$ is kept constant along the row followed by an isobaric transformation (line B-C) considering the cooling process. Fluid-dynamic losses are accounted for by means of a flow velocity reduction coefficient (φ) as explained in par. 2.2.2. Therefore velocity at the end of each expansion step is given by the following relationship:[7]

$$w_B=\varphi_r\sqrt{w_A^2+[2\cdot\Delta h_{is,i}-(u_i^2-u_{i+1}^2)]}. \tag{18}$$

The cooling flow per step is calculated after each expansion according to the methodology exposed in par. 2.3.1 and 2.3.2; heat transfer area is estimated by assuming that the chord portion $\Delta b/b$ spanned at each step is constant. Cooling flow at the ith step is therefore $\Delta b/b$ times the flow required to refrigerate a whole blade in contact with the main stream at the temperature $T_{gr,i}$.

Film cooling flow is mixed to the main stream during the isobaric transformation B-C. In order to approximate more closely phenomena taking place in a real turbine (where convective coolant leaves from the tip of the blade and at the trailing edge) convective cooling flow is mixed only at the end of the last step. Mass, momentum and energy conservation equations allow then to calculate conditions of the main stream at the end of each step:

$$m_{g,i+1}=m_{g,i}+m_{fc,i} \tag{19}$$

$$m_{g,i+1}w_C=m_{g,i}w_B+m_{fc,i}\theta w_6 \tag{20}$$

$$m_{g,i+1}\left(h_C+\frac{w_C^2}{2}-\frac{u_{i+1}^2}{2}\right)=m_{g,i}\left(h_A+\frac{w_A^2}{2}-\frac{u_i^2}{2}\right)+m_{fc,i}\left(h_4+\frac{u_m^2}{2}\right)-m_{cv,i}(h_5-h_4). \tag{21}$$

Coefficient θ (lower than 1) accounts for the fact that coolant is not injected parallel to the stream while the last term of the third equation takes into account the effect of heat released from the

[4]The two most important aspects related to E_h are the influence of the coolant Reynolds number on effectiveness of ribs and the effect of ribs on pressure drops. In this model $E_{h,\mathrm{ref}}$ is given as input for a reference Reynolds number ($\mathrm{Re}_{\mathrm{ref}}=50{,}000$); the actual value is corrected according to [16] through the rule: $E_h=E_{h,\mathrm{ref}}\cdot(\mathrm{Re}/\mathrm{Re}_{\mathrm{ref}})^{-0.2}$. The resulting increase in pressure drops (see par. 2.3.4) is given by $E_p=E_{h,\mathrm{ref}}^3$.

[5]$T_{bg,\max}$ is given as input parameter for stator blades. For rotor blades, input $T_{bg,\max}$ refers to a reference peripheral speed assumed equal to 400 m/s. $T_{bg,\max}$ is then corrected according to Larson-Miller parameter data from [17] to keep into account that higher speeds produce higher stresses in the blade so that a lower temperature is required to ensure the same lifetime. With current assumptions, when peripheral speed increases by about 20 m/s, the resulting correction determines a $T_{bg,\max}$ reduction of about 10°C.

[6]Parameter Z approximately varies from 100 for the first nozzle to 45 for rotors of the downstream stages; in comparison, [5] and [18] assumed for Z values of 100 and 71, respectively.

[7]The following equations hold for a rotor. Similar equations can be written for stators neglecting the change in the peripheral speed.

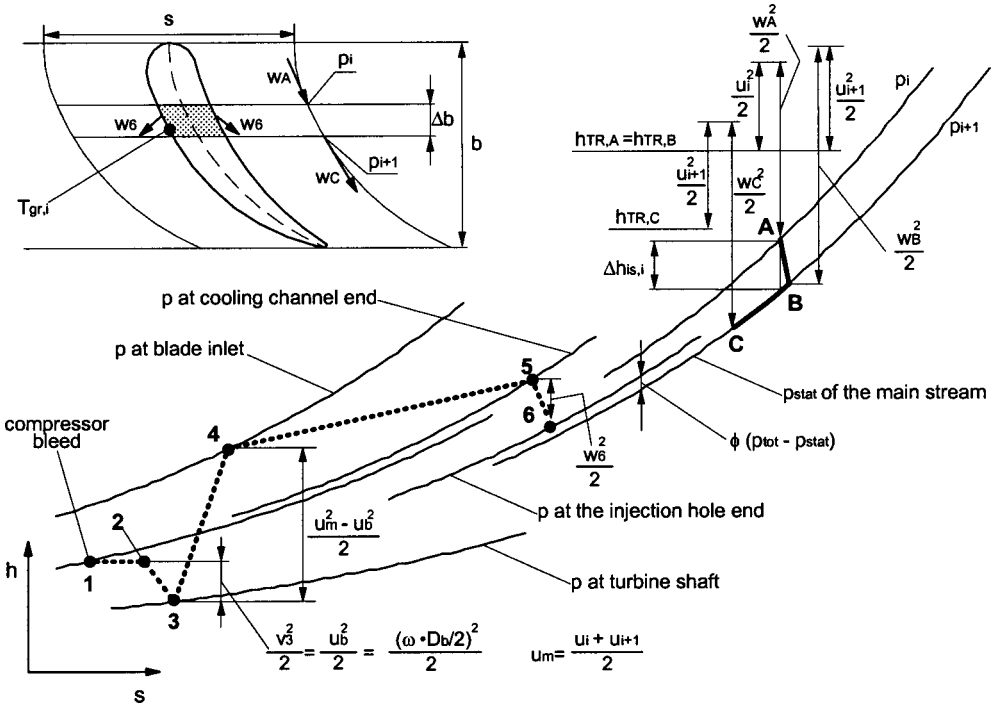

Fig. 5 Evolution of the thermodynamic conditions of cooling air (dotted bold line) and main gas stream (continuous bold line) in the specific enthalpy-entropy diagram. The figure refers to an intermediate pressure step (ten steps are considered for each blade) of a film-cooled rotor blade.

main stream to the convective cooling flow (both in open or closed loop). Note that these equations only hold for the intermediate steps of a row; in the last step also the convective coolant is injected in the main stream and additional terms compare in the equations.

2.3.4 Coolant History. Thermodynamic conditions of coolant at blade inlet are determined according to the approach illustrated in the left side of Fig. 5 that refers to the most complicated case of a rotor row. Coolant, bled from compressor at point 1, undergoes a 3% pressure drop along the duct to point 2. Since it must be injected into the disk (or the shaft) to reach the blade, the cooling flow is expanded to a lower pressure (line 2–3) in order to gain the swirl velocity v_3 that allows it entering the rotor in axial direction (in the relative reference frame). In performing calculations it is assumed that coolant is introduced at a diameter D_b equal to 60% of the diameter at the blade hub and axial velocity is neglected. Coolant is then centrifuged flowing through the disk and the blade from D_b to D_m and its pressure is increased. Adequate efficiencies for transformations 2–3 and 3–4 have been assumed. Note that for a stator, points 2, 3, and 4 coincide. Line 4–5 represents the transformation in the blade cooling channel. Temperature increase is calculated according to Eq. (12), while integration of the differential equation providing the pressure drop due to friction and heat transfer leads to the following expression:

$$\ln\frac{p_5}{p_4}=-\left[2\gamma\mathrm{Ma}^2\frac{1+(\gamma-1)\mathrm{Ma}^2}{1-\mathrm{Ma}^2}f\cdot\frac{L_{eq}}{c}\cdot\frac{c}{d}\right]-\left[\frac{4\gamma\mathrm{Ma}^2}{1-\mathrm{Ma}^2}\mathrm{St}_{cl}\left(\frac{T_{bcl}}{T_{cl}}-1\right)\frac{n\cdot h}{c}\frac{c}{d}\right] \quad (22)$$

where L_{eq} is the equivalent length of the cooling channel accounting for the presence of bends in multipass channels and ribs introduced to enhance the heat transfer coefficient.[8]

Coolant pressure drop is calculated only for the convective flow (open or closed loop) using the average fluid properties between channel inlet and outlet. For the film cooling flow and air used in open loop in CL-SC and CL-MC configurations pressure losses are not computed; in these cases a fixed fraction equal to $0.4\cdot(p_4-p_6)$ is assumed for drop p_4-p_5. At the channel end, coolant is accelerated through the injection holes and mixed to the main stream. For film cooling flows, expansion across the injection hole ends at a pressure higher than the mainstream pressure (as shown in Fig. 5) to consider the injection on the blade pressure side where pressure is higher than the average value p_i. While for the first row velocity at point 6 is found assuming that coolant at point 1 has the compressor exit pressure, for the following rows an iterative procedure is applied backward and the bleeding pressure required to inject the coolant through a choked expansion hole is found.[9]

Closed-loop cooling flows are not mixed with the main stream but are removed from the turbine. Therefore rotor flows move inbound through the disk reducing their pressure and are finally discharged at a peripheral speed u_b; only 50% of its dynamic head is assumed being recovered.

3 Model Calibration

3.1 Assumptions and Gas Turbine Model Calibration. A considerable set of assumptions is required in order to give valuable consistency to the calculation method. This has proved to be a very hard task because

- n_p is the number of cooling channel passages along the radial direction,
- d is the hydraulic diameter of cooling channels, and
- h is the blade height.

[8]In more detail $L_{eq}=n_p\cdot h\cdot E_p+55\cdot(n_p-1)\cdot d$ where the first term accounts for straight sections, the latter for bends according to [5] and

[9]The maximum pressure at which coolant is available is the compressor exit pressure. If this pressure value is not enough to choke the injection hole, then the forward procedure is used setting p_1 equal to the compressor exit pressure.

Table 2 Gas turbine data. Unless otherwise stated, these data are kept constant throughout the analysis.

Gas turbine efficiency assumptions: $\eta_{\infty,T,unc} = \eta_{\infty,T,olc} + 0.02$
$\eta_{\infty,T,clc} = \eta_{\infty,T,olc} + 0.01$
Axial/peripheral velocity at 1st stator exit = 0.38
Axial Mach number at last rotor exit = 0.45
Diffuser recovery = 0.55 of axial dynamic head
Blade metal thermal conductivity = 17.5 W/m–K
TBC / [metal blade] thermal conductivity = 0.2
Friction coefficient in cooling channels = 0.0028
Heat losses at combustor = 0.9% of fuel thermal input (LHV)
Heat losses at turbine exit = 0.3% of fuel thermal input (LHV)
Combustor pressure losses = 3%
Sequential combustor cooling flow = 2% of compressor inlet flow
Compressor stage average isentropic enthalpy drop = 27 kJ/kg
Compressor leakage = 0.75% of the compressor inlet mass flow
Turbine leakage = 0.75% of the turbine exit mass flow
Gas turbine organic efficiency = 0.99865 for each turbomachine
Electric generator efficiency = 0.987
Gas turbine auxiliary consumption = 0.35%
Inlet filter pressure loss = 1 kPa
HRSG pressure loss = 3 kPa
Fuel: natural gas available at p=40 bar, T=15 °C
composition (vol. %): CH_4 = 89.975; CO_2 = 1.316; C_2H_6 = 4.354; C_3H_8 = 0.101; N_2 = 4.253
LHV = 44.769 MJ/kg; HHV = 49.616 MJ/kg

- the simplified numerical model does not exactly describes the complex physical phenomena occurring in a real gas turbine blade (e.g., given the complicated geometry of cooling channels, the actual temperature distribution in the blade is unknown and impingement cooling, extensively adopted at 1st nozzle leading edge, has been neglected). Hence, parameters included in the model do not always have an exact correspondence in a real turbine and vice versa;
- manufacturers generally do not disclose all the machine features necessary to calibrate the model (i.e., cooling flow and thermal losses details, compressor and combustor outlet temperature, blade geometry, leakage flows, auxiliary consumption, etc.);
- some parameters have to be fixed somewhat arbitrarily since their actual value can vary in a wide range depending on different design criteria.

On the other hand, it is essential for the purpose of our work that the model predicts accurately the performance of state-of-the-art power plants, both for gas turbines and combined cycles. With such a goal, an alternative approach was tried. All the parameters included in the gas turbine model have been divided in two sets. Parameters of the first set have been fixed according to of the authors' best knowledge; Tables 1 to 3 provide a list of assumptions (next to the ones quoted during the previous description)

Table 3 Steam cycle data. Unless otherwise stated, these data are kept constant throughout the analysis.

Steam cycle data
3 pressure level: 166 / 36 / 4 bar
Maximum steam temperature SH and RH = 600 °C
Pinch point ΔT = 8 °C
Approach point ΔT = 25 °C
Pressure losses in economizers = 25%
Pressure losses in superheaters = 8%
Steam turbine exit velocity = 220 m/s
Condensation pressure = 0.0406 bar (1.2 in_{Hg})
HRSG thermal losses = 0.7% of the recovered thermal power
Steam cycle auxiliary = 1% of condenser thermal power

adopted for all the calculations carried out through the paper. Parameters of the second set have been calibrated in order to enable the model calculating as precisely as possible performance of the "reference" gas turbines listed in Table 4. Since performance data given by manufacturers, [20–28], typically limit to power, efficiency and TOT, calibration procedure reduces in finding a set of calibration variables that minimizes the value of a target function, that is defined as follows:

$$\Omega = \sum_{\text{mod el}}^{1 \text{ to } 4} \left[\left(\frac{W_{\text{calc}} - W_{\text{rep}}}{W_{\text{rep}}} \cdot 100 \right)^2 + \left(\frac{\eta_{\text{calc}} - \eta_{\text{rep}}}{\eta_{\text{rep}}} \cdot 100 \right)^2 + 0.0306 \cdot (\text{TOT}_{\text{calc}} - \text{TOT}_{\text{rep}})^2 \right] \tag{23}$$

where subscript "rep" refers to data reported by manufactures and "calc" denotes the result of the calculation based on the design parameters (number of stages, TIT, pressure ratio, mass flow rates) also reported in Table 4. The coefficient 0.0306 that multiplies the difference of TOT allows comparing homogeneously an intensive quantity like temperature with extensive quantities like power and efficiency.[10]

From a theoretical point of view, it is obvious that lower and lower values of Ω could be obtained by shifting more and more variables from the first to the second set. On the other hand, increasing the number of variables in the second set exponentially dilates computing time necessary to solve the minimization problem without allowing substantial benefits. Moreover, data available for calibration are limited and not necessarily accurate. Hence, the number of optimization variables has been limited to four and, since their choice is inevitably an arbitrary procedure, a clear physical connotation and a strong influence on results were the basic criteria for their selection. The selected variables are listed in Table 5.

Before discussing calibration results, it is important to estimate the expected accuracy. Checking the energy balance of the four reference gas turbines allows testing the coherence of manufacturers' data and validate assumptions regarding leakages, electric and organic efficiency, thermal losses and auxiliaries consumption. Row labeled "thermal balance error" in Table 4 refers to percentage values of the term:

$$1 - \frac{\eta_{\text{LHV}}}{W_{el}} [(m_{out} + m_{lkg}) \cdot (h(\text{TOT}) - h(T_0)) + W_{el}/\eta_e + \Delta W_{org} + \Delta W_{aux} + \Delta Q_{th} - Q_{in} + Q_{out}]. \tag{24}$$

Combination of manufacturers' data (W_{el}, η_{LHV}, TOT and m_{out}) and assumptions about energy losses allow to calculate precisely the energy balance when Q_{in} and Q_{out} are zero. The term Q_{in} accounts for extra heat introduced in the engine different from the chemical energy of the fuel (sensible heat of heated fuel is the only practical case). On the contrary, Q_{out} represents heat removed from the gas turbine due to combustor liners steam cooling (it's the case of Mitsubishi M701G), cooling air used for blade refrigeration (it's the case of Alstom GT26 and Mitsubishi M701G), closed-loop blade cooling, etc.

General Electric 7FB and Siemens V94.3A do not have any Q_{in} or Q_{out}, so these machines represent an ideal case to test consistency of assumptions; accuracy of their energy balance accounts for appropriateness of assumptions entering in Eq. (24). An analogous attempt has been tried also with the Alstom GT 26 where Q_{out} has been calculated on the basis of considerations about the once-through heat exchangers used for air cooling, [29]. The result obtained indicate that either Q_{out} estimation is too high or pessimistic assumption have been made about energy losses. For

[10]Value of that coefficient has been selected so that the temperature difference (expressed in °C or K) that determines a 1% deviation on calculated heat discharged at the turbine exhaust has about the same weight on Ω as a 1% deviation of the first two terms (which account for useful work and input heat).

Table 4 Manufacturers' data used in the calibration procedure. In performing calibration inlet and exhaust losses have been varied compared to values listed in Table 2 in order to meet manufacturers' assumptions. Values in brackets refer to the calibration result.

	General Electric PG7251 (7FB)	Siemens V94.3A	Alstom Power GT26	Mitsubishi M701G
References	[20][21][22]	[23][24]	[25]	[26][27][28]
Stages/Cooled rows/TBC coated rows/Film cooled rows	3 / 5 / 2 / 1	4 / 6 / 2 / 1	HP turbine 1 / 2 / 2 / 1 LP turbine 4 / 6 / 2 / 1	4 / 6 / 4 / 3
Exhaust mass flow rate, kg/s	448.4	644.0	562.0	737.1[a]
Pressure ratio	18.5	17	30	20
TIT, °C	1402	1350	1255[b]	1430
Simple cycle data				
Net electric power, MW	184.4 (185.5)	260.0 (259.3)	262.0 (264.9)	334.0 (330.1)
Net efficiency (LHV), %	36.92 (37.04)	38.20 (38.17)	38.20 (38.04)	39.55 (39.32)
TOT, °C	623.0 (623.1)	584.0 (582.7)	640.0 (638.8)	587.2 (585.6)
Thermal balance error, %	-0.03	-0.04	-0.75	0.00
Combined cycle data [c, d]				
Net electric power, MW	280.3 (280.4)	390.0 (388.3)	378.0 (392.6)	484.4 (481.1)
Net efficiency (LHV), %	57.30 (57.25)	57.30 (57.19)	57.00 (56.97)	58.00 (57.97)

[a] at compressor inlet

[b] value according to ISO definition. Since it is not clear whether this value is referred to HP or LP turbine, in our calibration TIT has been assumed 1250 °C and 1260 °C for HP and LP turbines respectively.

[c] Contrarily to assumption of tab. 3, maximum steam temperature of 565 °C has been here assumed. Condensation pressure declared for PG7251 (0.0406 bar) has been used in calculations of V94.3A and M701G gas turbines. In case of GT26 a 0.08 bar condensation pressure has been assumed since data refer to wet cooling tower.

[d] Differences in fuel thermal input between simple and combined cycle based on the same machine reflect different assumptions regarding pressure losses at compressor inlet (that affect the air mass flow rate) and fuel heating. Calculations are carried out according to manufactures' data.

the Mitsubishi turbine, no attempts were made to estimate temperature drop of cooling air: temperature at cooler exit has been set in order to verify the thermal balance.

Variables resulting from optimization process are summarized in Table 5, while values in Table 4 reporting calibration results, show a pretty good agreement with manufacturer's data. The corresponding value of Ω is 3.78; it means that the average error on variables entering in Eq. (23) is 0.56%. The sensitivity analysis of Fig. 6 shows the effect of single variations of the each optimizing variable on the target function Ω. The importance of including parameter K among calibration variables is clear. It is eventually to be noted that the assumptions about the bottoming steam cycle given in Table 3, based upon long time experience, proved to generate accurate predictions about the combined cycle performance, that, as indicated in Table 4, are in close agreement with manufacturers' data. The only significant difference is related to the power output of the combined cycle based on Alstom machine, where probably the gas turbine setting parameters vary between simple and combined cycle arrangement. Moreover, less recent manufacturer's data, [30], showed a better agreement with performance calculated.

Table 5 Calibration variables and respective values outcome from the optimization process

Compressor efficiency $\eta_{\infty,C}$	eq.(2)	0.924
Turbine cooled stage efficiency $\eta_{\infty,T}$	eq.(5)	0.927
Parameter r_{fc}	par.(2.3.2)	0.32
Coefficient K	eq.(8)	0.285

3.2 Assumptions for Closed-Loop Solutions. Extension of the model to closed-loop cooling calculation has been performed by maintaining the same sets of correlations and data developed for the open-loop circuit and neglecting film-cooling. A challenging problem rose in estimating the air flow rate used in these rows to refrigerate portions that cannot be cooled in closed loop (such as blade trailing edge, disks, etc.). In the solution devised, the cooling model is applied twice: once to a closed-loop circuit (considering steam or air as cooling medium), then to an open-loop air

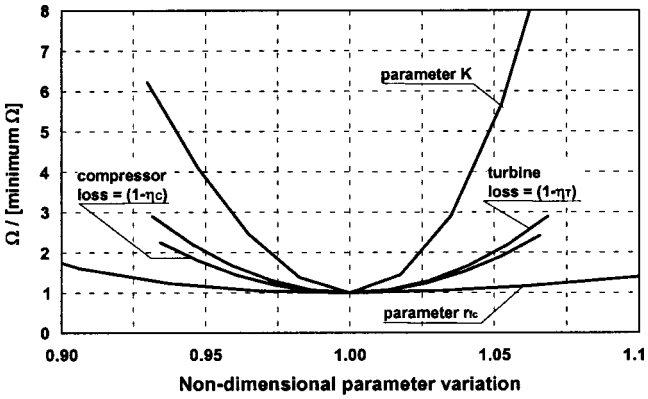

Fig. 6 Sensitivity analysis related to the calibration procedure: each curve refers to the variation of the target function obtained by varying one optimizing variable while keeping constant the other three to their optimum value

Table 6 Gas turbine characteristics and performance data for a General Electric 107H combined cycle, [31]

Stages / Cooled rows / TBC coated / Steam cooled	4 / 6 / 4 / 4
Inlet mass flow rate, kg/s	557.9
Pressure ratio	23
TIT, °C	1430
CC net electric power, MW	400
CC net efficiency (LHV), %	60.0

circuit without any film cooling. The final result is obtained by considering the fraction r_{cl} of the coolant mass flow rate found in the first case and the fraction $(1-r_{cl})$ of the second one. Calibration of r_{cl} has been performed comparing calculated results to available data of the GE H series combined cycle (see Table 6). Figure 7 shows the effect of variation of r_{cl} on the cycle performance. The bottom diagram shows the variation temperature drop across the nozzle ($\Delta T_{1,s}$ difference between combustor outlet temperature and TIT). Reducing r_{cl} brings about that more and more cooling air is mixed at the nozzle exit increasing the combustor outlet temperature and $\Delta T_{1,s}$ since a constant TIT (1430°C) has been assumed. Parameter r_{cl} has been selected in order to set $\Delta T_{1,s}$ in accordance with value provided by GE, [31]. Estimation of overall power output and efficiency (top diagrams of Fig. 7) and breakdown between gas and steam turbine power output, [32], are in good agreement with manufacturer's data.

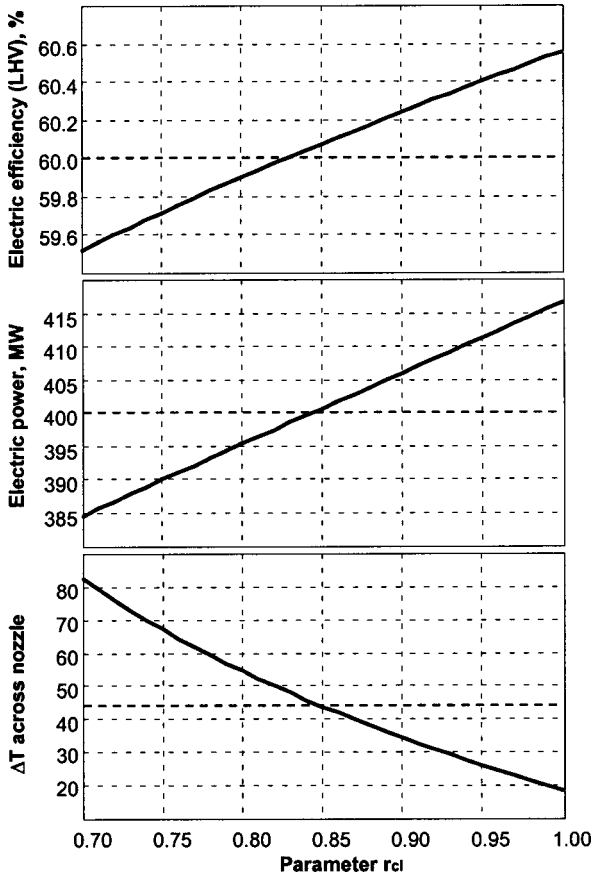

Fig. 7 Influence of the closed-loop cooling circuit parameter r_{cl} on the calculated performance of a GE 107H combined cycle. Bold dotted lines point out manufacturer's design data.

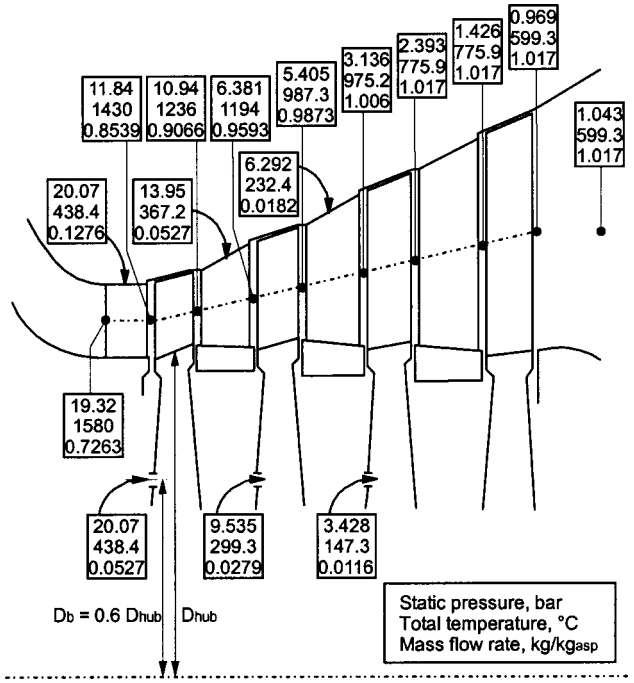

Fig. 8 The resulting blade geometry in the meridional plane of the "state-of-the-art" four-stage gas turbine (OL-AC case). Main stream data between blade rows refer to conditions after convective cooling flow mixing. At diffuser outlet total and static conditions coincide. Cooling flow rates include convective, film as well as disks contribution.

4 Presentation of Results

4.1 Results at Constant TIT. All results presented in this sections refer to "state-of-the-art" machines, as they are generated by the code, for the input data listed in Tables 1 to 3, "optimizing variables" listed in Table 5 and $r_{cl}=0.85$. The air mass flow rate at compressor inlet is maintained constant (700 kg/s, a value representative of large scale, 50 Hz machines). The selected "state-of-the-art" TIT (1430°C) is kept constant for all plant configurations,[11] while pressure ratio is varied to optimize performance, up to the maximum value of 30. An example of the resulting four stage machine for the "conventional" (OL-AC) solution is given in Fig. 8, that represents the meridional blade path, with the indication of the cooling flows. The corresponding expansion process in the temperature-specific entropy diagram is represented in Fig. 2. Other cycle configurations present different turbine geometry and different thermodynamic conditions, but the four stage solution was maintained for all cycles. For cases with sequential combustion, a nearly impulse HP stage expanding to 14.5 bar was added, so that the complete turbine becomes a five stage machine.

Detailed plant arrangements for the five schemes considered are represented in Figs. 9 to 13. In each figure, the most significant points are labeled, and the corresponding numerical values of pressure, temperature and mass flow rate are indicated in Table 7. The comparison among the considered plant arrangements in terms of efficiency and power is represented in Fig. 14. The following comments can be drawn:

- efficiency differences among the various plant configurations are significant, but relatively small: sequential combustion increases the efficiency of about one percentage point, closed loop cooling (either steam or mixed) of about two percentage points, the combined adoption of closed loop steam cooling

[11]The only exception is the case of TIT of HP turbine for the OL-AC+SC case, where a lower value (1290°C) is adopted, for reasons discussed in Section 4.3.

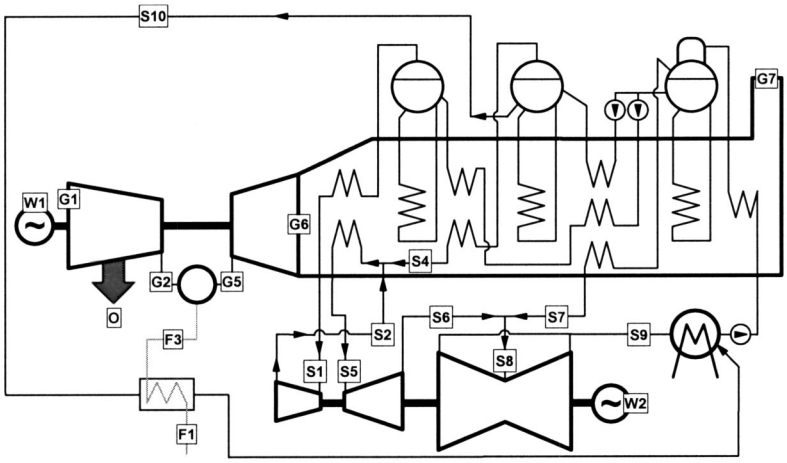

Fig. 9 Detailed plant configuration for the "state-of-the-art" OL-AC case

and sequential combustion (a configuration not yet considered by manufacturers) of about three percentage points.
- much larger gains (in the range of 15% for steam cooling, 20% for sequential combustion and as high as 36% for the combined adoption of the two practices) are found in terms of specific power.

4.2 Second-Law Analysis. A better understanding of the thermodynamic merits of the various plant configurations can be obtained by examining the results of the second-law analysis given in Table 8. Let's start from the "basic" configuration (OL-AC) without sequential combustion, where total "second law" irreversibilities amount to 43.45%, distributed as follows:

- as is well known, the largest fraction of these losses (58.64%) are related to the combustion process;[12]
- losses associated to blade cooling (including terms related to heat transfer and mixing processes) are the second largest contribution (about 8.7%);
- fluid-dynamic losses occurring in the three main turbomachines (air compressor, gas and steam turbine) have comparable weight and account for about 4% each[13]
- heat transfer irreversibilities in the HRSG account for about 4.6%;
- heat discharge to atmosphere accounts for about 8.5% (almost equally divided between condenser, stack and thermal losses);
- the remaining fraction (about 7%) is mostly related to organic and electrical losses and to auxiliaries consumption.

The adoption of sequential combustion has a positive, but not dramatic (corresponding to about 1.1 percentage points of efficiency increase) effect on combustion irreversibilities, due to the increase of the average temperature at which combustion heat is released.[14] However, part of this gain is lost because of the corresponding increase of blade cooling losses; hence, the sequential combustion yields a net efficiency increase somewhat lower than one percentage point.

The adoption of steam cooling in the first two turbine blade rows yields an overall better result, with a cycle efficiency gain of about two percentage points. The two positive effects of steam cooling are a significant decrease of blade cooling losses and, to a lesser extent, a decrease in the HRSG losses, only slightly offset by the increase in combustor losses.[15] It is interesting to point out that, even if air performs slightly worse than steam cooling in terms of heat transfer, most of the advantages brought about by closed-loop cooling are maintained when air is used as cooling medium in rotor rows. Therefore, if technological problems related to steam sealing experienced in the first trial tests cannot be solved, switching to closed-loop air cooling could be a valid solution.

The combined adoption of sequential combustion plus closed loop steam cooling yields, as expected, the best results, with a further gain of one percentage point in overall efficiency gain, mostly due to lower combustion losses.

4.3 Influence of TIT. The gas turbine history has been characterized by a continuous increase of turbine inlet temperatures (about 13°C/year, see [13]). It is therefore interesting to investigate how future TIT increases could affect performance of the considered advanced cycles. The results of this investigation are represented in Fig. 15 and can be summarized as follows:

- For "conventional" blade cooling, the influence of TIT on efficiency is significant (about 1 percentage point every 100°C TIT increase), and maintains a positive slope up to TIT as high as 1500°C. Extrapolating the curve, TITs as high as 1650°C would be required to achieve the 60% efficiency target.
- A similar behavior is found for closed loop steam cooling, where the efficiency gains related to a TIT increase are even higher. The 60% efficiency target is reached at TIT of about 1430°C and a further TIT increase up to 1500°C would bring about an additional 0.5 percentage gain.
- More complex is the situation for cycles adopting a sequential combustion, where two different values of TIT can be adopted for high and low pressure turbines respectively: for OL-AC cycles, the increase of the high pressure TIT over about 1300°C would not be beneficial, since it brings about significant blade cooling losses, while the increase of low pressure TIT is beneficial only for values below 1400°C; in other words, according to the present analysis, the sequential combustion with open loop air cooling is a brilliant solution to reach high efficiencies at relatively low and safe TITs, but is not capable of reaching the 60% efficiency target.

[12]This circumstance is the reason why dramatic efficiency improvements, say net cycle efficiency well above 70%, can be obtained only by substituting the highly irreversible combustion process by the more reversible thermochemical oxidation occurring in a high temperature fuel cell (see, for instance, [8]).

[13]Turbine losses include the losses in diffuser, that are significant both for gas and steam turbine.

[14]The adoption of a larger TIT for the high pressure turbine would further decrease the combustion losses, but the overall effect on efficiency would not be beneficial, owing to the relevant increase of blade cooling losses.

[15]The analysis is carried out at constant TIT. The adoption of steam cooling in the first turbine stator row allows a lower gas temperature at the combustor outlet. This effect, positive in terms of NO_x generation and combustor material thermal stresses, is seen by the second-law analysis as an increase of combustion irreversibilities.

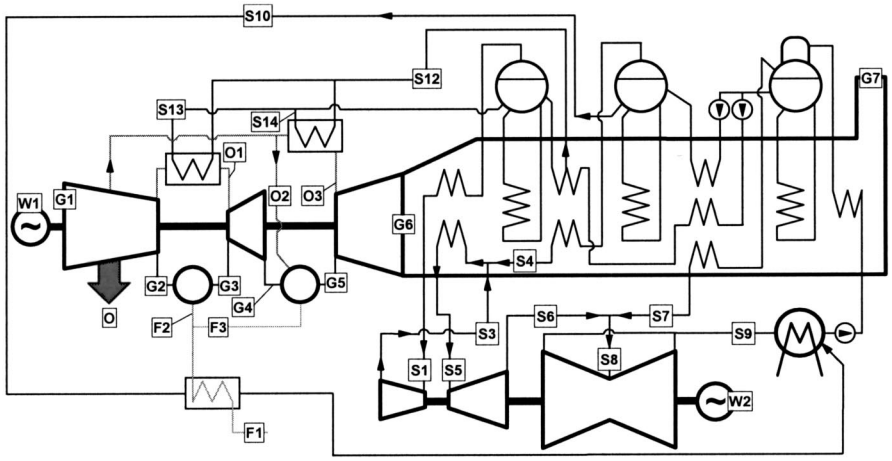

Fig. 10 Detailed plant configuration for the "state-of-the-art" OL-AC case, with SC (sequential combustion)

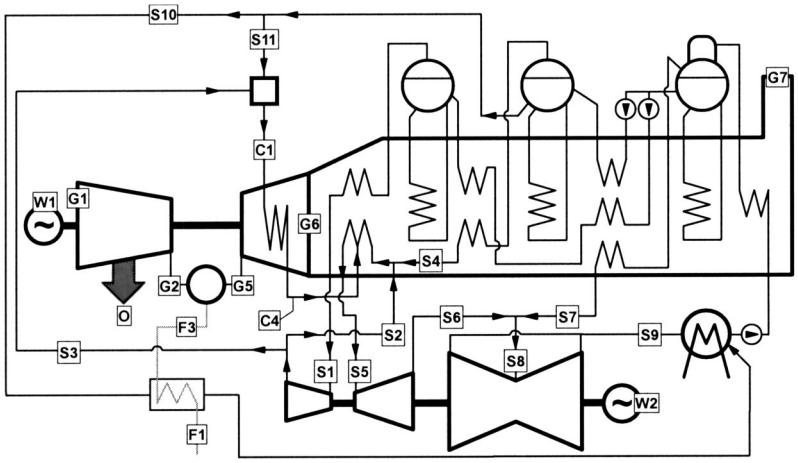

Fig. 11 Detailed plant configuration for the "state-of-the-art" CL-SC case. Flow rates and thermodynamic conditions in all relevant points are given in Table 7.

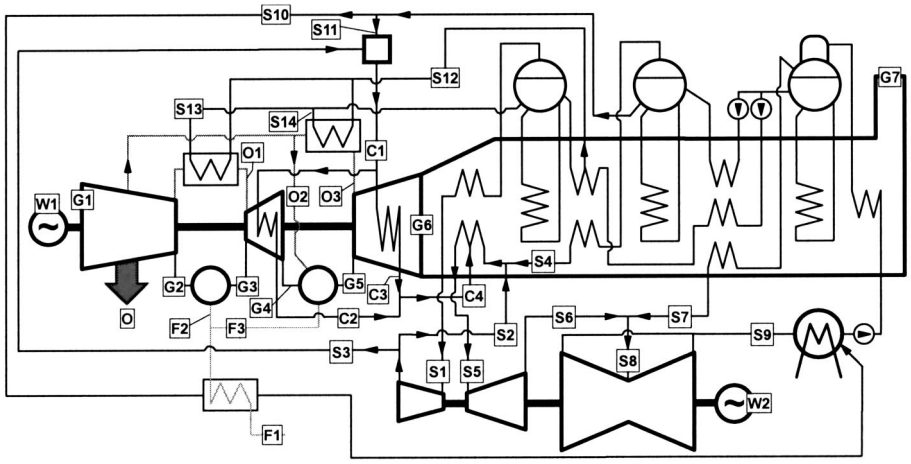

Fig. 12 Detailed plant configuration for the "state-of-the-art" CL-SC case, with sequential combustion

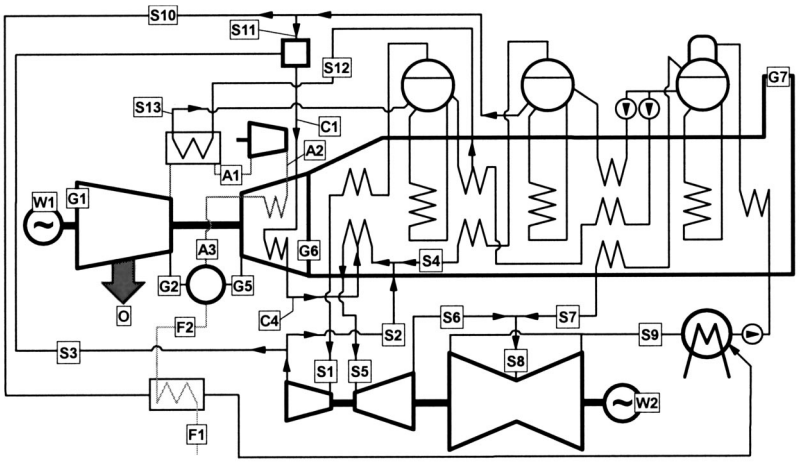

Fig. 13 Detailed plant configuration for the "state-of-the-art" CL-MC case. Details of flow rates and thermodynamic conditions in all relevant points are given in Table 7.

- The CL-SC+SC solution benefits significantly of TIT increase up to about 1350°C, while larger TITs induce marginal efficiency gains. The 60% target can be reached at TIT as low as 1270°C, while efficiency of about 61% are obtained for TIT close to 1400°C.

5 Conclusions

A comprehensive model for performance evaluation of combined cycle plants was developed and different industrial solutions presently adopted to increase conversion efficiency in large size electric power plant were compared in this paper. Although many aspects (such as reliability, capital cost, environmental issues) which can affect gas turbine design were neglected, thermodynamic analysis showed that efficiency higher than 61% can be achieved in the frame of current, available technology.

Analysis also showed that, for open-loop air cooling, sequential combustion, in the range of TIT lower than 1300°C, allows an efficiency gain corresponding to a 150°C TIT increase. In the range of higher TITs, this gain tends to vanish because of growing difficulties in HP turbine blade cooling and greater heat transfer irreversibilities in the HRSG due to higher TOT. The latter drawback asks for pressure ratios higher than the maximum here considered (30) but it probably would force to give up the simple, single spool arrangement in favor of a more expensive two spools arrangement.

Adoption of closed-loop cooling has opposite effects compared to sequential combustion, in the sense that efficiency gains increase as TIT goes up. Use of steam or air for rotor blade cooling does not produce substantial differences on both efficiency and specific power. Best performance are achieved through simultaneous introduction of closed-loop cooling and sequential combustion.

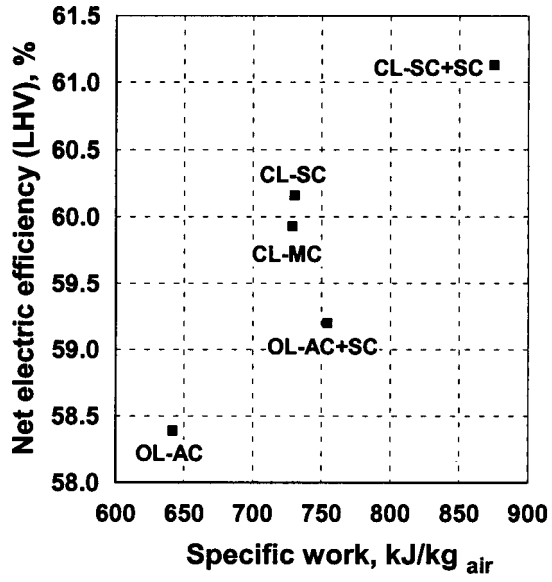

Fig. 14 Performance prediction for plants described in figures from 9 to 13 and Table 7. All the plants refer to the same "state-of-the-art" TIT of 1430°C.

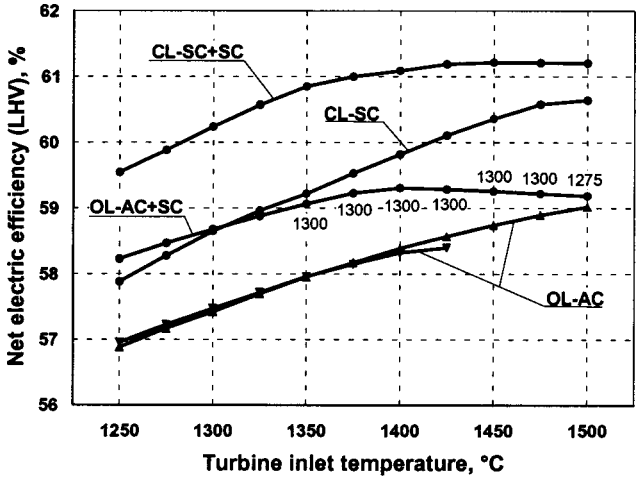

Fig. 15 Variation of cycle net LHV efficiency with turbine inlet temperature. The two curves related to OL-AC cycles refer to cases where cooling air is or is not cooled before entering gas turbine blades. In the first case, TIT cannot reach values above 1430°C. For cycles with sequential combustion, values in abscissa refers to TIT of both the turbines. Only for OL-AC+SC, when TIT of the LP turbine is higher than 1325°C, HP turbine TIT has been reduced to the values labeled in the figure in order to maximize the plant efficiency.

Table 7 Conditions of streams at the most relevant point of the combined cycles considered in figures from 9 to 13

		OL–AC			OL–AC+SC			CL–SC			CL–SC+SC			CL–MC		
		T, °C	p, bar	m, kg/s	T, °C	p, bar	m, kg/s	T, °C	p, bar	m, kg/s	T, °C	p, bar	m, kg/s	T, °C	p, bar	m, kg/s
Air at compressor inlet	G1	15.0	1.01	700.0	15.0	1.01	700.0	15.0	1.01	700.0	15.0	1.01	700.0	15.0	1.01	700.0
Air at compressor outlet	G2	438.4	20.07	491.2	525.9	30.10	488.0	467.5	23.07	619.3	525.8	30.10	589.5	467.5	23.07	589.9
Gas at HP combustor outlet	G3				1359.1	29.19	500.1				1465.8	29.19	606.2			
Gas at HP turbine outlet	G4				1087.9	14.50	549.9				1208.6	14.50	625.1			
Gas at combustor outlet	G5	1580	19.46	508.4	1492.4	14.07	571.7	1482.9	22.38	638.3	1455.5	14.07	644.8	1482.7	22.38	641.59
Gas at HRSG inlet	G6	595.4	1.04	711.8	648.5	1.04	714.5	592.3	1.04	713.8	669.1	1.04	717.3	593.0	1.04	713.6
Gas at HRSG outlet	G7	80.0	1.01	711.8	80.0	1.01	714.5	80.0	1.01	713.8	80.0	1.01	717.3	80.0	1.01	713.6
Air for HP turbine open-loop cooling at cooler outlet	O1				215.0	29.80	49.80									
Air for sequential combustor cooling	O2				380.3	14.94	14.00				380.2	14.94	14.00			
Air for open loop cooling at cooler outlet	O3				215.0	14.79	59.58									
Uncooled air for open loop cooling	O	variab.	variab.	203.5	variab.	variab.	83.38	variab.	variab.	75.48	variab.	variab.	63.81	variab.	variab.	30.26
Steam at closed-loop cooling circuit inlet	C1							295.2	36.00	59.92	313.4	36.00	99.65	296.3	36.00	43.04
Steam at HP turbine closed-loop cooling circuit outlet	C2										453.3	33.37	47.25			
Steam at LP closed-loop cooling circuit outlet	C3										562.5	33.43	52.08			
Steam from closed-loop cooling circuit	C4							507.7	33.76	59.75	510.5	33.37	99.33	489.1	34.21	43.04
Air for closed-loop cooling at cooler outlet	A1													215.0	22.84	45.64
Air for closed-loop cooling at boost compressor outlet	A2													243.4	27.15	45.64
Air at closed-loop cooling circuit outlet	A3													540.8	23.31	32.70
Fuel delivered at plant	F1	15.0	40.00	17.18	15.0	40.00	19.92	15.0	40.00	18.98	15.0	40.00	22.39	15.0	40.00	19.01
Heated fuel for HP combustor	F2				185.0	38.00	12.06				185.0	38.00	16.75			
Heated fuel for combustor	F3	185.0	38.00	17.18	185.0	38.00	7.86	185.0	38.00	18.98	185.0	38.00	5.64	185.0	38.00	19.01
Steam at HP turbine inlet	S1	570.4	152.7	80.89	600.0	152.7	95.88	567.3	152.7	89.05	600.0	152.7	117.94	568.0	152.7	84.86
Steam from HP turbine to RH	S2	364.0	36.00	79.97	385.5	36.00	94.90	359.4	36.00	32.98	385.1	36.00	25.08	360.8	36.00	44.35
Steam for gas turbine cooling	S3							359.4	36.00	55.12	385.1	36.00	91.68	360.8	36.00	39.60
Steam from IP level	S4	333.3	36.00	15.47	333.3	36.00	19.94	333.3	36.00	13.43	333.3	36.00	7.94	333.3	36.00	18.75
Steam at IP turbine inlet	S5	570.4	33.12	95.44	600.0	33.12	114.84	567.3	33.12	106.16	600.0	33.12	132.35	568.0	33.12	106.15
Steam at IP turbine outlet	S6	267.3	3.68	95.44	286.6	3.68	114.84	264.6	3.68	106.16	286.2	3.68	132.35	265.1	3.68	106.15
Steam from LP level	S7	300.0	4.00	13.16	300.0	4.00	12.93	300.0	4.00	11.11	300.0	4.00	6.96	300.0	4.00	12.84
Steam at LP turbine inlet	S8	271.2	3.68	108.61	287.9	3.68	127.77	268.0	3.68	117.27	286.9	3.68	139.31	269.1	3.68	118.98
Steam at turbine outlet	S9	29.2	0.041	108.10	29.2	0.041	123.38	29.2	0.041	115.02	29.2	0.041	132.68	29.2	0.041	116.34
IP BFW for fuel heating	S10	244.2	48.00	7.38	244.2	48.00	9.19	244.2	48.00	8.34	244.2	48.00	11.02	244.2	48.00	8.35
IP BFW for coolant desuperheating	S11							244.2	48.00	4.79	244.2	48.00	7.97	244.2	48.00	3.44
HP BFW at air cooler inlet	S12				182.0	221.3	28.05				182.0	221.3	8.10	182.0	221.3	13.62
HP BFW at air HP cooler outlet	S13				350.0	199.2	17.25				350.0	199.2	6.55	350.0	199.2	13.62
HP BFW at air cooler outlet	S14				350.0	199.2	10.80				350.0	199.2	1.55			
Gas cycle net power, MW	W1	299.5			343.5			348.0			401.9			346.6		
Steam cycle net power, MW	W2	149.5			184.5			163.2			210.7			163.4		

Table 8 Cycle efficiency losses related to the irreversibilities occurring in the various processes. Percentage losses are computed according to the second-law analysis method, with reference to the reversible work of the natural gas at plant boundaries (15°C, 40 bar). Differences between the numerical values of useful work and LHV efficiency reflect the difference among fuel reversible work (46.31 MJ/kg) and LHV (44.77 MJ/kg).

	OL-AC	OL-AC +SC	CL-SC	CL-SC +SC	CL-MC
combustion	25.48	24.39	25.93	24.38	25.89
overall blade cooling	3.77	3.98	2.18	2.84	2.38
cooling heat transfer	0.91	1.42	0.86	1.13	0.88
coolant discharge	2.79	2.49	1.31	1.70	1.39
coolant pressure losses	0.08	0.07	0.01	0.02	0.11
compressor	1.76	1.66	1.68	1.52	1.68
gas turbine fluid-dynamic loss	2.30	2.39	2.22	2.13	2.22
steam turbine	2.11	2.04	2.03	1.98	2.04
HRSG heat transfer	2.02	2.08	1.79	1.92	1.84
condenser	1.45	1.51	1.42	1.45	1.43
miscellaneous in steam cycle	0.25	0.29	0.25	0.30	0.24
elec./org./auxiliaries losses	1.69	1.67	1.69	1.66	1.69
thermal losses	1.11	1.21	1.09	1.15	1.09
leakages and filters	0.45	0.43	0.43	0.42	0.42
heat rejection at stack	1.14	1.13	1.13	1.13	1.13
combustor	25.48	24.39	25.93	24.38	25.89
useful work	56.45	57.23	58.16	59.10	57.94
LHV efficiency, %	58.39	59.20	60.16	61.13	59.93
specific work, kJ/kg$_{air}$	641.5	754.2	730.2	875.2	728.6
Operating conditions:					
Pressure ratio	20	30	23	30	23
HP turbine TIT, °C	—	1290	—	1430	—
TIT, °C	1430	1430	1430	1430	1430

Nomenclature

b = axial chord (m)
c = chord (m)
d = cooling channel diameter (m)
D = diameter (m)
D_b = rotor coolant injection diameter (m)
E_h = heat transfer enhancement factor
E_p = pressure loss multiplying factor
h = blade height (m)
h = specific enthalpy (J/kg)
h = heat transfer coefficient (W/m^2-K)
k_{is} = stage head factor$=2\cdot\Delta h_{is}/u_m^2$
K = multiplying coefficient in Eq. (8)
L_{eq} = equivalent length of the cooling (m) channels (see footnote 8)
m = mass flow rate (kg/s)
Ma = Mach number
n = number of cooling channel passages
Pr = Prandtl number
q = heat flux (W/m^2)
Q = thermal power (W)
r^* = reaction degree
r_{cl} = fraction of open-loop cooling (see par 3.2)
r_{fc} = fraction of cooling flow used for film cooling
Re = Reynolds number
S_c = cooling channels surface (m^2)
SP = size parameter (m) $V_{in}^{0.5}/\Delta h_{is}^{0.25}$ for compressor stages $V_{out}^{0.5}/\Delta h_{is}^{0.25}$ for turbine stages
St = Stanton number
t = thickness (m)
u = peripheral speed (m/s)
U = overall heat transfer coefficient (W/m^2-K)
v = velocity (m/s)
V = volume flow rate (m^3/s)
w = relative velocity (m/s)
W = mechanic or electric power (W)
α = (coolant passages cross section)/c^2
γ = stagger angle
η = efficiency
θ = component of the coolant velocity along the main stream direction (see Eq. (20))
λ = pattern factor (see Eq. (9))
φ = velocity loss coefficient
Φ = blade perimeter/chord
ψ = interference coefficient
ω = rotational speed$=2\cdot\pi\cdot$rpm/60 (rad/s)
ω_s = specific speed$=\omega\cdot V_{out}^{0.5}/\Delta h_{is}^{0.75}$ (rad)

Subscripts

a = axial
ad = adiabatic expansion
aux = auxiliaries
aw = adiabatic wall
b = coolant introduction in disks or shaft
bcl = blade surface, coolant side
bg = blade surface, gas side
blw = blade wall
C = compressor
cl = coolant side
clc = closed-loop cooled row
cv = convective coolant
el = electric
g = gas side
gr = gas recovery
in = inlet
is = isentropic
lkg = leakage
m = mean
olc = open-loop cooled row
org = organic
out = outlet
p = polytropic
r = rotor exit
ref = reference
s = stator exit
th = thermal
TT = total to total
unc = uncooled row
1 = first
∞ = large SP, i.e., no more scale effect

Acronyms

OL-AC = open-loop air cooled
CL-SC = closed-loop steam cooled
CL-MC = closed-loop mixed air/steam cooled
SC = sequential combustion
TIT = turbine inlet temperature
TBC = thermal barrier coating
TOT = turbine outlet temperature
LHV = lower heating value

References

[1] DuBose, P. E. et al., 2001, "Testing the World's Largest Gas Turbines," ASME Paper 2001-GT-0398.
[2] Maekawa, A. et al., 2001, "Development of H Series Gas Turbines," ASME 2001-GT-0500.
[3] Gaul, G. R., and Dodd, A. M., 2001, "The W501G Testing and Validation in the Siemens-Westinghouse Advanced Turbine Systems Program," ASME Paper 2001-GT-0399.
[4] Eckardt, D., and Rufli, P., 2001, "Advanced Gas Turbine Technology—ABB/BBC Historical Firsts," ASME Paper 2001-GT-0395.
[5] Consonni, S., 1992, "Performance Prediction of Gas/Steam Cycles for Power Generation," MAE Dept. Ph.D. Thesis n. 1983-T, Princeton University, Princeton, NJ.
[6] Young, J. B., and Wilcock, R. C., 2001, "Modelling the Air-Cooled Gas Turbine: Part 1—General Thermodynamics," ASME Paper 2001-GT-0385

[7] Chiesa, P., Consonni, S., and Lozza, G., 1998, ''A Comparative Analysis of IGCCs With CO2 Sequestration,'' *Proc. of 4th International Conference on Greenhouse Gas Control Technologies*, Interlaken, Switzerland, Pergamon, Oxford, pp. 107–112.
[8] Campanari, S., and Macchi, E., 1998, ''Thermodynamic Analysis of Advanced Power Cycles Based Upon Solid Oxide Fuel Cells, Gas Turbines And Rankine Cycles,'' ASME Paper 98-GT-585.
[9] Macchi, E. et al., 1995, ''An Assessment of the Thermodynamic Performance of Mixed Gas-Steam Cycles. Part A: Intercooled and Steam Injected Cycles—Part B: Water-Injected and HAT Cycles,'' ASME J. Eng. Gas Turbines Power, **117**, pp. 489–508.
[10] Lozza, G., 1990, ''Bottoming Steam Cycles for Combined Gas-Steam Power Plants: A Theoretical Estimation of Steam Turbine Performance and Cycle Analysis,'' *Proc. of 1990 ASME Cogen-Turbo*, New Orleans, LA, ASME, New York, pp. 83–92.
[11] Macchi, E., and Perdichizzi, A., 1981, ''Efficiency Prediction for Axial-Flow Turbines Operating With Non-Conventional Fluids,'' ASME J. Eng. Gas Turbines Power, **103**, pp. 718–724.
[12] Consonni et al., 1991, ''Gas-Turbine-Based Advanced Cycles for Power Generation. Part A: Calculation Model,'' Proc. of the Yokohama International Gas Turbine Congress, Yokohama, Japan.
[13] Chiesa et al., 1993, ''Predicting the Ultimate Performance of Advanced Power Cycles Based on Very High Temperature Gas Turbine Engines,'' ASME Paper 93-GT-223.
[14] Louis, J. F., 1997, ''Systematic Studies of Heat Transfer and Film Cooling Effectiveness,'' *AGARD CP-229*, Neuilly sur Seine, France.
[15] Dailey, G., 2003, ''Aero-Thermal Performance of Internal Cooling System in Turbomachines: Design and Calculation Issues,'' *von Karman Institute Lecture Series 2000-03*, Rhode Saint Genese, Belgium.
[16] Taslim, M. E., 2003, ''Aero-Thermal Performance of Internal Cooling System in Turbomachines: Convective Cooling in Non-Rotating and Rotating Channels: Experimental Aspects,'' *von Karman Institute Lecture Series 2000-03*, Rhode Saint Genese, Belgium.
[17] Strang, A., 1979, ''High Temperature Properties of Coated Superalloys,'' *Proc. of Behavior of High Temperature Alloys in Aggressive Environments*, Petten, The Netherlands, The Metals Society, London, pp. 595–611.
[18] Jorda, K., Torbidoni, L., and Massardo, A. F., 2001, ''Convective Blade Cooling Modelling for the Analysis of Innovative Gas Turbine Cycles,'' ASME Paper 2001-GT-0390.
[19] Goldstein, R. J., and Haji-Sheikh, H., 1967, ''Prediction of Film Cooling Effectiveness,'' *Proc. of 1967 Semi-International Symposium*, JSME, Tokyo, Japan, pp. 213–218.
[20] Johnston, J. R., 2000, ''Performance and Reliability Improvements for Heavy-Duty Gas Turbines,'' Report GER-3571H GE Power Systems, Schenectady, NY.
[21] Brooks, F. J., 2000, ''GE Gas Turbine: Performance Characteristics,'' Report GER-3567H, GE Power Systems, Schenectady NY.
[22] Chase, D. L., and Kehoe, P. T., 2000, ''GE Combined-Cycle Product Line and Performance,'' Report GER-3574G, GE Power Systems, Schenectady, NY.
[23] Streb, H. et al., 2001, ''Advanced Burner Development for the VX4.3A Gas Turbine,'' ASME Paper 2001-GT-0077.
[24] Siemens Power Generation website: www.pg.siemens.com/en/index.cfm.
[25] Alstom Power website: www.power.alstom.com.
[26] *Gas Turbine World 2000-2001 Handbook*, Vol. 21, Pequot Publishing, Fairfield, CT.
[27] Kallianpur, V., Akita, E., and Tsukuda, Y. 2001, ''Enhancing Reliability & Reducing O&M Expenditures in Advanced Combined Cycle Gas Turbine Power Plants,'' ASME Paper 2001-GT-0499.
[28] Fulton, K., and Farmer, R., 1997, ''Takasago 330-MW Combined Cycle is Tested for Steam-Cooled 501 G,'' Gas Turbine World, **27**(2), March/April.
[29] Anon., 1998, ''ABB Brings GT24 With Once-Through Boiler to New England Merchant Plant,'' Turbomachinery International, Jan.–Feb.
[30] ''The GT24/GT26 Gas Turbine,'' 1998, ABB Report PGT2186.
[31] Matta, R. K., Mercer, G. D., and Tuthill, R. S., 2000, ''Power Systems for the 21st Century—'H' Gas Turbine Combined-Cycles,'' GER-3935B, GE Power Systems, Schenectady, NY.
[32] Tomlinson, L. O. et al., 1995, ''Advanced Technology Combined Cycles,'' Report GER-3936, GE Power Systems, Schenectady, NY.

C. Cao

J. W. Chew

Fluids Research Center,
School of Engineering,
University of Surrey,
Guildford, Surrey GU2 7XH, UK

P. R. Millington

S. I. Hogg

Alstom Power,
Newbold Road,
Rugby, Warwickshire CV21 3NH, UK

Interaction of Rim Seal and Annulus Flows in an Axial Flow Turbine

A combined computational fluid dynamics (CFD) and experimental study of interaction of main gas path and rim sealing flow is reported. The experiments were conducted on a two stage axial turbine and included pressure measurements for the cavity formed between the stage 2 rotor disk and the upstream diaphragm for two values of the diaphragm-to-rotor axial clearance. The pressure measurements indicate that ingestion of the highly swirling annulus flow leads to increased vortex strength within the cavity. This effect is particularly strong for the larger axial clearance. Results from a number of steady and unsteady CFD models have been compared to the measured results. Good agreement between measurement and calculation for time-averaged pressures was obtained using unsteady CFD models, which predicted previously unknown unsteady flow features. This led to fast response pressure transducer measurements being made on the rig, and these confirmed the CFD prediction. [DOI: 10.1115/1.1772408]

1 Introduction

The present study considers interaction of rim sealing and main annulus flows in an axial flow turbine. In any such turbine with shrouded blades and vanes there will be gaps between rotating and stationary sections of the annulus walls. These gaps must accommodate relative movements of the rotating and stationary components, and will allow flow exchange between the main annulus and the cavity between the rotating and stationary disks. To avoid overheating of turbine disks it is sometimes necessary to channel cool, high pressure air from the compressor to the gap in the turbine inner annulus wall where it is ejected back into the main gas path. In this case the degree of hot gas ingestion, the level of sealing flow required, and the spoiling effects of the sealing flow in the turbine are all of interest. In lower pressure turbine stages ingestion of hot gas may not be of such concern, although the influence of flow through the gap on turbine performance is still of interest. A variety of disk cavity and rim seal geometries are found in current gas and steam turbines, and the influence of geometry on sealing and performance is of considerable interest.

Previous work on turbine rim sealing has noted both the effects of the rotating disk, which tends to draw flow in through the seal (e.g., Bayley and Owen [1]), and the importance of circumferential pressure gradients in the annulus, which can promote inflow and outflow around the seal circumference (e.g., Campbell [2]). It is now generally thought that, at engine conditions, circumferential pressure asymmetries are the primary cause of ingestion, with asymmetries from both stationary vanes and rotating blades contributing. The combined effects of rotating and stationary pressure asymmetries have been considered recently by Bohn et al. [3], Roy et al. [4], Hills et al. [5], and Gentilhomme et al. [6]. It may be concluded that predictive methods for rim seal ingestion must take account of the unsteady nature of the flow. Roy et al. measured pressures and ingestion in a turbine rig. Based on their unsteady pressure measurements and the observation that steady CFD models did not correctly predict ingestion they concluded that the unsteadiness was playing an important part in the ingestion process. Hills et al. showed that an unsteady CFD model gave considerably better agreement with previously published experimental ingestion data than steady models. For the conditions considered it was shown that the circumferential pressure asymmetry due to rotating blades had a large influence on ingestion despite being considerably smaller than the pressure asymmetry due to the stationary vanes. This was explained by considering inertial effects on the flow and the fact that the swirl velocity of the air was much closer to the rotor speed than to that of the vanes. An elementary model, taking some account of these effects was also shown to capture the experimental trends.

As noted by Smout et al. [7], the experimental rig described by Bohn et al. [8] has been used for research under the European collaborative ICAS-GT research program. At some conditions measurements indicated the presence of large-scale low-frequency pressure fluctuations with a characteristic wave length greater than that associated with the pitch of the blade or vanes. This result is very relevant to the present study. A further relevant and very recent result is that of Autef [9], as described by Chew et al. [10]. Autef found that unsteady CFD calculations for a rotor/stator disk cavity with axisymmetric, steady boundary conditions show three-dimensional unsteady flow at the rim seal for the case of weak external flow. This unsteady flow feature had not been identified previously and calculated levels of ingestion (due to disc pumping) showed much better agreement with experiment than earlier steady CFD models.

In this paper a combined CFD and experimental study of interaction of main gas path and rim sealing flow is reported. Emphasis is on the unsteady nature of the flow and ingestion into the disk cavity. The experiments were conducted on the two stage axial turbine described in the next section, and the FLUENT CFD code was used as described in Section 3. Results are presented and compared in Section 4, with the main conclusions being summarized in Section 5.

2 Experimental Rig and Tests

The experimental data were obtained using the ALSTOM two stage HP/IP model air turbine situated in Rugby, UK. The facility is primarily used to develop both impulse and reaction steam turbine blading and to provide high quality test data for CFD code validation.

A typical turbine configuration is shown in Fig. 1. The turbine incorporates a split shaft arrangement, each shaft having a torque meter, for accurate measurement of shaft power, and a hydraulic

Contributed by the International Gas Turbine Institute (IGTI) of THE AMERICAN SOCIETY OF MECHANICAL ENGINEERS for publication in the ASME JOURNAL OF ENGINEERING FOR GAS TURBINES AND POWER. Paper presented at the International Gas Turbine and Aeroengine Congress and Exhibition, Atlanta, GA, June 16–19, 2003, Paper No. 2003-GT-38368. Manuscript received by IGTI, October 2002, final revision, March 2003. Associate Editor: H. R. Simmons.

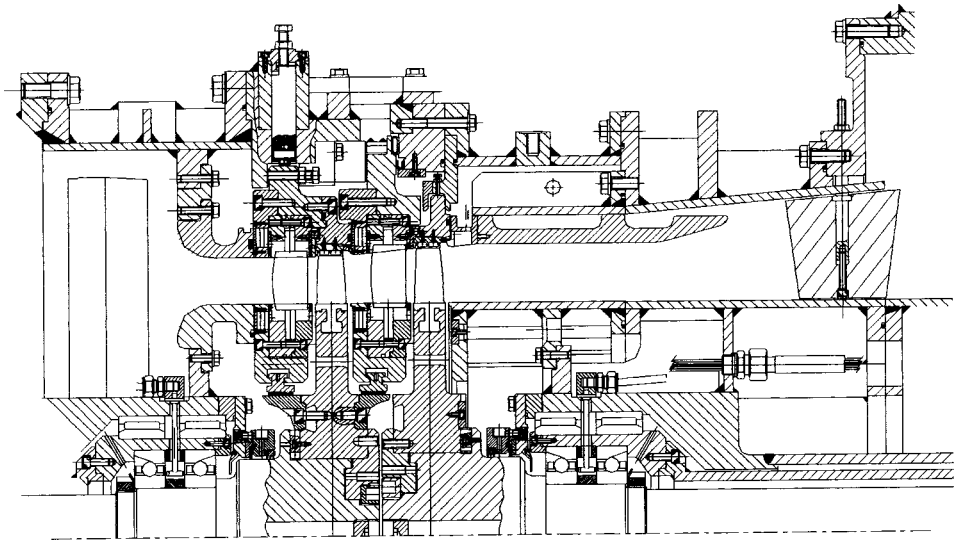

Fig. 1 Schematic of the two-stage turbine rig

dynamometer to absorb the power. Shaft bearing losses are measured separately using a ''balanced bearing system.''

The present tests were carried out using ALSTOM standard impulse HP/IP blading. The first stage of the turbine is used to provide representative flow conditions into the second stage. Interest is focused on interaction of sealing and main annulus flow at the disk rim gap, which is shown in Fig. 2. The second stage has 50 fixed vanes and 67 rotating blades. The moving blade root diameter is 609.6 mm. Balance holes in the rotor disks are provided to swallow most of the flow from the fixed-blade diaphragm gland, with the remaining leakage flow flowing radially outwards into the annulus. The standard disc to stator/diaphragm gap is 4 mm. In some tests this was reduced to 2 mm by gluing a spacer to the diaphragm face, with finishing to remove any step on the blade root and wall. The spacer extended 15 mm radially inwards from the root endwall.

The turbine is fully instrumented with kiel rakes, wall static pressure tappings, and thermocouples from which both the individual stage and turbine efficiencies can be obtained. In addition the stage 2 diaphragm has wall static pressure tappings on the exit face to measure the pressure variation in the disc/diaphragm space. These were calibrated statically to ± 5 mbar.

Two series of tests were carried out:

1. Efficiency measurements were performed with a blade radius ratio of 1.11 and disc/diaphragm gaps of 4 mm and 2 mm. Performance data and diaphragm face wall pressures were measured for dimensionless blade root speed (u/C_o) in the range 0.48 to 0.56.

2. Unsteady pressure measurements carried out with a blade radius ratio of 1.23 and a disc/diaphragm gap of 4 mm. As shown in Figs. 2 and 3, fast response pressure transducers were incorporated in the disk/diaphragm space on stage 2 for these tests. The transducers were surface mounted Endevco piezoresistive 8515C-50 (6.3 mm diameter$\times$0.76 mm thick). The transducer outputs were recorded at a tape speed that would allow frequencies

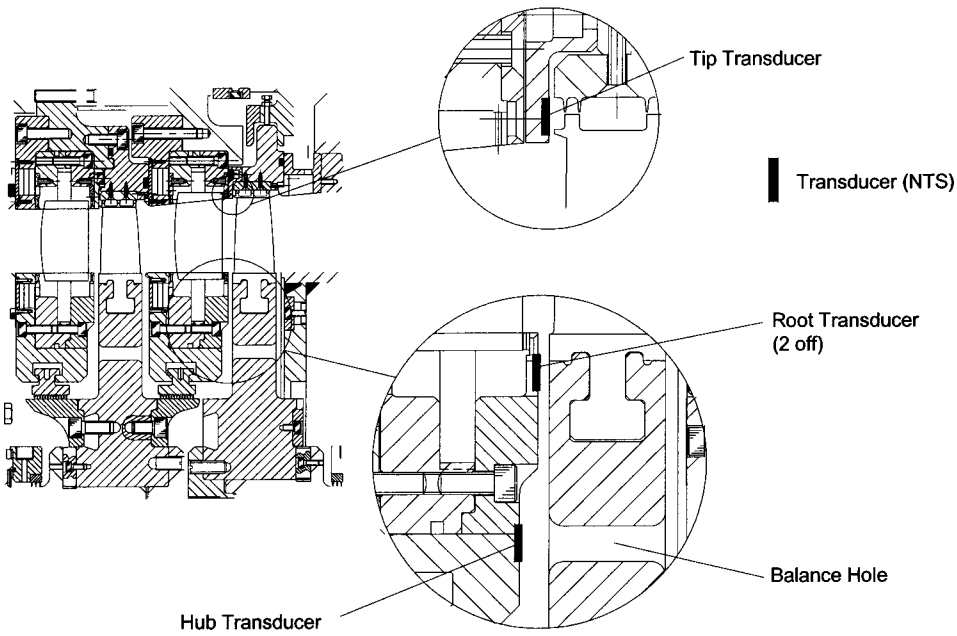

Fig. 2 Detail of the stage-two disk/diaphragm space

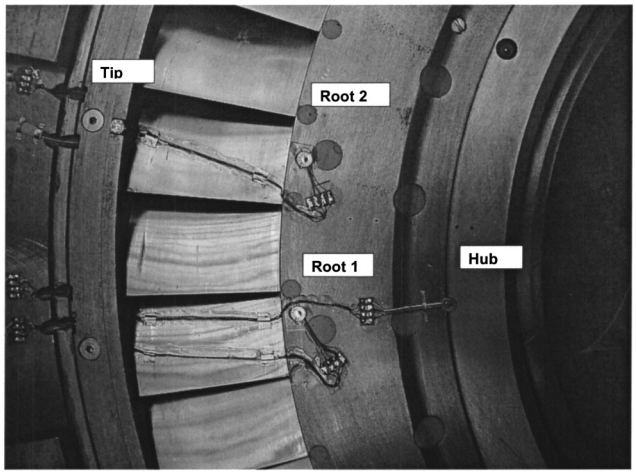

Fig. 3 Pressure transducer installation

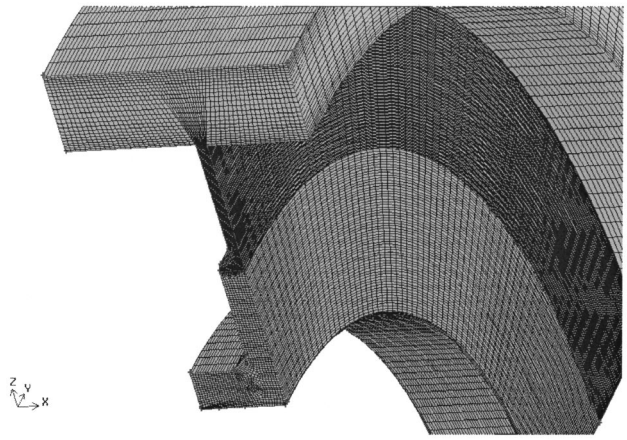

Fig. 5 Mesh 1: 4 mm axial gap on a 90 deg sector

up to 20 kHz to be postprocessed. The test data presented, however, were processed ''live'' using an ''in house'' LabVIEW based analysis tool. The transducers were calibrated statically to ± 5 mbar, and had a resonance frequency of 320 kHz, two orders of magnitude greater than the blade passing frequency.

Measurements were recorded at conditions of either constant pressure level (1.57 bar at exit) and ratio (1.562) with varying speed (2800–3500 rpm), or constant speed (2800, 3000, 3300 rpm) with varying pressure level and ratio. Note however that for all unsteady tests the absolute pressure at the measurement plane was maintained at 1.88 bar.

3 CFD Modeling

Meshes for the CFD models presented here were generated using the Gambit mesh generator versions 1.3 and 2.0 and the FLUENT solver versions 5.5 and 6.0, [11]. The basic solution domain and the coarser calculation mesh used for the initial axisymmetric study is illustrated in Fig. 4. This included the cavity between the rotating and stationary disks and a section of the annulus. The three-dimensional meshes covered a similar axisymmetric domain with either a 90 deg or full 360 deg sector being modeled. Neither the stationary vanes nor the rotating blades were included in any of the models, but some models included balance holes in the rotating disc. Where the balance holes are included, they are assumed to be four holes equally spaced around the circumference. This does not quite match the experiment in which the spacing is nonuniform.

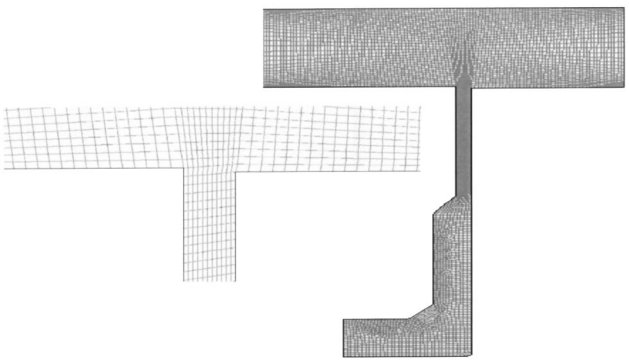

Fig. 4 Coarse mesh for the axisymmetric study

Two meshes were used for the axisymmetric models. The coarser of these, shown in Fig. 4, has 6000 quadrilateral cells while the finer mesh had 24,000 quadrilateral cells. The annulus inlet boundary conditions were set using the total pressure and flow angle profiles given by design calculations for the second-stage vane exit conditions. The static pressure was specified at the hub for the annulus outlet with the radial pressure distribution being given by the radial equilibrium condition. In the rig, flow entered the disk cavity at the inner radius through a labyrinth seal. The geometry of this region was not modeled exactly, but flow was introduced using a specified mass flow condition with zero swirl velocity at the cavity inner radius. When the balance holes were not modeled the specified seal flow was reduced so that the net flow from the cavity into the annulus would match the value estimated for the rig. When balance hole flow was modeled, the pressure was specified at the hole exit and this was adjusted to give the required mass flow. Unless otherwise stated no-slip conditions were applied at all solid boundaries. Compressible flow assumptions and standard relations for the properties of air were used in the axisymmetric models.

Five different meshes were used in the three-dimensional studies and these are summarized below. These include 90 deg and 360 deg sector models. The 90 deg models assume circumferential periodicity whereas, no such assumption is required with the full 360 deg.

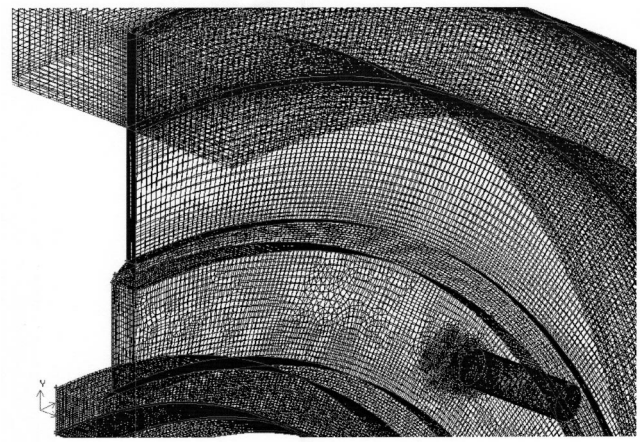

Fig. 6 Mesh 3: 4 mm axial gap with balance holes on a 90 deg sector

Mesh 1: An axisymmetric mesh for the 4-mm axial gap on a 90 deg sector with 380,000 hexahedral cells, as shown in Fig. 5. The mesh on each circumferential plane is identical, being obtained by rotation about the axis of revolution. There are no balance holes.

Mesh 2: Similar to mesh 1, for the 4-mm axial gap, but for a full 360 deg. This mesh is axisymmetric, has 1,190,000 hexahedral cells, and does not include balance holes.

Mesh 3: A 90 deg sector, for the 4-mm axial gap, containing one of the four balance holes. The mesh has 660,000 hexahedral cells and is shown in Fig. 6.

Mesh 4: Similar to mesh 3, for the 4-mm gap, but for a full 360 deg. This mesh, has 2,450,000 hexahedral cells, and includes four balance holes.

Mesh 5: This is a 360 deg axisymmetric mesh for the 2-mm axial gap having 1,420,000 hexahedral cells and not including any balance holes.

Boundary conditions applied for the three-dimensional models are as described above for the axisymmetric case, with rotational periodicity assumed for the 90 deg models. Compressibility was neglected for the three-dimensional cases, with density assumed constant. This involved little inaccuracy and enabled the energy equation to be dropped, saving some computing time. The standard k-ε turbulence model with wall functions was used throughout. The three momentum balance equations, the continuity equation, and the turbulence model equations are solved using the SIMPLE pressure correction algorithm. Second-order upwind spatial differencing was employed with a second-order pressure correction equation. These methods have been used successfully for other rotating disc cavity and turbomachinery flows. However, for the present problem, even when the geometry and boundary conditions were axisymmetric, attempts to find steady solutions produced three-dimensional flow fields, with doubtful convergence. This led to all three-dimensional models being solved in a time accurate fashion. This was done in the rotating frame of reference using implicit, second order time stepping. The time step used was 1.2×10^{-4} s corresponding to 0.0064 of a disk revolution, and the simulation was continued for about 0.5 s (or about 26 disk revolutions). Steady ''solutions'' were used as starting conditions for the unsteady calculations. For both two-dimensional and three-dimensional cases stable steady solutions were obtained by gradually increasing the rotor speed and the annulus inlet swirl to the desired values. Near-wall values were checked for all cases to ensure that the mesh was appropriate for application of the wall functions. Values of $y+$ in the cavity for the 4-mm gap solutions were the range 10 to 300. For the 2-mm gap solution the peak value was 500.

4 Results

CFD results were produced for a design point condition for which the rotational Reynolds number ($\mathrm{Re}_\phi=\rho\Omega r_o^2/\mu$) is 6.0×10^6, the mean annulus inlet Mach number and angle to the axial direction are 0.56 and 78 deg, with the mean inlet swirl equal to $1.83\Omega r_o$. The seal flow feeding the cavity and the balance hole flow are 1.09% and 0.73% of the main annulus flow, respectively. This gives a net flow from the cavity into the annulus of 0.36% of the annulus flow, corresponding to a nondimensional mass flow rate ($C_w=m/\mu r_o$) of 5867. This net flow rate is about 10% of the flow entrainment expected for a disk rotating in a quiescent environment at this rotational Reynolds number. The mean radial velocity based on the net mass flow is about 0.03 times the mean axial velocity in the annulus for the 4-mm axial gap, and twice this value for the 2-mm gap. The CFD solutions at these conditions are presented and compared with the experimental data in the following subsections.

4.1 Mean Pressure Distributions. Figure 7 shows the comparison of measurements from pressure tappings on the stationary disc with axisymmetric CFD solutions from the two meshes. Also

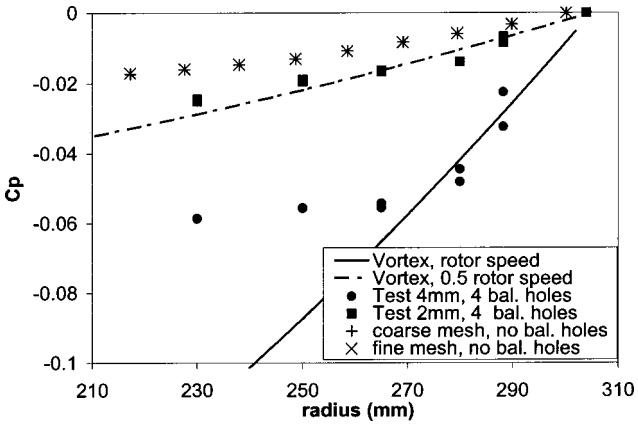

Fig. 7 Axisymmetric CFD results and measurements for the cavity pressure

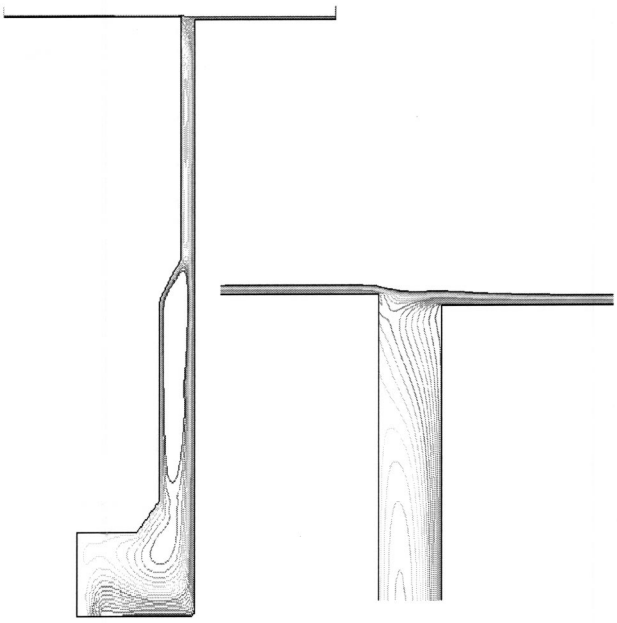

Fig. 8 Axisymmetric CFD flow streamlines for the fine mesh without balance hole flow

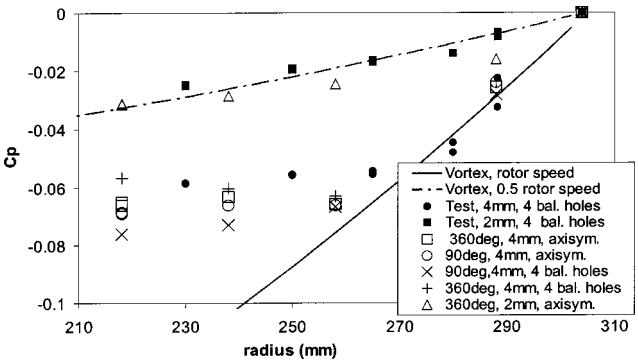

Fig. 9 Three-dimensional unsteady CFD results and measurements for the mean cavity pressure

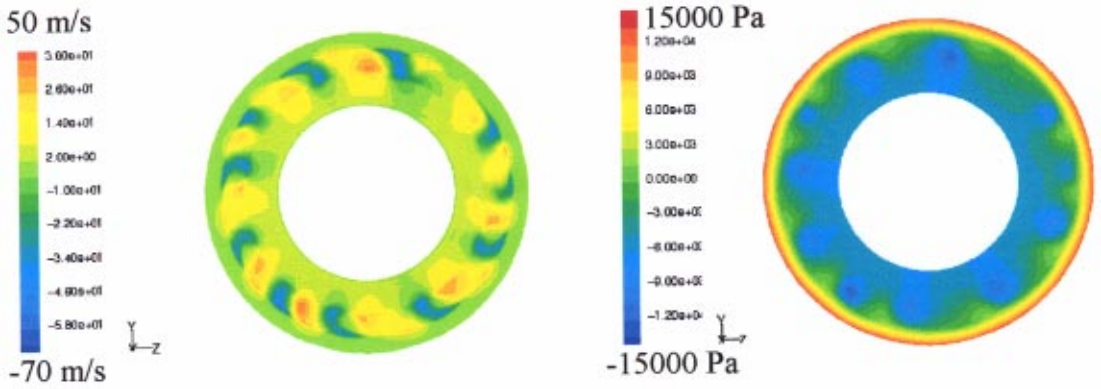

Fig. 10 Instantaneous radial velocities and pressure for the 4-mm gap, axisymmetric mesh, 360 deg model

shown, for reference, are the lines given by a forced vortex at disc speed and a forced vortex at half disk speed. These results are presented in the form of a pressure coefficient referenced to the pressure at the disk outer radius and nondimensionalized using the inlet dynamic head in the CFD solution. Note that an error of ± 5 mbar in the pressure measurements, would give an error in C_p of about ± 0.008. For a rotor-stator disk cavity with no through flow a ''core'' tangential velocity of about 40% of disk speed is expected. The much higher swirl levels indicated by the pressure measurements for the 4-mm axial gap may be attributed to ingestion of the highly swirling annulus gas into the cavity. Measurements for the 2-mm gap are fairly close to the half speed vortex line, indicating considerably less ingestion for the smaller gap. The CFD solutions for the 4-mm gap clearly under predict the pressure gradient and, by inference, the degree of ingestion into the cavity. Results from the two CFD meshes are very close, showing that the discrepancy with experiment is not due to numerical truncation error.

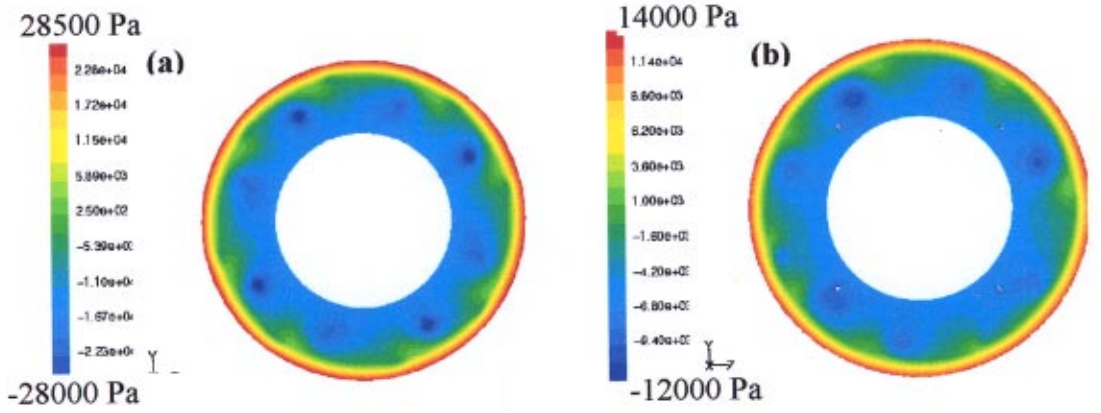

Fig. 11 Instantaneous pressure for (*a*) the 4-mm gap, axisymemtric mesh, 90 deg model and (*b*) the 4-mm gap, four balance holes, 360 deg model

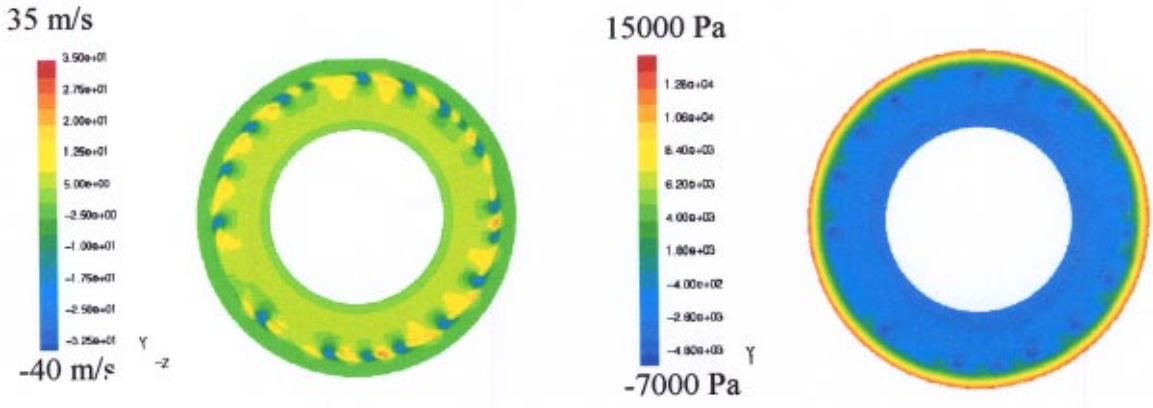

Fig. 12 Instantaneous radial velocities and pressure for the 2-mm gap, axisymmetric mesh, 360 deg model

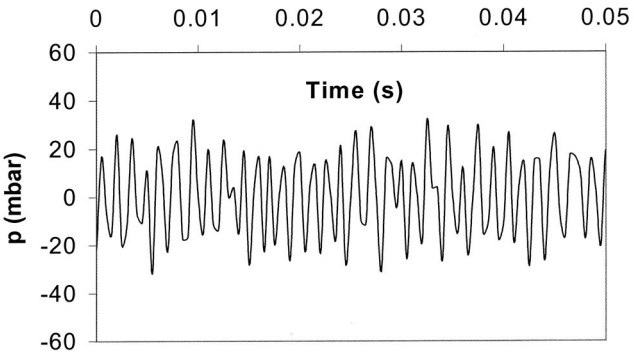

Fig. 13 Typical time trace for the filtered signal from the "root 2" transducer

The streamline plots in Fig. 8 confirm the lack of ingestion in the axisymmetric CFD results. As expected, the solution shows recirculation in the cavity due to the disk pumping effect. For a nonswirling annulus flow the pumping action might have been expected to draw flow into the cavity from the annulus, but this will be resisted by the highly swirling flow in this case. Further axisymmetric CFD solutions with the balance hole flow modeled by a slot exit in the rotating disk have shown that inclusion of the balance hole flow only affected the pressure gradient and flow structure in the inner part of the cavity. Insensitivity to the annulus hub boundary layer was also demonstrated, through a solution with the inlet hub boundary layer removed and the annulus hub wall upstream of the axial gap treated as a slip boundary.

Although not part of the present study, it is interesting to note the results of Chen [12], who did some earlier comparisons of CFD and measurements for this case. With a three-dimensional steady CFD model including one stationary vane and the disc cavity Chen also found that a CFD model of the 4-mm gap geometry gave a considerably lower cavity pressure gradient than shown by the measurements.

Time-averaged pressure predictions from the three-dimensional unsteady CFD models are compared with the measurements in Fig. 9. Checks on the numerical solutions showed that these time averages agreed with instantaneous circumferential averages. It is immediately apparent that these results for the 4-mm gap are much closer to the experimental data than the axisymmetric model. The 90 deg and 360 deg models without balance holes show very similar mean pressures although, as will be shown later, both these solutions show large-scale unsteady effects but differ in detail. The 90 deg model with balance holes shows the greatest overall pressure difference across the cavity, with the 360 deg model for the same geometry giving the best agreement with experiment. The difference between these 90 deg and 360 deg models is attributed to unsteadiness of the flow through the balance holes. The assumption of periodicity in the 90 deg model forces mass flow through all four holes to be synchronous. In the 360 deg model the balance hole flow variations are out of phase, and this reduces the overall degree of unsteadiness. CFD results for the 2-mm gap are in fair agreement with measurements, showing that the CFD models have captured the trend of ingestion decreasing as the gap is reduced.

4.2 Unsteady Flow Structure. Instantaneous pressure and radial velocity contours for the 4-mm gap, 360 deg model with an axisymmetric mesh are shown in Fig. 10. These contours are on an axial plane 0.529 mm upstream of the rotating disc. The axisymmetric contours in the outer part of the domain show the uniformity of the main annulus flow. At the rim gap, alternate regions of cavity inflow and outflow occur around the circumference. Associated pressure asymmetries are also evident. When viewed as a time series in the rotating frame these flow patterns rotate slowly in the opposite direction to the disc rotation. Thus in the absolute frame the flow patterns rotate at slightly less than disk speed. These large-scale structures are thought to arise from instability of the basic axisymmetric flow solution and are associated with interaction of the main annulus and cavity flows. They are concentrated in the region of the cavity where the axial gap is constant at 4 mm.

Figure 11(*a*) shows pressure contours on the same plane for the 4-mm gap, 90 deg model with an axisymmetric mesh. The enforced periodicity has clearly modified the structure compared to the 360 deg model, but the size of the structures are similar. As mentioned above, it appears that these differences in flow detail have little influence on the overall level of ingestion as the mean cavity pressure gradients given by the two solutions are very close. The pressure contours for the 360 deg model with balance holes again (Fig. 11(*b*)) shows some modification of the flow details but qualitatively very similar structures.

Instantaneous radial velocity and pressure contours from the 2-mm gap model are shown in Fig. 12. These show reductions in length scale and strength of the unsteady, three-dimensional effects compared to the 4-mm gap solutions. This may be associated with the reduced radial extent of the region of the cavity with minimum axial spacing as well as the change in gap. The reduction in the axial gap was expected to reduce ingestion and this effect appears to be captured by the model. Note also that the scale of the pressure asymmetries is now closer to that of the 50 vanes. For this case the pressure asymmetries due to the vanes might have as much effect on ingestion as the flow features shown in Fig. 12.

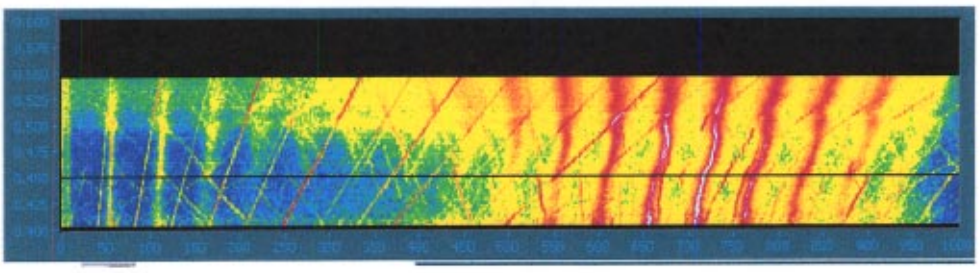

Fig. 14 Fourier analysis of results from "root 2" transducer from a run with varying rotor speed

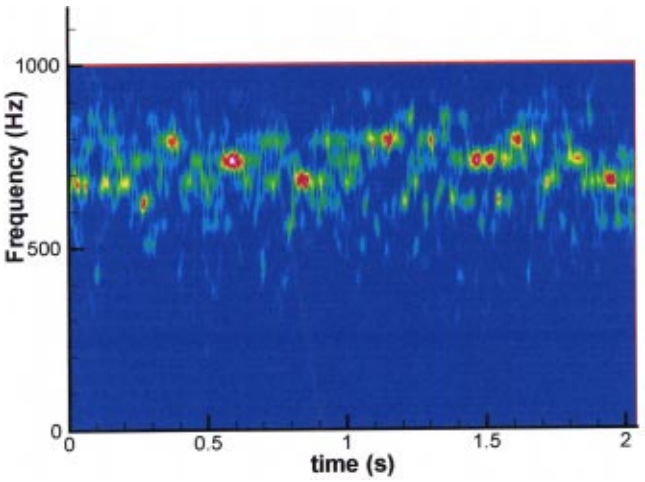

Fig. 15 Variation of intensity of frequency with time for the "root 2" transducer

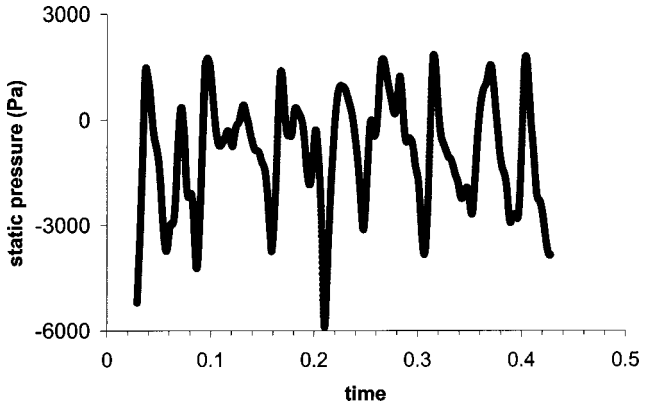

Fig. 16 Typical static pressure history (in the rotating frame) for the 360 deg, 4-mm gap model without balance holes

4.3 Unsteady Pressures. Results from the pressure transducer "root 2" (the position of which is shown in Fig. 3) are presented in Figs. 13–15. These have been processed in order to expose the low frequency events predicted by the CFD. The signals were sampled at 2000 Hz. Low pass filtering to 90% of the Nyquist frequency (i.e., 900 Hz) was undertaken prior to sampling digitally, so the signals are not influenced by frequencies above this value (for example blade passing at ~3.5 kHz). Unsteadiness in the 600 to 800 Hz range is apparent in these figures.

Figure 14 shows results for a range of rotor speeds at constant pressure level and ratio. The frequencies only increase slightly with speed, and can be compared with the engine order traces that are just visible as diagonal straight lines. Considering these and other results indicates that the frequency is a stronger function of annulus swirl velocity than rotor speed. The phase angle between measurements at different annular positions confirms that the events are rotating rather than pulsating with an angular speed slightly below the rotor speed and 11–14 events around the annulus. The unsteadiness was also found to be much stronger at the blade root positions than the rotor hub position shown in Fig. 3. The time-frequency plot in Fig. 15 suggests a degree of randomness with instabilities giving rise to a series of events in the 600 to 800 Hz frequency range. There may be a different number of events around the annulus at different times. This would concur with some of the effects seen in animations of the CFD results.

Time traces of pressure from the CFD simulations for the 4-mm and 2-mm gap, 360 deg geometries are shown in Figs. 16 and 17. These are for a reference point on the stator disc, but rotating with the frame of reference, at a radius of 304 mm. The 4-mm gap geometry of Fig. 16, corresponds to the experimental conditions, and the level of pressure variation is similar to that shown in the measurements in Fig. 13. The CFD results show some randomness (like the experiments), but the 2-mm gap CFD results are much closer to a periodic solution. The 4-mm gap, 90 deg sector model without balance holes, which are not shown here, also displayed a more periodic nature.

Comparison of experimental and CFD frequencies requires conversion between rotating and stationary frames. The speed of rotation of the flow pattern was estimated from changes over a small time period. This was not straightforward as the flow features change with time and do not all appear to move at exactly the same speed. However, in all cases examined the flow pattern tended to move (in the absolute frame) at slightly less than rotor speed, with estimates of 90 to 97% of rotor speed being typical.

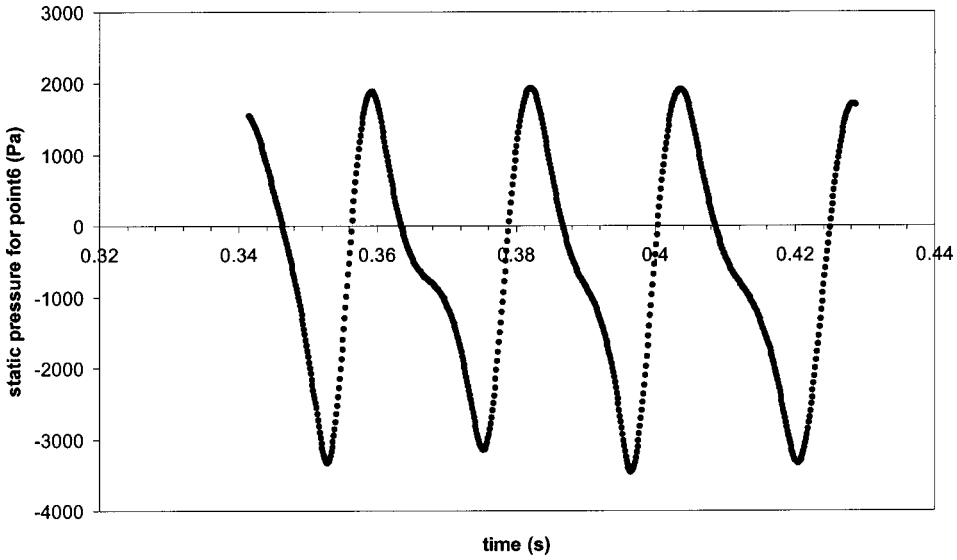

Fig. 17 Typical static pressure history (in the rotating frame) for the 360 deg, 2-mm gap model without balance holes

This is broadly in agreement with experiment. However, the observed flow patterns suggest fewer events around the circumference (say 6 to 12) than was deduced from the measurements. Combining these results it appears that the dominant frequencies given by the CFD in the stationary frame would be lower than the measured values (say about 400 to 600 Hz). Fourier analysis of the CFD results to identify the circumferential modes and tracking of these with time would give a more detailed comparison. This was attempted in one case, and better agreement with measurements was obtained, but further work would be needed to confirm this.

5 Conclusions

A combined CFD and experimental study has identified previously unknown unsteady flow features associated with interaction of rim seal and main annulus flows in an axial gas turbine. These unsteady features are clearly independent of blade passing events that have been shown in earlier studies to affect ingestion into the cavity in other geometries. The magnitude of the pressure perturbations is of order 10% of the dynamic head for the external flow, consistent with the disturbances arising from flow interaction as the rim seal and main gas path flows meet. The CFD models show that this is an incompressible flow phenomenon. The geometry considered here has a simple axial gap between rotor and stator disks with uniform cavity width at outer radii. The length scale for the disturbances may be linked to the radial extent of the uniform width region. As the gap width was reduced, keeping the same net rim seal flow, the ingestion was suppressed and the unsteadiness weakened. Although not demonstrated, it is expected that as the rim seal flow rate is increased, or the gap reduced further, the unsteadiness will be suppressed. The CFD results were obtained in advance of the unsteady pressure measurements, and so represent true predictions to a large extent. Excellent qualitative and some good quantitative agreement with measurement has been found. Time-averaged results for 90 deg sector models show largely good agreement with those for 360 deg models, although the details of the unsteady flow differ. An exception to this was the 90 deg model for the four balance holes configuration. In this case the periodic condition forced all balance hole flows to be equal at any instant, and the overall level of unsteadiness was greater than in the 360 deg model. The mesh sizes selected for the three-dimensional calculations were guided by numerical tests for axisymmetric flow, but some uncertainty as to numerical accuracy remains. Turbulence model inaccuracies may also be significant.

While identification of these unsteady effects is regarded as a significant advance in our understanding of this area, there is clearly more work that could be done. Use and development of CFD for design and research will no doubt continue to expand in this area, and so will use of fast response instrumentation. The present authors are currently investigating the particular question as to how the identified effects influence turbine efficiency.

Acknowledgments

The assistance of Dr. Nick Hills with computing issues is much appreciated. The authors also gratefully acknowledge useful discussions with many colleagues. In particular Dr. Jian-Xin Chen gave help with mesh generation and access to his initial CFD study, and Dr. David Bell, Mr. Tim Rice, and Dr. Peter Walker have given helpful input and advice.

Nomenclature

C_o = stage heat drop expressed as a velocity ($C_o^2/2$=stage specific heat drop)
C_p = pressure coefficient ($=2(p-p_o)/(\rho C_{in}^2)$)
C_w = rim seal mass flow coefficient ($=m/\mu r_o$)
C_{in} = inlet velocity
m = rim seal mass flow
p = pressure
p_o = static pressure at outer radius of disk
Re_ϕ = rotational Reynolds number ($=\rho\Omega r_o^2/\mu$)
u = moving blade root speed
r_o = outer radius of disk
μ = viscosity
ρ = density
Ω = angular velocity of rotor

References

[1] Bayley, F. J., and Owen, J. M., 1970, "The Fluid Dynamics of a Shrouded Disk System With a Radial Outflow of Coolant," ASME J. Eng. Power, **92**, pp. 335–341.
[2] Campbell, D. A., 1978, "Gas Turbine Disc Sealing System Design," Proc. AGARD conf. On Seal technology in Gas Turbine Engines, AGARD-CP-237.
[3] Bohn, D., Rudzinsky, B., Surken, N., and Gartner, W., 2000, "Experimental and Numerical Investigation of the Influence of Rotor Blades on Hot Gas Ingestion Into the Upstream Cavity of an Axial Turbine Stage," ASME Paper 2000-GT-284.
[4] Roy, R. P., Xu, G., Feng, J., and Kang, S., 2001, "Pressure Field and Main Stream Gas Ingestion in a Rotor Stator Disc Cavity," ASME Paper 2001-GT-564.
[5] Hills, N. J., Chew, J. W., and Turner, A. B., 2002, "Computational and Mathematical Modelling of Turbine Rim Seal Ingestion," ASME J. Turbomach., **124**, pp. 306–315.
[6] Gentilhomme, O., Hills, N. J., Chew, J. W., and Turner, A. B., 2002, "Measurement and Analysis of Ingestion Through a Turbine Rim Seal," ASME Paper GT-2002-30481.
[7] Smout, P. D., Chew, J. W., and Childs, P. R. N., 2002, "ICAS-GT: A European Collaborative Program on Internal Cooling Air Systems for Gas Turbines," ASME Paper GT-2002-30479.
[8] Bohn, D., Decker, A., and Wolff, M., 2003, "Influence of Sealing Air Mass Flow on the Unsteady Hot Gas Ingestion in the Upstream Cavity of a 1.5 Stage Turbine," proposed for ASME Turbo Expo.
[9] Autef, V., 2002, "Computation of Disc Cavity Rim Sealing," University of Surrey/Institut National Polytechnique de Grenoble project report.
[10] Chew, J. W., Hills, N. J., Hornsby, C., and Young, C., 2003, "Recent Developments in Application of CFD to Turbomachinery Internal Air Systems," submitted to the 5th European Turbomachinery Conf., Prague, March.
[11] Fluent Inc. http://www.fluent.com.
[12] Chen, J.-X., 2001, Alstom internal report, Whetstone, UK.

Development of a Two-Dimensional Computational Fluid Dynamics Approach for Computing Three-Dimensional Honeycomb Labyrinth Leakage

Dong-Chun Choi
Graduate Research Assistant

David L. Rhode
Professor

Mechanical Engineering Department,
Texas A&M University,
College Station, TX 77843

A new approach for employing a two-dimensional computational fluid dynamics (CFD) model to approximately compute a three-dimensional flow field such as that in a honeycomb labyrinth seal was developed. The advantage of this approach is that it greatly reduces the computer resource requirement needed to obtain a solution of the leakage for the three-dimensional flow through a honeycomb labyrinth. After the leakage through the stepped labyrinth seal was measured, it was used in numerically determining the value of one dimension (DTF1) of the simplified geometry two-dimensional approximate CFD model. Then the capability of the two-dimensional model approach was demonstrated by using it to compute the three-dimensional flow that had been measured at different operating conditions, and in some cases different distance to contact values. It was found that very close agreement with measurements was obtained in all cases, except for that of intermediate clearance and distance to contact for two sets of upstream and downstream pressure. The two-dimensional approach developed here offers interesting benefits relative to conventional algebraic-equation models, particularly for evaluating labyrinth geometries/operating conditions that are different from that of the data employed in developing the algebraic model. [DOI: 10.1115/1.1772405]

Introduction

The labyrinth seal is a noncontacting seal, and the major advantages of this seal are its; (a) simplicity, (b) reliability, (c) tolerance to dirty conditions, (d) system adaptability, (e) typically minimum effect on rotor dynamics, (f) lack of pressure limitations, (g) material selection flexibility, and (h) tolerance to large thermal and pressure variations. Because of the above advantages labyrinth seals have been used widely in turbomachinery. Labyrinth seals can be used to: (a) reduce the seal leakage flow, (b) control coolant flow for thermal reliability, or (c) prevent contaminants from entering a bearing chamber. Labyrinth seals work on the principle that fluid pressure energy is converted at each tooth tip clearance into kinetic energy that is either dissipated into heat by turbulence or enters the subsequent tooth clearance by kinetic energy carryover.

An optimization process for the labyrinth seal is required to obtain an efficient design of a new gas turbine engine. To reduce energy losses the labyrinth leakage must be minimized without starving the coolant flow to each component that is needed for thermal reliability. Therefore it is important to know accurately the leakage of many labyrinth alternatives over the increasingly wider range of operating conditions found in new engines.

Many years ago the basic fluid flow and thermodynamics details were discussed by Martin [1], Egli [2], and Kearton [3], among others. More recently a substantial number of investigators have studied several labyrinth aspects and parameters. Examples are: Stocker [4], Schramm et al. [5], Rhode et al. [6], Prasad et al. [7], Zimmerman et al. [8], Demko et al. [9], Brownell et al. [10], Bill and Shiembob [11], and Stoff [12]. Specifically, Stocker [4] used both two-dimensional planar as well as three-dimensional rotating seal test rigs to measure the air leakage through labyrinths with honeycomb, abradable, or solid stator walls. For a straight-through labyrinth with four teeth he found large increases of leakage relative to the solid wall for honeycomb at small tooth clearances. Recently Schramm et al. [5] obtained CFD results from a commercial code showing the leakage flow entering the honeycomb cells. They also found agreement with LDV measurements regarding the presence of a three-dimensional velocity field near the tooth tips. Regarding the effect of rub-grooves formed into an abradable surface, Rhode and Allen [6] obtained flow visualization digital images for large-scale stepped labyrinths that explain the effects on leakage that were measured. Further, Rhode and Adams [13] applied their in-house CFD code for better understanding of rub-groove effects on stepped labyrinths. Other details for rub-groove effects on straight-through labyrinths are found in Rhode and Allen [14]. In addition, cases with tooth tips located inside the rub-grooves were recently investigated experimentally by Denecke et al. [15] for stepped as well as straight-through labyrinths.

With today's computers and commercially available CFD codes, two-dimensional axisymmetric CFD is quite practical for obtaining enough solutions to gain, for example: (a) new flow field details, (b) new flow field overall insight, (c) a reduced number of experiments, (d) better interpretation of ambiguous measurements, (e) better design of experiments, etc. However, many geometries are inherently three-dimensional and it has therefore been assumed that a three-dimensional CFD model is required for such situations. Obviously, the use of two-dimensional axisymmetric CFD models compared to three-dimensional models has a huge impact on the practicalities of using CFD. An approach for approximately computing, without objectionable error, the three-

Contributed by the International Gas Turbine Institute (IGTI) of THE AMERICAN SOCIETY OF MECHANICAL ENGINEERS for publication in the ASME JOURNAL OF ENGINEERING FOR GAS TURBINES AND POWER. Paper presented at the International Gas Turbine and Aeroengine Congress and Exhibition, Atlanta, GA, June 16–19, 2003, Paper No. 2003-GT-38238. Manuscript received by IGTI, Oct. 2002, final revision, Mar. 2003. Associate Editor: H. R. Simmons.

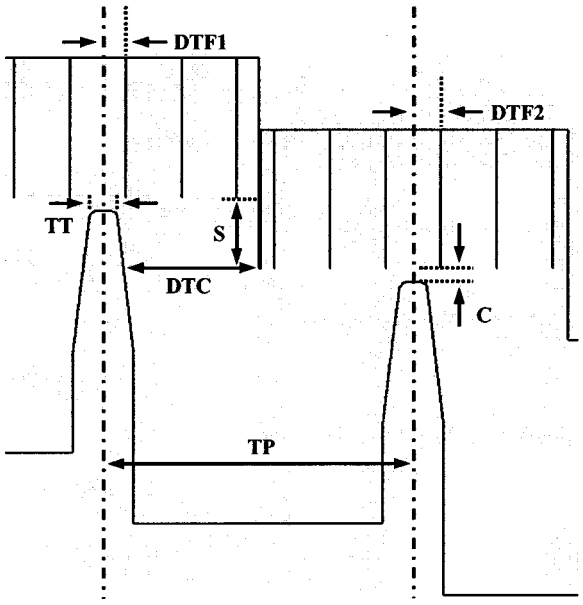

Fig. 1 Configuration and nomenclature of the stepped labyrinth considered (C/TT=0.20, 0.33, 0.50, DTF1/TT=0.57–1.05, DTF2/TT=1.05, 2.10, S/TT=2.67, DTC/TT=2.50, 5.83, 9.17, TP/TT=11.67, TT=0.762 mm)

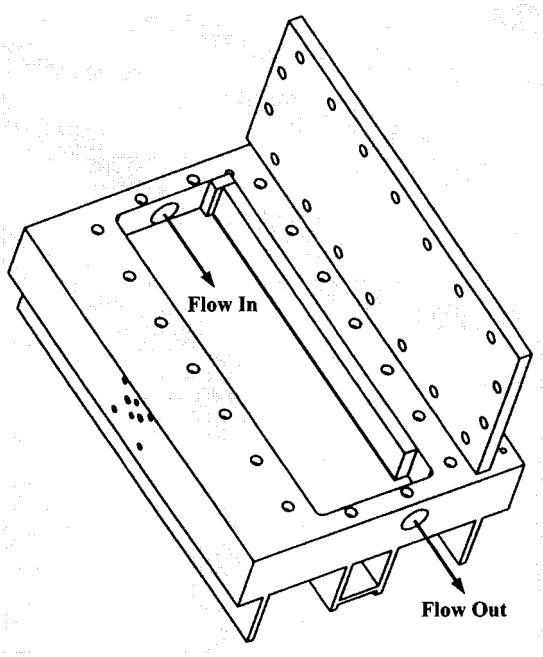

Fig. 2 Test section of the two-dimensional experimental facility

dimensional flow field using a two-dimensional CFD model will facilitate technical breakthroughs in many different fields of engineering and science.

The three-dimensional honeycomb matrix of a labyrinth seal provided the motivation for developing a two-dimensional axisymmetric CFD approach for approximately computing three-dimensional flow fields. Specifically, simple Martin-type [1] (i.e., algebraic-equation) seal leakage models for routine engine design sometimes give substantial leakage errors for seals with and without honeycomb. This is partly attributable to the use of data, a percentage of which is at laboratory (rather than at engine) pressure and temperature. It is also partly attributable to the fact that simple models must rely almost entirely on empirical curve fits and/or constants. Thus such simple models generally have a much narrower range of applicability than do CFD models. Particularly when developing a labyrinth seal with geometry and/or operating conditions that are different from that from which the model was developed, the two-dimensional CFD approach developed here will be very attractive.

Figure 1 shows the configuration and nomenclature of the stepped labyrinth seal considered in this study.

Objective

The objective of the present investigation is to: (a) measure the leakage through a simple labyrinth seal with honeycomb cells of two sizes (three-dimensional geometry), (b) use the labyrinth measurements to develop an approach for approximately computing the three-dimensional flow using a two-dimensional axisymmetric CFD model and (c) demonstrate the capability of the new approach by comparison with measurements at different conditions from that for which the two-dimensional approach was developed.

Experimental Facility

The air leakage seal facility (Fig. 2) allows easy installation of an extremely wide range of easily fabricated stator and rotor specimens in the test section housing. The upper specimen in the test section, with or without the honeycomb structure (honeycomb pitch of 3.2 mm or 1.6 mm), represents the stator and the lower one with the teeth represents the rotor. To ensure accurate positioning of the stator and rotor specimens, the test rig used two dowel pins for each specimen. In addition, it has extremely stiff (e.g., 150-mm thickness) walls in order to avoid a change in seal clearance and/or tooth axial position caused by pressurizing the test section.

The air was supplied by a compressor to the test section inlet. The upstream air pressure was controlled according to the test conditions by a pressure regulator and the upstream temperature was maintained at room temperature of approximately 294 K. Two stages of perforated plate were placed at the rig inlet as a turbulence settling chamber and to provide a uniform inlet velocity. For precise control of the seal radial clearance and axial tooth position shims were used.

An axial turbine flow meter of high accuracy and repeatability, ± 0.3 and $\pm 0.1\%$, respectively, was used to obtain the seal leakage flow rate. Two high accuracy, $\pm 0.25\%$, differential pressure transducers were used to measure the upstream and downstream test section pressures. Also an accurate temperature transducer was installed at the upstream chamber to obtain the inlet temperature.

The advantages of using two-dimensional planar seal test rigs for leakage measurement have been understood for many years. Specifically, measurement reliability employing two-dimensional planar specimens is easier to achieve due to the absence of centrifugal and thermal growth effects, for example. Thus small variations in leakage can be easily observed. The validity of the two-dimensional planar approach has been experimentally verified by numerous investigators (Stocker [4], Stoff [12], and Waschka et al. [16]). In particular, experimental verification using stepped labyrinths was conducted by Stocker [4], who found leakage variations of only about 1.7% on average between two-dimensional planar rig tests and corresponding rotating rig tests.

Numerical Model

The commercial finite volume CFD code STAR-CD was used to simulate the labyrinth seal flow with parallel processing to reduce the computational time. This code solves the compressible, Reynolds-averaged Navier-Stockes equations employing an advanced algorithm based on the well known SIMPLE algorithm

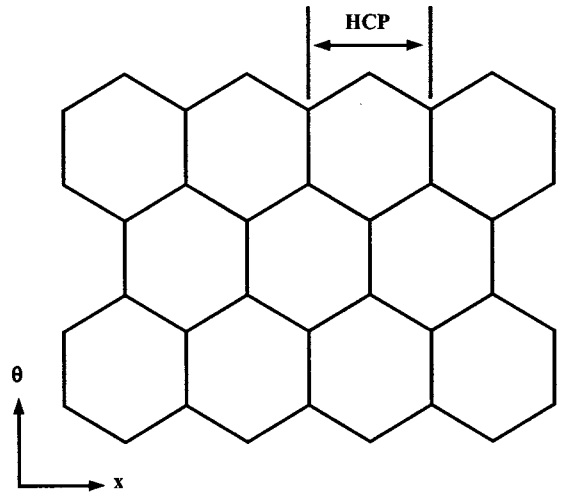

(a) Actual hexagonal honeycomb

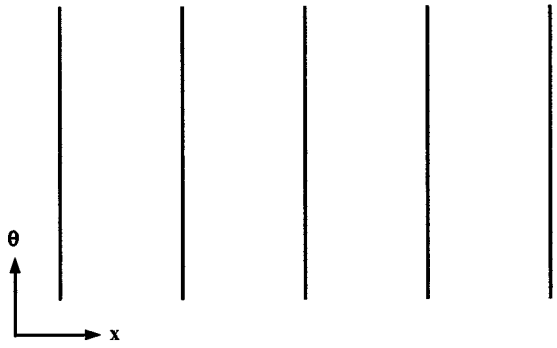

(b) New axisymmetric-CFD honeycomb model

Fig. 3 Honeycomb configuration for (*a*) the actual hexagonal honeycomb hardware and (*b*) the new two-dimensional axisymmetric approximation of the actual hexagonal honeycomb

(Patankar [17]). The meshes were nonorthogonal, body-fitted, structured grids with the collocated arrangement of variables. The high Reynolds number k-ε turbulent model (El Tahry [18]) was used. The standard wall function was used to describe the near wall velocity profile, and therefore the near wall grid was carefully monitored to ensure the proper range of y^+. The overall y^+ range was 12–90 for important geometry regions, however the y^+ values were lower in some unimportant regions inside the honeycomb far away from the tooth tip. But as shown in the previous research (Rhode et al. [19], Rhode et al. [13], Wittig et al. [20], and Schramm et al. [5]), this turbulent model using standard wall function was quite reasonable in simulating labyrinth seal flow.

In this research the geometry was simulated using a two-dimensional axisymmetric CFD model with baffles (zero-thickness two-dimensional fins) to describe the thin honeycomb walls. It was impossible to get a converged solution for some cases if the honeycomb fin was described as three-dimensional cells with thickness. The assumption of zero thickness for the fin is reasonable because honeycomb wall thickness is extremely thin compared to the honeycomb cell pitch HCP (see Fig. 3). Consequently the baffle can eliminate a large number of numerical cells. The properties of this baffle is similar to that of a solid wall, and this baffle cell can be placed between any two fluid or solid cells. Because of the difficulty of CFD cell connectivity at the interface

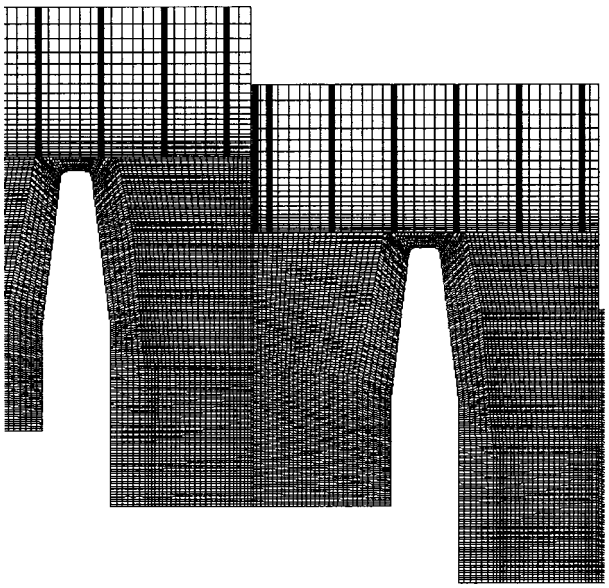

Fig. 4 Representative grid showing the two-dimensional axisymmetric approximate honeycomb fins

between honeycomb and labyrinth CFD cell faces, the arbitrary cell connectivity method was used during the mesh building operation. This kind of connectivity can be encountered at the interface between blocks of differing mesh structure, and it serves to connect the honeycomb and labyrinth cells in the current geometry. For improved numerical accuracy over a given portion of the solution domain, the embedded mesh refinement by internal subdivision of the coarse mesh for the honeycomb region was used.

Figure 4 shows the computational domain for the current study, and the grid consists of almost 33,000 cells. To ensure grid independence, additional testing with grids containing 152×23 and 78×23 cells for only the honeycomb region was considered. The result showed that the coarse computational grid gives only a 3% larger leakage than the refined one. Therefore 78×23 cells were used for honeycomb region.

On the stator and rotor walls no-slip, adiabatic, smooth surfaces were specified as boundary conditions. At the domain inlet, pressure and temperature were specified and at the outlet the pressure was specified. Also the turbulence intensity and length scale were specified for the inlet. To simulate the two-dimensional axisymmetric geometry the symmetric boundary conditions were specified in theta direction.

Two-Dimensional Approach for Three-Dimensional Flows

The two-dimensional CFD approach developed here is easily applied to other fluid flows throughout many fields of engineering and science. The development of the new two-dimensional approach involved the following four basic procedural steps in general terms:

(1) As a reasonable approximation choose a two-dimensional geometry (i.e., a simplified version of the three-dimensional geometry) that retains most of the flow characteristics of the actual three-dimensional geometry and has one unknown geometric dimension of significant importance.

(2) Divide the range of geometries to be considered into a few categories.

(3) Obtain a few two-dimensional approximate solutions of the simplified two-dimensional geometry to determine the unknown geometric dimension for each category that gives best agreement with measurements of the three-dimensional geometry.

(4) At different conditions from that of Step 3, obtain additional two-dimensional solutions to determine the capability (i.e., agreement with measurements) for the current choice of categories.

(5) If necessary further sub-divide the range of three-dimensional geometries into more categories, and repeat Steps 3 and 4 for each new category.

(6) Use a two-dimensional CFD model to compute the performance of the actual three-dimensional hardware design.

For the current labyrinth seal application, the three-dimensional geometry was simplified by replacing the actual hexagonal-cell matrix of Fig. 3(*a*) with a series of fins that are straight and continuous in the circumferential direction, as shown in Fig. 3(*b*). For such a stepped labyrinth it is necessary to properly fix the radial height of the honeycomb step at the proper axial location, and this was done by consistently placing an auxiliary honeycomb fin at the step axial location. Secondly, the axial distance from the center of each of the first and second labyrinth teeth (i.e., knives) to the nearest honeycomb fin (DTF1 and DTF2), along with the radial-distance clearance *C*, are very important geometric dimensions. Based on preliminary results showing that the leakage is too sensitive to DTF2, it was decided that DTF2 would be a constant with a value of half of the honeycomb matrix pitch (HCP in Fig. 3(*a*)) as shown in Figs. 1 and 4. It was further decided that DTF1 would be the unknown geometric dimension to be determined in Step 3 above. Note that the distance to contact DTC should not be used as the Step 3 geometric dimension because the leakage is not sufficiently sensitive to the DTC. In addition, changing the number of fins (see Fig. 3(*b*)) for the Step 3 geometric dimension would not work because this changes the design (i.e., the HCP) that is to be computed. Thus DTF1 should be interpreted as a computer-model-only geometric variable (i.e., not an actual design variable) that ''calibrates'' a two-dimensional CFD model to three-dimensional measurements. Stated differently, a change of DTF1 of the two-dimensional simplified geometry of Steps 1–4 has no effect on the seal design, but only changes the simplified two-dimensional domain and grid of the seal design.

The categories selected for Step 2 are defined by the clearance *C* and the honeycomb pitch HCP. Specifically, the six categories selected are: (*a*) $C=0.15$ mm and HCP=1.6 mm, (*b*) $C=0.15$ mm and HCP=3.2 mm, (*c*) $C=0.25$ mm and HCP=1.6 mm, (*d*) $C=0.25$ mm and HCP=3.2 mm, (*e*) $C=0.38$ mm and HCP=1.6 mm, and (*f*) $C=0.38$ mm and HCP=3.2 mm. The leakage solutions of Step 3 are given in Fig. 5 for all six categories. As expected from earlier work, DTF1 is less sensitive to HCP as C increases. For example at $C=0.38$ mm, observe in Fig. 5 that both honeycomb pitch values give DTF1 of about 0.64 mm.

To verify that DTF1 is not particularly sensitive to the operating condition, DTF1 was evaluated again for a higher pressure drop for the case of $C=0.15$ mm and HCP=1.6 mm. The leakage solutions are shown in Fig. 6 for comparison with that in Fig. 5. Observe that there is almost no difference in DTF1 as expected. The recommended values of DTF1 that were interpolated from Fig. 5 are given in Fig. 7 for user convenience.

Agreement With Measurements

The Cases Considered. The measurements and the corresponding computations were obtained for a stepped labyrinth configuration with: (a) step height $S=2.03$ mm, (b) tooth pitch $TP=8.89$ mm, (c) tooth tip thickness $TT=0.762$ mm, (d) honeycomb pitch HCP=1.6 mm or 3.2 mm, (e) and tooth clearance $C=0.15$ mm, 0.25 mm or 0.38 mm, and (f) distance to contact DTC=1.9 mm, 4.4 mm, or 7.0 mm. The tooth tip thickness considered is representative of that after the hardness coating (used in many gas turbines) is applied to the tooth tips. The number of the two-dimensional simplified honeycomb fins (see Fig. 3(*b*)) between the teeth for the HCP=1.6 mm and 3.2 mm cases is 5 and 3, respectively.

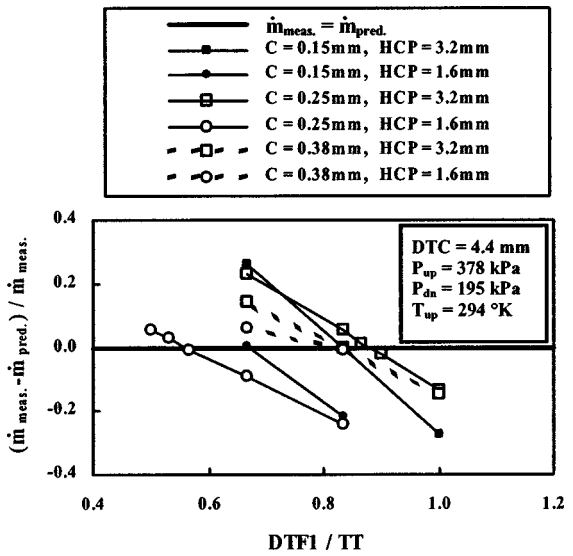

Fig. 5 Leakage solutions found in determining the DTF1 value for the two-dimensional axisymmetric CFD approach for $P_{up}=378$ kPa

Martin-Type Algebraic Models. Many versions of a simple algebraic model are in common usage for routine design of such seals. These generally were derived from the well-known Martin equation, [1]. The basic equation for the non-straight-through (i.e., stepped) labyrinth proposed by Egli [2] for example is

$$\dot{m} = A\alpha\varphi\sqrt{P_{up}/\nu_{up}}$$

where

$$\varphi = \sqrt{\frac{1-(P_{dn}/P_{up})^2}{N+\ln(P_{up}/P_{dn})}}$$

and the Gercke's [21] equation for the stepped labyrinth is

$$\dot{m} = \alpha\sqrt{\frac{P_{up}[1-(P_{dn}/P_{up})^2]}{\nu_{up}\left[\int_0^N \frac{1}{A^2}dx + \frac{1}{A_0A_n}\ln\left(\frac{A_0P_{up}}{A_nP_{dn}}\right)\right]}}.$$

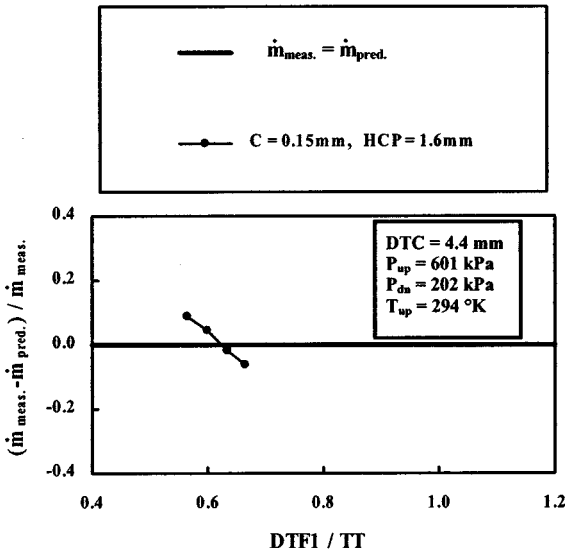

Fig. 6 Leakage solutions found in determining the DTF1 value for the higher upstream pressure of $P_{up}=601$ kPa

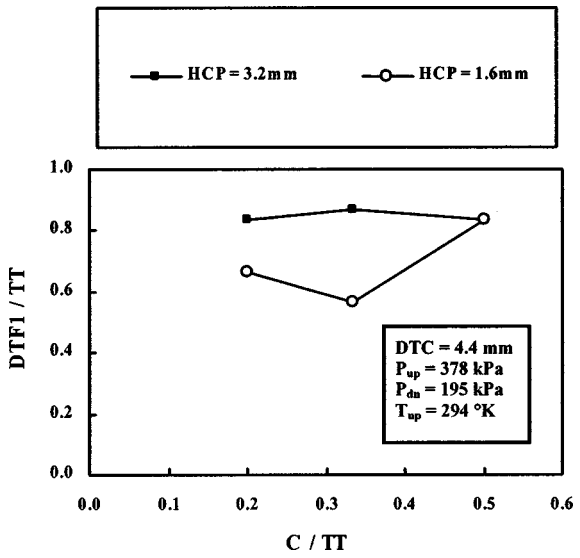

Fig. 7 Recommended values of DTF1 for application of the new two-dimensional CFD approach

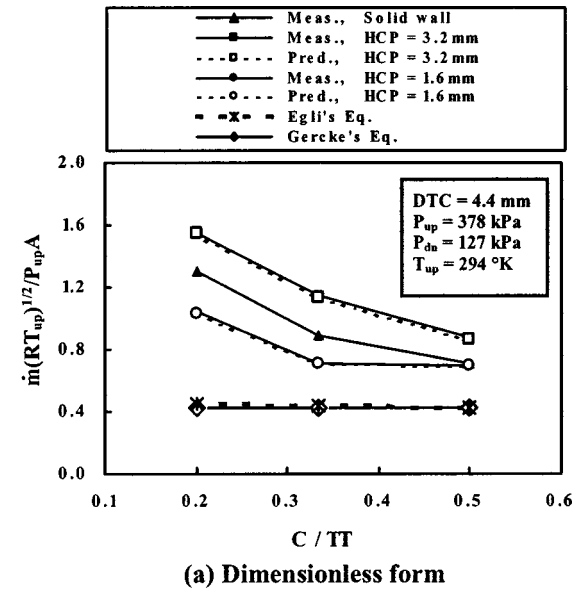

(a) Dimensionless form

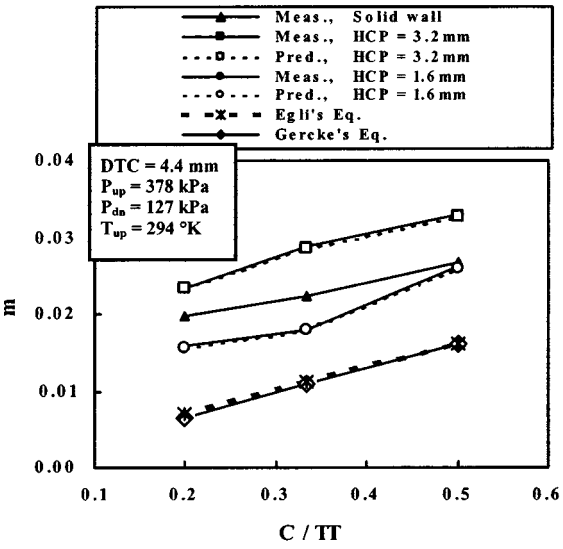

(b) Dimensional form

Fig. 8 Capability demonstration of the new two-dimensional CFD approach for various clearances and DTC=4.4 mm with P_{up}=378 kPa and P_{dn}=127 kPa

The kinetic energy carryover factor has been assumed as 1.0 for the Egli's equation, as it is generally assumed that the kinetic energy of the through-flow jet does not ''shoot through'' to the subsequent tooth clearance. Egli's model is based on the flow coefficient (or equivalent) curves that were extracted from measurements and Gercke recommended the flow coefficient as about 0.8. Naturally, for such simple algebraic models, when an operating condition or seal geometry outside the range for which the flow coefficient was experimentally determined is encountered, additional measurements and the subsequent flow coefficient data are needed.

Discussion. A very large number of computations using the DTF1 value for each of the six geometric categories of Fig. 7 were employed in a series of computations. These computations were obtained in order to demonstrate the capability of the two-dimensional approach developed herein. The first comparison series is shown in Fig. 8(*a*) in terms of the flow parameter (i.e., the dimensionless mass flow per unit area) and in Fig. 8(*b*) in terms of mass flow rate. Note that for every demonstration case in Figs. 8 and 10–15 the pressure drop (along with other conditions in some cases) is clearly different from that used to evaluate DTF1. Observe in Fig. 8 for axial distance to contact DTC=4.4 mm (i.e., the centered rotor axial position shown in Fig. 1) that for all six geometry categories of Fig. 7 the two-dimensional approach gives excellent agreement with measurements. Recall that the flow parameter is known to decrease as the clearance increases because of a well known vena contracta effect. Specifically, this effect is that the ratio of leakage jet minimum flow area to the geometric area at a tooth throttle is known to decrease as the tooth clearance increases. Also Figs. 8(*a*) and 8(*b*) show that Egli's and Gercke's models underpredict the measured leakage at the small clearance by 60% and 71% for HCP=1.6 mm and 3.2 mm, respectively. Naturally there are many important differences between these models and the present CFD model. For example, for such simple algebraic models the leakage is very sensitive to the flow coefficient curve, whereas for the proposed two-dimensional CFD approach the leakage is substantially less sensitive to DTF1. Also, recall that CFD is based on the complete Reynolds-averaged Navier-Stockes and turbulence transport equations rather than the simple Martin-type algebraic equation to give more realistic local distributions of each flow quantity. In addition, unlike Egli's and Gercke's models the CFD model includes the following: TP, TT, HCP, honeycomb cell depth, tooth edge rounding, and local variations of turbulence velocity and length scale.

Further, for each clearance the measured leakage increases substantially in the order of: (a) small cell honeycomb (smallest leakage), (b) solid (nonhoneycomb) wall, and (c) large cell honeycomb (largest leakage). Because the cell width of the large cell honeycomb (HCP=3.2 mm) is much larger than the tooth tip thickness (TT=0.762 mm), at the small clearances considered here the leakage jet penetrates into the honeycomb cell opposite of a tooth tip to give an increased effective flow area (see Fig. 9 for a similar case with HCP=1.6 mm). Therefore it is not surprising that the large cell size gives higher leakage than does the solid wall surface. Further, note that the small cell honeycomb gives significantly less leakage than does the solid wall. This is attributed to the increased overall turbulent friction that is expected with the increased number of honeycomb cells. Specifically, each honeycomb cell is the origin of a localized turbulent shear layer,

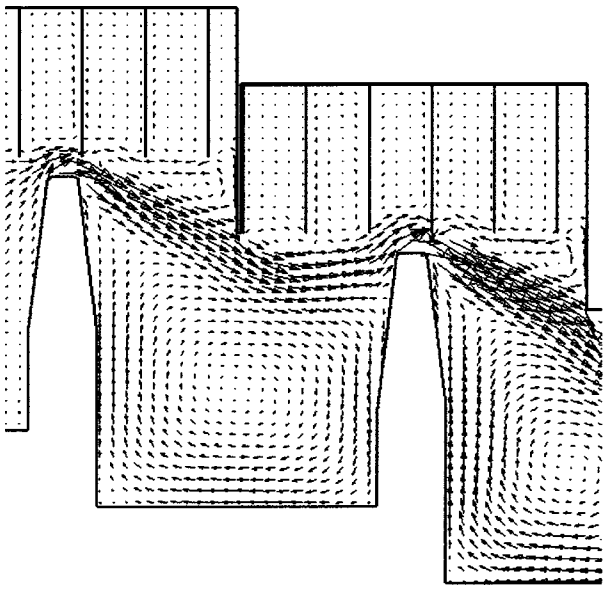

Fig. 9 Flow pattern example for a case where the two-dimensional axisymmetric honeycomb fin is not axially aligned with the tooth

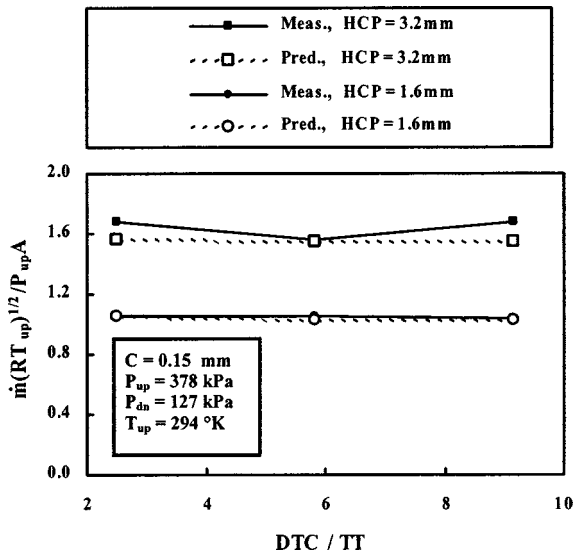

Fig. 11 Capability demonstration of the new two-dimensional CFD approach for various DTC values and $C=0.15$ mm with $P_{up}=378$ kPa and $P_{dn}=127$ kPa

the beginning of which is known to exhibit an intense local turbulent shear stress. In addition, at the large clearance of 0.38 mm it appears that the small cell honeycomb gives essentially the same overall turbulent friction as the solid wall, because it gives essentially the same mass flow as does the solid wall.

For a lower pressure difference and DTC=4.4 mm, Fig. 10 shows that very close agreement with measurements is found again. Also the same effect of large cell and small cell honeycomb relative to the solid wall is found.

Figures 11–13 demonstrate, for clearances of 0.15 mm, 0.25 mm, and 0.38 mm, respectively, the capability of the two-dimensional approach over a wide range of DTC values, as well as different pressure values from that used to determine the DTF1 values. For the smallest clearance, Fig. 11 shows very close agreement with measurements for all three DTC values with the small cell honeycomb as well as for DTC=4.4 mm with the large cell honeycomb. Further, for both of the extreme values of DTC with large cell honeycomb the two-dimensional approach underpredicts the measurement by only about 8%. For the intermediate clearance of 0.25 mm shown in Fig. 12, excellent agreement with measurements was found for all DTC values with the large cell size as well as for the small cell size. At the large clearance of 0.38 mm in Fig. 13, excellent agreement is again found for all six cases.

To demonstrate the two-dimensional capability at higher supply air density and overall pressure drop, Figs. 14 and 15 give additional comparisons for the small cell honeycomb. At $P_{up}=601$ kPa and $P_{dn}=202$ kPa Fig. 14 shows very close agreement with measurements except for the case with intermediate clearance and intermediate DTC. Note that the latter sole case exhibiting significant discrepancy with the measurements showed excellent agreement with the measurements in Fig. 12 at $P_{up}=378$ kPa and $P_{dn}=127$ kPa.

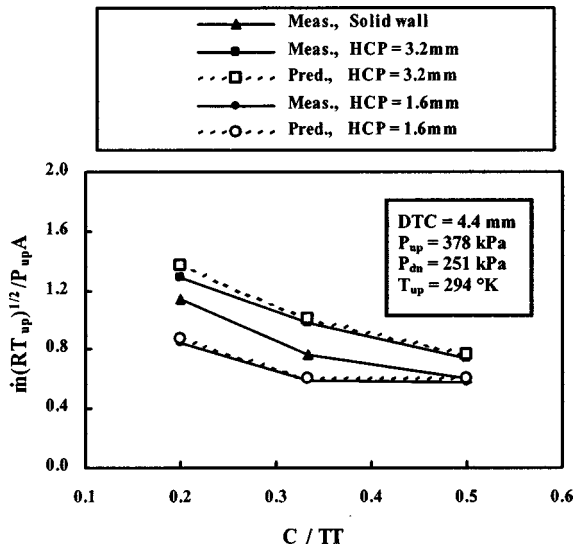

Fig. 10 Capability demonstration of the new two-dimensional CFD approach for various clearances and DTC=4.4 mm with $P_{up}=378$ kPa and $P_{dn}=251$ kPa

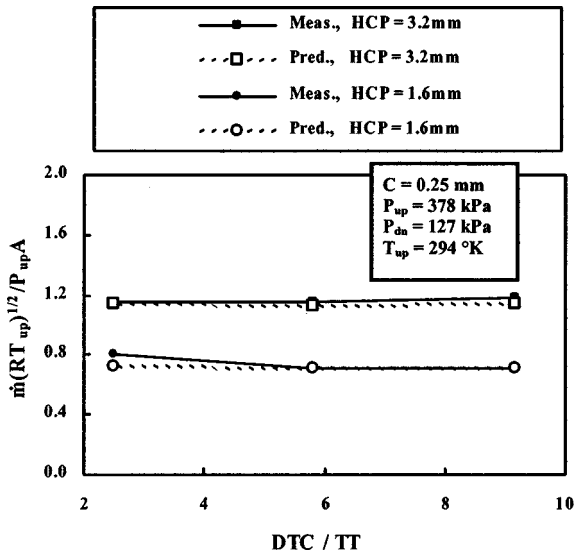

Fig. 12 Capability demonstration of the new two-dimensional CFD approach for various DTC values and $C=0.25$ mm with $P_{up}=378$ kPa and $P_{dn}=127$ kPa

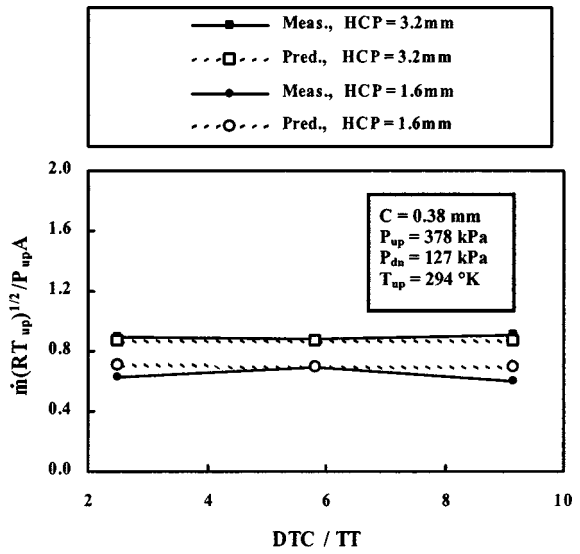

Fig. 13 Capability demonstration of the new two-dimensional CFD approach for various DTC values and $C=0.38$ mm with $P_{up}=378$ kPa and $P_{dn}=127$ kPa

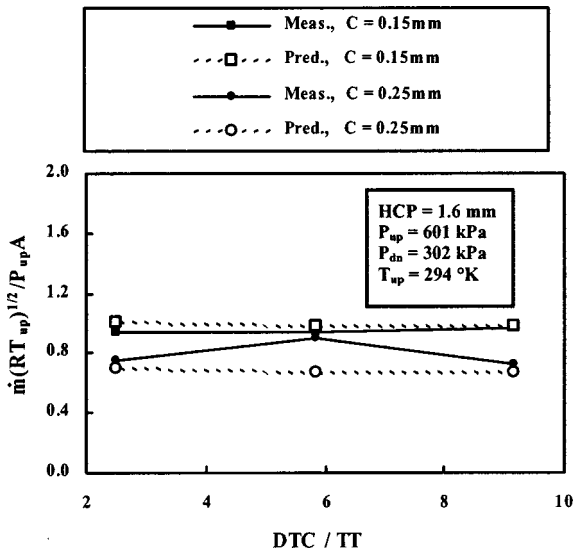

Fig. 15 Capability demonstration of the new two-dimensional CFD approach for various values of DTC and clearance with $P_{up}=601$ kPa and $P_{dn}=302$ kPa

Yet another set of pressures, $P_{up}=601$ kPa and $P_{dn}=302$ kPa, was used for the test cases of Fig. 15, which show essentially the same agreement with measurements as does Fig. 14. Observe for these pressures that, like Fig. 14, the case of intermediate clearance and intermediate DTC gives significant discrepancy, whereas that in Fig. 12 did not show it. Because this anomaly was found only at the higher P_{up} of 601 kPa and at the intermediate clearance, perhaps it can be attributed to Reynolds number effects that could not be captured by the turbulence model. Recall that measurements of such strongly recirculating turbulent flows are well known to exhibit unexpected effects at certain operating conditions. In summary, the new approach certainly shows significantly improved reliability over that of the Martin-type of leakage model (see Fig. 8 for an example).

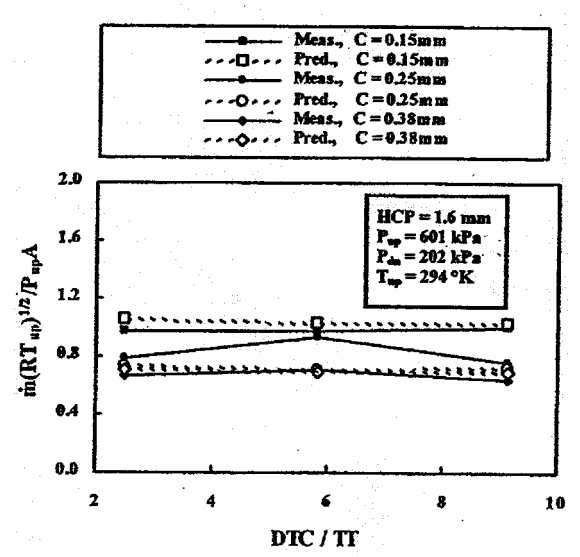

Fig. 14 Capability demonstration of the new two-dimensional CFD approach for various values of DTC and clearance with $P_{up}=601$ kPa and $P_{dn}=202$ kPa

It appears that the new approach demonstrated herein is very attractive. Further, when a new geometry category is encountered, measurements or reliable three-dimensional computations would naturally need to be obtained before the new approach can be applied. Although not included here, it is firmly believed that the reliability of the new approach for predicting seal exit swirl (heat transfer situations) will be considerably better than that of Martin-type algebraic models.

Figures 1 and 3 suggest that the local honeycomb geometry variations, i.e. circumferential variation of the hexagonal honeycomb cell walls, cause corresponding circumferential variations of the flow, especially at a tooth clearance. Specifically, at some circumferential locations a honeycomb fin is fairly well aligned with the tooth tip as shown in Fig. 16, and at other locations it will be more like that of Fig. 9. Comparison of the flow patterns shown in these figures gives an estimate of the degree of circumferential variation of the flow pattern. These flow patterns are very similar to that measured with an LDV by Schramm et al. [5] for a similar stepped honeycomb labyrinth.

Note in Fig. 16 that the leakage jet traverses the first tooth throttle with a somewhat radially inward (i.e., downward in Fig. 16) direction. Further, observe that the jet is immediately redirected slightly in the radially outward direction. This redirection results from the high-speed leakage jet entraining air from within the honeycomb cell near the downstream edge of the tooth tip. This entrainment of air from the honeycomb hexagonal cell into the leakage jet causes a slightly lowered pressure within the honeycomb cell, resulting in a pressure force that slightly re-directs the jet radially outward where it contacts the tip of the honeycomb fin immediately downstream. In addition, notice that circumferential locations exhibiting honeycomb fins positioned like that of Fig. 16 will give a somewhat different overall flow pattern from that of Fig. 9 as shown. In this case the leakage jet traversing the first tooth throttle impacts the tip of the honeycomb fin in such a way that the jet is re-directed more directly toward the radially inner corner of the step face.

Comparison of Figs. 16 and 17 shows the effect of a large change of DTC. Specifically, in Fig. 17 the major obstruction of the vertical face of the radial step formed in the honeycomb dramatically diverts the jet radially inward. The diverted jet reaches the rotor base of the cavity (horizontal surface between the teeth)

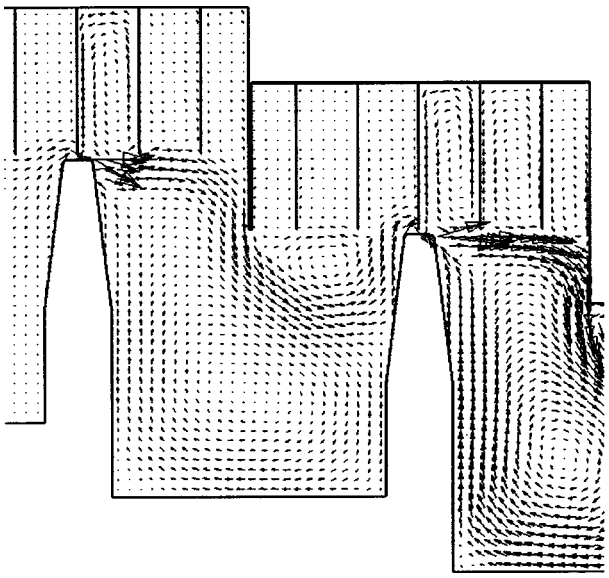

Fig. 16 Flow pattern example for a case where the two-dimensional axisymmetric honeycomb fin is axially aligned with the tooth DTC=4.4 mm

where it is diverted in the radially outward direction toward the second tooth throttle.

Summary and Conclusion

The following items summarize the current investigation:

1 Leakage measurements were obtained for two commonly used honeycomb cell sizes in a simple labyrinth seal.

2 The measurements were employed to develop a new two-dimensional approach for approximately computing the three-dimensional flow through honeycomb labyrinth seals.

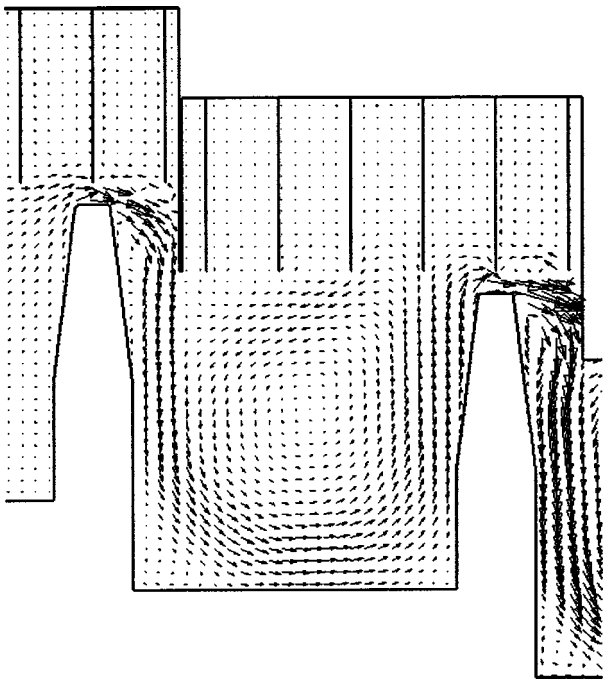

Fig. 17 Flow pattern example for a case where the two-dimensional axisymmetric honeycomb fin is axially aligned with the tooth and DTC=1.9 mm

3 The good capability of the new two-dimensional approach was demonstrated employing different operating conditions than that used for model development.

4 The two-dimensional CFD approach appears to offer interesting benefits relative to conventional Martin-type algebraic-equation models, particularly for labyrinth geometries/operating conditions that are different from that from which the algebraic models were developed. The Martin-type models by Egli and Gercke underpredict the leakage by a much larger margin (60% and 71% for HCP=1.6 mm and 3.2 mm, respectively, in Figs. 8(*a*) and 8(*b*)) than does the proposed two-dimensional CFD approach.

5 Based on two-dimensional solutions for different honeycomb fin positions (Figs. 9 and 16), the expected circumferential variation of flow pattern due to the circumferential variation of the honeycomb cell hexagonal walls near a tooth was presented.

6 A flow pattern that is much different from that commonly experienced was illustrated in Fig. 17 for cases where the DTC is very small. It results from the close proximity of a tooth throttle to the high pressure stagnation region on the step face.

7 At circumferential locations in the tooth throttle where a portion of the honeycomb hexagonal fin is axially aligned with the tooth tip, it was found that the leakage jet exiting the throttle is immediately redirected in the radially outward direction. This redirection is attributed to the suction effect in the hexagonal honeycomb cell due to the entrainment of air from the cell into the leakage jet.

Acknowledgment

The authors are grateful to the Texas ATP for partial support, and also to the Texas A&M University Supercomputer Center for a grant of computer resources. In addition, the assistance of L. Redd and B. Sramek with the measurements is appreciated.

Nomenclature

A = clearance flow area (m^2)
C = tooth tip clearance (m)
DTC = axial distance to contact (m)
DTF = axial distance to fin (m)
HCP = honeycomb pitch (m)
m = mass flow rate (kg/s)
N = number of teeth
P = absolute pressure (N/m^2)
R = specific gas constant (J/kg-K)
S = step height (m)
T = temperature (K)
TP = tooth pitch (m)
TT = tooth tip thickness (m)
x, r, θ = axial, radial, and circumferential coordinates
α = flow coefficient
ε = turbulent energy dissipation rate (m^2/s^3)
k = turbulent kinetic energy (m^2/s^2)
ν = specific volume (m^3/kg)

Subscripts

0 = first tooth
n = last tooth
meas. = measurement
pred. = prediction
up = upstream
dn = downstream

References

[1] Martin, H. M., 1908, "Labyrinth Packings," J. Engineering, **85**, pp. 33–36.
[2] Egli, A., 1935, "The Leakage of Steam Through Labyrinth Seals," Trans. ASME, **57**, pp. 115–122.
[3] Kearton, W. J., and Keh, T. H., 1952, "Leakage of Air Through Labyrinth Glands of the Staggered Type," Proc. Inst. Mech. Eng., **166**, pp. 180–188.
[4] Stocker, H. L., 1978, "Determining and Improving Labyrinth Seal Performance in Current and Advanced High Performance Gas Turbines," AGARD CP-237 Conference Proceedings, pp. 13/1–13/22.

[5] Schramm, V., Willenborg, K., Kim, S., and Wittig, S., 2002, ''Influence of a Honeycomb-Facing on the Flow Through a Stepped Labyrinth Seal,'' ASME J. Eng. Gas Turbines Power, **124**, pp. 140–146.
[6] Rhode, D. L., and Allen, B. F., 2001, ''Measurement and Visualization of Leakage Effects of Rounded Teeth Tips and Rub-Grooves on Stepped Labyrinths,'' ASME J. Eng. Gas Turbines Power, **123**, pp. 604–611.
[7] Prasad, B. V. S. S. S., Sethu Manavalan, V., and Nanjunda Rao, N., 1997, ''Computational and Experimental Investigations of Straight-Through Labyrinth Seals,'' ASME Paper No. 97-GT-326.
[8] Zimmermann, H., Kammerer, A., and Wolff, K. H., 1994, ''Performance of Worn Labyrinth Seals,'' ASME Paper No. 94-GT-131.
[9] Demko, J. A., Morrison, G. L., and Rhode, D. R., 1990, ''Effect of Shaft Rotation on the Incompressible Flow in a Labyrinth Seal,'' J. Propulsion, **6**, pp. 171–176.
[10] Brownell, J. B., Millward, J. A., and Parker, R. J., 1989, ''Nonintrusive Investigations Into Life-Size Labyrinth Seal Flow Fields,'' ASME J. Eng. Gas Turbines Power, **111**, pp. 335–342.
[11] Bill, R. C., and Shiembob, L. T., 1977, ''Friction and Wear of Sintered Fiber-Metal Abradable Seal Materials,'' NASA TM X73650.
[12] Stoff, H., 1980, ''Incompressible Flow in a Labyrinth Seal,'' J. Fluid Mech., **100**, pp. 817–829.
[13] Rhode, D. L., and Adams, R. G., 2001, ''Computed Effect of Rub-Groove Size on Stepped Labyrinth Seal Performance,'' Tribol. Trans., **44**, pp. 523–532.
[14] Rhode, D. L., and Allen, B. F., 1998, ''Visualization and Measurements of Leakage Effects on Straight-Through Labyrinth Seals,'' ASME Paper No. 98-GT-506.
[15] Denecke, J., Schramm, V., Kim, S., and Wittig, S., 2002, ''Influence of Rub-Grooves on Labyrinth Seal Leakage,'' ASME Paper No. GT-2002-30244.
[16] Waschka, W., Wittig, S., and Kim, S., 1992, ''Influence of High Rotational Speeds on the Heat Transfer and Discharge Coefficients in Labyrinth Seals,'' ASME J. Turbomach., **114**, pp. 462–468.
[17] Patankar, S. V., 1980, *Numerical Heat Transfer and Fluid Flow*, McGraw-Hill, New York.
[18] El Tahry, S. H., 1983, ''k-ε Equation for Compressible Reciprocating Engine Flows,'' J. Energy, **7**(4), pp. 345–353.
[19] Rhode, D. L., and Hibbs, R. I., 1993, ''Clearance Effects on Corresponding Annular and Labyrinth Seal Flow Leakage Characteristics,'' ASME J. Tribol., **115**, pp. 699–704.
[20] Wittig, S., Schelling, U., Kim, S., and Jacobsen, K., 1987, ''Numerical Predictions and Measurements of Discharge Coefficients in Labyrinth Seals,'' ASME Paper No. 87-GT-188.
[21] Gercke, Max Jobst, 1934, ''Flow Through Labyrinth Packing,'' Mech. Eng. (Am. Soc. Mech. Eng.), **56**(11), pp. 678–680.

Discharge Coefficients of Rotating Short Orifices With Radiused and Chamfered Inlets

M. Dittmann
e-mail: Mario.Dittmann@its.uni-karlsruhe.de

K. Dullenkopf

S. Wittig

Lehrstuhl und Institut für Thermische Strömungsmaschinen,
University of Karlsruhe,
76128 Karlsruhe, Germany

The secondary air system of modern gas turbine engines consists of numerous stationary or rotating passages to transport the cooling air, taken from the compressor, to thermally high loaded components that need cooling. Thereby the cooling air has to be metered by orifices to control the mass flow rate. Especially the discharge behavior of rotating holes may vary in a wide range depending on the actual geometry and the operating point. The exact knowledge of the discharge coefficients of these orifices is essential during the design process in order to guarantee a well adapted distribution of the cooling air inside the engine. This is crucial not only for a safe and efficient operation but also fundamental to predict the component's life and reliability. In this paper two different methods to correlate discharge coefficients of rotating orifices are described and compared, both in the stationary and rotating frame of reference. The benefits of defining the discharge coefficient in the relative frame of reference will be pointed out. Measurements were conducted for two different length-to-diameter ratios of the orifices with varying inlet geometries. The pressure ratio across the rotor was varied for rotational Reynolds numbers up to $Re_\Phi = 8.6 \times 10^5$. *The results demonstrate the strong influence of rotation on the discharge coefficient. An analysis of the complete data shows significant optimizing capabilities depending on the orifice geometry.* [DOI: 10.1115/1.1771685]

Introduction

Although CFD is commonly used in the design process of gas turbines, correlations to characterize flow elements are still necessary. Complex air system networks are established to predict pressure losses for all components and to calculate the flow distribution within the engine (Kutz and Speer [1]). Thereby, the reliability of the preliminary layout depends exclusively on the accuracy of one dimensional correlations. Especially the internal air system of gas turbines with its numerous variety of geometric configurations is difficult to design. But in particular the secondary air system is important concerning safety and performance of the engine. Furthermore, it has a strong impact on the component's life and thus the engine's life.

The cooling air of turbo engines is usually metered by stationary or rotating orifices. These tapping configurations cause most of the pressure losses and dominate the flow distribution. To guarantee the functionality of turbine disks and blades, a minimum amount of cooling air is needed. Therefore, the exact knowledge of the discharge behavior of all orifices is required during the design process of the air distribution system. The discharge coefficient has to be known not only for one operating point but also for the complete range of operating conditions. This is important especially for rotating orifices as their discharge behavior may vary strongly.

For turbulent flow the discharge coefficient of stationary holes is mainly influenced by geometrical parameters. Typical flow structures for different orifice configurations are shown in Fig. 1. It is evident that the inlet geometry influences the streamlines and separation regions and consequentially affects the discharge coefficient of the orifice.

The length-to-diameter ratio l/d of the hole is another important parameter as jet reattachment can occur inside the bore. The dynamic pressure is recovered behind the vena contracta and the discharge coefficient tends to result in higher values. Lichtarowicz et al. [2] investigated the discharge behavior of sharp edged orifices with l/d ratios up to 10 for noncompressible flow. A simple empirical expression for the discharge coefficients at high Reynolds numbers is given, which is also based on collected data from numerous experiments (see Fig. 2).

The influence of radiused and chamfered inlets was studied by Hay and Spencer [3] for numerous configurations. In general, their results showed that inlet radiusing and chamfering have beneficial effects on the discharge behavior. The discharge coefficient was found to increase up to 33% in comparison to sharp edged orifices. If the chamfer ratio c/d is raised beyond a critical value for short holes, c_D drops as the flow reattachment within the hole is incomplete.

Rhode et al. [4] studied the discharge behavior of long orifices with approaching flow perpendicular and inclined to the orifice axis. An increasing approach velocity results in lower c_D values.

Based on several experiments McGreehan and Schotsch [5] presented a method to predict the discharge coefficient of long orifices considering l/d, r/d, and relative tangential velocity effects on c_D. In Fig. 2 the discharge behavior of a stationary orifice is shown for a variation of the two geometric parameters l/d and r/d.

Especially in turbo engines rotational effects have to be considered to capture the discharge behavior of orifices depending on several operating conditions. Samoilovich and Morozov [6] and Meyfarth and Shine [7] performed basic measurements concerning the discharge coefficient of rotating orifices. More detailed investigations were conducted by Wittig et al. [8], who determined the flow field in the vicinity of the rotating orifices by LDV. In addition, numerical calculations were carried out. Based on experimental and numerical data Weissert [9] presented a correlation to predict the discharge coefficient of rotating holes. In Fig. 3 the numerically calculated flow field for a short sharp edged rotating orifice is shown. The velocity vectors are plotted relative to the rotor in the rotating frame of reference. A large separation region is located at the suction side of the hole reducing the dis-

Contributed by the International Gas Turbine Institute (IGTI) of THE AMERICAN SOCIETY OF MECHANICAL ENGINEERS for publication in the ASME JOURNAL OF ENGINEERING FOR GAS TURBINES AND POWER. Paper presented at the International Gas Turbine and Aeroengine Congress and Exhibition, Atlanta, GA, June 16–19, 2003, Paper No. 2003-GT-38314. Manuscript received by IGTI, October 2002, final revision, March 2003. Associate Editor: H. R. Simmons.

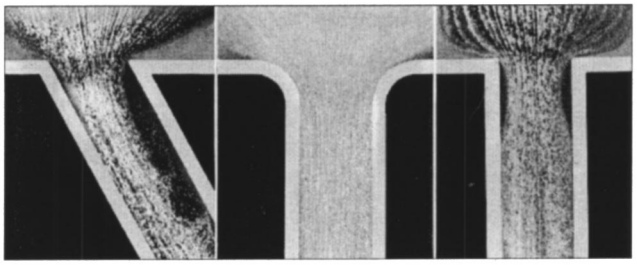

Fig. 1 Flow through stationary orifices, Nakayama [15]

charge coefficient. All relevant properties to characterize the discharge behavior of the orifice are added in Fig. 3.

Zimmermann et al. [10] compared the correlations for c_D values of rotating orifices of Samoilovich and Morozov [6], McGreehan Schotsch [5], and Weissert [9] but unfortunately observed a remarkable difference which could not be clarified. Nevertheless, several methods to correlate data of rotating orifices are discussed and highly appreciated recommendations are given. Another method to characterize the occurring losses of the flow through orifices is based on loss coefficients as presented by Idelchik [11] or Brillert et al. [12]. Obviously, new test data are required to refine existing correlations. As a well-designed internal air system is fundamental to realize high engine performance combined with increasing inspection intervals this is even more worthwhile.

Experimental Setup

To characterize the discharge behavior of orifices in high-speed rotating disks, a test facility was built up at the Institut für Thermische Strömungsmaschinen, Karlsruhe, Germany. A detailed description of the test rig is given by Wittig et al. [8]. As shown in Fig. 4, compressed air is discharged from a settling chamber through the flange of the rig to the rotor, which can be exchanged easily. A labyrinth seal was chosen to reduce the unavoidable

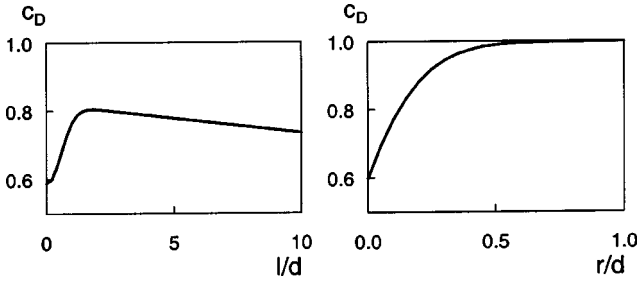

Fig. 2 Effect of orifice *l/d* and *r/d* for stationary configurations

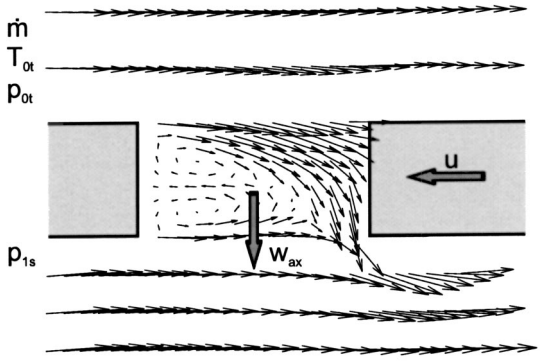

Fig. 3 Flow through a rotating short orifice

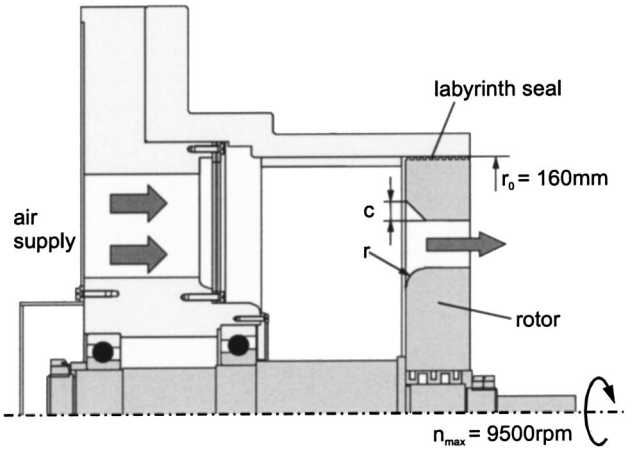

Fig. 4 Sketch of test rig

leakage flow between rotor and casing. To ensure a high level of accuracy extensive calibration measurements were performed in advance. Four holes with 15 mm in diameter were milled into each rotor, the inlet geometry was changed successively.

During the experiments the rotor was driven up to $n = 9500$ rpm which is equivalent to a rotational Reynolds number of $\mathrm{Re}_\Phi = 8.6 \times 10^5$. The pressure ratio was varied from 1.05 to 1.60 for each configuration. The mass flow rate discharged to the test section was measured by an orifice-metering system in accordance to European standards with an uncertainty of $\pm 1\%$. Total temperature and total pressure sensors were located at the pitch radius of the rotating holes 55 mm upstream of the rotor disk to determine the total properties of the fluid. The static pressure at the exit was set to be equal to the ambient pressure measured downstream of the rig. Temperatures were recorded with an uncertainty of ± 1 K. Differential pressure measurements were accomplished by several pressure transducers with an accuracy of $\pm 0.15\%$ in the range of $0-0.7 \times 10^5$ Pa.

The discharge behavior of all orifice geometries was investigated in the same range of operating conditions. Beginning at zero rotation the rotor disk speed was gradually increased while the pressure ratio was kept constant. Totally, 14 different orifice geometries were tested. All characteristic geometries are listed in Table 1. In all tests the chamfer angle was kept constant at 45 deg.

Theory of Rotating Orifices

The discharge behavior of an restricting flow element can be characterized by the c_D value. According to Eq. (1) the discharge coefficient is defined as the ratio of the actual mass flow rate $\dot{m}$ to the ideal mass flow rate $\dot{m}_{id}$.

$$c_D = \frac{\dot{m}}{\dot{m}_{id}} \tag{1}$$

To predict the discharge coefficient for specific geometry and flow conditions all influencing parameters have to be considered.

Table 1 Orifice geometries investigated

$l/d = 0.4$		$l/d = 1.25$	
r/d	c/d	r/d	c/d
0.00		0.00	
0.05	0.05	0.05	
0.10	0.10	0.10	0.10
0.20	0.20	0.20	0.20
		0.50	

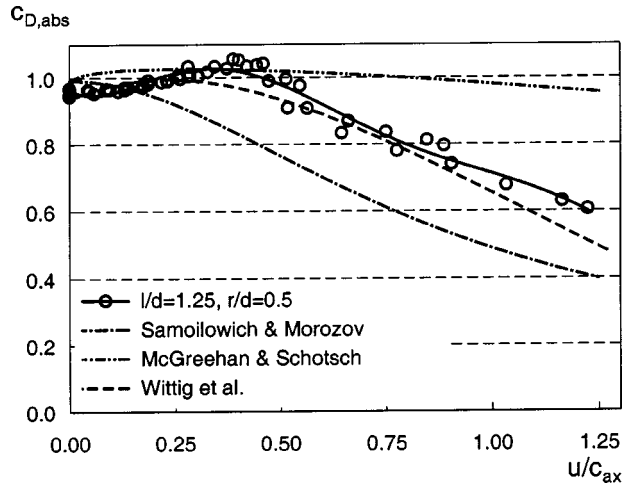

Fig. 5 Discharge coefficient defined in the absolute frame of reference, comparison of different correlations and experiments

Especially for rotating orifices different methods to correlate the data can be found in literature. The flow may be analyzed in the absolute or relative frame of reference. Both methods will be described. Afterwards, the new data will be compared and discussed.

Absolute Frame. The ideal mass flow rate of an rotating orifice in the absolute frame of reference is calculated according to Eq. (2). Total temperature T_{0t} and total pressure p_{0t} correspond to the total properties of the fluid upstream of the rotor disk, thus the dynamic head of the relative velocity is not considered. As the work done by the rotor which acts like an compressor is not taken into account, the real mass flow rate may even exceed the ideal mass flow rate. Depending on the orifice geometry and the operating point this can result in discharge coefficients higher than unity as shown in Fig. 5. To correlate the discharge behavior of rotating orifices in the absolute frame of reference $c_{D,abs}$ is usually plotted against the velocity ratio u/c_{ax}. Thereby, the ideal axial velocity is determined by the total properties of the fluid upstream and the static pressure downstream the rotor disk (Eq. (3)).

$$\dot{m}_{id}=\frac{p_{0t}A}{\sqrt{RT_{0t}}}\sqrt{\frac{2\kappa}{\kappa-1}\left[\left(\frac{p_{1s}}{p_{0t}}\right)^{2/\kappa}-\left(\frac{p_{1s}}{p_{0t}}\right)^{(\kappa+1)/\kappa}\right]} \tag{2}$$

$$c_{ax}=\sqrt{\frac{2\kappa}{\kappa-1}RT_{0t}\left[1-\left(\frac{p_{1s}}{p_{0t}}\right)^{(\kappa-1)/\kappa}\right]} \tag{3}$$

In Fig. 5 the newly gained discharge coefficients of an rotating orifice with $l/d=1.25$ and $r/d=0.5$ are compared to the predicted values of three different correlations. Due to the compressional work done by the rotor, the total pressure and total temperature is increased on the pressure side at the inlet region of the orifice. Thus, leading to higher discharge coefficients, which even exceed unity at certain operating conditions. When a critical velocity ratio is reached, the beneficial effects of rotation are overpowered by the deteriorating effects of flow separation at the suction side of the orifice. This results in a continuous decrease of the discharge coefficient with increasing velocity ratio. The discharge behavior of the investigated orifice geometry is characterized by the solid line, all data points are shown additionally.

Compared to the predicted discharge coefficients the maximum relative deviation at zero rotation is less than 3% in respect to the experimental value. But as already mentioned by Zimmermann et al. [10] an increasing difference was found for higher velocity ratios. The correlation based on the experiments of Samoilovich and Morozov [6] tends to predict lower c_D values. As seen in the original paper of McGreehan and Schotsch [5] their correlation however overestimates discharge coefficients at higher velocity ratios. Wittig et al. [13] presented a correlation called DIANA, capable of predicting Discharge coefficients And Nusselt numbers for internal Air systems. The new experimental data, which have not been available to built up DIANA, fit very well within the validity range of the existing correlation. However, a potential underprediction of c_D seems to exist for velocity ratios higher than 0.75. Deviations in the extrapolated range of the correlation were already mentioned by Dittmann et al. [14].

Relative Frame. Several essential benefits exist if the discharge behavior of rotating orifices is analyzed in the relative frame of reference, as already mentioned by Zimmermann et al. [10]. As the compressional work of the rotor is considered, c_D is limited by theoretical values. Discharge coefficients higher than unity, which are illogical under these circumstances, do not occur. Furthermore, if c_D is plotted against the velocity ratio in the relative frame of reference all possible operating conditions are limited to the theoretical range of $0\leqslant u/w_{ax}\leqslant 1$. As the ideal mass flow rate increases continuously with increasing rotational speed, c_D approaches zero for u/w_{ax} approaching unity. In comparison to the analysis in the absolute frame of reference, neither the velocity ratio is limited nor does a theoretical fixed point exist. Thus, extrapolations and correlations should be more reliable if the discharge behavior of rotating orifices is analyzed in the relative frame of reference.

Total properties, namely total temperature and total pressure, have to be transferred into the relative frame of reference in accordance to Eq. (4) and Eq. (5).

$$T_{0t,\mathrm{rel}}=T_{0t}\cdot\left(1+\frac{u^2}{2c_pT_{0t}}\right) \tag{4}$$

$$p_{0t,\mathrm{rel}}=p_{0t}\cdot\left(1+\frac{u^2}{2c_pT_{0t}}\right)^{\kappa/(\kappa-1)} \tag{5}$$

The discharge coefficient defined in the relative frame of reference is calculated by the total properties of the fluid in the relative system (Eq. (6)). Consequently, the ideal axial flow velocity is determined by Eq. (7).

$$c_D=\frac{\dot{m}}{\frac{p_{0t,\mathrm{rel}}A}{\sqrt{RT_{0t,\mathrm{rel}}}}\sqrt{\frac{2\kappa}{\kappa-1}\left[\left(\frac{p_{1s}}{p_{0t,\mathrm{rel}}}\right)^{2/\kappa}-\left(\frac{p_{1s}}{p_{0t,\mathrm{rel}}}\right)^{(\kappa+1)/\kappa}\right]}} \tag{6}$$

$$w_{ax}=\sqrt{\frac{2\kappa}{\kappa-1}RT_{0t,\mathrm{rel}}\left[1-\left(\frac{p_{1s}}{p_{0t,\mathrm{rel}}}\right)^{(\kappa-1)/\kappa}\right]} \tag{7}$$

In Fig. 6 the discharge coefficients determined in the absolute and relative frame of reference are shown for the same experimental results as already presented in Fig. 5. The discharge enhancement, due to the work done by the rotor, is graphically indicated. By analyzing the discharge behavior of the orifice with $l/d=1.25$ and $r/d=0.5$ in the relative frame of reference, the data points can even be better fitted by one characteristic curve. To distinguish the tested pressure ratios across the rotor disk different symbols are used. It can be clearly seen that the pressure ratio across the rotor disk and hence the Reynolds number does not influence the discharge behavior of the orifice. The investigated velocity ratio is gradually reduced with increasing pressure ratio as the maximum rotor speed was limited in the experimental setup to 9500 rpm.

Results

The analysis of the discharge behavior of rotating orifices in the absolute and relative frame of reference demonstrated the considerable advantages of defining c_D in the relative system. Therefore, the discharge behavior of all investigated orifice geometries will be discussed in the rotating system.

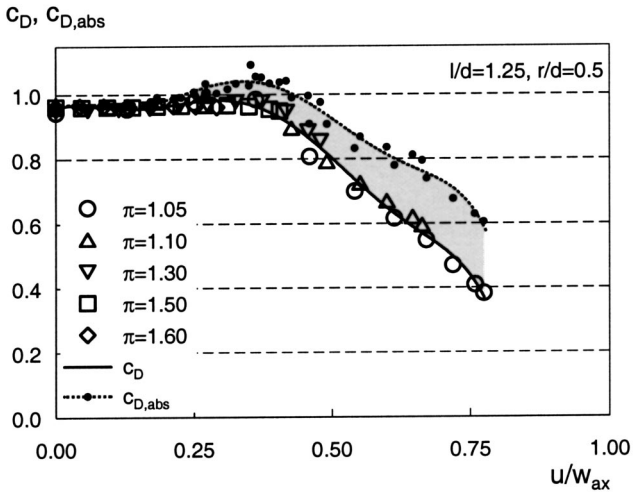

Fig. 6 Discharge coefficients defined in the absolute and relative frame of reference

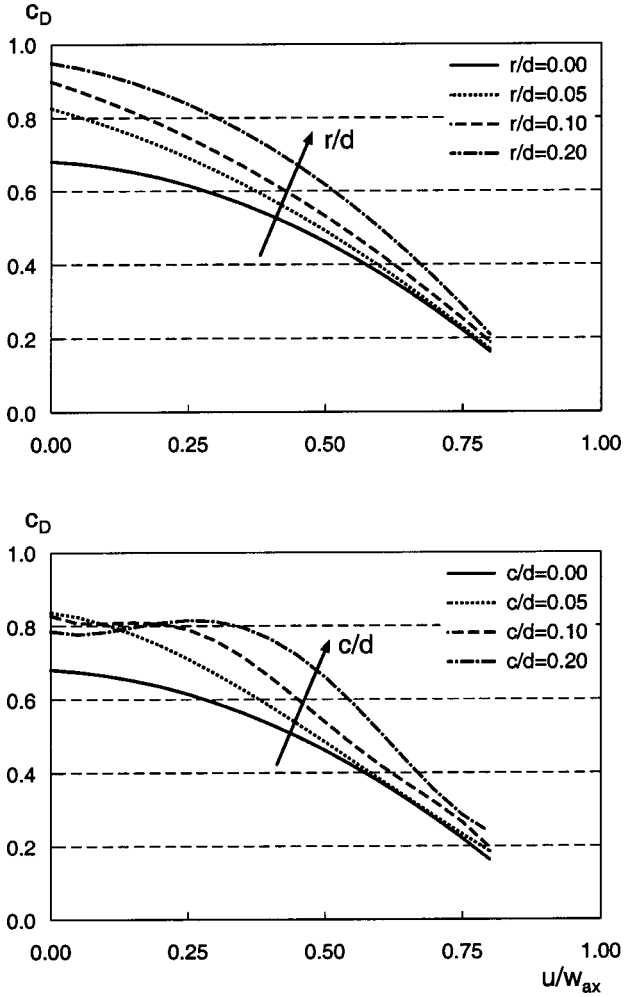

Fig. 7 Effect of orifice r/d and c/d on c_D for $l/d=0.4$

Effect of Inlet Geometry. In the present study the discharge behavior of short orifices was investigated. The l/d ratios were fixed at $l/d=0.4$ and $l/d=1.25$ while the inlet geometry was changed. Radiused and chamfered inlets were tested. The effects of r/d and c/d on the discharge behavior for each l/d ratio are discussed separately in Fig. 7 and Fig. 8.

Radiusing the inlet edge enhances the discharge coefficient of the orifice with $l/d=0.4$ for all operating conditions. Independent of the orifice geometry the discharge coefficient c_D gradually decreases with increasing velocity ratio. For a stationary setup, a small radius of $r/d=0.05$ increases the discharge coefficient by 21% with respect to the sharp edged orifice. At $r/d=0.2$ the improvement in c_D can reach up to 39%. Compared to the radiused inlet a chamfered inlet does not necessarily result in higher c_D values for all velocity ratios. This is only true for the smallest c/d ratio tested. A further increase of the chamfer depths deteriorates the discharge behavior for small velocity ratios as the effective length of the orifice is considerably reduced. According to Fig. 2, the l/d ratio has a strong impact on c_D, resulting in low discharge coefficients for small l/d ratios.

The discharge coefficient of a stationary sharp edged orifice with $l/d=1.25$ is 15% higher compared to the c_D of an orifice with $l/d=0.4$. Furthermore, c_D can be increased up to 21% for $r/d=0.5$ with respect to the sharp edged configuration of a stationary setup. Again, radiusing the inlet enhances the discharge behavior for all velocity ratios. But the discharge characteristics of the orifices with $l/d=1.25$ do not fully correspond to that with $l/d=0.4$. Only the discharge coefficient of the sharp-edged orifice is reduced continuously with increasing velocity ratio. For radiused inlets c_D remains nearly constant, until a critical velocity ratio is reached. A further acceleration of the rotor yields to a continuous decrease of c_D. Thereby, the critical velocity ratio is shifted to higher values with increasing inlet radius. The discharge behavior of an orifice with $l/d=1.25$ and chamfered inlet can be directly compared to that of an orifice with $l/d=0.4$. A chamfered inlet improves the inflow conditions, leading to smaller separation regions and therewith higher c_D values. However, the effective l/d ratio is reduced, deteriorating the discharge behavior.

A direct comparison concerning the effect of the orifice inlet geometry, whether radiused or chamfered, on c_D is given for $l/d=0.4$ in Fig. 9. Only two configurations are chosen. Nevertheless, all observed trends can be discussed. The solid lines represent the discharge characteristics of the radiused orifices whereas the dashed lines describe the discharge behavior of the chamfered ones. For small *r/d* and *c/d* ratios only very little differences can be found, respectively. At low velocity ratios the discharge behavior of the chamfered orifice seems to be more favorable. For velocity ratios higher than $u/w_{ax}=0.4$ the discharge behavior proves to be identical. An increase of inlet radius or chamfer depth results in a remarkable altered discharge characteristic only for the chamfered configuration. The discharge behavior of the orifice with $r/d=0.20$ can be compared to that with $r/d=0.05$. The inflow conditions are further optimized and the discharge coefficient is enhanced for all velocity ratios. In comparison, the discharge characteristic of the chamfered orifice is considerably altered. For a stationary setup with straight inflow, the enlargement of the chamfer depths results in a lower discharge coefficient. Due to the reduced effective l/d ratio, jet reattachment within the orifice is more incomplete. This results in lower c_D values for specific geometric configurations as shown by Hay and Spencer [3] in a stationary setup. When the velocity ratio is increased, c_D remains nearly constant or may be even enhanced before decreasing gradually for $u/w_{ax}>0.3$.

With respect to the discharge coefficient of the orifice with $r/d=0.2$ the c_D value for a straight inflow is reduced by 12%. However, the absolute deviation is continuously diminished with increasing velocity ratio. For operating conditions with velocity ratios between 0.3 and 0.6 the discharge coefficient of the rotating orifice with $c/d=0.2$ is even higher. This special behavior of the discharge characteristic of rotating chamfered orifices was observed for all other configurations investigated within the present study. Probably, the stagnation region on the pressure side of the orifice inlet is enlarged for these specific operating points com-

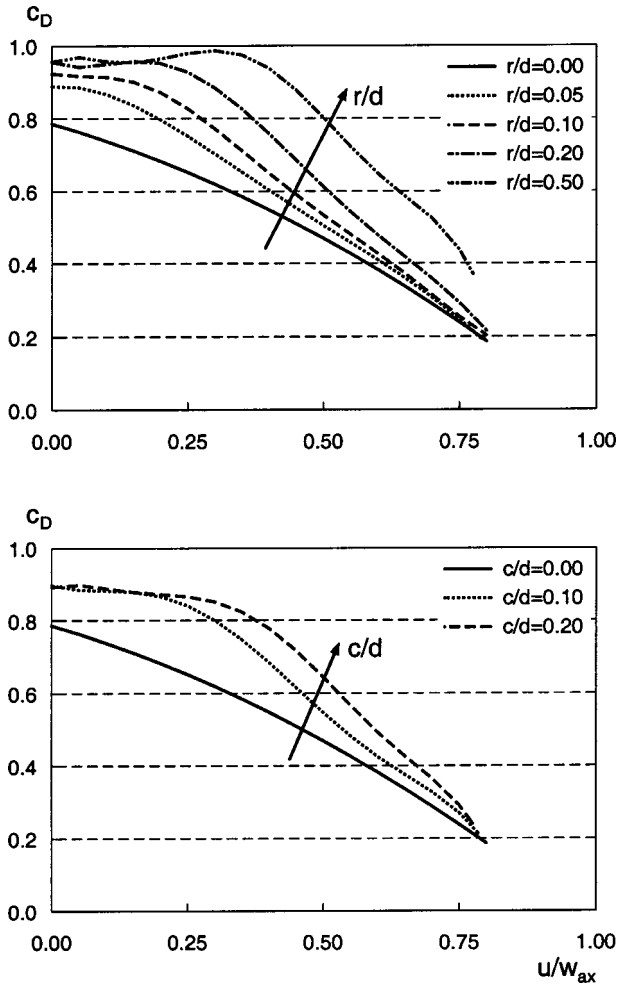

Fig. 8 Effect of orifice r/d and c/d on c_D for $l/d=1.25$

pared to the flow field of the radiused configuration. Successively, more compressional work is done by the rotor. This leads to an increase of the total pressure and total temperature directly at the inlet of the orifice and enhances the discharged mass flow rate. Further increasing of the rotor speed, the influence of the orifice geometry, whether radiused or chamfered, becomes negligible.

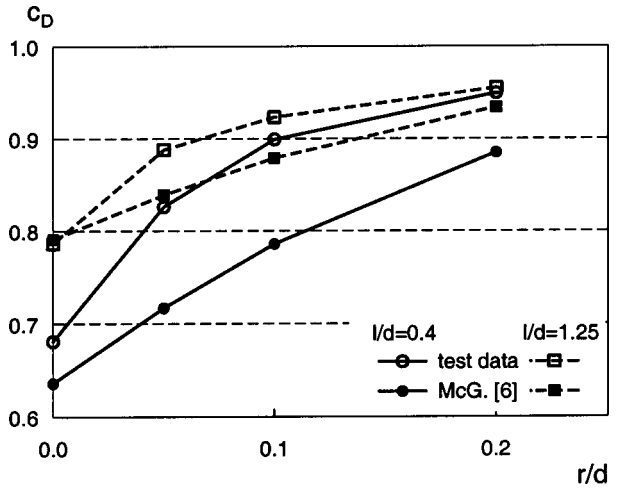

Fig. 10 Comparison of experimental results and predicted values for radiused inlets

In Fig. 10 the effect of r/d on c_D is compared to predicted discharge coefficients using the correlation of McGreehan and Schotsch [5]. The inlet radius is varied for both l/d ratios investigated. The experimental data were accomplished for operating points with stationary rotor. For $l/d=1.25$ the maximum relative deviation is less than 6% in respect to the experimental data. The discharge coefficient of the sharp edged orifice is even perfectly matched. If the l/d ratio is reduced to $l/d=0.4$ the deviation of the predicted values increases up to 13% for $r/d=0.05$ and 0.10. For the sharp edged configuration the c_D value is underpredicted by 7%. Concerning the c/d effect on c_D, all observed trends do agree very well with the results of Hay and Spencer [3].

Effect of l/d. The l/d ratio has a strong impact on the discharge coefficient of sharp-edged stationary orifices, especially for short holes. Therefore, a direct comparison of the discharge behavior of both tested l/d ratios is given in Fig. 11. The discharge characteristics of the orifice with $l/d=0.4$ are plotted as a solid line. The dashed lines represent the discharge behavior for $l/d=1.25$. Radiusing, as mentioned in the previous section, reduces the separation of the flow and consequently c_D is increased. According to Lichtarowicz et al. [2] the discharge coefficient of a sharp edged orifice with $l/d=1.25$ is higher than for $l/d=0.4$. At low velocity ratios this is also valid for rotating orifices. However,

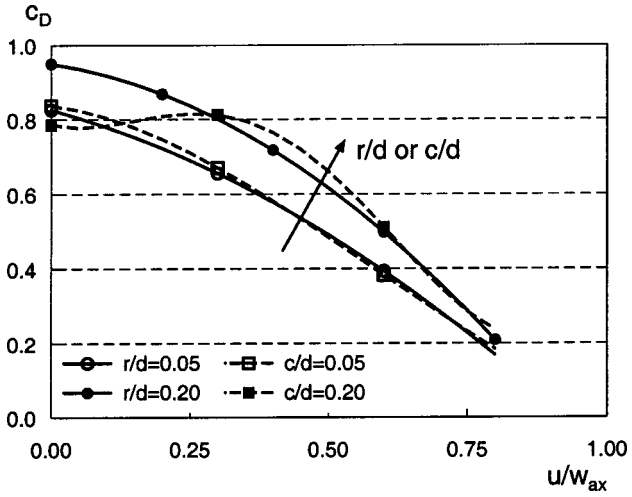

Fig. 9 Effect of inlet geometry for $l/d=0.4$

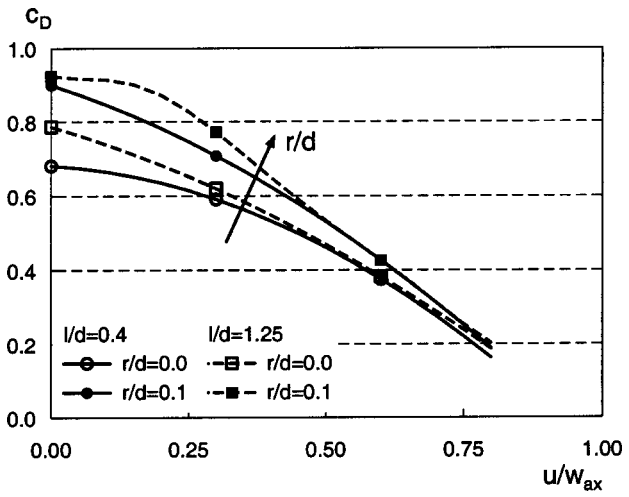

Fig. 11 Effect of orifice l/d on c_D for radiused inlets

the l/d effect on c_D can be neglected for high velocity ratios. For these operating points the discharge characteristic is dominated by the inlet geometry of the orifice.

Conclusions

In the present study two different methods to analyze the discharge behavior of rotating orifices are compared, either in the absolute or in the relative frame of reference. The benefits of defining the discharge coefficients in the relative system are pointed out. As the compressional work done by the rotor is taken into account, the discharge coefficient is limited by the theoretical values 0 and 1. To plot c_D against the relative velocity u/w_{ax} incorporates additional advantages. The theoretical velocity ratio cannot exceed unity. Furthermore, the ideal mass flow rate is continuously enhanced with increasing velocity ratio. The discharge coefficient is reduced and approaches zero for velocity ratios close to unity. Correlations and extrapolations are more reliable due to the theoretical limits and the additional fix point. Nevertheless, the influence of different geometry configurations can be captured precisely.

The pressure ratio does not have an influence on c_D as the Reynolds number is greater than 6×10^4 for all operating conditions. Radiusing the orifice inlet improves the discharge behavior for all operating conditions, independent of the l/d ratio. An enhancement in c_D of up to 39% compared to the sharp edged orifice could be achieved. Very small r/d ratios contribute to an improvement of the inflow condition, reducing separation regions and thus leading to higher discharge coefficients. Discharge coefficients of rotating holes with different chamfer depths do not allow a straight forward explanation. Small c/d ratios improve the discharge behavior of rotating orifices for all velocity ratios, whereas a further increase of the chamfer depths may result in lower c_D values at low velocity ratios. Compared to the inlet radius, the chamfer does influence the effective l/d ratio which has a strong influence on the discharge coefficient of short holes. Depending on the orifice geometry two typical discharge characteristics were observed. For some configurations a critical velocity ratio exists. The discharge coefficient remains nearly constant for low velocity ratios and decreases continuously for a further acceleration of the rotor beyond the critical operating point. The critical velocity ratio is shifted to higher values for increasing r/d or c/d ratios. For a specific range of velocity ratios chamfered inlets seem to be favorable compared to radiused inlets. However, at high velocity ratios the influence of the inlet geometry, whether radiused or chamfered, can be neglected. Even the l/d ratio does not affect the discharge coefficient for these operating conditions.

Predicted c_D values of stationary orifices with $l/d=1.25$ and radiused inlets were matched within an uncertainty of 6%. Remarkable differences between existing correlations to predict the discharge characteristic of rotating orifices made the need of new experimental data evident, to clarify the remaining discrepancies.

Acknowledgments

The work was funded by the German government within the Engine 3E project, phase II. The support of Rolls-Royce Deutschland Ltd. & Co. KG is greatly appreciated. Special thanks are due to D. Peitsch and W.-H. Friedl for technical discussions.

Nomenclature

A = cross-sectional area (m^2)
c = chamfer depth (m)
c_{ax} = axial velocity in the abs. frame of reference (m/s)
c_D = discharge coefficient
c_p = specific heat (J/kg K)
d = diameter of orifice (m)
l = length of orifice (m)
$\dot{m}$ = mass flow rate (kg/s)
n = rotational speed (1/min)
p = pressure (N/m^2)
r = radius (m)
r_0 = outer radius of the rotor (m)
r_m = pitch radius of the orifices (m)
R = specific gas constant (J/kg K)
Re_Φ = rotational Reynolds number, $\mathrm{Re}_\Phi=\omega r_m^2/\nu$
T = temperature (K)
u = circumferential velocity (m/s)
w_{ax} = axial velocity in the rel. frame of reference (m/s)
κ = isentropic exponent
ν = kinematic viscosity (m^2/s)
π = total pressure ratio, $\pi=p_{0t}/p_{1s}$
ω = angular velocity of rotor (1/s)

Subscripts

abs = absolute system
id = ideal
rel = relative system
s = static
t = total
0, 1 = upstream, downstream of orifice

References

[1] Kutz, K. J., and Speer, T. M., 1994, "Simulation of the Secondary Air System of Aero Engines," ASME J. Turbomach., **116**, pp. 306–315.
[2] Lichtarowicz, A., Duggins, R. K., and Markland, E., 1965, "Discharge Coefficients for Incompressible Non-Cavitating Flow Through Long Orifices," J. Mech. Eng. Sci., **7**(2), pp. 210–219.
[3] Hay, N., and Spencer, A., 1992, "Discharge Coefficients of Cooling Holes With Radiused and Chamfered Inlets," ASME J. Turbomach., **114**, pp. 701–706.
[4] Rhode, J. E., Richards, H. T., and Metger, G. W., 1969, "Discharge Coefficients for Thick Plate Orifices With Approach Flow Perpendicular and Inclined to the Orifice Axis," Tech. Rep. NASA-TN-D-5467.
[5] McGreehan, W. F., and Schotsch, M. J., 1988, "Flow Characteristics of Long Orifices With Rotation and Corner Radiusing," ASME J. Turbomach., **110**, pp. 213–217.
[6] Samoilovich, G. S., and Morozov, B. I., 1957, "Coefficients of Flow Through Pressure Equalizing Holes in Turbine Discs," Teploenergetica, **8**, pp. 16–23.
[7] Meyfarth, P. F., and Shine, A. J., 1965, "Experimental Study of Flow Through Moving Orifices," J. Basic Eng., **87**, pp. 1082–1083.
[8] Wittig, S., Kim, S., Jakoby, R., and Weißert, I., 1996, "Experimental and Numerical Study of Orifice Discharge Coefficients in High Speed Rotating Disks," ASME J. Turbomach., **118**(2), pp. 400–407.
[9] Weißert, I., 1997, "Numerische Simulation dreidimensionaler Strömungen in Sekundärluftsystemen von Gasturbinen unter besonderer Berücksichtigung der Rotation," Ph.D. thesis, Lehrstuhl und Institut für Thermische Strömungsmaschinen, Universität Karlsruhe (TH).
[10] Zimmermann, H., Kutz, J., and Fischer, R., 1998, "Air System Correlations Part 2: Rotating Holes and Two Phase Flow," ASME-Paper 98-GT-207.
[11] Idelchik, J. E., 1986, *Handbook of Hydraulic Resistance*, Springer-Verlag, Berlin.
[12] Brillert, D., Reichert, A.-W., and Simon, H., 1999, "Calculation of Flow Losses in Rotating Passages of Gas Turbine Cooling Systems," ASME Paper 99-GT-251.
[13] Wittig, S., Kim, S., Scherer, T., Jakoby, R., and Weißert, I., 1995, "Durchfluß an rotierenden Wellen- und Scheibenbohrungen und Wärmeübergang an rotierenden Wellen," Forschungsvereinigung Verbrennungskraftmaschinen (FVV), Abschlußbericht, Vorhaben Nr. 465 und 536, Heft 574.
[14] Dittmann, M., Geis, T., Schramm, V., Kim, S., and Wittig, S., 2002, "Discharge Coefficients of a Preswirl System in Secondary Air Systems," ASME J. Turbomach., **124**, pp. 119–124.
[15] Nakayama, Y., 1988, *Visualized Flow*, Pergamon Press, Oxford, UK.

Cooling Air Temperature Reduction in a Direct Transfer Preswirl System

T. Geis[1]
e-mail: torsten.geis@muc.mtu.de

M. Dittmann

K. Dullenkopf
Lehrstuhl und Institut fur Thermische Strömungsmaschinen,
University of Karlsruhe,
76128 Karlsruhe, Germany

This paper describes an experimental study of the cooling efficiency of a preswirl rotor-stator system equipped with a small number of preswirl nozzles of circular shape, located on a radius equal to that of the receiver disk holes. In the direct transfer cooling air system, total air temperatures were measured in the relative frame, i.e., inside the receiver holes by means of small total temperature probes for different throughflow rates, rotational Reynolds numbers and swirl ratios. The experimental data were compared with a simple theoretical model which predicts air temperatures in an "ideal" preswirl system. This comparison served to quantify the efficiency of this cooling scheme. In a subsequent one-dimensional analysis which took into account flow data obtained in an earlier experimental study by the same authors, two different mechanisms responsible for the elevated cooling air temperatures were determined. The new model considers in addition to the observed reduction of swirl due to viscous drag on the stator and mixing inside the rotor-stator cavity, the work put in by the rotor at high disk rotational Reynolds numbers and low cooling air flow rates. [DOI: 10.1115/1.1765124]

Introduction

The excellent performance and efficiency of modern gas turbine engines is among other reasons the result of advanced cooling schemes required to protect the engine components from temperatures in the hot gas path which are way above the allowed material limits. The conditions inside a turbomachine with two or more concentric shafts cause a very complex path of the cooling air with interactions of rotating and stationary components. In preswirl cooling air systems, nozzles are used to expand and thereby accelerate air in the circumferential direction of the rotor disk. By reducing the static temperature as well as the tangential relative speed between the fluid and the disk, the cooling air total temperature inside the rotor blades can drastically be reduced (Karabay et al. [1] and Popp et al. [2]). While total pressure losses at the inlet of the blade feed holes can be distinctively lower in such an air transfer system (Dittmann et al. [3]), total pressure losses in the nozzles make the establishment of a sufficient blade backflow margin more difficult.

For reversible flow conditions the cooling air temperature in the rotating frame is described as

$$\frac{T_{1\ \mathrm{tot,rel}}}{T_{1\ \mathrm{tot}}} = 1 + \frac{u_R^2 - 2u_R c_{1t}}{2c_p T_{1\ \mathrm{tot}}} \tag{1}$$

where u_R and c_{1t} denote the circumferential velocity of the receiver hole and the tangential component of the isentropic nozzle discharge velocity, respectively. For a given rotational Reynolds number, the total air temperature decreases with increasing nozzle pressure ratio, i.e., velocity c_1. At the same time, "cooling" of the cooling air is only feasible for velocity ratios in the range $0 < u_R/c_{1t} < 2$ (see also Wilson et al. [4]).

Equation (1) neither considers three-dimensional flow inside the preswirl cavity nor does it take into account mixing in the rotor-stator wheelspace. The latter effect was investigated by El-Oun and Owen [5] and Wilson and Owen [6] who showed that a radial outflow of coolant superposed on the preswirled main flow can deteriorate the efficiency of a preswirl system. Apart from the influence of radial outflow, no further parasitic effects were observed by these authors for the adiabatic case. The experimental apparatus employed by El-Oun and Owen ([6], see also El-Oun et al. [7]) roughly provided ideal geometric boundary conditions. For instance, large numbers of preswirl nozzles and receiver holes ($N=60$) were used such that quasi-axisymmetric flow could be assumed.

In the investigation reported here, a much smaller number of nozzles and blade feed holes ($N=12$) was used resulting in a fully three-dimensional flow field with large velocity gradients as earlier stated by Wilson et al. [4] and recently confirmed by experimental results from Geis et al. [8]. For this direct transfer preswirl system, it was the authors' intention to produce reliable cooling air temperature data and to derive equations which help to improve the design strategy for advanced cooling schemes in secondary air systems. Unlike Meierhofer and Franklin [9] who were among the first to measure temperatures inside a rotating disk, the present paper specifies very accurately the geometric and aerodynamic boundary conditions chosen in the experiments. Since air temperature measurements are difficult to perform inside rotating passages, the authors performed a comprehensive study to find a reliable technique. The result of this inquiry as well as a description of the whole test apparatus will be presented in the next section. Although heat transfer from the rotor does have an additional influence on the cooling air temperatures (see, e.g., Karabay et al. [10]) the present study was performed under nearly adiabatic conditions.

Experimental Setup

The experimental apparatus was the same as that used by Dittmann et al. [3] to study the discharge behavior. A schematic view of this direct transfer preswirl system is shown in Fig. 1. Details of the preswirl cavity are shown in Fig. 2.

[1]Present address: MTU Aero Engines GmbH, Dachauer Strasse 665, 80995 München, Germany.

Contributed by the International Gas Turbine Institute (IGTI) of THE AMERICAN SOCIETY OF MECHANICAL ENGINEERS for publication in the ASME JOURNAL OF ENGINEERING FOR GAS TURBINES AND POWER. Paper presented at the International Gas Turbine and Aeroengine Congress and Exhibition, Atlanta, GA, June 16–19, 2003, Paper No. 2003-GT-38231. Manuscript received by IGTI, October 2002, final revision, March 2003. Associate Editor: H. R. Simmons.

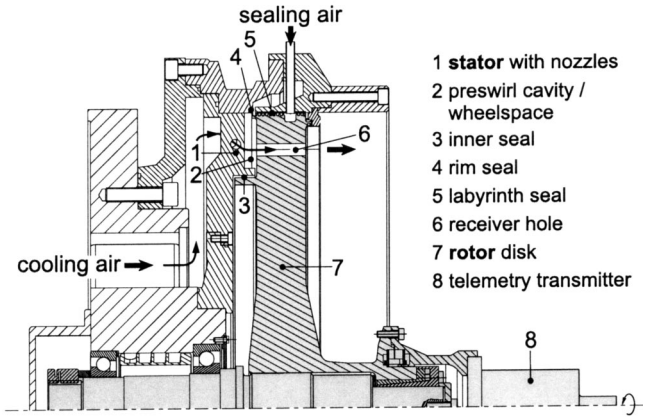

Fig. 1 Experimental apparatus

Cooling air was supplied to the test article by means of a compressor with nondimensional flow rates up to $c_w = 49{,}000$, and directed towards the preswirl plate which was equipped with $N_N = 12$ circular nozzles. The length to diameter ratio of these flow elements was fixed at $l/d = 3.8$. The nozzles were equally spaced on the circumference, inclined to the stator surface at $\alpha = 20°$ and oriented such that a jet following the nozzle axis would enter the receiver holes tangentially. The radial position of the nozzle outlet was at $r_e = 221.7$ mm and the one of the receiver holes at $r_m = 220$ mm (see Fig. 2). Discharge coefficients for both elements, i.e., holes and nozzles were determined in a recent study and presented by Dittmann et al. [3].

The axial spacing between the stator and the rotor disk, i.e., the width of the preswirl cavity was $s = 10$ mm and the height of this rotor-stator annulus $h = 46.5$ mm. The rotor contained $N_R = 12$ axial holes and the receiver total flow area was 1.56 times larger than that of the nozzles ($A_R/A_N = 1.56$). While their length equaled the thickness of the disk ($l = 40$ mm), the l/d was 4.0. Some of the rotating holes were instrumented with small stagnation probes which allowed the measurement of total temperatures of the cooling air. The diameter of these elements was adjusted to compensate for the blockage by the probe, resulting in a slightly smaller length to diameter ratio ($l/d = 3.57$ instead of $l/d = 4$). All disk holes were manufactured with chamfered inlets ($c/d = 0.04$).

The rotor was driven up to $n = 7000$ rpm resulting in a maximum disk hole circumferential velocity of $u_R = 161$ m/s and a rotational Reynolds number of $\mathrm{Re}_\varphi = 2.8 \cdot 10^6$. The swirl ratio β, i.e., the ratio of the flow tangential velocity to the disk hole circumferential velocity, was adjusted both by varying the pressure ratio and the angular speed of the rotor. The mass flow rate was measured by an orifice-metering system calibrated to an uncertainty of

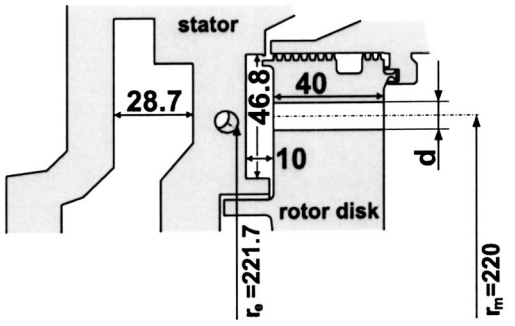

Fig. 2 Details of preswirl chamber, (dimensions in mm)

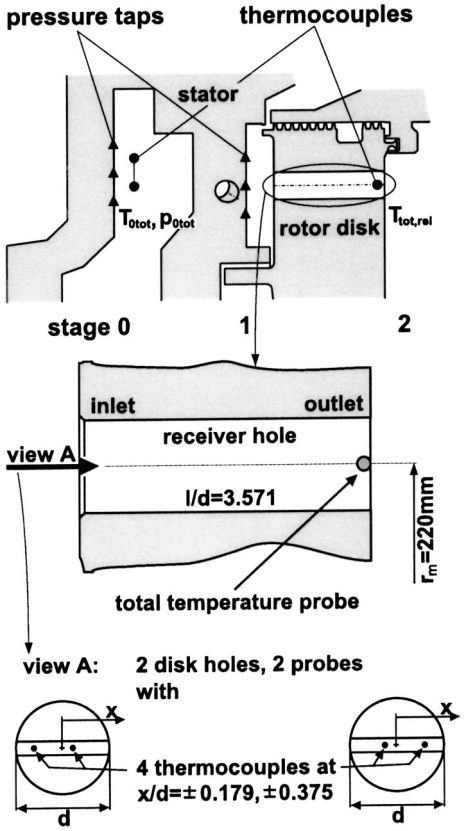

Fig. 3 Instrumentation of the receiver holes

±1%. Nozzle pressure ratios up to $\pi \approx 1.42$ were achieved in this study resulting in a subsonic flow through these elements.

The test facility allowed for superposing a radially directed cooling flow on the preswirled flow such that the influence of mixing between both flows could be investigated. However, since the authors of the present work were primarily interested in specifying the effects degrading the performance of a system without radial outflow, they did not make use of this option.

The air transfer system was shrouded by a massive steel casing, and a specific amount of sealing air was introduced at discrete positions on the circumference of the rotor disk to eliminate leakage between the disk and the stationary casing.

Instrumentation. A schematic view of the internal instrumentation of the apparatus is shown in Fig. 3. Pressure tappings and thermocouples used as total temperature sensors were installed inside the settling chamber and upstream of the preswirl plate to determine the inlet conditions to the system (referred to as stage "0"). In the outlet plane of the preswirl nozzles (stage "1"), various pressure taps ($d = 0.5$ mm) were used to measure static pressures at different angular and radial positions (for a more detailed description see Dittmann et al. [3]). In the outlet plane of the rotor disk, miniature total temperature probes were installed to measure the air stagnation temperatures relative to the disk (stage "2"). The probes used in this study were of cylindrical shape and based on a design described by Eck [11]. Unlike Eck [11] who introduced these instruments as stationary devices to measure total pressures, in the present study they were modified to fit in the rotating holes and to withstand the existing mechanical loads from the centrifugal forces. In addition, the new design admitts two thermocouples such that temperatures at two different locations could be measured employing one single probe (see Fig. 3, bottom and Fig. 4).

The instruments were built from a 2 mm diameter stainless steel

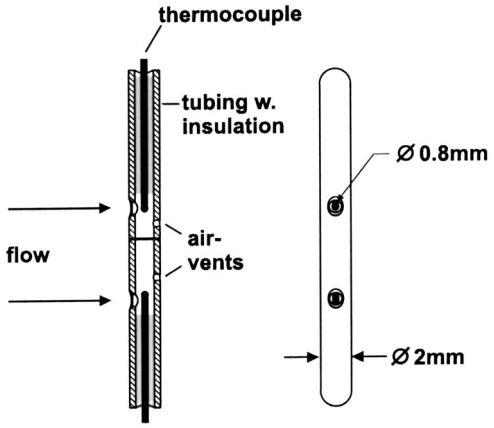

Fig. 4 Detailed view of one total temperature probe

tubing (thickness 0.4 mm) incorporating a teflon insulator which was placed between each thermocouple and the inner wall of the tube to reduce heat conduction between the sensor and the disk. The inlets of the probes ($d=0.8$ mm) were placed at various distances from the centerline of the rotating hole and chamfered to reduce the sensitivity to the flow angle (see Fig. 3). The latter feature accounted for the fact that in short rotating holes like the one investigated here, solid body rotation is unlikely to happen. On the downstream side vent holes were placed to minimize the response time of these instruments (see Fig. 4).

The determination of total temperatures in high velocity flows is critical if—like in this particular situation—the receiver exit velocity is not exactly known. Therefore, the dynamic head can only be ''captured'' and a high measuring accuracy achieved if the probe provides for a high temperature recovery:

$$T_{\text{probe}} = T_{\text{static}} + R \cdot \frac{w^2}{2c_p}. \tag{2}$$

In a calibration procedure similar to that described by Schoen [12], the cylindrical probes were installed near the outlet plane of the disk holes and the temperatures measured while the disk was stationary to determine the recovery factors of the probe. As can be concluded from Fig. 5, the dynamic temperature head ($w_{2ax}^2/2c_p$) is almost entirely recovered by these instruments. For axial flow velocities $w_{2ax} > 80$ m/s (the exit velocity was estimated employing the conservation of mass and energy), recovery factors close to 90% were measured. The observed decay at low

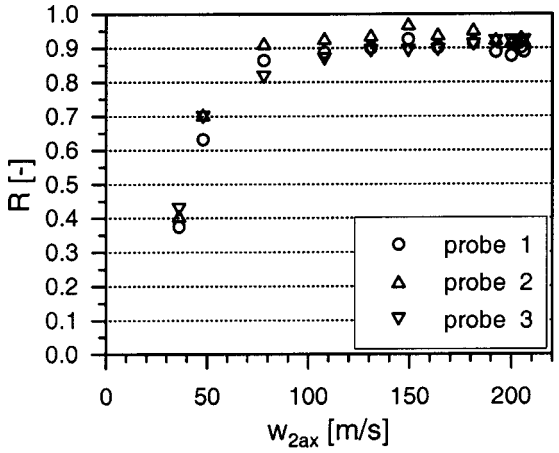

Fig. 5 Measured recovery factors for three cylindrical stagnation probes of equal shape

Table 1 Nondimensional parameters for the test cases

Noz. Pressure Ratio π	Nondim. Flow Rate c_w	Turb. Flow Parameter $\lambda_{\text{turb}} = c_w\,\text{Re}_\varphi^{-0.8}$
1.33 .. 1.37	48000–49000	0.33–1.49
1.26 .. 1.29	40000–41000	0.29–1.33
1.19 .. 1.21	31000–33000	0.23–1.11
1.09 .. 1.11	20000–23000	0.15–0.82

air velocities is due to a reduced stagnation zone (a more physical background is given in Hottel and Kalitinsky [13]) but does not impair the accuracy. Although the devices tested in this setup show slightly lower recovery factors R than the so-called ''Pratt & Whitney'' probes earlier presented by Hottel and Kalitinsky [13], a good measuring accuracy can be accomplished with the present technique. The scatter observed in Fig. 5 is in an acceptable range and certainly due to manufacturing tolerances.

For all temperature measurements, type K thermocouples were employed and the system accuracy determined to be better than ± 1 K. Pressures were recorded by means of a single transducer (accuracy 0.5%) coupled to a 48-channel Scanivalve rotary switch.

One major objective of this research study was not only to quantify the cooling efficiency of this preswirl system but also to separate those effects that are responsible for degrading its cooling performance. Concerning the latter task, e.g., the real flow conditions at the inlet of the rotating disk holes had to be exactly known (the relevance of c_{1t} is expressed by Eq. (1)). Due to a highly turbulent, fully three-dimensional flow field in this region, velocity measurements are extremely difficult to accomplish. In addition, neither temperatures nor total pressures can be measured accurately inside the cavity which could prove the assumption of isentropic flow made in earlier studies (Eq. (1)). Nevertheless, a nonintrusive laser-based measuring technique can successfully be employed to explore and analyze very accurately the flow field existing at close distance from the receiver inlet, as recently demonstrated by Geis et al. [8]. Although the cavity flow was determined to have large circumferential velocity gradients, the data acquired by the authors in the midplane between rotor and stator for different measuring positions relative to nozzle and disk hole were arithmetically averaged in the present work for each operating condition. Thus, a one-dimensional velocity could be derived which was taken to be representative for the entire wheelspace. The new data allowed the authors to specify an effective flow velocity at the rotor inlet which reduces the total temperature to be expected in the rotating frame. The result of this one-dimensional analysis is shown in the next section while the details about the PIV measuring technique can be found in Geis et al. [8].

Results and Discussion

Results are presented for different nozzle pressure ratios π although experiments were run at constant overall system pressure ratios (adjusting the latter parameter turned out to be less sensitive to the throughflow behavior of the disk holes). The resulting throughflow rates c_w are listed in Table 1. The variation of the rotational Reynolds number Re_φ is expressed in terms of the turbulent flow parameter λ_{turb}.

The tangential velocities measured by Geis et al. [8] in the midplane between the rotor disk and the preswirl plate at different distances from one nozzle exit and at different locations relative to a disk hole were arithmetically averaged and reduced to one single representative velocity, $v_{t,av}$. Although local effects are neglected by this method, it allows for comparing measured data with theoretical velocities expected for ideal system behavior. The result of such a comparison is illustrated in Fig. 6. As a matter of fact, the averaged flow velocities from the PIV measurements described in Geis et al. [8], $v_{t,av}$, were approximately 50% lower than the values calculated for reversible flow, $c_{1t,is}$. Experimental

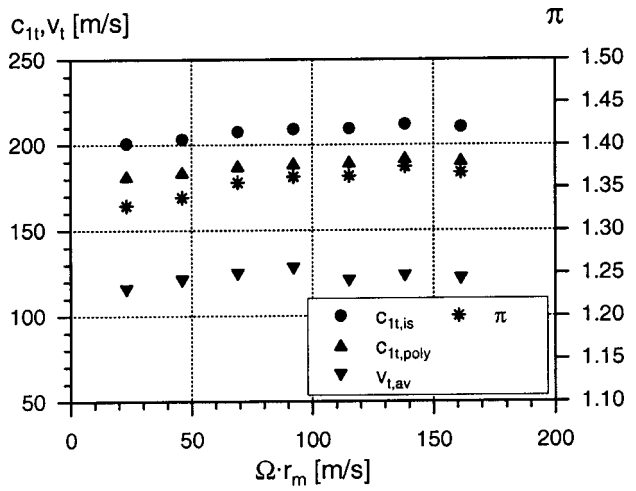

Fig. 6 Flow velocities inside the preswirl chamber

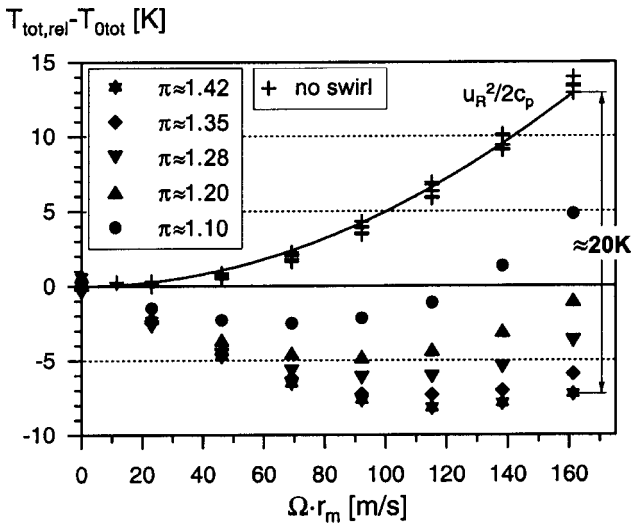

Fig. 8 Total temperatures ($s=10$ mm, $c/d=0.04$)

evaluation of pressures, temperatures and mass flow rates inside the system allowed the calculation of another nozzle discharge velocity assuming a polytropic expansion through these elements, $c_{1t,\mathrm{poly}}$ (the polytropic exponent was determined for each test point employing the conservation of mass and energy). These values were included in Fig. 6 to specify the flow condition at the inlet of the disk holes if losses would only occur inside the nozzle with the flow inside the rotor-stator annulus still being undisturbed. As expected, $c_{1t,\mathrm{poly}}$ lies in between $c_{1t,is}$ and $v_{t,av}$. For the nozzle pressure ratio chosen here ($\pi \approx 1.35$), all flow velocities are nearly independent from the rotational disk speed indicating a throughflow dominated regime. The slight increase in nozzle pressure ratio, observed in Fig. 6, is due to the discharge behavior of the disk holes.

In Fig. 7, the loss of momentum caused by the flow through the preswirl cavity is shown by plotting the effective swirl ratio $\overline{\beta}_{\mathrm{eff}} = v_{t,av}/\Omega \cdot r_m$ against the value determined for the outlet plane of the nozzle, $c_{1t,\mathrm{poly}}/\Omega \cdot r_m$. The relation between both velocity ratios is almost linear for the whole range of throughflow rates. Hence, for the geometry of the preswirl system tested here, an effective swirl ratio $\overline{\beta}_{\mathrm{eff}}$, describing the reduction of the initial swirl at the entry to such a system, can be correlated to give

$$\overline{\beta}_{\mathrm{eff}} = 0.0708 + 0.6261 \cdot c_{1t,\mathrm{poly}}/\Omega \cdot r_m . \tag{3}$$

Figure 8 shows total temperatures of the air measured inside the receiver holes using the rotating stagnation probes described in the previous section. The experiments were conducted for different nozzle pressure ratios π and disk speeds $u_R = \Omega \cdot r_m$ at $s = 10$ mm, $N = 12$, and $c/d = 0.04$. Additional experiments were performed for different throughflow rates with the preswirl nozzles removed from the apparatus to test the capability of the measuring technique to capture the total temperatures while the disk was rotating. $T_{\mathrm{tot,rel}}$ denotes the arithmetic average from the thermocouple readings taken inside the holes at four different locations (comp. Fig. 3).

The measured reduction of total temperature (the term $T_{\mathrm{tot,rel}} - T_{0\,\mathrm{tot}}$ becomes negative if "cooling" of the air is achieved) increases with the nozzle pressure ratio π, i.e., with the tangential absolute flow velocity at the inlet to the preswirl cavity. At the highest pressure ratio tested ($\pi \approx 1.42$), the total temperature "seen" by the rotor is almost 8K cooler than $T_{0\,\mathrm{tot}}$, the total temperature at the inlet to the system. The advantage gained from this air transfer system becomes more dramatic if $T_{\mathrm{tot,rel}}$ is compared with $u_R^2/2c_p$, the value obtained in a conventional system without preswirled cooling air: for the given geometry and pressure ratios tested, the maximum difference between both systems was determined to be 20K!

In Fig. 9, the temperature ratio $T_{\mathrm{tot,rel}}/T_{0\,\mathrm{tot}}$ is plotted against

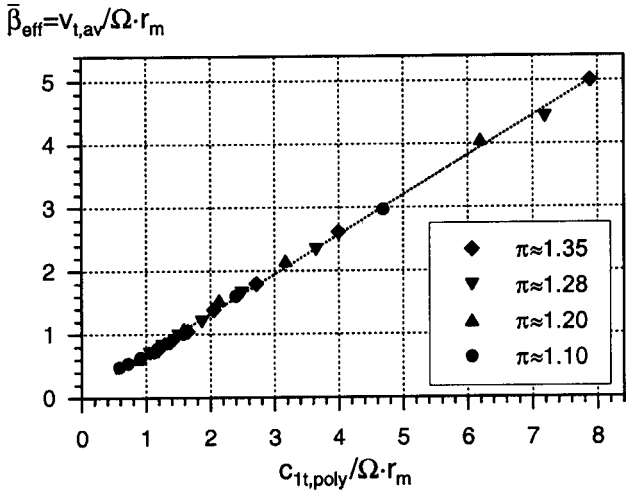

Fig. 7 Effective swirl ratio

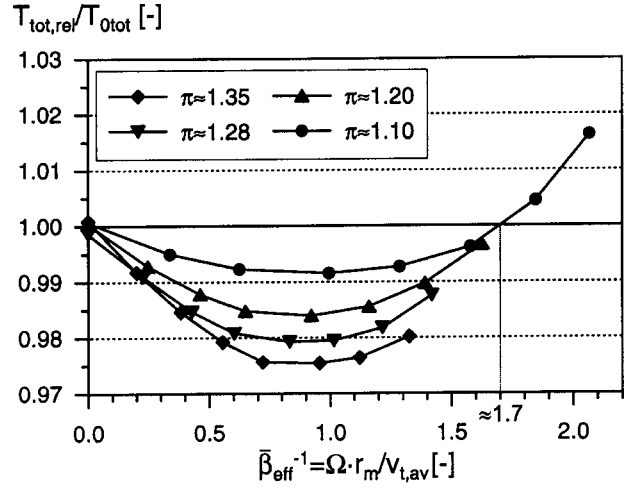

Fig. 9 Nondimensional temperature reduction ($s=10$ mm, $c/d=0.04$)

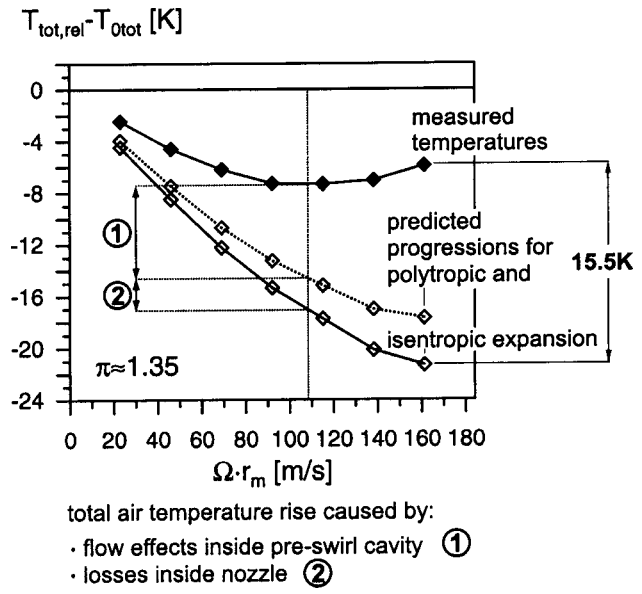

Fig. 10 Temperature elevation due to losses inside preswirl cavity and nozzle

the velocity ratio $1/\bar{\beta}_{\text{eff}}=\Omega\cdot r_m/v_{t,av}$. For all pressure ratios, the curves decrease until a minimum is reached at $\bar{\beta}_{\text{eff}}\approx 1$. If $u_R=\Omega\cdot r_m$ is further increased (and $v_{t,av}$ kept constant), all curves show an ascending behavior. $T_{\text{tot,rel}}/T_{0\text{ tot}}=1$ is finally reached at $1/\bar{\beta}_{\text{eff}}\approx 1.7$.

At a given pressure ratio, i.e., cooling flow rate, the maximum temperature reduction can be expected at $\bar{\beta}_{\text{eff}}=1$ in an ideal system. At the same time, heating (with respect to $T_{0\text{ tot}}$) occurs if $1/\bar{\beta}_{\text{eff}}\geqslant 2.0$ (see, e.g., Wilson et al. [4]). For the preswirl system tested here, the range of disk speeds where cooling can be achieved is smaller compared to an isentropic system: in the present work, temperatures smaller than $T_{0\text{ tot}}$ were measured for $\Omega\cdot r_m/v_{t,av}<1.7$. Hence, since the observed loss of momentum was already accounted for by employing $\bar{\beta}_{\text{eff}}$ in Fig. 9, another effect apart from $\bar{\beta}_{\text{eff}}$ is supposed to be responsible for degrading the cooling efficiency. A more profound analysis is required to reveal this additional mechanism.

Figure 10 shows measured temperatures and those values calculated assuming either isentropic or polytropic expansion through the nozzles at a given pressure ratio $\pi\approx 1.35$. Thereby, the ''isentropic expansion'' curve denotes a system that suffers neither from losses inside the nozzle nor from mixing losses inside the rotor-stator annulus. Inside such a system, the highest tangential flow velocities and hence, the lowest air total temperatures in the relative frame can be expected. The ''polytropic expansion'' curve characterizes a system that suffers merely from losses related to the preswirl nozzle. Fig. 10 illustrates that the air temperatures measured in a real system do drastically differ from those achieved under isentropic conditions. Thereby, the effects appearing inside the preswirl cavity seem to dominate the behavior of the real system. While the maximum difference between the ''isentropic'' and ''polytropic'' system is relatively small (≈4 K), a much larger difference can be observed between the graphs describing the real and ''isentropic'' system ($\Delta T\approx 15.5$ K).

Although Fig. 10 specifies the potential improvement of a well designed cooling air system, it does not give adequate information about the mechanisms responsible for real system behavior.

Following Eq. (1), the cooling air temperature in the relative frame can be approximated employing the tangential flow velocity measured inside the preswirl cavity, $v_{t,av}$:

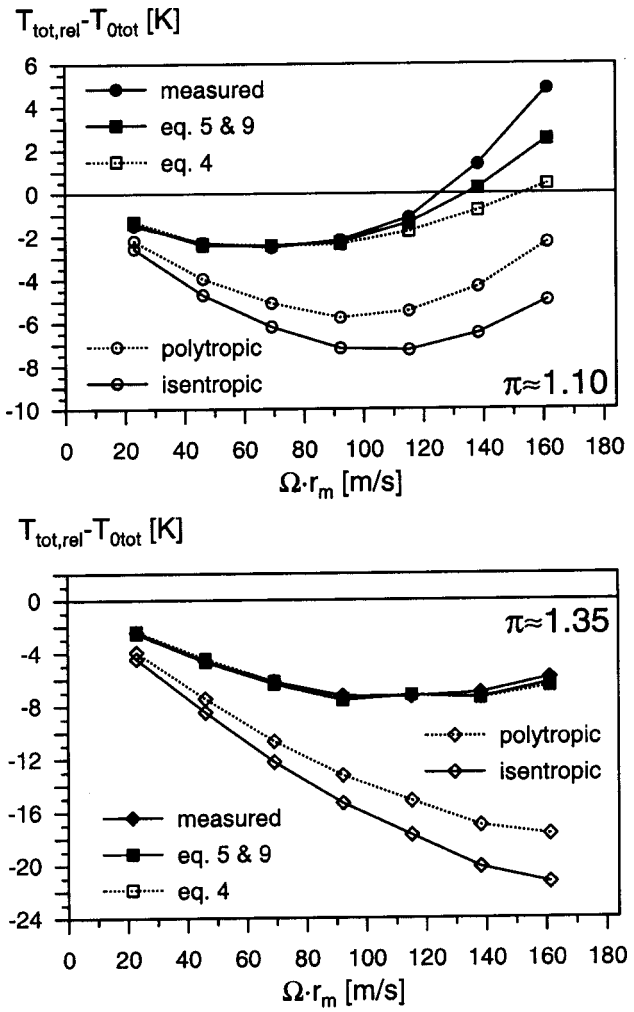

Fig. 11 Comparison between measured and theoretical temperatures—effect of $\bar{\beta}_{\text{eff}}$ and M_{rotor}

$$\frac{T_{1\text{ tot,rel}}}{T_{1\text{ tot}}}=1+\frac{u_R^2-2u_R v_{t,av}}{2c_p T_{1\text{ tot}}}. \tag{4}$$

Assuming that $T_{1\text{ tot}}$ equals $T_{0\text{ tot}}$—this is the case for an adiabatic expansion—the resulting relative total temperatures were plotted in Fig. 11 as squared open symbols. As can be seen, the semi-empirical model (Eq. (4)) predicts the measured values much better than the previous models employing either $c_{1t,is}$ or $c_{1t,\text{poly}}$. However, the agreement is only satisfying for large throughflow rates c_w and low rotational Reynolds numbers Re_φ. At the highest disk speeds and a nozzle pressure ratio of $\pi\approx 1.1$, the results deviated from the measured values by ≈5 K. This deviation is significant considering that in modern gas turbine engines, even higher disk rotational Reynolds numbers are achieved compared to those tested in the present experimental investigation. Viscous drag becomes increasingly relevant under these conditions and hence, can also be accounted for in the present study by the term

$$T_{1\text{ tot}}=T_{0\text{ tot}}+\Delta T_{\text{tot,abs}} \tag{5}$$

where

$$\Delta T_{\text{tot,abs}}=\frac{M_{\text{rotor}}\cdot\Omega}{\dot{m}\cdot c_p} \tag{6}$$

A simplified analytical solution was found for M_{rotor} employing an integral method presented by Goldstein [14]. The solution implied stationary turbulent flow with boundary layers according to the

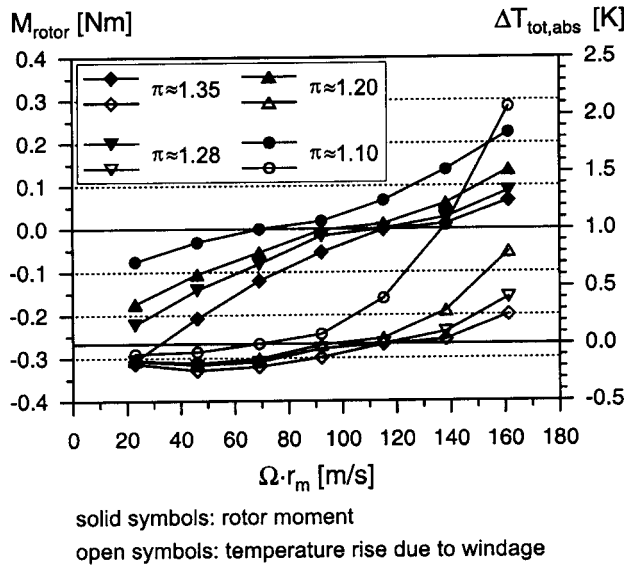

Fig. 12 Moment on rotor and corresponding temperature elevation

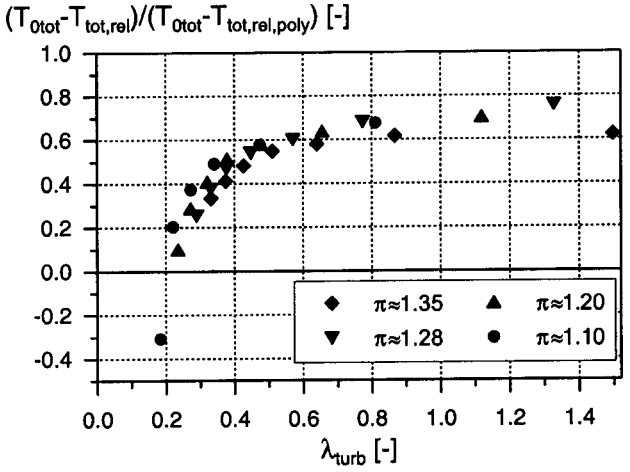

Fig. 13 Cooling efficiency

1/7th power law. Any perturbances generated by the preswirl jets and the rotating disk holes were neglected, the adjacent cavity walls were regarded to be smooth. Integrating from $r_1=0.203$ to $r_2=0.25$ m in the present study (the height of the preswirl cavity) finally results in

$$M_{\text{rotor}}=0.1676\rho\nu^{0.2}\frac{(r_2^{4.6}-r_1^{4.6})}{4.6}\cdot\left(\Omega-\frac{v_{t,av}}{r_m}\right)^{1.8}. \tag{7}$$

The moment of the rotor M_{rotor} as well as the rise of the total temperature in the absolute frame $\Delta T_{\text{tot,abs}}$ are plotted in Fig. 12. The diagram shows that windage heating takes place at positive values of M_{rotor}, i.e., at swirl ratios $\overline{\beta}_{\text{eff}}<1$. Vice versa, cooling can be expected for $\overline{\beta}_{\text{eff}}>1$, although the latter effect might be negligible in practical applications.

Considering $\Delta T_{\text{tot,abs}}$ in Eq. (4), the resulting progression of $T_{\text{tot,rel}}$ was also plotted in Fig. 11 and indicated by closed (squared) symbols. The measured data is reproduced much better by this extended model. Although the agreement between measured and modeled temperatures is satisfying for the range of parameters investigated in this work, a remaining deviation of ≈ 2 K must be acknowledged at the highest rotational speed and smallest flow rate, i.e., pressure ratio investigated here. At large rotational Reynolds numbers in conjunction with swirl ratios $\overline{\beta}_{\text{eff}}<1$, Eqs. (4) and (5) tend to underestimate the real system behavior, possibly due to the simplifications made in the integral solution for M_{rotor}.

Equations (6) and (7) can be rewritten in a nondimensional form to give

$$\frac{M_{\text{rotor}}}{\dot{m}\cdot u_R\cdot r_m}=\frac{r_2^{4.6}-r_1^{4.6}}{27.446\cdot r_m^{4.6}}\cdot(1-\overline{\beta}_{\text{eff}})^{1.8}\cdot\lambda_{\text{turb}}^{-1} \tag{8}$$

and

$$\Delta T_{\text{tot,abs}}=2\cdot\left(\frac{r_2^{4.6}-r_1^{4.6}}{27.446\cdot r_m^{4.6}}\cdot(1-\overline{\beta}_{\text{eff}})^{1.8}\cdot\lambda_{\text{turb}}^{-1}\right)\cdot\frac{u_R^2}{2c_p}. \tag{9}$$

If the measured temperature reduction is related to the reduction expected for the ''polytropic nozzle'' theory (see Fig. 10), this relation defines the cooling efficiency of a real system characterized by losses occurring inside the preswirl cavity. In nondimensional parameters this term can be written as

$$\frac{T_{0\,\text{tot}}-T_{\text{tot,rel}}}{T_{0\,\text{tot}}-T_{\text{tot,rel,poly}}}=\frac{\overline{\beta}_{\text{eff}}-\frac{1}{2}-\frac{M_{\text{rotor}}}{\dot{m}\cdot u_R\cdot r_m}}{\frac{c_{1t,\text{poly}}}{u_R}-\frac{1}{2}}. \tag{10}$$

According to Eq. (10), the cooling efficiency depends on the effective swirl ratio $\overline{\beta}_{\text{eff}}$ (comp. Eq. (3)), the geometry of the system and the turbulent flow parameter λ_{turb}. Thereby, windage heating must be considered at relatively high rotational Reynolds numbers Re_φ and low cooling flow rates c_w in those situations where the effective swirl ratio $\overline{\beta}_{\text{eff}}$ becomes smaller than unity.

Using measured values for $T_{\text{tot,rel}}$, a dependency between the cooling efficiency and the turbulent flow parameter λ_{turb} was determined which is illustrated in Fig. 13. It shows that, e.g., at $\lambda_{\text{turb}}\approx 0.4$, a cooling efficiency of only 50% (with respect to $T_{0\,\text{tot}}$) was achieved with the present preswirl system. The loss of momentum due to mixing detected inside the rotor-stator annulus where the preswirl air meets the rotating core flow (see, e.g., Geis et al. [8]) is certainly one major reason for this result. However, the descending slope observed for flow parameters $\lambda_{\text{turb}}<0.8$ is also due to frictional heating, as suggested by Eq. 10. Negative ratios of $(T_{0\,\text{tot}}-T_{\text{tot,rel}})/(T_{0\,\text{tot}}-T_{\text{tot,rel,poly}})$ indicate that heating took place compared to the total temperature at the entry to the system, $T_{0\,\text{tot}}$.

Conclusions

The results presented in this paper were obtained from an experimental investigation of a so-called direct transfer cooling air preswirl system. In this system, run under adiabatic conditions, no radial outflow of coolant was superposed on the preswirled flow. Despite these ''favorable'' constraints, the preswirl system was found to perform much worse in terms of cooling air temperature reduction than it was expected for isentropic flow. The mechanisms responsible for the inadequate system behavior—polytropic nozzle flow, significant mixing in the rotor-stator annulus and windage heating—could clearly be identified and separated. A thorough study was performed to evaluate their relevance.

Prior to determining the cooling efficiency of this air transfer system, a proper instrumentation technique had to be adapted to the apparatus allowing the measurement of total temperatures inside small rotating disk holes. The authors took advantage of small cylindrical stagnation pressure probes which were modified to accomplish temperature measurements. The recovery factors of these instruments were determined to be better than 85% for the relevant test cases and therefore, found to provide for the desired measuring accuracy.

With the instrumented rotor disk, measured temperatures exceeded those values predicted for an ''ideal'' system by approximately 15.5 K. While losses inside the preswirl nozzles were found to elevate the total temperatures in the relative frame by only 4 K, mixing inside the preswirl cavity turned out to be the dominant source for the observed decline in cooling performance. Circumferentially averaged flow velocities measured in an earlier study were approximately 50% smaller than the tangential velocities predicted for isentropic flow, confirming that a massive loss of momentum due to mixing took place in the rotor-stator annulus. A semi-empirical model was built based on the experimental flow data which underestimated the measured temperatures especially at large rotational Reynolds numbers Re_φ and small cooling flow rates c_w. An extended model was developed which considered the viscous drag of the rotor resulting in a distinctive heating of the coolant under certain flow conditions where the effective swirl ratio $\overline{\beta}_{\mathrm{eff}}$ became smaller than unity. The agreement between the theoretical and measured data was satisfying for the range of flow parameters tested in this investigation. However, at large Reynolds numbers and small throughflow rates, the simplifications made in the integral solution to determine the frictional moment of the rotor underestimated this additional effect. Windage heating was found to be negligible for many of the test cases but became increasingly important at turbulent flow parameters $\lambda_{\mathrm{turb}}<0.8$.

Future developments in gas turbine engines are directed towards higher overall thermal efficiencies, smaller specific fuel consumption and lower specific weight. To achieve these goals, secondary air systems must be more efficient, i.e., require less compressed cooling air to meet the demands in the hot turbine region. Reduced flow rates might result in turbulent flow parameters λ_{turb} much smaller than the ones investigated in the present study. Under these circumstances, parasitic effects like the ones detected here will become increasingly important and must be avoided by an optimized design of the preswirl apparatus. In specifying and evaluating the effects leading to a reduced cooling efficiency, the present work shows options how this task can be accomplished. Improvements are expected if mixing losses and windage can be minimized, and one promising approach would certainly be to increase the open circumference of the system. A large number of perfect nozzles and a very small rotor and stator wall surface might therefore be favored features in the design process of better cooling schemes.

Acknowledgment

This work was accomplished while all of the authors were present at the Institut für Thermische Strömungsmaschinen, University of Karlsruhe. The authors wish to thank the European Commission for partly funding the experimental research described in this paper.

Nomenclature

A = cross-sectional area (m^2)
c = depth of chamfer (m)
c = velocity in the absolute frame of reference (m/s)
c_w = nondimensional mass flow rate ($c_w=\dot{m}/(\mu r_2)$)
c_p = specific heat (J/(kgK))
d = diameter (m)
l = length of receiver holes (m)
$\dot{m}$ = mass flow rate (kg/s)
N = number of flow elements
n = disk rotational speed (1/min)
p = pressure ($\mathrm{N/m}^2$)
R = recovery factor
r = radius (m)
r_2 = outer radius of disk (m)
r_e = pitch radius of the preswirl nozzle exit (m)
r_m = pitch radius of the receiver holes (m)
Re_φ = rotational Reynolds number ($\mathrm{Re}_\varphi=\Omega r_m^2/\nu$)
s = axial spacing between rotor and stator (m)
T = temperature (K)
u = circumferential velocity (m/s)
v = measured absolute velocity (m/s)
w = velocity in the rotating frame of reference (m/s)
$\overline{\beta}_{\mathrm{eff}}$ = effective swirl ratio ($\overline{\beta}_{\mathrm{eff}}=v_{t,av}/(\Omega r_m)$)
λ_{turb} = turbulent flow parameter ($\lambda_{\mathrm{turb}}=c_w\,\mathrm{Re}_\varphi^{-0.8}$)
μ = dynamic viscosity ($\mathrm{Ns/m}^2$)
ν = kinematic viscosity (m^2/s)
π = nozzle pressure ratio ($\pi=p_{0\ \mathrm{tot}}/p_{1\ \mathrm{static}}$)
Ω = disk angular velocity (1/s)

Subscripts

abs = absolute system
av = average
ax = axial
is = isentropic
N = preswirl nozzle
poly = polytropic
R = receiver hole
rel = relative system
t = tangential
tot = total state
0,1,2 = stage 0,1,2

References

[1] Karabay, H., Chen, J.-X., Pilbrow, R., Wilson, M., and Owen, J. M., 1999, ''Flow in a ''Cover-Plate'' Preswirl Rotor-Stator System,'' ASME J. Turbomach., **121**, pp. 160–166.
[2] Popp, O., Zimmermann, H., and Kutz, J., 1998, ''CFD Analysis of Coverplate Receiver Flow,'' ASME J. Turbomach., **120**, pp. 43–49.
[3] Dittmann, M., Geis, T., Schramm, V., Kim, S., and Wittig, S., 2002, ''Discharge Coefficients of a Preswirl System in Secondary Air Systems,'' ASME J. Turbomach., **124**, pp. 119–124.
[4] Wilson, M., Pilbrow, R., and Owen, J. M., 1997, ''Flow and Heat Transfer in a Preswirl Rotor-Stator System,'' ASME J. Turbomach., **119**, pp. 364–373.
[5] El-Oun, Z. B., and Owen, J. M., 1989, ''Pre-swirl Blade-Cooling Effectiveness in an Adiabatic Rotor-Stator System,'' ASME J. Turbomach., **111**, pp. 522–529.
[6] Wilson, M., and Owen, J. M., 1994, ''Axisymmetric Computations of Flow and Heat Transfer in a Pre-Swirl Rotor-Stator System,'' presented at the First International Conference on Flow Interaction, Hong Kong.
[7] El-Oun, Z. B., Neller, P. H., and Turner, A. B., 1988, ''Sealing of a Shrouded Rotor-Stator System with Preswirl Coolant,'' ASME J. Turbomach., **110**, pp. 218–225.
[8] Geis, T., Rottenkolber, G., Dittmann, M., Richter, B., Dullenkopf, K., and Wittig, S., 2002, ''Endoscopic PIV-Measurements in an Enclosed Rotor-Stator System With Pre-Swirled Cooling Air,'' *Proceedings of the 11th International Symposium on Applications of Laser Techniques to Fluid Mechanics*, July 8–11.
[9] Meierhofer, B., and Franklin, C. J., 1981, ''An Investigation of the Preswirled Cooling Airflow of a Turbine Disc by Measuring the Air Temperature in the Rotating Channels,'' ASME Paper No. 81-GT-132.
[10] Karabay, H., Owen, J. M., and Wilson, M., 2001, ''Approximate Solutions for Flow and Heat Transfer in Pre-Swirl Rotating-Disc Systems,'' ASME Paper No. 2001-GT-0200.
[11] Eck, B., 1981, *Technische Strömungslehre, Sechste Auflage*, Springer-Verlag, Berlin.
[12] Schoen, J., 1951, ''Die Temperaturmessung in strömenden Gasen,'' Archiv für Technisches Messen V2165-1.
[13] Hottel, H. C., and Kalitinsky, A., 1945, ''Temperature Measurements in High-Velocity Air Streams,'' ASME J. Appl. Mech., **67**, pp. A25–A32.
[14] Goldstein, S., 1935, ''On the Resistance to the Rotation of a Disc Immersed in a Fluid,'' Proc. Cambridge Philos. Soc., **31**, pp. 232–241.

Analysis of Cycle Configurations for the Modernization of Combined Heat and Power Plant by Fitting a Gas Turbine System

Tadeusz Chmielniak

Gerard Kosman
e-mail: kosman@polsl.gliwice.pl

Wojciech Kosman

Silesian University of Technology,
Institute of Power Engineering and
Turbomachinery,
PL-44-100 Gliwice,
ul. Konarskiego 18, Poland

The application of a gas turbine generally allows to increase the number of possible configurations of cogenerated heat and electrical power systems, which became a significant substitute for classic, coal-fired power plants. They are characterized by better thermodynamical, economical, ecological, and operating indexes. Gas turbine units are also the best option for the modernization of existing power plants. This paper discusses the effectiveness of various technological configurations with gas turbines, which are to be applied during modernization projects of already existing conventional combined heat and power plants. In the analysis enthalpy and entropy methods were applied. Algorithms of the entropy method allow to determine the entropy generation in each section of a combined heat and power (CHP) plant. Several criteria were taken into consideration while analyzing the effectiveness of technological cycle configurations with gas turbines. These include the energy effectiveness, the efficiency of the HRSG and the steam cycle, the efficiency of the whole thermal electric power station, the exergetic efficiency of the HRSG and the steam cycle, and the fuel efficiency index. It was assumed that gas turbines operate under their nominal conditions. The composite curves were also taken into consideration while choosing the type of the turbine. The modernization project tends not to eliminate those existing power plant sections (machines and equipment), which are able to operate further. The project suggests that those units should remain in the system, which satisfy the applied durability criterion. The last phase of the optimization project focuses on the sensibility verification of several steam-gas CHP plant parameters and their influence on the whole system. [DOI: 10.1115/1.1765126]

Introduction

There are economical and ecological reasons for modernization of a considered CHP plant. The economical ones are high costs of energy and heat production. Some units have to be removed because of their poor technical condition. The ecological reasons derive from the necessity of satisfying the environmental law regulations. The CHP plant had to satisfy specified heat demand and provide safe operation during a specified period of time, [1–3].

The aim of the modernization is to

- increase the CHP plant competitiveness in electrical power and heat markets;
- reduce the influence on environment by:
  reducing the furnace gas and ashes emission,
- decreasing the rate of ash and slag wastes,
- restraining the railway and car transport maintaining the CHP plant,
- decreasing the noise level;
- exchange the inefficient units with new technologies.

The suggestion of technical modernization presented here is based on adding a gas turbine and a heat recovery steam generator (HRSG), [4]. Fueling a plant with natural gas:

- increases the fuel chemical utilization effectiveness, which is provided by cogeneration;
- decreases the harmful influence on natural environment by: elimination of SO_2 and flue dust;
- NO_x and CO_2 emission reduction;
- water losses reduction;
- reduces the investment cost.

Formulation of the Problem, Input Data

The simplified thermodynamical diagram of the CHP plant at present state is shown in Fig. 1. There are high and low pressure steam collectors separated by turbines. Livesteam is supplied by coal-fired steam boilers K-1, K-2, K-4, and K-5. Two condensing units with bleedings are modeled as one (TG-1,2). Their bleedings may be regulated. The mass flow rate of the steam in the low pressure collector and of the livesteam feeding the back-pressure TG-4 heating turbine depend on the heat demand in the main system heat exchangers (shaded gray), [4].

Anticipated heat demand and heat load that the CHP plant is supposed to satisfy is as follows:

- water 170 MW and
- steam 80 MW.

Before the main calculations could be done, input data for the modernization project had to be developed. They derived from the preliminary evaluation of the system concentrated on two aspects.

The first one was the *planned time of operation*. It describes the user expectations as for the future reliable unit operation. This is the required number of hours of the future operation and is specified by the user. Then the modernization project designer has to decide whether the units would be able to operate for the specified period of time.

The second aspect was that the preliminary technical state evaluation concerned not just the whole units but their main com-

Contributed by the International Gas Turbine Institute (IGTI) of THE AMERICAN SOCIETY OF MECHANICAL ENGINEERS for publication in the ASME JOURNAL OF ENGINEERING FOR GAS TURBINES AND POWER. Paper presented at the International Gas Turbine and Aeroengine Congress and Exhibition, Atlanta, GA, June 16–19, 2003, Paper No. 2003-GT-38240. Manuscript received by IGIT, October 2002, final revision, March 2003. Associate Editor: H. R. Simmons.

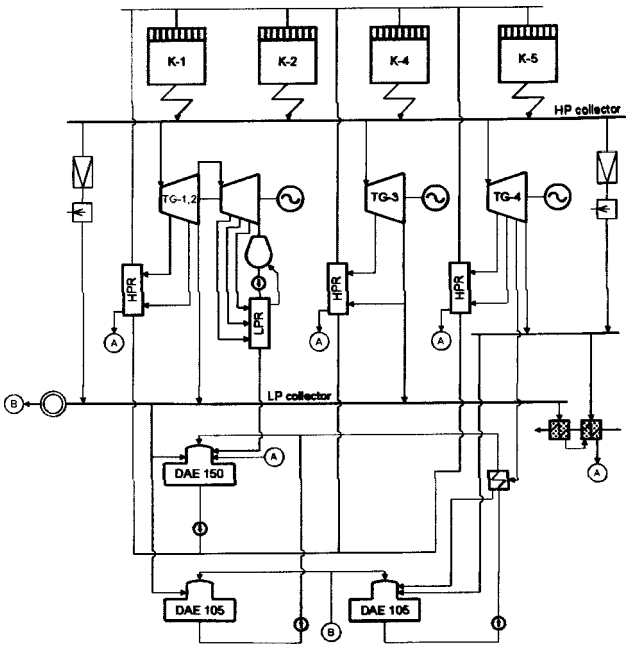

Fig. 1 Present state

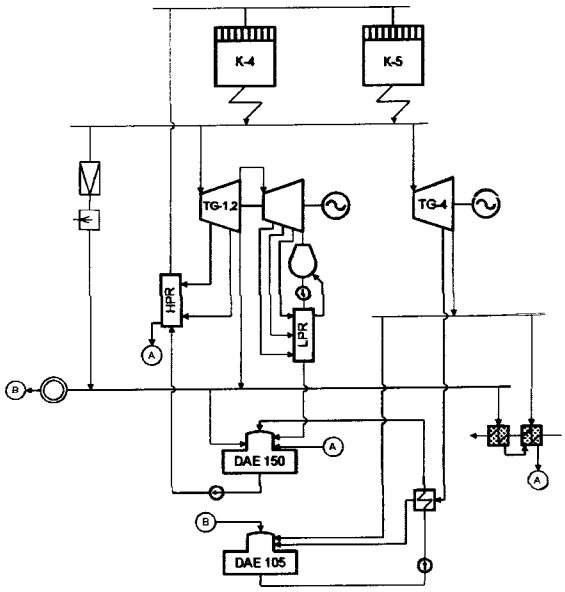

Fig. 2 Initial configuration

ponents such as rotors, cylinders, valves, and heat regeneration exchangers. Therefore a simple evaluation (''unit may or may not further operate'') was replaced with a more detailed one. This approach ensured that no unit would be unnecessarily withdrawn and more criteria affected the final solution.

The technical state might be described by efficiency indexes of the whole system and its components, by the degree of satisfying environmental protection law regulations and by the degree of material consumption of the machines components.

Several kinds of documentation were the basis of the evaluation. They were: machines operating history and processes reports (e.g., startups and shutoffs measurements), durability state analysis (numerical simulation of thermal and stress states), destructive and nondestructive tests results (done during repairs), [5,6]. (see Fig. 1.)

The initial analysis suggested that the following units or their components had to be withdrawn:

- steam boilers K-1 and K-2,
- back-pressure TG-3 turbine, and
- high pressure regeneration of TG-4 turbine.

The initial system configuration was defined. It is shown in Fig. 2. The exploited units and components are removed. This configuration does not however satisfy heat demand—the amount of produced livesteam is not enough.

Modernization Options

Five different options of fitting the gas turbine into the system were analyzed. Their simplified thermodynamical diagrams are shown throughout Figs. 3–7. These options regard different configurations of the heat recovery steam generator and the bottom steam cycle.

In the first option (Fig. 3; only the rearranged part of the system is shown) the applied gas turbine is linked to the already existing system through a heat recovery steam generator (HRSG). The steam cycle remains unchanged. The flow rate of livesteam at high pressure remains at its previous level. The amount of steam produced in the HRSG is equal to the livesteam mass flow rate produced previously in the both steam boilers. However, steam turbine TG-3 is already withdrawn and the additional steam must be reduced in pressure and temperature. This generates an exergy loss.

The next option (Fig. 4) is a modification of the previous one. The steam cycle still remains unchanged. Livesteam is produced in the steam recovery heat generator at two different pressure levels: 8900 kPa (High Pressure–HP) and 800 kPa (Low Pressure–LP). High-pressure steam feeds the steam turbines while the low-pressure one goes directly to the low pressure collector feeding thermal heat exchangers and sending the steam outside of the system as the process steam.

The first steam cycle modification occurs in option III (Fig. 5). The high-pressure recovery (HPR) of TG-1 and TG-2 is suspended and located instead in the heat recovery steam generator. The HRSG produces steam at two pressure levels, just as for option II.

Option IV (Fig. 6) provides further modification of the steam cycle. Both, high and low-pressure recovery (HPR and LPR) of TG-1 and TG-2, are located in the heat recovery steam generator. The HRSG produces steam at two pressure levels, just as for option II.

In the last option (Fig. 7) the 150 deaerator units are no longer fed by the steam from the low pressure steam collector. Livesteam for the deaerator units (DAE) is produced at the heat recovery steam generator at 550 kPa. Therefore the HRSG now produces livesteam at three different levels (HP, LP, and DAE). High and low-pressure recovery (HPR and LPR) is placed in the HRSG, just as they were in the previous option.

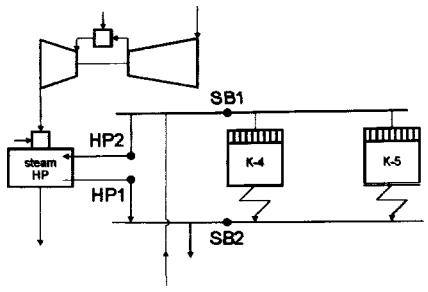

Fig. 3 Option I

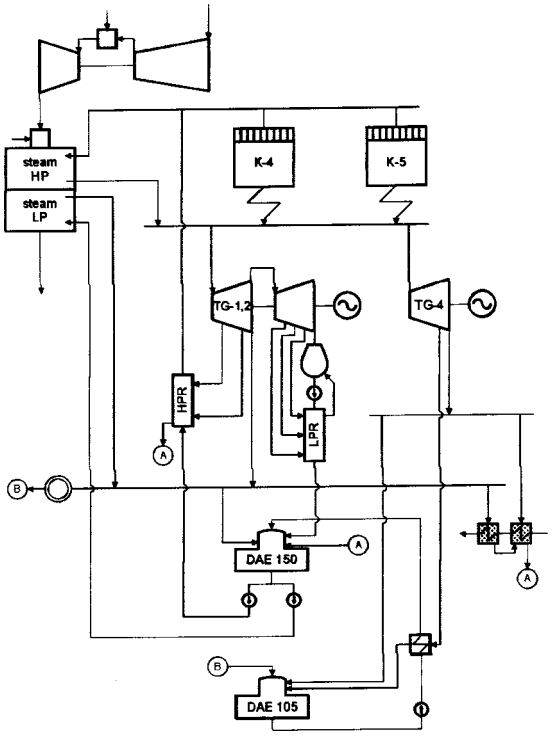

Fig. 4 Option II

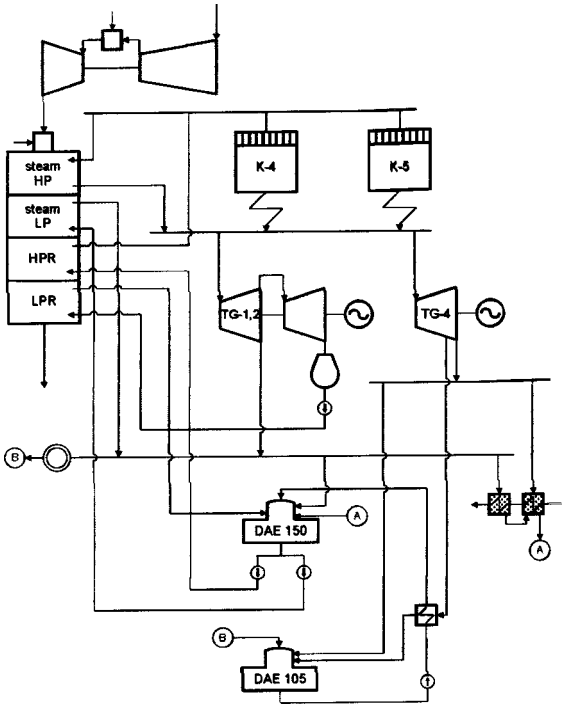

Fig. 6 Option IV

Enthalpy Analysis

The enthalpy analysis is in fact mass and energy balancing of the whole system. An own developed code was used for building the models of the steam turbines and determining steam pressures at bleedings by balancing them. The received data were used to build the Gate Cycle software, [7], models of the gas turbine, the heat recovery steam generator (with a reburner), the low pressure steam main collector and the 150 deaerator (DAE) for each of the options. Different types of gas turbines were applied for the models with their design parameters. Some of them were applied altogether with a reburner situated between the gas turbine exhaust gas outlet and the steam recovery steam generator. Several efficiencies and indexes were calculated to compare the options. Their list includes:

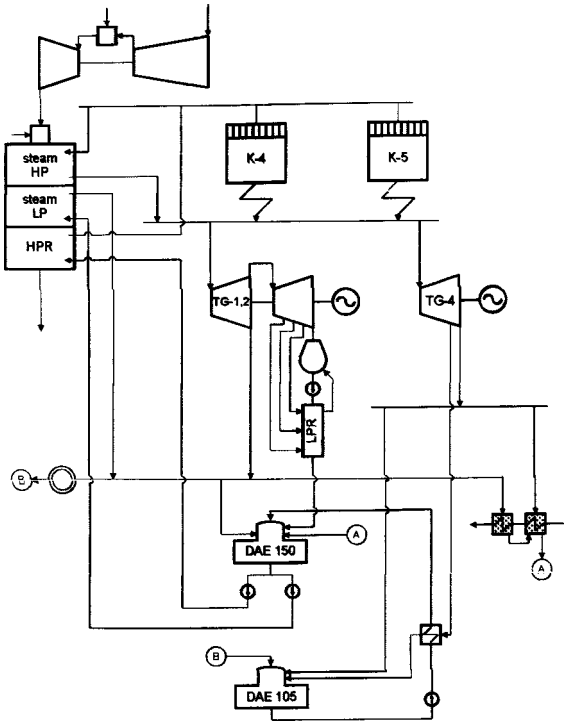

Fig. 5 Option III

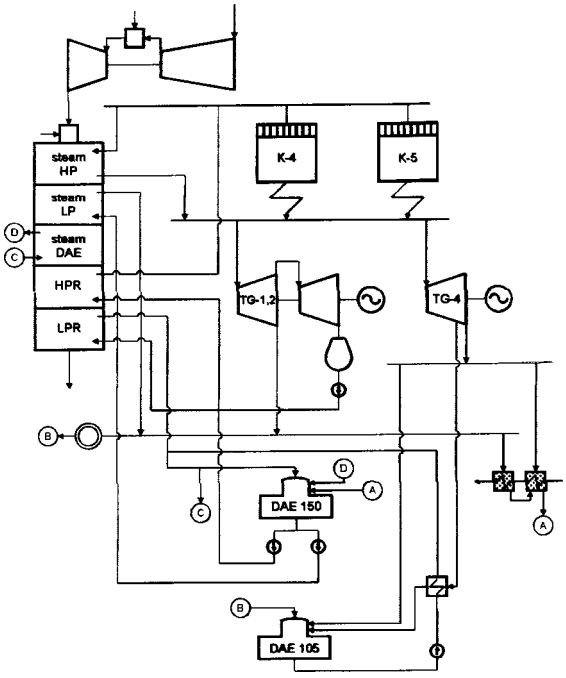

Fig. 7 Option V

Table 1 Calculation results

	I	II	III	IV	V
N_{GT}			84530		
$N_{el}+N_{GT}$ [kW]	151090	152590	159270	160330	160330
m_g			1170		
m_f			51.869		
m_{rbf}	1.8325	–	1.758	1.758	1.4611
t_{HRSGI}	570 C	545 C	569 C	569 C	565 C
η_{HRSG}	0.5973	0.6525	0.7255	0.7686	0.7738
η_{H+SC}	0.3329	0.3583	0.3746	0.3799	0.3830
ε	0.6044	0.6104	0.6371	0.6413	0.6413
η_{tot}	0.7032	0.7185	0.7181	0.7200	0.7220
$\varepsilon_{\mathrm{tot}}$	0.7898	0.7712	0.7638	0.7606	0.7584
t_{HRSG2}	233 C	192 C	157 C	132 C	128 C

- efficiency of the HRSG

$$\eta_{\mathrm{HRSG}}=\frac{Q_{\mathrm{HRSG}}}{H_{g1}} \tag{1}$$

- efficiency of the steam cycle and the HRSG

$$\eta_{H+SC}=\frac{N_{el}}{H_{g1}} \tag{2}$$

- efficiency index

$$\varepsilon=\frac{N_{el}+N_{GT}}{Q} \tag{3}$$

- efficiency of the whole CHP plant

$$\eta_{\mathrm{tot}}=\frac{N_{el}+N_{GT}+Q}{\dfrac{Q_{SB}}{\eta_{SB}}+(m_f+m_{rb})LHV_f} \tag{4}$$

- fuel efficiency index

$$\varepsilon_{\mathrm{tot}}=\frac{(m_f+m_{rb})LHV_f+\dfrac{Q_{SB}}{\eta_{SB}}}{\dfrac{N_{el}+N_{GT}}{\eta_{el}}+\dfrac{Q}{\eta_Q}}. \tag{5}$$

The efficiency of the HRSG is in fact a degree of a steam generator utilization. Installing a HRSG is generally reasonable if this efficiency is greater than 60%. The efficiency index, beside describing the cogeneration level, is also used as an indicator showing whether the power of the applied gas turbine is adequate to the steam cycle. The efficiency index close to 1 means that the gas turbine power is too big. Fuel efficiency index states the amount of fuel saved because of the cogeneration. The efficiency of the whole CHP plant is probably the most important indicator during the operation from plant owners point of view. It defines the amount of fuel energy converted into electric power and heat.

Results of the calculations are presented in Table 1 for a specified gas turbine, which is General Electrics PG7121. It proved to fit the system since it performed the best efficiencies and indexes when compared to other gas turbine types.

The analysis of the HRSG was carried out for the fixed mass flow rates of the steam and water at the inlets and outlets (of course the flow rates differ for each of the option). This was required since the steam cycle was not to be entirely changed—units were supposed to operate at the parameters as close to their design parameters as possible. Therefore livesteam pressure, temperature, and mass flow rates were adjusted but they were not the subject of optimization.

Entropy Method

Entropy method was another tool used for comparing modernization options. It has an advantage when compared to the standard energy balancing, [8]. When calculating system effectiveness by this method, entropy gains are calculated. They provide information about energy losses in system nodes and determine which units are essential when calculating the whole system efficiency.

System efficiency derives from energy and entropy balancing:

$$Q_1-Q_2-Q_3=N_{el} \tag{6}$$

$$\frac{Q_2}{T_2}+\frac{Q_3}{T_3}-\frac{Q_1}{T_1}=S_g \tag{7}$$

Heat transfers in the equations above are transfers at the upper heat source, bottom heat source, and where the

$$Q_1=Q_{\mathrm{HRSG}}+Q_{SB} \tag{8}$$

$$Q_2=Q_{\mathrm{cond}} \tag{9}$$

$$Q_3=Q_{XAB}+Q_{TS}. \tag{10}$$

Eliminating Q_{cond} and calculating N_{el} from Eqs. (6) and (7) the steam cycle efficiency (Eq. (2)) according to entropy method can be described as

$$\eta_{SC(S)}=\frac{Q_1\left(1-\dfrac{T_2}{T_1}\right)+Q_3\dfrac{T_2}{T_3}-S_gT_2}{Q_1}. \tag{11}$$

Temperatures that appear in the equations above are average entropic temperatures of according heat transfer at specified parts of the system. The average entropic temperature of supplied heat transfer equals

$$T_1=\frac{Q_{\mathrm{HRSG}}+Q_{SB}}{S_{out}-S_{in}} \tag{12}$$

where S_{in} and S_{out} are entropies of the flows at the HRSG and steam boilers respective inlets and outlets.

The form of this equation depends on the number of streams at the HRSG, which varies for each of the options. For option 1 formula (13) is

$$T_1=\frac{\boldsymbol{m}_{HP1}(\boldsymbol{h}_{HP2}-\boldsymbol{h}_{HP1})+\boldsymbol{m}_{SB1}(\boldsymbol{h}_{SB2}-\boldsymbol{h}_{SB1})}{\boldsymbol{m}_{HP1}(\boldsymbol{s}_{HP2}-\boldsymbol{s}_{HP2})+\boldsymbol{m}_{SB1}(\boldsymbol{s}_{SB2}-\boldsymbol{s}_{SB1})}. \tag{13}$$

Similar equations describe average temperatures at parts where heat is rejected from the system.

$$T_2=\frac{Q_{\mathrm{cond}}}{S_{in}-S_{out}} \tag{14}$$

Cooling water flows are not taken into consideration here because they do not belong to the system.

$$T_3=\frac{Q_{XAB}+Q_{TS}}{S_{XAB\ in}-S_{XAB\ out}+S_{TS\ in}-S_{TS\ out}} \tag{15}$$

Entropy gains in each part were calculated from individual entropy balances of these parts. The general equation is

$$S_g=S_{out}-S_{in}\pm S_{\mathrm{source}}. \tag{16}$$

The sign of the heat source entropy (S_{source}) depends whether the heat is supplied (−) or rejected (+).

Figure 8 presents entropy gains in parts of the system that change for each of the option. These are TG-1 and TG-2 units, their regenerations (HPR and LPR), as well as the HRSG. TG-4 unit parameters are the same for each of the option.

Total system efficiency calculated according to the entropy method is presented in Fig. 9 and is compared to the same index calculated in enthalpy analysis (Eq. (4)). Both methods should yield the same results. However models applied in commercial software and own developed code varied in details. Own code included more detailed model. This caused slight differences in results.

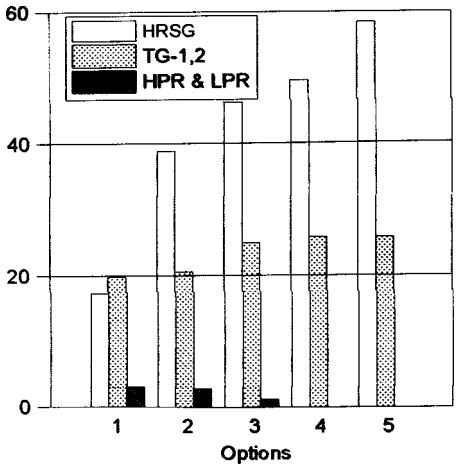

Fig. 8 Entropy gains

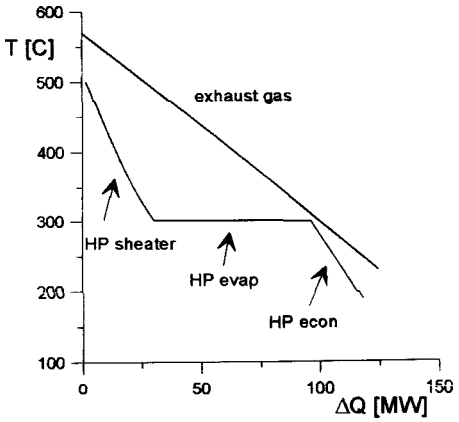

Fig. 10 Composite curves for option I

Exergy Calculations

When analyzing a combined energy production an exergy analysis is often regarded, [11]. It allows to compare different kinds of energy (e.g., electric power and heat power) in one simple equation.

The exergetic efficiency is defined as follows:

$$\eta_B = \frac{N_{el} + B_Q}{B_{g1} + B_{SB} + B_{HW_{in}}}. \tag{17}$$

This efficiency regards steam cycle and the HRSG. Gas turbine is omitted here in order to allow clear comparison of the modernization options. The efficiencies for each of the options are gathered in Table 2.

Pinch Point Analysis

The Pinch Point analysis, [9,10], was done for the HRSG. The input data for this analysis include pressures, temperatures and mass flow rates of all streams at HRSG inlet and outlet (steam, water, and exhaust gas). Another own developed code was built to analyze the heat exchange conditions. With this code composite curves and grand composite curves for the heat exchangers were drawn. The developed code allowed to assume temperature difference between hot and cold stream at the pinch point which affects the composition curves position. The lower the temperature difference, the closer to each other are the curves situated and the higher is the heat exchange surface area. However, if the temperature difference is too low, the heat exchange requires additional exchangers located at the HRSG inlet or outlet, depending where the hot or cold utility would be insufficient. If the composite curves at the according graph are situated one completely below the other, no additional exchangers are required.

Therefore using the Gate Cycle software and own developed code it was possible to determine the reburner minimum exit temperatures. Those temperatures should be applied in the real working system at the CHP plant.

Figures 10 and 11 present composite curves drawn for two options. In the second one heat exchangers surfaces operating at the same temperature rangers are located parallel.

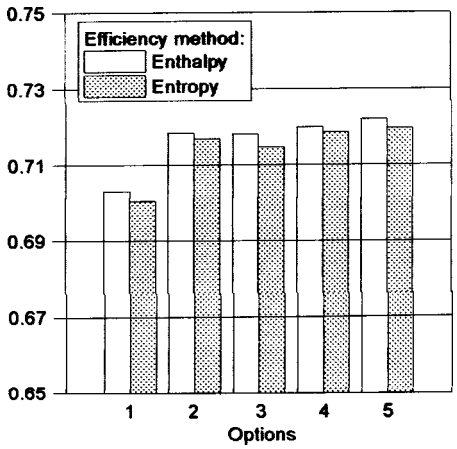

Fig. 9 Total efficiency comparison

Table 2 Exergy calculation results

	I	II	III	IV	V
η_B	0.6045	0.6266	0.6386	0.6429	0.6457

Cost Effectiveness

The modernization should be treated as an investment. Such project is successful only if it generates a profit from investment funds. The economy analysis of the modernization concentrates on *cash flows*.

Cash flows include:

1. investment costs (I_0),
2. future CHP plant annual cash flows, and
3. final investment expenses for closing down the project.

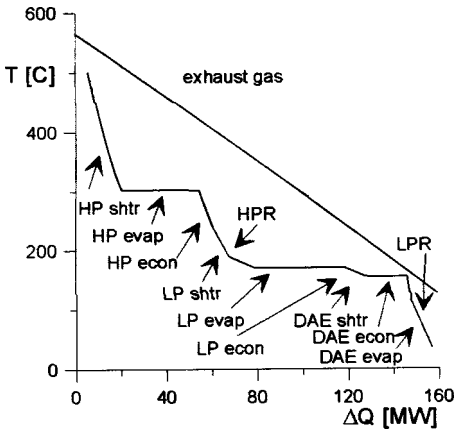

Fig. 11 Composite curves for option V

Table 3 Economic analysis results

NPV	7 248 913 USD
IRR	17.25%
DPB	7.15 years

Three investment evaluation indexes, which base on discounted cash flows, were used:

1. The net present value (NPV) method derives from the simple fact that an investment is reasonable if incomes exceed expenses and investment costs. The modernization is profitable only if net present value is positive in the last year of analyzed period of time. Obtained value is a financial surplus:

$$\mathrm{NPV}=\sum_{t=1}^{n}\frac{CF}{(1+r)^t}-I_0 \tag{14}$$

where n—analyzed time duration (here $n=10$ years).

2. The internal rate of return (IRR) defines a discount rate, which guarantees that total income amount is equal to investment cost. In other words it is the maximal loan interest rate that might be issued for the project. It is described as

$$\sum_{t=1}^{n}\frac{CF}{(1+\mathrm{IRR})^t}=I_0. \tag{15}$$

3. The discount pay back time (DPB) allows to determine the time, after which the amount of total discounted cash flows is equal to investment costs.

$$\sum_{t=1}^{\mathrm{DPB}}\frac{CF}{(1+r)^t}=I_0 \tag{16}$$

The results of economic calculations for option IV and gas turbine General Electrics PG7121 are shown in Table 3.

The NPV at the end of the last year is positive. It proves that the modernization is profitable. It begins to generate a profit at the beginning of the 8th year. A difference between internal rate of return and discount rate assumed for calculations is more than 5 percentage points, which guarantees immunity from unexpected changes of a financial cost of funds involved in the investment.

These results were verified against parameters that were assumed but are likely to change (e.g., natural gas price, selling prices of electric power and heat, discount rate).

Sensibility verification is presented as a set of diagrams (Figs. 12–14). They show the oscillation of the NPV when chosen parameters change and others remain as in economic analysis assumptions.

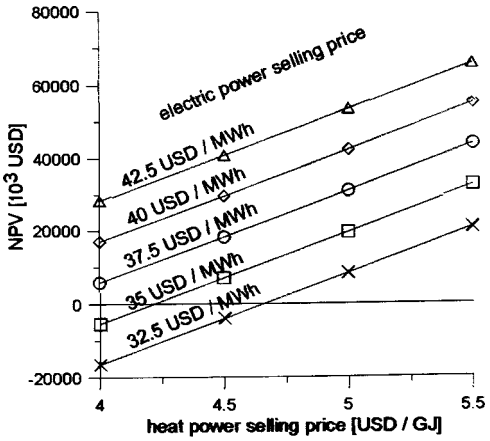

Fig. 13 NPV increase and produced power selling prices dependency

Conclusions

Each of the options throughout I to V shows some improvement. The efficiencies are increasing, while the fuel efficiency index and the flue gas temperature at the HRSG outlet are decreasing. It should be stressed that each of the options satisfies the heat demands (in hot water and process steam), so they are equally good from receivers point of view.

It might be observed that the total efficiency of the whole CHP plant is very similar for options II than and III. However, other efficiencies are worse for option II. The efficiency of the HRSG is low and that indicates low level of cogeneration. Also the fuel efficiency index is higher for that option, which decreases fuel savings in comparison to separated cycles generating heat and electric power. It proves that while comparing a modernization options, more feature factors should be taken into the consideration.

The gas turbine shaft power is also an important indicator. Too big turbine does not fit the already existing steam cycle—its overall efficiencies would be dropping. A smaller gas turbine with a reburner occurs to be the best choice for the existing combined heat and power plant. It provides the higher total efficiency and also the higher efficiency of the recovered heat from the flue gas.

The economic analysis demonstrates that the modernization project is profitable. Moreover, since the economic calculations assumptions were quite strict, it is very possible that the investment would generate a much higher profit than presented here.

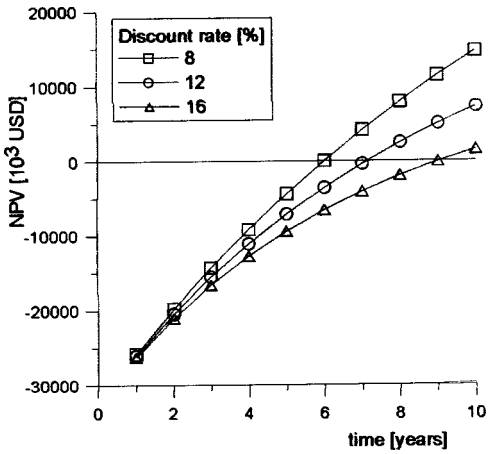

Fig. 12 NPV increase and discount rate dependency

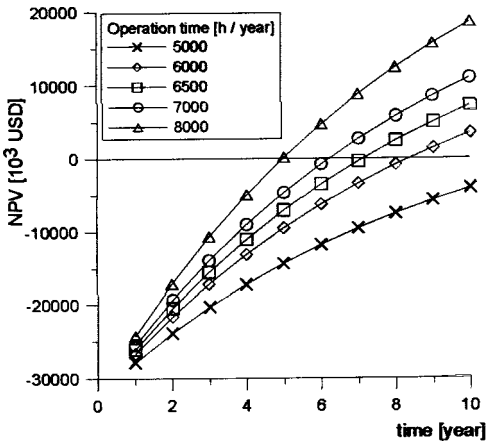

Fig. 14 NPV increase and number of operation hours during a year dependency

The sensibility verification guarantees quite large independence from financial conditions change. The modernization is profitable even if a tax rate, inflation rate, or loan interest rate would increase.

After the analyzed period of time is over, all of the new units would be depreciated and some additional funds (NPV) exist. This would allow further modernization of the CHP plant. Probably the older steam cycle would require modifications. The steam turbines are able to operate for 80,000 hours which is the maximum duration of time considered in the sensibility verification (Fig. 14).

Acknowledgment

A part of the calculations was carried out at the Department of Energetic ''Sergio Stecco'' at the University of Florence. The authors gratefully acknowledge the support of Prof. Giampaolo Manfrida in completing the calculations.

Nomenclature

B_{g1} = exergy rate of the flue gas at the HRSG inlet
$B_{HW\,in}$ = exergy rate of the heating water at the plant inlet
B_Q = total exergy rate of the produced heat in process steam and water
B_{SB} = exergy rate of the steam produced in the steam boilers
H_g = flue gas enthalpy
LHV_f = fuel lower heating value
m_f = mass flow rate of the fuel at the gas turbine inlet
m_g = flow rate of the exhaust gas at the gas turbine outlet
m_{rb} = mass flow rate of the fuel at the reburner
N_{el} = total electric power of the steam turbines
N_{GT} = electric power of the gas turbine
Q = total heat flow in process steam and water
Q_{HRSG} = heat transferred into steam and water in the HRSG
Q_{rb} = heat flow in reburner
Q_{SB} = heat transferred into livesteam in the steam boilers
Q_{TS} = heat flow generated in process steam
Q_{XAB} = heat flow generated in main system heat exchangers
t_{HRSG} = gas temperature at the HRSG inlet (1) and outlet (2)
η_{el} = efficiency of electrical power plant
η_{SB} = efficiency of the steam boilers
η_Q = efficiency of heat generating station

References

[1] Bejan, A., Tsatsaronis, G., and Moran, M., 1996, *Thermal Design & Optimization*, John Wiley and Sons, New York.
[2] Bonner, J. A., Elgawhary, A. M., and Tawney, R. K., ''Economic and Performance Evaluation of Combined Cycle Repowering Options,'' ASME Paper No. GT-2002-30565.
[3] Chmielniak, T., and Lukowicz, H., 1999, ''Steam CHP Plant Entropy Analysis,'' *Proceedings of Power Conference*, Warsaw University of Technology, Warsaw.
[4] Chmielniak, T., Kosman, G., and Kosman, W., 2002, ''Fitting a Gas Turbine Into an Existing Steam Cycle With Heating Turbines,'' *Proceedings of Gas Power Conference*, Szczyrk, Poland, Silesian University of Technology, Gliwice, Poland.
[5] GateCycle Version 5.40 GE Software.
[6] Kosman, G., Rusin, A., and Nowak, G., 1998, ''On-line & Off-line Steam Turbine Component Strain States Monitoring for the Diagnosis System,'' ASME Paper 97-GT-456.
[7] Linhoff March, 1998, *Introduction to Pinch Technology* Linchhoff March.
[8] Schmidt, D., and Sullivan, T., 2001, ''The Model Steam Turbine: A Method of Evaluating a Heat Recovery Steam Generator in a Combined Cycle Plant,'' ASME Paper No. 2001-GT-0501.
[9] Szargut, J., 1999, ''Energy and Ecological Effects of the Primary Gas Turbine Supplementing a Coal-Fired Power Plant,'' Int. J. Applied Thermodynamics, **2**(2), pp. 1–4.
[10] Szargut, J., Morris, D. R., and Steward, F. R., 1988, *Exergy Analysis of Thermal, Chemical and Metallurgical Processes*, Hemisphere, Washington, DC.
[11] ''TG-1,2 and TG-4 Units Technical State Evaluation,'' 1994–1995, Research Project, Silesian University of Technology, Gliwice, Poland.

Robust Optimal Design in Multistage Expansion of a Gas Turbine Cogeneration Plant Under Uncertain Energy Demands

Ryohei Yokoyama[1]
Associate Professor,
Mem. ASME
e-mail: yokoyama@ese.energy.osakafu-u.ac.jp

Koichi Ito
Professor,
Fellow ASME

Department of Energy Systems Engineering,
Osaka Prefecture University,
1-1 Gakuen-cho,
Sakai, Osaka 599-8531, Japan

Tatsuhiro Murata
Generator Systems Division,
Hitachi, Ltd.

In designing cogeneration plants, the estimation of energy demands is an important work. However, many conditions under which energy demands are estimated have some uncertainty at the design stage. Therefore, designers should consider that energy demands have some uncertainty, evaluate the robustness in the performance under uncertain energy demands, and design plants rationally in consideration of the robustness. The authors have developed a robust optimal design method based on the minimax regret criterion for the single-stage planning of energy supply plants. In this paper, the method is extended for the multistage expansion planning. Under uncertain energy demands increasing stepwise, equipment capacities and utility contract demands as well as energy flow rates for each expansion period are determined in consideration of their sequential relationships to minimize the maximum regret in the annual total cost and satisfy all the possible energy demands for all the expansion periods. Through a case study on a gas turbine cogeneration plant for district energy supply, features of the economic robustness and the robust optimal design are clarified in relation to the uncertainty in energy demands and the numbers of years for the expansion periods. [DOI: 10.1115/1.1771688]

Introduction

Because of their potential of high economic and energy saving characteristics by energy efficient utilization, cogeneration plants have been installed increasingly into districts and buildings in recent years. To utilize the potential and attain the highest economic and energy saving characteristics, design and operation are important issues.

In designing cogeneration plants, the estimation of energy demands is an important work. This is because designers are requested to rationally determine what types, numbers, and capacities of equipment should be installed in consideration of their operational strategies corresponding to seasonal and hourly variations in energy demands estimated, which significantly affects the economic and energy saving characteristics. In addition, for district energy supply, since energy demands increase stepwise with the construction of buildings, it is necessary to rationally expand equipment capacities correspondingly. Related with this issue, an optimal unit sizing method of energy supply plants has been proposed, by which equipment capacities and utility contract demands can be determined to minimize the annual total cost in consideration of equipment operational strategies for average energy demands estimated on several representative days, and satisfy peak energy demands in summer and winter, [1]. This method has been extended for the multistage expansion planning, [2]. The method can be a useful tool for unit sizing if energy demands can be estimated precisely.

However, many conditions under which energy demands are estimated have some uncertainty at the design stage, which makes it difficult to estimate energy demands precisely. Especially, for district energy supply, it is more difficult to estimate energy demands increasing stepwise for a long period. If the unit sizing is conducted by considering that energy demands estimated are certain, the economic and energy saving characteristics expected may not be attained and the deficit in energy supply may occur. This is because energy demands which occur at the operation stage differ from those estimated at the design stage. Therefore, designers should consider that energy demands have some uncertainty, evaluate the robustness in economic and energy saving characteristics under uncertain energy demands, and design plants rationally in consideration of the robustness.

An optimal unit sizing method of energy supply plants in consideration of the robustness under uncertain energy demands has been proposed for the single-stage and single-objective planning without increasing energy demands, [3], based on the minimax regret criterion, [4]. This method has been extended for the single-stage and multiobjective planning, [5]. However, no method has been proposed for the multistage expansion planning with increasing energy demands.

The first objective of this paper is to propose an optimal unit sizing method for the multistage expansion planning of energy supply plants in consideration of the robustness under uncertain energy demands increasing stepwise. The second objective is to evaluate the economic robustness of a gas turbine cogeneration plant and clarify its features through a case study. In the following, an optimal unit sizing problem for the multistage expansion planning is first described for a gas turbine cogeneration plant. Next, a robust optimal design problem based on the minimax regret criterion and its solution algorithm are described. Finally, a case study is conducted on a gas turbine cogeneration plant for district energy supply to investigate the features of the economic robustness and the robust optimal design. For simplicity of the optimization calculation, the two-stage expansion planning is considered for the problem formulation and case study. However, the proposed method can be extended for the expansion planning with more stages.

Optimal Unit Sizing for Multistage Expansion Planning

Concept of Multistage Expansion Planning. The multistage expansion planning of an energy supply plant is defined as fol-

[1]To whom correspondence should be addressed.

Contributed by the International Gas Turbine Institute (IGTI) of THE AMERICAN SOCIETY OF MECHANICAL ENGINEERS for publication in the ASME JOURNAL OF ENGINEERING FOR GAS TURBINES AND POWER. Paper presented at the International Gas Turbine and Aeroengine Congress and Exhibition, Atlanta, GA, June 16–19, 2003, Paper No. 2003-GT-38375. Manuscript received by IGTI, October 2002, final revision, March 2003. Associate Editor: H. R. Simmons.

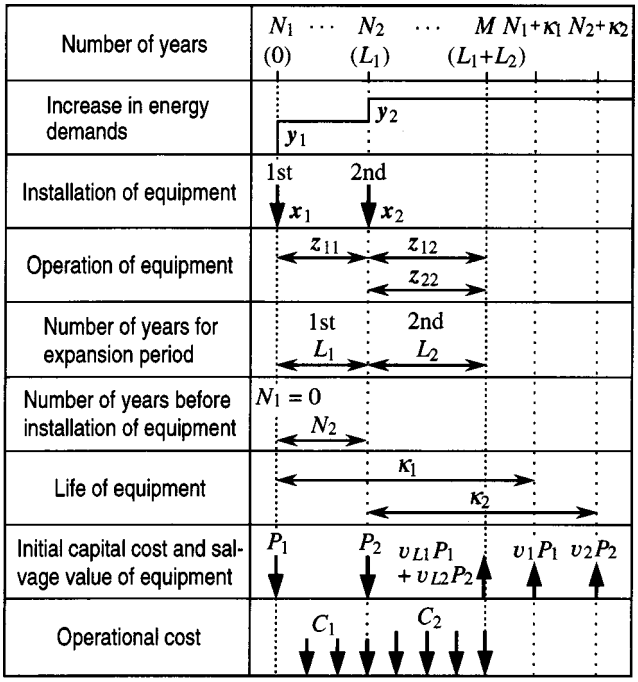

Fig. 1 Concept of multistage expansion planning of energy supply plant

lows. Its concept is shown in Fig. 1. Here, it is assumed that energy demands increase at two stages, and that equipment are installed and their numbers increase correspondingly. The first expansion period is defined as the one between the first and the second installations of equipment. The second expansion period is defined as the one between the second installation of equipment and the time when the annual total cost is evaluated. The increased energy demands which vary with season and time are designated by $\mathbf{y}_m$ for the mth expansion period ($m=1,2$). The equipment capacities and utility contract demands expanded for the mth expansion period are designated by $\mathbf{x}_m$. The equipment installed for the mth expansion period are operated corresponding to energy demands $\Sigma_{l=1}^{k}\mathbf{y}_l$ for the kth expansion period ($m \leqslant k \leqslant 2$), and their operational strategies are designated by $\mathbf{z}_{mk}$.

The number of years for the mth expansion period is designated by L_m. With this definition, the number of years for the period between the first and the mth installations of equipment N_m is expressed by

$$N_m = \begin{cases} 0 & (m=1) \\ \sum_{l=1}^{m-1} L_l & (m=2). \end{cases} \tag{1}$$

In addition, it is assumed that the numbers of years for the installed equipment life for the mth expansion period are identical, and are designated by κ_m.

The initial capital cost and the ratio of the salvage value after the life to the initial capital cost are designated by P_m and v_m, respectively, for the equipment installed for the mth expansion period. Here, P_m is a function with respect to $\mathbf{x}_m$. In addition, the ratio of the salvage value at the time when the annual total cost is evaluated is designated by v_{Lm}, and is related to v_m by

$$v_{Lm} = \frac{(1+i)^{\kappa_m} - (1+i)^{M-N_m} + v_m\{(1+i)^{M-N_m} - 1\}}{(1+i)^{\kappa_m} - 1} \quad (m=1,2) \tag{2}$$

where i is the interest rate, and $M = L_1 + L_2$ is the number of years for the period for which the annual total cost is evaluated. Equation (2) is derived by assuming that the annual capital cost of equipment with their life κ_m and the ratio of salvage value v_m is equivalent to that of equipment with their life $M-N_m$ and the ratio of salvage value v_{Lm}. On the other hand, the annual operational cost, which is the sum of utility demand and energy charges, is designated by C_m, and is a function with respect to $\mathbf{z}_{jm}$ ($1 \leqslant j \leqslant m$). The constraints mentioned below relate $\mathbf{z}_{jm}$ to $\mathbf{x}_j$ and $\mathbf{y}_j$, and consequently C_m is a function with respect to $\mathbf{x}_j$, $\mathbf{y}_j$, and $\mathbf{z}_{jm}$.

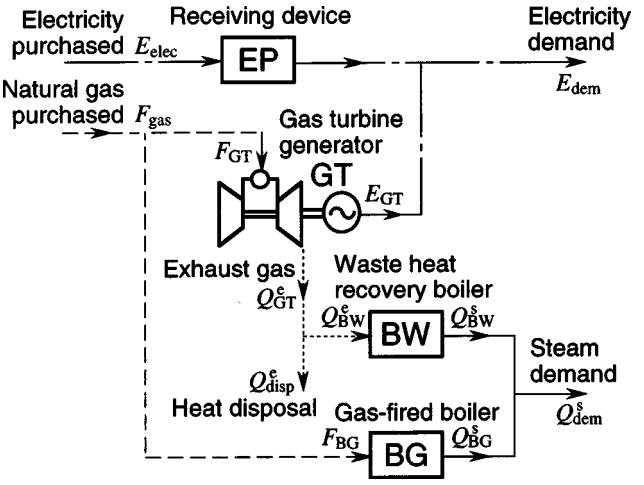

Fig. 2 Configuration of gas turbine cogeneration plant

Concept of Optimal Unit Sizing. An optimal unit sizing problem for the aforementioned multistage expansion planning of an energy supply plant is considered as follows. The annual total cost for the period M expressed by

$$f = \sum_{m=1}^{2}\left[\frac{iP_m\{(1+i)^{M-N_m} - v_{Lm}\}}{(1+i)^M - 1} + \sum_{l=1}^{L_m}\frac{iC_m(1+i)^{M-N_m-l}}{(1+i)^M - 1}\right] \tag{3}$$

is adopted as the objective function to be minimized. As constraints, performance characteristics of equipment, contract demand-consumption relationships of utilities, and energy balance and supply-demand relationships are considered for each time, each season, and each expansion period. As decision variables, equipment capacities and utility contract demands $\mathbf{x}_m$, and energy flow rates $\mathbf{z}_{mk}$ ($m \leqslant k \leqslant 2$) are considered. Here, it is assumed that P_m is a linear function with respect to $\mathbf{x}_m$. In addition, it is assumed that C_m is a linear function with respect to $\mathbf{z}_{jm}$ ($1 \leqslant j \leqslant m$). As aforementioned, $\mathbf{z}_{jm}$ is related to $\mathbf{x}_j$ and $\mathbf{y}_j$ through the constraints, and the constraints are also assumed to be linear functions with respect to $\mathbf{x}_j$, $\mathbf{y}_j$, and $\mathbf{z}_{jm}$.

As a result, the objective function f of Eq. (3) is expressed as the sum of the two terms, which are a function with respect to the variables only for the first expansion period f_1, and a function with respect to the variables for both the first and the second expansion periods f_2, as follows:

$$f = f_1(P_1, C_1) + f_2(P_2, C_2) = f_1(\mathbf{x}_1, \mathbf{y}_1, \mathbf{z}_{11}) + f_2(\mathbf{x}_1, \mathbf{x}_2, \mathbf{y}_1, \mathbf{y}_2, \mathbf{z}_{12}, \mathbf{z}_{22}). \tag{4}$$

Gas Turbine Cogeneration Plant and Its Optimal Unit Sizing Problem

Plant Configuration. A gas turbine cogeneration plant for district energy supply shown in Fig. 2 is considered in this paper. This plant is composed of a gas turbine generator (GT), a waste heat recovery boiler (BW), a gas-fired boiler (BG), and a receiving device (EP). Electricity is supplied to customers by operating

the gas turbine generator and by purchasing electricity from an outside electric power company. Exhaust heat generated from the gas turbine is recovered by the waste heat recovery boiler, and is used for steam supply. An excess of exhaust heat is disposed of through an exhaust gas dumper. A shortage of steam is supplemented by the gas-fired boiler. Steam is used for space cooling/heating and hot water supply. Here, steam demand is estimated on the assumption that steam absorption refrigerators are installed to produce cold water for space cooling.

The symbols used as energy flow rates in the following formulation are included in Fig. 2.

Formulation of Optimal Unit Sizing Problem. The symbols used for the formulation are defined, and the constraints and the objective function are formulated with the symbols. To take account of variations in energy demands, a typical year for each expansion period is divided into T sampling times. A quantity corresponding to each sampling time is identified by the argument (t) $(t=1,2,\ldots,T)$. The duration per year of each sampling time is designated by $d_m(t)$.

Performance characteristics of equipment are formulated as linear equations. For example, for the gas turbine generator, relationships among natural gas consumption $F_{\mathrm{GT}mk}(t)$, electric power generated $E_{\mathrm{GT}mk}(t)$, heat flow rate of exhaust gas $Q^{\mathrm{e}}_{\mathrm{GT}mk}(t)$, and power generating capacity $\overline{E}_{\mathrm{GT}m}$ are expressed by

$$\left.\begin{aligned} E_{\mathrm{GT}mk}(t)&=a_{\mathrm{GT}}F_{\mathrm{GT}mk}(t)\\ Q^{\mathrm{e}}_{\mathrm{GT}mk}(t)&=b_{\mathrm{GT}}F_{\mathrm{GT}mk}(t)\\ 0\leqslant E_{\mathrm{GT}mk}(t)&\leqslant\overline{E}_{\mathrm{GT}m}\end{aligned}\right\}\quad (m=1,2;m\leqslant k\leqslant 2;t=1,2,\ldots,T) \tag{5}$$

where a and b are performance characteristic values, and $\overline{(\ )}$ denotes an upper limit. The power and exhaust heat generating efficiencies depend on the capacity, part load, and inlet air temperature. However, the efficiencies are assumed to be constant, because the problem is formulated by linear equations. Similarly, performance characteristics of the waste heat recovery and gas-fired boilers are expressed by

$$\left.\begin{aligned} Q^{\mathrm{s}}_{\mathrm{BW}mk}(t)&=a_{\mathrm{BW}}Q^{\mathrm{e}}_{\mathrm{BW}mk}(t)\\ 0\leqslant Q^{\mathrm{s}}_{\mathrm{BW}mk}(t)&\leqslant\overline{Q}^{\mathrm{s}}_{\mathrm{BW}m}\end{aligned}\right\}\quad (m=1,2;m\leqslant k\leqslant 2;t=1,2,\ldots,T) \tag{6}$$

and

$$\left.\begin{aligned} Q^{\mathrm{s}}_{\mathrm{BG}mk}(t)&=a_{\mathrm{BG}}F_{\mathrm{BG}mk}(t)\\ 0\leqslant Q^{\mathrm{s}}_{\mathrm{BG}mk}(t)&\leqslant\overline{Q}^{\mathrm{s}}_{\mathrm{BG}m}\end{aligned}\right\}\quad (m=1,2;m\leqslant k\leqslant 2;t=1,2,\ldots,T) \tag{7}$$

respectively. In addition, the electricity and natural gas consumptions, $E_{\mathrm{elec}mk}(t)$ and $F_{\mathrm{gas}mk}(t)$, and their contract demands, $\overline{E}_{\mathrm{elec}m}$ and $\overline{F}_{\mathrm{gas}m}$, are related by

$$\left.\begin{aligned} 0\leqslant E_{\mathrm{elec}mk}(t)&\leqslant\overline{E}_{\mathrm{elec}m}\\ 0\leqslant F_{\mathrm{gas}mk}(t)&\leqslant\overline{F}_{\mathrm{gas}m}\end{aligned}\right\}\quad (m=1,2;m\leqslant k\leqslant 2;t=1,2,\ldots,T), \tag{8}$$

respectively. Here, the capacity of the receiving device $\overline{E}_{\mathrm{EP}m}$ is assumed to be equal to the contract demand of electricity purchased $\overline{E}_{\mathrm{elec}m}$ as follows:

$$\overline{E}_{\mathrm{EP}m}=\overline{E}_{\mathrm{elec}m}\quad (m=1,2). \tag{9}$$

Furthermore, energy balance and supply-demand relationships are expressed by

$$\left.\begin{aligned} \sum_{j=1}^{m}F_{\mathrm{gas}jm}(t)&=\sum_{j=1}^{m}F_{\mathrm{GT}jm}(t)+\sum_{j=1}^{m}F_{\mathrm{BG}jm}(t)\\ \sum_{j=1}^{m}E_{\mathrm{elec}jm}(t)+\sum_{j=1}^{m}E_{\mathrm{GT}jm}(t)&=\sum_{j=1}^{m}E_{\mathrm{dem}j}(t)\\ \sum_{j=1}^{m}Q^{\mathrm{e}}_{\mathrm{GT}jm}(t)&=\sum_{j=1}^{m}Q^{\mathrm{e}}_{\mathrm{BW}jm}(t)+\sum_{j=1}^{m}Q^{\mathrm{e}}_{\mathrm{disp}jm}(t)\\ \sum_{j=1}^{m}Q^{\mathrm{s}}_{\mathrm{BW}jm}(t)+\sum_{j=1}^{m}Q^{\mathrm{s}}_{\mathrm{BG}jm}(t)&=\sum_{j=1}^{m}Q^{\mathrm{s}}_{\mathrm{dem}j}(t)\end{aligned}\right\}$$
$$(m=1,2;t=1,2,\ldots,T). \tag{10}$$

The initial capital cost P_m and the annual operational cost C_m included in the annual total cost of Eq. (3) adopted as the objective function are expressed by

$$P_m=\Gamma_{\mathrm{EP}}\overline{E}_{\mathrm{EP}m}+\Gamma_{\mathrm{GT}}\overline{E}_{\mathrm{GT}m}+\Gamma_{\mathrm{BW}}\overline{Q}^{\mathrm{s}}_{\mathrm{BW}m}+\Gamma_{\mathrm{BG}}\overline{Q}^{\mathrm{s}}_{\mathrm{BG}m}\quad (m=1,2) \tag{11}$$

and

$$C_m=\sum_{j=1}^{m}\left\{12(\psi_{\mathrm{elec}}\overline{E}_{\mathrm{elec}j}+\psi_{\mathrm{gas}}\overline{F}_{\mathrm{gas}j})+\sum_{t=1}^{T}(\varphi_{\mathrm{elec}}E_{\mathrm{elec}jm}(t)+\varphi_{\mathrm{gas}}F_{\mathrm{gas}jm}(t))d_m(t)\right\}\quad (m=1,2), \tag{12}$$

respectively, where Γ is the capital unit cost of equipment, ψ is the monthly unit cost for demand charge of utility, and φ is the unit cost for energy charge of utility.

The design variable vector composed of equipment capacities and utility contract demands $\mathbf{x}_m$, the uncertain parameter vector composed of energy demands $\mathbf{y}_m$, and the operation variable vector composed of energy flow rates $\mathbf{z}_{mk}$ are defined as

$$\mathbf{x}_m=(\overline{E}_{\mathrm{EP}m},\overline{E}_{\mathrm{GT}m},\overline{Q}^{\mathrm{s}}_{\mathrm{BW}m},\overline{Q}^{\mathrm{s}}_{\mathrm{BG}m},\overline{E}_{\mathrm{elec}m},\overline{E}_{\mathrm{gas}m})^{\mathrm{T}}\quad (m=1,2) \tag{13}$$

$$\left.\begin{aligned} \mathbf{y}_m(t)&=(E_{\mathrm{dem}m}(t),Q^{\mathrm{s}}_{\mathrm{dem}m}(t))\quad (t=1,2,\ldots,T)\\ \mathbf{y}_m&=(\mathbf{y}_m(1),\mathbf{y}_m(2),\ldots,\mathbf{y}_m(T))^{\mathrm{T}}\end{aligned}\right\}\quad (m=1,2) \tag{14}$$

and

$$\left.\begin{aligned} \mathbf{z}_{mk}(t)&=(E_{\mathrm{GT}mk}(t),Q^{\mathrm{e}}_{\mathrm{GT}mk}(t),F_{\mathrm{GT}mk}(t),Q^{\mathrm{s}}_{\mathrm{BW}mk}(t),\\ &\quad Q^{\mathrm{e}}_{\mathrm{BW}mk}(t),Q^{\mathrm{s}}_{\mathrm{BG}mk}(t),F_{\mathrm{BG}mk}(t),Q^{\mathrm{e}}_{\mathrm{disp}mk}(t),\\ &\quad E_{\mathrm{elec}mk}(t),F_{\mathrm{gas}mk}(t)\ (t=1,2,\ldots,T)\\ \mathbf{z}_{mk}&=(\mathbf{z}_{mk}(1),z_{mk}(2),\ldots,\mathbf{z}_{mk}(T))^{\mathrm{T}}\end{aligned}\right\}$$
$$(m=1,2;m\leqslant k\leqslant 2), \tag{15}$$

respectively, where the superscript T means the transposition of a vector. As the feasible region X_m for $\mathbf{x}_m$, Eq. (9) and the nonnegative condition

$$\mathbf{x}_m\geqslant\mathbf{0}\quad (m=1,2) \tag{16}$$

are considered. As the feasible region Z_m for $\mathbf{z}_{jm}$ $(1\leqslant j\leqslant m)$, Eqs. (5) through (8) and Eq. (10) are considered. It should be noted that Z_m depends on the values of $\mathbf{x}_j$ and $\mathbf{y}_j$ $(1\leqslant j\leqslant m)$, which means that energy flow rates must be determined to satisfy performance characteristics of equipment, contract demand-consumption relationships of utilities, and energy balance and supply-demand relationships.

The optimal unit sizing problem is described as follows: the equipment capacities and utility contract demands $\mathbf{x}_m$ of Eq. (13) as well as the energy flow rates $\mathbf{z}_{mk}$ of Eq. (15) are determined to minimize the annual total cost f of Eq. (3) subject to the constraints of Eqs. (5) through (12) and Eq. (16) under energy demands $\mathbf{y}_m$ of Eq. (14).

Robust Optimal Design Based on Minimax Regret Criterion

Basic Concept. In designing an energy supply plant under uncertain energy demands, two criteria should be considered, i.e., flexibility and robustness, [6]. The former means the feasibility in energy supply for all the possible values of uncertain energy demands, and is related with constraints. The latter means the sensitivity of evaluation items for all the possible values of uncertain energy demands, and is related with objective functions. In this paper, the robustness is maximized while the flexibility is satisfied for all the possible values of uncertain energy demands. As a criterion for the robustness, the minimax regret (robust deviation) criterion is adopted here, [4]. The regret is defined as the difference in an objective function between the nonoptimal and the optimal designs for some values of uncertain parameters. The minimax regret criterion means that the maximum regret in the objective function is selected as the criterion for robustness among the regrets for all the possible values of uncertain parameters, and that the values of decision variables are determined to minimize the maximum regret or maximize the robustness. Therefore, if this criterion is adopted, the differences in the objective function between the resultant and the optimal designs can be small for all the possible values of uncertain parameters.

Formulation of Robust Optimal Design Problem. In formulating a robust optimal design problem, the possible region Y_m for $\mathbf{y}_m$ are assumed to be bounded by upper and lower limits estimated in advance as follows:

$$(1-\alpha_m)\tilde{\mathbf{y}}_m \leqslant \mathbf{y}_m \leqslant (1+\alpha_m)\tilde{\mathbf{y}}_m \quad (m=1,2) \tag{17}$$

where $\tilde{\mathbf{y}}_m$ and α_m are the averages and the parameter for the uncertainty of energy demands, respectively. According to the aforementioned basic concept, a robust optimal design problem is described as follows: the equipment capacities and utility contract demands $\mathbf{x}_m$ of Eq. (13) as well as the energy flow rates $\mathbf{z}_{mk}$ of Eq. (15) are determined to minimize the maximum regret in the annual total cost f of Eq. (3) subject to the constraints of Eqs. (5) through (12) and Eq. (16) for all the possible values of uncertain energy demands $\mathbf{y}_m$ of Eq. (14) bounded by Eq. (17). Here, it should be noted that although the design variables $\mathbf{x}_m$ must be determined at the design stage when energy demands $\mathbf{y}_m$ are uncertain, the operation variables $\mathbf{z}_{mk}$ can be determined at the operation stage when energy demands $\mathbf{y}_m$ become certain. In addition, the sequential relationship between the first and the second expansion periods must be considered. The sequential relationships among the design variables, the uncertain parameters, and the operation variables for the first and the second expansion periods are shown in Fig. 3. In consideration of these relationships, the robust optimal design problem is expressed by

$$\begin{aligned}
&\min_{\mathbf{x}_1\in X_1}\Bigg[\max_{\mathbf{y}_1\in Y_1}\Bigg\{\min_{\mathbf{z}_{11}\in Z_1} f_1(\mathbf{x}_1,\mathbf{y}_1,\mathbf{z}_{11}) \\
&\quad+\min_{\mathbf{x}_2\in X_2}\Bigg(\max_{\mathbf{y}_2\in Y_2}\Bigg[\min_{(\mathbf{z}_{12},\mathbf{z}_{22})\in Z_2} f_2(\mathbf{x}_1,\mathbf{x}_2,\mathbf{y}_1,\mathbf{y}_2,\mathbf{z}_{12},\mathbf{z}_{22}) \\
&\quad-\min_{\mathbf{x}_1'\in X_1}\Bigg\{\min_{\mathbf{z}_{11}'\in Z_1'} f_1(\mathbf{x}_1',\mathbf{y}_1,\mathbf{z}_{11}') \\
&\quad+\min_{\mathbf{x}_2'\in X_2}\Bigg(\min_{(\mathbf{z}_{12}',\mathbf{z}_{22}')\in Z_2'} f_2(\mathbf{x}_1',\mathbf{x}_2',\mathbf{y}_1,\mathbf{y}_2,\mathbf{z}_{12}',\mathbf{z}_{22}')\Bigg)\Bigg\}\Bigg]\Bigg)\Bigg\}\Bigg]
\end{aligned} \tag{18}$$

where the symbol $(\,)'$ is used to distinguish a different value or a set. In Eq. (18), the functions f_1 and f_2 of the first and the second terms, respectively, correspond to the robust optimal design, and the functions f_1 and f_2 of the third and the fourth terms, respectively, correspond to the ordinary optimal design. The difference in these terms denotes the regret in the objective function f.

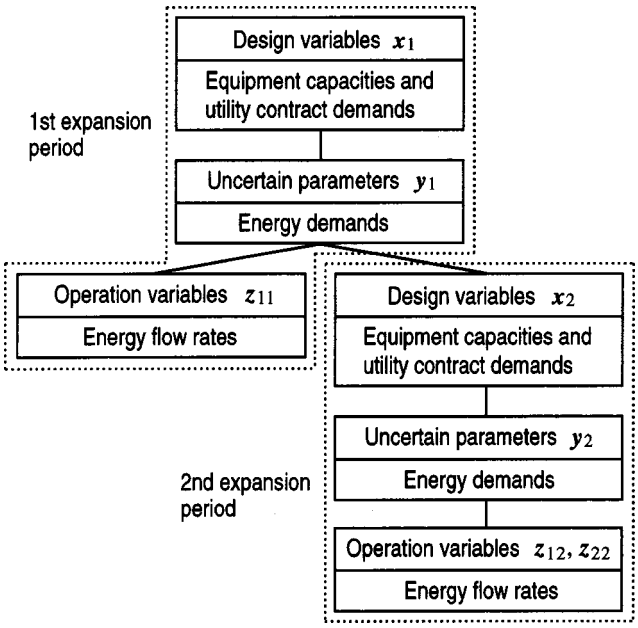

Fig. 3 Sequential relationships among design variables, uncertain parameters, and operation variables

Next, the flexibility, i.e., the feasibility in energy supply is incorporated into Eq. (18). To secure the flexibility for all the possible values of uncertain energy demands $\mathbf{y}_m$, an objective function which expresses the infeasibility in energy supply is introduced, [7], and the equipment capacities and utility contract demands $\mathbf{x}_m$ are determined to minimize (make zero) the maximum of this objective function for all the possible values of $\mathbf{y}_m$. This idea is applied to the ordinary and robust optimal designs for the first and the second expansion periods, and the resultant terms are added to Eq. (18) as penalty ones to take account of them prior to Eq. (18). Here, a detailed formulation is omitted.

Solution of Robust Optimal Design Problem. The aforementioned penalty terms for the flexibility can be treated as shown in the solution of the robust optimal design problem proposed previously, [3]. Here, only the solution of Eq. (18) is described. The optimization problem of Eq. (18) includes the operations of minimization and maximization hierarchically, and is formulated as a kind of multilevel linear programming problem, [8]. This problem is solved using the following procedure.

First, the operation of minimization with respect to $\mathbf{x}_1'$ and $\mathbf{x}_2'$ is moved forward to reformulate Eq. (18) as

$$\begin{aligned}
&\min_{\mathbf{x}_1\in X_1}\Bigg\{\max_{\mathbf{y}_1\in Y_1,\mathbf{x}_1'\in X_1}\Bigg(\min_{\mathbf{z}_{11}\in Z_1} f_1(\mathbf{x}_1,\mathbf{y}_1,\mathbf{z}_{11}) \\
&\quad+\min_{\mathbf{x}_2\in X_2}\Bigg[\max_{\mathbf{y}_2\in Y_2,\mathbf{x}_2'\in X_2}\Bigg\{\min_{(\mathbf{z}_{12},\mathbf{z}_{22})\in Z_2} f_2(\mathbf{x}_1,\mathbf{x}_2,\mathbf{y}_1,\mathbf{y}_2,\mathbf{z}_{12},\mathbf{z}_{22}) \\
&\quad-\Bigg(\min_{z_{11}'\in Z_1'} f_1(\mathbf{x}_1',\mathbf{y}_1,\mathbf{z}_{11}') \\
&\quad+\min_{(\mathbf{z}_{12}',\mathbf{z}_{22}')\in Z_2'} f_2(\mathbf{x}_1',\mathbf{x}_2',\mathbf{y}_1,\mathbf{y}_2,\mathbf{z}_{12}',\mathbf{z}_{22}')\Bigg)\Bigg\}\Bigg]\Bigg)\Bigg\}.
\end{aligned} \tag{19}$$

Evaluation of Upper Bound. Next, appropriate values of $\mathbf{x}_1$ and $\mathbf{x}_2$ are assumed in Eq. (19), and the operation of maximization with respect to $\mathbf{y}_2$ and $\mathbf{x}_2'$ is moved forward to consider the following optimization problem:

$$\max_{\mathbf{y}_1\in Y_1,\mathbf{x}_1'\in X_1,\mathbf{y}_2\in Y_2,\mathbf{x}_2'\in X_2}\Bigg\{\min_{\mathbf{z}_{11}\in Z_1} f_1(\mathbf{x}_1,\mathbf{y}_1,\mathbf{z}_{11}) + \min_{(\mathbf{z}_{12},\mathbf{z}_{22})\in Z_2} f_2(\mathbf{x}_1,\mathbf{x}_2,\mathbf{y}_1,\mathbf{y}_2,\mathbf{z}_{12},\mathbf{z}_{22}) - \Bigg(\min_{\mathbf{z}_{11}'\in Z_1'} f_1(\mathbf{x}_1',\mathbf{y}_1,\mathbf{z}_{11}') + \min_{(\mathbf{z}_{12}',\mathbf{z}_{22}')\in Z_2'} f_2(\mathbf{x}_1',\mathbf{x}_2',\mathbf{y}_1,\mathbf{y}_2,\mathbf{z}_{12}',\mathbf{z}_{22}')\Bigg)\Bigg\}. \tag{20}$$

The value of maximum regret corresponding to the optimal solution of this problem gives an upper bound for the minimum of maximum regret corresponding to the original problem of Eq. (19).

The problem of Eq. (20) is formulated as a bilevel linear programming one which includes the operations of maximization and minimization hierarchically. It can be reformulated as an ordinary one-level optimization problem by applying the Kuhn-Tucker optimality condition to its lower-level problem. This reformulation produces a complementarity condition which is an inner product of the inequality constraint vectors and the corresponding Lagrange multiplier vectors. To avoid the nonlinearity due to this complementarity condition, binary variables are introduced to linearize the nonlinear term, and the problem is reduced to a mixed-integer linear programming one, [9]. As a solution algorithm, the combination of the branch and bound, and the dual simplex algorithms is adopted, [10].

Evaluation of Lower Bound. On the other hand, the values of $\mathbf{y}_1$, $\mathbf{x}_1'$, $\mathbf{y}_2$, and $\mathbf{x}_2'$ are assumed to be selected only from the sets for combinations of those obtained by solving Eq. (20), and the following optimization problem is considered in place of Eq. (19):

$$\min_{\mathbf{x}_1\in X_1}\Bigg\{\max_{(\mathbf{y}_1,\mathbf{x}_1')\in A}\Bigg(\min_{\mathbf{z}_{11}\in Z_1} f_1(\mathbf{x}_1,\mathbf{y}_1,\mathbf{z}_{11}) + \min_{\mathbf{x}_2\in X_2}\Bigg[\max_{(\mathbf{y}_2,\mathbf{x}_2')\in B}\Bigg\{\min_{(\mathbf{z}_{12},\mathbf{z}_{22})\in Z_2} f_2(\mathbf{x}_1,\mathbf{x}_2,\mathbf{y}_1,\mathbf{y}_2,\mathbf{z}_{12},\mathbf{z}_{22}) - \Bigg(\min_{\mathbf{z}_{11}'\in Z_1'} f_1(\mathbf{x}_1',\mathbf{y}_1,\mathbf{z}_{11}') + \min_{(\mathbf{z}_{12}',\mathbf{z}_{22}')\in Z_2'} f_2(\mathbf{x}_1',\mathbf{x}_2',\mathbf{y}_1,\mathbf{y}_2,\mathbf{z}_{12}',\mathbf{z}_{22}')\Bigg)\Bigg\}\Bigg]\Bigg)\Bigg\} \tag{21}$$

where A and B are the sets for combinations of values of $(\mathbf{y}_1,\mathbf{x}_1')$ and $(\mathbf{y}_2,\mathbf{x}_2')$, respectively. The value of maximum regret corresponding to the optimal solution of this problem gives a lower bound for the minimum of maximum regret corresponding to the original problem of Eq. (19).

The problem of Eq. (21) is a three-level linear programming one which includes the operations of minimization and maximization hierarchically, and seems to be difficult to solve. However, the operations of maximization are only with respect to $(\mathbf{y}_1,\mathbf{x}_1')$ and $(\mathbf{y}_2,\mathbf{x}_2')$, and are conducted by selecting the values of $(\mathbf{y}_1,\mathbf{x}_1')$ and $(\mathbf{y}_2,\mathbf{x}_2')$ from their finite numbers of candidates in the sets A and B, respectively. Therefore, the introduction of variables for maxima with respect to $(\mathbf{y}_1,\mathbf{x}_1')$ and $(\mathbf{y}_2,\mathbf{x}_2')$, g_1 and g_2, respectively, as well as the corresponding inequality constraints transforms the problem of Eq. (21) into the following ordinary linear programming one:

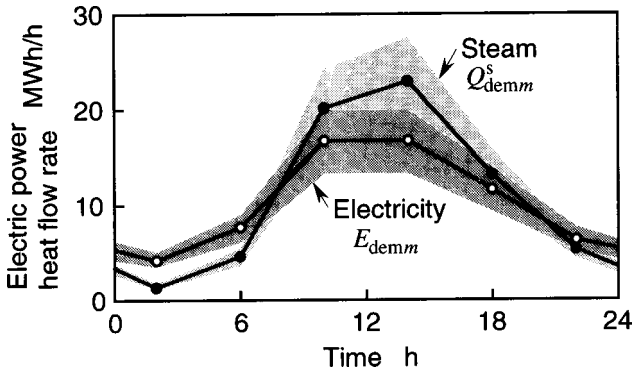

Fig. 4 Averages and uncertainty of energy demands (α_m=0.2)

$$\left.\begin{aligned}&\min_{\mathbf{x}_1\in X_1,\mathbf{z}_{11}\in Z_1,\mathbf{x}_2\in X_2,(\mathbf{z}_{12},\mathbf{z}_{22})\in Z_2} g_1\\ &\text{sub. to } g_1\geqslant f_1(\mathbf{x}_1,\mathbf{y}_1,\mathbf{z}_{11})+g_2(\mathbf{x}_1',\mathbf{y}_1)\\ &\qquad(\forall(\mathbf{y}_1,\mathbf{x}_1')\in A)\\ &\qquad g_2(\mathbf{x}_1',\mathbf{y}_1)\geqslant f_2(\mathbf{x}_1,\mathbf{x}_2,\mathbf{y}_1,\mathbf{y}_2,\mathbf{z}_{12},\mathbf{z}_{22})\\ &\qquad-(F_1(\mathbf{x}_1',\mathbf{y}_1)+F_2(x_1',\mathbf{x}_2',\mathbf{y}_1,\mathbf{y}_2))\\ &\qquad(\forall(\mathbf{y}_1,\mathbf{x}_1')\in A,\forall(\mathbf{y}_2,\mathbf{x}_2')\in B)\end{aligned}\right\} \tag{22}$$

where the arguments of g_2 mean that a variable is assigned to each combination of values of $(\mathbf{y}_1,\mathbf{x}_1')$. In addition, F_1 and F_2 are calculated as

$$\left.\begin{aligned}F_1(\mathbf{x}_1',\mathbf{y}_1)&=\min_{\mathbf{z}_{11}'\in Z_1'} f_1(\mathbf{x}_1',\mathbf{y}_1,\mathbf{z}_{11}')\\ F_2(\mathbf{x}_1',\mathbf{x}_2',\mathbf{y}_1,\mathbf{y}_2)&=\min_{(\mathbf{z}_{12}',\mathbf{z}_{22}')\in Z_2'} f_2(\mathbf{x}_1',\mathbf{x}_2',\mathbf{y}_1,\mathbf{y}_2,\mathbf{z}_{12}',\mathbf{z}_{22}')\end{aligned}\right\} \tag{23}$$

and are treated as constants in Eq. (22). The problem of Eq. (22) can be solved easily by the simplex algorithm.

Following the aforementioned procedure, the calculation of upper and lower bounds for the minimum of maximum regret in Eq. (19) is repeated. If upper and lower bounds coincide with each other, it is judged that the optimal solution of Eq. (19) is obtained, and the calculation is stopped.

Case Study

To investigate the features of the economic robustness and the robust optimal design, a case study is conducted on the gas turbine cogeneration plant for district energy supply shown in Fig. 1. As shown in the figure, since there are relationships between supplies and demands of electricity and steam, it is impossible to determine equipment capacities simply using the maxima of electricity and steam demands. Here, the unit sizing is conducted to minimize the maximum regret in the annual total cost.

Input Data. To conduct a fundamental study, a single representative day is considered in a typical year for the first and the second expansion periods, and the day is divided into six sampling times, each of which has four hours per day, i.e., $T=6$. Averages of electricity and steam demands for each sampling time are estimated. The same energy demands are assumed for the first and the second expansion periods. The values of α_m $(m=1,2)$ are changed as the parameters for the uncertainty in energy demands, and their effect on the robust optimal design is investigated. As an example, Fig. 4 shows the averages and uncertainty of electricity and steam demands in case that $\alpha_m=0.2$. In addition, the numbers of years for the first and the second expansion periods L_m $(m=1,2)$ are changed with that for the period for which the annual total cost is evaluated fixed as $M=L_1+L_2=15$ y, and their effect

Table 1 Input data

Item	Value
Duration of sampling time	$d_1(1)\sim d_1(6)=1460$ h/y $d_2(1)\sim d_2(6)=1460$ h/y
Capital unit cost of equipment	$\Gamma_{EP}=56.0\times10^3$ yen/kW $\Gamma_{GT}=230.0\times10^3$ yen/kW $\Gamma_{BW}=9.6\times10^3$ yen/kW $\Gamma_{BG}=6.9\times10^3$ yen/kW
Life of equipment	$\kappa_1=15$ y $\kappa_2=15$ y
Ratio of salvage value of equipment	$v_1=0.1$ $v_2=0.1$
Unit cost of utility	$\psi_{elec}=1.74\times10^3$ yen/(kW·month) $\psi_{gas}=2.37\times10^3$ yen/(m^3/h·month) $\varphi_{elec}=11.0$ yen/kWh $\varphi_{gas}=31.0$ yen/m^3
Interest rate	$i=0.1$

on the robust optimal design is also investigated. Other input data are given in Table 1. All values of costs are stated in yen, which is equivalent to about 8.0×10^{-3} dollars on the recent exchange rate.

Results and Discussion. Figures 5(*a*) and (*b*) show the relationships between the uncertainty in energy demands α_m and the optimal capacities of the gas turbine generator and the receiving device, in case that $L_1=5$ y and $L_2=10$ y, and $L_1=10$ y and $L_2=5$ y, respectively. Here, it is assumed that $\alpha_1=\alpha_2$. The optimal equipment capacities for the single-stage planning are also shown. In case that energy demands are certain, i.e., $\alpha_m=0$, the optimal

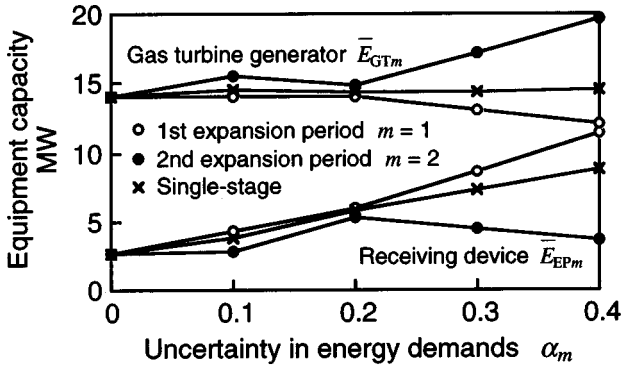

(a) $L_1=5$ y, $L_2=10$ y

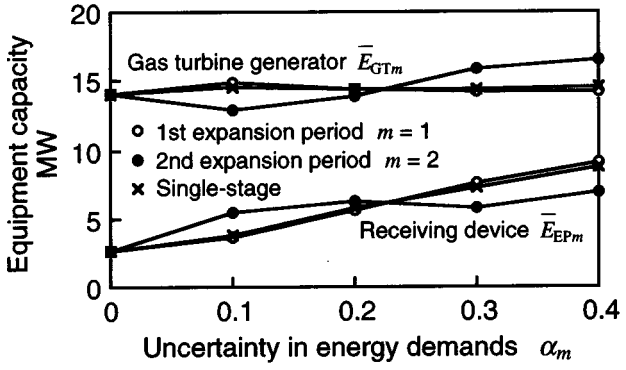

(b) $L_1=10$ y, $L_2=5$ y

Fig. 5 Relationships between uncertainty in energy demands and optimal equipment capacities ($\alpha_1=\alpha_2$); (*a*) $L_1=5$ y, $L_2=10$ y, (*b*) $L_1=10$ y, $L_2=5$ y

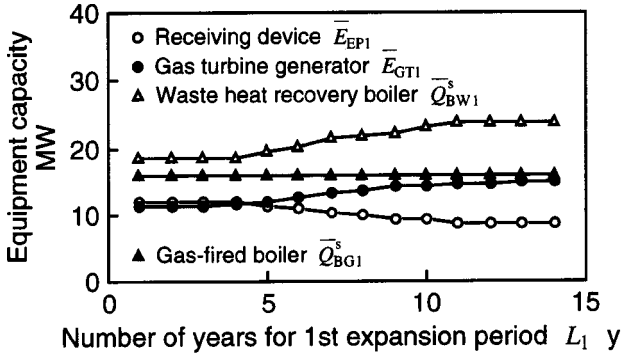

(a) 1st expansion period

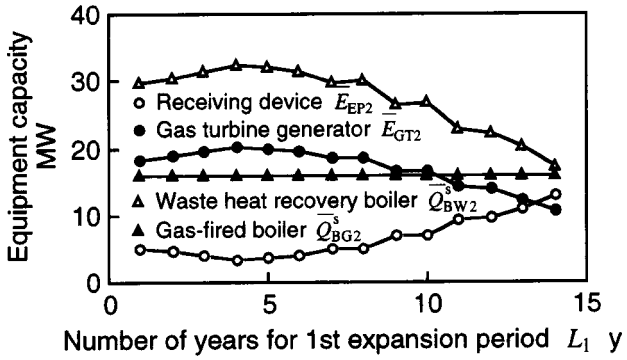

(b) 2nd expansion period

Fig. 6 Relationships between number of years for 1st expansion period and optimal equipment capacities ($\alpha_1=\alpha_2=0.4$); (*a*) 1st expansion period, (*b*) 2nd expansion period

equipment capacities for the first and the second expansion periods are identical regardless of the numbers of years for the expansion periods, and are equal to those for the single-stage planning. This is because of the linearity of the ordinary optimal design problem. However, in Fig. 5(a), with an increase in α_m, the optimal capacity of the gas turbine generator decreases and that of the receiving device increases for the first expansion period. On the other hand, with an increase in α_m, the optimal capacity of the gas turbine generator increases and that of the receiving device decreases for the second expansion period. In Fig. 5(b), although a similar tendency of changes in the optimal equipment capacities is found, their degrees are small. Especially, the optimal equipment capacities for the first expansion period approach to those for the single-stage planning. This is because of the nonlinearity of the robust optimal design problem.

Figures 6(*a*) and (*b*) show the relationships between the number of years for the first expansion period L_1 and the optimal equipment capacities for the first and the second expansion periods, respectively. Here, it is assumed that $\alpha_1=\alpha_2=0.4$. The features found in Fig. 5 are also shown in Fig. 6. Namely, with an increase in L_1, the optimal capacity of the gas turbine generator increases and that of the receiving device decreases for the first expansion period, and they approach to those for the single-stage planning. On the other hand, with an increase in L_1, the optimal capacity of the gas turbine generator decreases and that of the receiving device increases for the second expansion period. The results in Figs. 5 and 6 show that a large capacity of the cogeneration unit with a high capital cost and a possible reduction in the operational cost should be installed for a longer expansion period.

Figure 7 shows the relationship between the number of years for the first expansion period L_1 and the minimum of the maxi-

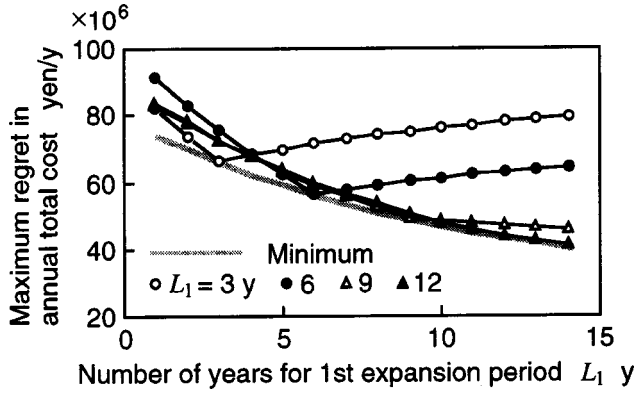

Fig. 7 Relationship between number of years for 1st expansion period and maximum regret in annual total cost ($\alpha_1=\alpha_2=0.4$)

mum regret in the annual total cost. Here, it is assumed that $\alpha_1=\alpha_2=0.4$. In addition, the changes in the maximum regret with respect to L_1 are also shown for the robust optimal designs in case that $L_1=3$, 6, 9, and 12 y. The former curve is the envelope of the latter ones. With an increase in L_1, the total energy demands for $M=15$ y decrease, the annual total cost decreases correspondingly, and its maximum regret also decreases. The following features are found by comparing the robust optimal designs in case that $L_1=3$, 6, 9, and 12 y. In case that $L_1=3$ or 6 y, the sensitivity of the maximum regret with respect to L_1 is high, and the maximum regret increases dramatically with a change in L_1 from 3 or 6 y. On the other hand, in case that $L_1=9$ or 12 y, the sensitivity of the maximum regret with respect to L_1 is low, and the maximum regret hardly increases even with a change in L_1 from 9 or 12 y. Although the uncertainty in the numbers of years for the expansion periods are not considered directly, it turns out that the robust optimal designs for $L_1=9$ and 12 y are suitable from the viewpoint of robustness against the uncertainty in the numbers of years for the expansion periods.

Figures 8(*a*) and (*b*) show the relationships between the uncertainty in energy demands α_1 and α_2, and the optimal capacities of the gas turbine generator and the receiving device for the first and the second expansion periods, respectively, in case that $L_1=5$ y and $L_2=10$ y. Here, the values of α_1 and α_2 are changed independently. For the first expansion period, only in case that α_1 and α_2 are both large, the capacity of the gas turbine generator decreases, and that of the receiving device increases dramatically. In the other cases, the capacity of the gas turbine generator remains almost constant, and that of the receiving device increases with α_1. On the other hand, for the second expansion period, when α_1 is small, the capacity of the gas turbine generator remains almost constant regardless of α_2, and that of the receiving device increases with α_2. However, when α_1 is large, the capacity of the gas turbine generator decreases in case that α_2 is small, and increases in case that α_2 is large. In addition, that of the receiving device increases in case that α_2 is small, and decreases in case that α_2 is large. Since the optimal equipment capacities depend significantly on the uncertainty in energy demands as shown here, it is necessary to evaluate the uncertainty in energy demands and determine the equipment capacities appropriately.

Figure 9 shows the relationship between the uncertainty in energy demands α_1 and α_2, and the minimum of the maximum regret in the annual total cost, in case that $L_1=5$ y and $L_2=10$ y. Here, the values of α_1 and α_2 are changed independently. The minimum of the maximum regret increases with α_1 and α_2. Its increasing rate is large especially in case that $\alpha_1+\alpha_2>0.3$. This is because the electricity and steam demands become more unbalanced with increases in α_1 and α_2, which makes the cogeneration plant disadvantageous.

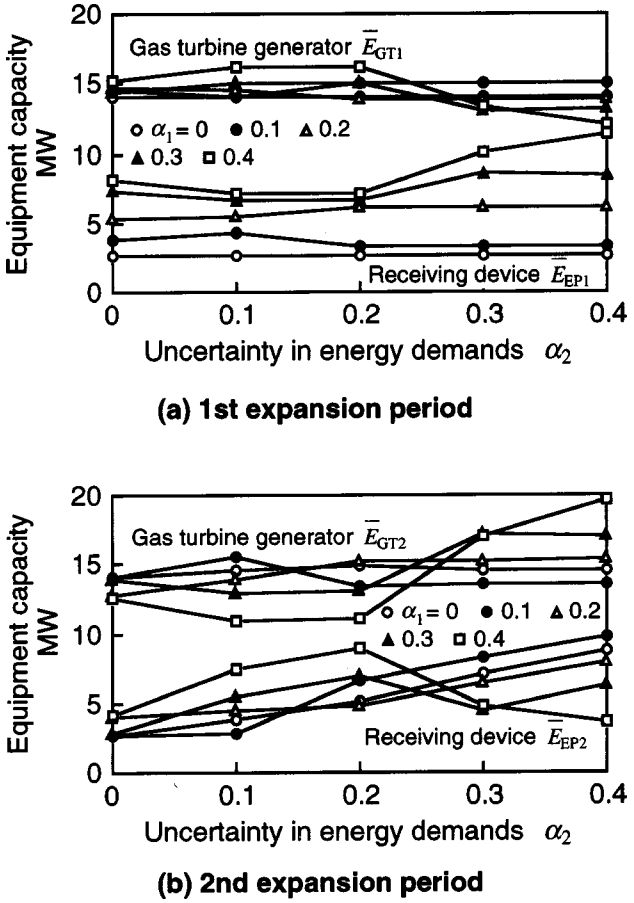

Fig. 8 Relationships between uncertainty in energy demands and optimal equipment capacities ($L_1=5$ y, $L_2=10$ y); (*a*) 1st expansion period, (*b*) 2nd expansion period

Conclusions

An optimal unit sizing method for the multistage expansion planning of energy supply plants has been proposed in consideration of the robustness under uncertain energy demands based on the minimax regret criterion. Under uncertain energy demands increasing stepwise, equipment capacities and utility contract demands as well as energy flow rates for each expansion period are determined in consideration of their sequential relationships to minimize the maximum regret in the annual total cost and satisfy

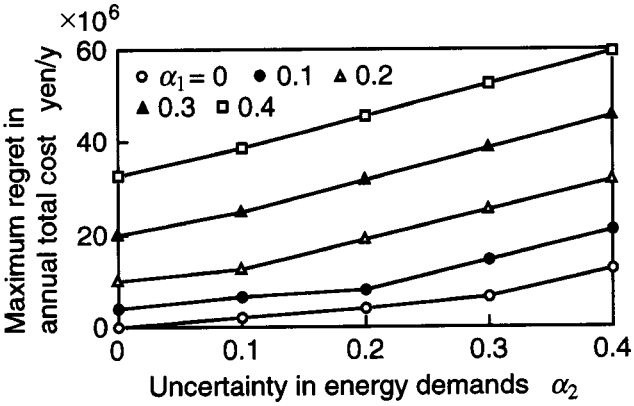

Fig. 9 Relationship between uncertainty in energy demands and minimum of maximum regret in annual total cost ($L_1=5$ y, $L_2=10$ y)

all the possible energy demands for all the expansion periods. This robust optimal design problem has been formulated as a kind of multilevel linear programming one, and its solution algorithm has been proposed. A case study has been conducted on a gas turbine cogeneration plant for district energy supply to evaluate its economic robustness by changing the uncertainty in energy demands and the numbers of years for the expansion periods. Through the case study, the features of the economic robustness and the robust optimal design have been clarified in relation to the uncertainty in energy demands and the numbers of years for the expansion periods, and it has turned out that it is necessary to evaluate the uncertainty in energy demands and determine the equipment capacities appropriately. It has also turned out that a large capacity of the cogeneration unit with a high capital cost and a possible reduction in the operational cost should be installed for a longer expansion period. In addition, it has turned out that the robust optimal design for the longer first expansion period is advantageous regardless of the uncertainty in the numbers of years for the expansion periods.

Nomenclature

a, b = performance characteristic values of equipment ($kW/(m^3/h)$, kW/kW)
C = annual operational cost (yen/y)
d = duration per year of sampling time (h/y)
E = electric power (kWh/h)
F = natural gas consumption (m^3/h)
f = objective function (annual total cost) (yen/y)
g = variable for minimum
i = interest rate
L = number of years for expansion period (y)
M = number of years for period for which annual total cost is evaluated (y)
N = number of years for period before installation of equipment (y)
P = initial capital cost of equipment (yen)
Q = heat flow rate (kWh/h)
T = number of sampling times
t = index for sampling times
v = ratio of salvage value after life to initial capital cost of equipment
v_L = ratio of salvage value at time when annual total cost is evaluated to initial capital cost of equipment
X = feasible region for $\mathbf{x}$
$\mathbf{x}$ = design variables (equipment capacities and utility contract demands) (kW, m^3/h)
Y = possible region for $\mathbf{y}$
$\mathbf{y}$ = uncertain parameters (energy demands) (kWh/h)
Z = feasible region for $\mathbf{z}$
$\mathbf{z}$ = operation variables (energy flow rates) (kWh/h, m^3/h)
α = parameter for uncertainty in energy demands
Γ = capital unit cost of equipment (yen/kW)
κ = number of years for life of equipment (y)
φ = unit cost for energy charge of utility (yen/kWh, yen/m^3)
ψ = monthly unit cost for demand charge of utility (yen/(kW·month), $yen/(m^3/h \cdot month)$)
$\overline{(\ )}$ = upper limit
$\tilde{(\ )}$ = average
$(\ )'$ = different value or set

Subscripts

BG = gas-fired boiler
BW = waste heat recovery boiler
dem = energy demand
disp = heat disposal
EP = receiving device
elec = electricity purchased
GT = gas turbine generator
gas = natural gas purchased
j, k, l, m = indices for expansion periods

Superscripts

e = exhaust gas
s = steam
T = transposition of vector

References

[1] Yokoyama, R., Ito, K., and Matsumoto, Y., 1994, "Optimal Sizing of a Gas Turbine Cogeneration Plant in Consideration of Its Operational Strategy," ASME J. Eng. Gas Turbines Power, **116**, pp. 32–38.
[2] Yokoyama, R., Ito, K., and Matsumoto, Y., 1996, "Optimal Multistage Expansion Planning of a Gas Turbine Cogeneration Plant," ASME J. Eng. Gas Turbines Power, **118**, pp. 803–809.
[3] Yokoyama, R., and Ito, K., 1999, "Robust Optimal Design of a Gas Turbine Cogeneration Plant Based on Minimax Regret Criterion," Paper No. 99-GT-128.
[4] Kouvelis, P., and Yu, G., 1997, *Robust Discrete Optimization and Its Applications*, Kluwer Academic Publishers, Dordrecht, The Netherlands.
[5] Yokoyama, R., and Ito, K., 2001, "Multiobjective Robust Optimal Design of a Gas Turbine Cogeneration Plant Under Uncertain Energy Demands," Paper No. 2001-GT-208.
[6] Parkinson, A., Sorensen, C., and Pourhassan, N., 1993, "A General Approach for Robust Optimal Design," ASME J. Mech. Des., **115**, pp. 74–80.
[7] Biegler, L. T., Grossmann, I. E., and Westerberg, A. W., 1997, *Systematic Methods of Chemical Process Design*, Prentice-Hall, Upper Saddle River, NJ.
[8] Migdalas, A., Pardalos, P. M., and Värbrand, P., 1998, *Multilevel Optimization: Algorithms and Applications*, Kluwer Academic Publishers, Dordrecht, The Netherlands.
[9] Fortuny-Amat, J., and McCarl, B., 1981, "A Representation and Economic Interpretation of a Two-Level Programming Problem," J. Oper. Res. Soc. Am., **32**(9), pp. 783–792.
[10] Brooke, A., Kendrick, D., and Meeraus, A., 1996, *GAMS Release 2.25 a User's Guide*, GAMS Development Corp., Washington, DC.

Evaluation of Operational Performance of Gas Turbine Cogeneration Plants Using an Optimization Tool: OPS-Operation

Ryohei Yokoyama[1]
Associate Professor,
Mem. ASME
e-mail: yokoyama@ese.energy.osakafu-u.ac.jp

Koichi Ito
Professor,
Fellow ASME

Department of Energy Systems Engineering,
Osaka Prefecture University,
1-1 Gakuen-cho,
Sakai, Osaka 599-8531, Japan

To attain the highest performance of gas turbine cogeneration plants, it is necessary to rationally select the numbers and capacities of gas turbines and auxiliary equipment in consideration of their operational strategies corresponding to energy demands which change with season and time. It is also important to rationally select the options such as the variable heat to power by the steam injection or combined cycle, and the inlet air cooling by the ice storage combined with electric compression refrigeration or steam absorption refrigeration. The evaluation of the effects of these alternatives on the performance is an important work for designers. However, it takes much time to conduct the work thoroughly. The authors have developed an optimization tool named "OPS-Operation" to assess the operational strategies for given configurations and specifications of energy supply plants. This tool has a user-friendly interface for the functions of data registration, graphical flowsheet editing, automatic programming and optimization calculation, and graphical representation of results. In this paper, the effects of the aforementioned alternatives on the operational performance of gas turbine cogeneration plants are evaluated using the optimization tool in terms of many criteria including operational cost, energy consumption, and CO_2 emission. It is demonstrated that the tool is very effective to evaluate the performance rationally, flexibly, and easily.
[DOI: 10.1115/1.1771689]

Introduction

For the purpose of energy efficient utilization, cogeneration plants have been increasingly installed into industrial and commercial sectors. Especially, gas turbine cogeneration plants have been installed into industries and districts with relatively large energy demands. However, gas turbines as prime movers of cogeneration plants have the following deficiencies: decreases in power generating efficiencies for part load status, constant heat to power output ratios, and decreases in maximum power outputs for high ambient air temperature.

To overcome these deficiencies, several technologies have been developed. Variable heat to power outputs can be realized by the steam injection and combined cycle, [1–3]. These options can also increase maximum power outputs. Decreases in maximum power outputs for high ambient air temperature can be recovered by the inlet air cooling, [4]. There are several options for the inlet air cooling. One is to use cold water generated by ice storage units combined with electric compression refrigerators, [5]. Another is to use cold water generated by steam absorption refrigerators, [6]. These options may be effective from the viewpoint of increasing power generating efficiencies and maximum power outputs of gas turbines only. However, it is not clear if they can increase overall efficiencies and economics of gas turbine cogeneration plants.

To attain the highest performance of gas turbine cogeneration plants, it is necessary to rationally select the numbers and capacities of gas turbines and auxiliary equipment in consideration of their operational strategies corresponding to energy demands which change with season and time. It is also important to rationally select the aforementioned options such as the variable heat to power by the steam injection or combined cycle, and the inlet air cooling by the ice storage combined with electric compression refrigeration or steam absorption refrigeration. The evaluation of the effects of these alternatives on the performance is an important work for designers. However, it takes much time to conduct the work thoroughly.

The authors have proposed an optimal operational planning method based on the mathematical programming to assess the operational strategies for given configurations and specifications of energy supply plants, [7,8]. On the basis of the methods, they have also developed an optimization tool named ''OPS-Operation'' with a user-friendly interface for the functions of data registration, graphical flowsheet editing, automatic programming and optimization calculation, and graphical representation of results, [9,10], and have extended some functions.

In this paper, the effects of the aforementioned alternatives on the operational performance of gas turbine cogeneration plants are evaluated using the optimization tool in terms of many criteria including operational cost, energy consumption, and CO_2 emission. It is demonstrated that the tool is very effective to evaluate the performance rationally, flexibly, and easily.

Operational Planning of Energy Supply Plants

Overall Planning Process. The operational planning of energy supply plants is conducted as one procedure in the overall planning process shown in Fig. 1. A summary of each procedure in the process is described in the following.

First, demands of energy such as electricity, space heating and cooling, hot water, and steam are estimated for a building, a district, or a factory to be supplied with energy. Performance characteristics of some types of equipment such as gas turbines and

[1]To whom correspondence should be addressed.

Contributed by the International Gas Turbine Institute (IGTI) of THE AMERICAN SOCIETY OF MECHANICAL ENGINEERS for publication in the ASME JOURNAL OF ENGINEERING FOR GAS TURBINES AND POWER. Paper presented at the International Gas Turbine and Aeroengine Congress and Exhibition, Atlanta, GA, June 16–19, 2003, Paper No. 2003-GT-38381. Manuscript received by IGTI, October 2002, final revision, March 2003. Associate Editor: H. R. Simmons.

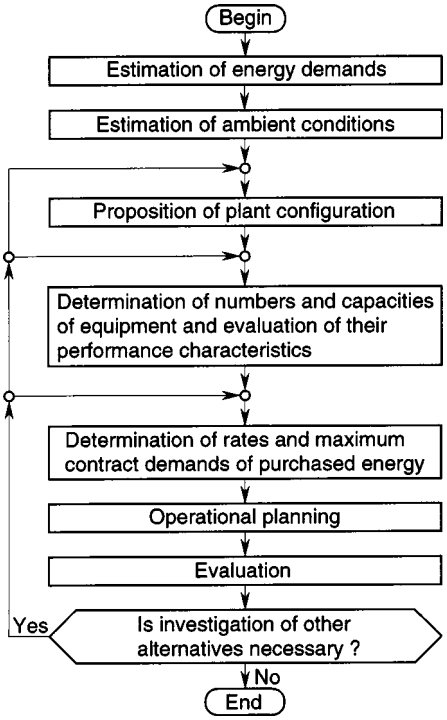

Fig. 1 Overall planning process

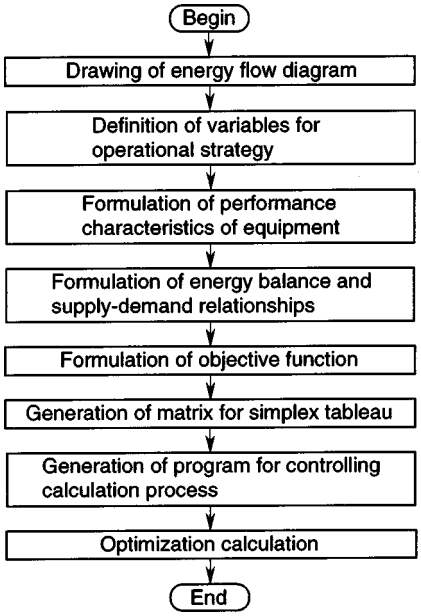

Fig. 2 Optimal operational planning process

heat pumps depend on ambient conditions such as air and water temperatures. To take account of this dependence, ambient conditions are also estimated. Here, seasonal and hourly variations in energy demands and ambient conditions are considered by setting multiple representative days per year and multiple sampling times per each representative day.

Next, a plant configuration is proposed by selecting several types of equipment and connecting them by energy flows. The number and capacities of each type of equipment are determined. Performance characteristics of each piece of equipment are also evaluated at the rated and part load status. Rates for energy charge and maximum contract demands of energy purchased from outside utility companies are determined. Here, the energy charge is a part of the operational cost due to the consumptions of purchased energy.

Finally, the operational planning is conducted for the proposed alternative, i.e., the operational strategy such as the on/off status, and energy flow rates and storage levels of equipment corresponding to seasonal and hourly variations in energy demands is assessed under the aforementioned planning conditions—energy demands, ambient conditions, plant configuration, numbers, capacities, and performance characteristics of equipment, and rates and maximum contract demands of purchased energy. Additionally, on the basis of the obtained operational strategy, the energy charge, energy consumption, and CO_2 emission, etc., are evaluated as criteria from the viewpoints of economics, energy savings, and environmental protection, etc., respectively. Furthermore, the total cost is evaluated by adding the capital cost of equipment and the demand charge of purchased energy to the energy charge. Here, the demand charge is a part of the operational cost due to the maximum contract demands of purchased energy.

The operational planning and evaluation are conducted for other alternatives, and they are compared with one another.

Optimal Operational Planning. Many alternatives exist concerning the operational strategy. The operational planning has been conducted conventionally by introducing operational rules such as preference order of equipment operation and determining the operational strategy by trial and error. In contrast with this conventional approach, the authors have proposed an optimal operational planning method based on the mathematical programming to assess the operational strategy rationally, [7,8]. A series of procedures in the optimal operational planning process is shown in Fig. 2. A summary of each procedure in the process is described as follows.

First, an energy flow diagram is drawn which illustrates the energy conversion process from supplies to demands through equipment, and the variables for the operational strategy are defined correspondingly. They are composed of continuous variables $\mathbf{x}$ for the energy flows rates and storage levels of equipment, and binary ones $\mathbf{y}$ for the on/off status of equipment.

Next, performance characteristics of equipment are formulated using the variables. They are expressed approximately as linear equations with respect to the variables. Here, since binary variables are employed to consider the discontinuity of performance characteristics due to the on/off status, even the linear equations can express a change in the thermal efficiency or the coefficient of performance due to the rated/part load status. If strongly nonlinear performance characteristics of equipment should be considered, they can be expressed approximately using piece-wise linear equations along with additional binary variables. Energy balance and supply-demand relationships are also formulated for each energy flow. These are based on the first law of thermodynamics and expressed as linear equations with respect to the energy flow rates at branching points in the energy flow diagram. All these equations are considered as constraints of the optimization problem. Furthermore, the objective function of the optimization problem is formulated using both continuous and binary variables. For example, the energy charge is adopted as the objective function to be minimized. This optimization problem results in a mixed-integer linear programming one, and it can be solved using the branch and bound algorithm along with the dual simplex one.

The aforementioned optimization problem can be expressed mathematically as

$$\left.\begin{aligned} \text{min.} \quad & f(\mathbf{x},\mathbf{y}|\mathbf{d},\mathbf{c},\mathbf{p}(\mathbf{a})) \\ \text{sub. to} \quad & \mathbf{g}(\mathbf{x},\mathbf{y}|\mathbf{d},\mathbf{c},\mathbf{p}(\mathbf{a})) \leqslant \mathbf{0} \\ & \mathbf{h}(\mathbf{x},\mathbf{y}|\mathbf{d},\mathbf{c},\mathbf{p}(\mathbf{a})) = \mathbf{0} \\ & \mathbf{x} \geqslant 0 \\ & \mathbf{y} \in \{0,1\}^n \end{aligned}\right\} \tag{1}$$

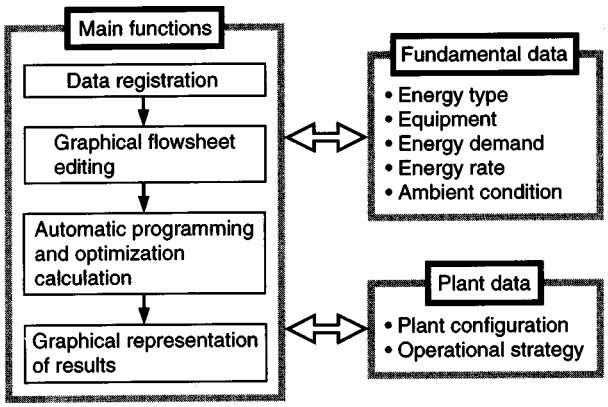

Fig. 3 Fundamental structure of optimization tool

where f is the objective function to be minimized, **g** and **h** are the functions for inequality and equality constraints, respectively, and **d**, **c**, **p**, and **a** are the vectors for energy demands, rates and maximum contract demands of purchased energy, performance characteristic values of equipment, and ambient conditions, respectively, and are treated as parameters whose values are given as input data. The performance characteristic values **p** may be functions with respect to ambient conditions **a**. In addition, the superscript n is the number of binary variables. For an energy supply plant without equipment for energy storage, this optimization problem is defined independently for each representative day and each sampling time. On the other hand, for an energy supply plant with equipment for energy storage, this optimization problem is defined for each representative day, on the assumption that the energy demands change cyclically with a period of a day.

Finally, according to the aforementioned formulation, the matrix for simplex tableau is generated as input data for solving the mixed-integer linear programming problem. The program for controlling the overall calculation process—data input, optimization calculation, and data output—is also generated. The optimization calculation is conducted to find the optimal values of variables for the operational strategy.

Optimization Tool: OPS-Operation

Even if the optimal operational planning method is employed, it is difficult for designers to conduct the aforementioned overall planning thoroughly. To assist designers to conduct the planning flexibly and easily, an optimization tool named ''OPS-Operation'' has been developed, [9,10], and its functions have been extended.

The software of the tool is written using C and FORTRAN languages. X-Window is employed for the software related with graphics. The tool can be executed on UNIX and LINUX.

A fundamental structure of the tool is shown in Fig. 3. The tool has the following main functions: data registration, graphical flowsheet editing, automatic programming and optimization calculation, and graphical representation of results. Data are divided into two categories: fundamental and plant data. The following are some features of the main functions.

Data Registration. Various types of fundamental data can be registered in advance in a data base, and are utilized for the graphical flowsheet editing to prepare plant data. Each type of data can be saved to any stock data base, and can be retrieved to the current data base. This function enables designers to construct the data base flexibly according to their needs. The types and structure of data are shown in Fig. 4.

Energy demands, energy rates, and ambient conditions can be changed seasonally and hourly by setting representative days and sampling times. To ensure the independence among these different types of data, representative days and sampling times can be defined independently for each type of data. However, they are made

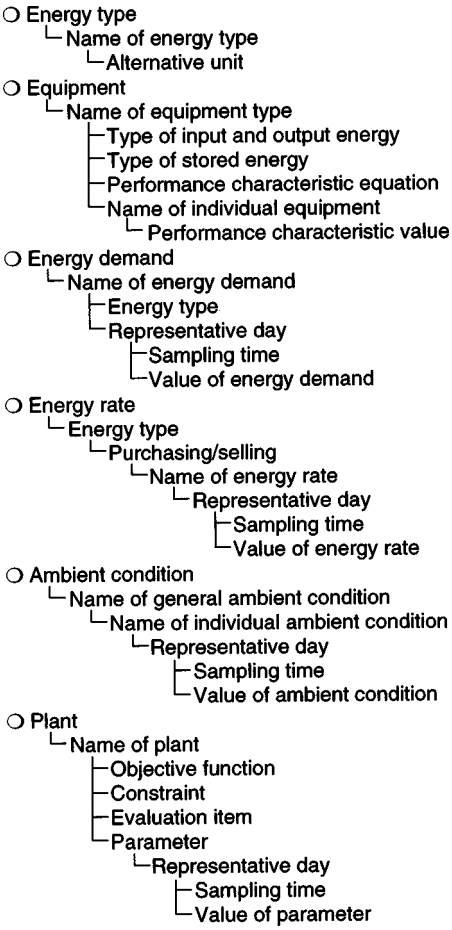

Fig. 4 Types and structure of data

consistent with one another prior to the optimization calculation, if they are selected simultaneously as planning conditions. This procedure enables designers to conduct the operational planning with various degrees of details concerning seasonal and hourly variations in planning conditions. The types of equipment are categorized into the ones for energy conversion and storage. Performance characteristics of the former are defined as the relationships among flow rates of input and output energy. Performance characteristics of the latter are defined as the differential energy balance relationships with respect to energy storage levels. Performance characteristic values can be identified with catalogued or measured data on the flow rates of input and output energy for the rated/part load status.

Data input windows are prepared as a user-friendly interface for data registration. Corresponding to the hierarchical structure of data shown in Fig. 4, the data input windows are also structured hierarchically, which helps designers to understand the data input task easily. As an example, the windows for registering and defining data on equipment types are shown in Fig. 5. With these windows, names of equipment types can be registered in the data base, and types of input and output energy, types of stored energy, performance characteristic equations, and graphical data for the flowsheet editor can be defined for each type of equipment. Figure 5 shows the registration and definition of data on gas turbine generators.

Graphical Flowsheet Editing. A graphical flowsheet editor is prepared as a user-friendly interface for defining energy supply plants. Plant data are defined by energy flow diagrams in place of

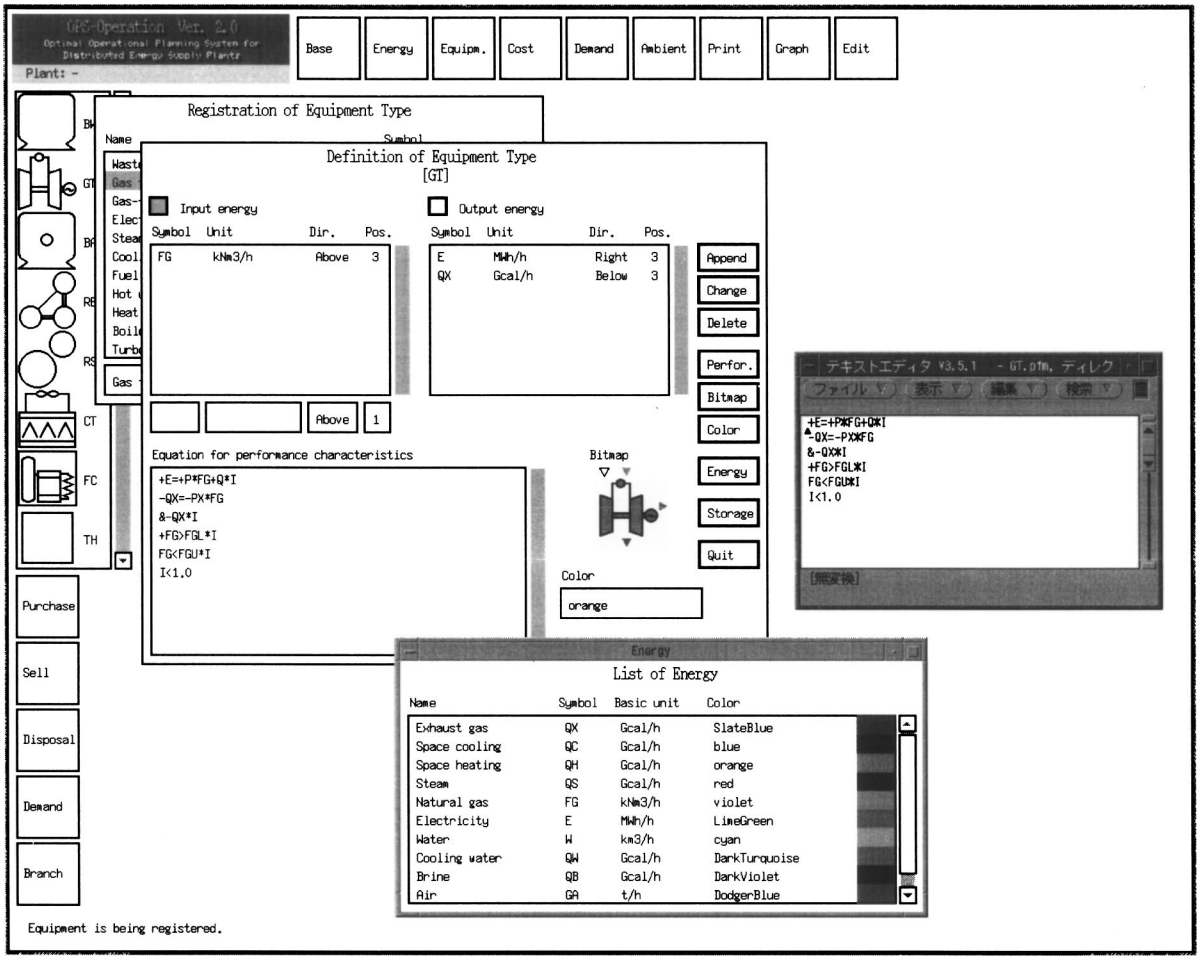

Fig. 5 Data registration

numerical and character data. This function enables designers to compose or change plant data flexibly and easily by drawing or modifying energy flow diagrams.

Energy flow diagrams are drawn by setting several elements denoted by icons, connecting elements by energy flows, selecting several types of data registered in the data base, and inputting relevant numerical data. The elements include equipment, energy flow terminals, and nodes. Four types of energy flow terminals, i.e., ''purchase,'' ''sell,'' ''demand,'' and ''disposal,'' are prepared to express boundaries between energy supply plants and the environment. The nodes are prepared to express the branching of energy flows. As an example, an energy flow diagram for a simple Brayton cycle gas turbine cogeneration plant drawn by the graphical flowsheet editor is shown in Fig. 6.

Automatic Programming and Optimization Calculation. The operational planning can be conducted automatically for energy supply plants defined by the graphical flowsheet editor, i.e., all the procedures needed for the aforementioned operational planning—formulation of the optimal operational planning problem, generation of the matrix for simplex tableau and the program for controlling the overall calculation process, and execution of optimization calculation—can be conducted automatically by analyzing energy flow diagrams and converting them into numerical and character data. This function enables designers to conduct the operational planning easily and efficiently. In addition, the adoption of the optimization approach enables designers to conduct the operational planning rationally, because it does not need to determine the operational strategy according to operational rules assumed by trial and error. Not only the optimal operational strategy but also the energy deficit due to insufficient capacities of equipment against required energy demands are obtained through the optimization calculation. The latter information helps designers to check capacities of equipment of energy supply plants with complex configurations.

As complementary functions for the optimization calculation, various conditions can be incorporated as objective functions, constraints, evaluation items, and parameters.

Objective Functions. The energy charge is selected as the standard objective function for the operational planning. However, designers often need to select other objective functions such as the ones related with energy savings or environmental protection. Alternative objective functions can be registered and one of them can be selected for each energy supply plant. This function enables designers to obtain the operational strategy rational from various viewpoints.

Constraints. As standard constraints, performance characteristics of equipment, and energy balance and supply-demand relationships are considered. Besides these constraints, operational restraints which must be obeyed in practical operation should often be considered. For example, the following operational restraints can be conceived:

- on/off status of equipment,
- preference order of equipment operation,
- load level control of same type of equipment, and
- preference order of energy utilization.

Alternative sets of additional constraints can be registered and

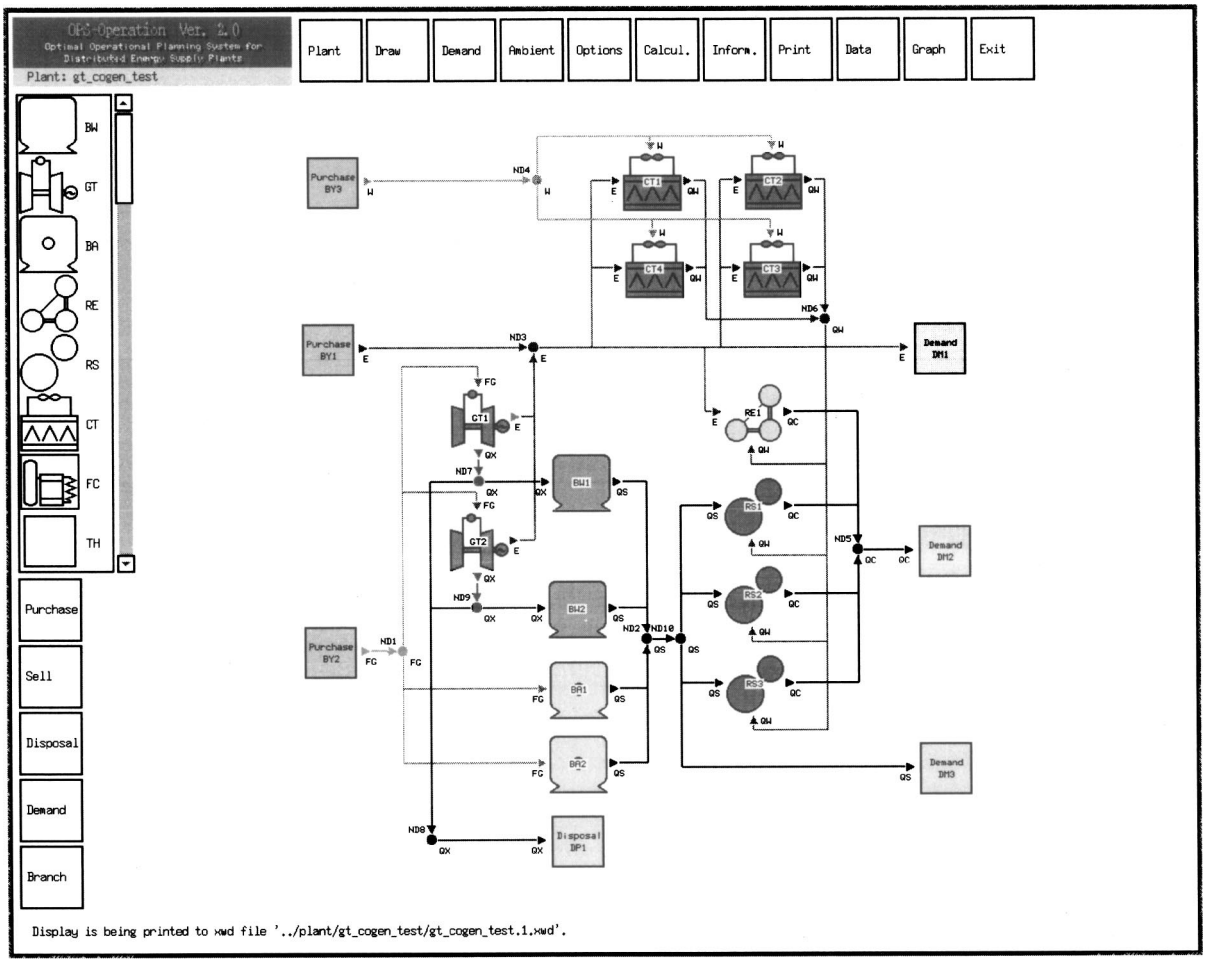

Fig. 6 Graphical flowsheet editing

selected for each energy supply plant. This function enables designers to conduct the operational planning subject to practical operational restraints.

Evaluation Items. Besides the variables defined automatically, designers often need to evaluate important criteria in addition to the objective function as evaluation items. Alternative sets of evaluation items can be registered and selected for each energy supply plant. This function enables designers to obtain the values of evaluation items simultaneously through the optimization calculation.

Parameters. The objective functions, constraints, and evaluation items may be defined using parameters whose values can be changed with representative days and sampling times. For example, operational restrictions can be made active or inactive according to representative days and sampling times. Representative days and sampling times for parameters can also be set independently from those for energy demands, energy rates, and ambient conditions. This function enables designers to conduct the operational planning on a wide variety of conditions.

Graphical Representation of Results. The operational strategy obtained through the optimization calculation can be represented graphically. Since a large number of data on the operational strategy are obtained, designers can select data necessary to evaluate the performance of energy supply plants. For example, if a piece of equipment on the energy flow diagram is selected, seasonal and hourly variations are obtained for the flow rates of input and output energy and the energy storage level of the equipment. Furthermore, if a branching point is selected, seasonal and hourly variations are obtained for the flow rate allocations of input and output energy at the branching point. For each representative day, the daily changes in the hourly energy flow rates and storage levels are represented. For a year, the annual changes in the daily energy flow rates or the annual duration curves for the hourly energy flow rates and storage levels are represented. This function enables designers to understand the operational strategy visually and change plant data for proposing better alternatives. As an example, Fig. 7 shows a graphical representation of the optimal operational strategy obtained for the simple Brayton cycle gas turbine cogeneration plant shown in Fig. 6.

Application of Optimization Tool

Plant Configuration. The operational performance of a gas turbine cogeneration plant shown in Fig. 8 is evaluated using the optimization tool. This plant is composed of a gas turbine cogeneration unit (CU), a gas-fired auxiliary boiler (BG), a steam absorption refrigerator (RS), a cooling tower (CT), a heat exchanger (HE), an air cooler (AC), and a receiving device for purchasing electricity (EP).

Electricity is supplied to customers by operating the cogeneration unit and purchasing electricity from an outside electric power company. Exhaust heat generated from the gas turbine is recovered in the form of steam by the waste heat recovery boiler in the cogeneration unit, and is used for heat supply. An excess of exhaust heat is disposed of to the environment in the form of exhaust gas. A shortage of steam is supplemented by the gas-fired auxiliary boiler. Steam is used by the steam absorption refrigerator and heat exchanger to supply cold water for inlet air and space cool-

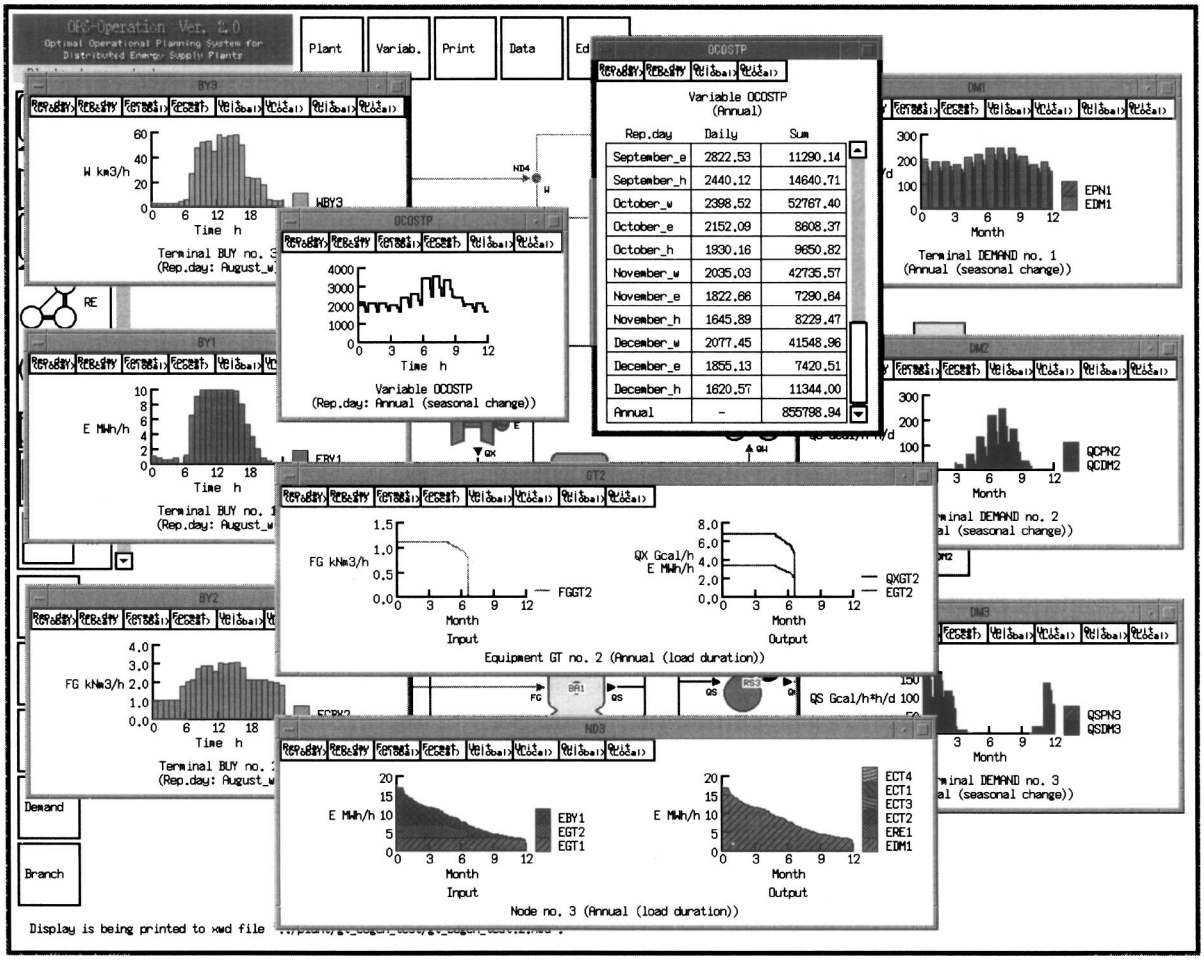

Fig. 7 Graphical representation of results

ing, and hot water for space heating and hot water supply, respectively. The air cooler cools air supplied to the cogeneration unit. Water is consumed by the cogeneration unit and cooling tower.

The effects of some alternatives for the plant configuration on the operational performance are investigated. As for the cogeneration unit, the following alternatives are considered:

- with simple Brayton cycle unit (SC),
- with steam injected unit (SI),
- with combined cycle unit (CC), and
- without cogeneration unit (N).

The simple Brayton cycle unit is equipped with a gas turbine generator and a waste heat recovery boiler. The combined cycle unit is equipped with a gas turbine generator, a waste heat recovery boiler, and a steam turbine generator. The steam injected unit is equipped with a steam injected gas turbine generator and a waste heat recovery boiler. A conventional plant without any cogeneration unit is also investigated to clarify the effect of the types for the cogeneration unit as compared with that of cogeneration. As for the inlet air cooling, the following alternatives are considered:

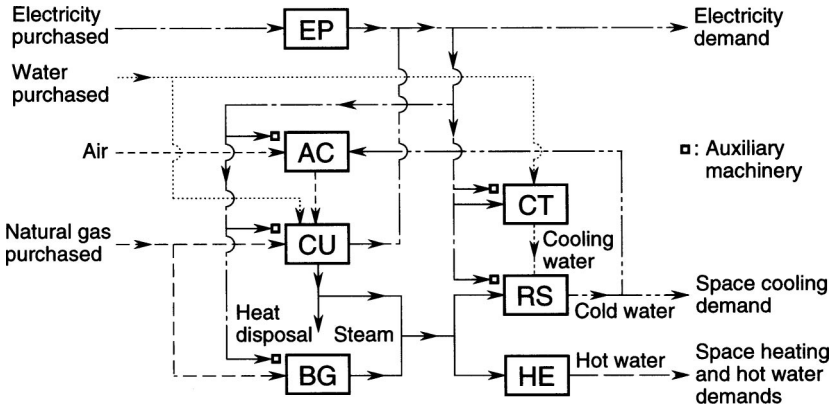

Fig. 8 Configuration of gas turbine cogeneration plant

Table 1 Summary of energy demands

Energy	Hourly maximum MW	Annual total GWh/y
Electricity	17.14	73.29
Cold water	26.28	27.28
Hot water	21.39	19.83

- with inlet air cooling (IC) and
- without inlet air cooling (N).

The optimization calculation is conducted for all the combinations of the alternatives for the cogeneration unit and inlet air cooling. The names of plants are expressed using the abbreviations for the alternatives. For example, the plant with the steam injected unit and inlet air cooling is expressed as SI/IC.

Input Data and Conditions. A district in Osaka, Japan which is supplied with energy is investigated as an example. It is composed of hotels and office buildings, and its total floor area is 383.7×10^3 m^2. Energy demands are estimated by setting 36 representative days per year, i.e., a weekday, a Saturday, and a holiday per month, and dividing each representative day into 24 sampling times each of which has an hour. A summary of energy demands is shown in Table 1. To evaluate the cooling energy for the inlet air cooling, the ambient air temperature and humidity are also estimated by setting 12 representative days each of which corresponds to a month, and dividing each representative day into 24 sampling times. These data are omitted here.

The capacities and performance characteristic values of main equipment are given in Tables 2 and 3, respectively. Although the performance characteristic values are shown only at the rated load status, their changes at the part load status are also taken into account. In addition, the capacities and performance characteristic values of the cogeneration units are shown only for the inlet air temperature of 15°C, their changes with the inlet air temperature are also taken into account. As for the inlet air cooling, the bypass factor of the air cooler is assumed to be 0.2, and the temperature of air after it is cooled is assumed to be 15°C. Here, the bypass factor means the ratio of the amount of the air whose heat cannot be exchanged in the air cooler.

As the operational strategy of the plants, the on/off status of operation and energy flow rates of each piece of equipment are determined. In addition, the on/off status of steam injection, steam extraction, and inlet air cooling are also determined for the steam injected unit, combined cycle unit, and air cooler, respectively.

The energy charge of purchased electricity, natural gas, and water is adopted as the objective function to be minimized. The following items are considered as criteria: operational cost, energy consumption, CO_2 emission, and exhaust heat disposal. The operational cost is the sum of the demand and energy charges of purchased energy. The energy consumption is evaluated as the sum of the lower heating values of the fuel consumed by the electric power company and the natural gas. The CO_2 emission is evaluated as the sum of those due to the consumptions of the aforementioned fuel and the natural gas. The exhaust heat disposal is evaluated as the heat of steam generated when it is recovered by the waste heat recovery boiler. The data on the rates of purchased electricity, natural gas, and water, and the energy consumptions and CO_2 emissions of purchased electricity and natural gas are omitted here.

Table 2 Capacities of main equipment

Equipment	Item	Value
Simple Brayton cycle unit*1	Power generation	4.22 MW
	Steam generation	6.01 MW
Steam injected unit*1	Power generation	4.22 MW*2
		6.36 MW*3
	Steam generation	6.01 MW*2
		1.77 MW*3
Combined cycle unit*1	Power generation	5.72 MW*4
		4.51 MW*5
	Steam generation	0.0 MW*4
		4.98 MW*5
Gas-fired auxiliary boiler	Steam generation	21.4 MW
Steam absorption refrigerator	Cold water generation	27.0 MW
Heat exchanger	Hot water generation	21.4 MW
Air cooler	Air cooling	74.0 t/h

*1 Inlet air temperature is assumed to be 15 °C.
*2 Without steam injection.
*3 With maximum steam injection.
*4 Without steam extraction.
*5 With maximum steam extraction.

Table 3 Performance characteristic values at rated load status of main equipment

Equipment	Item	Value
Simple Brayton cycle unit*1	Power generating efficiency	0.300
	Steam generating efficiency	0.427
Steam injected unit*1	Power generating efficiency	0.300*2
		0.367*3
	Steam generating efficiency	0.427*2
		0.102*3
Combined cycle unit*1	Power generating efficiency	0.406*4
		0.320*5
	Steam generating efficiency	0.0*4
		0.354*5
Gas-fired auxiliary boiler	Thermal efficiency	0.920
Steam absorption refrigerator	Coefficient of performance	1.25
Heat exchanger	Thermal efficiency	1.00
Air cooler	Thermal efficiency	1.00

*1 Inlet air temperature is assumed to be 15 °C.
*2 Without steam injection.
*3 With maximum steam injection.
*4 Without steam extraction.
*5 With maximum steam extraction.

Results and Discussion. The operational strategies and values of criteria for all the combinations of the alternatives for the cogeneration unit and inlet air cooling can be obtained easily using the optimization tool.

Table 4 shows the values of criteria and maximum contract demands of purchased energy for the alternative plants. All the values of criteria are expressed on the annual basis. All values of costs are stated in yen, which is equivalent to about 8.0×10^{-3} dollars on the recent exchange rate. Reduction rates of the criteria are calculated by adopting those for the conventional plant N/N or the cogeneration plant with the simple Brayton cycle unit and without the inlet air cooling SC/N as the references. The reduction rates in the following is obtained by adopting N/N as the reference.

Results on SC. The cogeneration plant with the simple Brayton cycle unit and without the inlet air cooling SC/N has a reduction rate of the operational cost of 10.7%, but has smaller reduction rates of the energy consumption and CO_2 emission. This is because the energy charge of purchased energy is adopted as the objective function to be minimized, the simple Brayton cycle unit is operated mostly at the rated load status with a high power generating efficiency, and much exhaust heat is disposed of. The cogeneration plant with the inlet air cooling SC/IC can reduce the operational cost further by 0.8%. This is because, although the energy charge can hardly be reduced, the demand charge can be reduced because of a reduction of the maximum contract demand of purchased electricity.

Results on SI. The cogeneration plant with the steam injected unit and without the inlet air cooling SI/N has higher reduction rates of the operational cost, energy consumption, and CO_2 emission than that with the simple Brayton cycle one SC/N. For example, SI/N has reduction rates of the operational cost and energy

Table 4 Values of criteria and maximum contract demands of purchased energy for alternative plants

Plant		N/N	SC/N	SC/AC	SI/N	SI/N*	SI/AC	SI/AC*	CC/N	CC/N*	CC/AC	CC/AC*
Operational cost $\times 10^6$ yen/y		1366.6	1219.3	1207.8	1186.4	1153.9	1175.5	1146.1	1169.7	1151.5	1158.5	1142.5
Energy charge $\times 10^6$ yen/y		916.6	824.4	822.5	791.6	791.8	790.4	790.8	778.2	778.6	776.8	777.2
Demand charge $\times 10^6$ yen/y		450.0	394.9	385.2	394.9	362.1	385.1	355.3	391.5	372.9	381.8	365.3
Energy consumption GWh/y		261.8	256.7	256.6	246.4	247.1	246.4	247.3	243.9	244.2	243.9	244.3
CO_2 emission $\times 10^3$ t-CO_2/y		61.57	57.00	56.87	54.23	54.29	54.15	54.22	53.85	53.91	53.75	53.83
Exhaust heat disposal GWh/y		0.0	22.43	22.20	1.21	1.21	1.16	1.16	0.0	0.0	0.0	0.0
Max. cont. dem. of electricity MW		19.15	15.71	15.25	15.71	13.62	15.24	13.14	15.43	14.30	14.97	13.78
Max. cont. dem. of natural gas $\times 10^3$ m^3/h		2.05	2.74	2.74	2.74	3.19	2.74	3.32	2.84	3.05	2.84	3.18
Reduction rate with N/N as reference %	Operational cost	–	10.78	11.62	13.18	15.56	13.99	16.13	14.41	15.74	15.22	16.40
	Energy charge	–	10.06	10.26	13.64	13.61	13.77	13.73	15.10	15.06	15.26	15.20
	Demand charge	–	12.25	14.39	12.25	19.53	14.42	21.04	13.00	17.13	15.16	18.83
	Primary energy consumption	–	1.97	2.01	5.85	5.60	5.85	5.57	6.86	6.70	6.87	6.67
	CO_2 emission	–	7.43	7.64	11.92	11.83	12.05	11.95	12.55	12.45	12.70	12.58
Reduction rate with SC/N as reference %	Operational cost	–	–	0.95	2.70	5.36	3.60	6.00	4.07	5.56	4.98	6.30
	Energy charge	–	–	0.23	3.99	3.95	4.13	4.08	5.61	5.56	5.78	5.72
	Demand charge	–	–	2.44	0.0	8.30	2.47	10.02	0.85	5.57	3.32	7.50
	Primary energy consumption	–	–	0.04	3.95	3.70	3.96	3.68	4.99	4.82	4.99	4.79
	CO_2 emission	–	–	0.22	4.85	4.75	4.99	4.88	5.53	5.42	5.70	5.57

* Maximum contract demand of purchased electricity is minimized.

charge of 13.1 and 13.6%, respectively. This is because the steam injected unit has a variable heat to power output ratio, and can change it flexibly corresponding to heat and power demands. However, SI/N has the same reduction rate of the demand charge of 12.2% as SC/N. This is because the steam injected unit is operated without power augmentation by steam injection even during the period with the maximum electricity demand, and the maximum contract demand of purchased electricity cannot be reduced, since the maximum space cooling demand occurs simultaneously, and it is more advantageous that the unit is operated without steam injection. Therefore, the optimization calculation is also conducted to minimize the maximum contract demand of purchased electricity. As a result, the demand charge is also reduced by 7.2%, and consequently the operational cost is reduced further by 2.3%. The cogeneration plant with the inlet air cooling SI/IC can reduce the operational cost by 0.5 to 0.8%, as compared with SI/N.

Results on CC. The cogeneration plant with the combined cycle unit and without the inlet air cooling CC/N has higher reduction rates of the operational cost, energy consumption, and CO_2 emission than that with the steam injected one SI/N. For example, CC/N has reduction rates of the operational cost and energy charge of 14.4 and 15.1%, respectively. This is because the combined cycle unit has a variable heat to power output ratio and a high power generating efficiency without steam extraction by combining the gas and steam turbine generators. In addition, CC/N has a slightly higher reduction rate of the demand charge of 13.0% than SI/N. This is because the steam turbine generator generates electricity even with the maximum steam extraction during the period with the maximum electricity and space cooling demands. The optimization calculation is also conducted to minimize the maximum contract demand of purchased electricity. As a result, the demand charge is reduced further by 4.1%, and consequently the operational cost is reduced further by 1.3%. The effect of minimizing the maximum contract demand of purchased electricity of CC/N is smaller than that of SI/N. This is because the increase in the power generating capacity by the combined cycle unit is smaller than that by the steam injected one. The cogeneration plant with the inlet air cooling CC/IC can reduce the operational cost by 0.6 to 0.8%, as compared with CC/N.

Conclusions

The effects of the variable heat to power and inlet air cooling on the operational performance of gas turbine cogeneration plants have been evaluated using the optimization tool which the authors have developed. It has been demonstrated that the tool is very effective to evaluate the performance rationally, flexibly, and easily. Through case studies, it has turned out that the variable heat to power by the steam injection or combined cycle reduces the operational cost, energy consumption, and CO_2 emission, and that this effect on the operational cost becomes larger by increasing the power generating capacity with the maximum steam injection or without the steam extraction during the period with the maximum electricity and space cooling demands, and minimizing the maximum contract demand of purchased electricity. It has also turned out that the inlet air cooling by the steam absorption refrigeration reduces the demand charge of purchased electricity and consequently the operational cost.

Nomenclature

- **a** = ambient conditions
- **c** = rates and maximum contract demands of purchased energy
- **d** = energy demands
- f = objective function
- **g** = inequality constraints
- **h** = equality constraints
- n = number of binary variables
- **p** = performance characteristic values of equipment
- **x** = continuous variables for energy flow rates and storage levels of equipment
- **y** = binary variables for on/off status of equipment

Abbreviations for Equipment

- AC = air cooler
- BG = gas-fired auxiliary boiler
- CT = cooling tower
- CU = gas turbine cogeneration unit
- EP = receiving device for purchasing electricity
- HE = heat exchanger
- RS = steam absorption refrigerator

Abbreviations for Plants

- CC = with combined cycle unit
- IC = with inlet air cooling
- N = without cogeneration unit or without inlet air cooling
- SC = with simple Brayton cycle unit
- SI = with steam injected unit

References

[1] Tuzson, J., 1992, "Status of Steam-Injected Gas Turbines," ASME J. Eng. Gas Turbines Power, **114**, pp. 682–686.

[2] Miura, S., 1997, "The Flexible Cogeneration System/Variable Power-Heat Ratio," Energy Resources, **18**(1), pp. 53–62 (in Japanese).

[3] Miura, S., 1999, "Small Gas Turbine Co-generation With Variable Heat and

Power Ratios,'' Cogeneration, **14**(1), pp. 51–58 (in Japanese).
[4] Lukas, H., 1997, ''Power Augmentation Through Inlet Cooling,'' Global Gas Turb. News, **37**(3), pp. 12–15.
[5] Ebeling, J. A., Halil, R., Bantam, D., Bakenhus, B., Schreiber, H., and Wendland, R., 1992, ''Peaking Gas Turbine Capacity Enhancement Using Ice Storage for Compressor Inlet Air Cooling,'' ASME Paper No. 92-GT-265.
[6] Bies, D., Johänntgen, U., and Scharfe, J., 1999, ''Optimised Cooling of the Compressor Intake Air—A New Way for the Improvement of Power and Efficiency in Gas Turbine Plants,'' *Proceedings of the International Gas Turbine Congress 1999 Kobe*, **I**, pp. 429–436.
[7] Ito, K., Yokoyama, R., Akagi, S., and Matsumoto, Y., 1990, ''Influence of Fuel Cost on the Operation of a Gas Turbine-Waste Heat Boiler Cogeneration Plant,'' ASME J. Eng. Gas Turbines Power, **112**, pp. 122–128.
[8] Ito, K., Yokoyama, R., and Shiba, T., 1992, ''Optimal Operation of a Diesel Engine Cogeneration Plant Including a Heat Storage Tank,'' ASME J. Eng. Gas Turbines Power, **114**, pp. 687–694.
[9] Yokoyama, R., Ito, K., Kamimura, K., and Miyasaka, F., 1994, ''Development of a General-Purpose Optimal Operational Planning System for Energy Supply Plants,'' ASME J. Energy Resour. Technol., **116**, pp. 290–296.
[10] Kamimura, K., Mukai, T., Nishi, Y., Yokoyama, R., and Ito, K., 1999, ''Development of an Optimal Operational Planning System Using an Object-Oriented Framework for Energy Supply Plants,'' *Proceedings of the 6th International Building Performance Simulation Association Conference*, **III**, pp. 1269–1276.

Turbocharger Unstable Operation Diagnosis Using Vibroacoustic Measurements

N. Aretakis
Research Associate

K. Mathioudakis
Associate Professor

M. Kefalakis
Research Assistant

K. Papailiou
Professor

Laboratory of Thermal Turbomachines,
National Technical University of Athens,
Iroon Polytechniou 9,
Athens 15773, Greece

The possibility to detect unstable operating condition (stall or surge) of an automotive turbocharger using vibration or acoustic measurements is studied. An experimental study is performed, in order to acquire and analyze test data, to find out whether vibration or acoustic measurements can be correlated to aerothermodynamic operating condition. An instrumentation set allowing the definition of the operating point on the map of the compressor of the turbocharger is used. Hot wires at the compressor inlet serve as flow condition indicators and provide a clear indicator of the presence or not of instabilities, such as rotating stall or surge. Accelerometers are mounted on the casing and microphones are placed in the vicinity of the compressor casing, to measure vibration and sound emission. Data covering an extensive range of the compressor performance map have been collected and analyzed. Signal features from the different measuring instruments are discussed. Using such features, a bi-parametric criterion is established for determination of whether the compressor operates in the stable part of its performance characteristic or in the presence of unstable operation phenomena (rotating stall, surge). The possibility of generalizing the validity of observations is supported, by presenting results from testing a second turbocharger, which is shown to exhibit similar behavior. [DOI: 10.1115/1.1771686]

Introduction

Operation of turbo compressors is restricted by the occurrence of unstable phenomena, namely rotating stall and surge. These phenomena limit the operating range of engines which comprise compressors, due to the fact that their presence may be harmful or even dangerous for the integrity of the engine. Out of the two, rotating stall is of a weaker character and its presence could be tolerated, even though for high rotational speed it can lead to destruction after a short period of time. Surge is a more severe situation that cannot usually be tolerated, as it may cause immediately severe damage.

The possibility to detect the presence of such phenomena is of great importance for the controls of the engine comprising the compressor, in order to take appropriate action once they are detected. On the other hand, methods of active control are very much interested in the detection of ''precursors,'' namely signals that announce the appearance of unstable operation, before it is actually established. For example, a recent study on stall inception in high-speed centrifugal compressor has been presented by Kang [1].

The detection of unstable operation type and its features is usually achieved using aerodynamic measuring instruments: fast response pressure sensors, hot wires or hot films are instruments that can be used to sense flow fluctuations and derive from them dynamic characteristics, such as frequency of the phenomena, or number and propagation speed of rotating stall cells. Study of aerodynamic characteristics has been the subject of a large number of works. A review of existing techniques was presented by Pampreen [2]. Reviews have also been presented by Ribi [3] and Gravahl and Engeland [4,5].

The disadvantage of such instruments for use in field operating machines, is that they are rather sensitive in other than laboratory environment while they have to be placed intrusively, in contact with the flow path of the compressor. It is thus desirable to have the possibility to detect the phenomena using the least intrusive means. Research in this direction has been performed very recently. Bently et al. [6,7], have studied the possibility to detect rotating stall, by exploiting data from displacement probes, such as those used in industrial compressors for shaft position monitoring. A test case where rotating stall was thus identified was reported by Teeling [8]. On the other hand, methods using a number of performance instruments and appropriate processing algorithms have been patented recently, [9–11].

The present paper presents the results of an investigation aiming to establish methods for diagnosing the presence of unstable operation by means of least intrusive measurements. Sound and casing vibration measurements are used for this purpose. The possibility of using such measurements presents an advantage over the methods of [6,7], since it can be applied in every compressor and not only on compressors equipped with an *X*, *Y* displacement system (usually available in larger industrial compressors). The particular field of interest for application is the detection of compressor surge in automotive turbochargers. For such application, it is interesting to examine the possibility of automated instability detection with very simple means. Detecting such conditions is very important for the operation of a turbocharged reciprocating engine (see, for example, [12]).

To the authors' knowledge it is the first time that vibroacoustic data are systematically correlated to the performance of centrifugal compressor for the diagnosis of unstable operating conditions. Use of vibroacoustic data for diagnosing mechanical faults has already been examined in the past by the research group of the authors, [13,14]. On the other hand, microphones inside the gas path have been used by a number of investigators and the fact that sound is altered, when unstable operation is encountered, has been used since a long time as a means of indicating such operation (e.g., Kyrtatos and Watson [15]). No systematic interrelation with operating conditions or criteria for stall and surge occurrence have nevertheless been reported.

Contributed by the International Gas Turbine Institute (IGTI) of THE AMERICAN SOCIETY OF MECHANICAL ENGINEERS for publication in the ASME JOURNAL OF ENGINEERING FOR GAS TURBINES AND POWER. Paper presented at the International Gas Turbine and Aeroengine Congress and Exhibition, Atlanta, GA, June 16–19, 2003, Paper No. 2003-GT-38321. Manuscript received by IGTI, October 2002, final revision, March 2003. Associate Editor: H. R. Simmons.

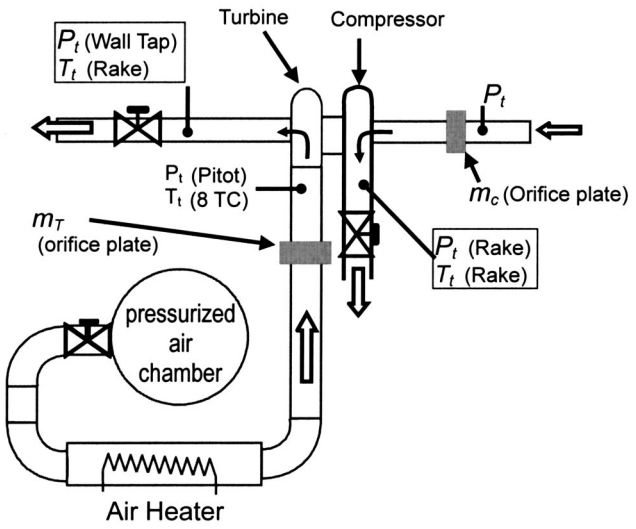

Fig. 1 Turbocharger test facility schematic

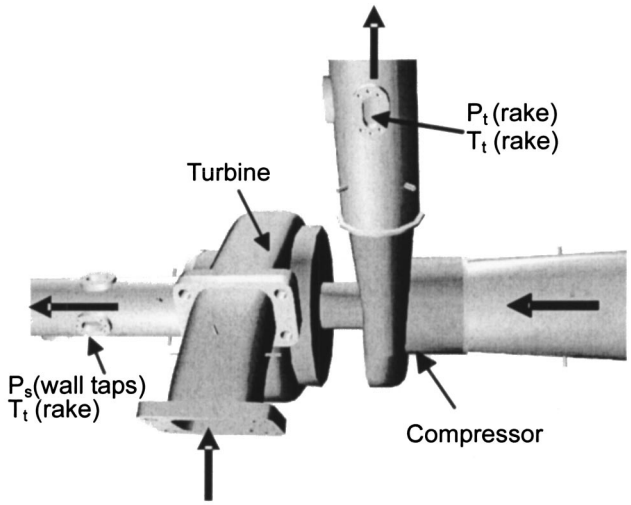

Fig. 2 Close up on the turbocharger under test

Experimental Investigation Setup

The setup of the experimental investigation and the procedure followed was dictated by the main purpose of the investigation, which was to establish a means for diagnosing unstable operation. The guidelines for setting up diagnostic systems given by Loukis et al. [16] were taken into account for this purpose. The Facility used and the choice of instrumentation are presented in the following.

Test Facility. The experiments were carried out on the turbocharger test rig of the Lab of Thermal Turbomachines, National Technical University of Athens presented schematically in Fig. 1. On this test rig the turbocharger under test is operated in an open circuit, while the inlet and outlet ducting is equipped with pneumatically driven throttle valves, which allow both inlet and outlet throttling. The turbocharger is driven from a pressurized air circuit. If desired, the compressed air is heated by an electric heater before fed to the turbine inlet. The operating points for the compressor and the turbine are set by appropriate adjustment of the throttle valves covering the entire compressor and turbine performance map.

Test Engine and Operating Conditions. A turbocharger suited for seven liter truck engines has been used for the present experiments. It comprises a single stage compressor with seven blades and seven splitters, tip diameter of 9 cm and a single-stage turbine with ten blades. The tests were performed at different operating points of the compressor. Operating points were chosen to cover the entire useful operating range of the compressor, starting from fully open throttle and reaching or passing the surge limit. The setting of the operating point is achieved by closing the throttling valve at the compressor outlet while the rotational speed is controlled by changing the valve settings at both turbine inlet and outlet.

Measurements for Performance Evaluation. The turbocharger is fitted with instrumentation allowing measurement of the quantities necessary to derive the compressor and turbine performance maps, as shown in Figs. 1 and 2.

The compressor mass flow rate is measured with an orifice plate positioned at the compressor inlet duct. The compressor inlet total pressure was derived from a measurement upstream of the orifice plate, adjusted by the total pressure drop produced by the orifice plate. At compressor outlet, the total pressure and temperature were being measured using pressure and temperature rakes, with five sensing points each.

For the turbine mass flow rate, an orifice plate has been also used. The turbine inlet temperature derived from an average of eight thermocouples positioned inside the tube. The total inlet pressure was measured using a total pressure Pitot probe. At the turbine outlet, a total temperature rake was used to measure the total temperature, while the static pressure was measured as the average pressure of four wall pressure taps. Although swirl was present in some cases, after checking with pressure probe traverses we found that the error in this static pressure measurement was less than 1%.

Temperature was measured using type-K thermocouples and pressure by means of pressure transducers. The errors in performance variables of the compressor map are estimated to be 0.5% in pressure ratio, 1% in efficiency, 0.8% in mass flow rate and 0.1% in rotational speed.

All performance measurements were recorded using a data acquisition system based on a PC, fitted with a data acquisition card with 12-bit A/D converter, maximum aggregate sampling rate of 100 kHz and adjustable input ranges. The measurements were obtained as time average of 100 samples over one second for each measuring channel.

Measurements for Unstable Operation Determination. In order to have a reliable and sensitive indicator of stable and unstable operation, a measurement of unsteady flow velocity at the inlet of the compressor was performed. Two hot wires at compressor inlet were used for this purpose. The position of the hot wires is shown in Fig. 3. The hotwires used in this study were of the type 55P11 with Pt-plated tungsten wire manufactured by Dantec. Although this measurement is very accurate and sensitive, it is intrusive. Its use is thus limited for investigation in laboratory environment. The hot wires can be used to identify the precise features of the stall patterns (cells numbers and rotational speed). Although such features are of interest for aerodynamic internal flow studies, in the present work data were not elaborated in this direction, and hot wires were used only as primary stall indicators.

Other fast response measurements that are less intrusive and are examined here for their suitability for instability identification, are casing vibrations and the sound emitted by the turbocharger. This choice was dictated by the empirical fact that during unstable operation, vibrations and sound levels increase significantly.

Two small accelerometers measuring compressor vertical and axial casing vibration were used. The accelerometers were of the type 4393, manufactured by Bruel & Kjaer with frequency range 0–12 kHz. For sound measurements three omni-directional microphones of Electret condenser-type were used with maximum fre-

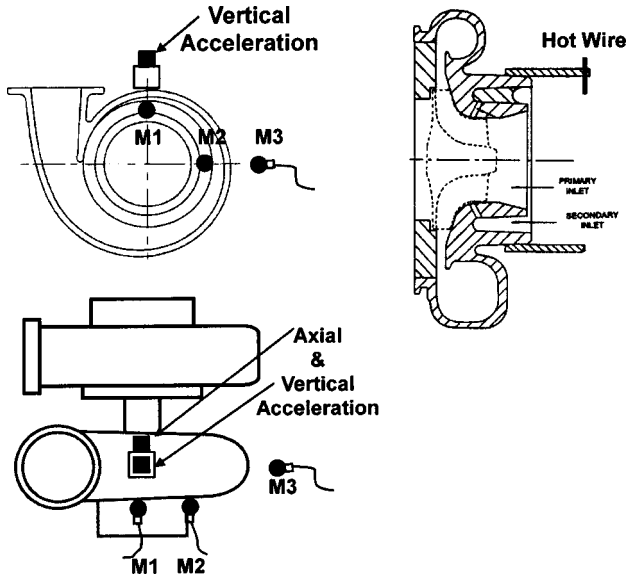

Fig. 3 Instruments location for vibroacoustical measurements

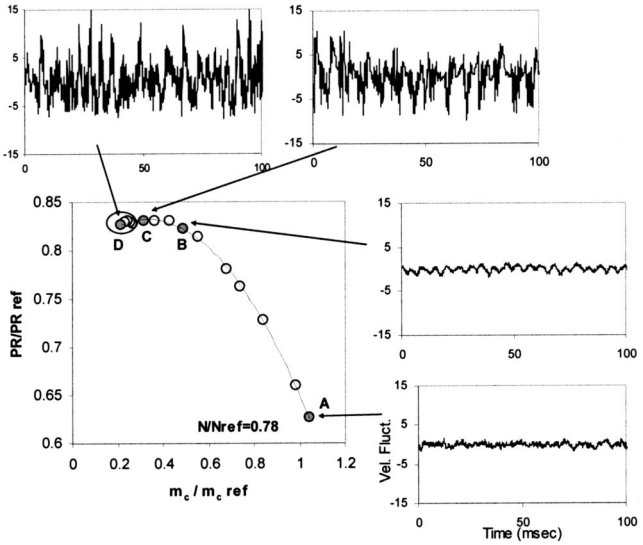

Fig. 4 Unsteady flow velocity fluctuation signals for different operating points along compressor characteristic curve

quency 18 kHz. Two of them were located at compressor inlet facing the compressor casing while the third facing the compressor from the side. The location of measuring instruments is shown in Fig. 3. The microphones were of condenser type with frequency range 0–14 kHz, battery operated. They were series production inexpensive type of microphones, chosen to be such in view of the fact that the diagnostic system sought by this investigation is desired to be as simple and easy to acquire as possible. Such microphones have been used in the past for rotating stall investigations by Lawless and Fleeter [17].

The fast response data were acquired by a PC based data acquisition system fitted with an acquisition card with 12-bit A/D converter, maximum aggregate sampling rate of 500 kHz and adjustable input ranges.

Before presenting measurement results, it should be mentioned that all the fast response results presented were derived from data strings of 8192 samples per channel, with a sampling frequency of 30,000 Hz.

Performance Characteristics and Operating Regimes

We first examine how different operating regimes of the compressor are manifested. Operating points along a constant speed characteristic are examined, Fig. 4.

Starting from fully open throttle (maximum mass flow rate) different regimes are characterized by the magnitude of velocity fluctuations at the inlet. The stable operation region, extending between points A and B, is characterized by very low amplitude fluctuations. The stall onset point B is characterized by an increase in the amplitude of fluctuations. Surge onset, point C is accompanied by a significant rise of fluctuation magnitude.

For operating points within the surge operating regime very large fluctuations are observed. Such points are indicated inside circle D in Fig. 4. It should be noted that the points in the circle are drawn on the basis of the readings of the performance measuring instruments, but do not represent actual operating points (the actual operating points would form a surge cycle and could be measured by instantaneous flow and pressure measurements using fast response instrumentation). The estimation of the mass flow rate and the pressure ratio for those points is not accurate.

Similar results derived from microphone M1 facing compressor casing from the inlet side are shown in Figs. 5 and 6.

In Fig. 5 the behavior of acoustic pressure signals along the same characteristic curve is shown. From this figure we can see that the reduction of the mass flow rate is leading to an increase of acoustic pressure level. On the other hand there are no clearly defined operating regions as in the case of hot wire. This is due to the fact that the kind of instabilities examined are low frequency phenomena and well hidden when there is a predominant high frequency, as in case of acoustic pressure. This can be further understood observing the behavior of acoustic pressure spectra presented in Fig. 6.

The *x*-axis in the spectra is presented in terms of ''rotor orders'' which is multiples of rotational frequency. From this figure we can see that the rotational frequency is predominant for all the points along characteristic curve except in deep surge operation. On the other hand an increase in low frequency energy content (below rotational frequency) is observed as the operating points moves from the stable into the unstable operation regime (moving from A to D). In the deep surge operating region a predominant peak at very low frequency appears (~15 Hz), which is the surge frequency.

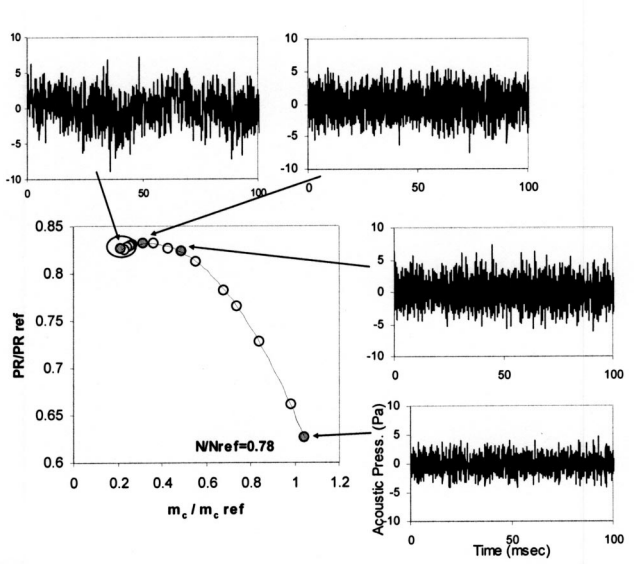

Fig. 5 Acoustic pressure signals for different operating points along compressor characteristic curve

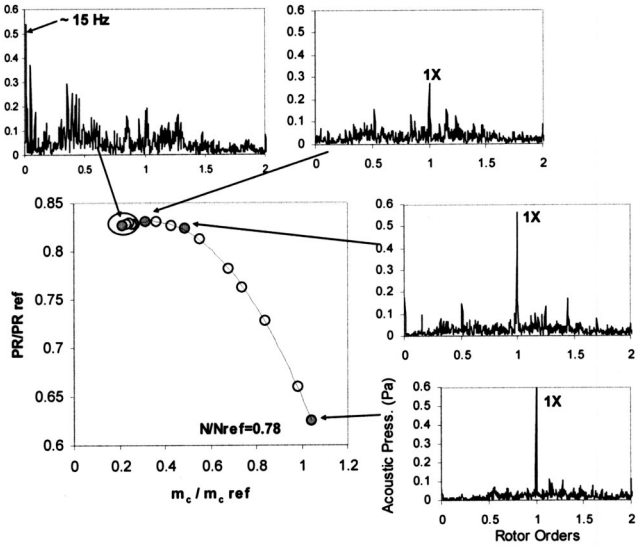

Fig. 6 Acoustic pressure spectra for different operating points along compressor characteristic curve

Similar information was found to be produced by the other microphones positioned at different locations. The most sensitive to changes of operational conditions was found to be the microphone facing the compressor from the inlet side at 0 deg (M1, Fig. 3). The acoustic pressure results presented in the following come from this particular microphone.

Unsteady Signal Features for Different Operating Conditions

In order to reveal the features of the measured signals, spectra of acoustic pressure for different operating conditions are examined. In Fig. 7, successions of spectra for operating points on a constant speed characteristic are shown. The bottom spectrum corresponds to fully open throttle and the top one to almost fully closed.

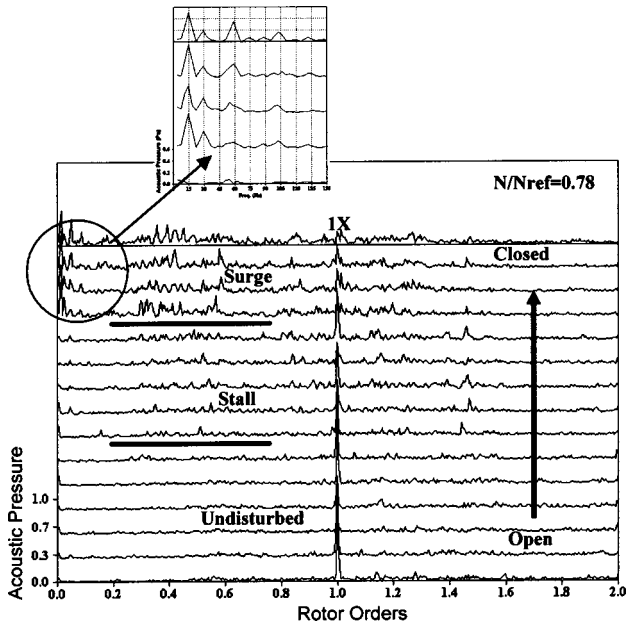

Fig. 7 Acoustic pressure spectra for different operating points for a constant speed characteristic curve

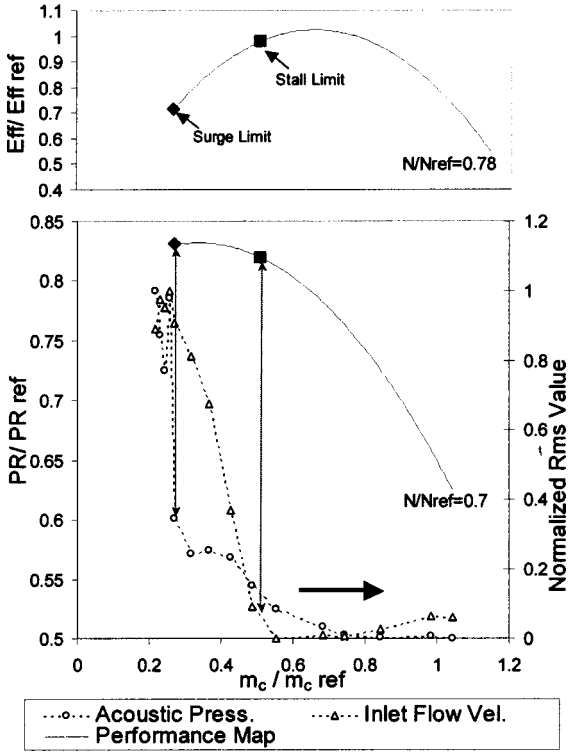

Fig. 8 Acoustic pressure and Inlet flow velocity rms level along compressor characteristic curve

The following observations can be made: most of the energy content of the signals is at the rotational frequency, with peaks clearly present for almost all operation points. The stable and unstable operating regions can be distinguished by a change in the form of the spectrum. The transition between these regions comes with a level increase of spectra components in a frequency range between 0 and 1X. Sound is produced in the subharmonic frequency range, when operational instabilities are present. Surge operation is clearly marked with the appearance of the low frequency of 15 Hz at the last four operating points. This frequency does not change with operating point and was found to be the same for different rotational speeds, pointing to the conclusion that it characterizes the occurrence of surge. Presence of surge, with overall mass flow oscillations, was also visually verified for these operating points with the help of tufts visualizing flow direction at the compressor inlet.

Similar behavior was found to be exhibited by casing vibration measurement signals, with the difference that this measurement was not found to be that sensitive to changes of small magnitude disturbances, caused by rotating stall. Changes due to surge are noticeable, as will also become apparent from overall levels presented later in the paper.

The above results have shown that the acoustic pressure level at a sub harmonic frequency range can be used for determination of unstable operation. Among the different parameters examined for quantification of that level the most suitable was found to be the RMS value corresponding to a sub harmonic frequency range (0–F Hz) defined by the following equation:

$$\sigma_F = \sqrt{\frac{1}{F}\int_0^F S_{pp}(f)\cdot df} \tag{1}$$

where $S_{pp}(f)$ is the power spectral density component corresponding to frequency f, and $F = 0.9\text{X}$ namely 90% of shaft speed.

The behavior of this parameter for acoustic and inlet velocity signals, along a constant speed characteristic, is shown in Fig. 8.

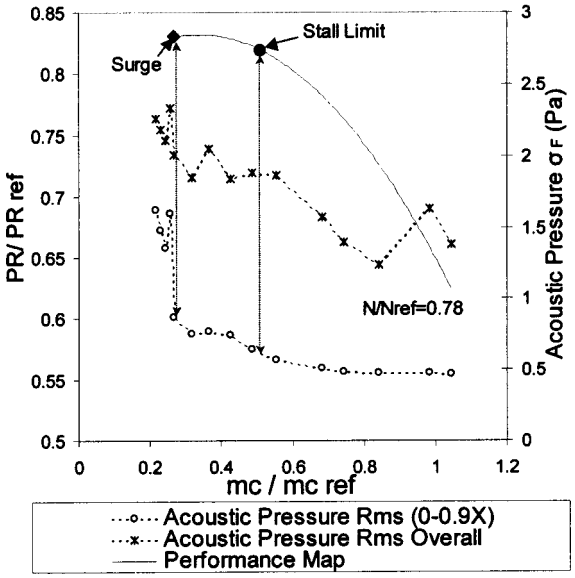

Fig. 9 Acoustic pressure rms level for different frequency ranges along a compressor characteristic curve

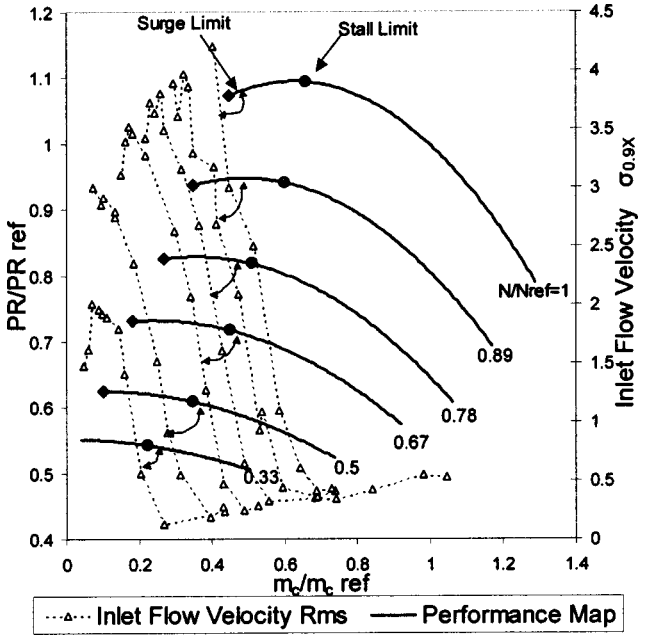

Fig. 10 Inlet flow velocity rms level along compressor characteristic curves

The efficiency characteristic is also included in the upper part of the figure.

The presented σ_F values have been normalized over their corresponding maximum values, in order to have the possibility to compare the two trends, even though their absolute magnitudes differ significantly. It is observed that both parameters present similar behavior: values are small at stable operation and increase as stall is approached. Velocity σ_F increases sharply as rotating stall is approached, and keeps increasing within the stall operating region. Acoustic signal σ_F increases first to some value larger than that for stable operation, which does not change much for stalled operation, and then increases sharply as surge is encountered.

At this point it is useful to comment on the selection of the sub synchronous frequency interval. The frequency range [0,0.9X] was selected because it offers a clear variation when unstable operation is entered. This is due to the fact that the frequencies associated with rotating stall and surge are always below the frequency of rotation (sub harmonic range). In order to show that unless this frequency range is selected, distinction is not as clear, a comparison to the signal RMS over the entire available bandwidth is shown in Fig. 9.

In this figure the acoustic pressure RMS levels for the two frequency ranges and for one characteristic curve are presented. We can see that by inclusion of all available frequency components the change in magnitude when entering unstable operation is not sharp. So the frequency range between 0 and 0.9 X is a better choice than overall frequency range. The results presented in the following are calculated at this frequency range.

We can now examine how the values of σ_F vary over the performance map of the compressor, at different speeds of operation. For comparison purposes, results for the three types of unsteady signals examined will be presented.

Figure 10 shows results for flow velocity fluctuations rms. The features observed on the single constant speed characteristic of Fig. 8 are exhibited for all the other characteristics as well. This quantity would be appropriate as an indicator of operating regime, but the measuring instrument does not possess the robustness characteristics that one would require for industrial use.

Establishment of Acoustic Criteria for Surge Detection

Examination of the results of the previous section has indicated that acoustic signals features show a systematic variation with operating regime. It will now be shown that a correlation of the value of σ_F to operating region can be established, offering thus a stall and surge operation criteria.

Observation of Fig. 11 shows that the σ_F depends on both rotational speed and operating region on a constant speed characteristic. It is noted that similar behavior but with weaker dependence on speed is exhibited by casing vibration (Fig. 12). In order to establish acoustic surge detection criteria, the possibility to correlate acoustic pressure levels to rotational speed is examined. For this purpose the following physical reasoning is taken into account.

First, we examine how the stall and surge occurrence points are located on a nondimensional performance curve of the compressor. The Φ-Ψ characteristics for all the rotational speeds of the performance maps presented previously are shown in Fig. 13. It is

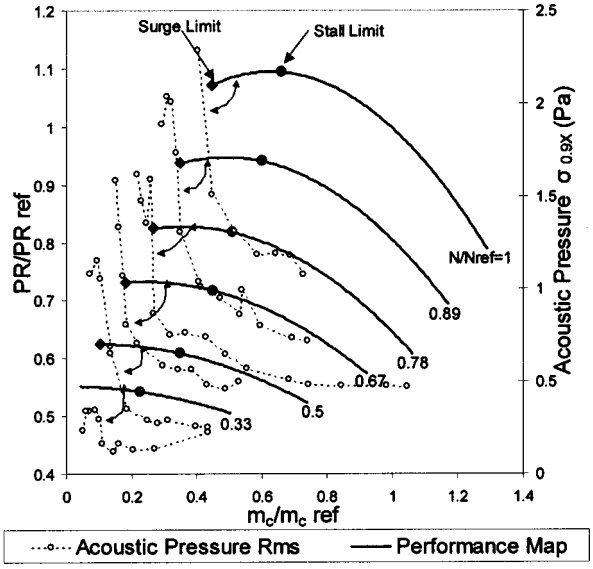

Fig. 11 Acoustic pressure rms level along compressor characteristic curves

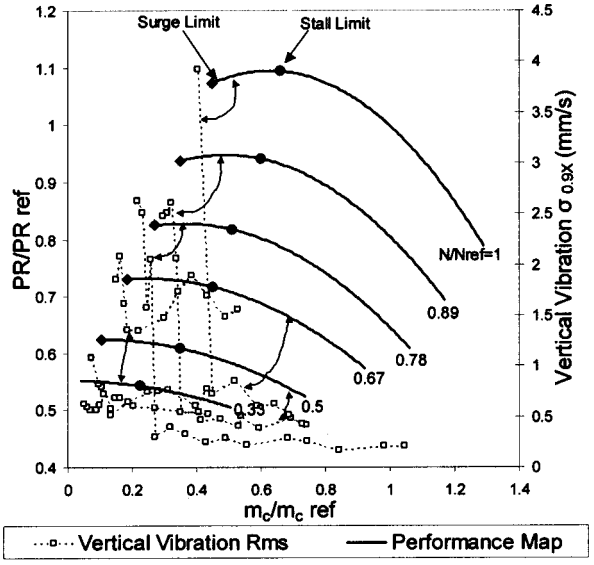

Fig. 12 Vertical casing vibration rms level along compressor characteristic curves

observed that they very closely collapse to a single curve. It is interesting to note that the stall occurrence points are very closely spaced for all the curves. We can therefore say that stall occurs at a particular value of Φ. This fact can be further exploited for correlating with sound pressure levels. Reasoning is presented in the Appendix, to support the claim that the rms value at the stall occurrence point would have a dependence primarily on rotational speed.

The validity of this assessment is checked on the data presented previously, which have been used to plot Fig. 14. In this figure the acoustic levels for all operating speeds are plotted versus rotational speed. The stall and surge limit points are also indicated. It's observed that the stall and surge limits follow a certain trend with operational speed. A best fit line following a power law is fitted to these data and is shown on the figure.

For a given compressor, once these two functions for stall and surge operation respectively are established, the operational condition can be easily identified, from the value of σ_F and the rotating speed. The three regions of operating situation are clearly

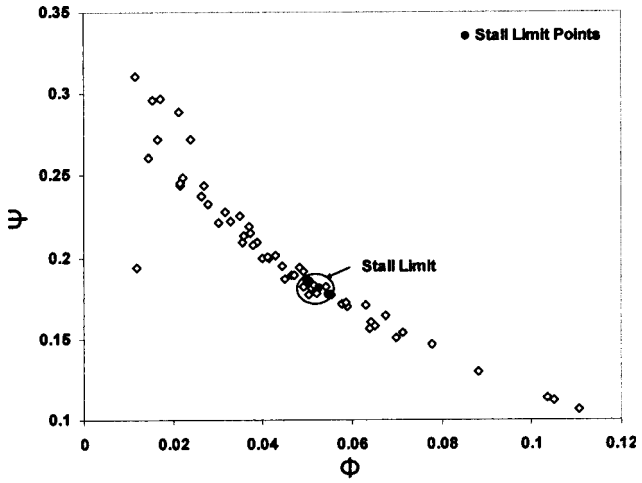

$$\Phi = \frac{m_c}{\rho \cdot A \cdot U}, \quad \Psi = \frac{\Delta H_c}{U^2}$$

Fig. 13 Compressor Φ-Ψ characteristic

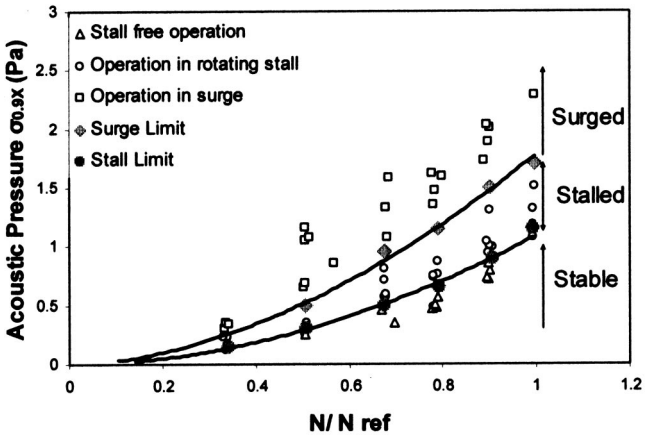

Fig. 14 Correlation between acoustic pressure rms level and compressor speed

marked in Fig. 14. The flow chart of a procedure that could be used for implementation of a detection system is shown in the diagram of Fig. 15.

The proposed procedure would be useful as a means to diagnose what is the condition in which the compressor is operating, and if rotating stall or surge is present. In this respect, it would provide an alternative to the means discussed in [9–11], but in the present case, using a much simpler measurement setup.

Possibility for Criteria Generalization. A question that would require further research before being answered is what the level of generality of the present approach is. A first answer to this question is given from results obtained on another turbocharger that was also tested at the turbocharger test rig. It is of similar type, but bigger than the one used for the tests reported above. The compressor tip diameter is 11 cm and is used for 12 lt truck engines.

Results derived from experiments on this turbocharger, corresponding to those of Fig. 14, are presented in Fig. 16. It is seen that the second turbocharger shows a behavior similar to the first one, in terms of acoustic signal features and their relation to op-

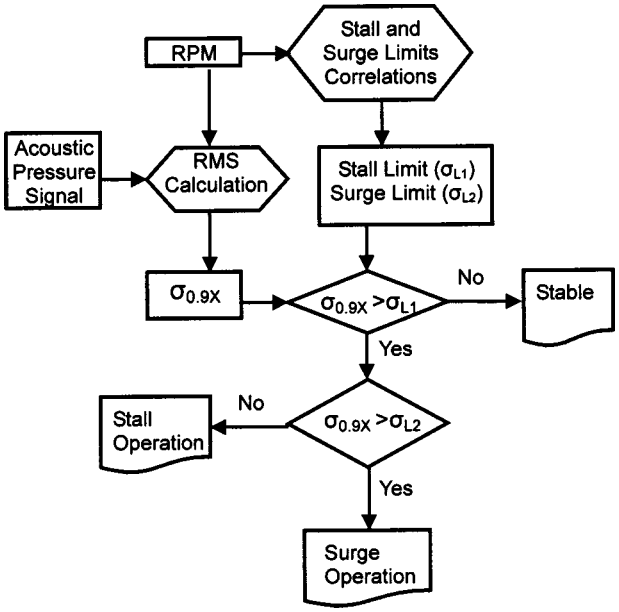

Fig. 15 Flow chart of a stall and surge diagnostic procedure for a radial compressor

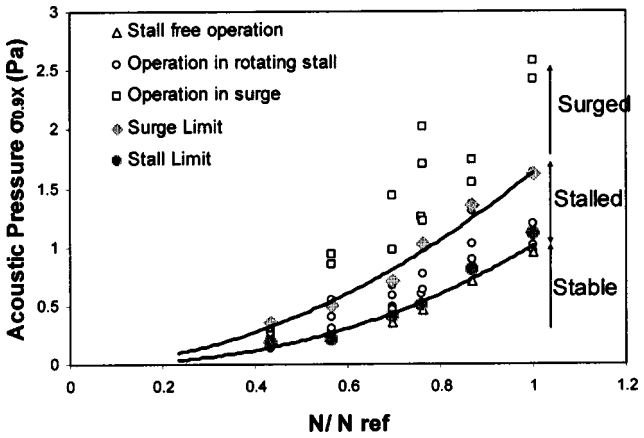

Fig. 16 Correlation between acoustic pressure rms level and compressor speed for turbocharger II

erating regime. Lines of a similar form can also be derived here, separating unstable, stall and surge operating conditions.

Conclusions

An experimental study for investigation of turbocharger operational instabilities in relation to vibroacoustic measurements has been presented. Measurements of unsteady flow velocity, sound emission, and casing vibration have been performed for a wide range of operating points of the turbocharger compressor.

It was shown that acoustic signal features can be extracted, that exhibit a good correlation with operating condition. In particular, a parameter that gives the possibility to distinguish between stall free, stalled and operation with surge present was introduced. This parameter is the rms value of acoustic signals, filtered in the subsynchronous part of the spectrum. Well defined limits of this parameter for different operating regimes have been established, in function of compressor rotational speed.

The conclusions drawn on the basis of observation on the test turbocharger were found to hold for a second one that was also tested in the same manner. These results provide an indication that the method proposed here may be of general validity for use in detecting unstable compressor operating conditions.

Acknowledgments

The experimental work for this paper has been carried out in the frame of project ATECS (Contract No: G3RD CT-1999-0015) and financial support of the Commission of the European Union is gratefully acknowledged.

Nomenclature

a = speed of sound
A = compressor inlet area
BPF = blade passing frequency
D = tip diameter
f = frequency
He = Helmholz number ($=fD/a$)
m = mass flow rate
Mi = microphone i
N = rotational speed
P = pressure
PR = pressure ratio
S_{pp} = power spectral density
St = Strouhal number ($=f/\mathrm{BPF}$)
T = temperature
U = peripheral velocity
ΔH = enthalpy increase
ρ = air density
σ_F = rms value for frequency range 0–F Hz (Eq. (1))
σ_{L1} = rms stall limit (Fig. 15)
σ_{L2} = rms surge limit (Fig. 15)
Φ = nondimensional mass flow parameter (Fig. 13)
Ψ = nondimensional pressure rise parameter (Fig. 13)
1X = shaft rotational frequency

Sub and Superscripts

C = compressor
ref = reference value
s = static
t = total
T = turbine

Appendix

It has been discussed by Mongeau et al. [18,19] that the spectral density of sound emitted from turbomachines follows a law of the form

$$\sqrt{S_{pp}(f)}=\rho U^2\sqrt{D/U}F(\mathrm{St},\phi)G(\mathrm{He},\phi) \tag{2}$$

When a specific value of the flow coefficient Φ is considered (such as the one for stall occurrence), for unique functions F and G (as was the case for the turbomachines of [18,19]), a simplified dependence of the sub synchronous σ_F can be anticipated. Since the integration of Eq. (2) extends over a fixed percentage of rotational speed, this means that it covers a certain range of values for the Strouhal number, independent of speed of rotation (St range is $[0,0.9/Z]$, where Z the impeller number of blades). Using this consideration and the definition of the σ_F, we can conclude that for a given compressor the σ_F should exhibit a strong dependence on rotational speed, which could be the primary parameter for correlating sound pressure at specific nondimensional operating conditions.

Strictly speaking, Eq. (2) should apply for measurement of airborne sound, and the assumptions made stem from the results of [18,19], driven in low-speed centrifugal turbomachines. This reasoning, however, provides good indication of the parameter used to detect stall and surge operating limits in the present study.

References

[1] Kang, J. S., and Kang, S. H., 2001, "Stall Inception in a High Speed Centrifugal Compressor," ASME Paper 2001-FT-0301.
[2] Pampreen, R. C., 1993, *Compressor Surge and Stall*, Concepts ETI.
[3] Ribi, B., 1996, *Instability Phenomena in Centrifugal Compressors* (von Karman Institute Lecture Series), VKI LS 1996-01, Jan 15–19.
[4] Gravdhl, J. T., and Engeland, O., 1999, *Compressor Surge and Rotating Stall*, Springer-Verlag, London.
[5] Gravdahl, J. T., and Egeland, O. E., 1999, *Compressor Surge and Rotating Stall: Modeling and Control*, Springer, London.
[6] Bently, D., Goldman, P., and Yuan, J., 2001, *Rotor Dynamics of Centrifugal Compressor in Rotating Stall*, Orbit 2Q01, pp. 40–50.
[7] Bently, D., and Goldman, P., 2000, *Vibrational Diagnostics of Rotating Stall in Centrifugal Compressors*, Orbit 1Q01, pp. 32–40.
[8] Teeling, S., 1998, *Using Data Manger 2000 to Remotely Diagnose Compressor Rotating Stall*, Orbit, Dec., pp. 26–29.
[9] Wang, Y. Y., 2001, "Turbocharger Compressor Diagnostic System," U.S. Patent 6,298,718, Oct.
[10] Beaverson, G. K., Schnetzka, H. R., and Frank, T. M., 1999, "Methods and Apparatus for Detecting Surge in Centrifugal Compressors," U.S. Patent 5894736, Apr.
[11] Haugen, R. L., and Kann, M. J., 2001, "Method for Detecting the Occurrence of Surge in a Cetrifugal Compressor by Detecting the Change in the Mass Flow Rate," US patent No 6213724, Apr.
[12] Chesse, P., Hetet, J. F., Tauzia, X., Roy, P., and Inozu, B., 2000, "Performance Simulation of Sequentially Turbocharged Marine Diesel Engines With Applications to Compressor Surge," ASME J. Eng. Gas Turbines Power, **122**, pp. 562–569.
[13] Aretakis, N., and Mathioudakis, K., 1996, "Radial Compressor Fault Identification Using Dynamic Measurement Data," ASME Paper 96-GT-102.
[14] Aretakis, N., and Mathioudakis, K., 1998, "Classification of Radial Compressor Faults Using Pattern Recognition Techniques," Control Eng. Prac., **6**, pp. 1217–1223.
[15] Kyrtatos, N., and Watson, N., 1980, "Application of Aerodynamically Induced Prewirl to a Small Turbocharger Compressor," ASME Paper 80-GT-23.

[16] Loukis, E., Mathioudakis, K., and Papiliou, K.: ''A Methodology for the Design of Automated Gas Turbine Diagnostic Systems,'' presented at the 38th ASME International Gas Turbine and Aeroengine Congress and Exposition, May, Cincinnati OH.
[17] Lawless, P. B., and Fleeter, S., 1993, ''Rotating Stall Acoustic Signature in a Low Speed Centrifugal Compressor: Part 1—Vaneless Diffuser,'' ASME Paper 93-GT-297.
[18] Mongeau, L., Thompson, D. E., and McLaughlin, D. K., 1993, ''Sound Generation by Rotating Stall in Centrifugal Turbomachines,'' J. Sound Vib., **163**(1), pp. 1–30.
[19] Mongeau, L., Thompson, D. E., and McLaughlin, D. K., 1995, ''A Method for Characterizing Aerodynamic Sound Sources in Turbomachines,'' J. Sound Vib., **181**(1), pp. 369–389.

Feasibility of Applying Active Lubrication to Reduce Vibration in Industrial Compressors

Ilmar F. Santos
Department of Mechanical Engineering,
Technical University of Denmark,
Lyngby 2800, Denmark
e-mail: ifs@mek.dtu.dk

Rodrigo Nicoletti
MSX International do Brasil,
Complexo Industrial Ford Nordeste,
COPEC 428-900, Brazil
e-mail: rnicoletti@ford.com

Alexandre Scalabrin
Empresa Brasileira de Aeronáutica S.A.,
São José dos Campos 12227-901, Brazil
e-mail: scalabrin@embraer.com.br

In this paper the complete set of modified Reynolds' equations for the active lubrication is presented. The solution of such a set of equations allows the determination of stiffness and damping coefficients of actively lubricated bearings. These coefficients are not just dependent on Sommerfeld number, as it would be the case of conventional hydrodynamic bearings, but they are also dependent on the excitation frequencies and gains of the control loop. Stiffness as well as damping coefficients can be strongly influenced by the choice of the control strategy, servo valve dynamics and geometry of the orifices distributed over the sliding surface. The dynamic coefficients of tilting-pad bearings with and without active lubrication and their influence on an industrial compressor of 391 Kg, which operates with a maximum speed of 10,200 rpm, are analyzed. In the original compressor design, the bearing housings are mounted on squeeze-film dampers in order to ensure reasonable stability margins during full load condition (high maximum continuous speed). Instead of having a combination of tilting-pad bearings and squeeze-film dampers, another design solution is proposed and theoretically investigated in the present paper, i.e., using actively lubricated bearings. By choosing a suitable set of control gains, it is possible not only to increase the stability of the rotor-bearing system, but also enlarge its operational frequency range. [DOI: 10.1115/1.1765123]

Introduction

The development of new mechanisms for dissipating vibration energy is of fundamental importance to keep low vibration levels in rotating machines. Among these mechanisms are seal dampers (Vance and Li, [1]) squeeze-film dampers (San Andrés and Lubell [2]), hybrid squeeze-film dampers (El-Shafei and Hathout [3]), hydraulic active chamber systems (Ulbrich and Althaus [4], Althaus et al. [5], and Santos [6]), variable impedance hydrodynamic journal bearings (Goodwin et al. [7]), actively lubricated bearings (Santos [8], Santos and Russo [9], Santos and Nicoletti [10], and Santos and Scalabrin [11]), active-control fluid bearings (Bently et al. [12]), and magnetized journal bearings lubricated with ferrofluids (Osman et al. [13]).

When the hydrostatic and the hydrodynamic lubrication are simultaneously combined in a journal bearing, with the aim of reducing wear between machine elements, one refers to the *hybrid lubrication*, which offers the advantages of both lubrication mechanisms. When part of the hydrostatic pressure is also dynamically modified by means of hydraulic control systems, one refers to the *active lubrication*. By the association of electronics, control design, and hydraulics, the active lubrication simultaneously allows the reduction of wear between rotating and nonrotating parts of the machinery and, in addition, the attenuation of rotor vibration.

Recent theoretical (Santos [8], Santos and Russo [9], Santos and Nicoletti [10], Santos and Nicoletti [14], and Nicoletti and Santos [15]) and experimental (Santos and Scalabrin [11] and Santos et al. [16]) investigations related to active lubrication showed the feasibility of attenuating rotor vibrations in test rigs with rigid rotors. The use of active lubrication in tilting-pad journal bearings (TPJB) has the strong advantage of resulting to bearings with negligible cross-coupling effects between orthogonal directions. However, this kind of active strategy can also be applied to hydrostatic (Bently et al. [12]) and to multilobed bearings (Santos et al. [16]).

In the present work, the application of active lubrication to an industrial compressor is analyzed, and this is the main original contribution of this theoretical investigation. The rotor flexibility is considered in the analyzes by using finite elements in the modeling. The bearings are included into the global model with help of the linearized dynamic coefficients. Such coefficients are calculated for both passive and active cases, by solving the complete set of modified Reynolds' equations for the active lubrication. This set of equations takes into account the fluid dynamics of the oil film, the servo valve dynamics, and the feedback control gains. The feasibility of enlarging the operational range by properly designing the control system is focused on this work.

Industrial Compressor Modeling

High-efficiency rotating machines, working at severe pressure and flow conditions, demand continuous monitoring and control of vibration levels. One of the ways of reducing vibration amplitudes in rotating machines is the use of hydrodynamic bearings. Among the hydrodynamic bearings, the tilting-pad bearings are those which show the best stability properties. Nevertheless, in many cases, due to aerodynamic excitations (cross-coupling effect) instabilities can occur, if the amount of bearing damping (at full load condition, i.e., high maximum continuous speed) is not enough to ensure a reasonable stability margin. One of the ways of improving this stability margin is by applying active lubrication.

The rotating machine whose dynamics under active lubrication will be analyzed is a gas compressor. The compressor is composed of five impellers, weights 391 kg and operates in the range of 6942 rpm (115.7 Hz) to 10,170 rpm (169.7 Hz).

By applying the finite shaft elements proposed by Nelson and McVaugh [17], the compressor is modeled with 56 elements (57 nodes—Fig. 1). Impellers and other machine elements attached to the shaft are considered as rigid discs, whose dynamics are incorporated into the model by adding inertia to the respective nodes. Hence, in the model, the impellers are at nodes 20, 24, 28, 32, and

Contributed by the International Gas Turbine Institute (IGTI) of THE AMERICAN SOCIETY OF MECHANICAL ENGINEERS for publication in the ASME JOURNAL OF ENGINEERING FOR GAS TURBINES AND POWER. Paper presented at the International Gas Turbine and Aeroengine Congress and Exhibition, Atlanta, GA, June 16–19; 2003, Paper No. 2003-GT-38225. Manuscript received by IGTI, October 2002, final revision, March 2003. Associate Editor: H. R. Simmons.

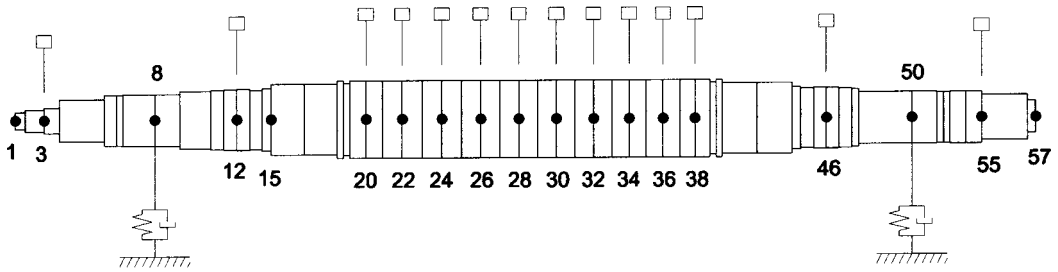

Fig. 1 Mechanical model of the compressor by finite shaft elements

36; bushes are at nodes 22, 26, 30, and 34; a thrust disk sleeve is locate at node 3; a balance piston is located at node 38; seal bushes are located at nodes 12 and 46; and the coupling is at node 55. The bearings are located at nodes 8 and 50.

Active Lubrication—Principle and Preliminary Results

In order to achieve an active lubrication, four pads are assembled in the bearing, two in horizontal and two in vertical directions, with bores machined on their surfaces, as illustrated in Fig. 2. Each pair of pads is connected to a servo-valve. By changing the control signal of the servo-valves, pressurized oil is injected into the oil film through the bores in the pads (Fig. 3). This allows changes of the oil film pressure in the bearing gap. Since the bearing damping and stiffness depend on the hydrodynamic pressure, the bearing dynamic coefficients can therefore be altered and the rotor-bearing stability improved.

The test rig of such active bearing can be seen in Fig. 4. The rigid shaft (2) is driven by an electric motor (1), and supported by the active TPJB (3). Oil to the conventional lubrication is supplied through pipelines (6), whereas the pressurized oil from the servo valves (4) is supplied to the bearing through pipelines (5). This test rig has a relatively light rotor, which operates at a low rotational speed of 650 rpm. Such a combination of parameters inevitably leads to nearly overdamped vibration responses. Despite of these conditions, a further increase of damping is achieved when the active lubrication is turned on. The experimental results presented in Fig. 5 show a nearly 50% reduction of vibration amplitude, after transient fades away. In this figure, the control system is activated at 0.5 s.

Modified Reynolds' Equation and Active Lubrication

According to Santos et al. [16], the hydrodynamic pressure distribution over the four pad surfaces of the active lubricated bearing can be calculated by solving a pair of coupled partial differential equations for each orthogonal direction. For the horizontal direction, the pair of equations is given by Eqs. (1) and (2):

$$\frac{\partial}{\partial \bar{x}}\left(\frac{h_1^3}{\mu}\frac{\partial p_1}{\partial \bar{x}}\right)+\frac{\partial}{\partial \bar{z}}\left(\frac{h_1^3}{\mu}\frac{\partial p_1}{\partial \bar{z}}\right)-\frac{3}{\mu l_o}\sum_{m=1}^{no}\mathcal{F}_m[p_1(1-C_1)-C_2p_3]$$
$$=6U\frac{\partial h_1}{\partial \bar{z}}+12\frac{\partial h_1}{\partial t}-\frac{3}{\mu l_o}\sum_{m=1}^{no}\mathcal{F}_m\left[P_{inj_{st1}}+C_3\omega_v^2K_VY_h\sqrt{\frac{G_{1y}^2+(\omega G_{2y})^2}{(-\omega^2+\omega_v^2)^2+(2\xi_v\omega_v\omega)^2}}\,e^{j(\omega t+\phi_y)}\right] \quad (1)$$

$$\frac{\partial}{\partial \bar{x}}\left(\frac{h_3^3}{\mu}\frac{\partial p_3}{\partial \bar{x}}\right)+\frac{\partial}{\partial \bar{z}}\left(\frac{h_3^3}{\mu}\frac{\partial p_3}{\partial \bar{z}}\right)-\frac{3}{\mu l_o}\sum_{m=1}^{no}\mathcal{F}_m[p_3(1-C_1)-C_2p_1]$$
$$=6U\frac{\partial h_3}{\partial \bar{z}}+12\frac{\partial h_3}{\partial t}-\frac{3}{\mu l_o}\sum_{m=1}^{no}\mathcal{F}_m\left[P_{inj_{st3}}+C_3\omega_v^2K_VY_h\sqrt{\frac{G_{1y}^2+(\omega G_{2y})^2}{(-\omega^2+\omega_v^2)^2+(2\xi_v\omega_v\omega)^2}}\,e^{j(\omega t+\phi_y)}\right] \quad (2)$$

where the phase

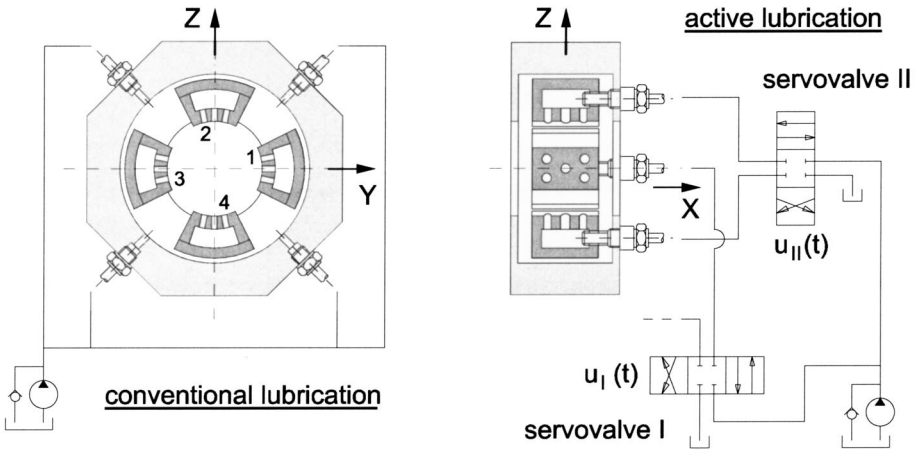

Fig. 2 Tilting-pad journal bearing with active lubrication—pads connected to the servo-valves

$$\phi_y = \arctan[-G_{1y} 2\xi_v \omega_v \omega + \omega G_{2y}(\omega_v^2 - \omega^2)/G_{1y}(\omega_v^2 - \omega^2) + \omega G_{2y} 2\xi_v \omega_v].$$

For the vertical direction (*Z*-direction), the pair of coupled equations are similar to Eqs. (1) and (2), but referring to pads 2 and 4 instead of pads 1 and 3. These coupled equations are called the modified Reynolds' equations for the active lubrication. Such equations relate the pressure distribution, over each pair of pads arranged in *Y* and *Z*-directions, with the gains of the adopted PD controller by considering the servo-valve dynamics. G_{1y} and G_{1z} are the proportional gains, whereas G_{2y} and G_{2z} are the derivative gains. The servo-valve dynamics is described using the constants K_V, ω_v, ξ_v, and K_{PQ}. The coeficients C_1, C_2, and C_3 are given by

$$C_1 = \frac{\sum_1^{no} \frac{\pi d_0^2}{128\mu l_0} - K_{PQ}}{\sum_1^{no} \frac{\pi d_0^2}{128\mu l_0} - 2K_{PQ}} \qquad C_2 = \frac{-K_{PQ}}{\sum_1^{no} \frac{\pi d_0^2}{128\mu l_0} - 2K_{PQ}} \tag{3}$$

$$C_3 = \frac{1}{\sum_1^{no} \frac{\pi d_0^2}{128\mu l_0} - 2K_{PQ}}.$$

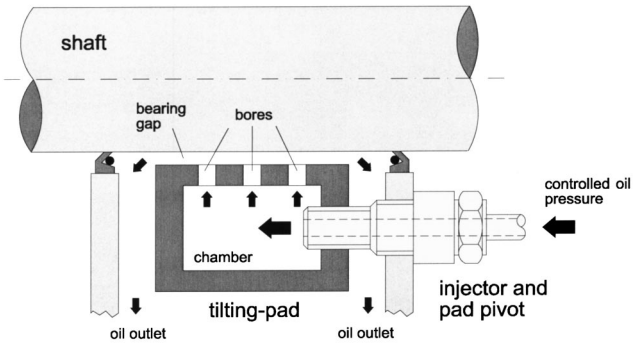

Fig. 3 Tilting-pad journal bearing with active lubrication—oil injection through orifices in the pads

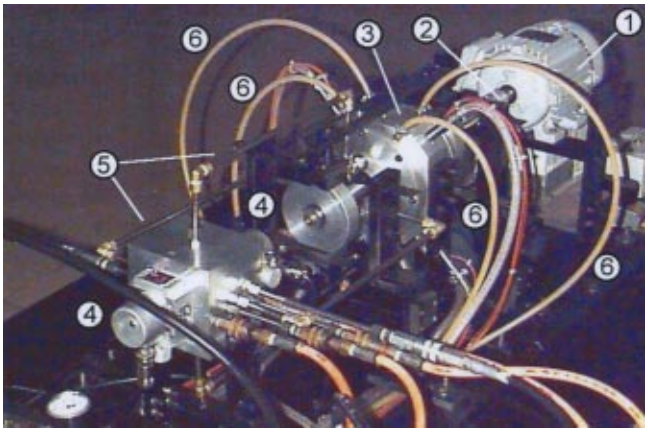

Fig. 4 Test rig of the tilting-pad journal bearing: (1) motor; (2) rigid shaft; (3) active lubricated TPJB; (4) servo-valves; (5) pipelines (active lubrication); (6) pipelines (passive lubrication)

The coeficients C_1 and C_2 are the coupling terms between the hydrodynamic pressures over the pair of pads in a given direction. The coeficient C_3 multiplies the term related to the active radial oil injection.

Hence, by a given set of controller gains (G_{1y}, G_{1z}, G_{2y}, and G_{2z}), it is possible to calculate the resultant oil film pressure distribution over each pair of pads, considering the effects of the additional radial oil injection.

Bearing Dynamic Coefficients as Function of the Control Gains

The dynamic coefficients of the bearing with active lubrication can be estimated by applying a Taylor series and assuming harmonic variation of the oil pressure distribution (Lund and Thomsen [18], Ghosh et al. [19], and Hamrock [20]). Thus, the oil pressure distribution over the *i*th pad can be approximated by

$$p_i = p_i(\overline{x,z},t) = \mathcal{P}_{st_i} + \mathcal{P}_{y_i}\Delta Y_h e^{j\omega t} + \mathcal{P}_{z_i}\Delta Z_h e^{j\omega t} + \mathcal{P}_{\alpha_i}\Delta A_i e^{j\omega t} \tag{4}$$

where

$$\mathcal{P}_{st_i} = p_i|_{eq} \qquad \mathcal{P}_{y_i} = \left.\frac{\partial p_i}{\partial Y_h}\right|_{eq} + j\omega \left.\frac{\partial p_i}{\partial Y_h}\right|_{eq}$$

$$\mathcal{P}_{z_i} = \left.\frac{\partial p_i}{\partial Z_h}\right|_{eq} + j\omega \left.\frac{\partial p_i}{\partial Z_h}\right|_{eq} \qquad \mathcal{P}_{\alpha_i} = \left.\frac{\partial p_i}{\partial \alpha_i}\right|_{eq} + j\omega \left.\frac{\partial p_i}{\partial \alpha_i}\right|_{eq}. \tag{5}$$

The terms $\mathcal{P}_{st_i}$, $\mathcal{P}_{y_i}$, $\mathcal{P}_{z_i}$, and $\mathcal{P}_{\alpha_i}$ are obtained by applying small perturbations to the equilibrium position of the bearing system, and then solving the Reynolds' equation for each pair of pads in the horizontal and vertical directions. Since there are four terms to be calculated for each pad, and the active bearing has four pads, one arrives to a set of sixteen partial equations. By solving numerically this system of equations, one can build for each pad the following matrix:

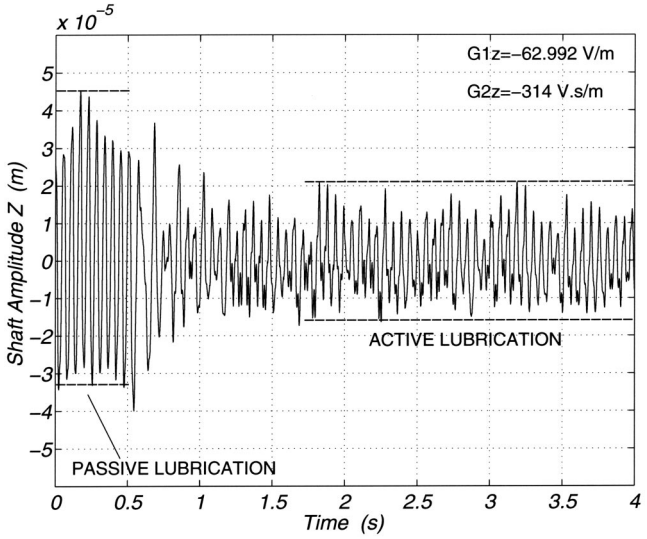

Fig. 5 Experimental results illustrating vibration reduction of shaft amplitudes in time domain, when active lubrication is turned on at 0.5*s* (G_{1z} and G_{2z} are the PD controller gains)

$$\mathbf{A}_i=\int_{\bar{x}}\int_{\bar{z}}\begin{bmatrix}\mathcal{P}_{y_i}\cos\left(\frac{\bar{z}}{R_s}\right) & \mathcal{P}_{y_i}\sin\left(\frac{\bar{z}}{R_s}\right) & \mathcal{P}_{y_i}(R_s+\Delta s)\sin\left(\frac{\bar{z}}{R_s}\right)\\ \mathcal{P}_{z_i}\cos\left(\frac{\bar{z}}{R_s}\right) & \mathcal{P}_{z_i}\sin\left(\frac{\bar{z}}{R_s}\right) & \mathcal{P}_{z_i}(R_s+\Delta s)\sin\left(\frac{\bar{z}}{R_s}\right)\\ \mathcal{P}_{\alpha_i}\cos\left(\frac{\bar{z}}{R_s}\right) & \mathcal{P}_{\alpha_i}\sin\left(\frac{\bar{z}}{R_s}\right) & \mathcal{P}_{\alpha_i}(R_s+\Delta s)\sin\left(\frac{\bar{z}}{R_s}\right)\end{bmatrix}d\bar{z}d\bar{x}. \tag{6}$$

Such a matrix is an implicit function of the Sommerfeld number ($S=2\mu L\Omega R^3/|W|(R_s-R)^2$), the excitation frequency (ω), the servo-valve dynamics ($K_V,\omega_v,\xi_v,K_{PQ}$), and the control gains of the PD controller ($G_{1y},G_{1z},G_{2y},G_{2z}$). In the present work, the excitation frequency ω is considered synchronous, due to unbalance, i.e., $\Omega=\omega$. The stiffness and damping matrices of the ith rotor-pad subsystem are obtained by the real and imaginary parts of $\mathbf{A}_i$, as follows:

$$\mathbf{K}_i=\mathcal{R}(\mathbf{A}_i)\qquad \mathbf{D}_i=\frac{1}{\omega}\mathcal{I}(\mathbf{A}_i). \tag{7}$$

By using a transformation matrix $\mathbf{T}_i$ which depends on the position of the pad in the bearing and on the angular displacement of the pad (Allaire et al. [21]), the stiffness and damping coefficients can be calculated in the inertial referential system, for the global rotor-bearing system:

$$\mathbf{K}=\sum_{i=1}^{4}\mathbf{T}_i^T\mathbf{K}_i\mathbf{T}_i=\begin{bmatrix}k_{yy} & k_{yz} & k_{y\alpha_1} & k_{y\alpha_2} & k_{y\alpha_3} & k_{y\alpha_4}\\ k_{zy} & k_{zz} & k_{z\alpha_1} & k_{z\alpha_2} & k_{z\alpha_3} & k_{z\alpha_4}\\ k_{\alpha_1 y} & k_{\alpha_1 z} & k_{\alpha_1\alpha_1} & 0 & 0 & 0\\ k_{\alpha_2 y} & k_{\alpha_2 z} & 0 & k_{\alpha_2\alpha_2} & 0 & 0\\ k_{\alpha_3 y} & k_{\alpha_3 z} & 0 & 0 & k_{\alpha_2\alpha_3} & 0\\ k_{\alpha_4 y} & k_{\alpha_4 z} & 0 & 0 & 0 & k_{\alpha_4\alpha_4}\end{bmatrix} \tag{8}$$

$$\mathbf{D}=\sum_{i=1}^{4}\mathbf{T}_i^T\mathbf{D}_i\mathbf{T}_i=\begin{bmatrix}d_{yy} & d_{yz} & d_{y\alpha_1} & d_{y\alpha_2} & d_{y\alpha_3} & d_{y\alpha_4}\\ d_{zy} & d_{zz} & d_{z\alpha_1} & d_{z\alpha_2} & d_{z\alpha_3} & d_{z\alpha_4}\\ d_{\alpha_1 y} & d_{\alpha_1 z} & d_{\alpha_1\alpha_1} & 0 & 0 & 0\\ d_{\alpha_2 y} & d_{\alpha_2 z} & 0 & d_{\alpha_2\alpha_2} & 0 & 0\\ d_{\alpha_3 y} & d_{\alpha_3 z} & 0 & 0 & d_{\alpha_3\alpha_3} & 0\\ d_{\alpha_4 y} & d_{\alpha_4 z} & 0 & 0 & 0 & d_{\alpha_4\alpha_4}\end{bmatrix} \tag{9}$$

where

$$\mathbf{T}_i=\begin{bmatrix}\cos(\varphi_i+\alpha_i) & \text{sen}(\varphi_i+\alpha_i) & 0\\ -\text{sen}(\varphi_i+\alpha_i) & \cos(\varphi_i+\alpha_i) & 0\\ 0 & 0 & 1\end{bmatrix}. \tag{10}$$

In the case of bearings without tilting-pads, the stiffness and damping matrices reduce to the size 2×2, by discharging variable α_i.

$$\frac{|u_y|}{|Y_h|}=\sqrt{G_{1y}^2+\omega^2G_{2y}^2}\leqslant\frac{0.25}{0.3h_0}$$
$$\frac{|u_z|}{|Z_h|}=\sqrt{G_{1z}^2+\omega^2G_{2z}^2}\leqslant\frac{0.25}{0.3h_0} \tag{11}$$

where an amplitude limitation of 30% of the assembled clearance was chosen.

Numerical Results

Table 1 presents the bearing and servo valve characteristics adopted in the numerical simulations.

The operational linear range of servo valves is limited to 5% of its nominal maximum control signal (Schäfer [22] and Althaus [23]). Besides, dynamic coefficients are only theoretically valid for infinitesimal displacements. However, according to Lund and Thomsen [18], dynamic coefficients may be used in practical applications for amplitudes up to 50% of the bearing clearance. With this in mind, the following restrictions of control signal and vibration amplitude were applied to the dynamic coefficients calculations:

Table 1 Bearing and servo-valve characteristics

Journal radius (R)	50.800	mm
Pad inner radius (R_s)	50.921	mm
Pad aperture angle (α_0)	76.2	deg
Offset	0.6	
Pad width (L)	44,450	mm
Distance from pad surface to pivot (Δs)	17.377	mm
Orifice length (l_0) and diameter (d_0)	5.0	mm
Number of orifices per pad (n_0)	5	
Assembled bearing gap (h_0)	76.0	μm
Oil dynamic viscosity (μ)	0.015	Pa.s
Servo-valve eigenfrequency (ω_v)	320.0	Hz
Servo-valve damping factor (ξ_v)	0.48	
Servo-valve gain (K_V)	16.7×10^{-6}	m^3/s.V
Servo-valve linear factor (K_{PQ})	1.13×10^{-12}	m^3/s.Pa
Pressure supply (P_S)	22,0	MPa

Bearing Stiffness Coefficients. By setting the control gains G_{1y}, G_{1z}, G_{2y}, and G_{2z}, to zero and varying the values of the static injection pressure ($P_{inj_{st}}$), one sensitively modifies the bearing stiffness coefficients, whereas damping coefficients remain almost constant. Such theoretical and experimental results are extensively discussed in Russo [24].

On the other hand, by adopting static pressures of 0.1 MPa in all pads, and varying the proportional control gains (G_{1y} and G_{1z}), while keeping the derivative gains as zero, one also achieves a modification of the stiffness coefficients, while the damping is not much altered. Figures 6 and 7 illustrate the behavior of the horizontal and vertical main stiffness coefficients as a function of the proportional gains and rotating frequency. In these figures, for a given control gain, the coefficients K_{yy} and K_{zz} have a standard behavior as function of the rotating frequency, i.e. they almost increase with the frequency (Someya [25]). Nevertheless, for a given frequency and varying the control gain, one can detect three different regions in these same figures: region (I) with control gains between $-1.5\cdot10^4$ V/m and $+1.5\cdot10^4$ V/m; region (II) with control gains smaller than $-1.5\cdot10^4$ V/m; and region (III) with control gains larger than $+1.5\cdot10^4$ V/m. In region (I), the coefficients K_{yy} and K_{zz} vary linearly as function of the control gains. When the control voltage reaches the limits established by Eq. (11), the coefficients stop varying and remain constant in the so far achieved values, thus forming regions (II) and (III).

As mentioned previously, the damping coefficients are not much altered by the proportional gains, thus being not presented in this subsection. The cross-coupling stiffness coefficients are also not presented since they are negligible, as in the conventional lubrication case of TPJB.

Bearing Damping Coefficients. By setting once again the static pressures to 0.1 MPa, but varying the derivative control gains (G_{2y} and G_{2z}), while keeping proportional gains as zero, one achieves a sensitive modification of the damping coefficients. By this time, the stiffness coefficients are not much altered. Figures 8 and 9 illustrate the behavior of the horizontal and vertical main damping coefficients as a function of the derivative gains and rotating frequency.

In these figures, for a given control gain, the coefficients D_{yy} and D_{zz} have a standard behavior as function of the rotating frequency, i.e., they almost decrease with the frequency (Someya [25]). However, for a given frequency and varying the control gain, one can detect three different regions in Figs. 8 and 9 similar to those found in Figs. 6 and 7. In region (I), the coefficients D_{yy} and D_{zz} vary linearly as function of the control gains. Nevertheless, such a region narrows with the increase of the rotating frequency. When the control voltage reaches the limits established by Eq. (11), the coefficients stop varying and remain constant in the so far achieved values, thus forming regions (II) and (III). The narrowing of the region (I) is caused by the term ω in Eq. (11), leading the maximum allowed derivative gain to be a function of the inverse of the frequency $G_{2y}^{\max}=|u_y|/|(Y_h|\cdot\omega)=0.25/(0.3h_0\cdot\omega)$ and $G_{2z}^{\max}=|u_z|/|(Z_h|\cdot\omega)=0.25/(0.3h_0\cdot\omega)$.

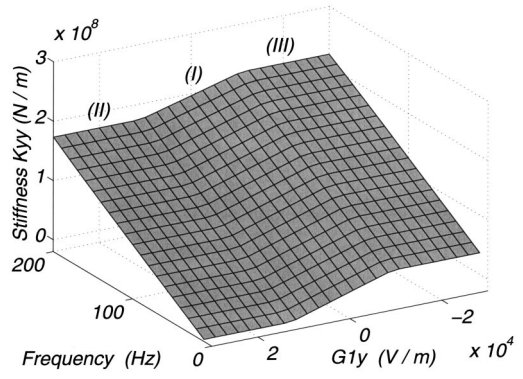

Fig. 6 Bearing stiffness in horizontal direction as function of the rotating frequency and proportional gain G_{1y}

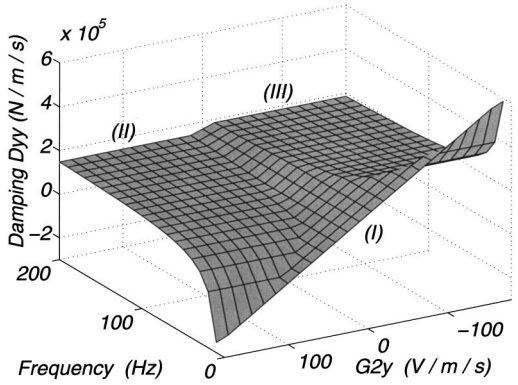

Fig. 8 Bearing damping in horizontal direction as function of the rotating frequency and derivative gain G_{2y}

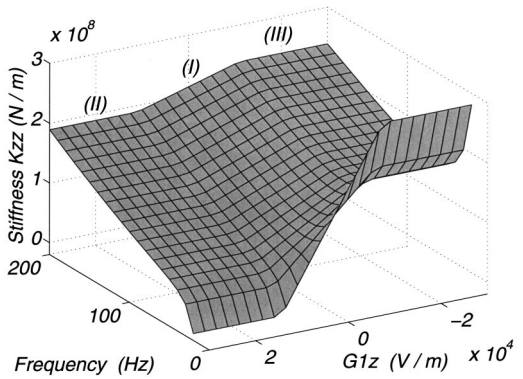

Fig. 7 Bearing stiffness in vertical direction as function of the rotating frequency and proportional gain G_{1z}

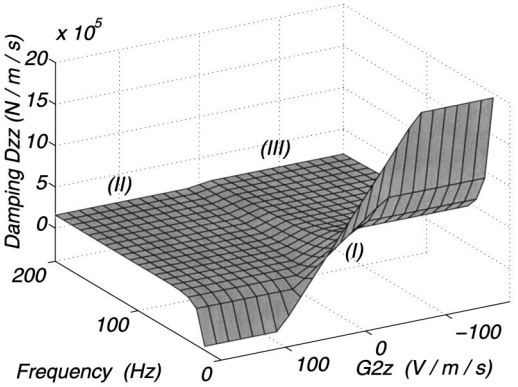

Fig. 9 Bearing damping in vertical direction as function of the rotating frequency and derivative gain G_{2z}

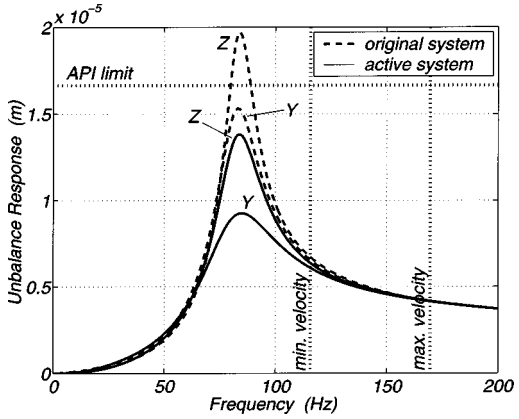

Fig. 10 Unbalance response of the compressor supported by original and active bearings—node of maximum displacements

As mentioned previously, the stiffness coefficients are not much altered by the derivative gains, thus being not presented in this subsection. The cross-coupling damping coefficients are also not presented since they are negligible, as in the conventional lubrication case.

Lateral Dynamic Analysis of the Gas Compressor. The four first eigenmodes of the compressor are overdamped and related to rigid body motions. The first two bending modes, in *Y* and *Z*-directions, are not overdamped. Such modes are chosen to be controlled by the active lubricated bearings, once the compressor operational range is situated above these first critical frequencies. The criteria for choosing the best set of control gains is based on the increasing of the damping factor of such bending modes. The chosen set of coefficients is

$$G_{1y} = +1.05 \cdot 10^4 \ \text{V/m}$$

$$G_{1z} = +1.05 \cdot 10^4 \ \text{V/m}$$

$$G_{2y} = +10.5 \ \text{V/(m/s)}$$

$$G_{2z} = +12.9 \ \text{V/(m/s)}.$$

With these gains, the dynamic coefficients are obtained from Figs. 6 to 9 as a function of the frequency. Inserting the dynamic coefficients of the active lubricated bearings into the finite element model of the gas compressor, one can analyze its unbalance response, following the criteria established by the norm API 617 [26].

According to the norm API 617, for the case in study, the unbalance mass to be applied in the node of maximum displacement of the model is given by

$$m_u = 720.0 \ \text{g.mm.} \tag{12}$$

According to this same norm, the vibration amplitude limit for the case in study is

$$L_v = 16.65 \ \mu\text{m}. \tag{13}$$

The results for the original compressor, with conventional bearings, and for the same compressor supported by active bearings are shown in Fig. 10. In this figure, it is displayed the unbalance response of the node with maximum displacements (node 28—Fig. 1).

In Fig. 10, one can see that the compressor supported by the original conventional bearings is not in accordance with norm API 617. The node of maximum deflection (node 28) presents vibration amplitudes which surpass the limit established by the norm (*Z*-direction). Inserting the dynamic coefficients of the active lubricated bearings into the model, one achieves lower vibration amplitudes, in both *Y* and *Z*-directions, in comparison to the response of the original system. By applying the active lubrication, the damping factors of the first bending modes of the compressor are clearly increased. Such an increase in damping factor is evidenced by the reduction of vibration amplitudes. As a result, the lateral vibration amplitudes of the gas compressor remain in accordance with the API 617.

Table 2 Separation margins for the compressor supported by conventional and active bearings (API 617)

	Conventional Bearings	Active Bearings
Y-direction	$SM = 9.7$	$SM = 0.0$
Z-direction	$SM = 13.8$	$SM = 8.4$

SM in % of minimum operational velocity

Norm API 617 defines a way of calculating separation margins between system resonances and operational velocities. By calculating the necessary separation margins for the cases of original and active lubricated bearings, according to the norm and based on the results presented in Fig. 10, one achieves the values shown in Table 2.

One can see, in Table 2, that the required separation margins are reduced by using the active lubricated bearings. This means that the operational range of the gas compressor can be expanded.

Conclusion

The theoretical limits of the active lubrication and the feasibility of its application to an industrial gas compressor were investigated. The set of modified Reynolds equations for the active lubrication is solved, considering the servo valve dynamics and obeying its restrictions related to the input voltage linear range. Such an investigation allows to conclude that:

(a) The stiffness coefficients of the oil film can be significantly altered by changing the proportional gains. Such a modification is feasible in a large range of frequencies, and the stiffness coefficients vary linearly with the proportional gains. Due to the restriction of input voltage in the servo-valves, two saturation regions appear, where the variation of the coefficients stops, and the coefficients remain constant in the maximum and minimum achieved values.

(b) The damping coefficients of the oil film can be significantly altered by varying the derivative gains. Such a modification is also feasible in a quite large range of frequencies, and the damping coefficients also vary linearly with the derivative gains. Due to the restriction of input voltage in the servo-valves, two saturation regions appear, where this variation of the coefficients stops, and the latter remain constant in the maximum and minimum achieved values. The higher the frequencies are, the narrower the range of variation of the damping coefficients is. At higher frequencies (above approx. 150 Hz), no significant changes between maximum and minimum damping values are detectable. This shows a frequency limitation of the active lubrication. It is important to highlight, that this frequency limitation is related to the adopted control strategy (PD controller) and not to the servo valve eigenfrequency ($\omega_v = 320$ Hz).

(c) If a larger variation of dynamic coefficients is necessary to improve the lateral dynamics of the gas compressor, an additional possibility is the increase of the supply pressure to the servo-valves. Such an action results in the increase of the slope of region (I) (Figs. 6 to 9) as a function of the gains, thus leading the system to present higher maximum and minimum coefficient values.

(d) One of the most important theoretical conclusions is related to the feasibility of controlling the first bending vibration mode of a flexible rotor via its bearings. Despite of the limitation of rotor displacements in the bearing gap (30% of the assembled clearance), it is possible to reduce the rotor vibration by active forces (active lubrication) acting on the bearings.

Acknowledgment

The Brazilian research foundation FAPESP—Fundação de Amparo àPesquisa do Estado de São Paulo—is gratefully acknowledged for the support given to this project.

Nomenclature

d_0 = orifice diameter
eq = equilibrium position
$\mathcal{F}$ = positioning function of orifice distribution over pad surface
G_{1y}, G_{1z} = proportional gains in Y and Z-directions
G_{2y}, G_{2z} = derivative gains in Y and Z-directions
h_0 = assembled bearing clearance
h_i = oil film thickness on ith pad
K_{PQ} = servo-valve linearization factor
K_V = servo-valve gain
$\mathbf{K}$, $\mathbf{D}$ = stiffness and damping matrices
l_0 = orifice length
L = pad width
L_v = vibration limit
m_u = unbalance mass
no = number of orifices over pad
p_i = hydrodynamic pressure on ith pad
$P_{inj_{st}}$ = static injection pressure
R = journal radius
R_s = pad inner radius
t = time
$\mathbf{T}_i$ = transformation matrix of ith pad
u_y, u_z = servo-valve control signals
U = linear velocity of rotor surface
W = external static load on the bearing
X, Y, Z = inertial reference frame
$\overline{x,y}$ = pad local reference frame
Y_h, Z_h = rotor displacements
α_i = angular displacement of ith pad
ΔA_i = perturbation on the pad displacements
Δs = distance from pad surface to pad pivot
$\Delta Y_h, \Delta Z_h$ = perturbation on the rotor displacements
ϕ_y, ϕ_z = phase angle of control signal
φ_i = angular location of ith pad in the bearing
μ = oil dynamic viscosity
ξ_v = servo-valve damping factor
ω = excitation frequency
ω_v = servo-valve eigenfrequency
Ω = rotor angular velocity

References

[1] Vance, J. M., and Li, J., 1996, ''Test Results of a New Damper Seal for Vibration Reduction in Turbomachinery,'' ASME J. Eng. Gas Turbines Power, **118**, pp. 843–846.
[2] San Andrés, L., and Lubell, D., 1998, ''Imbalance Response of a Test Rotor Supported on Squeeze Film Dampers,'' ASME J. Eng. Gas Turbines Power, **120**, pp. 397–404.
[3] El-Shafei, A., and Hathout, J. P., 1995, ''Development and Control of HSFDs for Active Control of Rotor-Bearing Systems,'' ASME J. Eng. Gas Turbines Power, **117**, pp. 757–766.
[4] Ulbrich H., and Althaus, J., 1989, ''Actuator Design for Rotor Control,'' *12th Biennial ASME Conference on Vibration and Noise*, Montreal, Sept. 17–21, ASME, New York, pp. 17–22.
[5] Althaus, J., Stelter, P., Feldkamp, B., and Adam, H., 1993, ''Aktives hydraulisches Lager für eine Schneckenzentrifuge,'' *Schwingungen in rotierenden Machinen II*, H. Irretier, R. Nordmann, and H. Springer, eds., Vieweg-Verlag, Braunschweig, Germany, **2**, pp. 28–36.
[6] Santos, I. F., 1995, ''On the Adjusting of the Dynamic coefficients of Tilting-Pad Journal Bearings,'' STLE Tribol. Trans., **38**(3), pp. 700–706.
[7] Goodwin, M. J., Boroomand, T., and Hooke, C. J., 1989, ''Variable Impedance Hydrodynamic Journal Bearings for Controlling Flexible Rotor Vibrations,'' *12th Biennial ASME Conference on Vibration and Noise*, Montreal, Sept. 17–21, ASME, New York, pp. 261–267.
[8] Santos, I. F., 1994, ''Design and Evaluation of Two Types of Active Tilting-Pad Journal Bearings,'' *IUTAM Symposium on Active Control of Vibration*, Bath, England, Kluwer, Dordreicht, The Netherlands, pp. 79–87.
[9] Santos, I. F., and Russo, F. H., 1998, ''Tilting-Pad Journal Bearings with Electronic Radial Oil Injection,'' ASME J. Tribol., **120**, pp. 583–594.
[10] Santos, I. F., and Nicoletti, R., 1999, ''THD Analysis in Tilting-Pad Journal Bearings Using Multiple Orifice Hybrid Lubrication,'' ASME J. Tribol., **121**, pp. 892–900.
[11] Santos, I. F., and Scalabrin, A., 2000, ''Control System Design for Active Lubrication with Theoretical and Experimental Examples,'' ASME Paper No. 2000-GT-643.
[12] Bently, D. E., Grant J. W., and Hanifan P., 1999, ''Active Controlled Hydrostatic Bearings for a New Generation of Machines,'' ASME Paper No. 2000-GT-354.
[13] Osman, T. A., Nada, G. S., and Safar, Z. S., 2001, ''Static and Dynamic Characteristics of Magnetized Journal Bearings Lubricated With Ferrofluid,'' Tribol. Int., **34**(6), pp. 369–380.
[14] Santos, I. F., and Nicoletti, R., 2001, ''Influence of Orifice Distribution on the Thermal and Static Properties of Hybridly Lubricated Bearings,'' Int. J. Solids Struct., **38**(10–13), pp. 2069–2081.
[15] Nicoletti, R., and Santos, I. F., 2001, ''Vibration Control of Rotating Machinery Using Active Tilting-Pad Bearings,'' *Proceedings of the IEEE/ASME International Conference on Advanced Intelligent Mechatronics*, Como, Italy, July 8–11, pp. 589–594.
[16] Santos, I. F., Scalabrin A., and Nicoletti, R., 2001, ''Ein Beitrag zur aktiven Schmierungstheorie,'' *Schwingungen in rotierenden Machinen VI*, edited by H. Irretier, R. Nordmann, and H. Springer, eds., Vieweg-Verlag, Braunschweig, Germany, **5**, pp. 21–30.
[17] Nelson, H. D., and McVaugh, J. M., 1976, ''The Dynamics of Rotor-Bearing Systems Using Finite Element,'' J. Eng. Ind., **98**, pp. 593–600.
[18] Lund, J. W., and Thomsen, K. K., 1978, ''A Calculation Method and Data for the Dynamic Coefficients of Oil-Lubricated Journal Bearings,'' *Topics in Fluid Film Bearing and Rotor Bearing System Design and Optimization*, S. M. Rhode, P. E. Allaire, and C. J. Maday, eds., ASME, New York, pp. 1–28.
[19] Ghosh, M. K., Guha, S. K., and Majumdar, B. C., 1989, ''Rotordynamic Coefficients of Multirecess Hybrid Journal Bearings—Part I,'' Wear, **129**, pp. 245–259.
[20] Hamrock, B. J., 1994, *Fundamentals of Fluid Film Lubrication*, Mechanical Engineering Series, McGraw-Hill, New York.
[21] Allaire, P. E., Parsell, J. A., and Barret, L. E., 1981, ''A Pad Perturbation Method for the Dynamic Coefficients of Tilting Pad Journal Bearings,'' Wear, **72**, pp. 29–44.
[22] Schäfer, K. D., 1977, ''Elektrohydraulische regelsysteme,'' MOOG Bulletin D, **1**(180), WA 2000 N.
[23] Althaus, J., 1991, *Eine aktive hydraulische Lagerung für Rotorsysteme*, Fortschritt-Berichte VDI, Series 11, N. 154, VDI-Verlag GmbH.
[24] Russo, F. H., 1999, ''Identification of Hybrid Tilting-Pad Bearings Dynamic Properties—Theory and Experiment,'' Master thesis, State University of Campinas, Brazil (in Portuguese).
[25] Someya, T., *Journal Bearing Data Book*, Springer-Verlag, Berlin.
[26] API, 1995, *617—Centrifugal Compressors for Petroleum, Chemical, and Gas Service Industries, 6*, American Petroleum Institute, Washington, DC.

A Study of the Nonlinear Interaction Between an Eccentric Squeeze Film Damper and an Unbalanced Flexible Rotor

Philip Bonello[1]

Michael J. Brennan

Institute of Sound and Vibration Research,
University of Southampton,
Highfield, Southampton SO17 1BJ, UK

Roy Holmes

School of Engineering Sciences,
University of Southampton,
Highfield, Southampton SO17 1BJ, UK

In this paper, the nonlinear interaction between an eccentric squeeze film damper and an unbalanced flexible rotor is investigated, paying particular attention to the effect of cavitation in the damper. A harmonic balance method that uses the receptance functions of the rotating linear part of the system to determine periodic solutions to the nonlinear problem is used to predict vibration levels in a test rig. By comparing predictions obtained respectively with, and without, lower pressure limits for the squeeze film damper model, it is concluded that cavitation is promoted by increasing static eccentricity and/or unbalance level. This, in turn, is found to have a profound effect on the predictions for the critical vibration levels, which such dampers are designed to attenuate. Experimental results are presented to support the findings. [DOI: 10.1115/1.1787503]

Introduction

Squeeze film dampers (SFD's) are nonlinear elements used in aero-engine assemblies primarily to attenuate vibrations and transmitted forces. Such a damper is essentially equivalent to a journal bearing with the journal (a ring fixed to the outer race of a rolling element bearing) mechanically prevented from rotating but free to orbit within an oil-filled annular clearance, forming the SFD. A retainer spring placed in parallel with the oil film is often used to support the gravity load on the journal. By centralizing the journal in the housing (e.g., by preloading the spring), vibration that is synchronous with the rotational speed can be obtained. In such a condition, the SFD is generally found to behave approximately linearly over an appreciable range of vibration amplitude [1], with the nonlinearity becoming very significant at the larger amplitudes where it manifests itself as amplitude jumps on runup or rundown in rotational speed [2]. However, there are many practical situations where there is a significant degree of static eccentricity (i.e., offset) of the journal within the bearing housing. This may be due to preloading error, omission of the centralising mechanism for constructional simplicity, or, in extreme cases, partial failure of the retainer spring in service. This offset results in nonlinearity that is evident by the presence of nonsynchronous frequency components in the vibration. This paper deals with a sprung eccentric SFD.

Various nonlinear periodic solution techniques for the unbalance response have been developed as efficient alternatives to time-consuming step-by-step time domain numerical integration. Periodic solution techniques for circular, concentric, and synchronous whirl motion are well documented, e.g., Ref. [3]. Equivalent linearization methods, e.g., [4] can cater for noncircular (elliptical) orbits, but do not allow for the presence of nonsynchronous frequency components, making them not very useful for the study of rotors with eccentric SFD's. A recently developed ''receptance harmonic balance'' (RHB) technique [5] can be used for the determination of the periodic response of flexible rotors under such conditions. This method uses frequency response functions (''receptances'') of the linear subsystem to determine iteratively the response in each harmonic at the nonlinear degrees of freedom.

As observed in Ref. [3], only a few researchers have attempted to obtain the nonlinear response of SFD supported multimode rotors, and, as in Ref. [3], these mainly considered perfectly centralized SFD's. The validity of the nonlinear response will depend on the models used for both linear (rotor) and nonlinear (SFD) parts of the system. The work in Refs. [6,7] used the same flexible rotor test rig as the research presented in this paper and an eccentric SFD was considered. However, a linear analysis was performed in Ref. [6]. In Ref. [7], a nonlinear model was used for the SFD and time domain numerical integration was used to solve the nonlinear equations of motion. A simplified lumped parameter model with three equivalent masses was used for the rotor in Ref. [7], in order to alleviate the computational burden. However, as a result of this simplification, the results obtained were considered reliable only within a frequency range of 0–60 Hz [8]. This not only restricted the operating speed of the rig, which could otherwise be driven up to 100 rev/s, but must have affected the supersynchronous frequency content of the predictions within the speed range considered (0–50 rev/s).

As regards the model used for the SFD, a major assumption is the extent of cavitation (oil film rupture). Such cavitation can be either vaporous or gaseous [9]. Both forms of cavitation involve the formation of bubbles, resulting in discrepancies in the conventional models used for the SFD, which assume an incompressible fluid [9–11]. The term gas (or air) entrainment has been used to describe the formation of bubbles by either form of cavitation [2,10]. Gaseous cavitation is defined in Ref. [9] as arising from the ingestion of ambient air into the low-pressure regions of the SFD and is usually associated with a jumpup in amplitude on runup in rotational speed [2,12]. In the case of vaporous cavitation, vapor comes out from within the liquid in the low-pressure regions of the SFD and the bubbles so formed include gases that were previously dissolved in the oil, rather than ingested air [9]. Such bubbles are known to persist despite re-entry into high-pressure regions [9]. A model for a SFD with a bubbly (compressible) fluid resulting from vaporous cavitation was devised in Ref. [9]. This model is too complicated to use on all but the simplest of systems, like the rigid rotor rig with centralized damper considered in Ref. [10]. However, in Ref. [10], simulations and experiments showed that a SFD model based on an incompressible film that ruptured at absolute zero pressure gave predictions that were

[1]Present address: School of Engineering, University of Manchester, Oxford Road, Manchester M13 9PL, UK.

Contributed by the Structure and Dynamics Division of THE AMERICAN SOCIETY OF MECHANICAL ENGINEERS for publication in the ASME JOURNAL OF ENGINEERING FOR GAS TURBINES AND POWER. Manuscript received by the S&D Division November 22, 2002; final revision received November 20, 2003. Associate Editor: N. K. Arakere.

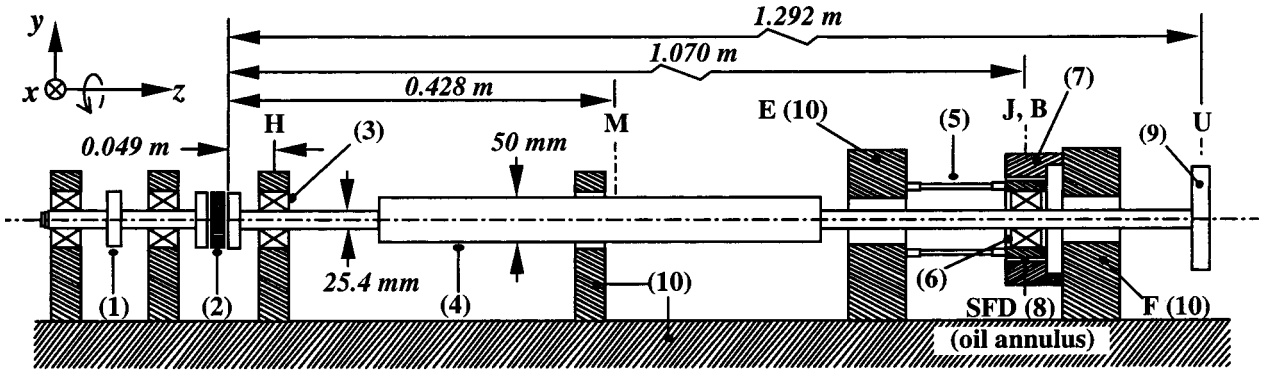

(1) Motor driven pulley
(2) Flexible rubber coupling
(3) Self-aligning ball bearing
(4) Shaft (density 7860kg/m^3, Young's Modulus 200 GPa)
(5) Flexible bar × 4 (retainer spring)
(6) Self-aligning ball bearing and damper journal (centre J)
(7) Bearing housing (centre B)
(8) Oil annulus (SFD)
(9) Unbalance disc
(10) Frame and bedplate

Fig. 1 Test rig

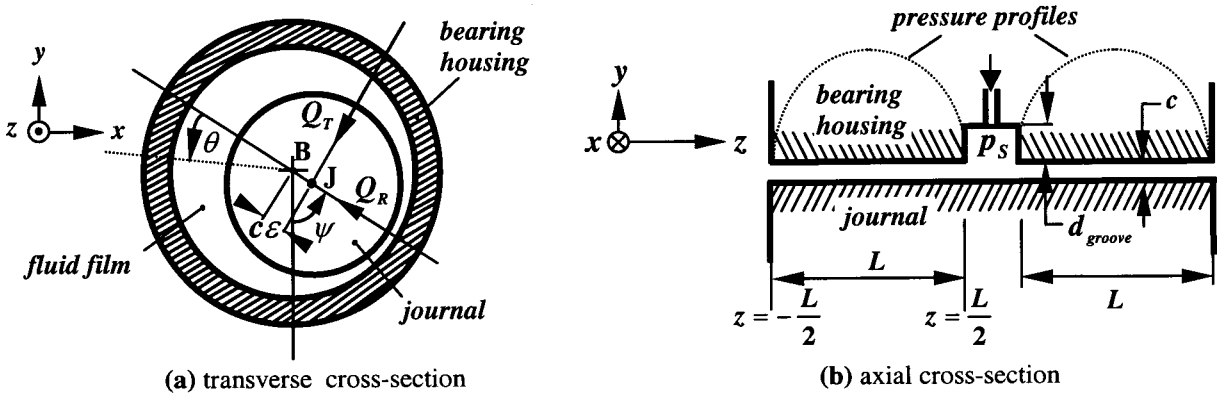

Fig. 2 Sections through squeeze film damper

satisfactory and superior to the "π" film model frequently used in theoretical studies, e.g., Ref. [4]. The absolute zero pressure cavitation model for the SFD was used in Ref. [12] on various rigid rotor configurations with eccentric SFD's and is also used here.

In the present work, a flexible rotor test rig is analyzed for periodic solutions using the RHB technique. The use of this technique is justified by comparing the results with alternative results obtained by numerically integrating the time-domain modal equations of the system. The analysis then focuses on the influence of damper static eccentricity and unbalance level on cavitation and its resulting effect on vibration levels.

Test Facility

A drawing of the experimental rig is given in Fig. 1. Its configuration is described in Ref. [6] as being typical of a small centrifugal pump. The mild steel stepped shaft (4) runs in self-aligning ball bearings (3) and (6) at H and J, respectively. The ball bearing at H is rigidly supported. A ring is fixed to the outer race of the ball bearing (6) and four flexible bars (5) connect it to the frame at E, forming an isotropic retainer spring. The rotor is then free to orbit in the oil-filled annular clearance within the bearing housing (7), forming the SFD (8). In Fig. 1, J refers to the center of the SFD journal (i.e., the ring fixed to the outer race of the ball bearing (6)), and B refers to the center of the bearing housing (7). If the pedestals E and F are considered rigid and the bearing housing (7) is rigidly bolted to F, then the retainer spring is effectively in parallel with the SFD. The static eccentricity of J from B can be varied by adjusting the position of the housing (7). The squeeze film damper has two lands separated by a deep groove, and is shown schematically in Fig. 2. Table 1 gives the dimensions of the SFD.

Oil of viscosity $\eta = 0.0045$ N s m^{-2} is supplied at a pressure p_s of up to 1.2 bars (gauge) through three holes, equally spaced around the groove. Unbalance masses are attached to the overhung disc at U. The x and y vibration is monitored at three positions J, U, and M. Point M is referred to here as the "mid-shaft" position, although the distance HM is actually 0.4 times the span HJ. Assuming that the frame and ball bearings have infinite stiffness (i.e., are rigid), the first two undamped critical speeds of the rig were calculated at 14 rev/s and 40 rev/s, using the mechanical impedance (MI) technique [13,14]. The first two undamped critical speeds of the rig with the damper "locked" by inserting shims into the radial clearance, were computed at 31 and 91 rev/s.

Table 1 Dimensions of SFD

$c = 0.132 \times 10^{-3}$ m	$d_{groove} = 5.25 \times 10^{-3}$ m
$L = 9.72 \times 10^{-3}$ m	$R = 50.022 \times 10^{-3}$ m

Theoretical Modeling

Referring to Fig. 2, the SFD forces are given by

$$Q_x = Q_x(X_J, Y_J, \dot{X}_J, \dot{Y}_J) = -\{Q_R(\varepsilon, \dot{\varepsilon}, \dot{\psi})\sin\psi + Q_T(\varepsilon, \dot{\varepsilon}, \dot{\psi})\cos\psi\}, \tag{1a}$$

$$Q_y = Q_y(X_J, Y_J, \dot{X}_J, \dot{Y}_J) = Q_R(\varepsilon, \dot{\varepsilon}, \dot{\psi})\cos\psi - Q_T(\varepsilon, \dot{\varepsilon}, \dot{\psi})\sin\psi. \tag{1b}$$

The radial and tangential squeeze film forces Q_R, Q_T are obtained by integrating the instantaneous pressure distribution within the squeeze film $p(\theta,z)$, after truncating it at a cavitation pressure p_c:

$$Q_R = -2R\int_{-L/2}^{L/2}\int_0^{2\pi} p_t(\theta,z)\cos\theta \; d\theta \; dz, \tag{2a}$$

$$Q_T = -2R\int_{-L/2}^{L/2}\int_0^{2\pi} p_t(\theta,z)\sin\theta \; d\theta \; dz, \tag{2b}$$

where

$$p_t(\theta,z) = \begin{matrix} p(\theta,z), & p(\theta,z) > p_c \\ p_c, & p(\theta,z) \leq p_c \end{matrix}. \tag{3}$$

The pressure distribution $p(\theta,z)$ is given by the short bearing solution to the incompressible Reynolds equation [12]:

$$p(\theta,z) = \frac{6\eta}{c^2}\frac{\{\varepsilon\dot{\psi}\sin\theta + \dot{\varepsilon}\cos\theta\}}{\{1+\varepsilon\cos\theta\}^3}\left(z^2 - \frac{L^2}{4}\right) + p_s\left(\frac{z}{L} + \frac{1}{2}\right). \tag{4}$$

This approximate model for the SFD under consideration is justified since (i) it is unsealed at its ends, and (ii) the ratio L/R is only around 0.2 [10]. Moreover, the groove depth is well over ten times the radial clearance, justifying the two-land model.

The derivation of the general RHB model is described in some detail in Ref. [5], and only an application of the method is described here. Equilibrium periodic solutions of fundamental frequency ϖ (rad/s) are sought where

$$\varpi = \Omega/N, \tag{5}$$

Ω rad/s being the rotational speed and N a positive integer. Accordingly, both the displacements X_J, Y_J, and the motion-dependent squeeze film forces can be expressed as Fourier series approximated to m harmonics:

$$X_J = \overline{X}_J + \sum_{s=1}^{m}(a_{XJ}^{(s)}\cos s\varpi t + b_{XJ}^{(s)}\sin s\varpi t), \tag{6a}$$

$$Y_J = \overline{Y}_J + \sum_{s=1}^{m}(a_{YJ}^{(s)}\cos s\varpi t + b_{YJ}^{(s)}\sin s\varpi t), \tag{6b}$$

$$Q_x = \overline{Q}_x + \sum_{s=1}^{m}(p_x^{(s)}\cos s\varpi t + q_x^{(s)}\sin s\varpi t), \tag{7a}$$

$$Q_y = \overline{Q}_y + \sum_{s=1}^{m}(p_y^{(s)}\cos s\varpi t + q_y^{(s)}\sin s\varpi t). \tag{7b}$$

The SFD force Fourier coefficients in Eqs. 7(a) and 7(b) are given by

$$\overline{Q}_{x,y} = \frac{1}{\Gamma}\int_0^{\Gamma} Q_{x,y}\, dt, \tag{8a}$$

$$p_{x,y}^{(s)} = \frac{2}{\Gamma}\int_0^{\Gamma} Q_{x,y}\cos s\varpi t \; dt, \tag{8b}$$

$$q_{x,y}^{(s)} = \frac{2}{\Gamma}\int_0^{\Gamma} Q_{x,y}\sin s\varpi t \; dt, \tag{8c}$$

where the period $\Gamma = 2\pi/\varpi$, $s = 1, \ldots, m$, and $Q_{x,y}$ are given by Eqs. (1) and (2).

The polar moment of inertia of the disc is sufficiently small for gyroscopic effects to be neglected, hence so is any cross coupling between the xz and yz planes. The SFD is assumed to be the only source of damping. The SFD forces are considered as external forces, which, along with the unbalance forces, act on the linear subsystem. The RHB equations of the rotor for an unbalance U at U can then be written as

$$\overline{X}_J - X_{J0} = \overline{Q}_x\alpha_{JJ}(0), \tag{9a1}$$

$$\overline{Y}_J - Y_{J0} = \overline{Q}_y\beta_{JJ}(0), \tag{9a2}$$

$$a_{XJ}^{(s)} = \alpha_{JJ}(s\varpi)p_x^{(s)}, \tag{9b1}$$

$$a_{YJ}^{(s)} = \beta_{JJ}(s\varpi)p_y^{(s)} - \delta_{Ns}\beta_{JU}(s\varpi)U\Omega^2, \quad s = 1, \ldots, m, \tag{9b2}$$

$$b_{XJ}^{(s)} = \alpha_{JJ}(s\varpi)q_x^{(s)} + \delta_{Ns}\alpha_{JU}(s\varpi)U\Omega^2, \tag{9c1}$$

$$b_{YJ}^{(s)} = \beta_{JJ}(s\varpi)q_y^{(s)}, \quad s = 1, \ldots, m, \tag{9c2}$$

where

$$\delta_{Ns} = 0 \quad \text{for } s \neq N, \quad \delta_{Ns} = 1 \quad \text{for } s = N. \tag{10}$$

$\alpha_{ij}(s\varpi)$, $\beta_{ij}(s\varpi)$ (where $s = 0,1, \ldots, m$) are the receptance functions connecting the forces at position j in the x and y directions, respectively, with the responses (displacements) in the corresponding directions at position i. These receptances are for the linear subsystem, which is the rotor pinned at H and sprung at J, and for the case studied, $\alpha_{ij}(s\varpi) = \beta_{ij}(s\varpi)$. The receptances were computed using the mechanical impedance (MI) method, which is described in Refs. [13,14]. Only the attachments to the shaft (e.g., the disc at U, the ball bearing and damper journal at J, ... etc.) were considered as lumped inertias. The impedance matrices of the shaft elements for each plane xz, yz were based on the exact solution of the harmonic wave equation of a uniform section beam of distributed inertia in transverse vibration [14]. Hence these matrices were exact, irrespective of element length, and only eight shaft elements needed to be used in the MI model of the rotor. Matrix assembly of the shaft element matrices was similar to that used in finite element analysis, the impedance matrices of the inertia attachments to the shaft and the point supports being inserted at the appropriate areas of the global impedance matrix. This matrix was then inverted at each frequency and divided by a factor $j\omega$ (where $j = \sqrt{-1}$) to yield the receptance matrix. The detailed input into the MI modeling program for the test rig is given in Table 2. The flexible rubber coupling (marked (2) in Fig. 1) was assumed to exert no restraint in either bending plane.

Equations (9) constitute a system of $2(2m+1)$ nonlinear algebraic equations in an equal number of unknowns contained in the vector

$$\mathbf{v} = [\overline{X}_J \; \overline{Y}_J \; a_{XJ}^{(1)} \; a_{YJ}^{(1)} \cdots a_{XJ}^{(m)} \; a_{YJ}^{(m)} \; b_{XJ}^{(1)} \; b_{YJ}^{(1)} \cdots b_{XJ}^{(m)} \; b_{YJ}^{(m)}]^{\Gamma}. \tag{11}$$

This enables expression of Eqs. (9) in the standard form $\mathbf{f}(\mathbf{v}) = \mathbf{0}$, where $\mathbf{f}$ is a nonlinear vector function of $\mathbf{v}$. Solution is possible using the Newton-Raphson iterative procedure [15]. At each stage of the iteration $\mathbf{f}(\mathbf{v})$ is computed as follows: for an assumed $\mathbf{v}$ and given Ω and N (and hence ϖ and Γ), the SFD response is computed from Eqs. (6). The SFD forces can then be computed from Eqs. (1), (2), and their Fourier coefficients from Eqs. (8). Arc-length continuation [15] is employed to trace out a speed response curve (i.e., a set of solutions over a range of speeds) for a given unbalance. For each solution on this curve, knowledge of the Fourier coefficients of $Q_{x,y}$ enables the direct determination of the

Table 2 Mechanical impedance model for linear part (i.e., excluding SFD)

Station no.	1	2	3 (H)	4	5	6 (J)	7	8 (U)	9
Attached mass (kg)	0.1518*	0.0692*				1.3567		6.4039	
Support stiffness (kN/m)			∞			123.4			
Element	**1-2**	**2-3**	**3-4**	**4-5**	**5-6**	**6-7**	**7-8**	**8-9**	
Length (mm)	20.0	29.0	44.0	715.0	262.0	13.0	209.3	12.7	
Diameter (mm)	16.000	25.405	25.405	50.000	25.405	25.405	25.385	25.385	

*the mass of the hub at the left hand end of shaft (Fig. 1) is shared between stations 1 and 2

Fourier coefficients of the displacement response at a general position P on the rotor (measured from the static position of P), by using Eqs. (9) modified as follows: (i) omitting the terms X_{J0}, Y_{J0}; (ii) replacing the subscript J by P in the displacement Fourier coefficients on the left-hand side of Eqs. (9); (iii) replacing the *first* subscript J by P in the receptance terms on the right-hand side of Eqs. (9).

In general, the RHB-computed periodic solutions can be either stable or unstable. Floquet stability analysis is carried out as in Ref. [5].

As a verification of the RHB solution, and to justify its relevance to the present study, the numerical integration of the modal equations is performed. These equations, and the determination of the modal parameters, are outlined in the Appendix. In the modal equations, the first four modes of the linear subsystem (i.e., the rotor pinned at H, sprung at J) in each plane xz, yz were considered. This is justified in Fig. 3, where the exact receptance $\alpha_{JU}(\omega)$ (computed by MI) is compared with the approximate one, reconstructed from the first four terms in its modal series expansion (given by Eq. (*A*4) of the Appendix). It is evident that excellent agreement prevails over a frequency range of 0–500 Hz, covering five harmonics of the maximum rotational speed of the rig (100 rev/s).

At the maximum speed of 100 rev/s, the Reynolds number [16] for the SFD is 2 (taking the oil density to be 841 kg/m^3). An upper bound for the fluid inertia effect at the SFD was estimated using the method in Ref. [16] to be 0.17 kg, which is negligible when compared to the effective mass at J of the linear subsystem in each of the modes considered. From Eq. (*A*4) of the Appendix, these latter masses are equal to the inverse of the values in the third column of Table 3 in the Appendix.

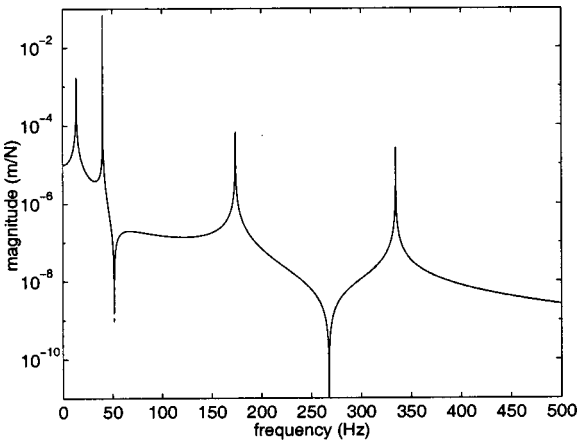

Fig. 3 (Reproduced from Ref. [5]) Comparison of exact rotor receptance function $\alpha_{JU}(\omega)$ computed by the mechanical impedance method (——) with the approximation synthesised from four modes (– – –) (Both lines overlay)

Experimental Work

Two static offset conditions $(X_{J0}/c, Y_{J0}/c)$ of $(0,-0.6)$ and $(0,-0.8)$, respectively, were considered, i.e., the static eccentricity was entirely in the (negative) y direction. The static eccentricity adjustment was complicated by a static runout of the shaft. By rotating the shaft slowly by hand and using a micrometer dial indicator with its stem pressed to the shaft at M, and at locations as close as possible to J and U, it was found that the amplitude of the fluctuation in the reading was 0.015, 0.022, and 0.05 mm, respectively, for the y direction. The runout in the x direction was negligible. The runout at J was confirmed by the readings of the displacement transducers. This meant that the runout was not due to lack of roundness of the shaft surface since the displacement transducers at J were aimed at projections on the (nonrotating) journal rather than at the shaft. This also meant that the static eccentricity of J was different for different angular positions of the shaft. At first this appeared unusual since the shaft was pivoted at H and, regardless of whether the shaft was distorted (due to the machining process, gravity, and temperature), the restoring force from the retainer spring should have maintained J at a fixed position within the clearance. The most likely explanation is that the distortion of the shaft resulted in angular misalignment of the hubs at the flexible rubber coupling (marked (2) in Fig. 1), resulting in a slight restraining torque that varied with the angular position of the shaft. This slight restraint was thought to affect the position of J, because of the low stiffness of the retainer spring (123.4 kN/m). In view of this problem, the static eccentricity was adjusted for each of four angular positions (0, 90, 180, and 270°) of the shaft. The average values of X_{J0}/c, Y_{J0}/c over the four angular positions were brought as close as possible to the desired values. The static eccentricity was rechecked after each experiment, when the rig was hot.

The displacement transducers at J, U, and M were connected through voltage amplifiers to a PC-operated spectrum analyzer, which was set to acquire data in the form of a time history 0.5 s long. The vibration data in the x and y directions were obtained for a given unbalance at U and a fixed oil supply pressure of 1 bar over a range of speeds (10–100 rev/s) in steps of 2 rev/s. The rotor speed was measured using an optical sensor and the observed fluctuation in speed over each acquisition was within ± 0.5 rev/s. Two unbalance levels were considered, $U=2.59\times10^{-4}$ kg m and $U=5.10\times10^{-4}$ kg m.

Results and Discussion

In this section, theoretical and experimental results are presented and discussed. In the theoretical treatment no attempt is made to compensate for the small residual unbalance left after the rig was balanced when first commissioned. The residual unbalance response was investigated experimentally in Ref. [17] and found to be adequately small. Unless otherwise stated, in the theoretical treatment the cavitation pressure $p_c=-101.325\times10^3$ Pa (absolute zero). All RHB predictions are for $N=1$, which means that subharmonics of the rotational speed are not considered.

The choice of the number of harmonics m to use is first considered. Figure 4 shows one example of how the RHB solution converges to the modal numerical integration result as m is increased from 1 to 5. It is concluded that the inclusion of further harmonics in the RHB solution is unnecessary. The example in Fig. 4 illustrates the varying influence of the harmonics on the orbital motion at the three locations J, U, and M, evidenced by the corresponding degree of orbital distortion from an ellipse. It is seen that, while the presence of these harmonics is a symptom of the nonlinearity of the system, the harmonics do not necessarily manifest themselves significantly at the actual source of the nonlinearity (i.e., at J). This effect is also observed in the measurements shown in Fig. 5, where the kinked outline of the orbit at M is adequately predicted. In the example shown, the transfer receptance function linking M to J amplifies the responses at M to the individual harmonic components of the SFD forces at J. The high degree of correlation between the $N=1$ RHB solutions with $m=5$ and the (steady-state) numerical integration results over the entire operating speed range is illustrated in the amplitude-speed curves of Fig. 6, which refer to the vibration at M for a static eccentricity of 0.8 and $U=5.1\times10^{-4}$ kg m. The vertical axes show the displacement amplitude normalized with respect to the radial clearance c. The displacement amplitudes in the x and y

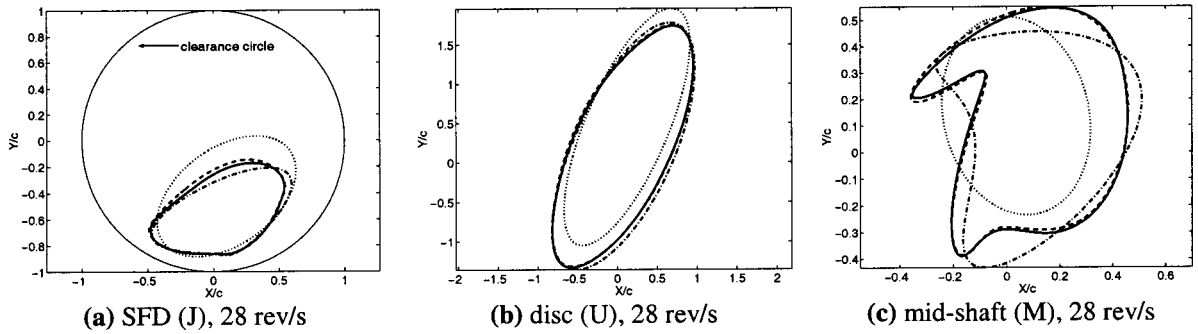

Fig. 4 Convergence of RHB $N=1$ as the number of harmonics m is increased for X_{J0}/c, $Y_{J0}/c=0$, -0.8 and $U=5.10\times10^{-4}$ kg m. $m=1$ (· · · ·), $m=2$ (·-·-·), $m=5$ (– – –); modal numerical integration (——).

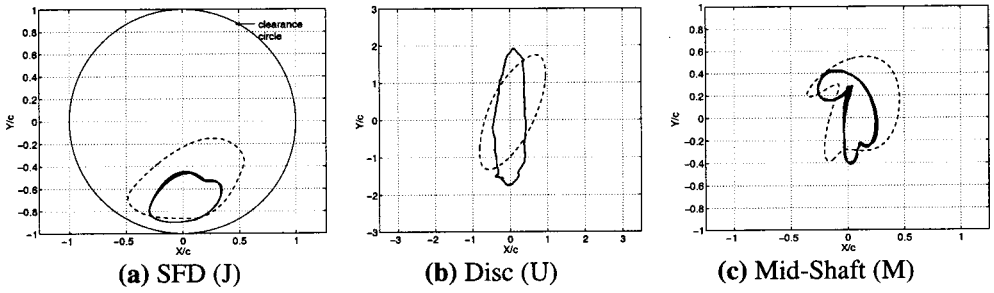

Fig. 5 (reproduced from Ref. [5]): Comparison of predicted and measured orbital motion at J, U, and M at 28 rev/s for X_{J0}/c, $Y_{J0}/c=0$, -0.8 and $U=5.10\times10^{-4}$ kg m. RHB, $N=1$, $m=5$ (– – –), measurement over 0.5 s (——).

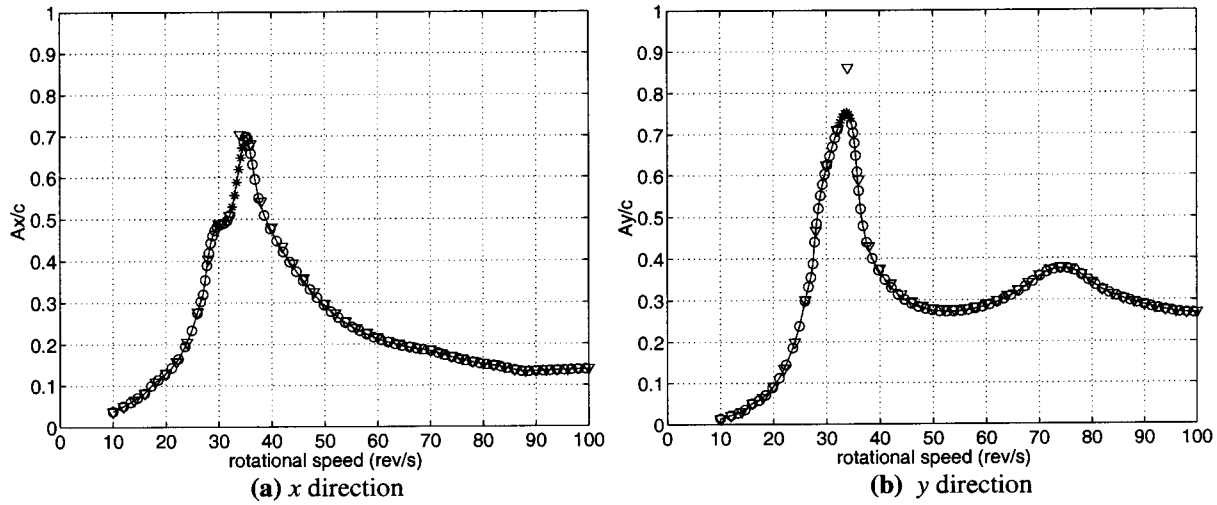

Fig. 6 Correlation between RHB and numerical integration predictions for amplitude at M with X_{J0}/c, $Y_{J0}/c=0$, -0.8 and $U=5.10\times10^{-4}$ kg m. RHB $N=1$, $m=5$: -○- (stable), -*- (unstable); numerical integration: ∇. Vertical axes show ratio of half the peak-to-peak displacement to c.

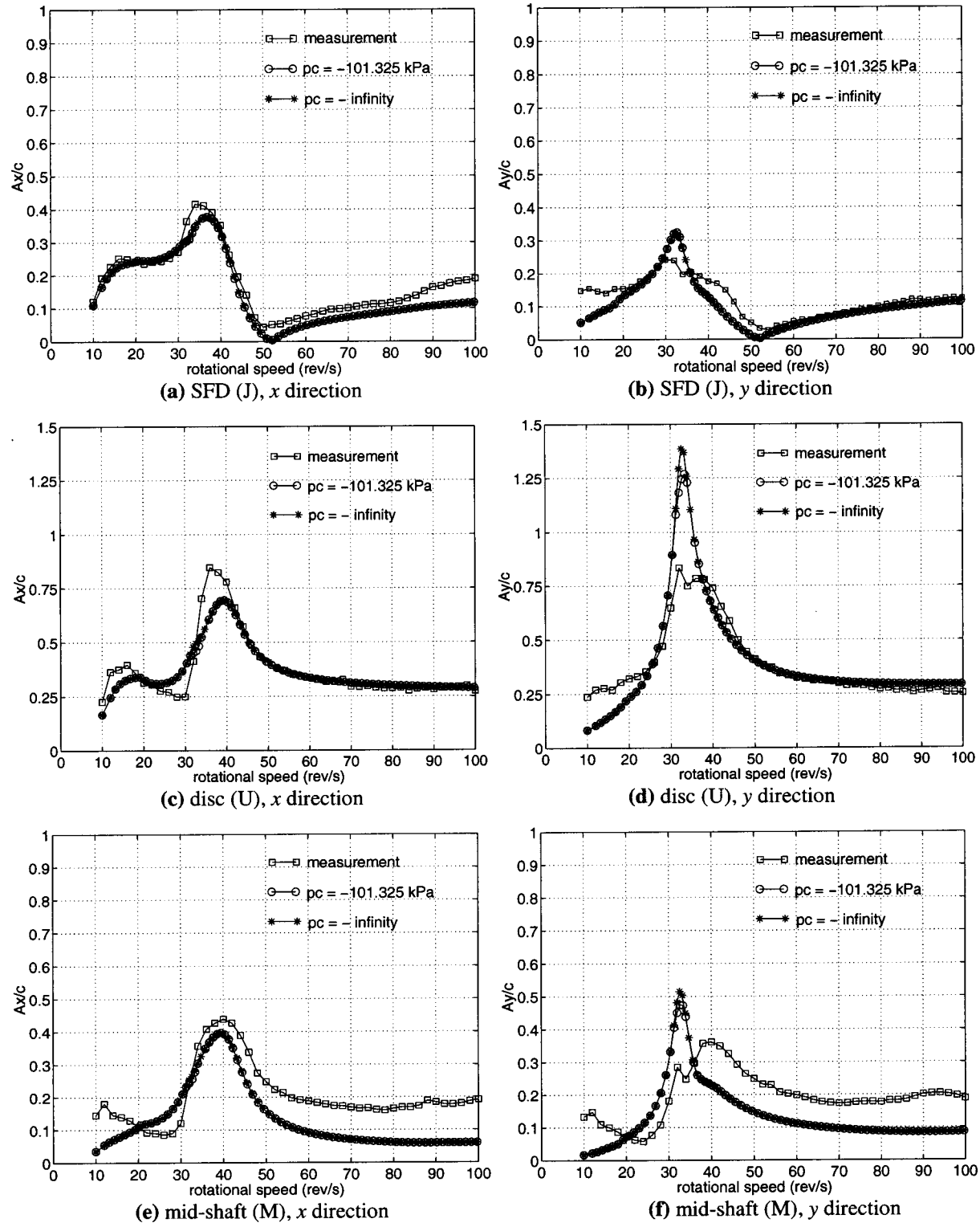

Fig. 7 Unbalance response for X_{J0}/c, $Y_{J0}/c = 0, -0.6$ and $U = 2.59\times10^{-4}$ kg m. All predictions are RHB $N=1$, $m=5$. Vertical axes show ratio of half peak-to-peak displacement to c.

directions are defined as half the peak-to-peak fluctuation in the respective displacement time histories. Arc-length continuation is used to trace out the RHB solution curve, so the rotational speed corresponding to each solution is not pre-selected, but comes out as part of the solution process [15]. On the other hand, the numerical integration results are performed at discrete preselected speeds, in steps of 2 rev/s, and the corresponding solution points are not joined in Fig. 6 for emphasis. In Fig. 6, the disagreement between the numerical integration and RHB results at 34 rev/s is due to the fact that, over the range 32–35 rev/s, the $N=1$ RHB results are unstable, as reported in Ref. [5]. The numerical integration result gives the stable motion, which is quasiperiodic with subsynchronous frequency components. The corresponding measured motion was similarly aperiodic. With $p_c = -101.325$

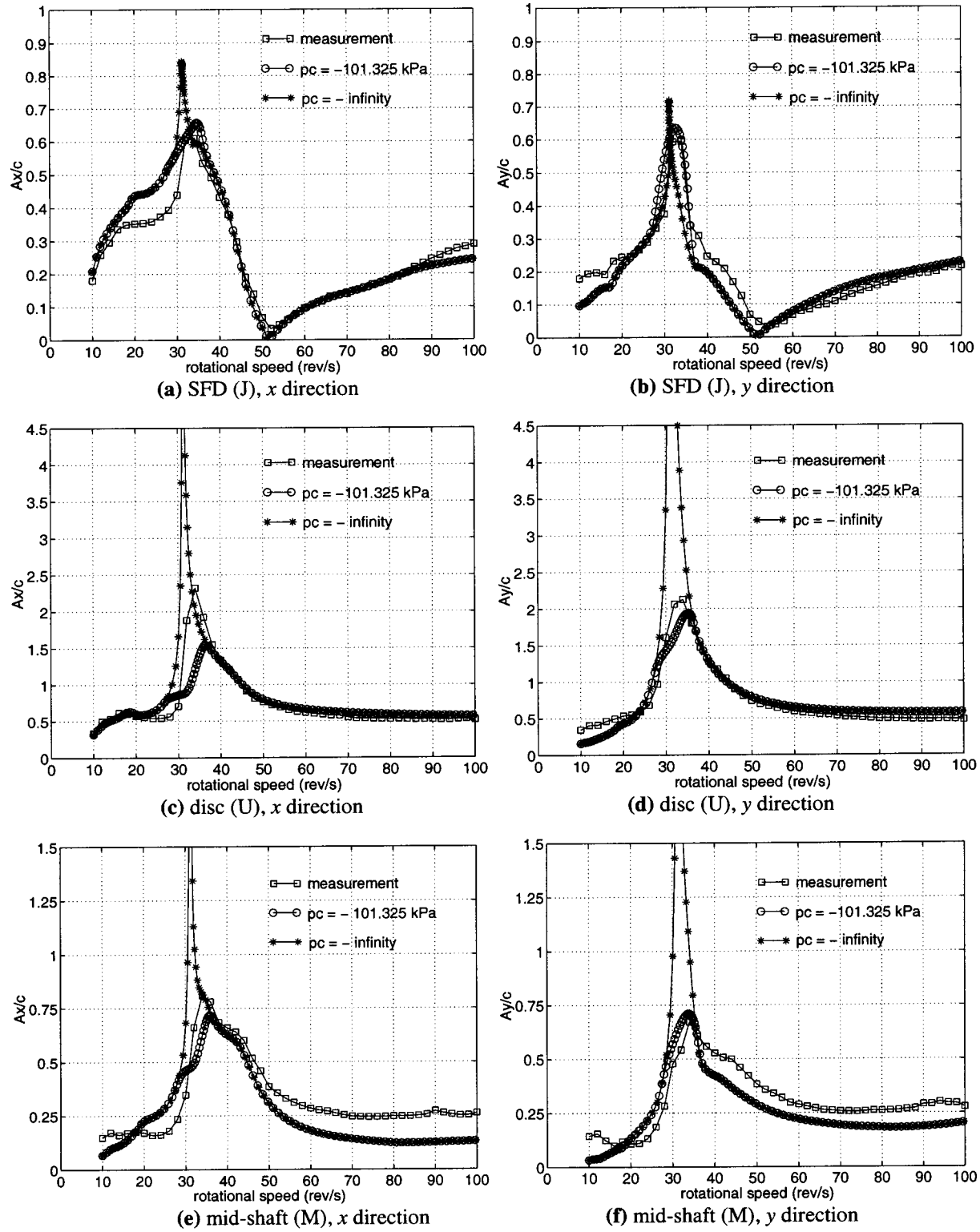

Fig. 8 Unbalance response for X_{J0}/c, $Y_{J0}/c=0$, -0.6 and $U=5.10\times10^{-4}$ kg m. All predictions are RHB $N=1$, $m=5$. Vertical axes show ratio of half peak-to-peak displacement to c.

$\times10^3$ Pa, this instability of the $N=1$ periodic motion was found to occur only for the static eccentricity of 0.8 with $U=5.10\times10^{-4}$ kg m (highest static eccentricity considered under highest unbalance). Even in this condition, the difference in amplitude between the RHB and numerical integration predictions over the narrow speed range (32–35 rev/s) was not large and so the issue of stability is ignored and the RHB $N=1$ predictions are used throughout.

The predicted and measured amplitude-speed plots are shown in Figs. 7–10. In addition to the lower pressure limit of $p_c=$

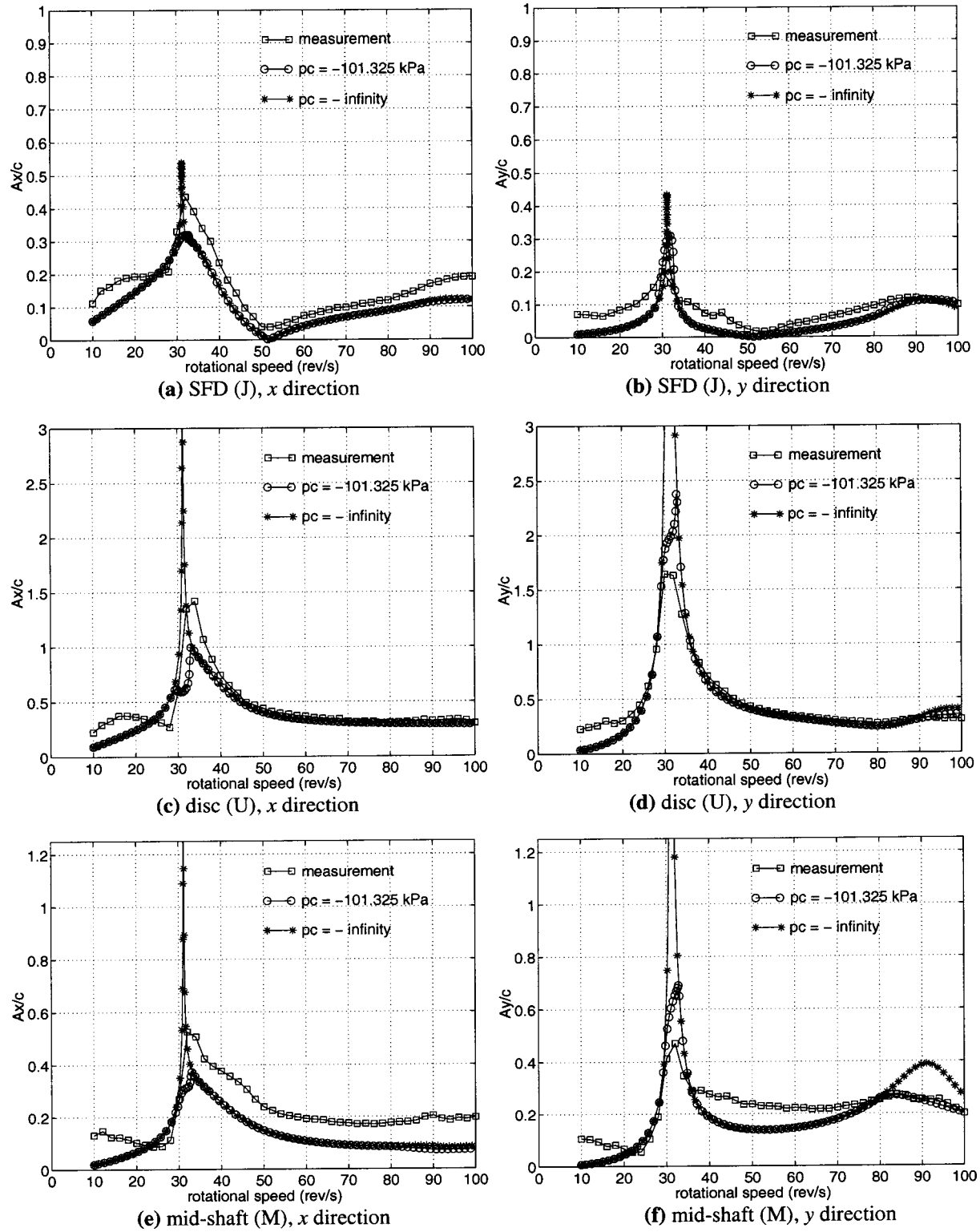

Fig. 9 Unbalance response for X_{J0}/c, $Y_{J0}/c=0$, -0.8 and $U=2.59\times10^{-4}$ kg m. All predictions are RHB $N=1$, $m=5$. Vertical axes show ratio of half peak-to-peak displacement to c.

-101.325×10^3 Pa, another set of $N=1$ RHB solutions was generated by taking $p_c=-\infty$ (no lower pressure limit imposed, i.e., a full film at the SFD under all conditions). Notice that, for the latter case only, closed form expressions for the SFD forces can be used in the computation [18]. The predictions obtained with $p_c=-101.325\times10^3$ Pa are referred to here as the ''absolute zero cavitation'' results, while those obtained with $p_c=-\infty$ are referred to as the ''full film'' results. Those regimes of operation for which cavitation occurs are identified by those regimes for which divergence occurs between the results obtained by the two different values of p_c. The reason for this is that the divergence would be the result of the minimum oil film pressure in the full film model

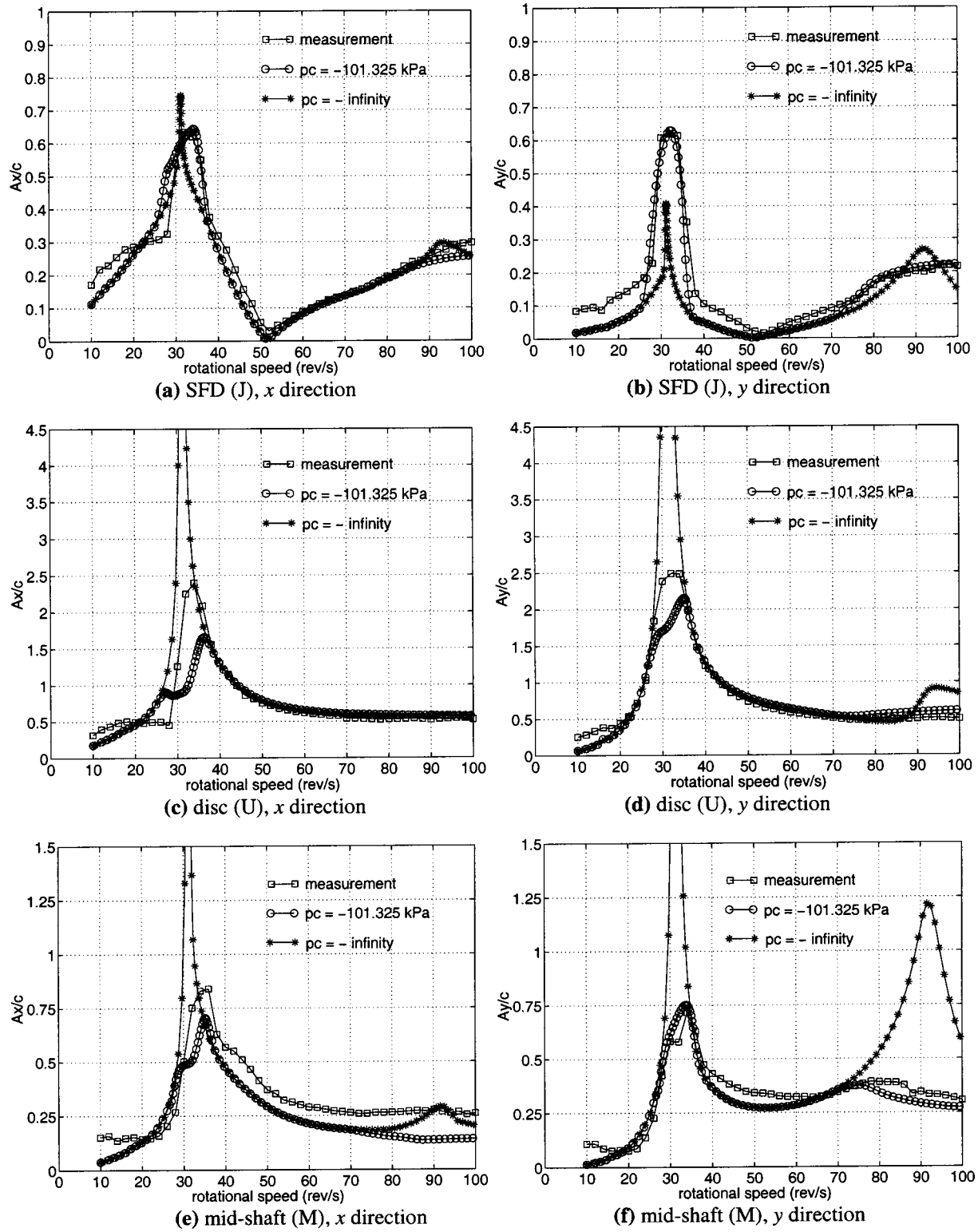

Fig. 10 Unbalance response for X_{J0}/c, $Y_{J0}/c = 0, -0.8$ and $U = 5.10 \times 10^{-4}$ kg m. All predictions are RHB $N = 1$, $m = 5$. Vertical axes show ratio of half peak-to-peak displacement to c.

going below absolute zero. In this way, one can study the influence of static eccentricity and unbalance on cavitation within the SFD at a fixed supply pressure (1 bar) and observe how the cavitation affects the predicted vibration levels.

Figures 7(*a*) and (*b*) show the vibration levels at the SFD for a static eccentricity of 0.6 and the lower unbalance ($U = 2.59 \times 10^{-4}$ kgm). It is clear that both the absolute zero pressure cavitation model and the full film model yield virtually identical results, suggesting that negligible cavitation is predicted under such conditions. The predictions for the vibration levels at the other locations of the rotor are consequently very close for both models (Figs. 7(*c*)–(*f*)), with maximum divergence being registered at the disc position (U) in the *y* direction (Fig. 7(*d*)). It should be noted

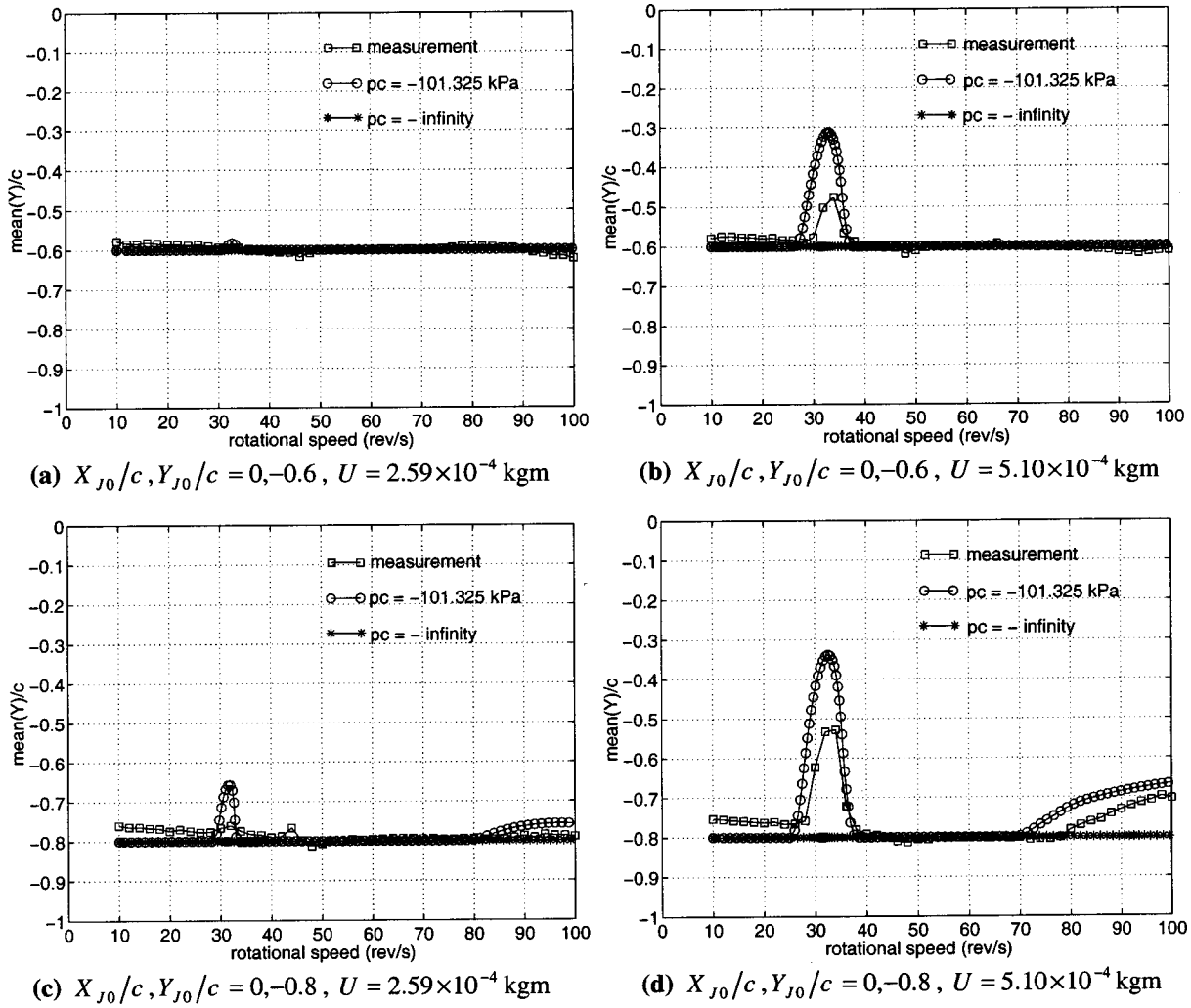

Fig. 11 Variation of normalized mean *y* displacement ($\bar{Y}_J/c$) of J relative to housing center with rotational speed. All predictions are RHB $N=1$, $m=5$.

that in Figs. 7(*a*) and (*c*), which refer to the *x* direction (for which the SFD is centralized), two maxima are observed in both measurement and prediction. The lower predicted maximum is less defined, especially for the SFD *x* vibration, Fig. 7(*a*). These maxima may be related to the undamped natural frequencies of the test rig (14, 40 rev/s). In the *y* direction (in which the SFD is offset), Figs. 7(*b*), (*d*), and (*f*), the first maximum is entirely absent from the prediction, while the second one is predicted at a lower speed (around 32 rev/s). Hence the predicted behavior in the *y* direction is more akin to the pin-pin configuration of the test rig (i.e., with SFD locked, where the first critical speed is 31 rev/s). Figure 8 shows the effect of nearly doubling the previous unbalance to $U=5.1\times10^{-4}$ kg m for the same static eccentricity of 0.6. Large discrepancies emerge between the cavitated and uncavitated model predictions within the range 28–36 rev/s. As previously discussed, this means that within this speed range, in the full film model, the oil film would support a region below absolute zero pressure (i.e., absolute tension) and hence cavitation would occur in the absolute zero cavitation model. Within the zone of maximum amplitude, 30–34 rev/s, the full film model predicts extremely high vibration in the *y* direction at positions other than the SFD (i.e., at U and M), which were not observed in the measurements. In the *x* direction, the uncavitated predictions for the vibration at U and M are extremely large in the immediate vicinity of 31 rev/s. Figure 9 shows the vibration levels for the higher static eccentricity of 0.8 and the lower unbalance ($U=2.59\times10^{-4}$ kg m). It shows that differences between the predictions from the two SFD models appear in the vicinity of 31 rev/s and, for M in the *y* direction, beyond 80 rev/s as well (Fig. 9(*f*)). This effect becomes more striking at the higher unbalance ($U=5.1\times10^{-4}$ kg m) for the same static eccentricity (0.8), Fig. 10. Large differences between the predictions from the two SFD models emerge not just in the 27–37-rev/s zone, but for the *y* direction especially, above 70 rev/s (Figs. 10(*b*), (*d*), and (*f*)). This implies an additional predicted cavitation regime.

From the full film unbalance response predictions in Figs. 8–10, it is evident that as the static eccentricity and/or unbalance is increased, an uncavitated SFD (i.e., a full film) would cause the rotor to behave in certain speed ranges as though it were pinned at the SFD journal J. This tendency is especially strong in the *y* direction at the higher static eccentricity (0.8): the critical speeds tend to 31 rev/s for the static eccentricity of 0.6, and 31 and 91 rev/s for the static eccentricity of 0.8. However, the truncation of the pressure in the SFD at absolute zero (i.e., the model used for cavitation) mitigates this effect and maintains the predicted vibration within safe limits at all positions along the rotor. In the case of the static eccentricity of 0.8, cavitation completely attenuates the predicted peak at the second pin-pin critical speed of 91 rev/s (Fig. 10(*f*)), which agrees more closely with measurement. The reason for this striking difference in vibration amplitudes predicted by the two SFD models is a direct consequence of the centralizing effect cavitation has on the SFD journal. Cavitation in

an eccentric damper produces a steady component of displacement counter to the direction of the static offset. In Ref. [18] it is shown that an uncavitated squeeze film that is unsupported by a parallel retainer spring cannot produce a sustained lift to counter the gravity load. In the present case, the full film model does not produce any lift (of the mean position of vibration) from the statically offset position of J. Hence, as the static eccentricity and/or unbalance are increased, the vibration is limited by the clearance circle (i.e., there is less room for vibration) and the SFD forces become very large, especially in the *y* direction (the direction of the offset), but also at the limits of the *x* vibration. These large SFD forces would render the SFD ineffective, and the resulting effect at the other locations M and U would approach that obtained by locking the SFD. However, in the present case, this adverse effect is prevented by the centralising effect of cavitation.

Figure 11 shows the variation of the mean *y* displacement at the SFD (i.e., $\overline{Y}_J/c$ in Eq. (6*b*)) with rotational speed for four different conditions. It is clear that, under all conditions, the full film model produces no lift from the static position. On the other hand, the cavitation regimes are clearly defined by those speed ranges where the absolute zero pressure cavitation prediction rises from the static position. The measurements in Fig. 11 follow the trend predicted by the absolute zero pressure cavitation model. In fact, approximately over the cavitation regimes predicted in Fig. 11, pinhole bubbles were observed within the oil flowing out of the damper, indicating cavitation, and these observations tend to agree with those made in a previous investigation [17]. Since no amplitude jump was observed on runup, it is presumed that these bubbles were due to the release of air that was previously dissolved in the oil in the sump, rather than the result of air ingestion into the SFD from the ambient. Despite the presence of such bubbles, Figs. 7–11 show that, overall, the assumption of an incompressible film rupturing at absolute zero pressure gives satisfactory predictions for the vibration levels.

It is noted that Figs. 8(*a*) and (*b*), 9(*a*) and (*b*), and 10(*a*) indicate that the amplitude at the SFD in the immediate vicinity of 31 rev/s (first pin-pin critical speed) is greater with the full film than with the cavitated film. This may at first appear to contradict previous studies, e.g., Ref. [4], which show that an uncavitated film results in a smaller SFD journal orbit than a cavitated one. However, it is very important to note that studies like Ref. [4] were restricted to rigid rotors and their results should not be extended to rotor vibration in the region of the flexural critical speeds. It is noted that a similar effect to that observed in Figs. 8(*a*) and (*b*)–10(*a*) and (*b*) at 31 rev/s would be obtained if the SFD and retainer spring were replaced by a very large but still finite stiffness: since the right hand node of the resulting system will not be located exactly at J, in the absence of any other damping in the system a spike at 31 Hz would appear in the frequency response function $\alpha_{JU}(\omega)$ (see Eq. (*A*4) of the Appendix). Hence it would appear that in the region of 31 rev/s, the uncavitated SFD force has a very large equivalent stiffness coefficient and very small equivalent damping coefficient, most probably due to the vibration being limited by the clearance circle due to the lack of lift from the eccentric static position, as observed earlier.

In Figs. 7–10, the very low level in the SFD vibration at 50–52 rev/s corresponds to the antiresonance at 52 Hz in the calculated transfer receptance function between J and U for the linear subsystem (i.e., $\alpha_{JU}(\omega)$ in Fig. 3). At 50–52 rev/s, the measured orbit at J was practically a "dot" of amplitude much less than the static runout there. This indicates that the runout at J has little or no effect on the alternating part of the displacement, i.e., the runout is a purely static or, at worst, a low frequency (quasistatic) phenomenon.

Conclusions

A recently developed receptance harmonic balance technique has been applied to a flexible rotor rig fitted with an eccentric squeeze film damper with the aim of studying its interaction with an unbalanced rotor. For a fixed supply pressure, it is concluded that cavitation is promoted by increased static eccentricity and/or unbalance. For the configuration studied, the centralising effect of such cavitation is seen to be beneficial in that it prevents excessive vibration along the shaft. Hence for a statically determinate flexible rotor-rigid pedestal system with a SFD at one of its bearings it is not recommended that cavitation be suppressed by increasing the supply pressure or removing dissolved air in the sump, under conditions of high static eccentricity and unbalance.

Nomenclature

$a_{XJ}^{(s)}$, $a_{YJ}^{(s)}$ = Displacement cosine coefficients
A_x, A_y = *x*, *y* half peak-to-peak displacements (m)
$b_{XJ}^{(s)}$, $b_{YJ}^{(s)}$ = Displacement sine coefficients
c = Radial clearance (m)
$\mathbf{f}$ = Nonlinear vector function of $\mathbf{v}$
L = Land length (m)
m = Total number of harmonics
N = Positive integer
$p(\theta,z)$ = Pressure distribution (Pa, gauge)
p_c = Cavitation pressure (Pa, gauge)
$p_t(\theta,z)$ = Truncated pressure distribution (Pa, gauge)
p_S = Supply pressure (Pa, gauge)
$p_x^{(s)}$, $p_y^{(s)}$ = SFD force cosine coefficients
P = Arbitrary position on rotor
$q_x^{(s)}$, $q_y^{(s)}$ = SFD force sine coefficients
q_{xr}, q_{yr} = *x*, *y* modal coordinates for mode no. *r*
Q_R, Q_T = Radial, tangential SFD forces (N)
Q_x, Q_y = Cartesian SFD forces (N)
Q_x, Q_y = Mean SFD forces (N)
R = Bearing housing bore radius (m)
s = Harmonic number
t = Time (s)
U = Unbalance (kg m)
$\mathbf{v}$ = Vector of response Fourier coefficients
x, y, z = Cartesian axes
X_J, Y_J = Cartesian coordinates of J relative to B (m)
X_{J0}, Y_{J0} = Static values of X_J, Y_J (m)
X_J, Y_J = Mean values of X_J, Y_J (m)
z = SFD axial dimension (m)
η = Viscosity ($\mathrm{N\,s\,m^{-2}}$)
ε = Nondimensional eccentricity, $=\sqrt{X_J^2+Y_J^2}/c$
ψ = Attitude angle (rad)
ϖ = Fundamental frequency (rad/s)
Ω = Rotational speed (rad/s)
Γ = Period of response, $=2\pi/\varpi$ (s)
$\alpha_{ij}(s\varpi)$, $\beta_{ij}(s\varpi)$ = Receptance functions (m/N)
δ_{Ns} = $=0$ for $s\neq N$, $=1$ for $s=N$
θ = SFD angular dimension (rad)
ω_{xr}, ω_{yr} = *x*, *y* natural frequencies for mode no. *r*
$\phi_P^{(xr)}$, $\phi_P^{(yr)}$ = *x*, *y* mode shapes at P for mode no. *r*
∞ = Infinity

Appendix

The first four modes of the linear subsystem (i.e., the rotor pinned at H, sprung at J) in each plane *xz*, *yz* were considered. Hence the modal equations can be written as

$$\ddot{q}_{xr}+\omega_{xr}^2 q_{xr}=\phi_J^{(xr)}Q_x(X_J,Y_J,\dot{X}_J,\dot{Y}_J)+\phi_U^{(xr)}U\sin\Omega t, \quad (A1a)$$

Table 3 Undamped modal parameters for linear part in one plane of vibration

Mode no. r	$\omega_{xr}/(2\pi)$ (Hz)	$\phi_J^{(xr)}\phi_J^{(xr)}$ ($\times 10^{-3}$ kg^{-1})	$\phi_J^{(xr)}\phi_U^{(xr)}$ ($\times 10^{-3}$ kg^{-1})	$\phi_J^{(xr)}\phi_M^{(xr)}$ ($\times 10^{-3}$ kg^{-1})
1	13.74	54.220	77.796	18.152
2	40.40	38.495	−34.148	43.012
3	173.86	251.269	−38.753	−131.688
4	334.68	106.073	−13.540	72.685

$$\ddot{q}_{yr}+\omega_{yr}^2 q_{yr}=\phi_J^{(yr)}Q_y(X_J,Y_J,\dot{X}_J,\dot{Y}_J) - \phi_U^{(yr)}U\cos\Omega t, \quad \text{where } r=1,\ldots,4. \tag{A1b}$$

In the above equations, ω_{xr}, ω_{yr}, $r=1,\ldots,4$ are the natural frequencies in the xz and yz planes, respectively, and $\phi_P^{(xr)}$, $\phi_P^{(yr)}$ are the corresponding mass-normalized mode shapes, evaluated at position P in the x and y directions, respectively. Note that $\omega_{xr}=\omega_{yr}$ and $\phi_P^{(xr)}=\phi_P^{(yr)}$. In Eqs. (*A*1*a*) and (*A*1*b*), the SFD forces are evaluated from Eqs. (1) and (2) with

$$X_J=X_{J0}+\sum_{r=1}^{4}\phi_J^{(xr)}q_{xr}, \tag{A2a}$$

$$Y_J=Y_{J0}+\sum_{r=1}^{4}\phi_J^{(yr)}q_{yr}. \tag{A2b}$$

The displacement response at a general position P, measured from its static position, is given by

$$X_P=\sum_{r=1}^{4}\phi_P^{(xr)}q_{xr}, \tag{A3a}$$

$$Y_P=\sum_{r=1}^{4}\phi_P^{(yr)}q_{yr}. \tag{A3b}$$

The evaluation of the modal parameters in Eqs. (*A*1) (i.e., natural frequencies and mode shapes) is now considered. The natural frequencies were found from the resonance locations of a typical receptance function. Knowing these frequencies, the required mode shapes were then determined by fitting the four modes to the exact receptance function (computed by the mechanical impedance method) over a range of frequencies using the truncated series expansion [19]:

$$\alpha_{ij}(\omega)\approx\sum_{r=1}^{4}\frac{\phi_i^{(xr)}\phi_j^{(xr)}}{\omega_{xr}^2-\omega^2}. \tag{A4}$$

The relevant modal parameters (which are the same for either plane) are given in Table 3.

Equations (*A*1) were expressed in terms of 16 first-order differential equations and solved using a standard numerical integration routine suitable for numerically ''stiff'' differential equations [20].

References

[1] De Santiago, O., San Andrés, L. A., and Oliveras, J., 1999, ''Imbalance Response of a Rotor Supported on Open-Ends, Integral Squeeze Film Dampers,'' ASME J. Eng. Gas Turbines Power, **121, 4**, pp. 718–724.

[2] Zeidan, F., and Vance, J., 1990, ''Cavitation and Air Entrainment Effects on the Response of Squeeze Film Supported Rotors,'' ASME J. Tribol., **109**, pp. 149–154.

[3] Yakoub, R. Y., and El-Shafei, A., 2001, ''The Nonlinear Response of Multimode Rotors Supported on Squeeze Film Dampers,'' ASME J. Eng. Gas Turbines Power, **123**, pp. 839–848.

[4] El-Shafei, A., and Eranki, R. V., 1994, ''Dynamic Analysis of Squeeze Film Damper Supported Rotors Using Equivalent Linearisation,'' ASME J. Eng. Gas Turbines Power, **116**, pp. 682–691.

[5] Bonello, P., Brennan, M. J., and Holmes, R., 2002, ''Non-Linear Modelling of Rotor Dynamic Systems With Squeeze Film Dampers—An Efficient Integrated Approach,'' J. Sound Vib., **249**(4), pp. 743–773.

[6] Chu, F., and Holmes, R., 1998, ''The Effect of Squeeze Film Damper Parameters on the Unbalance Response and Stability of a Flexible Rotor,'' ASME J. Eng. Gas Turbines Power, **120**, pp. 1–9.

[7] Chu, F., and Holmes, R., 2000, ''The Damping Capacity of the Squeeze Film Damper in Suppressing the Vibration of a Rotating Assembly,'' Tribol. Int., **33(2)**, pp. 81–97.

[8] Chu, F., 1993, *The Vibration Control of a Flexible Rotor by Means of a Squeeze Film Damper*, Ph.D. thesis, University of Southampton, UK.

[9] Feng, N. S., and Hahn, E. J., 1985, ''Density and Viscosity Models for Two-Phase Homogeneous Hydrodynamic Damper Fluids,'' ASLE Trans., **29**(3), pp. 361–369.

[10] Feng, N. S., and Hahn, E. J., 1987, ''Effects of Gas Entrainment on Squeeze Film Damper Performance,'' ASME J. Tribol., **109**, pp. 149–154.

[11] Diaz, S. E., and San Andrés, L. A., 1998, ''Measurements of Pressure in a Squeeze Film Damper With an Air/Oil Bubbly Mixture,'' STLE Tribol. Trans., **41**(2), pp. 282–288.

[12] Sykes, J. E. H., and Holmes, R., 1990, ''The Effects of Bearing Misalignment on the Non-linear Vibration of Aero-engine Rotor-Damper Assemblies,'' Proc. Inst. Mech. Eng., Part G: J. Aerospace Eng., **204**(2), pp. 83–99.

[13] Neubert, V. H., 1987, *Mechanical Impedance: Modelling/Analysis of Structures*, Naval sea systems command, Code NSEA-55N.

[14] Bonello, P., and Brennan, M. J., 2001, ''Modelling the Dynamic Behavior of a Supercritical Rotor on a Flexible Foundation Using the Mechanical Impedance Technique,'' J. Sound Vib., **239**(3), pp. 445–466.

[15] Seydel, R., 1988, *From Equilibrium to Chaos: Practical Bifurcation and Stability Analysis*, Elsevier Science, New York.

[16] San Andrés, L. A., and Vance, J. M., 1986, ''Effects of Fluid Inertia and Turbulence on the Force Coefficients for Squeeze Film Dampers,'' ASME J. Eng. Gas Turbines Power, **108**, pp. 332–339.

[17] Burghardt, M., 1998, *An Investigation of The Squeeze Film Damping of A Super-Critical Rotor*, M.Sc. thesis, University of Southampton, UK.

[18] Humes, B., and Holmes, R., 1978, ''The Role of Subatmospheric Film Pressures in the Vibration Performance of Squeeze-Film Bearings,'' J. Mech. Eng. Sci., **20** (5), pp. 283–289.

[19] Ewins, D. J., 1984, *Modal Testing: Theory and Practice*, Research Student Press, Letchworth, UK.

[20] The Mathworks Inc., 1999, MATLAB®, Version 5.3.1.29215a (R11.1).

The Oxidation of Metal Alloy Foils in the Presence of Water Vapor

James M. Rakowski
Allegheny Ludlum Technical Center,
Alabama and Pacific Avenues,
Brackenridge, PA 15014-1597

Water vapor can be detrimental to the elevated temperature oxidation resistance of alloys that rely on the formation of a protective chromium oxide layer. The resulting degradation can be significant, particularly when such alloys are in the form of light gauge sheet and strip. Long-term test results will be presented for commercially available wrought austenitic stainless steels and nickel-base superalloys exposed at 1300°F and 1400°F in environments containing various levels of water vapor. [DOI: 10.1115/1.1787508]

Introduction

Basic 18Cr-8Ni austenitic stainless steels are often specified for use at elevated temperatures because they retain significant mechanical strength and exhibit resistance to creep deformation, particularly when alloyed with carbide-forming and solid-solution-strengthening elements. They are relatively resistant to oxidation but are not truly heat resistant alloys—the risk of breakaway oxidation must be considered when selecting them for certain elevated temperature applications, particularly when they are used in thin sections. Breakaway oxidation can occur when chromium is depleted from the substrate to the extent that damage to the protective oxide layer will not heal. A thin foil, which has an intrinsically high surface area to volume ratio, can be rapidly depleted in chromium during oxidation when compared to a heavy section. The result is that a disruption in the initially formed chromia scale can result in rapid oxidation and subsequent degradation of the foil.

Water vapor is encountered as a minor component in ambient air and in larger concentrations as a by-product of combustion processes. It has been known for some time that the presence of water vapor in oxidizing environments can alter the degradation process for many different metals [1]. When present in oxygen-bearing atmospheres or as the primary oxidant, water vapor appears to hasten the onset of rapid oxidation of Fe-Cr and Fe-Ni-Cr alloys at elevated temperatures [2–23]. The results vary from study to study, but general trends are that the presence of water vapor accelerates the rate of oxidation, leads to the formation of layered scales, and increases the amount of chromium required to form a protective oxide film.

One mechanism proposed for the actions of water vapor on several systems is the increase in the rate of formation of volatile species [24,25]. Chromium oxide evaporates in the absence of water vapor as gaseous chromium oxides, an effect most pronounced at elevated temperatures (>1000°C). Recent work on austenitic stainless steels has shown that water vapor can increase the evaporative rate loss to levels where it is significant at lower temperatures, particularly in rapidly flowing gas streams, due to the formation of volatile oxy-hydroxides such as $CrO_2(OH)_2$ [26,16–19].

Recent studies on 18Cr-8Ni stainless-steel thin foils found that a thin chromium oxide layer is established on the sample surface during initial exposure to air containing water vapor. The amount of chromium incorporated into this scale is not significant enough to result in breakaway oxidation due solely to chromium depletion of the substrate. Rapid weight gain occurs due to the formation and growth of mixed oxide nodules. These nucleate after an incubation time and then spread, consuming the initially formed protective oxide layer. This is supported by the finding that remnants of the initial chromium oxide layer survive on heavily degraded samples. It is unclear if the nodules form as a direct result of the action of water vapor or if it plays a role in inhibiting healing of flaws, cracks, and spalled regions by the formation of new chromium oxide [21,22].

Experimental Procedure

Oxidation test samples were prepared from commercially obtained stainless steel and nickel-base superalloy foils ranging from 75 to 100 μm (0.0035 to 0.0040 in.) thick. The sample coupons were left in the mill-finished bright annealed condition, commonly referred to commercially as a 2BA surface finish. Some material was prepared at the Allegheny Ludlum Technical Center. Ingots weighing fifty pounds were vacuum induction melted and processed to foil using laboratory-scale hot and cold rolling mills. The finished laboratory-produced foil is similar in nature to production material with respect to composition, grain size, surface finish, etc. All samples were degreased, rinsed in acetone, and dried in hot air prior to testing.

Samples were exposed at 1300°F and 1400°F (704°C and 760°C) in both ambient laboratory air and in air containing a deliberate addition of water vapor. Samples were tested in ambient air, which contains approximately 0.5% water vapor by volume, in large box furnaces. Gas flow in such furnaces was solely by convection. Exposures in air containing a controlled addition of water vapor were done in retort tube furnaces. The gas flow velocity in these furnaces was relatively low at 0.004 ft/s (0.0012 m/s) and directional. The water vapor contents were fixed at 7% and 10% by volume, corresponding to dew points of 102°F (39°C) and 115°F (46°C), respectively. Details of water vapor addition were discussed in a previous publication [21]. The rate of oxidation was measured by periodic weighing of the samples using a semi-microanalytical balance with a resolution of 0.01 mg. The average thermal cycle length due to sample weighing was about 160 h.

Results: Austenitic Stainless Steels

UNS S34700, a niobium (columbium) stabilized 18Cr-8Ni stainless steel commonly referred to as Type 347, was used as a baseline. Type 347 steel oxidizes slowly in ambient air (Fig. 1). When plotted against the square root of time, the weight change kinetics are essentially linear. This indicates that the growth rate is controlled by diffusion through a thin, compact chromium-rich oxide scale. Samples tested at 1400°F did exhibit a shift to a slightly higher rate after about 1000 h of exposure, but did not exhibit accelerated oxidation.

The addition of water vapor resulted in much higher weight gains for Type 347 steel (Fig. 2). Oxidation was initially rapid and then slowed considerably. The samples exposed in air+10% water

Contributed by the International Gas Turbine Institute (IGTI) of THE AMERICAN SOCIETY OF MECHANICAL ENGINEERS for publication in the ASME JOURNAL OF ENGINEERING FOR GAS TURBINES AND POWER. Paper presented at the International Gas Turbine and Aeroengine Congress and Exhibition, Atlanta, GA, June 16–19, 2003, Paper No. 2003-GT-38059. Manuscript received by IGTI, October 2002, final revision, March 2003. Associate Editor: H. R. Simmons.

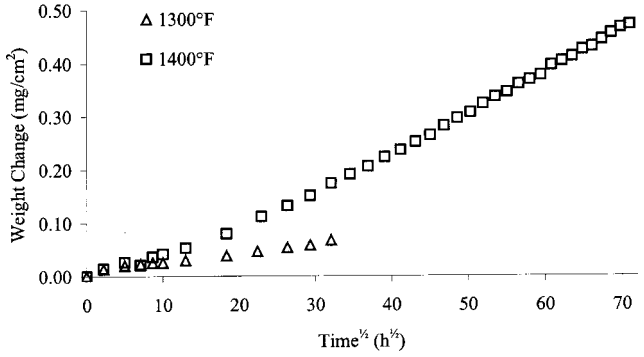

Fig. 1 Oxidation of Type 347 in ambient air

vapor gained less weight than samples exposed in air+7% water vapor. The weight gain was higher at 1400°F than at 1300°F, as would be expected.

The surfaces of the samples oxidized at 1300°F were covered with a mixture of iron and chromium oxides (Fig. 3). The fine-grained low-lying areas were relatively rich in chromium while the smooth raised areas were essentially pure iron oxide.

The sample exposed at 1400°F in air+7% water vapor was visually distinct from the two samples exposed at 1300°F. It was dark matte brown in color rather than a lustrous silvery gray. When examined in the scanning electron microscope (SEM), the surface is relatively uniform except for numerous shallow surface pits. Microchemical analysis revealed that the surface was very rich in iron (Fig. 4).

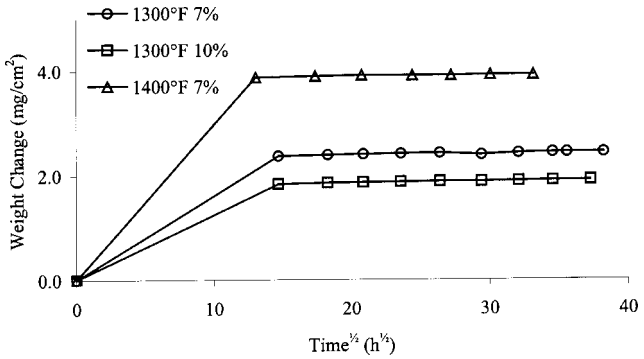

Fig. 2 Effect of water vapor on the oxidation of Type 347

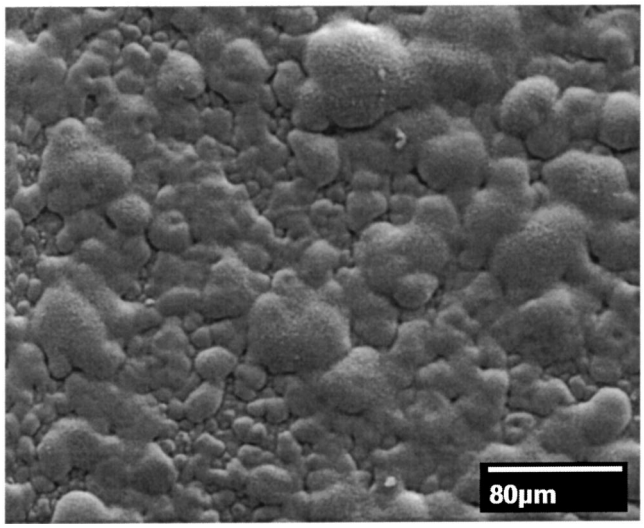

Fig. 3 SEM micrograph of the surface of Type 347 after 1000 h at 1300°F in air+10% water vapor

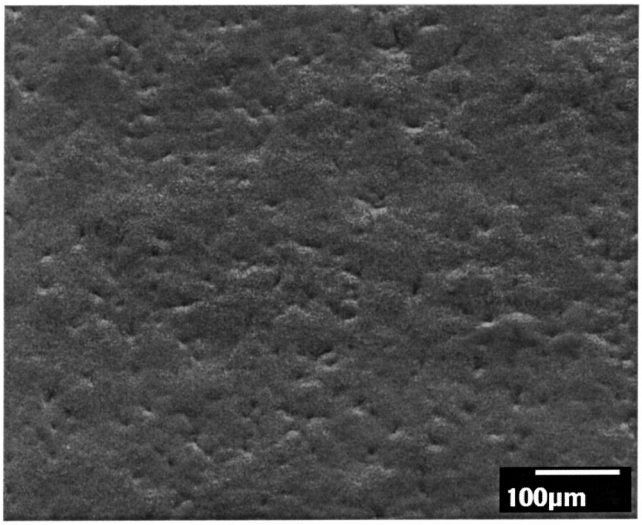

Fig. 4 SEM micrograph of the surface of Type 347 after 1000 h at 1400°F in air+7% water vapor

Previous tests using the same general exposure conditions were run on Type 347 steel in a gas-tight box furnace with an interior volume of about 1 ft^3 (0.03 m^3) [21]. The gas flow velocity in such a large chamber is essentially zero and is nondirectional. Testing under such conditions resulted in a significant lag before accelerated oxidation began when compared to tests performed in the tube furnaces (Fig. 5).

UNS S30215, commonly referred to as Type 302B steel, has similar nickel and chromium levels as Type 347, with the addition

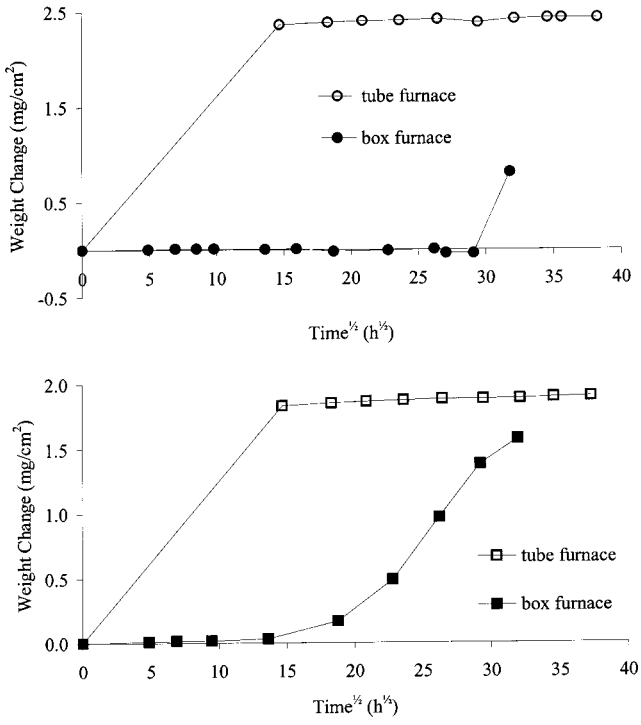

Fig. 5 Effect of flow rate on the oxidation of Type 347 in air containing water vapor at 1300°F (top—7% water vapor; bottom—10% water vapor)

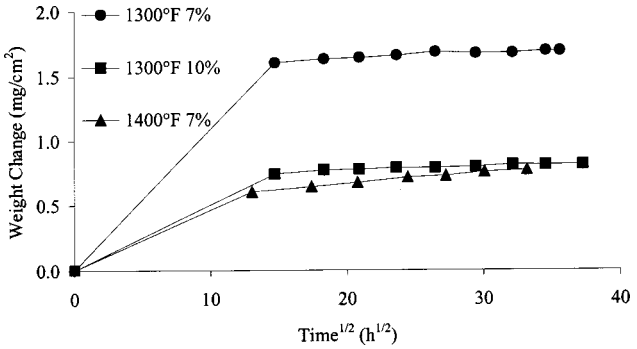

Fig. 6 Effect of water vapor on the oxidation of Type 302B (high silicon)

of about 2.5% silicon by weight (replacing iron). The Type 302B samples did not offer significantly better oxidation resistance than Type 347 (Fig. 6).

The surfaces of the Type 302B samples exposed at 1300°F looked very similar to their Type 347 counterparts (Fig. 7). The Type 302B sample exposed at 1400°F in air+7% water vapor exhibited regions of heavy spallation, which appears to be taking place between the iron-rich oxide cap and a chromium-rich oxide sublayer (Fig. 8).

The role of chromium in iron-base alloys was investigated by melting and processing a laboratory-scale quantity of a model austenitic stainless steel containing about 21% chromium by weight. Accelerated oxidation was not observed after several thousand hours of exposure (Fig. 9).

Metallographic observations revealed that the oxide scale is thin and compact after 1500 h of exposure. Microchemical analysis in the SEM reveals that the oxide is primarily chromium-rich, with some iron segregated to the scale/gas interface. Note that the oxide is less than 1 μm thick, so independent microanalysis is difficult to perform. Both samples exposed at 1300°F exhibit oxide thickening over metal grain boundaries (Fig. 10).

The oxide is somewhat more uniform on the 1400°F sample (Fig. 11). Microchemical analysis in the SEM indicates that the oxide is again chromium-rich with iron segregated to the scale/gas interface.

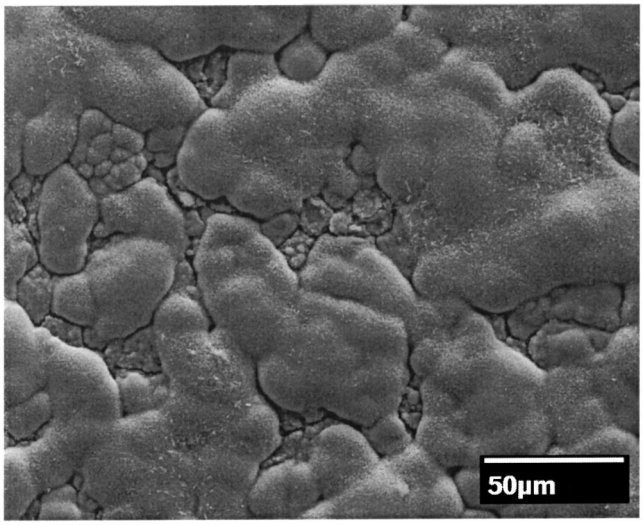

Fig. 7 SEM micrograph of the surface of Type 302B after 1500 h at 1300°F in air+7% water vapor

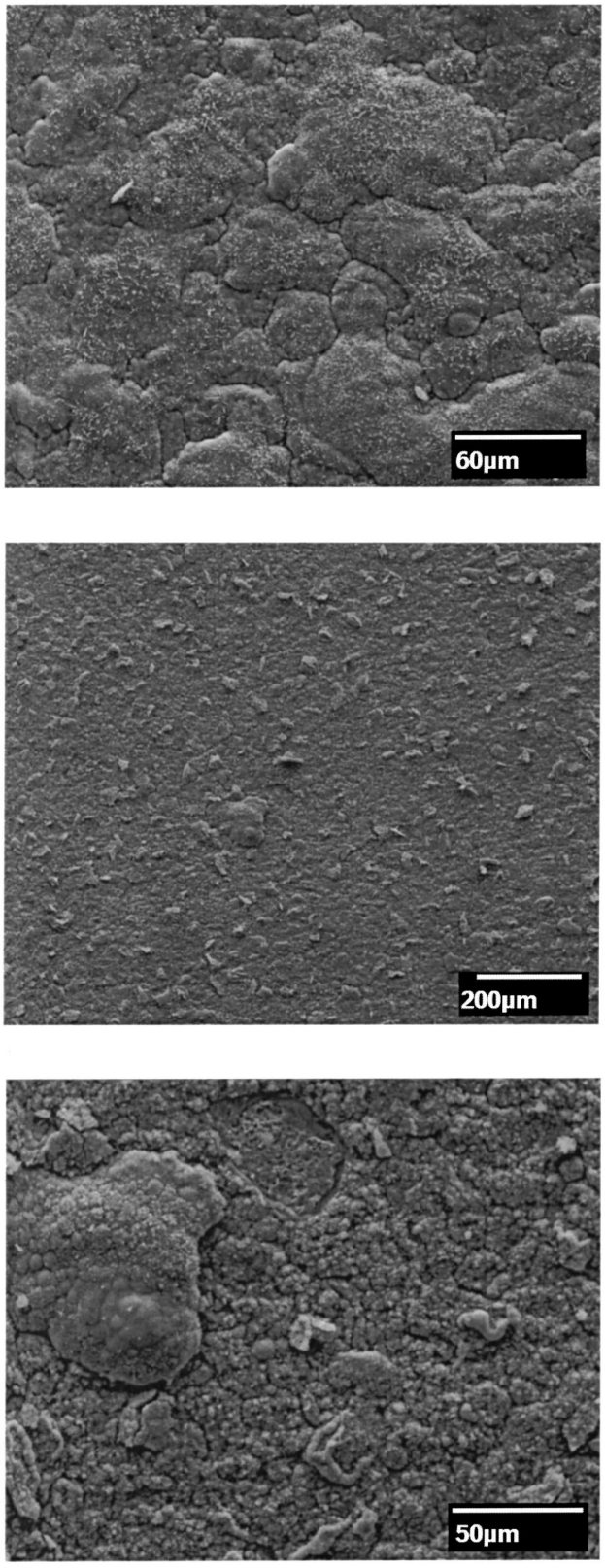

Fig. 8 SEM micrographs of the surface of Type 302B after 1000 h at 1400°F in air+7% water vapor (top—typical; middle and bottom—spalled)

Results: Nickel-Base Alloys

Nickel-base alloys are often specified when conditions are too severe for the application of austenitic stainless steels. Such alloys

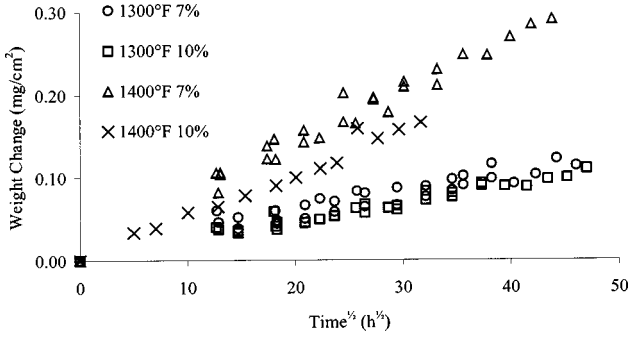

Fig. 9 Effect of higher chromium on the oxidation of austenitic stainless steels in air containing water vapor

are generally more resistant to oxidation and elevated temperature deformation and creep. Two common alloys were examined—UNS N06002 and N06625—which both contain about 21 wt. % chromium (the same as in the model austenitic alloy discussed above) and 9 wt. % molybdenum. The primary difference between the two is in secondary alloying elements. UNS N06002 (commonly referred to as the HX alloy) contains about 18 wt. % iron while UNS N06625 (commonly referred to as the 625 alloy) contains about 3 wt. % niobium and has a relatively low iron content.

The HX alloy samples exhibited resistance to oxidation at 1300°F in air containing water vapor when compared to identical samples exposed in ambient air (Fig. 12). The sample exposed in 7% water vapor appeared to gain a slightly larger amount of weight and the sample exposed in 10% water vapor appeared to gain a slightly smaller amount of weight. The difference was not significant in either case.

Significant deviations from oxidation behavior in ambient air were noted for the HX alloy samples exposed in air containing water vapor at 1400°F (Fig. 13). A gradual weight loss is evident, particularly in air+10% water vapor. Spalling of the samples was not observed (exposures were done in nonmetallic segmented boats that would collect a fraction of spalled scale particles), so it is possible that the weight loss was due to scale volatilization.

The 625 alloy samples deviated slightly from ambient oxidation behavior at 1300°F in air containing water vapor (Fig. 14). The measured weight changes were slightly higher for exposures in air+7% water vapor and air+10% water vapor.

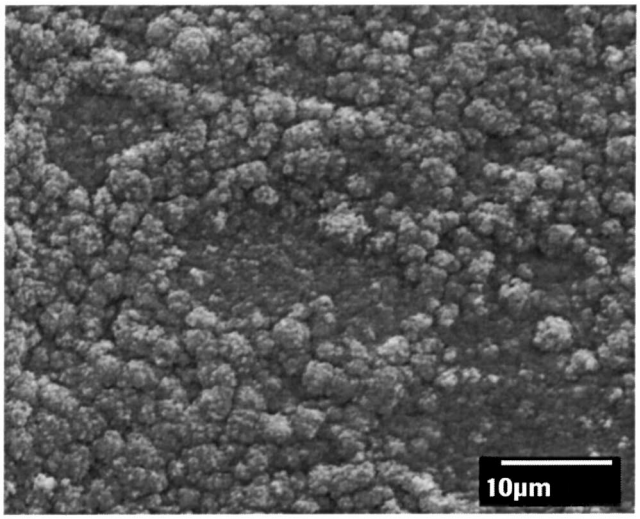

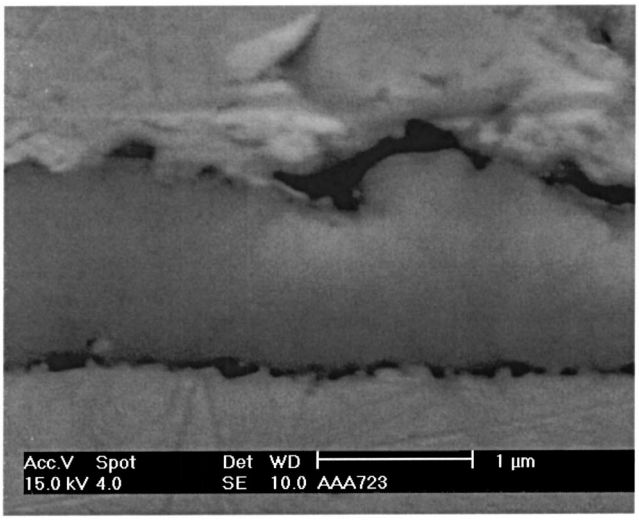

Fig. 11 SEM micrographs of the surface and of the scale in cross section of a high Cr austenitic alloy after 1500 h at 1400°F in air+7% water vapor

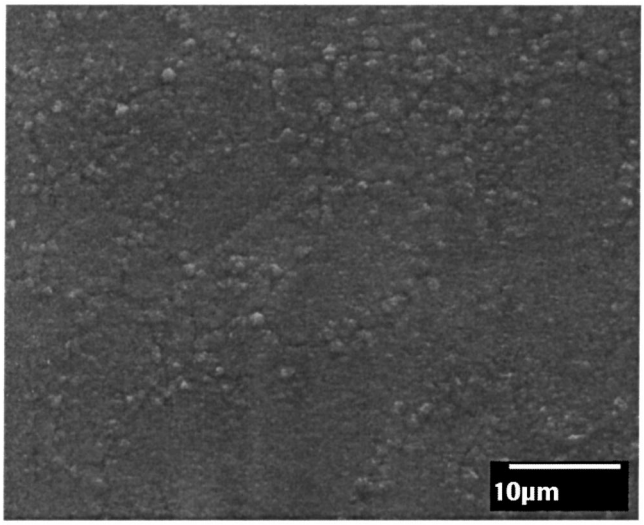

Fig. 10 SEM micrograph of the surface of a high Cr austenitic alloy after 1500 h at 1300°F in air+10% water vapor

Significant deviations from oxidation behavior in ambient air were noted for the 625 alloy samples exposed in air containing water vapor at 1400°F (Fig. 15). The results were similar to those observed for the HX alloy. The 625 alloy sample exposed in air +10% water vapor exhibited a net weight loss after 1000 h.

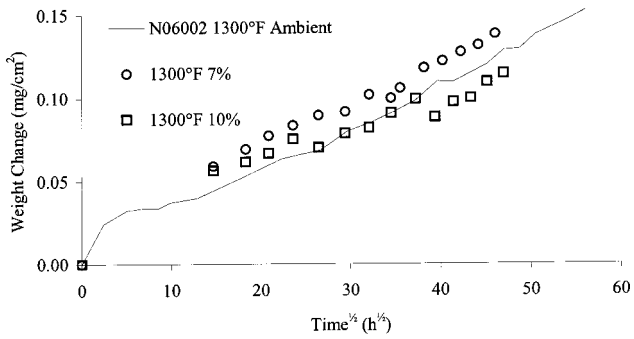

Fig. 12 Effect of water vapor on the oxidation of the HX alloy at 1300°F

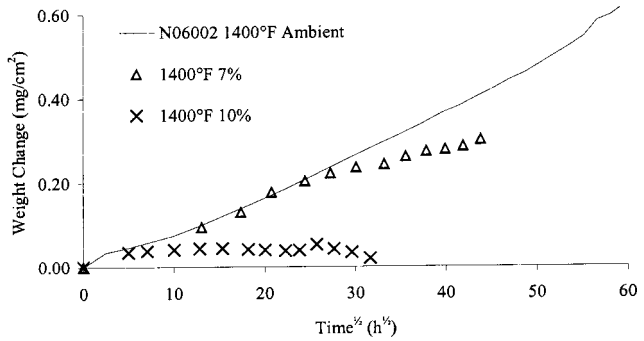

Fig. 13 Effect of water vapor on the oxidation of the HX alloy at 1400°F

Again, spallation of the samples was not observed so it is assumed that the weight loss was due to scale volatilization.

Samples of the 625 alloy were removed from the test and examined after 500 and 1500 h of exposure in humidified air. The samples exposed at 1300°F were covered with a thin oxide (less than 1 μm thick), which is rich in chromium (Fig. 16). Small nickel-rich patches were present at the scale/gas surface.

The oxide scale is thicker at 1400°F and is primarily chromium oxide (Fig. 17). A second phase has formed in the metal beneath the scale, particularly along substrate grain boundaries. Semiquantitiative (standardless) microanalysis in the SEM indicates that the second phase particles are nickel-rich and contain about 25 wt. % niobium. Unambiguous identification of this phase was not carried out. A review of the literature suggests that bulk 625 alloy can form δ phase (Ni_3Nb) under similar time–temperature exposure conditions [26,27]. Internal oxidation of aluminum, particularly along metal grain boundaries was observed after 1500 h at temperature.

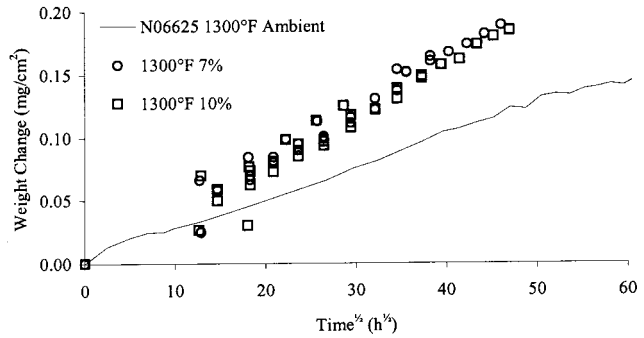

Fig. 14 Effect of water vapor on the oxidation of the 625 alloy at 1300°F

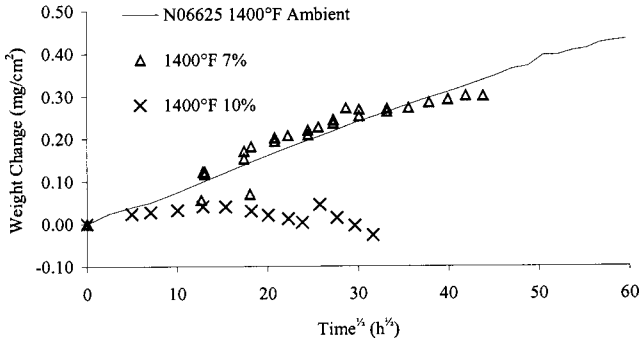

Fig. 15 Effect of water vapor on the oxidation of the 625 alloy at 1400°F

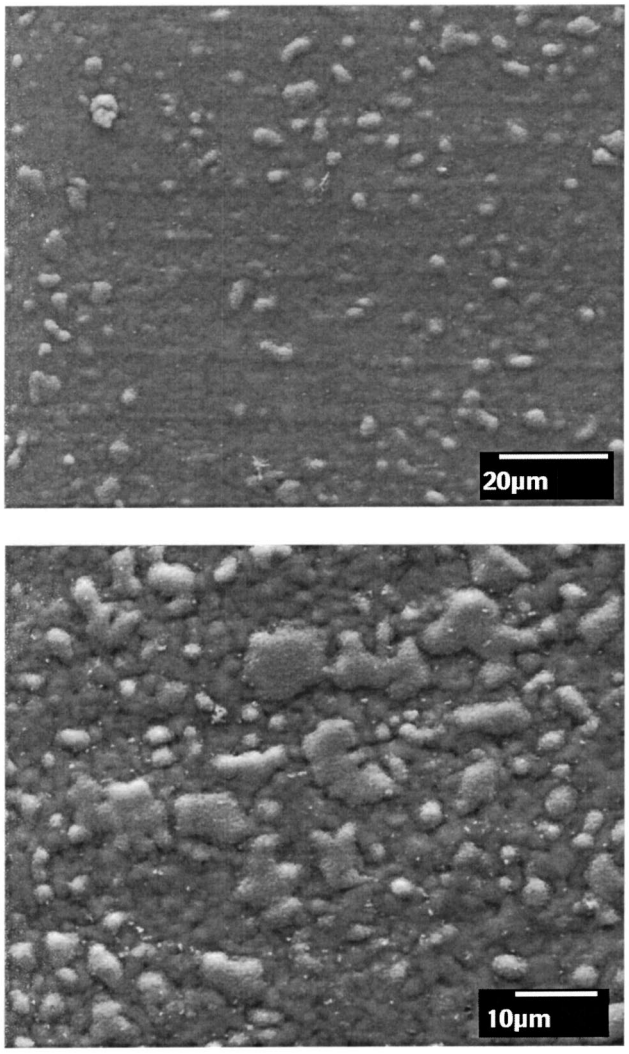

Fig. 16 SEM micrograph of the surface of a 625 alloy sample after 1500 h at 1300°F in air (top—air+7% water vapor; bottom—air+10% water vapor)

X-ray microanalysis in the scanning electron microscope was used to measure the depletion of chromium from the subscale regions of the 625 alloy foil. The results were quantified using a standardless ZAF routine built into the software supplied by the detector manufacturer. The performance of the software routine was checked by analyzing a piece of unexposed 625 alloy foil included in the metallographic mount. The measured composition was in agreement with the known bulk composition of the foil as determined by standard analytical chemistry techniques. No depletion was detected for the samples exposed for 500 h at 1300°F. The samples exposed for 1500 h exhibited limited chromium depletion to a depth of less than 10 μm (Fig. 18). The sample exposed in air+10% water vapor may be slightly more affected than the sample exposed in air+7% water vapor.

Measurable chromium depletion was observed at 4500 and 1500 h of exposure in air+7% water vapor at 1400°F (Fig. 19). Calculations indicate that the measured scale thickness of about 2 μm can account for the observed value for chromium depletion. This indicates that scale evaporation is not causing excessive chromium loss from the metal at 1500 h. This is in agreement with the oxidation data presented in Fig. 15.

The oxidized surfaces of the 625 samples were examined using a scanning Auger microprobe (SAM). The unit used for this analysis is equipped with an ion gun which can sputter a known thick-

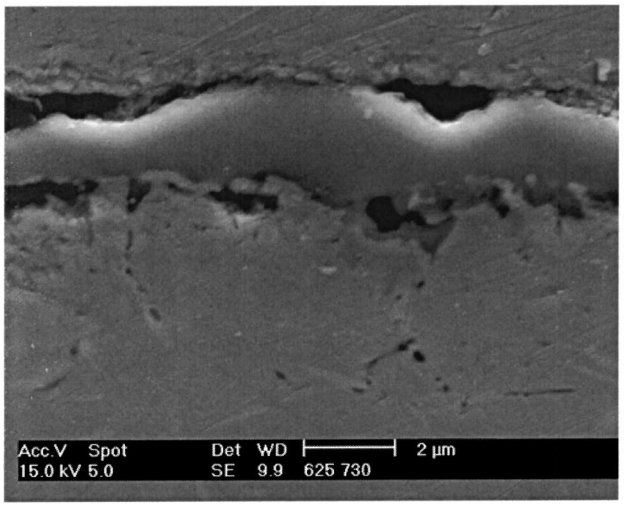

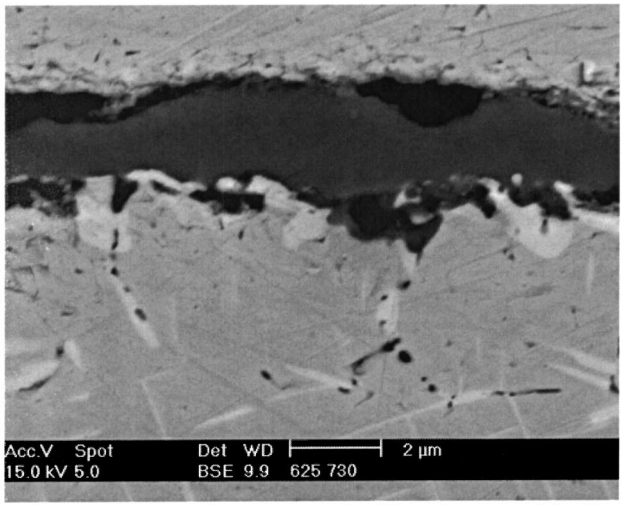

Fig. 17 SEM micrographs (secondary and backscattered electron modes) of the scale in cross section of a UNS N06625 sample after 1500 h at 1400°F in air+7% water vapor

ness of material off of the surface using energetic argon ions. Auger spectra were collected between the sputtering sessions, resulting in depth-resolved sample composition profiles to a depth of more than 1 μm from the original scale/gas interface.

Analysis of the chromium and nickel profiles reveals significant nickel segregation to the scale/gas interface after exposure to hu-

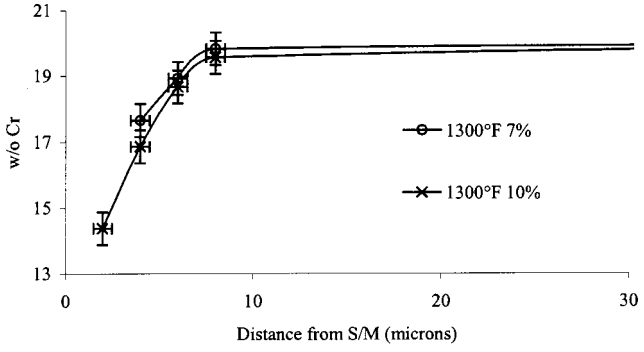

Fig. 18 Chromium profiles as a function of distance from the scale/metal interface for 625 alloy samples exposed for 1500 h at 1300°F (SEM microprobe analysis)

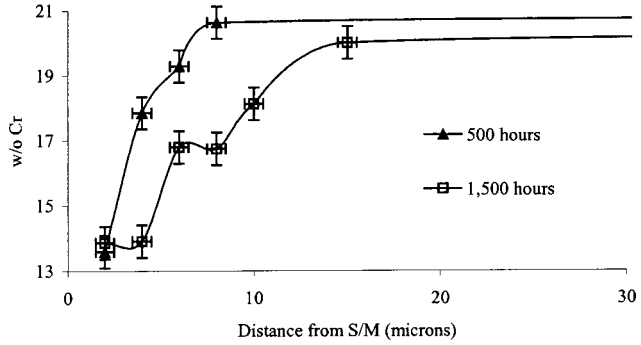

Fig. 19 Chromium profiles as a function of distance from the scale/metal interface for 625 alloy samples exposed at 1400°F (SEM microprobe analysis)

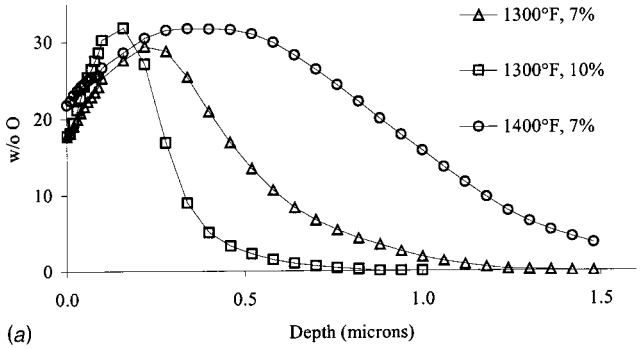

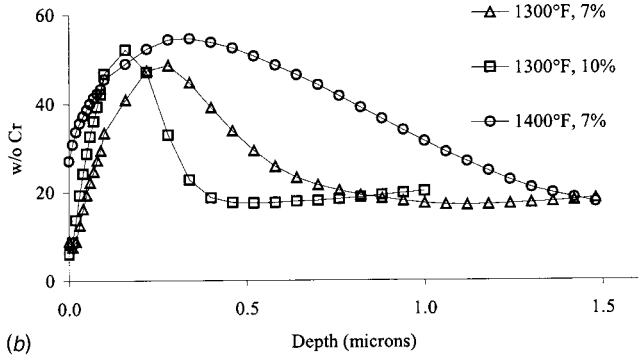

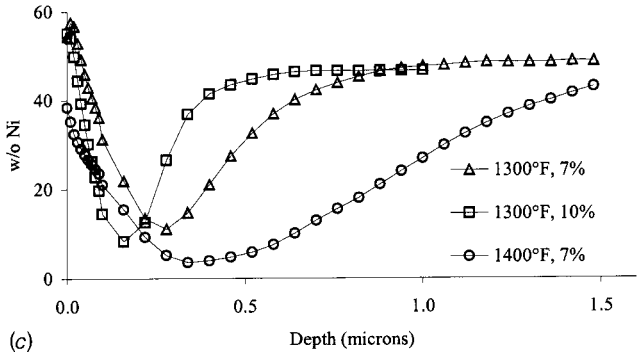

Fig. 20 SAM compositional depth profiles from 625 alloy samples after 500 h exposure in air containing various levels of water vapor (*a*, oxygen; *b*, chromium; *c*, nickel)

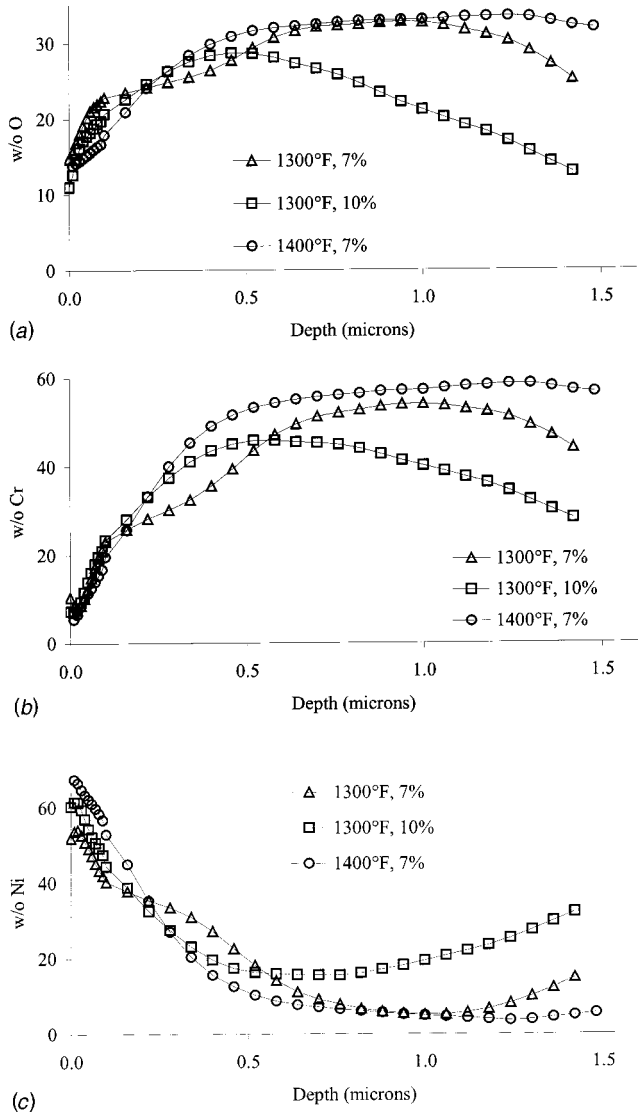

Fig. 21 SAM compositional depth profiles from 625 alloy samples after 1500 h exposure in air containing various levels of water vapor (*a*, oxygen; *b*, chromium; *c*, nickel)

midified air (Fig. 20). A chromium-rich oxide is present adjacent to the metal directly beneath the nickel-rich outer layer. The chromium oxide layer formed on the 625 alloy sample exposed for 500 h in air+7% water vapor at 1300°F was significantly thicker than the chromium oxide layer formed on the sample exposed in air+10% water vapor, as determined by monitoring the location and breadth of the peaks in the oxygen and chromium traces. It is possible that the higher levels of water vapor result in the formation of higher levels of volatile species. The oxide scale formed on the sample exposed at 1400°F in air+7% water vapor is thicker but is otherwise similar to the compositional profiles observed for the scales formed at 1300°F.

The same pattern in oxide thickness observed after 500 h holds true after 1500 h (Fig. 21). The segregation of nickel to the surface appears to be more pronounced. It is unclear whether nickel continues to migrate through the chromia layer or if it were initially present as transient oxide phases and then enriched by the evaporation of chromium-bearing species from the surface.

Conclusions

The presence of water vapor in oxidizing environments has been shown to alter the oxidation behavior of thin stainless steel and nickel-base alloy foils. Low alloy austenitic stainless steels undergo accelerated oxidation due to the formation of a thick outer layer of iron oxide. The severity of attack appears to be dependant on the temperature, the amount of water vapor, and the velocity of the oxidizing gas stream. Increasing the amount of chromium in austenitic stainless steels resulted in improved oxidation resistance, while adding silicon did not.

Water vapor did not result in accelerated oxidation for nickel-base alloys during the duration of the testing. Chromium loss via oxide scale evaporation was a factor, particularly at 1400°F at longer times. Significant chromium depletion was detected in the substrate prior to evaporation becoming significant. This trend is expected to accelerate as the magnitude of the weight loss increases and may lead to increased risk of elevated temperature degradation during extended term applications.

Acknowledgments

This work was partially funded by the Department of Energy under contract DE-FC02-00CH11062. Thanks are owed to Mike Lancet for performing the SAM analysis and to Catherine Kijowski for performing the oxidation testing.

References

[1] Kubaschewski, O., and Hopkins, B. E., 1962, *Oxidation of Metals and Alloys*, Butterworths, London.
[2] Caplan, D., and Cohen, M., 1959, Corrosion (Houston), **15**, pp. 57–62.
[3] Fujii, C. T., and Meussner, R. A., 1963, J. Electrochem. Soc., **110**, pp. 1195–1204.
[4] Fujii, C. T., and Meussner, R. A., 1964, J. Electrochem. Soc., **111**, pp. 1215–1221.
[5] Wood, G. C. et al., 1970, Werkst. Korros., **8**, pp. 900–910.
[6] Graham, H. C., and Davis, H. H., 1971, J. Am. Ceram. Soc., **54.2**, pp. 89–93.
[7] Kvernes, I. et al., 1977, Corros. Sci., **17**, pp. 237–252.
[8] Kofstad, P., 1988, *High Temperature Corrosion*, Elsevier, London.
[9] Khanna, A. S., and Kofstad, P., 1991, *Proceedings of the International Conference Held at the University of Cambridge, March 26–28, 1990*, M. J. Bennett and G. Lorimer, eds, IOM, London.
[10] Chaudanson, H. et al., 1991, *Proceedings of Eurocorr '91 Budapest, October 21–25, 1991*, I. Karl and M. Bod, eds., European Federation of Corrosion, Budapest, Hungary.
[11] Saeki, I. et al., 1995, Corros. Sci., **38**, pp. 19–31.
[12] Jianian, S. et al., 1997, Oxid. Met., **48**, pp. 347–356.
[13] Saeki, I. et al., 1998, Corros. Sci., **40**, pp. 191–200.
[14] Lee, Y. et al., 1996, *Proceedings of the Third International Conference on the Microscopy of Oxidation Held at Trinity Hall the University of Cambridge, September 16–18, 1996*, S. B. Newcomb and J. A. Little, eds., IOM, London.
[15] Ozturk, B., and Matway, R., 1997, ISIJ Int., **37.2**, pp. 169–197.
[16] Asteman, H. et al., 1999, Oxid. Met., **52**, pp. 95–111.
[17] Asteman, H. et al., 2000, Oxid. Met., **54**, pp. 11–26.
[18] Asteman, H. et al., 2002, Oxid. Met., **57**, pp. 193–216.
[19] Asteman, H. et al., 2002, Corros. Sci., **44**, pp. 2635–2649.
[20] Pint, B. A., and Rakowski, J. M., "Paper 00259 Effect of Water Vapor on the Oxidation Resistance of Stainless Steels," in *Proceedings of NACE/2000, Orlando FL, March 26–31, 2000*, NACE International, Houston.
[21] Rakowski, J. M., and Pint, B. A., 2000, "Paper 00517 Observations of the Effect of Water Vapor on the Elevated Temperature Oxidation of Austenitic Stainless Steel Foil," in *Proceedings of NACE/2000, Orlando FL, March 26–31, 2000*, NACE International, Houston.
[22] Rakowski, J. M., 2001, "The Oxidation of Austenitic Stainless Steel Foil in Humidified Air," in *Proceedings of the ASME IGTI Turbo Expo, New Orleans LA, June 4–7, 2001*, ASME International, New York.
[23] Kofstad, P., 1966, *High Temperature Oxidation of Metals*, Wiley, New York.
[24] Meier, G. H., and Birks, N., 1983, *Introduction to High Temperature Oxidation of Metals*, Edward Arnold, London.
[25] Ebbinghaus, B. B., 1993, Combust. Flame, **93**, pp. 119–137.
[26] Radavich, J. F., and Fort, A., 1994, in *Proceedings of the International Symposium on Superalloys 718, 625, 706 and Various Derivatives, Pittsburgh PA, June 1994*, E. Loria, ed., TMS, Warrendale PA, pp. 635–647.
[27] Xie, X. et al., 1990, in *Long Term Stability of High Temperature Materials: Proceedings of a Symposium Sponsored by the High Temperature Alloys Committee and the Physical Metallurgy Committee of the SMD Division of TMS Held During the 1999 TMS Annual Meeting in San Diego, California February 28–March 4, 1999*, G. E. Fuchs et al., eds., TMS, Warrendale PA, pp. 135–146.

Numerical Analysis and Experimental Investigation of a Common Rail-Type Diesel Injector

Marco Coppo
e-mail: marco.coppo@polito.it

Claudio Dongiovanni
e-mail: claudio.dongiovanni@polito.it

Claudio Negri
e-mail: claudio.negri@polito.it

Dipartimento di Energetica,
Polecnico di Torino,
Turin, Italy

A production common rail-type injector has been investigated via numerical simulation and experimentation. The functioning principle of the injector has been carefully analyzed so as to obtain a mathematical model of the device. A zero-dimensional approach has been used for modeling the injector, thus considering the variables as function of time only. The analysis of the hydraulic part of the injector resulted in the definition of an equivalent hydraulic scheme, on which basis both the equations of continuity in chambers and flow through nozzles were written. The connecting pipe between common rail and injector, as well as the injector internal line, were modeled according to a one-dimensional approach. The moving mechanical components of the injector, such as needle, pressure rod, and control valve have been modeled using the mass-spring-damper scheme, thus obtaining the equation governing their motion. An electromagnetic model of the control valve solenoid has also been realized, in order to work out the attraction force on the anchor, generated by the electric current when flowing into its coil. The model obtained has been implemented using the MATLAB® toolbox SIMULINK®; the ordinary differential equations were solved by means of an implicit scheme of the second-order accuracy, suitable for problems with high level of stiffness, while the partial differential equations were integrated using the finite-difference Lax-Friedrichs method. The experimental investigation on the common-rail injection system was performed on a test bench at some standard test conditions. Electric current flowing through the injector coil, oil pressure in the common rail and at the injector inlet, injection rate, needle lift, and control valve lift were gauged and recorded during several injection phases. The mean reflux-flow rate and the mean quantity of fuel injected per stroke were also measured. Temperature and pressure of the feeding oil as well as pressure in the rail were continuously controlled during the experimental test. The numerical and experimental results were compared. Afterwards, the model was used to investigate the effect of control volume feeding and discharge holes and of their inlet fillet, as well as the effect of the control volume capacity, on the injector performance.
[DOI: 10.1115/1.1787502]

Introduction

The design of high-performance fuel-injection systems, or modification of existing configurations, in the light of the increasing demands placed by energy-saving and emission regulations on the performance of diesel engines dictates the need for sophisticated analytical investigation tools. In the last years the common-rail injection system has been proposed [1,2] as the injection system to fulfil future emission limits [3–5]. In this system the pressure generation is totally independent from the fuel metering and the injection timing can be defined independently on the engine speed and on the car load [1,2].

Many research activities are directed towards common-rail system improvement in order to obtain linear dependency between injector energizing time and injected flow rate, reduction of the dwell time between two consecutive injections, and leakage minimization [6,7]. Other researchers have developed alternative common-rail injection systems with two rails at different pressure level in order to modulate the injected flow rate shape [8].

In this context numerical simulation offers the means of evaluating the geometry and operation effects on the unsteady flow phenomena in common-rail injection systems [7,9–11], allowing a significant reduction of experimental tests.

One of the older common-rail injector model was presented in Ref. [9] and successively improved and employed for the analysis of the instability phenomena due to the control valve behavior [10]. An important input parameter in this model was the magnetic attraction force in the control valve dynamic model. This was calculated interpolating the experimental curve between driving current and magnetic force measured at fixed control valve position. In Refs. [7,12] a lumped parameter model, in which the magnetic field was represented by an equivalent magnetic circuit, was used to calculate the solenoid magnetic force at the control valve. The ordinary differential equations of the injector models were solved numerically using fourth-order Runge-Kutta procedures, which are not very suitable for stiff problems. In Refs. [13,14] the electromagnetic attraction force was evaluated by means of a phenomenological model. The force was considered directly proportional to the square of the magnetic flux and the proportionality constant was experimentally determined under stationary conditions.

In the present work, the equivalent hydraulic scheme of a commercial common-rail injector was defined. The moving mechanical components of the injector were modeled following a mass-spring-damper model. An electromagnetic model of the control

Contributed by the Internal Combustion Engine Division of THE AMERICAN SOCIETY OF MECHANICAL ENGINEERS for publication in the ASME JOURNAL OF ENGINEERING FOR GAS TURBINES AND POWER. Manuscript received by the ICE Division, October 15, 2002; final revision received September 1, 2003. Associate Editor: D. Assanis.

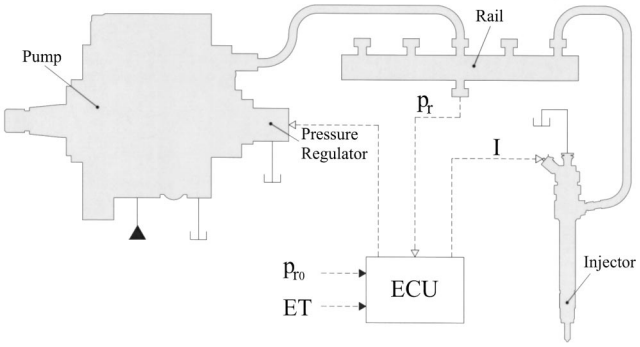

Fig. 1 Injection system layout

valve solenoid has also been realized, in order to work out the attraction force on the control valve, generated by the electric current when flowing into its coil. The model obtained has been implemented using the MATLAB® toolbox SIMULINK®, taking advantage of its ability to solve ordinary differential equations by means of the NDF (numerical differentiation formulas) implicit scheme, suitable for problems with high level of stiffness. The partial differential equations, arising from the one-dimensional model of the flow in pipes, were solved by means of a dedicated SIMULINK® routine in which the Lax-Friedrichs' finite difference scheme was implemented.

Injection System

The injection system under investigation was a commercial injection system of the common-rail type for passenger cars. It was made up of a volumetric high-pressure pump, a pressure regulator, a fuel rail, a rail pressure sensor, four electric injectors, and connecting pipes. In the present study, only one injector was connected to the common rail in order to minimize the rail pressure oscillation and thus allowing a more precise validation of the injector model.

The high-pressure pump (Fig. 1), a three-piston Bosch unit with a displacement of 0.657 cm^3/rev, was provided with an embedded pressure regulator displaced on its delivery port. The regulator, controlled by the system electronic control unit (ECU), is responsible for maintaining the value of the oil pressure in the rail (p_r) at the desired level (p_{r0}).

The common rail had a trapped volume of 20 cm^3 and was capable of feeding four injectors. The rail and injector feeding pipes were 305 and 200 mm long, respectively.

The electric injector under investigation was a standard Bosch unit (Fig. 2) fitted with a nozzle of microsac type. It presented five cylindrical holes that had been finished with a hydro-erosion process that guarantees a flow rate increase of about 10%. A stationary flow rate of 9.0 ± 0.17 cm^3/s at a constant injection pressure of 10 MPa characterizes the nozzle. Figure 2 shows an enlargement of the solenoid control valve of the injector, of the control piston-needle displacement sensor, and of the needle tip.

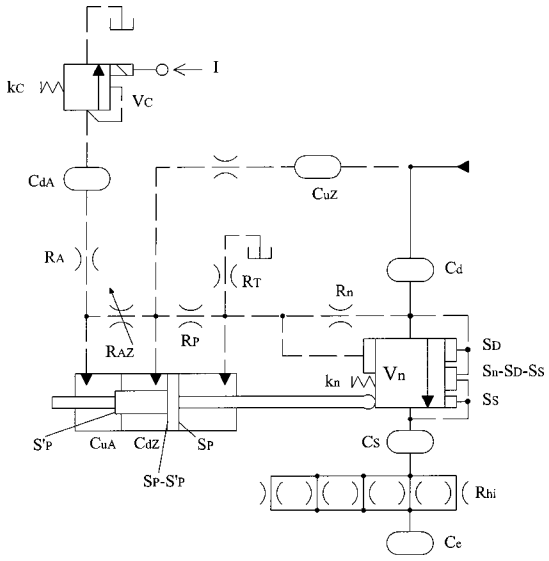

Fig. 3 Injector equivalent hydraulic circuit

Mathematical Model

The injector under investigation has been thoroughly disassembled so as to work out its functioning principle, internal layout, and key elements. The analysis resulted in the definition of three models of the component: the hydraulic, the mechanical, and the electromagnetic one.

Hydraulic Model. Figure 3 shows the equivalent hydraulic circuit of the injector, drawn following ISO 1219 standards. Continuous lines represent the main connecting ducts, while dashed lines represent pilot and vent connections. The hydraulic parts of the injector were modeled with ideal components such as uniform pressure chambers and laminar or turbulent hydraulic resistances, according to a zero-dimensional modeling approach. The internal pipe connecting the injector inlet to the nozzle delivery chamber was modeled according to a one-dimensional modeling approach.

The equivalent hydraulic circuit of the injector will be explained by considering the circuit of the control valve and the one of the control piston and nozzle separately.

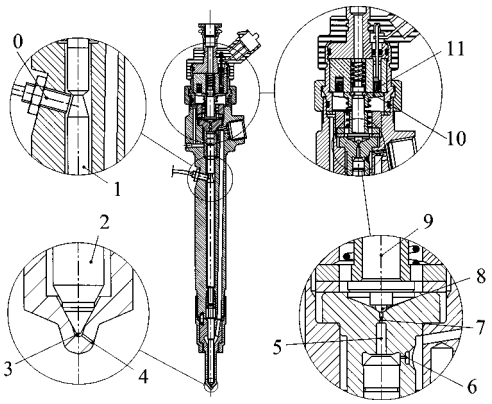

0	displacement sensor
1	control piston
2	needle
3	sac volume
4	nozzle hole
5	control volume
6	feeding hole (Z)
7	discharge hole (A)
8	ball
9	pin
10	anchor
11	solenoid

Fig. 2 Injector

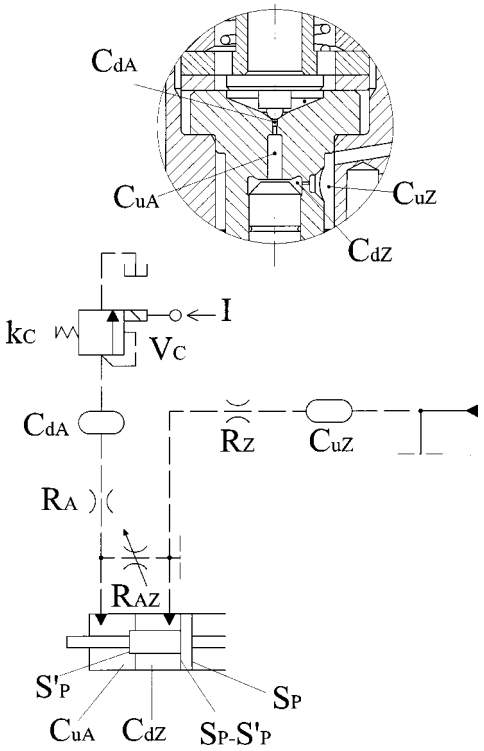

Fig. 4 Control valve and relative equivalent hydraulic circuit

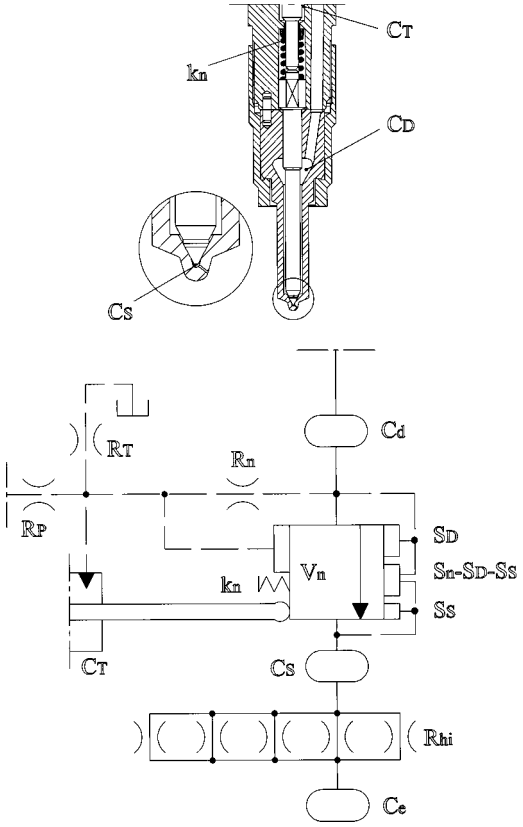

Fig. 5 Control piston-nozzle and relative equivalent hydraulic circuit

Figure 4 shows the control valve and the relative portion of the equivalent hydraulic circuit. R_A and R_Z are the hydraulic resistances used for modeling flow through control-volume orifices A (discharge) and Z (feeding), respectively. The variable resistance R_{AZ} models the flow between chambers C_{dZ} and C_{uA}, taking into account the effect of the control piston position on the actual flow area between the aforementioned chambers. The solenoid control valve V_c is represented using its standard symbol, which shows the forces that act in the opening (one generated by the current I flowing through the solenoid, the other by the pressure in the chamber C_{dA}) and closing direction (spring force).

Figure 5 illustrates the control piston and nozzle along with the relative portion of equivalent hydraulic circuit. The needle valve V_n is represented with all the actions governing the needle motion, such as pressures acting on different surface areas, force applied by the control piston and spring force. The chamber C_D models the nozzle delivery volume, C_S is the sac volume, whereas the hydraulic resistance R_{hi} represents the ith nozzle hole, through which fuel flows into the injection environment C_e. The control piston model was realized considering two different surface areas on one side, so as to take into account the different contribution of pressure in the chambers C_{uA} and C_{dZ} to the total force applied in the needle valve closing direction.

Leakages both between control valve and piston and between needle and its liner were modeled by means of the resistances R_P and R_n, respectively, and the resulting flow, which gathers in chamber C_T (the annular chamber around the control piston), is then returned to tank after passing a small opening, modeled with the resistance R_T, between control valve and injector body.

The continuity and compressibility equation was written for every chamber of the model,

$$\sum Q = \frac{V}{E_l}\frac{dp}{dt} + \frac{dV}{dt}, \tag{1}$$

where ΣQ was the net flow rate coming into the chamber, $(V/E_l)(dp/dt)$ the rate of increase of the fluid volume in the chamber due to the fluid compressibility, and dV/dt the deformation rate of the chamber volume.

Fluid leakages occurring between coupled mechanical elements in relative motion (e.g., needle and its liner, or control piston and control valve body) were modeled using laminar flow hydraulic resistances, characterized by a flow rate proportional to the pressure drop Δp across the element,

$$Q = K_L \Delta p, \tag{2}$$

where the theoretical value of K_L, for an annulus shaped cross-section flow area, can be obtained by

$$K_L = \frac{\pi d_m g^3}{12 l \rho \nu}. \tag{3}$$

The leakage flow rate, Eqs. (2) and (3), depends on the third power of the radial gap g. At high pressure the material deformation strongly affects the gap entity and its value is not constant along the gap length l because pressure decreases in the gap when approaching the low-pressure side [6]. In order to take into account these effects on the leakage flow rate, the value of K_L has to be experimentally evaluated in the real injector working conditions.

Flow through orifices (such as nozzle holes and needle-seat opening passage, as well as control-volume feeding and discharge holes) was modeled assuming turbulent flow, therefore assuming the flow rate proportional to the square root of the pressure drop Δp across the orifice, as shown by Eq. (4),

$$Q = \mu A \sqrt{\frac{2\Delta p}{\rho}}. \tag{4}$$

The hole discharge coefficient of control volume orifices A and Z was evaluated according to the model proposed in Ref. [15].

This model considers four flow regimes inside the hole: laminar, turbulent, reattaching, and fully cavitating. Neglecting cavitation occurrence, a preliminary estimation of the hole discharge coefficient is

$$1/\mu = \sqrt{K_M + f\frac{l}{d} + 1}, \tag{5}$$

where K_M is the inlet loss coefficient, which is a function of inlet geometry [16], l is the hole axial length, d is the hole diameter, and f is the wall friction coefficient,

$$f = \mathrm{MAX}(64/\mathrm{Re}, 0.316/\mathrm{Re}^{0.25}), \tag{6}$$

where Re is the Reynolds number. It follows that the pressure in the vena contracta is

$$p_{vc} = p_v - \frac{\rho_l}{2}\left(\frac{Q}{AK_{vc}}\right)^2, \tag{7}$$

where the contraction coefficient K_{vc} is

$$\frac{1}{K_{vc}^2} = \frac{1}{K_{vc_0}^2} - 11.4\frac{r}{d}, \tag{8}$$

where $K_{vc_0} = 0.61$ and r is the fillet radius of the hole inlet.

If the pressure in the vena contracta (p_{vc}) is higher then the oil vapor pressure (p_v), cavitation does not occur and the value of the hole discharge coefficient is given by Eq. (5). Otherwise, cavitation occurs and the discharge coefficient is evaluated in according to

$$\mu = K_{vc}\sqrt{\frac{p_u - p_v}{p_u - p_d}}. \tag{9}$$

The nozzle-hole and needle-seat discharge coefficients were assumed as needle lift dependent in according to Ref. [17]. In Ref. [17] these nonstationary coefficients were experimentally evaluated for a minisac nozzle in the real working conditions of a distributor pump-valve–pipe-injector-type injection system. This approach takes into account the unsteadiness, compressibility flow effects, the dynamic effects of the needle lift, and the influence of the needle seat passage area on the hole discharge coefficient.

Pipe Model. A one-dimensional modeling approach was followed in order to model the fluid flow in the pipe connecting injector and rail and in the injector internal duct that delivers the fluid from the inlet to the delivery chamber. This was necessary to correctly take into account pressure waves propagation that occurs in those elements. The pipe flow conservation equations were written for a single-phase fluid. An isothermal flow was assumed in the present study and only the momentum and conservation equations were written

$$\frac{\partial \mathbf{w}}{\partial t} + A\frac{\partial \mathbf{w}}{\partial x} = \mathbf{b}, \tag{10}$$

where

$$\mathbf{w} = \begin{Bmatrix} u \\ p \end{Bmatrix}, \quad A = \begin{bmatrix} u & 1/\rho \\ \rho c^2 & u \end{bmatrix}, \quad \mathbf{b} = \begin{Bmatrix} -4\tau/\rho d \\ 0 \end{Bmatrix}$$

and τ is the wall shear stress that was evaluated under the assumption of steady-state friction. The eigenvalues of the hyperbolic system of partial differential Eqs. (10) are $\lambda = u \pm c$, real and distinct.

The wave propagation speed c was evaluated as

$$c = \sqrt{\frac{E_l/\rho}{\left(1 + K_p\frac{E_l}{E_p}\frac{d_p}{t_p}\right)}}, \tag{11}$$

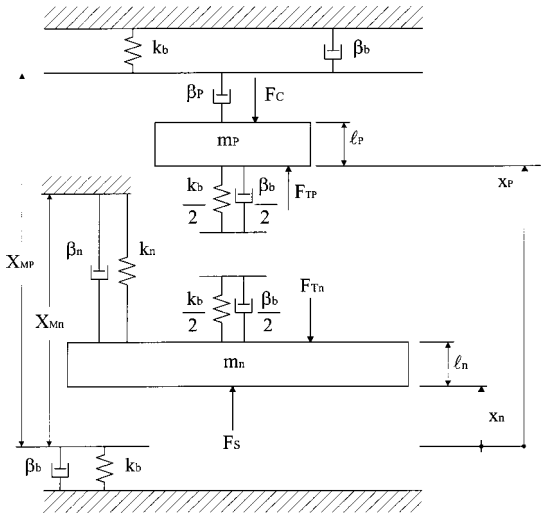

Fig. 6 Schematic of dynamic model of control piston needle

where the second term within brackets takes into account the effect of the pipe elasticity; K_p is the pipe constraint factor, depending on pipe support layout, E_p the Young's modulus of elasticity of the pipe material, and t_p the pipe wall thickness.

In the present study the model works with imposed constant pressure in the common rail. Junctions were treated as minor losses and only the continuity equation was locally written.

Fluid Model. Density, wave propagation speed, and kinematic viscosity of the ISO 4113 test oil had been evaluated as function of pressure and temperature [18]. These oil properties were approximated with analytic functions of the exponential type in the range of pressures from 0.1 to 200 MPa and temperatures from 10 to 120°C. These analytic formulas were derived from the actual value of properties, which were supplied by the oil company, by using the least-square method for non-linear approximation functions with two independent variables.

Mechanical Model. All mechanical devices whose position can vary during injector functioning (i.e., needle, control piston, and control valve) were modeled using the conventional mass-spring-damper scheme, governed by a mechanical equilibrium equation, in which the dynamic parameters are functions of element displacement.

Injector needle and control piston form a two degrees of freedom mechanical system, which can be modeled as shown by Fig. 6. Two equilibrium equations are needed to describe the system motion, one for each element. With reference to Figs. 3 and 6, the needle and the control piston dynamic equilibrium equations were written,

$$m_n\frac{d^2x_n}{dt^2} + \overline{\beta}_n\frac{dx_n}{dt} + \overline{k}_n x_n + \overline{F}_{0n} = F_S - F_{Tn} - F_R, \tag{12}$$

$$m_P\frac{d^2x_P}{dt^2} + \overline{\beta}_P\frac{dx_P}{dt} + \overline{k}_P x_P + \overline{F}_{0P} = -F_c + F_{TP} + F_R, \tag{13}$$

where

$$F_S = p_S S_S + p_D S_D + \frac{p_S + p_D}{2}(S_n - S_S - S_D), \quad F_{Tn} = p_T S_n,$$

$$F_c = p_{uA} S'_P + p_{dZ}(S_P - S'_P), \quad F_{TP} = p_T S_P,$$

$$F_R = \begin{cases} k_b(x_n + l_n - x_P) + \beta_S\left(\dfrac{dx_n}{dt} - \dfrac{dx_P}{dt}\right) \\ \qquad \text{if } x_P \leqslant x_n + l_n \\ 0 \qquad \text{if } x_P > x_n + l_n \end{cases},$$

$x_n < 0$	$\overline{\beta}_n = \beta_b + \beta_n$	$\overline{k}_n = k_b + k_n$	$\overline{F}_{0n} = F_{0n}$
$0 \leqslant x_n < X_{Mn} - l_n$	$\overline{\beta}_n = \beta_n$	$\overline{k}_n = k_n$	$\overline{F}_{0n} = F_{0n}$
$X_{Mn} - l_n \leqslant x_n$	$\overline{\beta}_n = \beta_b + \beta_n$	$\overline{k}_n = k_b + k_n$	$\overline{F}_{0n} = F_{0n} - k_b X_{Mn}$

and

$x_P < X_{MP} - l_P$	$\overline{\beta}_P = \beta_P$	$\overline{k}_P = 0$	$\overline{F}_{0P} = 0$
$X_{MP} - l_P \leqslant x_P$	$\overline{\beta}_P = \beta_b + \beta_P$	$\overline{k}_P = k_b$	$\overline{F}_{0P} = -k_b(X_{MP} - l_P)$.

F_R represents the force that needle and control piston apply to each other when they are in contact.

The axial deformation of some mechanical elements (i.e., needle, nozzle, and control piston) was taken into account. These elements were considered only axially stressed, while the effects of the radial stress were neglected. As a result the axial length of control piston (l_P), needle (l_n), and nozzle (X_{Mn}) in Eqs. (12) and (13) was evaluated as function of the axial compressive load (F_N) in each element. Therefore the deformed length l of these elements was evaluated as follows:

$$l = l_0\left(1 - \frac{F_N}{EA}\right), \tag{14}$$

where l_0 is the not deformed element length, A the cross section, and E the Young's modulus of elasticity of the element material.

The mobile device of the control valve can be modeled following the two degrees of freedom scheme shown by Fig. 7. The mobile device was divided in the pin element having mass m_c and in the anchor element of mass m_a. The two dynamic equilibrium equations were written

$$m_c \frac{d^2 x_c}{dt^2} + \overline{\beta}_c \frac{dx_c}{dt} + \overline{k}_c x_c + \overline{F}_{0c} = (p_{dA} - p_T) S_c + F'_R, \tag{15}$$

$$m_a \frac{d^2 x_a}{dt^2} + \beta_a \frac{dx_a}{dt} + k_a x_a - F_{0a} = F_{\mathrm{Ea}} - F'_R, \tag{16}$$

where

$$F'_R = \begin{cases} k_b(x_a + X_{Mc} - x_c - l_{Mc}) + \beta_b\left(\dfrac{dx_a}{dt} - \dfrac{dx_c}{dt}\right) \\ \qquad \text{if } x_c + l_{Mc} \leqslant x_a + X_{Mc} \\ 0 \qquad \text{if } x_c + l_{Mc} > x_a + X_{Mc} \end{cases}$$

$x_c < 0$	$\overline{\beta}_c = \beta_b + \beta_c$	$\overline{k}_c = k_b + k_c$	$\overline{F}_{0c} = F_{0c}$
$0 \leqslant x_c < X_{Mc} - l_c$	$\overline{\beta}_c = \beta_c$	$\overline{k}_c = k_c$	$\overline{F}_{0c} = F_{0c}$
$X_{Mc} - l_c \leqslant x_c$	$\overline{\beta}_c = \beta_b + \beta_c$	$\overline{k}_c = k_b + k_c$	$\overline{F}_{0c} = F_{0c} - k_b(X_{Mc} - l_c)$.

The force F_{Ea} represents the electromagnetic action that the current generates when it flows in the coil.

Electromagnetic Model. A model of the electromechanical actuator that drives the control valve was realized in order to work out the net mechanical force applied by the solenoid on the mobile device anchor, for a given current flowing in the solenoid.

The magnetic force applied by the solenoid on the anchor, F_{Ea} can be obtained by applying the principle of energy conservation to the anchorcoil system [19,20]. In the general form it can be written as follows:

$$VIdt = F_{\mathrm{Ea}} dx_a + dW_m, \tag{17}$$

where $VIdt$ represents the electric energy input to the system, $F_{\mathrm{Ea}} dx_a$ is the mechanical work done on the anchor, and dW_m is the change in the magnetic energy.

From Faraday's law, voltage V may be expressed in terms of flux linkage ($N\Phi$) and Eq. (17) becomes

$$NId\Phi = F_{\mathrm{Ea}} dx_a + dW_m \tag{18}$$

as shown in Refs. [19,20]; by considering Φ and x_a as independent variables, Eq. (18) can be reduced to

$$F_{\mathrm{Ea}} = -\left.\frac{\partial W_m}{\partial x_a}\right|_{\Phi}. \tag{19}$$

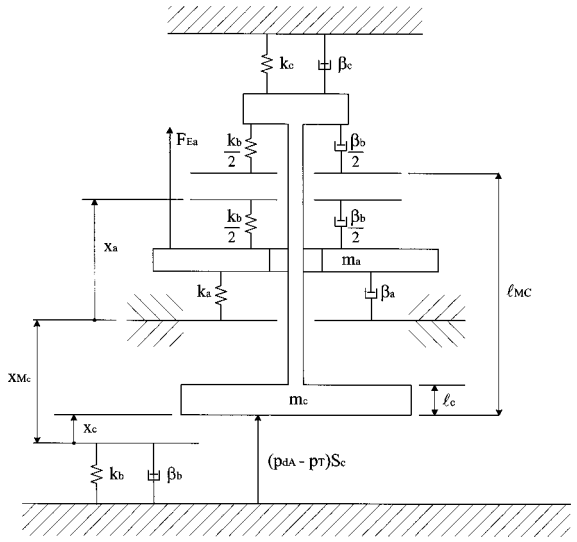

Fig. 7 Schematic of dynamic model of control valve

The magnetic circuit geometry of the control valve has been thoroughly analyzed in order to evaluate the magnetic energy stored in the gap. Figure 8 shows the path of the significant magnetic fluxes, having neglected secondary leakage fluxes and flux fringing.

Exploiting the analogy between Ohm's and Hopkinson's law, we obtained the magnetic equivalent circuit of Fig. 9 where NI is the ampere turns in the exciting coil and $\Re_j$ $(j=1,\ldots,5)$ are the magnetic reluctances. When the magnetic flux flows across a cross section area A_a constant along the path length l, the value of the jth reluctance can be obtained by

$$\Re_j=\frac{l_j}{\mu_0 A_{aj}} \quad (j=1,2). \tag{20a}$$

When the flux flows across a radial path, the reluctance can be evaluated as

$$\Re_j=\frac{1}{2\pi\mu_0 t_j}\ln(d_e/d_i)_j \quad (j=3,4,5), \tag{20b}$$

where t is the radial thickness, and d_e and d_i are the external and internal diameter of the gap volume. Reluctance of the ferromagnetic components was neglected because it is several order of magnitude lower than the corresponding gap reluctance.

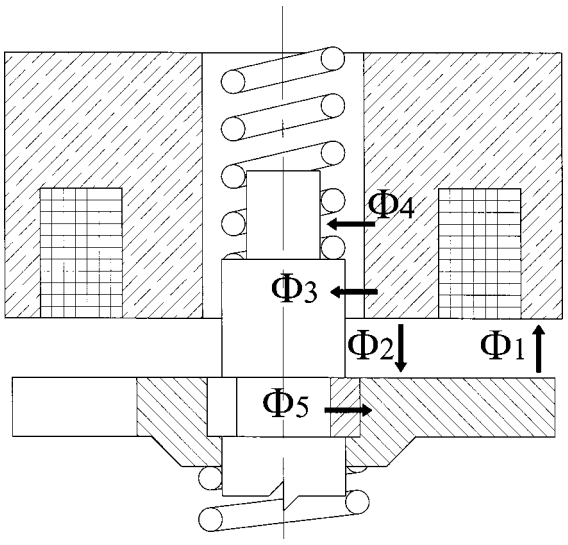

Fig. 8 Magnetic flux path

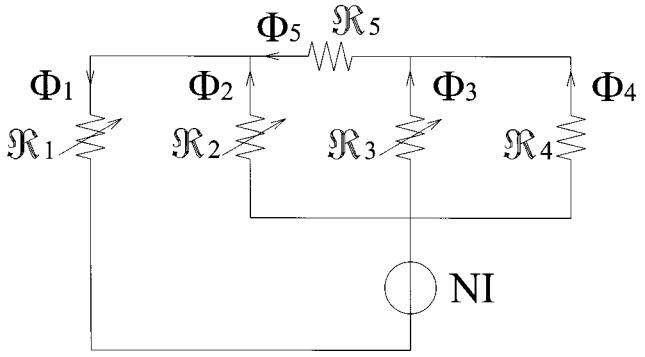

Fig. 9 Equivalent magnetic circuit

Circuit of Fig. 9 was solved using Thevenin's theorem, and the equivalent circuit reluctance connected to the magnetomotive force generator was determined as

$$\Re=\Re_1+\frac{\Re_2\Re_3\Re_4+\Re_2\Re_5(\Re_3+\Re_4)}{\Re_3\Re_4+(\Re_2+\Re_5)(\Re_3+\Re_4)}. \tag{21}$$

The magnetic energy W_m is stored in the volume of the electromechanical actuator, but only the portion of energy stored in the gap between control-valve body and magnetic core depends on the anchor lift x_a. Consequently, being the magnetization curve of nonferromagnetic materials (oil in the gaps) linear, Eq. (19) can be written as

$$F_{\mathrm{Ea}}=-\frac{1}{2}\Phi_1^2\frac{d\Re}{dx_a}=-\frac{1}{2}\left(\frac{NI}{\Re}\right)^2\frac{d\Re}{dx_a}. \tag{22}$$

To complete the model, it was necessary to take into account the saturation phenomenon that occurs to every ferromagnetic material. That is, a magnetic flux cannot increase indefinitely, as the material presents a maximum magnetic flux density after which the curve B-H is almost flat. In this model we assumed a simplified magnetization curve, given by

$$B=\begin{cases}\mu H & \text{if } H<H^*\\ \mu H^*+\mu_0(H-H^*) & \\ & \text{if } H\geqslant H^*\end{cases} \tag{23}$$

thus neglecting material hysteresis and nonlinearity.

As a result of the saturation phenomenon, the maximum force of attraction is limited because the maximum magnetic flux which can be obtained in the jth branch of the circuit is approximately

$$\Phi_{Mj}\cong\mu H_j^* A_j \tag{24}$$

being μ_0 negligible with respect μ.

Numerical Algorithm

Equations obtained during injector functioning analysis and modeling were implemented in SIMULINK®, a MATLAB® Toolbox designed for modeling dynamic systems.

The system of second-order ordinary differential equations, representing the hydraulic, mechanical, and electromagnetic analytical model of the injector, was preliminary reduced to a system of the first order. Then a NDF implicit multistep scheme of second-order accuracy was used to solve the resulting first-order differential equation system that can be written as

$$y'=F(t,y). \tag{25}$$

The NDF scheme is an improvement of the BDF (backward differentiation formulas) that is very popular for solving stiff problems and was previously employed in the numerical models of pump-valve–pipe-injector injection system [17,18].

Table 1 Test points

Test	p_r (MPa)	ET (μs)
A	135	730
B	135	280
C	80	700
D	80	300

In order to explain the difference between NDF and BDF, a constant temporal step size Δt in the computational grid is considered. The second-order NDF takes the form [21]

$$\tfrac{1}{2}(3y^k_{n+1}-4y_n+y_{n-1})-F(t_{n+1},y^k_{n+1})\Delta t+\tfrac{1}{6}(y^k_{n+1}-3y_{n+}+3y_{n-1}-y_{n-2})=0, \quad (26)$$

where the subscripts indicate the time-marching coordinate in the computational grid, while the superscript indicates the iterative approximation of the solution. The last term in Eq. (26) represents the correction to the second-order BDF [21]. This term implies that for sufficiently small step sizes, the second-order NDF can achieve the same accuracy as second order BDF with a step size about 26% bigger.

The Lax-Friedrichs finite difference scheme [22] was used to discretize the partial differential equations that describe the flow into the injector feeding pipe and injector internal main duct. The conservative scheme adopted is of the first-order accuracy and presents a minimum diffusion term when the Courant number $(c\Delta t/\Delta x)$ is chosen to be equal to 1. An iterative process was chosen in order to synchronize the NDF solver, which works with a varying time increment, and the Lax-Friedrichs algorithm, which operates with constant time step, in order to maintain the Courant number as close to one as possible.

Experimental Analysis

Experimental investigation of injector performance was carried out on a test bench designed for testing both traditional and common-rail-type diesel fuel injection systems.

The oil employed during the test was compliant with ISO 4113 specifications and was supplied at a temperature of 40 ± 1°C and a relative pressure of $0.08\pm5\%$ MPa to the injection system. Temperature of the injector body was continuously measured so as to identify the stationary working conditions of the injection system.

The experiments were carried out under four different sets of boundary conditions which characterize the injector working field. The injection-system operative conditions (rail pressure reference value p_{r0}, injector energizing time ET—see Fig. 1), which were imposed through the injection-system test bench, are shown in Table 1. Tests A and C refer to a main injection, while tests B and D refer to a pilot injection.

For every test condition, pressure in the rail (p_r) and at the injector inlet (p_{in}), injection flow-rate (Q), control piston-needle lift (x_P), control valve lift (x_c), and current flowing in the coil (I) time history were gauged. The pressure p_{in} was measured in the injector feeding pipe (30 mm from the injector inlet), while the rail pressure p_r was measured at the end of a short dead-ended pipe mounted on one of the unused injector connections. Both signals were gauged by means of piezoresistive transducers (Kistler 4067). The injection flow rate was measured by means of a Bosch measure tube (EVI equipment). A noncontact eddy current displacement sensor ($\mu\varepsilon$ S05) was employed for the measurement of the control piston lift and its installation is shown in Fig. 2. The gauging of the control valve lift was performed by means of an inductive transducer (AVL 423) whose magnetic core was connected to the valve body by means of an extension rod brazed to the valve head. A hall effect transducer measured the electric current flowing through the solenoid coil. An EMI equipment was used to measure the mean injected flow rate, while the mean injector reflux flow rate was measured by means of graduated burettes.

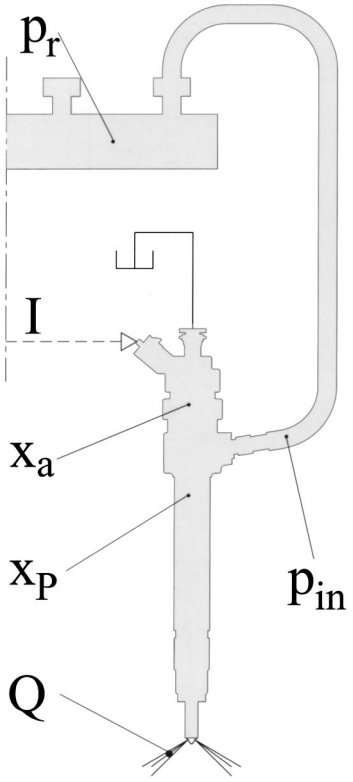

Fig. 10 Layout of the analyzed system

Pursuing the aim of reducing the random error effects, at least 20 consecutive injection cycles were acquired after stationary working conditions of the injection system were reached.

The mass of the injector mechanical elements, the stiffness of the springs and the geometrical dimensions were experimentally evaluated with an uncertainty of $\pm1\%$.

Results

Model performance was assessed by comparing numerically obtained and experimentally measured data. Figure 10 shows the portion of the injection system under analysis and the measured quantities. The electric current signals gauged during experimentation (Fig. 11) were fed to the model, so as to compare simulated and actual injector behavior when driven by the same input. The model works with imposed constant pressure in the common rail. This assumption is justified by the limited fluctuation of the rail pressure (lower than 3 MPa in the considered test cases), as shown in Fig. 12. This is the result of the choice of connecting only one injector to the rail.

Oil pressure at injector inlet (p_{in}), control valve lift (x_c), control piston-needle lift (x_P), and injected flow rate (Q) were used to evaluate the model accuracy. For every test condition (Table 1) both numerical and experimental values of p_{in}, x_c, x_P, and Q were plotted versus time t in Figs. 13–16. The experimental results were the ensemble values of 20 consecutive injection cycles and were drawn with circular symbols. The numerical results were drawn with continuous lines. Moreover, numerically simulated and experimentally gauged values of the injected oil volume per cycle were compared, leading to the results presented in Table 2.

The numerical results were obtained after a fine-tuning process of the model in order to define the appropriate value of the inlet loss coefficients K_M of the control volume holes, Eq. (5), which

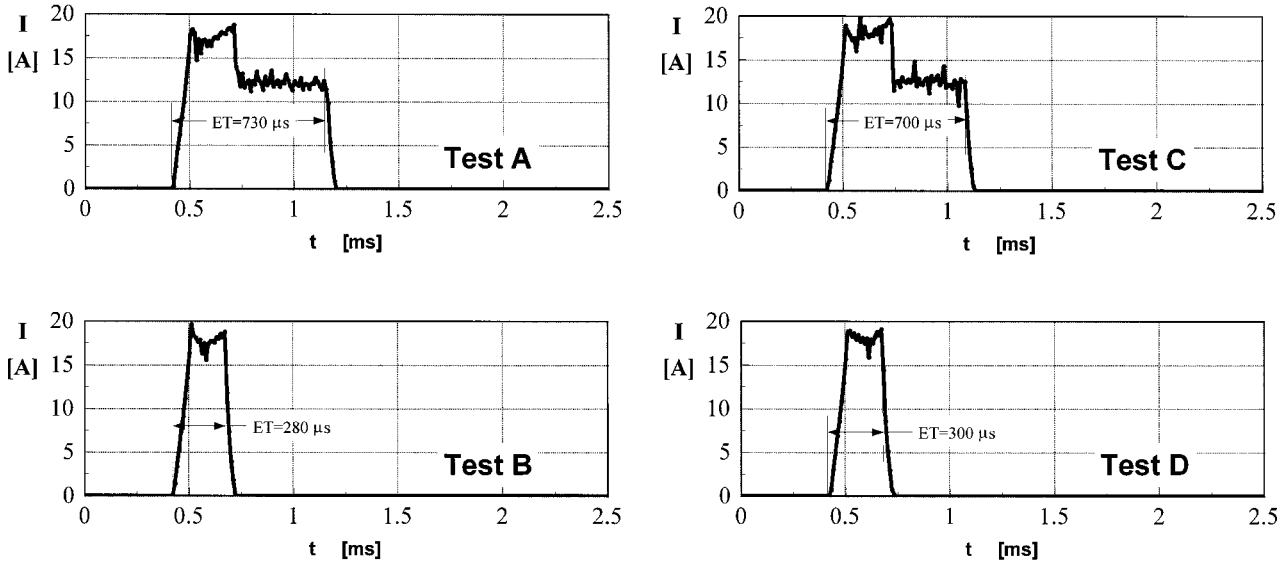

Fig. 11 Injector energizing current—model input

cannot be easily evaluated by direct investigation. Similarly, the evaluation of the damping factors β, Eqs. (12)–(16), was performed indirectly, comparing the model prediction to the experimental data regarding control valve and piston-needle motion. At the end of this tuning phase, sensible values of the control volume holes discharge coefficients (in the range 0.68–0.83) were obtained, as well as damping factors congruent to those of underdamped mechanical systems.

Numerical results shown in Figs. 13–16 were obtained by imposing the driving current (Fig. 11) and the reference rail pressure (Fig. 12) to the model, without any intervention on any other parameter. On this basis, the model was judged capable of reproducing injector functioning with a discrete accuracy.

As Figs. 13(*b*)–16(*b*) show, the control valve presents bounces at the upper and lower seats. The quick control valve reopening after having completed the main opening cycle slows down the needle during its closing motion. Numerical analysis of this phenomenon helped in understanding the cause of the control valve reopening, thus identifying the anchor as the responsible. During the closing stage of the control valve, in fact, while the ball reaches its seat and stops its descending motion, the anchor, which is not rigidly bounded to the pin, continues its downward motion, thus further compressing the relative spring. The energy stored in the elastic element is partially dissipated by friction forces and partially released, causing the anchor to move upward until reaching the contact with the pin. The anchor kinetic energy is then converted into work against the main control valve spring, thus causing valve reopening.

Figures 13(*c*)–16(*c*) show an initial phase during which the control piston needle starts moving without any injection (Figs. 13(*d*)–16(*d*)). This is caused by the reduction of the nozzle, needle, and control piston axial deformation, a consequence of the control volume pressure decrease.

Finally, the model was used to investigate the effect of some of the most important injector parameters on the injected flow rate curve. This analysis was performed with reference to the *A* test point (p_r=135 MPa, ET=730 μs) and the control piston-needle lift (x_P), the force on control piston (F_c), modulated by the control volume pressure, and the flow rate (Q) time histories were drawn in Figs. 17–20.

Figure 17 shows the effect of reducing the control volume feeding hole diameter on the injection rate curve. The injector original

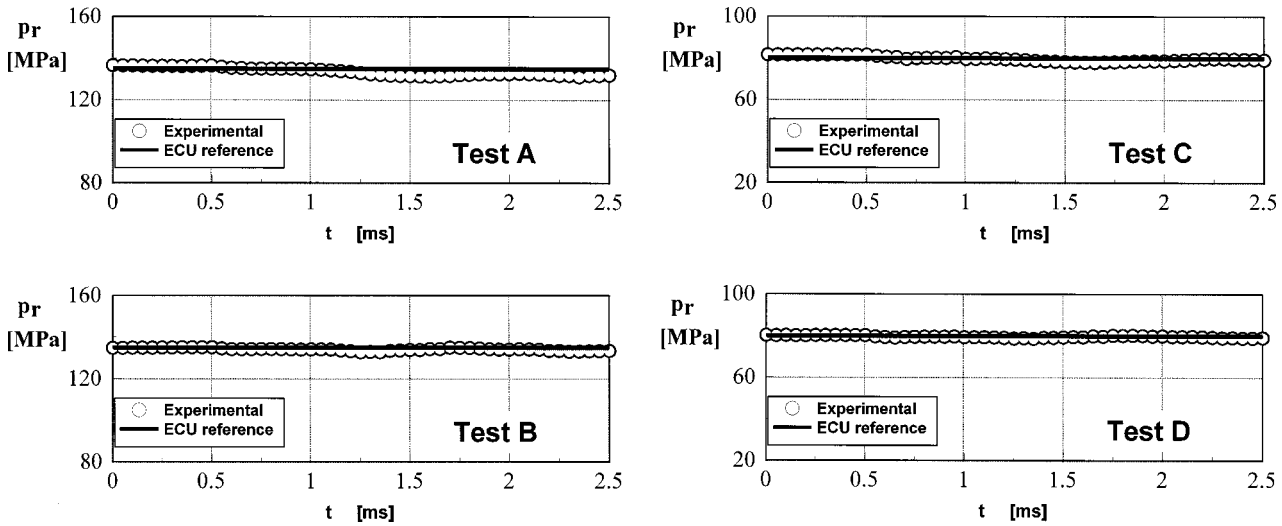

Fig. 12 Measured rail pressure versus reference value

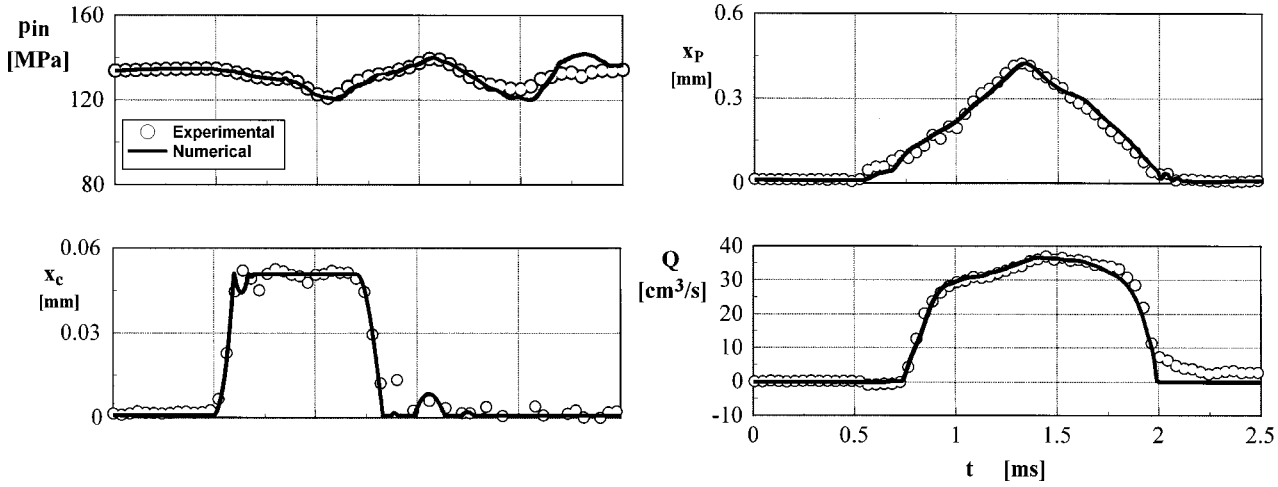

Fig. 13 Test A (p_r=135 MPa, ET=730 μs)

configuration (d_z in Fig. 17) was compared to two configurations having a diameter of the *Z* hole reduced by 10% ($0.90d_z$ in Fig. 17) and by 20% ($0.80d_z$ in Fig. 17). Both opening and closing sides of the curve are affected by the reduction of the *Z* hole. Precisely, the opening stage results anticipated, as the pressure in the control volume drops more rapidly, while the closing stage results delayed, thus increasing the injected volume.

Figure 18 shows the effects of enlarging the *A* hole diameter on

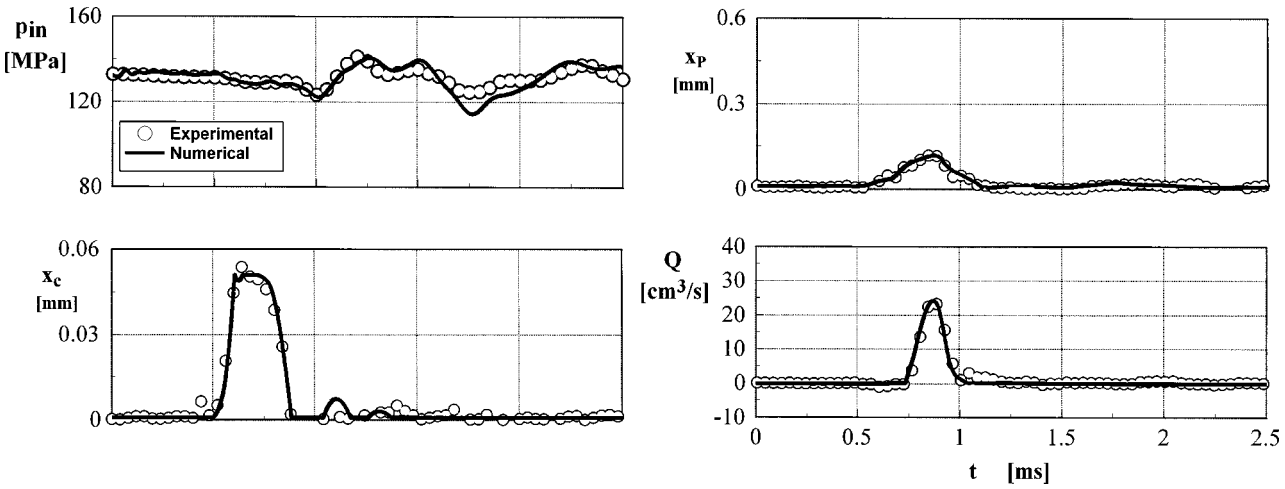

Fig. 14 Test B (p_r=135 MPa, ET=280 μs)

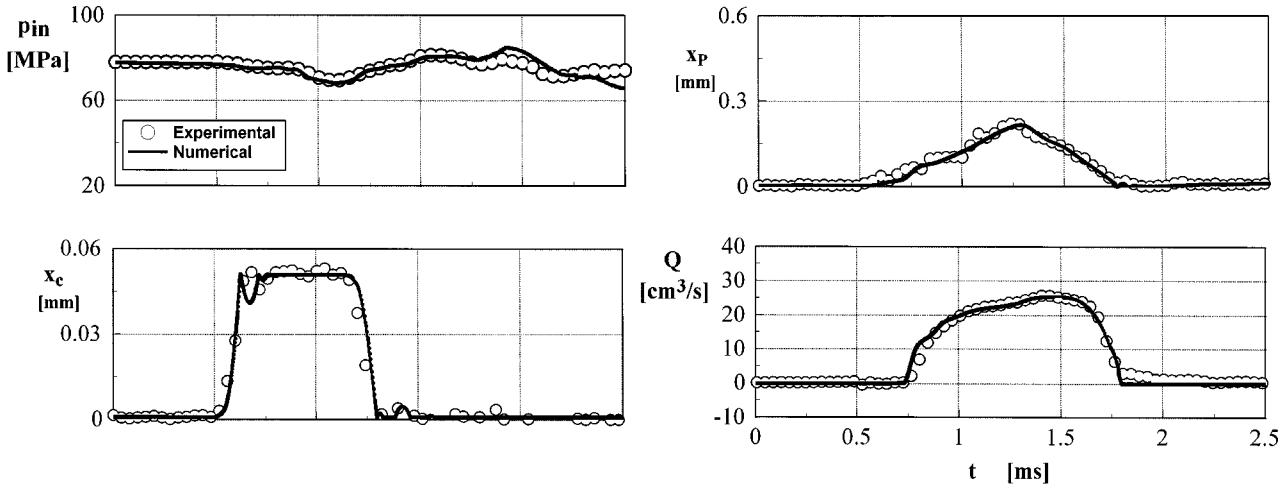

Fig. 15 Test C (p_r=80 MPa, ET=700 μs)

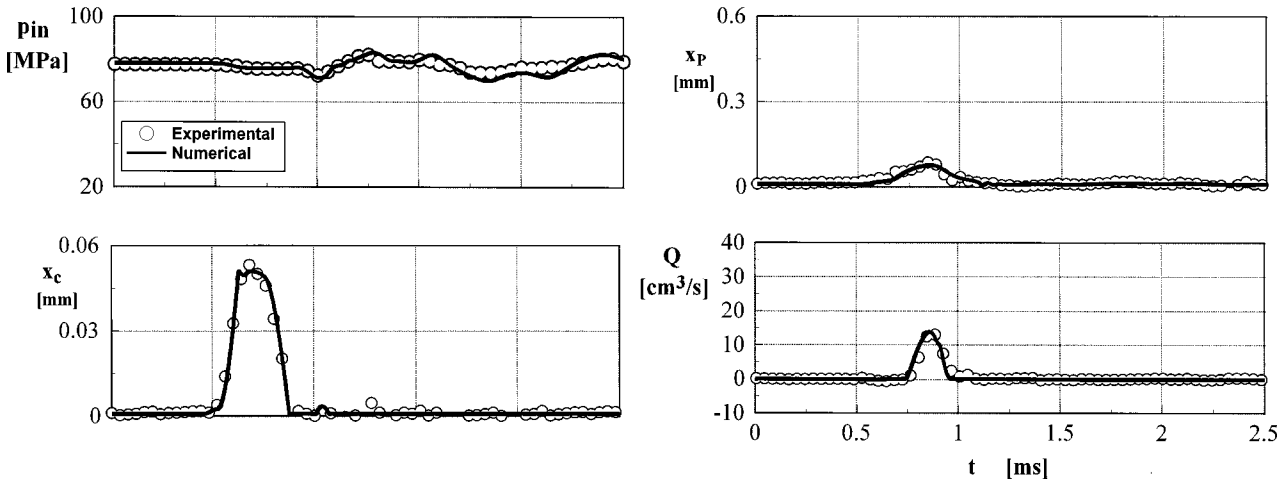

Fig. 16 Test D (p_r=80 MPa, ET=300 μs)

the injector performances. The hole diameter was increased by 10% and by 20%. The obvious effect on anticipating the opening stage is accompanied by a less obvious effect on the closing stage. This can be explained analysing the needle lift time histories. It shows that the needle raises more when enlarging the *A* hole. Therefore the delay observed is the result of the longer time taken by the needle to reach its seat, as required by the enlarged traveling distance.

Table 2 Fluid volume injected per cycle

Test	V_f (Experimental) [mm^3/stroke]	V_f (Numerical) [mm^3/stroke]
A	37.3±0.1	37.4
B	3.7±0.6	3.7
C	20.7±0.1	20.5
D	1.6±0.6	1.6

The effects of control volume capacity on the injector performances were investigated and shown in Fig. 19. In this theoretical analysis the original value of the control volume capacity (V_c in Fig. 19) was reduced by 40% ($0.6V_c$ in Fig. 19) and tripled ($3.0V_c$ in Fig. 19). This parameter does not seem to be greatly affecting the injector behavior. However, a faster injector response can be seen when the control volume is reduced. Also, a higher maximum injection rate is reached as a results of a higher needle lift, which slightly improves the flow through the nozzle.

Usually the control volume holes and the nozzle orifice are made with rounded corners. This is achieved by flowing abrasive material through the parts. The main reason for this is to make sure that the performance of the injector remains relatively un-

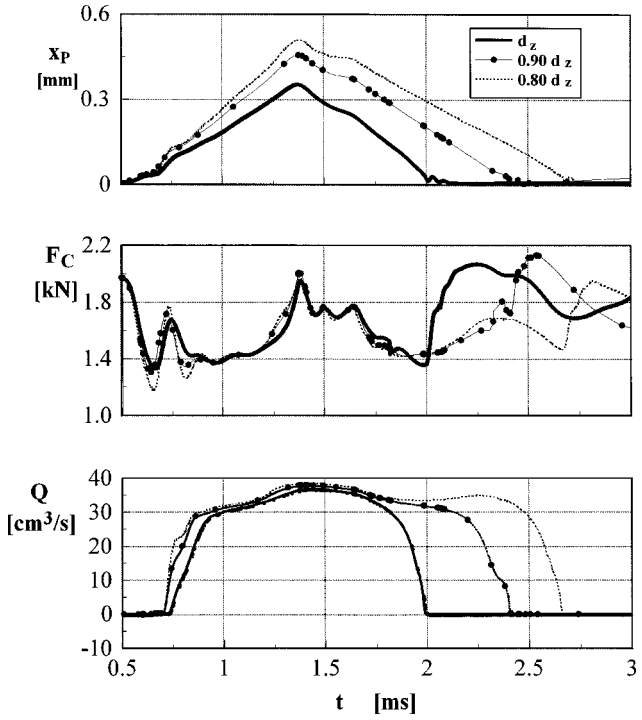

Fig. 17 Theoretical effect of the control volume feeding hole

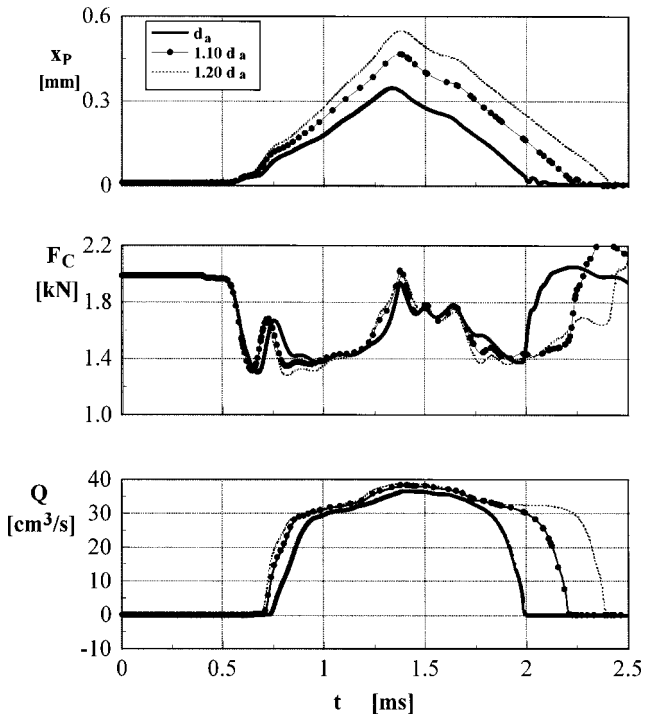

Fig. 18 Theoretical effect of the control volume discharge hole

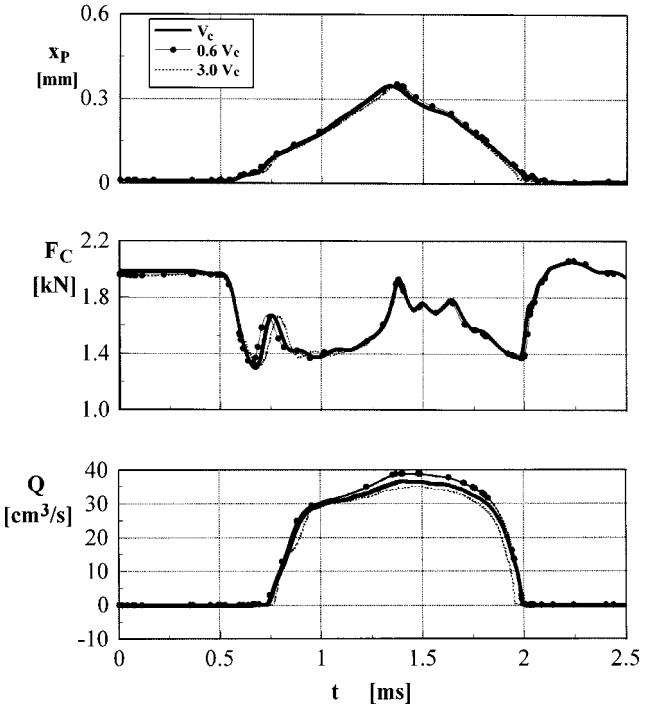

Fig. 19 Theoretical effect of the control volume capacity

changed over a long period of operation. In order to show the effects of hole inlet wear, the design hole configuration, which was numerically evaluated during model tuning, was compared to a sharp edged hole configuration (Fig. 20).

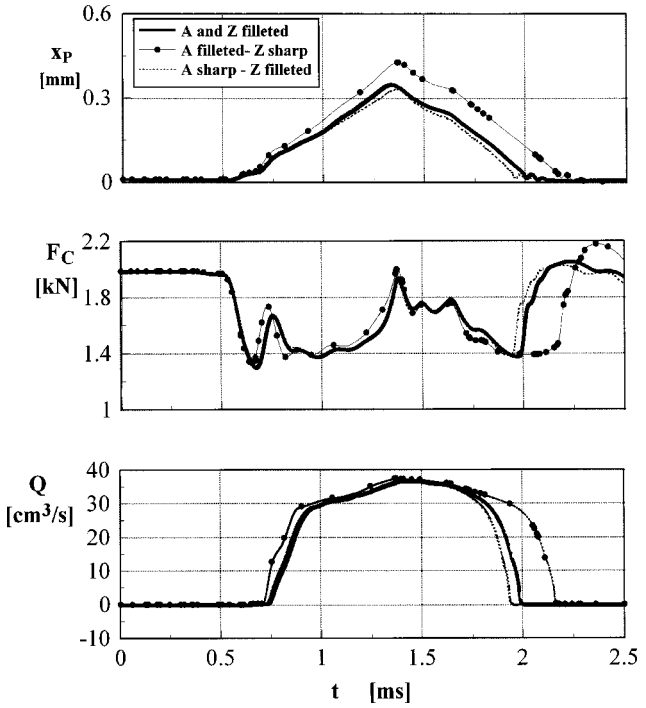

Fig. 20 Effect of control volume holes inlet geometry

Conclusions

A mathematical model of a commercial-type common-rail injector was developed and proposed. The equivalent hydraulic scheme of the injector, the dynamic model of moving mechanical components, and a new electromagnetic model of the control valve solenoid were realized and discussed. Leakages and axial deformation of needle, control piston, and nozzle were taken into account. The mathematical model obtained was implemented using the MATLAB® toolbox SIMULINK®, but it can be easily and completely coded in other simulation environments and used for simulating other common rail injectors, at the only expense of entering appropriate geometrical and physical data.

Experimental investigation on the common-rail injection system was performed at standard working conditions ranging from small pilot to full load main injections. Electric current flowing through the injector coil, oil pressure in the rail and at the injector inlet, control valve lift, control piston-needle lift, and oil injection rate were gauged. The numerical results, which were obtained by changing only rail pressure and injector driving current, were compared with the relative experimental data. The good agreement between experimental and theoretical data allowed us to use the model to investigate the influence of some injector design parameters on the injector performance.

Model predictions showed the great importance of the correct dimensioning of the control volume feeding and discharge holes, as it determines significant variations of the injector hydraulic performance. Seeking constant injector behavior over a long time span, particular care must be taken when choosing the control volume holes finishing level and materials, as the inlet shape of these holes, which changes in time due to wear, significantly affects the injected flow rate. On the other hand, the control piston-needle dynamics seems to be only slightly influenced by the control volume capacity.

Acknowledgments

This work was financially supported by M.I.U.R.–P.R.I.N 2001.

The authors would like to thank the CRF (FIAT Research Center) for its technical support.

Nomenclature

- A = Geometrical area
- B = Magnetic flux density
- C = Chamber
- c = Wave propagation speed
- d = Diameter
- E = Bulk modulus of elasticity, Young's modulus of elasticity
- ET = Injector energizing time
- F = Force
- f = Friction factor
- g = Radial allowance between coupled elements
- H = Magnetic field intensity
- I = Electric current
- K = Constant
- k = Spring stiffness
- l = Length
- m = Mass
- N = Number of coil turns
- p = Pressure
- Q = Flow rate
- R = Hydraulic resistance
- r = Radius
- Re = Reynolds number
- S = Surface
- t = Time, thickness
- u = Average cross-sectional velocity of the fluid
- V = Volume, valve, electric tension

W = Energy
x = Lift, distance
β = Damping factor
Δ = Increment
Φ = Magnetic flux
μ = Discharge coefficient, magnetic permeability
μ_0 = Magnetic permeability of the free space
ρ = Density
τ = Wall shear stress
ν = Kinematic viscosity
$\mathfrak{R}$ = Reluctance

Subscripts

A = Control-volume discharge hole
a = Anchor
b = Seat
c = Control valve
D = Delivery
d = Downstream
E = Electromechanical
e = Injection environment, external
f = Fuel injected per cycle
h = Hole
i = Internal
in = Injector inlet
L = Leakage
l = Liquid
M = Maximum value, minor losses
m = Magnetic, mean
N = In the axial direction
n = Nozzle, needle
P = Piston
p = Pipe
R = Reaction
r = Rail
S = Sac
T = Tank
u = Upstream
v = Vapor
vc = Vena contract
Z = Control-volume feeding hole
0 = Reference value

References

[1] Stumpp, G., and Ricco, M., 1996, ''Common Rail—An Attractive Fuel Injection System for Passenger Car DI Diesel Engines,'' SAE paper 960870.
[2] Boehner, W., and Kummel, K., 1997, ''Common Rail Injection System for Commercial Diesel Vehicles,'' SAE paper 970345.
[3] Schommers, J., Duvinage, F., Stotz, M., Peters, A., Ellwanger, S., Koyanagi, K., and Gildein, H., 2000, ''Potential of Common Rail Injection System for Passenger Car DI Diesel Engines,'' SAE paper 2000-01-0944.
[4] Bianchi, G. M., Pelloni, P., and Corcione, E., 2000, ''Numerical Analysis of Passenger Car HSDI Diesel Engines With the 2nd Generation of Common Rail Injection Systems: The Effect of Multiple Injections on Emissions,'' SAE paper 2001-01-1068.
[5] Flaig, U., Polach, W., and Ziegler, G., 1999, ''Common Rail System (CR-System) for Passenger Car DI Diesel Engines; Experiences With Applications for Series Production Projects,'' SAE paper 1999-01-0191.
[6] Ganser, M. A., 2000, ''Common Rail Injectors for 2000 Bar and Beyond,'' SAE paper 2000-01-0706.
[7] Wickman, D. D., Tanin, K. V., Senecal, P. K., Reitz, R. D., Gebert, K., Barkhimer, R. L., and Beck, N. J., 2000, ''Methods and Results From the Developmentof a 2600 Bar Diesel Fuel Injection System,'' SAE paper 2000-01-0947.
[8] Kohketsu, S., Tanabe, K., and Mori, K., 2000, ''Flexibly Controlled Injection Rate Shape With Next Generation Common Rail System for Heavy Duty DI Diesel Engines,'' SAE paper 2000-01-0705.
[9] Amoia, V., Ficarella, A., Laforgia, D., De Matthaeis, S., and Genco, C., 1997, ''A Theoretical Code to Simulate the Behavior of an Electro-Injector for Diesel Engines and Parametric Analysis,'' SAE paper 970349.
[10] Ficarella, A., Laforgia, D., and Landriscina, V., 1999, ''Evaluation of Instability Phenomena in a Common Rail Injection System for High Speed Diesel Engines,'' SAE paper 1999-01-0192.
[11] Lasa, M., Heinkel, H. M., Moser, E., and Rothfuß, R., 2000, ''Expeditious Design of Mechatronic Systems Using a VHDL-AMS Based Standard Element Library—A Common Rail Example,'' SAE paper 2000-01-0581.
[12] Gebert, K., Barkhimer, R. L., Beck, N. J., Wickman, D. D., Tanin, K. V., Das, S., and Reitz, R. D., 1998, ''An Evaluation of Common Rail, Hydraulically Intensified Diesel Fuel Injection System Concepts and Rate Shapes,'' SAE paper 981930.
[13] Bianchi, G. M., Pelloni, P., Filicori, F., and Vannini, G., 2000, ''Optimization of the Solenoid Valve Behavior in Common-Rail Injection Systems,'' SAE paper 2000-01-2042.
[14] Bianchi, G. M., Falfari, S., Pelloni, P., Kong, S. C., and Reitz, R. D., 2002, ''Numerical Analysis of High-Pressure Fast-Response Common Rail Injector Dynamics,'' SAE paper 2002-01-0213.
[15] Von Kuensberg Sarre, C., Kong, S. C., and Reitz, R. D., 1999, ''Modeling the Effects of Injector Nozzle Geometry on Diesel Sprays,'' SAE paper 1999-01-0912.
[16] Munson, B. R., Young, D. F., and Okiishi, T. H., 1990, *Fundamentals of Fluid Mechanics*, Wiley, New York.
[17] Catania, A. E., Dongiovanni, C., Mittica, A., Badami, M., and Lovisolo, F., 1994, ''Numerical Analysis vs. Experimental Investigation of a Distribution Type Diesel Fuel Injection System,'' ASME J. Eng. Gas Turbines Power, **116**, pp. 814–830.
[18] Dongiovanni, C., 1997, ''Influence of Oil Thermodynamic Properties on the Simulation of a High Pressure Injection System by Means of a Refined Second Order Accurate Implicit Algorithm,'' ATA Automotive Engineering, pp. 530–541.
[19] Nasar, S. A., 1995, *Electric Machines and Power Systems: Vol. 1, Electric Machines*, McGraw-Hill, New York.
[20] Chai, H. D., 1998, *Electromechanical Motion Devices*, Prince All, NJ.
[21] Klopfenstein, R. W., 1971, ''Numerical Differentiation Formulas for Stiff Systems of Ordinary Differential Equations,'' RCA Rev., **32**, pp. 447–462.
[22] LeVeque, R. J., 1990, *Numerical Methods for Conservation Laws*, Birkhäuser Verlag, Basel.

A Diagnostic Method for Heavy-Duty Diesel Engines Used in Stationary Applications

D. T. Hountalas

D. A. Kouremenos

Mechanical Engineering Department,
Thermal Engineering Section,
National Technical University of Athens,
Heroon Polytechniou 9,
15773 Athens, Greece

M. Sideris

Hellenic Public Power Corporation,
Island Production Division,
Syggrou Avenue 112,
11741 Athens, Greece

The diesel engine is used for power generation in stationary applications especially in isolated areas not connected to the main distribution network due to its relatively high efficiency, durability, and flexibility compared to alternative power sources. The diesel engine can easily follow power fluctuations. For this reason it is widely used for power generation in Islands in Greece. The diesel engine is a complex machine and requires intensive maintenance to insure proper and efficient operation. This is amplified by the interaction between the engine and the exhaust gas turbocharger. The present work describes an advanced troubleshooting method, based mainly on thermodynamics, for stationary engine monitoring and fault detection. The method is based on the processing of measured engine data using a simulation model and provides the current engine condition and its tuning. An application of the method on a slow speed diesel engine used for power generation is presented. The method is applied in the field and the results reveal the condition of the engine and its subsystems. Furthermore, proposals are made to improve engine performance. The method is most useful since it is possible to detect faults at their initial stage that may in the future result in serious problems and limit the availability of the engine. [DOI: 10.1115/1.1787500]

Introduction

Diesel engines are widely used for power generation in stationary applications isolated from the main network because of their durability, high efficiency, power concentration, and flexibility, [1,2]. These engines can operate at loads ranging from 25% up to 100% with no problem while maintaining a high level of efficiency for loads exceeding 40%. This is a great advantage since they are suitable for cases with high power fluctuations. Furthermore, increasing the number of units allows us to have a number of them operating close to their optimum point. For this reason diesel engines are widely used in the area of Greece for power production in islands that are not connected to the main power network. It is extremely important that these engines are kept in an excellent condition that enables a high degree of availability and relatively low fuel consumption, which is a major factor due to the number of operating hours. To achieve this the engineer has to face a series of problems related to their operation. A major challenge related to these engines is that due to their relatively large size it is extremely difficult to detect an engine malfunction using trial and error methods. To maintain the engine properly, the engineer usually makes use of overall data taken from the engine subsystems [1,2]. These data, even though essential, do not provide the means to detect accurately and in a time efficient way the actual cause for an engine malfunction. One of the most difficult problems is to determine the cause for low power output or high exhaust gas temperature in cases where no obvious fault or damage exists.

In the past, various methods have been proposed for heavy-duty diesel engines fault diagnosis with minor success. These methods [3–7] are statistical and are based on the correlation of measured engine data with data obtained under a known engine fault condition or on the comparison of the current engine state with an ideal one. However, it is extremely difficult or even impossible to correlate properly the current engine state with one from the engine shop tests and even if this is accomplished, it is very difficult to detect the actual cause of an engine fault. Currently modern techniques for fault detection are under development from engine manufacturers using neural networks. Even though it is relatively early to have an indication concerning their efficiency one problem is recognized by people involved in the field, these methods are usually dedicated to a specific engine design. Furthermore, they require a great amount of data that are usually not easily available for field applications and provide little information concerning engine tuning.

In the present work, a completely different approach to the problem of heavy-duty diesel engine troubleshooting is proposed which aims to offer an applicable, time economic, and relatively simple solution to the problem. Considering the economical impact of improper engine operation and low efficiency or power output on power production makes the case for introducing such a method. An additional reason for introducing such methods is the reduction of pollutant emissions since they are closely related to the condition of the engine and its subsystems. The proposed method offers a large amount of information enabling detection of an engine fault at its early stage before resulting in a serious malfunction.

The proposed method is based on thermodynamics and makes use of a detailed simulation model of the engine and its components and experimental data [8,9]. The required engine data are measured easily on the field using conventional instrumentation requiring no modification of the engine and its subsystems. The proposed method is fully automatic requiring no interactive action from the engineer eliminating thus another source of possible error. The method provides the condition of the engine in a few minutes and makes proposals for required adjustments to achieve optimum engine performance at the present state. This is an important advantage since for an old and worn-out engine the required tuning for optimum performance differs considerably from that of a new one. Up to now the method has been used in marine applications giving promising results [8,9]. In the present work, the application of an improved version to a large-scale two-stroke slow speed diesel engine used for power generation is given. The improved version is faster compared to the previous one and its main advantage is that it is completely automatic requiring no

Contributed by the Internal Combustion Engine Division of THE AMERICAN SOCIETY OF MECHANICAL ENGINEERS for publication in the ASME JOURNAL OF ENGINEERING FOR GAS TURBINES AND POWER. Manuscript received by the ICE Division, September 2002; final revision received November 2003. Associate Editor: D. Assanis.

interaction from the user. This automatic procedure involves both initial calibration of the model and the diagnostic procedure itself.

In the present work a brief description is given of the modifications conducted on the simulation model to improve its predictive ability and the general philosophy of the diagnosis procedure. Furthermore, a description is given of the diagnosis methodology and the procedure used to estimate the model constants and relate them with the condition of the engine and its subsystems. A detailed description of the application of the method on a two-stroke diesel engine used for power generation is given. The method is applied before the initiation of the high power demand period (summer) to estimate the present engine condition and the need for additional tuning. From the analysis of measured engine data, using the diagnosis method, the actual condition of the engine and its subsystems is revealed and compared to the one expected for a new engine (with proper tuning and new component condition). The latter provides a clear picture of the engine condition to the engineer and can be accomplished only with the use of modeling, since shop test data refer to the conditions at which these were conducted.

Description of the Engine Simulation Model

The heart of the diagnosis method is an existing simulation model capable of describing a variety of engine configurations [10]. Since the purpose of the present work is not the development of a simulation code but its use for diagnostic purposes we will only give a general description and focus our attention on modifications conducted to improve its predictive capability.

Engine Cylinder Simulation

Heat-Transfer Model. A turbulent kinetic energy viscous dissipation rate $k\sim\varepsilon_t$ model [10] is used to determine the characteristic velocity for the heat-transfer calculations as proposed by Assanis and Heywood [11] and described in detail in previous publications [8,10]. The heat-transfer coefficient is estimated using the following relation [2,11]:

$$h_c = c\ \mathrm{Re}^{0.8}\ \mathrm{Pr}^{0.33}\frac{\lambda}{l_{\mathrm{car}}}. \tag{1}$$

Cylinder Blowby. An important parameter involved in engine diagnosis is blowby that affects the compression and combustion expansion pressure diagram [1,2]. In the present work a rather simple model is used instead of a detailed one developed in the past [12] since the latter requires knowledge of detailed engine data that in most cases are not available for field applications. For this reason blowby rate is estimated using an equivalent blowby area between the cylinder rings and the cylinder bore [8]. The mass flow is calculated using isentropic compressible flow relations. The equivalent blowby area A is equal to

$$A = \pi D\,\delta r, \tag{2}$$

where δr is the equivalent cylinder-ring clearance.

Jet Model. Up to now for diagnostic purposes a relatively simple jet formation model was used to estimate the air entrainment rate inside the combustion zone. During its application on marine diesel engines various problems were realized that affected the diagnosis procedure. The simulation required in some cases tuning of model constants to adequately predict engine performance with the variation of engine operating conditions. This affected the diagnosis procedure since, as described in the next section, it is based on the comparison of model constants. For this reason we modified the jet formation model to account for the various physical mechanisms involved in the air-fuel mixing mechanism as described below.

The resulting fuel jet is assumed to have the shape of a cone penetrating inside the engine cylinder consuming the surrounding air. Its penetration length inside the cylinder is estimated from empirical correlations that provide the velocity along the spray axis [2,13,14],

$$\begin{aligned} u = u_{\mathrm{inj}} &= C_d\left(\frac{2\Delta \mathrm{P}}{\rho_{\mathrm{l}}}\right)^{0.5} \quad \text{for } x < L, \\ u &= u_{\mathrm{inj}}\left(\frac{L}{x}\right)^{n} \quad \text{for } x \geqslant L, \end{aligned} \tag{3}$$

where now is considered the breakup length "L" given by the following expression [14,15]:

$$L = u_{\mathrm{inj}} t_{\mathrm{break}} \cong c_l\left(\frac{\rho_l}{\rho_a}\right)^{0.5} d_{\mathrm{inj}} \tag{4}$$

and c_l is a constant and ρ_a, ρ_l the densities of air and fuel, respectively.

The jet angle is now considered variable and obtained from the following relation [2,13–15]:

$$\alpha = 0.05\left(\frac{d_{\mathrm{inj}}^2 \rho_a \Delta P}{\mu_a^2}\right)^{0.25}. \tag{5}$$

Furthermore, in the improved model the effect of air swirl upon jet penetration and cone angle is considered for using the following well tested relations [15]:

$$x_s = x\left(1 + \frac{c_s}{1 + c_s}\right)^{-1}, \tag{6}$$

$$\alpha_s = \alpha\left(1 + \frac{c_s}{1 + c_s}\right), \tag{7}$$

where c_s is given by

$$c_s = \frac{u_a r}{30\pi N} \tag{8}$$

and r is the radial distance from the cylinder axis.

Air swirl results in an increase of the air entrainment rate inside the jet and subsequent wall impingement. The instantaneous swirl ratio c_s is obtained from the conservation of angular momentum inside the engine cylinder as described in Ref. [13].

After impingement on the cylinder walls, the wall jet theory of Glauert [16] is used to determine the jet history upon the cylinder walls. Details concerning this mechanism together with the analytical expressions can be found in Refs. [10,13].

Estimation of Air Entrainment Rate. To estimate the rate of air entrainment into the burning zone we consider the volume change rate of the jet. The air entrainment rate is thus obtained from

$$\frac{dm_{\mathrm{in}}}{dt} = \rho\frac{dV_j}{dt}. \tag{9}$$

Estimation of the Combustion Rate. Another improvement introduced in the present model is that the injected fuel is now divided into groups having the same Sauter mean diameter depending on their time of entrance into the burning zone. The Sauter mean diameter of each group D_{SM} is obtained from the following semiempirical expressions used by various researchers in multi-zone codes [13,14] derived by analyzing experimental data:

$$D_{\mathrm{SM},1} = 0.38\ \mathrm{Re}_{\mathrm{inj}}^{0.25}\ \mathrm{We}_{\mathrm{inj}}^{-0.32}(\nu_l/\nu_a)^{0.37}(\rho_l/\rho_a)^{-0.47} d_{\mathrm{inj}}, \tag{10a}$$

$$D_{\mathrm{SM},2} = 4.12\ \mathrm{Re}_{\mathrm{inj}}^{0.12}\ \mathrm{We}_{\mathrm{inj}}^{-0.75}(\nu_l/\nu_a)^{0.54}(\rho_l/\rho_a)^{0.18} d_{\mathrm{inj}} \tag{10b}$$

where subscripts "1" and "2" denote complete and incomplete sprays, respectively. The Reynolds and Weber numbers are given by

$$\mathrm{Re}_{\mathrm{inj}}=\frac{u_{\mathrm{inj}}d_{\mathrm{inj}}}{\nu_l},\quad \mathrm{We}_{\mathrm{inj}}=\frac{u_{\mathrm{inj}}^2 d_{\mathrm{inj}}\rho_l}{\sigma}. \tag{11}$$

The Sauter mean diameter is taken to be the maximum of these two values calculated in Eqs. (10*a*) and (10*b*). The fuel droplets evaporate and the resulting vapor mixes with the surrounding air to form a combustible mixture. The mixing rate is controlled by turbulent diffusion; the evaporated fuel and the air entrained are divided into two portions; a macromixed one and a micromixed one [10]. The corresponding rates are given by

$$\dot{m}_{\mathrm{fmic}}=D_t(u)(m_{\mathrm{fmac}}-m_{\mathrm{fmic}}), \tag{12a}$$

$$\dot{m}_{\mathrm{amic}}=D_t(u)(m_{\mathrm{amac}}-m_{\mathrm{amic}}), \tag{12b}$$

$$D_t(u)=a_{\mathrm{mix}}u, \tag{13}$$

where a_{mix} is a constant and u the relative velocity of the burning zone element with respect to the surrounding air. Ignition delay is determined from the relation [1,2,17]

$$S_{pr}=\int_0^t \frac{1}{a_{\mathrm{del}}P_g^{-2.5}\Phi_{\mathrm{eq}}^{-1.04}\exp(5000/T_g)}\,dt-1, \tag{14}$$

where "Φ_{eq}" is the local equivalence ratio of the fuel air mixture inside the zone and T_g, P_g the cylinder temperature and pressure respectively expressed in K and bars.

The combustion rate of fuel is modeled using an Arrhenius type equation of the form [1,2,10]

$$m_{\mathrm{fb}}=\left\{K_b\frac{m_{\mathrm{fmic}}-m_{\mathrm{fb}}}{T^{0.5}}e^{-E_c/T}P_{\mathrm{O}_2}\right\},\quad \text{if } (\mathrm{AFR})>(\mathrm{AFR})_{\mathrm{st}},$$
$$m_{\mathrm{fb}}=\left\{K_b\frac{m_{\mathrm{fmic}}-m_{\mathrm{fb}}}{(\mathrm{AFR})_{\mathrm{st}}T^{0.5}}e^{-E_c/T}P_{\mathrm{O}_2}\right\},\quad \text{if } (\mathrm{AFR})\leqslant(\mathrm{AFR})_{\mathrm{st}}, \tag{15}$$

where K_b is a constant, E_c the reduced activation energy (K), AFR the air fuel ratio, and $\mathrm{P}_{\mathrm{O}_2}$ the partial pressure of oxygen inside the zone.

The Fuel Injection System. A detailed simulation model has been developed in the past for the fuel injection system [18] requiring a great number of geometrical data that are extremely difficult to obtain for commercial engines. For this reason a simpler model is used for diagnostic purposes [19]. In this model the following control volumes are considered: *high-pressure pump chamber (1), delivery valve chamber (2), delivery pipe from pump to injector (3), injector (4).*

The simulation of each control volume is accomplished by considering the incoming and outgoing volume flow rates and the fuel compressibility, obtaining the following relation [19]:

$$\frac{dP_j}{dt}=\frac{K_f}{V_j}\left(\frac{dV_j}{dt}-\dot{Q}_{tj}\right), \tag{16}$$

where $\dot{Q}_{tj}=\Sigma\,\dot{Q}_j$ is the total net volume flow rate into the control volume and dV_j/dt is the rate of its volume change. The volumetric flow rate through orifices, various openings, or ports is given by the formula

$$\dot{Q}_j=A_jC_{dj}\left(\frac{2\Delta P_j}{\rho_j}\right)^{0.5}, \tag{17}$$

where "j" is the corresponding volume. The delivery valve is modeled in a rather simple way that has been found to give relatively accurate results for engine performance prediction. It is considered as a check valve allowing the fuel to flow only from the delivery chamber to the fuel pipe. The injector is modeled in a similar way, as a check valve, allowing fuel to flow towards the combustion chamber only when the pressure exceeds its opening pressure. The pressure history inside the fuel pipe is obtained using the method of characteristics to solve unsteady flow equations [19].

Simulation of the Inlet and Exhaust System. Since the most common turbocharging system used in two-stroke stationary diesel engines is the constant pressure one [20,21] the filling-emptying method is used in the present work [2,11,20,21] to estimate the pressure-temperature versus time history in the two manifolds (intake-exhaust). The mass flow rate through the turbine nozzle is calculated using isentropic flow relations and the effective area A_{eff} of the turbine nozzle.

Scavenging Model. An important mechanism for two-stroke turbocharged engine operation is scavenging [1]. For this reason a new two-zone scavenging model has been developed while in the past simple correlations were used for marine engine diagnosis. During gas exchange, the cylinder contents are divided into two parts: one consisting only of fresh entrained air, and a second consisting of combustion products from the previous cycle and fresh entrained air. During scavenging, part of the intake air escapes directly into the exhaust manifold (short-circuiting) reducing the exhaust gas temperature considerably [2]. If $dm_{a,\mathrm{inl}}$ is the total amount of air entering the cylinder at a certain time during intake, one part $dm_{a,\mathrm{exh}}$ escapes to the exhaust manifold directly, while the remaining one enters the fresh air and combustion products zone. These amounts are given by the following two relations:

$$dm_{a,\mathrm{fz}}=(dm_{a,\mathrm{inl}}-dm_{a,\mathrm{exh}})(1-C_{1\mathrm{scav}}), \tag{18a}$$

$$dm_{a,\mathrm{cz}}=(dm_{a,\mathrm{inl}}-dm_{a,\mathrm{exh}})C_{1\mathrm{scav}}. \tag{18b}$$

If $dm_{g,\mathrm{exh}}$ is the total amount of exhausted cylinder mass to the exhaust manifold; this is taken partially from the fresh air zone and the combustion products one. Thus the gas masses taken from the two zones are given from the following relations:

$$dm_{g,\mathrm{fz}}=(dm_{g,\mathrm{exh}}-dm_{a,\mathrm{exh}})C_{2\mathrm{scav}}, \tag{19a}$$

$$dm_{g,\mathrm{cz}}=(dm_{g,\mathrm{ex}}-dm_{a,\mathrm{exh}})(1-C_{2\mathrm{scav}}), \tag{19b}$$

where $C_{1\mathrm{scav}}$ and $C_{2\mathrm{scav}}$ are the constants of the scavenging model. At the end of scavenging (start of compression stroke), perfect mixing between the two zones is assumed resulting in a single zone that is a mixture of fresh entrained air and combustion products from the previous cycle.

Turbocharger. It is often difficult to obtain characteristic charts for the compressor and the turbine especially for existing engines. To overcome the problem the method of operation similarity [9,22] is used from which we manage to reproduce the charts from existing experimental data. The method is efficient for engine loads in the range of 40–100% and is as follows: We calculate, using a least-squares method and data from the official shop tests, the constants of polynomial curves fitting the following functions:

$$\eta_{\mathrm{is}_C}=f_1(\phi), \tag{20}$$

$$\eta_{\mathrm{is}_T}=f_2(\phi), \tag{21}$$

$$k_{\mathrm{is}}=f_3(\phi)=\Delta h_{\mathrm{is}}/U^2, \tag{22}$$

where $\phi=m/(\rho AU)$ is the flow coefficient.

The data required for the calculation of the turbine and compressor characteristic maps in the above form are: pressure before and after the compressor, pressure before and after the turbine, air temperature before and after the compressor, exhaust gas temperature before and after the turbine, rotational speed of the turbocharger, air and exhaust gas mass flow rate obtained from the simulation using the previous data.

Then using the previous relations and the current "ϕ" value T/C performance is estimated. The mass flow rate through the

turbine nozzle is estimated using compressible flow relations [20,21] and the equivalent nozzle flow area "A_{eff}."

Air Cooler. The pressure drop and effectiveness are functions of the mass flow rate through it [8,20],

$$\varepsilon = 1 - b\dot{m}^2, \tag{23}$$

$$\Delta P_{\text{ac}} = a_{\text{ac}}\dot{m}^2, \tag{24}$$

where effectiveness "ε" is defined as

$$\varepsilon = \frac{T_{a,\text{in}} - T_{a,\text{out}}}{T_{a,\text{in}} - T_{c,\text{in}}} \tag{25}$$

and subscripts "a, c, in, out" denote, respectively, air, cooling medium, inlet, and outlet from air cooler. Constants "a_{ac} and b" are determined so that the values match the ones calculated from the engine shop tests. The mass flow rate of air is calculated from the simulation model using measured engine data.

Outline of the Proposed Diagnostic Methodology

It is widely recognized that a number of engine subsystems have a serious effect on overall engine performance [11,20,21]. For this reason it is extremely difficult to detect the actual cause for an engine malfunction or improper operation. It would be extremely important if one could provide in a direct way the actual cause for an engine fault. This would result in savings in both labor and spare parts and would increase greatly the availability of the unit.

To perform a diagnosis the engineer mainly utilizes data obtained from measurable engine parameters such as pressure, temperature, etc. These parameters are usually influenced by a number of subsystems making the distinction of the actual cause for a fault extremely difficult if not impossible. As an example let us assume that a lower than normal peak combustion pressure is observed. In this case, there are a number of possible reasons, i.e., low fuel flow rate, faulty injector, improper injection timing, low boost pressure, increased blowby, etc.

To solve the previous problem it is required to develop a method that can distinguish for the effect of each parameter using mainly the measured cylinder pressure trace and injection pressure diagram if available. For this reason in the proposed method a stepwise approach is adopted that distinguishes between the parameters affecting the compression stroke, the ones affecting the combustion expansion stroke, and finally the ones affecting the gas exchange system [8,9]. The method is based on a simulation model developed by the authors [10] focusing mainly on the accurate prediction of engine performance rather than to a detailed description of the fundamental mechanisms. This is the best way to proceed, since simple models are most adequate for such applications. The simulation model is calibrated to provide engine behavior at the reference state (new engine) and then the process is repeated at the current state. For this reason an autocalibration method is used to estimate constants values that describe the condition of each engine subsystem [8,9]. In Fig. 1(a) is given the procedure followed to estimate model constants "β" so that the output "Y" is predicted using the input (engine operating conditions) and the constants β involved in the modeling. We assume that an error or malfunction exists if the following criterion is satisfied:

$$\left|\frac{\beta - \beta_0}{\beta_0}\right| x100 \geqslant 3, \tag{26}$$

where β are the constants determined at the present state and β_0 their corresponding values at the reference state, i.e., new engine condition. The three percent error limit is used to account for measurement errors on the field.

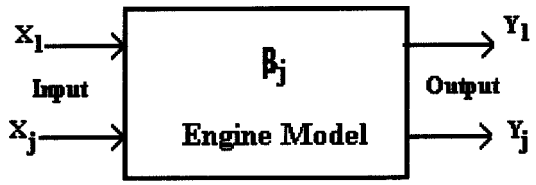

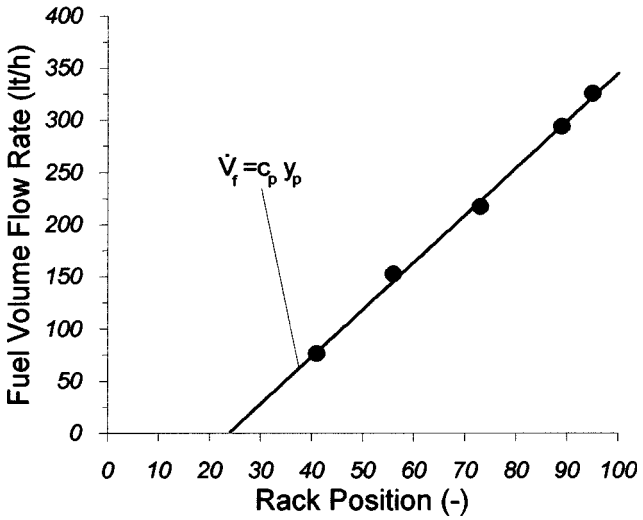

Fig. 1 (*a*) Constant determination philosophy (*b*) Fuel pump volumetric flow rate versus rack position

Estimation of Model's Constants

The model constants are related to the condition of various engine subsystems and their reference values are determined from shop test data. The relation between an engine constant and the condition of an engine subsystem is determined from a sensitivity analysis, described in Ref. [9].

For constant estimation a completely automatic methodology has been developed using measured engine data obtained from the engine shop tests or from measurements conducted in the field. All constants are determined so that the values of various computational parameters Y_{calc} obtained from the simulation model match with reasonable accuracy the measured ones Y_{expt}.

Assume that the number of constants to be determined is "j," while the available number of measured values is "i." A least-squares method is used, aiming for the minimization of the following function:

$$f_{\text{err}}(\beta_{1,2,\ldots,j}) = \sum_{\text{i}} (Y_{\text{expt},i} - Y_{\text{calc},i})^2, \tag{27}$$

where Y_{expt} and Y_{calc} are the matrices of the experimental and calculated values, respectively. The problem is thus reduced to the minimization of the sum of squares function f_{err} which is nonlinear in parameters [23,24]. The algorithm for the solution is as follows:

$$\beta^{k+1} = \beta^k + Z^k X^{T(k)} (Y_{\text{expt}} - Y_{\text{calc}}^{(k)}),$$

where

$$Z^{-1(k)} \equiv X^{T(k)} W X^{(k)}. \tag{28}$$

Table 1 Constants values determined during the current diagnosis procedure

Constant name	Indicative values
CR	19.62
c	0.023
δr	0.30×10^{-4} m
T_w	430K
a_{del}	0.32
a_{mix}	0.40
K_b	5.5×10^{6}
A_{eff}	0.067m^2
c_p	1.02×10^{-3} m^3 s^{-1}
a_{ac}	2.89kg^{-1} m^{-1}
b	2.24×10^{-4} kg^{-2} s^2

In this relation β represents the constants or parameters vector to be determined, k is the iteration number, X is the sensitivity matrix defined by

$$X=\begin{bmatrix} X_{ll} & \cdot & X_{lj} \\ \cdot & \cdot & \cdot \\ X_{il} & \cdot & X_{ij} \end{bmatrix}=\begin{bmatrix} \dfrac{\partial Y_{l,\text{calc}}}{\partial \beta_1} & \cdot & \dfrac{\partial Y_{l,\text{calc}}}{\partial \beta_j} \\ \cdot & \cdot & \cdot \\ \dfrac{\partial Y_{i,\text{calc}}}{\partial \beta_1} & \cdot & \dfrac{\partial Y_{i,\text{calc}}}{\partial \beta_j} \end{bmatrix} \tag{29}$$

and W is a weighting matrix defined in a way that takes into account the importance of each parameter by either including or excluding it from the current calculation step (values 1 and 0, respectively).

The constants determined during the present application and their estimated values are shown in Table 1. The constants determination procedure initiates using only the compression part of the measured cylinder pressure trace. First the ignition point is determined and then the part of the simulation describing the compression stroke up to this point is used. The constants determination procedure is applied until the calculated cylinder pressure trace matches the measured one. From this procedure the constants affecting the compression stroke are estimated. Then the simulation makes trial runs to estimate the ignition delay period and the relevant constant value a_{del}. After this is finished it goes on to the combustion expansion phase estimating the fuel mass flow rate and constants K_b, a_{mix} to match the pressure rise rate and peak cylinder pressure. Once this process is completed the entire open cycle simulation is used to estimate constant A_{eff} to have a mean pressure at the exhaust manifold equal to the measured. Once the process is completed new conditions at the inlet port closure are determined and the entire process is repeated until all constants converge. At the end the constants of the gas exchange system, i.e., T/C and A/C, are estimated. This is in brief the procedure followed to estimate model constants on the field.

Determination of the Correlation Between Engine Parameters and Constants Values

A sensitivity analysis is conducted using the simulation model to determine the relation between constants and measurable engine parameters. For this reason the value of each constant β_j is varied by $\delta\beta_j$ and the corresponding effect on the measured output value $Y_{\text{expt},i}$ is estimated. The sensitivity coefficient is then obtained from the following relation:

$$\delta s_{j,i}=\frac{\delta\beta_j}{\delta Y_{\text{expt},i}}. \tag{30}$$

Applying the previous procedure determines the relation between model constants and engine parameters.

Constants Related to the Compression Stroke. In the case of the compression stroke it is difficult to distinguish for the actual effect of each constant if only the peak cylinder pressure is used. For this reason we use the entire cylinder pressure trace because it has been observed in a previous detailed investigation [25] that each parameter affects different parts of the cylinder pressure diagram:

- CR affects the entire cylinder pressure trace and has significant affect on the initial part of the compression stroke.
- Parameter δr affects the part around TDC and during expansion. It has the most significant effect on the peak compression pressure angle shifting its value to the left relatively to TDC position. Its value is used to estimate the degree of cylinder/ring wear.
- T_w has a significant effect around TDC.
- The constant c is taken equal to the value estimated from the shop test data since it is characteristic for a specific engine.

Thus the constants values are estimated so that the calculated cylinder compression diagram matches accurately the measured one for all operating conditions examined. During this procedure the values of CR and δr should remain relatively unchanged since they represent geometrical data of the engine.

Constants Related to the Combustion Expansion Stroke The constant a_{del} is related to the ignition delay period and thus to the fuel cetane number while constant a_{mix} is related to the peak combustion pressure. Injector quality is expressed considering the current value of constant a_{mix} in comparison to the one obtained for a new engine. Finally the constant K_b is related to the rate of pressure rise during the initial part of combustion.

Constants Related to the Fuel Injection System. The high-pressure pump barrel-cylinder clearance δr_p, expressing the condition of the fuel pump is related to the derivative of the fuel pressure inside the pipe at injection start that affects the dynamic injection delay period, i.e., the time between the static start of delivery and the injector opening. The delivery valve leakage area A_{dval} is related to the residual pressure inside the fuel pipeline. In cases where no fuel injection pressure diagram is available, which is a common case for engines operating in the field, use is made of the fuel rack position. The mass flow rate of fuel supplied by the high-pressure pump is related to the pump index by the following relation:

$$\dot{m}_f=c_p\rho_f y_p, \tag{31}$$

where y_p is the fuel rack position and c_p a constant related to the overall condition of the fuel pump. The validity of the previous linear relation is verified observing Fig. 1(*b*) obtained from the shop test data, providing the variation of the fuel pump volumetric flow rate with rack position. Constant c_p is the tangent of the curve and provides an estimate of the condition of the fuel pump.

Constants Related to the Inlet/Exhaust System. The constant a_{ac} is related to the air cooler pressure drop and determines the degree of pollution while the constant b is related to the air cooler effectiveness and is used to express its efficiency.

The constant A_{eff} is related to the mean pressure before the turbine and is used to estimate the condition of the inlet nozzle (i.e., pollution). Finally the coefficients of the polynomials involved in Eqs. (20)–(22) are used to estimate the condition of the compressor and the turbine.

Determination of Constants Values at the Reference State

As mentioned, the diagnosis procedure is based on the comparison of constants values determined for a new engine condition with the ones at the present state. Thus the model must be calibrated using available experimental data before diagnosis. For this purpose a special calibration procedure has been developed which is fully automatic and makes use of engine data that are provided in the engine shop tests (see Table 2).

Table 2 Shop test data required for model calibration

Main engine data	Inlet/exhaust system data
Engine speed	Gas pressure before/after the turbine
Fuel flow rate	Turbine rotational speed
Brake power output	Air pressure before/after compressor
Peak firing pressure	Gas temperature before/after the turbine
Peak compression pressure	Compressor air inlet temperature
Fuel mass flow rate	Air temperature before/after the air cooler
Fuel rack setting	Water temperature before/after air cooler
VIT Index setting	Air cooler pressure drop

For a new engine with minimum cylinder-ring wear and known CR the model can be calibrated without using the entire cylinder pressure diagram. The knowledge of specific points, i.e., peak compression pressure and peak firing pressure, is adequate. This is important since for such large engines it is not usually possible to have detailed experimental data in the required form, i.e., a cylinder pressure trace. The process followed to estimate constants values is similar to the one described in the ''estimation of constant's values'' section. During this process we estimate the constant c of the heat-transfer model, which is then maintained the same since it is a characteristic of the specific engine.

Estimation of Cylinder Fuel Flow Rate

For a multi-cylinder engine operating on the field, it is extremely difficult if not impossible to estimate the fuel flow rate to each cylinder especially in cases where injection pressure is not available. For this reason, we have developed a method to estimate the fuel flow rate based on the processing of the measured cylinder pressure diagram. An estimate of the amount of fuel mass burned inside the engine cylinder is obtained from the heat release rate analysis as follows [2]:

$$m_{\text{finj}} = \frac{Q_{g,\text{cum}}}{H_{\text{calor}}}, \tag{32}$$

where H_{calor} is the lower heating value of the fuel used. Term $Q_{g,\text{cum}}$ is the cumulative gross heat release obtained from the net heat release [1,2] and the calculated heat losses to the cylinder wall using the engine simulation model. The instantaneous gas temperature for the heat release rate analysis is obtained using the perfect gas state equation and the measured cylinder pressure value as follows:

$$T_g = \frac{P_{\text{expt}} V}{mR}. \tag{33}$$

The method has been validated by laboratory experiments and its accuracy is around 2.0%.

Experimental Procedure

The diagnosis method requires specific engine operating data. The most important data are the cylinder pressure trace and if available the fuel injection system pressure history. The latter for the present application, as mentioned, was not available because the engine was not equipped with a suitable transducer mounting position. Prior to the initiation of the measurement procedure absolute pressure sensors and thermocouples were mounted on the inlet and exhaust manifolds. Special attention was paid to the accurate measurement of the pressure history inside the exhaust and inlet manifolds since their pressure difference controls the scavenging process.

Figure 2 gives the layout of the experimental procedure where we observe the engine and the various measurement points. Cylinder pressure data are recorded using a fast data acquisition system at a sampling rate of 1 deg engine crank angle [26]. A total of 40 cycles are recorded from which a mean pressure diagram is estimated.

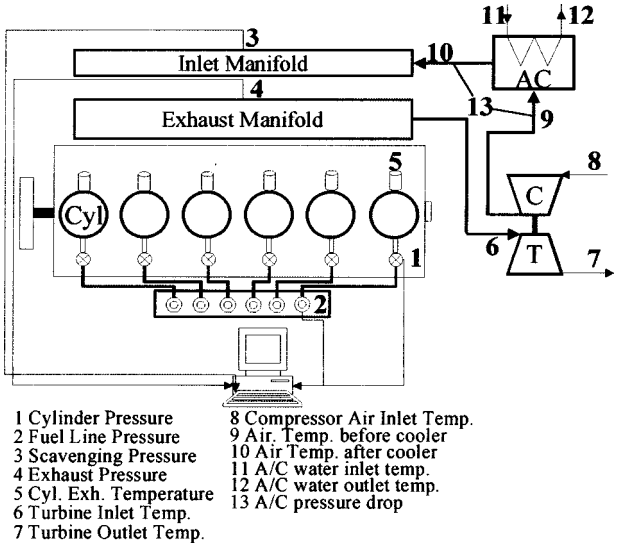

Fig. 2 Diagram of the experimental method

A serious problem in the case of field applications is the accurate estimation of TDC position especially when no specific installation exists. For this reason, a thermodynamic method for TDC estimation using the compression part of the measured cylinder pressure diagram was developed and validated. The accuracy of the method has been verified in previously reported work [8,27] by comparing the measured TDC position with the theoretically calculated one. The accuracy of the method is ± 0.2 deg CA. The method has been used in the present work and its accuracy has been verified by comparing the estimated power output of the unit with the one of the generator by considering for its mechanical losses. The mechanical efficiency of the engine is estimated from the official shop tests where it is given the indicated power output of the engine and its brake power output. The mechanical losses of the generator are estimated using data from the official acceptance tests, where the indicated power output and the electrical power generated were measured (using the mechanical efficiency of the engine estimated from the shop tests).

Application of the Diagnosis Procedure on a Stationary Two-Stroke Diesel Engine

The proposed method is applied on a stationary two-stroke turbocharged diesel engine used for power generation in a power station of the Hellenic Islands. The main purpose of the investigation is to determine the condition of the engine and its tuning before the initiation of the high power demand period. Measurements are taken using laboratory instrumentation properly modified for application on the field at two engine loads, namely 67.5 and 92.5% as shown in Table 3. Table 4 shows the main data of the engine. A short list of the test conditions for all measurements conducted is given in Table 3.

Table 3 Test conditions examined

Test number	Engine speed	Load
1	136.7 rpm	67.5%
2	136.7 rpm	92.5%

Table 4 Main engine data

Type: MAN KMC607S	7 Cyl
Cylinder bore	600mm
Stroke	1650mm
Connecting rod length	2280mm
CR (nominal)	19.8
Number of turbochargers	1
Number of air coolers	1

Results of the Diagnosis Procedure

Analysis of Cylinder Pressure Data Determination of Cylinder Compression Condition

Measured Cylinder Pressure Data. The pressure diagrams of all cylinders are given in Figs. 3(*a*) and (*b*) for 67.5 and 92.5% engine load, respectively at 136.7 rpm engine speed. These are the mean values estimated from a series of 40 successive cycles, a number that is quite adequate for a slow speed diesel engine. This was verified during the measurement where no significant cycle variability was observed. The results given in the next paragraphs

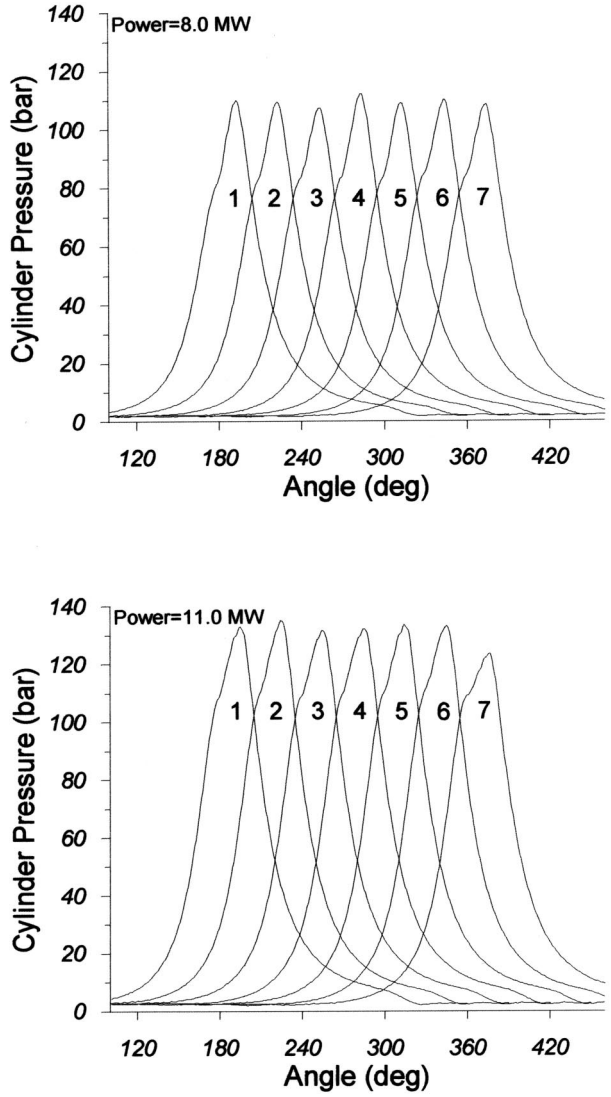

Fig. 3 (*a*) Measured cylinder pressure diagrams at 136.7 rpm and 92.5% load (*b*) Measured cylinder pressure diagrams at 136.7 rpm and 67.5% load

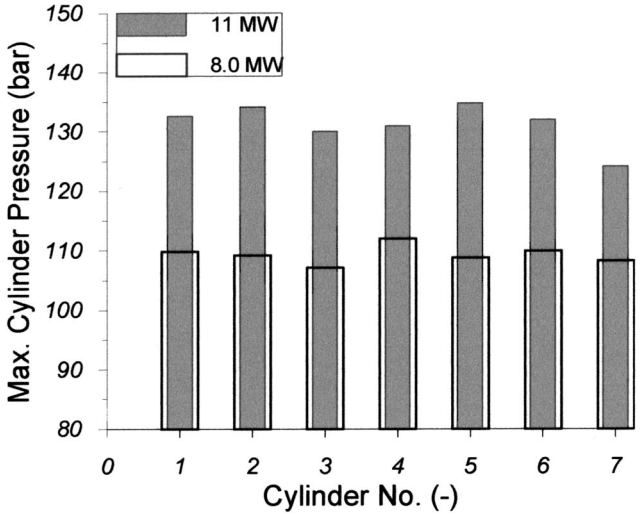

Fig. 4 Maximum combustion pressures at 136.7 rpm engine speed

are obtained using the mean cylinder pressure trace. It is obvious that differences exist between the engine cylinders. The cylinder pressure history is altered when load is increased from 67.5 to 92.5%. As shown later, this is mainly due to improper operation of the engine VIT system and power fluctuations during the measurement procedure.

The differences between cylinders is made even more obvious when observing the peak combustion pressure for both engine loads considered, Fig. 4, where for some cylinders the deviation from the mean value is higher than normal. The actual cause for these differences is derived from the application of the diagnosis method as shown below.

Cylinder Compression Condition. Figures 5(*a* and *b*) show the cylinder compression pressure value and compression condition respectively, for both engine loads. The compression pressure value is obtained from the simulation code and corresponds to the peak cylinder pressure we would have if the fuel flow to the cylinder where interrupted. Figure 5(*a*) indicates that cylinders 1, 3, and 7 have a slightly lower value compared to the others but no direct conclusion can be derived since peak compression pressure is affected by a number of parameters. From the diagnosis method, we estimate for each cylinder the value of "δr" and by comparison to the reference value of compression quality, Fig. 5(*b*). All cylinders have a value lower than 100% but higher than 90%. This is normal since the engine has been operating for several thousands of hours, but it reveals the initiation of wear.

Cylinder Power Output. Having determined the TDC position for each cylinder its indicated power output is estimated. Using the mechanical efficiency obtained from the engine shop tests as already described, the brake power output for all engine cylinders is determined. The results obtained are given in Fig. 6 for both engine loads. As observed, cylinders nos. 1 and 4 have in general the highest power output and cylinders nos. 2 and 7 the lowest. The picture is altered for some cylinders when decreasing engine load from 92.5 to 67.5% due to power fluctuations during the measurement. In both cases, the maximum deviation is around 5% that is quite acceptable and reveals in general uniform operation even though the condition can be improved by adjusting the fuel rack position of some cylinders using the fuel consumption data given in the following paragraph.

Fuel Consumption. To determine the fuel flow rate to each cylinder (a parameter practically impossible to measure), which is one of the most important parameters for cylinder diagnosis, the

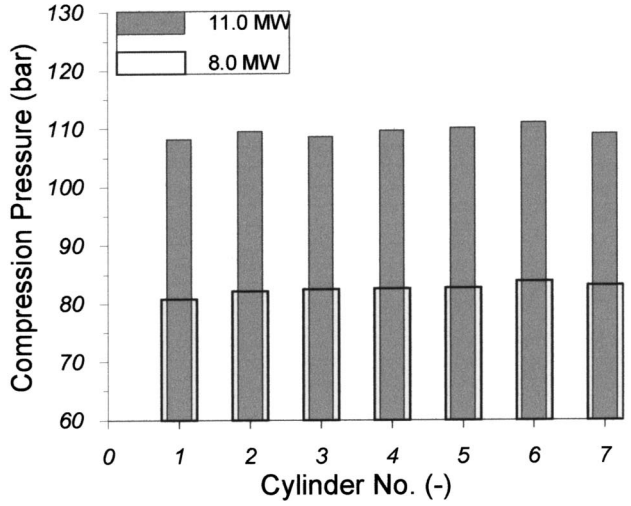

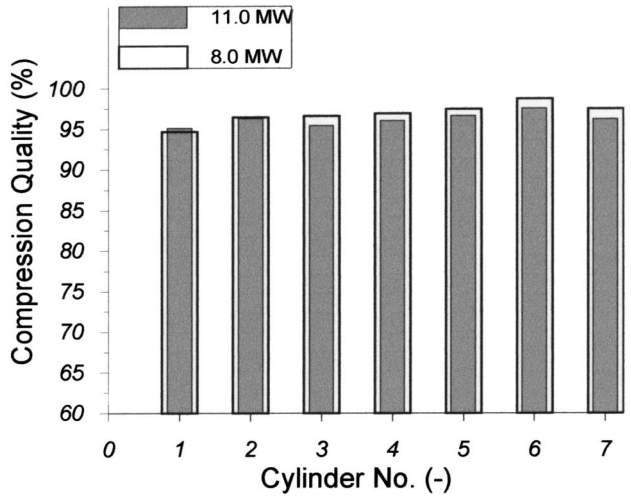

Fig. 5 (*a*) Maximum compression pressures at 136.7 rpm engine speed (*b*) Cylinder compression quality for both loads examined

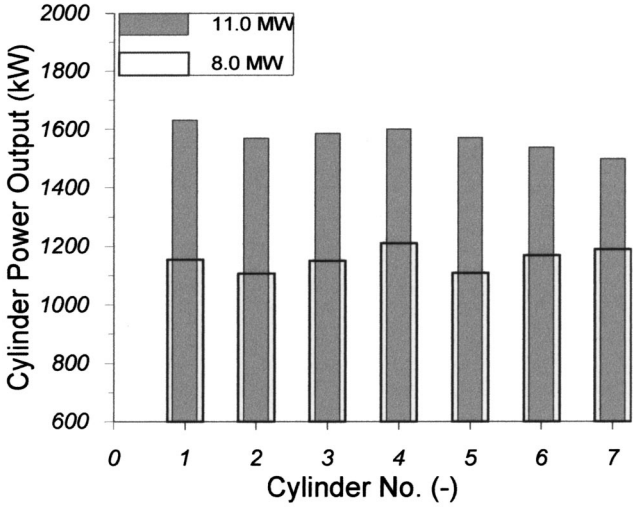

Fig. 6 Estimated brake power output for all engine cylinders at 67.5 and 92.5% load

method based on heat release analysis described in the previous sections is used. The results obtained are shown in Figs. 7(*a*) and (*b*). Figure 7(*a*) reveals differences in fuel flow rate between individual cylinders similar to those of power output. With the exception of cylinders 6 and 7 the situation is similar for both load cases examined. The differences observed for these two cylinders between the two load cases examined are due to power fluctuations during the measurement. For this reason we consider the values from both test cases to estimate a mean deviation as shown in Fig. 7(*b*). The deviation around the mean value is less than 5% for all cylinders revealing a relatively good tuning of fuel pumps. With reference to Fig. 7(*b*), the situation can be improved by adjusting the fuel racks of cylinders 2 and 4.

Ignition Point and Injection Timing Data. Having determined the TDC position, the ignition point for each cylinder is obtained. The results are given in Fig. 8(*a*) for both loads examined. As shown, there is variability between the cylinders on the order of 2 deg CA, which is a relatively high value for slow speed two stroke diesel engines. Cylinder nos. 3, 6, and 7 have the lowest ignition angle. In the present application, as already mentioned, it was not possible to measure the fuel injection pressure history. For this reason dynamic injection timing is computed using the estimated ignition point and the ignition delay obtained from Eq. (16), using the simulation model. The method is very accurate for slow speed engines and has been verified in the past using measured fuel injection system data. For injection timing tuning, we prefer to use the injection timing values at 92.5% load because according to the official shop tests the VIT index at this load is close to zero, i.e., the VIT mechanism is not affecting the injection timing. The normal injection timing for 92.5% load is 3° BTDC and thus comparing the dynamic injection of all cylinders with this value reveals that the injection timing of cylinder nos. 3, 6, and especially 7 is retarded.

This is verified by comparing the cylinder pressure traces and the computed heat release rates of cylinder nos. 1 and 7 as shown in Figs. 9(*a*) and (*b*). It is obvious that combustion initiates later for cylinder no. 7. From Fig. 8(*b*) we observe that at 67.5% load due to the operation of the VIT system the injection timing compared to 92.5% load is increased as expected. However, the operation of the VIT system is improper for cylinder nos. 2, 5, and especially 7. Using the data of Fig. 8(*b*), injection timing can be adjusted to match the normal value. This will not solve the problem at other loads if the VIT operation is not restored.

Condition of Fuel Injector Nozzles. The diagnostic system can be used to estimate the condition of the injector nozzles. The results are given in Fig. 10. Injector quality is an overall term expressing the condition of the fuel injector. It is estimated comparing the constant a_{mix} to its value estimated from shop trial data corresponding to a new engine condition. As observed most injectors are in good condition with the exception of cylinder nos. 3, 4, and 7 where quality is around 93–95%. For this reason it is proposed to check the relative nozzles, i.e., the nozzle opening pressure and the spray pattern. This has been done and the findings of the diagnosis procedure were verified. In this case, since the problem is not yet severe, an initial nozzle wear is detected which in the near future could create a bigger problem.

Condition of the Gas Exchange System. Based on measured engine data, i.e., turbine inlet/outlet temperatures and pressures, the isentropic efficiencies for the turbine and the compressor are determined and compared to the reference value corresponding to a new engine condition using Eqs. (20)–(22). This method defines the turbine and compressor condition. For the specific application the temperatures at the cylinder exit and before/after the turbine where each is measured using two temperature sensors, a cali-

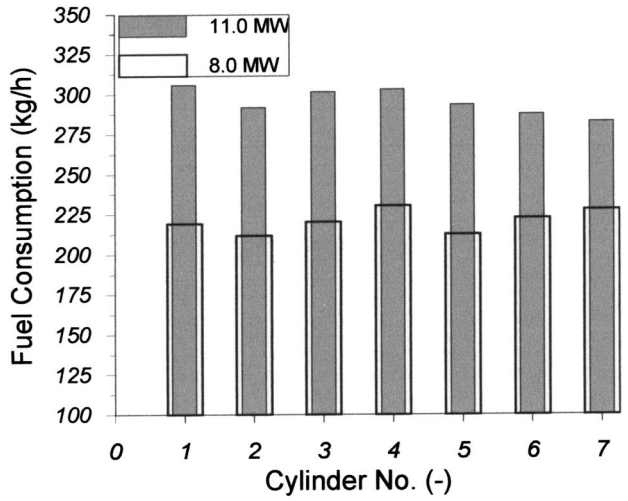

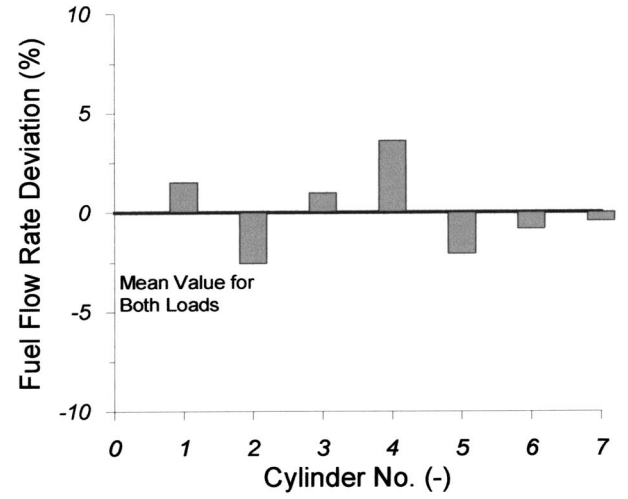

Fig. 7 (*a*) Estimated fuel consumption for all engine cylinders at 67.5 and 92.5% load (*b*) Deviation of fuel consumption for all cylinders at 67.5 and 92.5% load

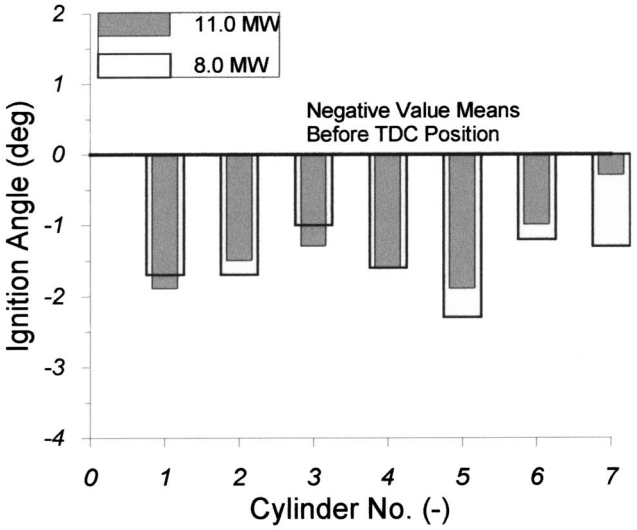

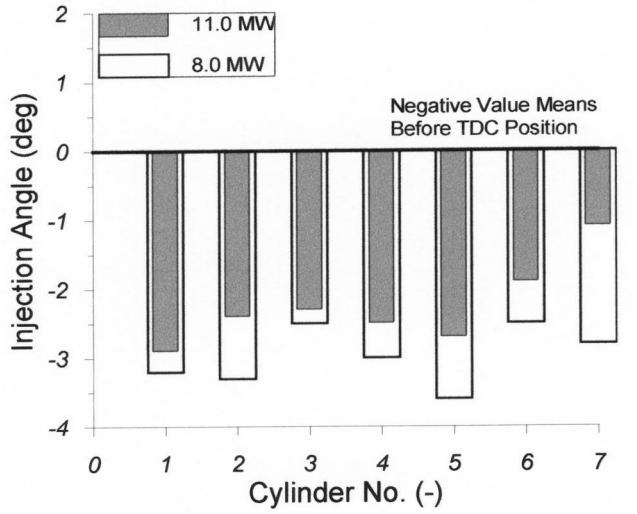

Fig. 8 (*a*) Estimated ignition angle at 67 and 92.5% load (*b*) Estimated dynamic injection timing at 67 and 92.5% load

brated thermocouple and the conventional instrumentation of the engine, both showing approximately the same readings.

Table 5 gives the estimated condition of the compressor and the turbine. Compressor efficiency is lower than normal while for the turbine a small reduction of its efficiency is observed which is not serious. Based on the analysis of the pressure data before the turbine a reduction of turbine effective flow area close to 8% is observed revealing pollution of the turbine inlet nozzle. This finding was verified during inspection and results in a slightly higher boost pressure, exhaust pressure, and mainly exhaust gas temperature before the turbine, as shown in Table 7.

Air Cooler Condition. Based on the measured A/C air inlet and outlet temperatures and the cooling water inlet and outlet temperatures its effectiveness is determined. The air cooler condition is estimated comparing the present effectiveness with the one corresponding to a new engine condition estimated from shop trial data. The comparison reveals that the air cooler functions properly, with no reduction of the heat exchange area (see Table 6).

Comparison of Current Engine Performance With That Corresponding to a New Engine

An indication of engine condition is usually obtained by comparing engine output values with the corresponding ones obtained from the official shop tests. This comparison is not valid because it is impossible to have the same operating conditions between the two test points (i.e., different ambient conditions, tuning, etc.). For this reason we use the simulation model and the reference constants values estimated from the shop test data to predict the expected output of a new engine at the current operating conditions using the same type of fuel. The results for both methods are given in Table 7 for 92.5% load in comparison with the current engine data. In Fig. 11 is also given the comparison of cylinder pressure for cylinder no. 1 at the current state against the one expected for a new engine operating at the same conditions.

Comparing the measured engine data with the shop test data, a significant difference is revealed in various values that initially leads to wrong conclusions. When comparing the measured engine data with the one obtained from the simulation model, corresponding to a new engine at the current site conditions, a smaller difference is revealed. For this reason the values reported in Table 7 are analyzed to understand the source for these differences and the advantages obtained from the use of the diagnostic model.

• *Peak combustion pressure*: Peak combustion pressure is lower compared to the one predicted for a new engine and the one ob-

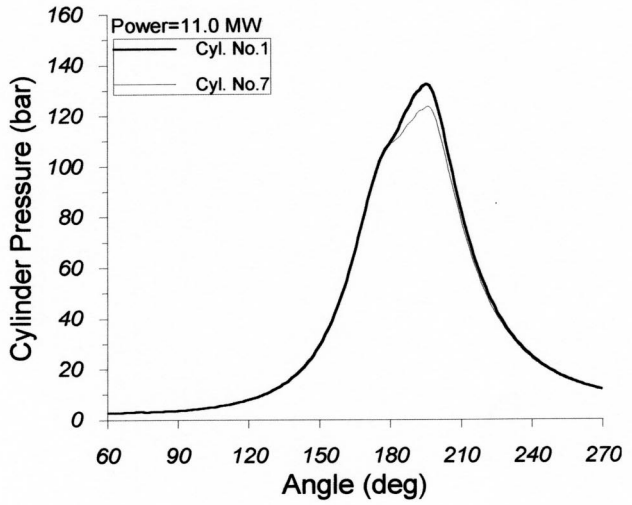

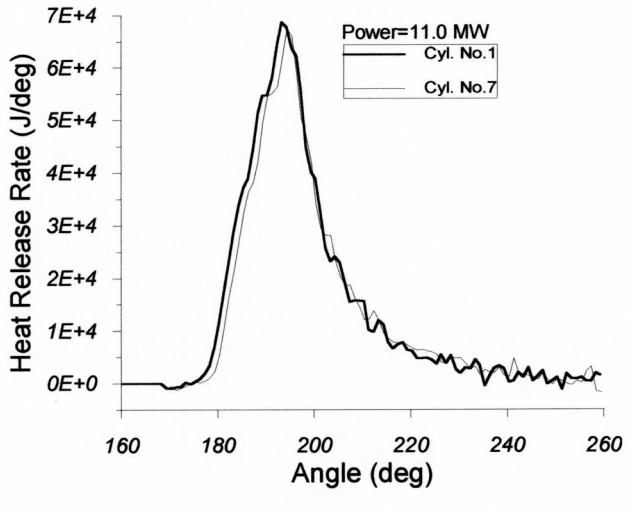

Fig. 9 (*a*) Comparison of pressure diagrams for cylinders 1 and 7 at 92.5% load (*b*) Comparison of heat release Rates for cylinders 1 and 7 at 92.5% load

tained from the engine shop tests. This is due to the lower injection timing of most cylinders and the lower compression quality as already shown.

• *Compression pressure*: Here the difference is obvious: the compression pressure of the engine is lower when compared to both the predicted value for new engine and the one obtained from the shop tests. The reason, as already shown, is the increase of cylinder-ring clearance.

• *Brake specific fuel consumption*: The current value is higher compared to both values obtained from the simulation model and the shop tests. The difference is due mainly to improper tuning, lower compression quality, and higher ambient temperature. The shop test value is the lowest because the fuel used during testing had a higher heating value compared to the fuel oil used at the site during the measurement procedure.

• *Boost pressure*: The boost pressure values are relatively similar. The boost pressure at the current condition would be lower, due to reduced compression efficiency, if the turbine inlet nozzle was clean, i.e., if it was not restricting the flow of air and exhaust gases through the engine.

• *Exhaust manifold pressure*: The current exhaust manifold pressure is higher compared to the shop test value and the one for

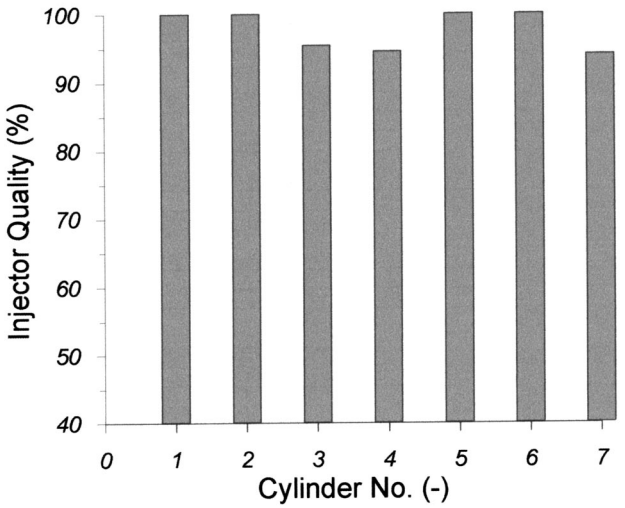

Fig. 10 Injector nozzle condition for all engine cylinders

a new engine at the given ambient conditions. This is the result of turbine inlet nozzle deposits as determined from the diagnosis procedure, but does not yet cause a serious problem. The increased value contributes to an increase of the exhaust gas temperature before the turbine.

• *Exhaust gas temperatures*: Compared to the shop tests, current engine values are significantly higher. This is misleading since the values of the official shop tests where recorded at a lower ambient temperature of about 18°C, compared to the current value of 30°C. Comparing the current values with the ones corresponding to a new engine predicted from the simulation model, at site conditions, shows differences, especially after the cylinders. The higher measured values before the turbine are mainly due to the pollution of the turbine inlet nozzle. Thus the actual condition is revealed when comparing the measured values with the ones corresponding to a new engine, at site conditions, obtained from the simulation model. As observed in Table 7 the temperature at the cylinder exit is lower compared to the one at the turbine inlet, as in the official shop tests, due to the high velocity of the exhaust gas as it exits the combustion chamber.

• *Air temperature*: The air cooler air inlet temperature is significantly higher compared to the one obtained from the engine shop tests because the latter has been measured at a significantly lower ambient temperature. The measured value is closer to the one corresponding to a new engine at the current site conditions, but still higher due to lower compressor isentropic efficiency. Finally, as far as the A/C air outlet temperature is concerned the picture is relatively similar. The measured value is significantly higher compared to the one obtained from the shop tests, due to the difference

Table 5 Compressor and turbine condition

Load %	Compressor condition	Turbine condition	Turbine nozzle condition
92.5	87%	96%	92%
67.5	85%	97%	92%

Table 6 Air cooler condition

Load %	Air cooler condition
92.5	98%
67.5	99%

Table 7 Current engine data compared to shop test and new engine condition

Parameter	Units	Data from engine shop tests	New engine at present conditions	Current condition
Total fuel consumption	kg/h	1983	2064	2064
Total brake power output	kW	11,397	11,326	10,993
Brake specific fuel consumption	g/kWh	174	182	187.8
Peak combustion pressure	bar	132.5	137.9	131.2
Peak compression pressure	bar	113.4	112.1	109.4
Scavenging air pressure	bar	3.21	3.23	3.20
Exhaust manifold pressure	bar	2.92	2.95	2.95
Cyl. exhaust temperature	°C	282	328	330
Turbine inlet temperature	°C	337	352	385
Turbine outlet temperature	°C	216	229	245
Turbine speed	rpm	10,088	10,323	10,000
Air cooler temperature in	°C	142	167	180
Air cooler temperature out	°C	37	42	44

in ambient conditions, while it is relatively close to the one obtained from the simulation. This verifies the previous finding that the air cooler is in a good condition.

In summary, it is obvious that a direct comparison of measured data with ones obtained from the engine shop tests is not valid due to differences mainly in ambient and engine operating conditions. If one follows this procedure incorrect conclusions may be derived that do not reveal in any case the actual condition of the engine and its subsystems. The recommended procedure is to compare measured data with one obtained from the simulation model using reference constants values corresponding to a new engine and the site operating conditions.

Conclusions

In the present work, is given the description of a diagnosis method for stationary diesel engines used for power generation. The proposed method is completely automatic requiring no interaction from the user. It can be applied on any type of diesel engine, using data obtained from the official shop tests for calibration of the model. The engineer can determine in a few minutes the condition of the engine and required adjustments to obtain optimum performance.

To validate the method for stationary diesel engines, the method is applied to a slow speed two-stroke diesel engine used for power generation on a Greek Island. The diagnostics are performed on site to determine the condition of the engine before the initiation of the high power demand period. Based on the derived information the specific engine is in a relatively good condition, but various problems are detected that could lead to improper operation in the near future. As observed, all engine cylinders have a compression quality lower than normal, which is an indication of cylinder liner or ring wear. The problem is not yet severe but an indication for inspection is revealed. It is also observed that three injectors are not functioning properly and inspection or replacement is required. A need for fuel rack adjustment is also revealed that will result in more uniform cylinder operation. On the other hand, a need for injection timing adjustment is indicated since some cylinders have retarded injection. Another important finding is that the VIT system is not functioning properly for some cylinders since their injection timing is not varied properly with engine load. As far as the condition of the other subsystems is concerned, a reduction of compressor efficiency and pollution of the turbine inlet nozzle area are detected. If the engine is kept at the present condition exhaust gas temperatures would increase leading possibly to engine de-rating in the near future.

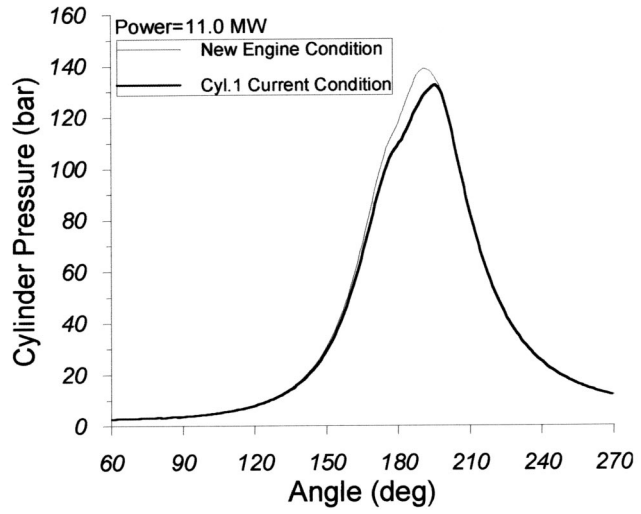

Fig. 11 Comparison of cylinder 1 pressure diagram with calculated one corresponding to a new engine condition

As shown, the proposed method can be used to predict new engine performance at the given operating conditions. This makes it possible to compare measured engine data directly with the predicted ones and derive conclusions concerning the engine and its subsystem condition. As revealed from the analysis it is not correct to compare directly measured engine data with ones obtained from the official shop tests, since these have been recorded at different operating and ambient conditions.

The proposed method can detect the cause for an engine malfunction, thus reducing repair time. Furthermore, through the detection of faults at their initial stage it can contribute to the increase of the availability of power generation units.

Nomenclature

a = Constant
A = Area (m^2)
b = Constant
c = Constant, swirl ratio
C = Constant
C_d = Discharge coefficient (−)
d_{inj} = Injector hole diameter (m)
D = Cylinder bore (m)
D_{SM} = Sauter mean diameter (m)
D_t = Turbulent diffusivity (m^{-1})
E_c = Activation energy (K)
f = Function
h_c = Heat-transfer coefficient (W/m^2 K)
H_{calor} = Lower calorific value (J/kg)
k = Turbulent kinetic energy (J)
K_b = Constant

K_f = Bulk modulus of fuel compressibility (N/m^2)
k_{is} = Load parameter (−)
l = Length (m)
L = Breakup length (m)
m = mass (kg)
$\dot{m}$ = Mass flow rate (kg/s)
N = Rotational speed (rpm)
P = Pressure (N/m^2)
$\dot{Q}$ = Volumetric flow rate (m^3/s)
$Q_{g,cum}$ = Cumulative gross heat released (J)
r = Radius (m)
R = Ideal gas constant (J/kg/K)
S_{pr} = Integral value in ignition delay correlation
t = Time (s)
T = Temperature (K)
u = Velocity (m/s)
U = Rotor tip velocity (m/s)
V = Volume (m^3)
W = Weighting matrix
x = Penetration length (m)
X = Matrix
y_p = Rack position (−)
Y, Z = Matrices

Greek letters

α = Jet angle (deg)
β = Matrix
β_0 = Marix
δr = Equivalent cylinder ring clearance (m)
δr_p = High pressure pump barrel-cylinder clearance (m)
δs = Sensitivity coefficient
Δh_{is} = Isentropic specific enthalpy rise or drop (m^2/s^2)
ΔP = Pressure difference (N/m^2)
ε = Air cooler effectiveness (−)
ε_t = Viscous dissipation rate (W/kg)
η_{is} = Isentropic efficiency (−)
λ = Thermal conductivity (W/m/K)
μ = Dynamic viscosity (kg/ms)
ν = Kinematic viscosity (m^2/s)
ρ = Density (kg/m^3)
σ = Surface tension (N/m)
ϕ = Flow parameter
Φ_{eq} = Equivalence ratio

Subscripts

a = Air
ac = Air cooler
b = Burned
c = Constant
C = Compressor
calc = Calculated
car = Characteristic
del = Delay
eff = Effective
exh = Exhaust
expt = Experimental
f = Fuel
fc = Combustion zone
fz = Fresh air zone
g = Gas
inl = Inlet
inj = Injector
j = Index
l = Liquid
mac = Macromixed
mic = Micromixed
mix = Mixing
p = Pump
s = Swirl
scav = Scavenging
st = Stoichiometric
t = Total
T = Turbine
w = Wall

Abbreviations

A/C = Air cooler
AFR = Air fuel ratio
CA = Crank angle
CR = Geometrical Compression ratio
DI = Direct injection
T/C = Turbocharger
TDC = Top dead center
VIT = Variable injection timing

Dimensionless Groups

Nu = Nusselt number
Pr = Prandtl number
Re = Reynolds number
We = Weber number

References

[1] Heywood, J. B., 1988, *Internal Combustion Engine Fundamentals*, McGraw-Hill, New York.
[2] Benson, R. S., and Whitehouse, N. D., 1973, *Internal Combustion Engines*, Pergamon, Oxford.
[3] Fredriksen, P. S., 1976, "Advanced Condition Monitoring System Based on Microprocessor Components," Symposium on Ship Operation Automation, Washington, DC.
[4] Terano, T., 1976, "Trouble Diagnosis System of Marine Engine-Its System Analysis," Symposium on Ship Operation Automation, Washington, DC.
[5] Holtrop, J., and Menner, G. J., 1978, "A Statistical Power Prediction Method," Int. Shipbuilding Progress, **25**(290), pp. 253–256.
[6] Bruel, and Kjaer, 1980, *Machine Health Monitoring Using FFT Frequency Analyzer Type 2031 or 2033 With Desk-Top Calculator*, Denmark.
[7] Collacot, R. V., 1997, *Mechanical Fault Diagnosis and Condition Monitoring*, Vols. I and II, Chapman and Hall, London.
[8] Kouremenos, D. A., Hountalas, D. T., and Kotsiopoulos, P. N., 1995, "Development of a Thermodynamic Method for Diagnosis and Tuning of Diesel Engines and Its Application on Marine Engines," Proceeding of the Institution of Mechanical Engineers, Part A: Journal for Power and Energy, **209**, pp. 125–139.
[9] Kouremenos, D. A., and Hountalas, D. T., 1997, "Diagnosis and Condition Monitoring of Medium Speed Marine Diesel Engines," Tribotest Intern. Journal, **4**(1), pp. 63–91.
[10] Kouremenos, D. A., Rakopoulos, C. D., and Hountalas, D. T., 1990, "Thermodynamic Analysis of Indirect Injection Diesel Engines by Two-Zone Modeling of Combustion," ASME J. Eng. Gas Turbines Power, **112**, pp. 138–149.
[11] Assanis, D. N., and Heywood, J. B., 1986, "Development and Use of a Computer Simulation of the Turbocompounded Diesel System for Engine Performance and Component Heat Transfer Studies," SAE Paper No. 860329, pp. 95–120.
[12] Kouremenos, D. A., Rakopoulos, C. D., Kotsos, K. G., and Hountalas, D. T., 1987, "Modeling the Blowby Rate in a Reciprocating Internal Combustion Engine," Proc. 16th IASTED IMS Int. Conf., Paris, pp. 465–468.
[13] Kouremenos, D. A., Rakopoulos, C. D., and Hountalas, D. T., 1997, "Multi-Zone Combustion Modeling for the Prediction of Pollutants Emissions and Performance of DI Diesel Engines," SAE Paper No. 970635.
[14] Jung, D., and Assanis, D. N., 2001, "Multi-Zone DI Diesel Spray Combustion Model for Cycle Simulation Studies of Engine Performance and Emissions," SAE Paper No. 2001-01-1246.
[15] Ramos, J. I., 1989, *Internal Combustion Engine Modeling*, Hemisphere Publishing Corp., Washington, DC.
[16] Glauert, M. B., 1956, "The Wall Jet," J. Fluid Mech., **1**, pp. 625–643.
[17] Kadota, T., Hiroyasu, H., and Oya, H., 1976, "Spontaneous Ignition Delay of A Fuel Droplet In High Pressure And High Temperature Gaseous Environments," Bull. JSME, **19**(130), pp. 437–445.
[18] Kouremenos, D. A., Rakopoulos, C. D., Hountalas, D. T., and Kotsiopoulos, P. N., 1991, "A Simulation Technique for the Fuel Injection System of Diesel Engines," ASME-WA Meeting, Atlanta, GA, Dec. 1–6, *Proc. AES*, **24**, pp. 91–102.
[19] Hountalas, D. T., and Kouremenos, A. D., 1998, "Development of a Fast and Simple Simulation Model for the Fuel Injection System of Diesel Engines," Advances in Engineering Software, Elsevier Science, New York, **29**(1), pp. 13–28.
[20] Watson, N., and Janota, M. S., 1982, *Turbocharging the Internal Combustion Engine*, MacMillan, London.
[21] Marzouk, M., 1976, "Simulation of Turbocharged Diesel Engines Under Transient Conditions," Ph.D. thesis, Imperial College, University of London.
[22] Vavra, M. H., 1974, *Aero-Thermodynamics and Flow in Turbomachines*, Krieger, New York.

[23] Beck, J. V., and Arnold, K. J., 1977, *Parameter Estimation in Engineering and Science*, Wiley, New York.
[24] Sage, A. R., and Melsa, J. L., 1971, *System Identification*, Academic, New York.
[25] Kouremenos, D. A., Rakopoulos, C. D., and Hountalas, D. T., 1995, ''Parametric Study of the Variables Affecting the Compression Stroke of Reciprocating Internal Combustion Engines,'' ASME International Mechanical Engineering Congress & Exposition, Anaheim, CA.
[26] Marzouk, M., and Watson, N., 1976, ''Some Problems in Diesel Engine Research With Special Reference to Computer Control and Data Acquisition,'' Proc. Inst. Mech. Eng., **190**(23), pp. 137–151.
[27] Hountalas, D. T., and Kouremenos, A. D., 1995, ''Evaluation of a Thermodynamic Method for the Determination of the TDC Position in Reciprocating Internal Combustion Engines,'' ECOS'95 ASME International Conference, Istanbul Turkey, Paper C4-60, pp. 677–682.

Flamelet Modeling of Pollutant Formation in a Gas Turbine Combustion Chamber Using Detailed Chemistry for a Kerosene Model Fuel

E. Riesmeier
e-mail: e.riesmeier@itm.rwth-aachen.de

S. Honnet
e-mail: s.honnet@itm.rwth-aachen.de

N. Peters
e-mail: n.peters@itm.rwth-aachen.de

Institut für Technische Mechanik,
RWTH Aachen,
Templergraben 64,
D-52056 Aachen, Germany

Combustion and pollutant formation in a gas turbine combustion chamber is investigated numerically using the Eulerian particle flamelet model. The code solving the unsteady flamelet equations is coupled to an unstructured computational fluid dynamics (CFD) code providing solutions for the flow and mixture field from which the flamelet parameters can be extracted. Flamelets are initialized in the fuel-rich region close to the fuel injectors of the combustor. They are represented by marker particles that are convected through the flow field. Each flamelet takes a different pathway through the combustor, leading to different histories for the flamelet parameters. Equations for the probability of finding a flamelet at a certain position and time are additionally solved in the CFD code. To model the chemical properties of kerosene, a detailed reaction mechanism for a mixture of n-decane and 1,2,4-trimethylbenzene is used. It includes a detailed NO_x submechanism and the buildup of polycyclic aromatic hydrocarbons up to four aromatic rings. The kinetically based soot model describes the formation of soot particles by inception, further growth by coagulation, and condensation as well as surface growth and oxidation. Simulation results are compared to experimental data obtained on a high-pressure rig. The influence of the model on pollutant formation is shown, and the effect of the number of flamelets on the model is investigated. [DOI: 10.1115/1.1787507]

1 Introduction

As future legislation for exhaust emission of internal combustion engines becomes more and more stringent, effective ways of redesigning and modifying furnace geometry and setup are sought after. Three-dimensional modeling of the combustion process in gas turbine combustion chambers including major pollutant formation allows engine developers to quickly perform trend studies, varying several parameters. By using enhanced models for turbulent mixing and combustion, a revised depiction of flow physics and chemistry and improvement of design will be faciliated.

Numerical simulation of combustion processes including the formation of pollutants requires detailed chemical mechanisms for adequate accuracy. This can be achieved by using the Eulerian particle flamelet model (EPFM), which is an extension of the highly validated representative interactive flamelet model (RIF). The latter is based on the laminar flamelet concept for nonpremixed combustion by Peters [1] and has the advantage of separating the numerical effort associated with the resolution of the small chemical time and length scales from the computational fluid dynamics (CFD) computation of the flow field. In this model turbulent flames are treated as an ensemble of thin locally one-dimensional laminar flamelets that are strained and stretched by the turbulent flow field. In a gas turbine combustor the smallest chemical time and length scales can be assumed to be smaller than those of the turbulence, ensuring that the laminar structure of the flame is disturbed but preserved.

The chemistry is solved in a one-dimensional flamelet code calculating species and temperature profiles as functions of a conserved scalar, the mixture fraction. This solution procedure allows high resolution in time for the chemistry independent of CFD calculations and therefore the usage of a detailed mechanism for model fuel. In this case a kerosene model fuel consisting of 80 wt. % *n*-decane (representing the aliphatic component) and 20 wt. % 1,2,4-trimethylbenzene (representing the aromatic component) is applied.

The EPFM model was first applied to a gas turbine combustion chamber burning in steady state using *n*-heptane as model fuel by Barths et al. [2]. Pollutant formation was investigated by introducing Eulerian particles transported unsteadily in the steady-state flow field computed with a CFD code. Each particle represents an unsteady flamelet accounting for different pathways and thereby different histories of the flamelet parameters and different residence times for the flamelets. The same concept was successfully applied to a combustor with high preheat and high level internal exhaust gas recirculation (EGR) [3].

Combustion in several diesel engines ranging from small to large bore, from low to part load, including exhaust gas recirculation, was simulated using the RIF concept [4–7]. By using multiple RIFs based on the Eulerian particle method for the simulation of a Volkswagen 1.9 l DI diesel engine [8], significant improvement for the prediction of the partially premixed burning phase and subsequent pollutant formation was achieved.

In the present study, the governing equations describing the mathematical basis of the flamelet model, the extension leading to the formulation of the EPFM model, and its interaction with the CFD code will be discussed in Sec. 2. Next the model fuel chosen for kerosene and its detailed chemistry and pollutant submechanisms will be outlined. Numerical simulations used to validate the chemistry model against experimental data from the literature are presented. The experimental setup for the gas turbine combustion

Contributed by the Internal Combustion Engine Division of THE AMERICAN SOCIETY OF MECHANICAL ENGINEERS for publication in the ASME JOURNAL OF ENGINEERING FOR GAS TURBINES AND POWER. Manuscript received by the ICE Division Jan. 20, 2003; final revision received by the ASME Headquarters March 12, 2004. Associate Editor: D. Assanis.

chamber, operating conditions, and measurement techniques are given. Finally simulation results from the application to the preceeding setup will be discussed.

2 Mathematical Model

In nonpremixed combustion as it occurs in the gas turbine combustion chamber, the mixing of fuel and oxidizer takes place within the reaction zone during combustion. This system of two inlet flows (1,2) allows the description of local mixture by the mixture fraction Z. It is defined at any location in the system as the ratio of the mass flux originating from the fuel feed to the sum of the mass fluxes originating from both the fuel and the oxidizer feed:

$$Z = \frac{\dot{m}_1}{\dot{m}_1 + \dot{m}_2}. \tag{1}$$

Generally the boundary conditions for the mixture fraction are $Z=1$ in the pure fuel feed and $Z=0$ in the pure oxidizer feed. Introducing the following transport equation for this conserved scalar,

$$\rho \frac{\partial Z}{\partial t} + \rho v_\alpha \frac{\partial Z}{\partial x_\alpha} - \frac{\partial}{\partial x_\alpha}\left(\rho D_Z \frac{\partial Z}{\partial x_\alpha}\right) = 0, \tag{2}$$

one can show that the gradient of Z is perpendicular to the reaction zone. The diffusion coefficient D_Z in Eq. (2) can be defined arbitrarily and was chosen such that the mixture fraction Lewis number Le_Z is equal to unity.

2.1 Flamelet Equations. Considering a locally defined coordinate system where one coordinate x_1 is perpendicular to the reaction zone and is thereby equivalent to the mixture fraction Z, and the other two coordinates x_2, x_3 run within the reaction zone, the conservation equations for species and temperature can be transformed. An order of magnitude analysis showing that the terms containing x_2 or x_3 are small to leading order leads to the one-dimensional form of these transport equations, called flamelet equations. Assuming unity Lewis numbers for the species $\mathrm{Le}_i = 1$ yields

$$\rho \frac{\partial Y_i}{\partial t} - \rho \frac{\chi}{2} \frac{\partial^2 Y_i}{\partial Z^2} - \dot{m}_i = 0 \tag{3}$$

for the species Y_i and

$$\rho \frac{\partial T}{\partial t} - \rho \frac{\chi}{2} \frac{\partial^2 T}{\partial Z^2} - \rho \frac{\chi}{2c_p}\left(\sum_{i=1}^{N} c_{p_i} \frac{\partial Y_i}{\partial Z} \frac{\partial c_p}{\partial Z}\right) \frac{\partial T}{\partial Z} + \frac{1}{c_p} \times \left(\sum_{i=1}^{N} h_i \dot{m}_i - \frac{\partial p}{\partial t} - \dot{q}_R''' \right) = 0 \tag{4}$$

for the temperature T. The influence of the flow field on transport in mixture fraction space is represented by the scalar dissipation rate,

$$\chi = 2D_z \left(\frac{\partial Z}{\partial x_\alpha}\right)^2 = \chi(Z), \tag{5}$$

a crucial parameter in flamelet modeling as it accounts for strain effects. Together with the pressure p these are the so-called flamelet parameters. In addition to those time-dependent parameters the flamelet solution is defined by the initial and boundary conditions. In gas turbine combustors the initial conditions do not vary in space. Assuming the composition of the fuel and oxidizer stream not to vary in time as well, the boundary conditions for the species conservation equations also remain constant.

2.2 CFD Code. To derive species mass fractions from the flamelet solution $Y_i(\eta,t)$, a presumed probability density function (β-PDF) is used that has been shown to be a good approximation for turbulent jets [9]. The spatial distribution of the mean species mass fractions can be computed from

$$\tilde{Y}_i(\mathbf{x},t) = \int_0^1 \tilde{f}_Z(\eta;\mathbf{x},t) Y_i(\eta,t) d\eta. \tag{6}$$

The shape of the β-PDF is determined by the local mean and variance of the mixture fraction. Therefore transport equations for these two parameters have to be solved additionally in the CFD code as given by

$$\frac{\partial(\overline{\rho}\tilde{Z})}{\partial t} + \nabla \cdot (\overline{\rho}\mathbf{u}\tilde{Z}) = \nabla \cdot \left[\frac{\mu_t}{\mathrm{Sc}_{\tilde{Z}}} \nabla \tilde{Z}\right], \tag{7}$$

$$\frac{\partial(\overline{\rho}\widetilde{Z''^2})}{\partial t} + \nabla \cdot (\overline{\rho}\mathbf{u}\widetilde{Z''^2}) = \nabla \cdot \left[\frac{\mu_t}{\mathrm{Sc}_{\widetilde{Z''^2}}} \nabla \widetilde{Z''^2}\right] + \frac{2\mu_t}{\mathrm{Sc}_{\widetilde{Z''^2}}} (\nabla \tilde{Z})^2 - \overline{\rho}\widetilde{\chi}. \tag{8}$$

The formulation of the energy equation was changed from the internal energy to enthalpy H including the chemical heat of formation of species given by

$$H = \Delta h_f^0 + \int_{T^0}^{T} c_p dT. \tag{9}$$

Replacing the energy transport equation with the following transport equation for the mean enthalpy $\tilde{H}$

$$\frac{\partial \overline{\rho}\tilde{H}}{\partial t} + \nabla \cdot (\overline{\rho}\mathbf{u}\tilde{H}) = \frac{D\tilde{p}}{Dt} - \nabla \cdot \mathbf{J} + \overline{\rho}\widetilde{\varepsilon} + \tilde{q}_R''' \tag{10}$$

in the CFD code leads to the absence of a chemical source term in this equation. The heat flux vector $\mathbf{J}$ accounts for the contributions from heat conduction and the enthalpy flux term, and $\dot{q}_R'''$ represents the radiative heat loss.

The mean enthalpy $\tilde{H}$ is defined as the sum over the species enthalpies h_i weighted by the mean mass fractions $\tilde{Y}_i$. By using the relation given in Eq. (11) and the spatial distribution of the mean mass fractions the temperature can be computed iteratively:

$$\tilde{H} = \sum_{i=1}^{N} \tilde{Y}_i h_i(\tilde{T}). \tag{11}$$

2.3 Modeling of the Flamelet Parameters. While in most technical applications the pressure can be taken to be spatially constant, the scalar dissipation rate varies in space due to the nonhomogeneous turbulent flow and mixture fields. The mixture fraction dependence of χ is taken from Peters [1]:

$$\chi(Z) = \frac{a}{\pi} \exp\{-2[\mathrm{erfc}^{-1}(2Z)]^2\} = \frac{a}{\pi} f_{\mathrm{erfc}}(Z). \tag{12}$$

This can be expressed as

$$\chi(Z,\mathbf{x}) = \frac{\chi_{\mathrm{st}}(\mathbf{x})}{f_{\mathrm{erfc}}(Z_{\mathrm{st}})} f_{\mathrm{erfc}}(Z). \tag{13}$$

The local value of the conditional scalar dissipation rate at stoichiometric mixture χ_{st} is obtained from

$$\tilde{\chi}_{\mathrm{st}} = \frac{\tilde{\chi} f_{\mathrm{erfc}}(Z_{\mathrm{st}})}{\int_0^1 f_{\mathrm{erfc}}(\eta) \tilde{f}_Z(\eta) d\eta} \tag{14}$$

where $\tilde{\chi}$ is modeled following Jones and Whitelaw [10],

$$\tilde{\chi} = c_\chi \frac{\tilde{\varepsilon}}{\tilde{k}} \widetilde{Z''^2}, \tag{15}$$

with $c_\chi = 2.0$. A volume-averaged value for the scalar dissipation rate at stoichiometric mixture for each flamelet is computed fol-

lowing Pitsch, Chen, and Peters [11] by converting surface into volume integrals. In addition it is weighted with the probability $\tilde{I}_l$ of finding a particle l:

$$\hat{\chi}_{st}(l) = \frac{\int_V \tilde{I}_l(\mathbf{x})\overline{\rho}(\mathbf{x})\tilde{\chi}_{st}^{3/2}(\mathbf{x})\tilde{f}_Z(Z_{st})dV'}{\int_V \tilde{I}_l(\mathbf{x})\overline{\rho}(\mathbf{x})\tilde{\chi}_{st}^{1/2}(\mathbf{x})\tilde{f}_Z(Z_{st})dV'}. \quad (16)$$

2.4 The Eulerian Particle Flamelet Model. Different mass particles with initially different locations will be transported through the flow field on different pathways. Since the scalar dissipation rate varies in space, they will experience different histories of the flamelet parameters. To track the mass-weighted fractions of particles related to the flamelet l, marker equations for each particle and therefore for each flamelet are solved which for a turbulent flow field have the form

$$\frac{\partial\overline{\rho}\tilde{I}_l}{\partial t} + \nabla\cdot(\overline{\rho}\tilde{\mathbf{v}}\tilde{I}_l) - \nabla\cdot\left(\overline{\rho}\frac{\nu_t}{Sc_l}\nabla\tilde{I}_l\right) = 0. \quad (17)$$

Here the probability I_l of finding a particle l at location $\mathbf{x}$ and time t is obtained. The local steady-state mass fractions can be derived from Eq. (6) by integration over time and summation over the number of particles, weighted by the temporal integration of the summation over the number of particles:

$$\tilde{Y}_i(\mathbf{x},t) = \frac{\int_0^{t_{end}}\left(\sum_{l=1}^{n_i}\tilde{I}_l(\mathbf{x},t)\int_0^1\tilde{f}_Z(\eta;\mathbf{x},t)Y_{i,l}(\eta,t)d\eta\right)dt}{\int_0^{t_{end}}\sum_l\tilde{I}_l(\mathbf{x},t)dt}. \quad (18)$$

3 Chemistry Model

The chemical mechanism for the kerosene model fuel consists of two detailed reaction submechanisms, one for *n*-decane, and the other for 1,2,4-trimethylbenzene. Both mechanisms describe low- and high-temperature autoignition, fuel decomposition, and oxidation.

3.1 Chemistry of *n*-Decane and 1,2,4-Trimethylbenzene. The *n*-decane submechanism features about 600 reactions between 67 chemical species. It was validated against various experimental data and is described in detail by Bikas and Peters [12]. The submechanism for 1,2,4-trimethylbenzene [13] accounts for the aromatic component in a two-component mixture representing kerosene and is based on a reaction scheme for toluene. The reaction rates for similar reactions have been adjusted to account for the higher reactivity of 1,2,4-trimethylbenzene compared to toluene, a phenomenological approach for describing the oxidation and ignition characteristics of 1,2,4-trimethylbenzene in a broad range of initial conditions. Nevertheless this submechanism is also highly validated against experimental data as seen in the literature mentioned above.

3.2 Pollutant Formation. The NO_x submechanism taken from Hewson and Bollig [14] accounts for thermal, prompt, and nitrous oxide contributions to NO_x formation as well as for NO_x reburn by hydrocarbon radicals and amines (NH_x). Soot precursor chemistry is described up to benzene following Mauss [15] based on work by Frenklach and Warnatz [16] and Miller and Melius [17] and simplified by Pitsch [18]. Further formation and growth of small PAHs is included in the mechanisms up to PAHs consisting of four aromatic rings. The formation of soot particles and their growth and oxidation are described by a kinetically based model. A method using statistical models is employed as described by Mauss [15] and Frenklach and Harris [19]. Together with the pollutant formation submechanisms the overall reaction mechanism comprises 1171 reactions between 132 chemical species.

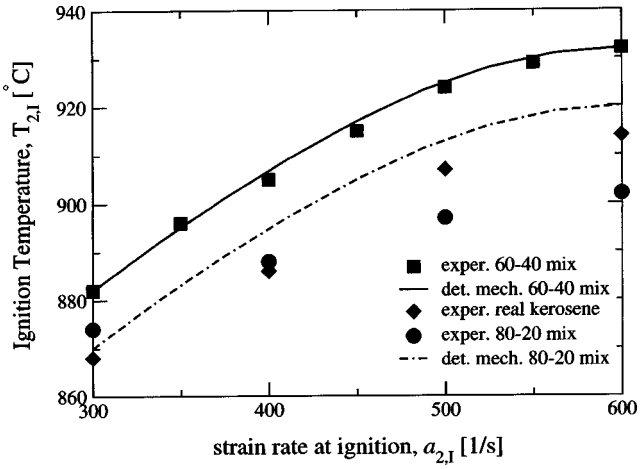

Fig. 1 Oxidizer temperatures at autoignition as a function of the strain rate *a*

3.3 Validation of the Kinetic Mechanism. To illustrate the applicability of the kinetic mechanism, experimental data taken from the literature are compared to calculations using a one-dimensional flamelet code. The mixture of 80 wt. % *n*-decane and 20 wt. % 1,2,4-trimethylbenzene was found to be a good choice for modeling kerosene. The comparison of calculated and experimental [20] oxidizer temperatures $T_{2,I}$ at autoignition as given in Fig. 1 for a counterflow diffusion flame shows that the chosen mixture reproduces real kerosene in a satisfying manner.

Figures 2 and 3 show the comparison of calculated major species mole fractions to experimental data gathered from a premixed burner stabilized flame [21]. The mole fractions for these major species are reproduced quite well. However, the simulation results for acetylene differ from the measurements by a factor of 2 as shown in Fig. 4, while ethylene is reproduced well again.

4 Experiments

To fulfill the aeroengine emissions certification requirements an axially staged kerosene-fueled combustor has been developed at BMW Rolls-Royce. The combustor is divided into a pilot and a main stage with the respective swirl flow injectors. The main fuel injector supplies most of the fuel into the combustor at high-load

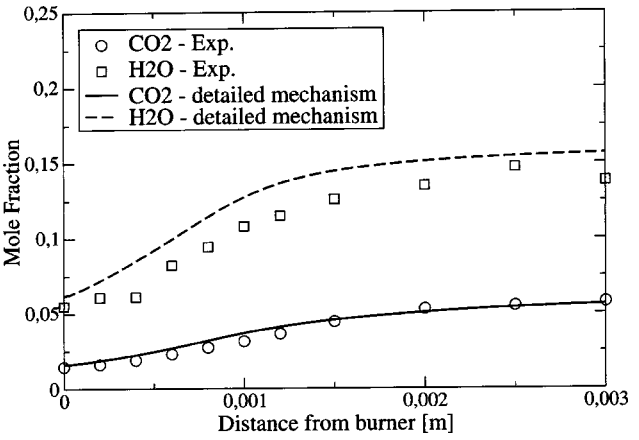

Fig. 2 Mole fractions of CO_2 and H_2O in a rich premixed kerosene/O_2/N_2 flame

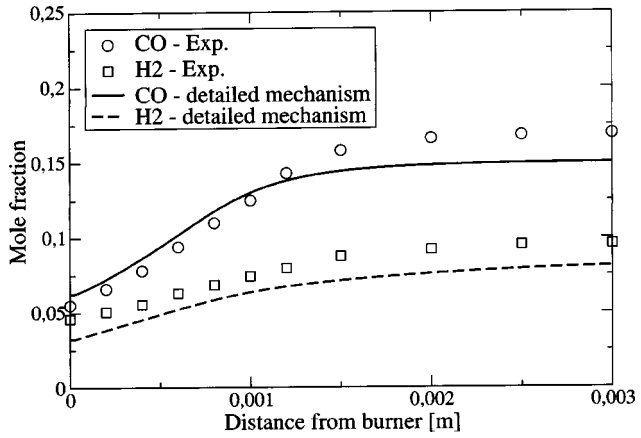

Fig. 3 Mole fractions of CO and H_2 in a rich premixed kerosene/O_2/N_2 flame

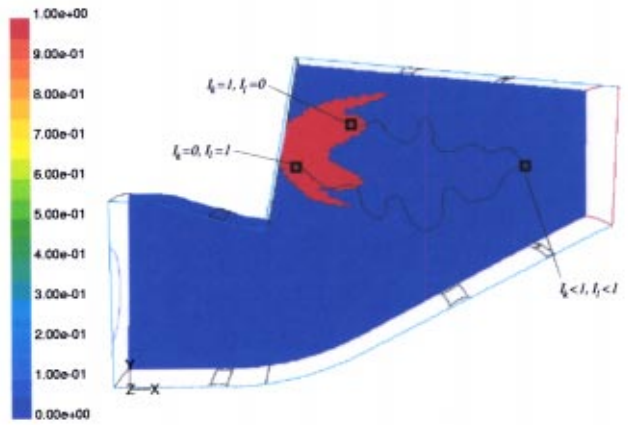

Fig. 5 Probability of finding flamelet l in the cross section through the axis of the main injector

operating conditions. However, it can be switched off at low load operating conditions. The pilot stage is designed for good altitude relight, weak extinction, idle emissions, and efficiency at low load. The main stage primarily yields low NO_x emissions at high load.

The research combustor investigated experimentally was set up in a 90° sector high pressure rig consisting of 5 segments each containing one pilot and main fuel injector. The investigated operating conditions were reduced take-off conditions scaled down to a pressure of 20 bar. A full radially and circumferentially resolved traverse of exhaust emissions of CO, CO_2, and H_2O were measured. Exhaust conditions were measured by sweeping with an exhaust rake in circumferential direction. Exhaust gas temperature was determined from concentrations of CO and CO_2. The emission index of NO_x was measured with the rake run in parallel mode, collecting and mixing the exhaust gas from five radial positions simultaneously and later averaging over the middle portion of the sector. The average NO_x emission index calculated as NO_2 is 26 g NO_x/kg fuel. A typical average level of soot concentrations was derived from measurements in terms of the Hartree smoke unit (HSU) over the three segments from which an order of magnitude of 3 ± 2 mg/m^3 could be estimated.

5 Numerical Implementation

Prior to using the flamelet code as subsequent postprocessing, the turbulent reacting flow and mixture field were computed using the commercial unstructured FLUENT code. The code solves the Favre averaged conservation equations for mass, momentum, and energy on a block structured grid consisting of 350,000 grid points using the standard k, ε turbulence model as well as an equlilibrium chemistry combustion model to derive main species mass fractions. In addition, transport equations for the mean and the variance of the mixture fraction as well as the enthalpy are solved as described in Eqs. (7), (8), and (10).

Based on the steady-state solution, pollutants are calculated with the EPFM in a postprocessing step solving the unsteady transport equations for the probability I_l of finding a flamelet l given by Eq. (17). Since after 10 ms about 99% of the initial particle mass left the combustion chamber, unsteady calculations comprise this time interval for the postprocessing.

The fuel boundary conditions were adjusted to meet real fuel injection and evaporation by modeling the atomizer nozzle as described in the following. Fuel is injected as a mixture of fuel and air in a narrow annular inlet. The value for the mixture fraction of the fuel inlet results from fuel and oxidizer mass fractions at the injector. By choosing maximum mixture fraction variance the fuel and oxidizer are statistically ''unmixed'' without combustion since the PDF yields two δ peaks at $Z=0$ and $Z=1$. Close to the fuel inlets no chemical reactions take place, and fuel break up and evaporation are reproduced. For the main injector the fuel temperature was set to 586 K, and for the pilot injector to 675 K. Combustion air enters the domain at 846 K.

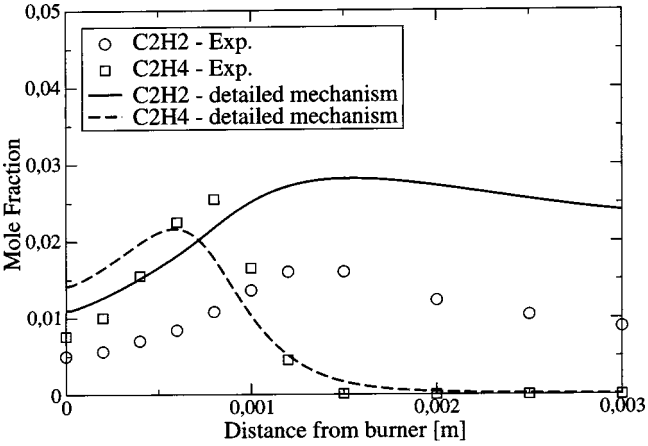

Fig. 4 Mole fractions of C_2H_2 and C_2H_4 in a rich premixed kerosene/O_2/N_2 flame

5.1 Flamelet Initialization. The particle initialization region in the combustion chamber is determined by comparing the temperature and the mean mixture fraction cell values to a particular value. Computational cells with a mean mixture fraction greater than Z_{st} and a temperature lower than 1800 K were included:

$$\tilde{I}_l(\mathbf{x}) = \begin{cases} 1 & \text{if } \tilde{Z}(\mathbf{x}) > Z_{st} \wedge T < 1800 \text{ K} \\ 0 & \text{otherwise} \end{cases} . \quad (19)$$

This range was chosen in order to initialize particles in the fuel stream where the temperature is low enough for NO_x and soot formation to be negligible. The temperature was evaluated from a preceding calculation using a simple combustion model with equilibrium chemistry.

The resulting initial particle distribution for one flamelet is shown in Fig. 5. The flamelet computation was started from steady-state solutions for the scalar dissipation rate that is an average over all cells where particles l have been initialized. Due to the low temperature in these cells the pollutant concentrations were initially set to zero.

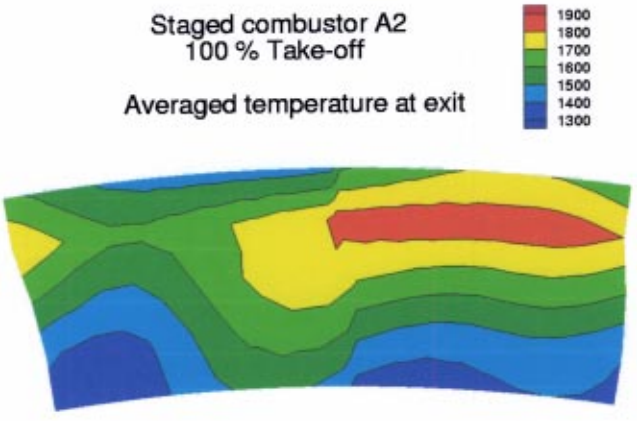

Fig. 6 Experimental exhaust temperature distribution

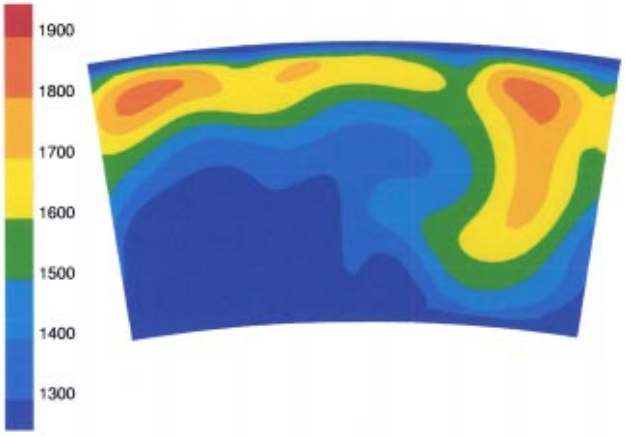

Fig. 7 Exhaust temperature distribution in the simulation

5.1.1 Subdivision of Flamelets. One simulation with only one particle ($l=1$) and a second simulation with five particles ($l=1,\ldots,5$) were performed. In the case with five particles the cells were additionally subdivided corresponding to the level of the local scalar dissipation rate.

While in Diesel engine simulations the mixing field must first evolve with start of injection and therefore at that time only one flamelet is representative for the whole computational domain [22], the stationary mixing field in a gas turbine combustion chamber yields a wide variety of local scalar dissipation rates at start of the postprocessing. In case of more than one flamelet to be used the initialization regions are grouped from high to low scalar dissipation rates such that the total cell mass in each region and thereby for each flamelet was similar.

6 Results and Discussion

The pollutant mass fractions calculated using Eq. (18) and the temperature iterated using Eq. (11) are shown in the following. For the computation with one particle, an emission index EI NO_x calculated as NO_2 of 10.4 g NO_2 /kg fuel and a soot mass concentration of 0.72 mg/m^3 was obtained. For the computation with five particles the emission index EI NO_x changed marginally to 10.6 g NO_2 /kg fuel, and soot was lower by 0.01 mg/m^3.

From the experiment a maximum temperature of approximately 1940 K is observed as seen in Fig. 6. The temperature traverse shows the dilatation of a hot spot of approximately 1900 K at approximately 80% of the height of the measuring plane. The hot spot extends only over the right half of the sector, whereas the simulation (Fig. 7) shows the dilatation of this high-temperature region nearly over the whole width of the exhaust plane.

Low-temperature regions at the bottom of the plane can be observed in both the experiment and the simulation. These regions are caused by the mixing jets integrated in the bottom and top walls of the combustor, producing a vertical temperature gradient. However, while in the experiment the temperature traverse at the bottom is quite homogeneous, a horizontal gradient is observed from the simulation. Since in the experiment the data were gathered about one-fourth of the combustor length behind the exhaust plane, the exhaust flow had more time for mixing, which might have decreased the temperature gradients. In addition the measured data were averaged over the combustor segments. The influence of the cooling films near the walls seen in the simulation cannot be seen in the experiment, since the measured region covers only 10%–90% duct height.

The weaker mixing in the simulation may stem from an underestimation of the mixing process by the k, ε model, whose capability of describing highly swirling flow accurately is limited. Therefore in an additional step the turbulent Schmidt numbers were reduced to 0.4 in order to enhance the scalar mixing in the simulations. The effect on the emission indices is listed in Table 1 and shown in Figs. 8–11. These figures show vertical cut views through the axis of the main stage injector.

Figures 8 and 9 show the strong dependence of the NO_x mass fraction on the temperature. It can be seen that near the main stage injector at the surface of stoichiometric mixture, where temperatures are high, the NO_x mass fraction has a maximum value of around 0.0006. The pilot stage injector not seen in this cut view yields the high-temperature region on the lower left side, where an even stronger correlation of temperature level and NO_x is observed.

By comparing those figures to Figs. 10 and 11 the effect of reducing the turbulent Schmidt numbers becomes visual. The strong dependence of the NO_x mass fraction on temperature is observed. But due to the enhanced mixing process the temperature distribution reflects a smearing of high-temperature regions, tending to a broader dilatation of NO_x.

Table 1 Emission index for NO_x and soot

	EI of NO_x (g/kg fuel)	EI of soot (mg/m^3)
Experiment	26	3±2
1 flamelet, $Sc_t=0.9$	10.4	0.72
5 flamelets, $Sc_t=0.9$	10.6	0.71
5 flamelets, $Sc_t=0.4$	10.0	1.57

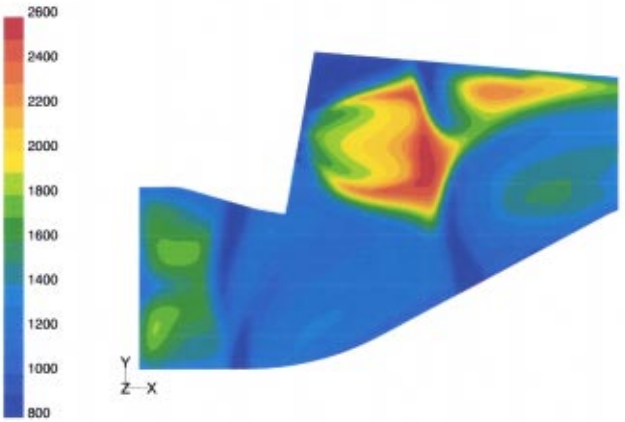

Fig. 8 Cut view temperature distribution in the simulation

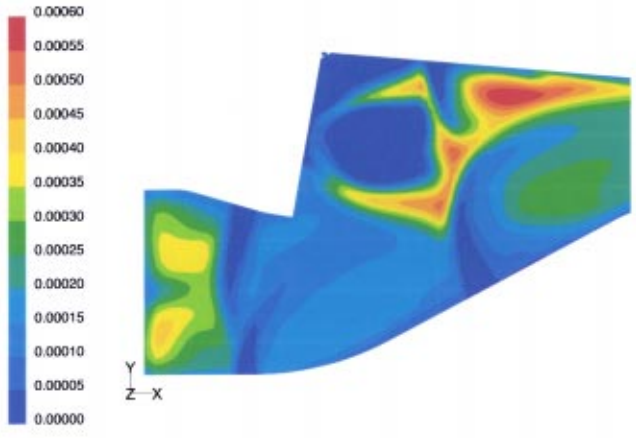

Fig. 9 Cut view NO_x distribution in the simulation

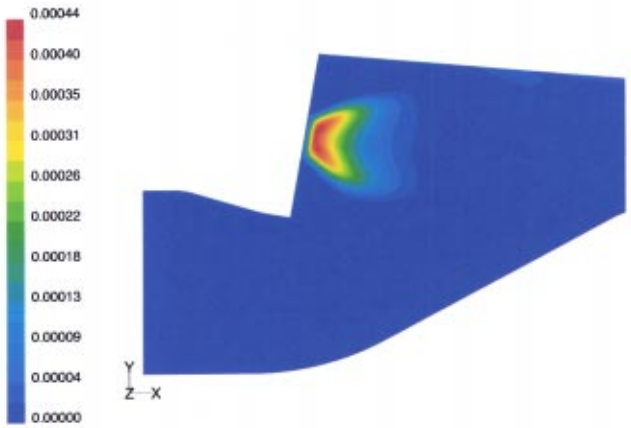

Fig. 12 Cut view soot mass concentration distribution in the simulation, reduced Schmidt numbers

Figure 12 shows the spatial distribution of the soot mass concentration. Figure 13 shows the mean mixture fraction distribution, and by comparing both figures, it can be seen that a significant amount of soot is formed close to the main stage injector under fuel rich conditions. Hence, in this region high concentrations of soot precursors are located. When passing the surface of stoichiometric mixture, soot is subsequently oxidized, leading to the small amount of soot observed in the exhaust gas.

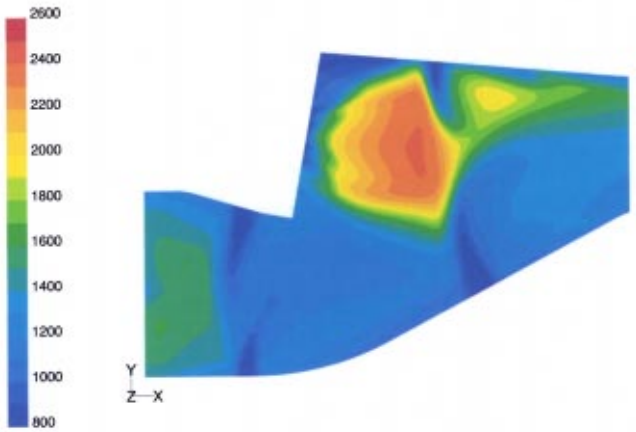

Fig. 10 Cut view temperature distribution in the simulation, reduced Schmidt numbers

7 Summary and Conclusions

Pollutant formation in a staged diffusion flame combustor was investigated numerically using a detailed mechanism for a kerosene model fuel. The simulations were performed in two steps. First the turbulent reacting flow and mixture field were computed with the commerical CFD code FLUENT. Combustion was considered using a basic combustion model such as the equilibrium chemistry model. The pollutant formation was then modeled by solving so-called marker equations for tracer particles, each representing an unsteady flamelet. The comparison of the results that were obtained with one and five flamelets revealed that they differed only marginally in the averaged exhaust values for the NO_x emission index and the soot mass concentration as well as in the spatial distribution in the combustor.

A more considerable effect was observed from reducing the turbulent Schmidt numbers from their default value to 0.4, resulting in a more efficient turbulent mixing. Calculations using the reduced Schmidt numbers yielded smaller temperature gradients, resulting in slightly lower peak values for NO_x and higher soot concentrations. Experimentally, an emission index for NO_x of 26 g NO_2 /kg fuel and a soot mass concentration of 3 ± 2 mg/m^3

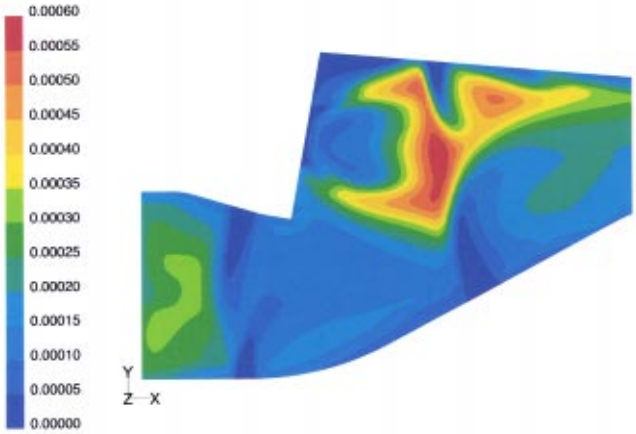

Fig. 11 Cut view NO_x distribution in the simulation, reduced Schmidt numbers

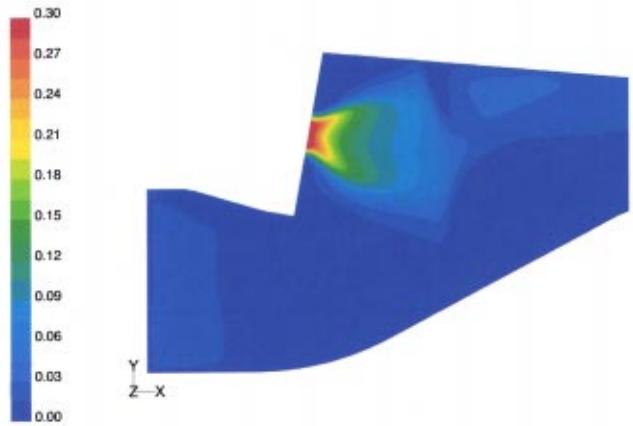

Fig. 13 Cut view mean mixture fraction distribution in the simulation

were measured for the kerosene-fueled test rig. The simulations using a mixture of *n*-decane and 1,2,4-trimethylbenzene predicted 10.6 g NO_2/kg fuel and 0.7 mg/m^3 soot for default Schmidt numbers compared to 10 g NO_2/kg fuel and 1.6 mg/m^3 soot for reduced Schmidt numbers.

The low value for NO_x is attributed to the presumably underestimated turbulent mixing process, whereas the low value for soot may depend on the sensitivity of the soot model on soot precursors probably not yet calculated with sufficient accuracy. Nevertheless the simulations show that the soot mass concentration can in fuel-rich regions locally exceed the exhaust values by several orders of magnitude, and soot is oxidized almost completely when passing the surface of stoichiometric mixture where OH radicals appear in high concentrations.

Acknowledgments

The authors wish to thank Rolls Royce Germany for providing experimental data and support on the grid structure setup. This work has been partially supported by the European Commission within the project GRD1-1999-10325 (CFD4C).

Nomenclature

Acronyms

CFD = Computational fluid dynamics
EGR = exhaust gas recirculation
EPFM = Eulerian particle flamelet model
PAH = Polycyclic aromatic hydrocarbons
PDF = Probability density function
RIF = Representative interactive flamelet

Variables

a = Strain rate (s^{-1})
c_p = Specific heat capacity ($J\,kg^{-1}\,K^{-1}$)
D_Z = Diffusion coefficient for mixture fraction Z ($m^2\,s^{-1}$)
f_v = Soot volume fraction (dimensionless)
$\tilde{f}_Z$ = Probability density function of mixture fraction (dimensionless)
h_i = Specific enthalpy of species i ($J\,kg^{-1}$)
I_l = Probability of finding a particle l (dimensionless)
$\mathbf{J}$ = Heat flux vector ($J\,m^{-3}\,s^{-1}$)
k = Turbulent kinetic energy ($m^2\,s^{-2}$)
$\dot{m}_i$ = Chemical production rate for species i ($kg\,m^{-3}\,s^{-1}$)
p = Pressure (Pa)
$\dot{q}_R'''$ = Radiative heat loss ($J\,m^{-3}\,s^{-1}$)
t = Time (s)
T = Temperature (K)
$\mathbf{u}$ = Sample space vector of velocity vector ($m\,s^{-1}$)
$\mathbf{v}$ = Velocity vector ($m\,s^{-1}$)
$\mathbf{x}$ = Spatial vector (m)
x_α = α component of spatial coordinate x (m)
Y_i = Mass fraction of species i (dimensionless)
Z = Mixture fraction (dimensionless)
η = Sample space variable (dimensionless)
ε = Turbulent dissipation ($m^2\,s^{-3}$)
χ = Scalar dissipation rate (s^{-1})
ρ = Density ($kg\,m^{-3}$)

Constants

c_χ = Time scale ratio for scalar dissipation and velocity fluctuations, 2.0
Sc_l = Turbulent Schmidt number in the transport equation for the flamelet marker particles, default value 0.9
Sc_t = Turbulent Schmidt number, default value 0.9
$Sc_{\tilde{Z}}$ = Schmidt number in the transport equation for the turbulent mean value of the mixture fraction, default value 0.9
$Sc_{\tilde{Z}''^2}$ = Schmidt number in the transport equation for the mixture fraction variance, default value 0.9

References

[1] Peters, N., 1984, Prog. Energy Combust. Sci., **10**, pp. 319–339.
[2] Barths, H., Peters, N., Brehm, N., Mack, A., Pfitzner, M., and Smiljanowski, V., 1998, Proc. Combust. Inst., **27**, pp. 1841–1847.
[3] Coelho, P. J., and Peters, N., 2001, Combust. Flame, **124**, pp. 503–518.
[4] Pitsch, H., Barths, H., and Peters, N., SAE paper no. 95-2357.
[5] Barths, H., Pitsch, H., and Peters, N., 1997, in *Proceedings of the Third International Conference on High Performance Computing in the Automotive Industry*, M. Sheh, ed., Cray Research Inc., Eagan, MN, pp. 11–18.
[6] Hasse, C., Barths, H., and Peters, N., SAE paper no. 1999-01-3547.
[7] Hergart, C. A., Barths, H., and Peters, N., SAE paper no. 1999-01-3550.
[8] Barths, H., Antoni, C., and Peters, N., SAE paper no. 98-2459.
[9] Jones, W. P., and McGuirk, J. J., 1980, in *Second International Symposium on Turbulence and Shear Flows*, L. J. S. Bradbury, F. Durst, B. E. Launde, F. W. Schmidt, and J. H. Whitelaw, eds., Springer-Verlag, Berlin, pp. 233–245.
[10] Jones, W. P., and Whitelaw, J. H., 1982, Combust. Flame, **48**, pp. 1–26.
[11] Pitsch, H., Chen, M., and Peters, N., 1998, Proc. Combust. Inst., **27**, pp. 1057–1064.
[12] Bikas, G., and Peters, N., 2001, Combust. Flame, **126**, pp. 1456–1471.
[13] Bikas, G., 2001, ''Kinetic Mechanisms forc Hydrocarbon Ignition,'' Ph.D. thesis, Rheinisch-Westfälische Technische Hochschule, Aachen, Germany.
[14] Hewson, J. C., and Bollig, M., 1996, Proc. Combust. Inst., **26**, pp. 2171–2180.
[15] Mauss, F., 1997, ''Entwicklung eines kinetischen Modells der Rußbildung mit schneller Polymerisation,'' Ph.D. thesis, Rheinisch-Westfälische Technische Hochschule, Aachen, Germany.
[16] Frenklach, M., and Warnatz, J., 1987, Combust. Sci. Technol., **51**, pp. 265–283.
[17] Miller, J. A., and Melius, C. F., 1992, Combust. Flame, **91**, pp. 21–39.
[18] Pitsch, H., 1997, ''Modellierung der Zündung und Schadstoffbildung bei der dieselmotorischen Verbrennung mit Hilfe eines interaktiven Flamelet-Modells,'' Ph.D. thesis, Rheinisch-Westfälische Technische Hochschule, Aachen, Germany.
[19] Frenklach, M., and Harris, S. J., 1987, J. Colloid Interface Sci., **118**, pp. 252–261.
[20] Kortschik, C., private communications, 2000.
[21] Douté, C., Delfau, J. L., Akrich, R., and Vovelle, C., 1995, Combust. Sci. Technol., **106**, pp. 327–344.
[22] Barths, H., Hasse, C., Bikas, G., and Peters, N., 2000, Proc. Combust. Inst., **28**, pp. 1161–1168.

Three-Way Catalytic Converter Modeling as a Modern Engineering Design Tool

G. N. Pontikakis

G. S. Konstantas

A. M. Stamatelos[1]

e-mail: stam@uth.gr

Mechanical and Industrial Engineering Department,
University of Thessaly,
383 34 Volos, Greece

The competition to deliver ultra low emitting vehicles at a reasonable cost is driving the automotive industry to invest significant manpower and test lab resources in the design optimization of increasingly complex exhaust aftertreatment systems. Optimization can no longer be based on traditional approaches, which are intensive in hardware use and lab testing. This paper discusses the extents and limitations of applicability of state-of-the-art mathematical models of catalytic converter performance. In-house software from the authors' lab, already in use during the last decade in design optimization studies, updated with recent, important model improvements, is employed as a reference in this discussion. Emphasis is on the engineering methodology of the computational tools and their application, which covers quality assurance of input data, advanced parameter estimation procedures, and a suggested performance measure that drives the parameter estimation code to optimum results and also allows a less subjective assessment of model prediction accuracy. Extensive comparisons between measured and computed instantaneous emissions over full cycles are presented, aiming to give a good picture of the capabilities of state of the art engineering models of automotive catalytic converter systems.
[DOI: 10.1115/1.1787506]

Introduction

The catalytic converter has been in use for the past 30 years as an efficient and economic solution for the reduction of pollutants emitted by the internal combustion engine, the latter being the powertrain for almost all vehicles in use today. The widespread use of the catalytic converter was the response of the automotive industry to the legislation of developed countries, which poses limits to the most important gaseous pollutants emitted by both gasoline and diesel engines.

Since the concern about the environmental impact of the emissions of the vehicles fleet is steadily growing—especially in urban areas, where air pollution has become a major issue—emission legislation becomes gradually stricter. Accordingly, this has led to continuous efforts of the automotive industry to improve the efficiency of the catalytic converter [1]. Today's emission standards have been lowered so much that the catalytic converter technology has been pushed to its limits and it became apparent that, in order to build vehicles that comply with the legislation, automotive engineers should tune the whole system of engine, piping, and catalytic converter [2]. Thus there emerged the need to view the catalytic converter as a component of an integrated *exhaust aftertreatment system* that should be designed very accurately.

In this context, the role of modeling of the components of exhaust aftertreatment systems is becoming increasingly important, especially as regards the catalytic converter, which is the most crucial device of such systems. Since the introduction of catalytic converters in production vehicles, catalytic converter models have been appearing in the literature in parallel with the development of new catalytic converter technologies. Nevertheless, the accuracy, reliability, and application range of catalytic converter models is still questioned. The number of modeling applications in the automotive industry remains limited, especially when contrasted to the plethora of models that appear in the literature [3–15]. It seems that a complicated landscape of approaches and methodologies has been created, causing an uncertainty as regards their validity and applicability. Most probably, this adversely affects their application in everyday practice, although modern modeling methodologies have been greatly improved and, in many cases, they have been successfully incorporated in the process of exhaust aftertreatment systems design [16–20].

In what follows, we attempt to inverse this situation, first by sketching an overview of modeling approaches that could help the navigation through the complicated landscape of this field of research. Subsequently, we present our choice of modeling approaches along with some supporting tools, in order to compile a complete methodology that provides the required high accuracy levels for the current state-of-the-art exhaust aftertreatment systems design. This methodology combines a significantly updated version of the CATRAN [21] modeling code with optimization tools tailored to the computer-aided estimation of the model's chemical kinetics parameters. The first steps of the developed optimization methodology have already been presented elsewhere [22]. Here we update and enhance it by incorporating recent improvements of the catalytic converter model and better integration with the supporting tools.

Navigation in the Modeling Landscape

A great number of models have been presented until today, featuring a multitude of approaches and levels of modeling detail. The diversity of published works on the field indicates that no definite answers have been given to the catalytic converter modeling problem [23]. There are several reasons for this situation:

• *Modeling objectives and application range*. Not all published works share common objectives and application range, varying from fast, approximate models to very detailed, computationally intensive models. Fundamental research models formulation usually attempts to describe phenomena as accurately as possible, require a lot of input data and usually can be tested only in extremely simplified catalyst behavior scenarios. For application-oriented models, formulation depends on the system or device where modeling is applied as well as the design parameters under investigation. In this case, accuracy may be sacrificed because of constraints such as simplicity or flexibility.

[1]Author to whom correspondence should be addressed.

Contributed by the Internal Combustion Engine Division of THE AMERICAN SOCIETY OF MECHANICAL ENGINEERS for publication in the ASME JOURNAL OF ENGINEERING FOR GAS TURBINES AND POWER. Manuscript received by the ICE Division, December 1, 2002; final revision received September 1, 2003. Associate Editor: D. Assanis.

• *Problem complexity*. Catalytic converter operation involves heterogeneous catalytic chemical reactions, which are coupled with simultaneous heat and mass transfer and take place under highly transient conditions. Under such conditions, it is difficult to describe chemical phenomena quantitatively or even qualitatively Each set of inevitable approximations and simplifying assumptions that are included essentially defines a different modeling approach, and no one can a priori be considered better or worse than any other one.

• *Rapidly changing washcoat technology*. Catalytic converter manufacturers continuously improve the chemical characteristics of the catalytic converter washcoats, in an effort to produce efficient as well as low-cost designs. Thus chemical kinetics research has to keep track of most modern washcoat developments, which inhibits the acquisition of in-depth knowledge about the washcoats chemical behavior and may lead to system-specific conclusions and results.

• *Performance assessment difficulty*. Finally, there is no consensus on how to assess model performance, so that models with similar scope can be compared. The introduction of such a methodological tool should help towards identifying the weaknesses and advantages of different approaches and provide with a quantitative criterion for model comparison.

The variety of modeling approaches that have been proposed and tested until today can be largely attributed to the above points. Nevertheless, similarities may be noticed among many different models and the majority of them share a common structure, which is dictated by the structure and operating concept of the catalytic converter itself.

Specifically, the catalytic converter is essentially a batch of parallel channels, which have been covered in their interior by a chemically active washcoat layer. The structure of most published models follows the structure of the converter itself so that each model can be divided into three distinct levels: The washcoat level, the channel level, and the reactor level. Below, we attempt to clarify what is modeled at each level and discuss which are the most common choices that one has to make when developing a catalytic converter model.

Washcoat Level. Washcoat modeling is local in nature. At this level, local phenomena at each point of the washcoat along the channel axis are considered. Two dominant phenomena should be modeled: diffusion and simultaneous reaction within the washcoat.

Heat and mass transport through the boundary layer of the flow is normally accounted for by employing mass and heat-transfer coefficients. Heat transfer through the washcoat is normally omitted, since the washcoat is approximately isothermal [24]. Finally, several approaches exist for the modeling of mass transport through the washcoat: from completely neglecting washcoat diffusion to detailed calculation of species profiles diffusing–reacting in the washcoat solving the corresponding balance equations. The former can be viewed as a zero-dimensional approach, while the latter is one- or two-dimensional and implies significant added computational cost.

For the reaction modeling, the mission of the model is twofold:

(i) To identify the prevailing physical and chemical phenomena and formulate an appropriate reaction scheme.

(ii) To assign a rate expression to each reaction.

When building the reaction scheme, the primary choice is between elementary or overall reactions. Elementary reactions describe in detail the real steps with which heterogeneous catalysis proceeds. On the other hand, overall reactions view heterogeneous catalysis phenomenologically as a one-step reaction and no intermediate steps are considered.

Elementary reactions usually employ simple Arrhenius-type rate expressions [25,26]. Overall reactions use more complicated rate expressions, which are either totally empirical or they are based on the Langmuir-Hinshelwood formalism and containing some empirical terms [9,12,27]. Essentially, the overall reaction approach favours the simplification of the reaction scheme, at the expense of using more complicated and highly empirical rate expressions; in a sense, the complexity of the reaction scheme details is hidden into the mathematical formulation of the rate expressions. An interesting fact that is not yet fully understood by fundamental researchers in chemistry and chemical kinetics is that the above-mentioned engineering approach has succeeded in producing unexpectedly high accuracy in matching the performance of catalytic converters in real cycles [7,23].

Channel Level. At the channel level, the local information provided by the washcoat model is exploited. The objectives of the model are the following:

(i) to determine the mass and heat transfer between the exhaust gas and the solid phase (substrate and washcoat) of the converter;

(ii) to determine the exhaust gas characteristics (temperature and species concentrations) along the channel.

At this level, chemical and physical phenomena in the washcoat are viewed as heat or mass sinks/sources. Profiles of gas temperature and species concentration between the channel wall and the bulk flow are computed along the channel axis.

The exhaust gas flow through the channel is laminar and is usually approximated with plug flow. Thus one-dimensional heat and mass balance equations for the exhaust gas are formulated at this level of modeling. The option here is between a transient and a quasisteady approach. If transient (time-dependent) terms of the equations are omitted, steady-state balances remain. The quasisteady approach implies that these steady-state balances are solved for each time step as solution proceeds in time for different boundary conditions. The boundary conditions are imposed by the transient reactor model.

By omitting transient terms, the steady-state approach essentially assumes that the there is no accumulation of heat or mass in the gas flow, which is a realistic assumption [28]. The objective of this approximation is to simplify the balance equations and reduce the computational cost that is involved in their solution.

Reactor Level. At the reactor level, channel-level information is exploited. Specifically, channels interact with each other only via heat transfer. Thus channels are viewed as heat sinks/sources and only one problem is tackled: Heat transfer in the solid phase, i.e., conductive heat transfer in the monolith and convection–radiation to the surrounding air. At this level, the heat sources computed for each channel at the kinetics and channel level calculations are used to estimate the temperature field of the monolith.

Heat-transfer calculations may be one, two, or three dimensional, depending on the desired accuracy. One-dimensional (1D) reactor level models treat all the channels of the monolith identically (i.e., subject to identical boundary conditions). On the other hand, 2D computations divide the monolith into sectors (clusters of channels) and the channel level computations are done for each one of the distinct sectors [10]. Finite-volume or finite element approaches may be employed in the 3D computation [6,11,15].

Evidently, each catalytic converter model incorporates a lot of assumptions and approximations. At each level of catalytic converter modeling, choices have to be made regarding modeling complexity and detail, which affect the accuracy and applicability of the resulting model. For the engineer, modeling detail is always dictated by the engineered object. Thus before deciding for a specific model formulation, the model's purpose should be clarified. Therefore we give below a brief discussion about the role of catalytic converter modeling within the process of modern exhaust aftertreatment systems design and operation.

Role of Modeling in the Design of Ultra Low Emission Exhaust Aftertreatment Systems

According to emission legislations for passenger cars and vans, emissions are measured over an engine or vehicle test cycle, which is an important part of every emission standard. These test

cycles are supposed to create repeatable emission measurement conditions and, at the same time, simulate a real driving condition of a given application.

Consequently, the primary objective of the automotive industry is to build cost-effective exhaust lines that will enable the vehicle to succeed in the legislated driving cycle tests. Because of the increasingly stringent emission standards, we observe a trend towards more complicated exhaust lines. For successful design, the engineer must consider not only the catalytic converter but, instead, the exhaust line (engine settings and control–exhaust piping–catalytic converter) as a system—an exhaust aftertreatment system. This progressively makes the experimental testing of the exhaust line more difficult and more expensive, requiring more time and experimental data to tune it appropriately.

In order to decrease cost and design time for development, modeling of the whole exhaust aftertreatment system would be extremely helpful. If fast, reliable models were available to the industry, new exhaust line configurations could be tested rapidly and at a reasonable cost; additionally, optimization of the exhaust line components could be aided by numerical optimization procedures to achieve improved configurations and lower overall emissions. The underlying notion is the incorporation of computer-aided engineering (CAE) practices in the design of exhaust lines, which is currently under way in the automotive industry.

Consequently, the targets for the exhaust line modeling are set by the industry. Currently, an indicative wish list for an ideal modeling tool of the kind is the following:

• *Reliability*. It should be cross checked and validated thoroughly in real-world case studies before conclusions and design decisions can be drawn using it.

• *Speed*. It should run reasonably fast (that is, faster than real time), with common computer equipment so that it can be tested, adjusted, and used within the time and cost constraints of the automotive industry.

• *Versatility*. It should be easy to modify and apply to different system configurations, in order to enable their assessment and tuning.

• *Ease of use*. It should be easy to validate and use by automotive engineers who are not modeling experts.

• *Minimum input data*. It should require input data that may be acquired by routine experiments, in order to keep cost low and to prevent input data uncertainty and errors.

• *Simplicity*. It should follow the fundamental engineering rule of thumb to keep complexity low. In this way, engineers–users can easily have control over their modeling tools and easily gain insight to model behavior and results.

Traditionally, modeling tools and CAE procedures in general are used in many areas of automobile design. The modeling of the catalytic converter proved to be a very complex problem, though, and this area resisted the extensive application of modeling. As of today, such modeling tools are not fully accepted in the field of catalytic converter optimization, let alone the CAE-driven design of the whole exhaust line.

Nevertheless, progress on this field of research is fast. The automotive industry clearly identifies the importance of modeling tools and recent improvements of catalytic converter models are a response to this trend. Below, we present some work in this direction. We employ an updated version of a catalytic converter modeling code, which has been continuously developed since 1996 [10] and has been employed on various design projects. The software is combined with the development of a performance measure for the assessment of modeling quality, which is utilized within a genetic algorithm optimization procedure for the computer-aided estimation of reaction kinetics parameters. Our purpose is to provide a demonstration of the role and applicability of current modeling software in the design process of modern exhaust aftertreatment systems.

Model Description

Below, we present an updated version of the CATRAN catalytic converter model. The model's design concept is the minimization of degrees of freedom and the elimination of any superfluous complexity in general. The main features of the model are the following:

• transient, one-dimensional temperature profile for the solid phase of the converter (reactor level modeling);

• quasisteady, 1D computation of temperature and concentration axial distributions for the gaseous phase (channel level modeling);

• simplified reaction scheme featuring a minimum set of redox reactions and an oxygen storage submodel (washcoat level modeling).

Below, the detailed description of model formulation is given for each modeling level.

Washcoat Level Modeling. The first task of washcoat modeling is to define how the simultaneous phenomena of diffusion and reaction in the washcoat will be taken into account. What will be adopted in this work is the ''film model'' approach, which is the simplest and most widely used one (e.g., Refs. [9], [11]). The film model approximates the washcoat with a solid–gas interface, where it is assumed that all reactions occur. This approximation essentially neglects diffusion effects completely, and assumes that all catalytically active cites are directly available to gaseous-phase species at this solid–gas interface.

This has been questioned by Zygourakis and Aris [24] and Hayes and Kolaczkowski [29]. They provide evidence that concentration gradients in the washcoat are present and may significantly affect the operation of the monolithic converter, especially in high temperatures. Nevertheless, significant complexity is introduced in the models in order to explicitly consider diffusion in the washcoat. Therefore washcoat diffusion is not implemented here and its effect is lumped into the kinetic parameters of the model.

The approximation for the solid–gas interface states that all species that diffuse to it through the boundary layer are removed from the gas phase due to reactions:

$$\frac{\rho_g}{M_g} k_{m,j} S (c_j - c_{j,s}) = R_j . \tag{1}$$

The left-hand side of the above equation describes mass transfer through the boundary layer of the gas flow. Parameter k_m is the mass transfer coefficient in the boundary layer, c_j denotes species concentration at the gaseous phase, and $c_{s,j}$ is corresponding concentration at the gas–solid interface. S is the geometrical surface area of the washcoat, i.e., channel wall area per channel volume. For a channel with hydraulic diameter d_h, we readily find: $S = 4/d_h$.

On the right-hand side of Eq. (1), the rate R_j refers to the production or consumption of each species at the solid–gas interface. For N_R reactions, each taking place with a rate r_k, the rate of consumption or production of a species j is

$$R_{\mathrm{rea},j} = \delta \gamma S \sum_{k=1}^{N_R} (a_{j,k} r_k), \tag{2}$$

where $a_{j,k}$ is the stoichiometric coefficient of species j in reaction k, δ is the washcoat thickness, and γ is the specific catalyst area, i.e., catalytically active area per washcoat volume.

The second task of washcoat modeling is to choose a reaction scheme and the appropriate expressions for the reaction rates r_k. We opt for overall reactions, because they provide the user with a more compact and comprehensible reaction scheme and they are computationally less expensive. Here, the three-way catalytic converter (3WCC) will be considered, which is designed for spark-ignition engines exhaust. Below, we briefly discuss what we choose to implement in this case.

Table 1 Reaction scheme and rate expressions of the model

	Reaction	Rate expression
	Oxidation reactions	
1	$CO+1/2O_2 \rightarrow CO_2$	$r_1=\frac{A_1 e^{-E_1/R_gT} c_{CO} c_{O_2}}{G}$
2	$H_2+1/2O_2 \rightarrow H_2O$	$r_2=\frac{A_2 e^{-E_2/R_gT} c_{H_2} c_{O_2}}{G}$
3, 4	$C_\alpha H_\beta+(\alpha+0.25\beta)O_2 \rightarrow \alpha CO_2+0.5\beta H_2O$	$r_k=\frac{A_k e^{-E_k/R_gT} c_{C_\alpha H_\beta} c_{O_2}}{G}, \quad k=3,4$
	NO reduction	
5	$2CO+2NO \rightarrow 2CO_2+N_2$	$r_5=A_5 e^{-E_5/R_gT} c_{CO} c_{NO}$
	Oxygen storage	
6	$2CeO_2+CO \rightarrow Ce_2O_3+CO_2$	$r_6=A_6 e^{-E_6/R_gT} c_{CO} \psi \Psi_{cap}$
7, 8	$C_\alpha H_\beta+(2\alpha+\beta)CeO_2 \rightarrow (\alpha+0.5\beta)Ce_2O_3+\alpha CO+0.5\beta H_2O$	$r_k=A_k e^{-E_k/R_gT} c_{C_\alpha H_\beta} \psi \Psi_{cap}, \; k=7, 8$
9	$Ce_2O_3+1/2O_2 \rightarrow 2CeO_2$	$r_9=A_9 e^{-E_9/R_gT} c_{O_2} (1-\psi) \Psi_{cap}$
10	$Ce_2O_3+NO \rightarrow 2CeO_2+1/2N_2$	$r_{10}=A_{10} e^{-E_{10}/R_gT} c_{NO} (1-\psi) \Psi_{cap}$
	Inhibition term	
	$G=T(1+K_1 c_{CO}+K_2 c_{CxHy})^2 (1+K_3 c_{CO}^2 c_{CxHy}^2)(1+K_4 c_{NO}^{0.7}), \quad K_i=k_i \exp(-E_i/R_gT)$	
	$K_1=65.5 \quad K_2=2080 \quad K_3=3.98 \quad K_4=4.79\times 10^5$	
	$E_1=-7990 \quad E_2=-3000 \quad E_3=-96{,}534 \quad E_4=31{,}036$	
	Auxiliary quantities	
	$\psi=\frac{2\times \text{moles } CeO_2}{2\times \text{moles } CeO_2+\text{moles } Ce_2O_3}, \quad \frac{d\psi}{dt}=-\frac{r_9+r_{10}}{\Psi_{cap}}+\frac{r_6+r_7+r_8}{\Psi_{cap}}$	

In the present model, the oxidation reactions rates of CO and HC are based on the expressions by Voltz et al. [27]. It is interesting to note that the expressions developed by Voltz et al. about 30 years ago for a Pt oxidation catalyst continue to be successful, with little variation, in describing the performance of Pt:Rh, Pd, Pd:Rh, and even tri-metal catalysts. For the HC oxidation, we have to note the real exhaust gas contains a very complex mixture of several hundreds of different hydrocarbon species with variability in composition depending on the driving conditions [30]. In practice, the diversity of the HC mixture is usually taken into account by considering two categories of hydrocarbons, each being oxidized in different temperature: an easily oxidizing HC (''fast'' HC), and a less-easily oxidizing HC (''slow'' HC). Here, the ''fast'' HC is represented by propene (C_3H_6) and the ''slow'' HC is represented by propane (C_3H_8). In practice, only the total hydrocarbon content of the exhaust is measured. Throughout this work, it is assumed that the exhaust HC consisted of 85% ''fast'' HC and 15% ''slow'' HC. This assumption was done for modeling purposes due to the lack of more accurate data and, according to our experience, it gives satisfactory results.

For the reaction between CO and NO we use an empirical reaction rate adopted from Pattas et al. [31], which predicts a variable order of reaction for the CO oxidation from NO, depending on CO concentration. The expression is qualitatively consistent with the results of Koberstein and Wannemacher [32], which predict that the reaction order for CO in the CO–NO reaction tends to unity as the reactants' concentrations tend to vanish. Finally, hydrogen oxidation is also included in the model.

All reduction–oxidation reactions employed in the model, along with their rate expressions, are given in Table 1.

Apart from the redox reactions, oxygen storage phenomena play a principal role in the efficiency of the 3WCC. Oxygen storage occurs on the ceria (Ce), which is contained in large quantities in the catalyst's washcoat (at the order of 30% wt). Under net oxidizing conditions, 3-valent Ce oxide (Ce_2O_3) may react with O_2, NO, or H_2O and oxidize to its four-valent state (CeO_2). Under net reducing conditions, CeO_2 may function as an oxidizing agent for CO, HC, and H_2.

Oxygen storage is taken into account by an updated reaction scheme. The new scheme consists of five reactions which account for (i) Ce_2O_3 oxidation by O_2 and NO, and (ii) CeO_2 reduction by CO and fast/slow hydrocarbons The model uses the auxiliary quantity ψ to express the fractional extent of oxidation of the oxygen storage component. It is defined as

$$\psi=\frac{2\times \text{moles } CeO_2}{2\times \text{moles } CeO_2+\text{moles } Ce_2O_3}. \tag{3}$$

The extent of oxidation ψ is continuously changing during transient converter operation. Its value is affected by the relative reaction rates of reaction nos. 6–10. The rates of reactions, also given in Table 1, are expected to be linear functions of ψ. Specifically, the oxidation rate of the oxygen storage component is assumed proportional to the active sites of Ce_2O_3, i.e., to $\Psi_{cap}(1-\psi)$. On the other hand, the oxidation rate of CO and HC by CeO_2 is assumed proportional to ($\Psi_{cap}\psi$). Moreover, the rates of these reactions should be linearly dependent on the local concentration of the corresponding gaseous phase reactant.

The rate of variation of ψ is the difference between the rate that Ce_2O_3 is oxidized and reduced:

$$\frac{d\psi}{dt}=-\frac{r_9+r_{10}}{\Psi_{cap}}+\frac{r_6+r_7+r_8}{\Psi_{cap}}. \tag{4}$$

The updated model includes an analytical solution for Eq. (4) for ψ at each node along the catalyst channels.

Channel Level Modeling. For the formulation of the channel-level model, two usual simplifications are employed [26,33], namely:

• The axial diffusion of mass and heat in the gas phase is negligible.

• The mass and heat accumulation in the gas phase is negligible. (This comprises the assumption for the quasi-steady-state nature of the problem.)

The first assumption is generally accepted and is employed in most models, e.g., those of Chen et al. [11] and Siemund et al. [9]. Only the boundary layer effect on mass transfer is accounted for, using a mass transfer coefficient k_m, which is a function of the Sherwood number. Bulk flow is approximated with plug flow with uniform temperature T_g and species concentrations c_j. The velocity of the flow readily results from the mass flow rate: $u_z = 4\dot{m}/(\rho \pi d_h^2)$.

The second assumption is more controversial and both the quasi-steady and the transient approach have been tested in the literature. Shamim et al. [15] have presented a model that incorporates transient terms at channel level modeling. On the other hand, Young and Finlayson [8] and Oh and Cavendish [3] argue about the validity of the quasi-steady approximation. They provide justification on the basis of the large ratio of thermal to mass time constants of the problem. Following this line of thought, the quasi-steady approach is used here as well, for simplicity and low computational cost.

In order to write the mass balance for the exhaust gas, a mean bulk value c_j is employed for the gas–phase concentration of each species. Likewise, a value $c_{s,j}$ is considered for the concentration of each species at the solid–gas interface. Using the quasi-steady-state approximation and neglecting diffusion and accumulation terms, the mass balance for the gas phase becomes

$$\rho_g u_z \frac{\partial c_j(z)}{\partial z} = \rho_g k_{m,j} S[c_j(z) - c_{s,j}(z)]. \tag{5}$$

Similarly to the above, a mean bulk value T_g is used for the exhaust gas temperature, and a solid phase temperature T_s is introduced for the monolith and the solid–gas interface. Energy is transferred to and from the exhaust gas only due to convection with the channel walls. Thus the energy balance for the gas phase becomes

$$\rho_s c_p u_z \frac{\partial T_g(z)}{\partial z} = hS[T_s(z) - T_g(z)]. \tag{6}$$

Parameter h is the heat-transfer coefficient and is calculated as a function of the Nusselt dimensionless number.

Finally, the boundary conditions for the temperature, mass flow rate, and concentrations are given from measurement at the converter's inlet:

$$\begin{aligned} c_j(t, z=0) &= c_{j,\text{in}}(t), \\ T_g(t, z=0) &= T_{g,\text{in}}(t), \\ \dot{m}(t, z=0) &= \dot{m}_{\text{in}}(t). \end{aligned} \tag{7}$$

The species that are considered in the exhaust gas flow are the following: $j = \text{CO}, \text{O}_2, \text{H}_2, \text{HC}_{\text{fast}}, \text{HC}_{\text{slow}}, \text{NO}_x, \text{N}_2$.

Reactor Level Modeling. At the reactor level modeling, heat transfer between channels and between the reactor and its surrounding are modeled. The principal issue here is to decide if one-, two-, or three-dimensional modeling of the heat transfer should be employed.

The reactor model presented in this work is a one-dimensional heat-transfer model for the transient heat conduction in the monolith. Heat losses to the environment via convection and radiation are also taken into account. Its primary assumptions are the following:

• Heat losses from the front and the rear face of the monolith are neglected. (To our knowledge, this is the case with all models that have appeared in the literature.)

• Since the catalytic converter is always insulated, simpler models approximate the convert as adiabatic. Heat losses to the surrounding are taken into account but, owing to the model's 1D nature, they are inevitably distributed uniformly in each monolith's cross section.

• Flow rate and temperature profiles of the exhaust gas at the inlet of the filter are considered uniform. An average value for flow rate and temperature is measured, and gas flow is distributed uniformly to each channel.

The temperature field in the converter is described by the equation of transient heat conduction in one dimension, with heat sources being convection from the exhaust gas, the enthalpy released from the reactions, and convection to ambient air,

$$\rho_s c_{p,s} \frac{\partial T_s}{\partial t} = k_{s,z} \frac{\partial^2 T_s}{\partial z^2} + hS(T_g - T_s) + \sum_{k=1}^{N_R} (-\Delta H_k) r_k + Q_{\text{amb}}. \tag{8}$$

Finally, the boundary condition needed for the solution of the heat conduction equation refers to the heat losses to ambient air:

$$Q_{\text{amb}} = S_{\text{mon}}[h_{\text{amb}}(T_s - T_{\text{amb}}) + \varepsilon \sigma (T_s^4 - T_{\text{amb}}^4)]. \tag{9}$$

Two- and three-dimensional reactor models have also appeared in the literature, e.g., the models of Heck et al. [34], Chen et al. [11], Zygourakis [35], and Jahn et al. [36]. These models are indispensable if the exhaust gas at the converter inlet exhibits a severely nonuniform flow profile but also require mass flow rate and temperature profiles at the inlet of the catalytic converter. Such data are not usually available in routine engine-bench or driving cycle converter tests, which are the main application field for our model. Therefore the 1D approach is preferred, since its modeling detail matches routine input data quality, provides sufficient accuracy, and has low computational power requirements.

Tuning Procedure

General. The kinetics submodel introduces into the catalytic converter model a set of parameters that have to be estimated with reference to a set of experimental data. The introduction of tunable parameters is inevitable regardless of the formulation of the reaction scheme. Tunable parameters take into account the reactivity of the specific washcoat formulation as well as any other aspect of catalytic converter operation that is not included in the model explicitly.

In the present model, the tunable parameters are the activation energy E_k and the preexponential factor A_k that are included in the reaction rate r_k of each reaction k. In total, there is a maximum number of 20 tunable parameters, however, the values of activation energies are more or less known from Arrhenius plots and thus only the pre-exponential factors are tuned (ten tunable parameters). Apart from reaction activity, tunable parameters values include the approximations that have been done during model formulation. Among them, the most important are:

• effect of reaction scheme and rate expressions simplifications;
• effect of exhaust gas input data uncertainty;
• effect of neglection of diffusion in the washcoat;
• effect of 1D reactor model approximation.

Since (i) the rate expressions of the model are empirical and (ii) effects of model approximations are lumped into the tunable parameters, the latter do not correspond to real kinetic parameters. Rather, they should be viewed as fitting parameters of the model.

The traditional method to tune a model was to manually adjust the parameters by a trial-and-error procedure, starting from a set of realistic values (known from previous experience) and modifying them gradually, so that the model results compare well with the measured ones. The usual method for computation versus measurement comparison is inspection of plotted results. Thus manual tuning introduces human intuition and experience in order to (i) assess model performance, and (ii) fit the model to the given experimental data. This is a questionable practice because

• inspection is dependent on the scale that results are viewed and it may therefore be misleading;

• there is considerable difficulty to compare the performance of different models that are presented in the literature;

• it does not provide any confidence about the quality of the tuning.

The above drawbacks of manual performance assessment and parameter tuning have led to efforts for the development of a corresponding computer-aided procedure. Since model tuning is essentially a parameter-fitting problem, the underlying idea of all attempts has been to express the problem mathematically as an optimization problem. This involves the introduction of an iterative optimization method, which maximizes or minimizes an objective function that indicates goodness of fit. The objective function required by the optimization procedure is thus a *performance measure* of the model, i.e., a mathematical measure that assesses a model's performance in a quantitative manner.

A few attempts for the development of a complete computer-aided tuning methodology have been presented in the past. Montreuil et al. [12] were the first to present a systematic attempt for the tuning of the parameters of their steady-state three-way catalytic converter model. Dubien and Schweich [37] also published a methodology to determine the pre-exponential factor and the activation energy of simple rate expressions from light-off experiments. Pontikakis and Stamatelos [7,38] introduced a computer-aided tuning procedure for the determination of kinetic parameters of a three-way catalytic converter model from driving cycle tests based on the conjugate gradients method. Glielmo and Santini [39] presented a simplified three-way catalytic converter model oriented to the design and test of warm-up control strategies and tuned it using a genetic algorithm.

All of the above efforts used a performance measure based on the least-squares error [40] between measured and computed results. Except for Glielmo and Santini, all other works are based on gradient-based methods for the optimization of the performance measure [41]. Gradient methods are faster, more accurate, and may be used as black-box methods, but assume that the optimization space is unimodal (i.e., it contains a single extremum). Genetic algorithms, used by Glielmo and Santini, are better suited to multi-modal optimization but they are slower, less accurate, and have to be appropriately adapted to the target problem.

In the present work, we present recent progress that has been made in the field of computer-aided parameter estimation. It is a continuation of the work of Pontikakis and Stamatelos [7] and updates both performance measure definition and optimization methodology. In the following sections the requirements that a performance measure should comply with are presented, and a performance measure that satisfies these requirements is defined. Finally, a genetic algorithm is applied as an optimization methodology [23].

Formulation of the Performance Measure. The performance measure that is formulated below exploits the information of species concentrations measurements at the inlet and the outlet of the catalytic converter. Specifically, it is based on the conversion efficiency E_j for a pollutant j. Herein, we take into account the three legislated pollutants, thus $j=\mathrm{CO,\ HC,\ NO}_x$.

To account for the goodness of computation results compared with a measurement that spans over a certain time period, an error e for each time instance must be defined. The latter should give the deviation between computation and measurement for the conversion efficiency E. Summation over time should then be performed to calculate an overall error value for the whole extent of the measurement. Here, the error is defined as

$$|e| = |E - \hat{E}|. \tag{10}$$

Absolute values are taken to ensure error positiveness. This error definition also ensures that $0 \leqslant |e| \leqslant 1$, since it is based on conversion efficiency.

The error between computation and measurement is a function of time and the tunable paremeter vector: $e=e(t;\vartheta)$, where ϑ is the formed by the pre-exponential factor and activation energy of each reaction of the model:

$$\vartheta = [A_1, E_1, A_2, E_2, \ldots, A_{N_p}, E_{N_p}]^T. \tag{11}$$

We name *performance function* $f(t;\vartheta)=f(e(t;\vartheta))$ a function of the error e, which is subsequently summed over some time period τ to give the performance measure F. Here, the performance function is defined as

$$f(t_n;\vartheta) = \frac{|e(t_n;\vartheta)|}{e_{\max}(t_n)}. \tag{12}$$

Time t take discrete values, $t_n = n\Delta t$, with Δt being the discretization interval which corresponds to the frequency data measured. The quantity $e_{\max}$ is the maximum error between computation and measurement, and it is defined as

$$e_{\max}(t_n) = \max\{\hat{E}(t_n), 1-\hat{E}(t_n)\}. \tag{13}$$

The performance measure can be subsequently formed using some function of the sum of the performance function over time:

$$F(\vartheta) = F\left(\sum_{n=0}^{N} f(t_n;\vartheta)\right), \quad N = \tau/\Delta t. \tag{14}$$

In this work, we define the performance measure F as the mean value of the performance function over the time period of interest:

$$F(\vartheta) = \frac{1}{N}\sum_{n=0}^{N} f(t_n;\vartheta) = \frac{1}{N}\sum_{n=0}^{N} \frac{|e(t_n;\vartheta)|}{e_{\max}(t_n)}. \tag{15}$$

The performance measure defined in Eq. (15) is used for the assessment of the performance of each of the three pollutants CO, HC, NO_x. The total performance measure is computed as the mean of these three values:

$$F = \frac{F_{\mathrm{CO}} + F_{\mathrm{HC}} + F_{\mathrm{NO}_x}}{3}. \tag{16}$$

The above performance measure presents advantageous features compared to the classical least-squares performance measure:

• It ranges between two, previously known, finite extreme values. Extremes correspond to zero and maximum deviation between calculation and experiment.

• The extrema of the performance measure are the same for all physical quantities that may be used and all different measurements where the performance measure may be applied. That is, the performance measure is normalized so that its extrema do not depend on the either the measured quantities or the experimental protocol.

Furthermore, out of the different versions of performance measure tested within the specific genetic algorithm optimization procedure, the specific one gave us the best convergence, without the need to rely on empirical weight factors [23].

Optimization Procedure. Having defined the performance measure for the model, the problem of tunable parameter estimation reduces in finding a tunable parameter vector ϑ that maximizes F.

The parameter vector ϑ is not used directly in the optimization procedure. Instead, we perform parameter reparametrization for the pre-exponential factor A, defined as

$$A = 10^{\tilde{A}} \Leftrightarrow \tilde{A} = \log A \tag{17}$$

and the transformed tunable parameters vector becomes

$$\tilde{\vartheta} = [\tilde{A}_1, E_1, \tilde{A}_2, E_2, \ldots, \tilde{A}_{N_p}, E_{N_p}]^T. \tag{18}$$

Then, the problem of tunable parameter estimation is expressed as

Table 2 Parameters of the genetic algorithm

Encoding type	binary
Crossover operator	one-point crossover
Mutation operator	binary mutation
Population size	100
Crossover probability	0.6
Mutation probability	0.03
Encoding resolution	10 bit ($\ell=10$)
Limits	$10^{07}<A_i<10^{23}$

$$\text{Maximize } F'(\tilde{\vartheta}) = 1 - F(\tilde{\vartheta}) = \frac{1}{3N} \sum_{j=\text{CO,HC,NO}_x} \sum_{n=0}^{N} \frac{|e_j(t_n;\tilde{\vartheta})|}{e_{j,\max}(t_n)}, \quad N=\tau/\Delta t. \tag{19}$$

This is a constraint maximization problem, since the components of vector ϑ are allowed to vary between two extreme values, i.e., $\vartheta_{i,\min} \leqslant \vartheta_i \leqslant \vartheta_{i,\max}$. Previous experience [7] has shown that the parameter space that results from this problem formulation is multimodal. Thus an appropriate optimization procedure should be used. Here, a genetic algorithm has been employed for the maximization of Eq. (19). A brief description of the genetic algorithms operation concept and the main features of the implementation used herein are presented below.

A genetic algorithm is a kind of artificial evolution. What evolves is a population of solutions to a problem; each solution is an individual of the population. Individuals are born, mate, reproduce, are mutated, and die analogously to nature's paradigm. The cornerstone of this evolution process is that more fit individuals are given more advantage to live longer and propagate their genetic material to the next generations.

The main steps taken by the algorithm are the following:

(i) *Initialization*. A set of points in the optimization space is chosen at random. This is the initial population of the genetic algorithm, with each point corresponding to an individual of the population.

(ii) *Encoding*. Each individual is encoded to a finite binary string (chromosome). In brief, each real interval $[\tilde{\vartheta}_{i,\min}, \tilde{\vartheta}_{i,\max}]$ is mapped to the integer interval $[0,2^{\ell}]$ and subsequently transform from integer to binary. Then, the chromosome is built by concatenating the binary strings that correspond to the value of each parameter ϑ_i. This encoding is called ''concatenated, multiparameter, mapped, fixed-point coding'' [42].

(iii) *Fitness calculation*. The fitness of each individual in the population is computed using Eq. (19). It should be noticed that fitness calculation requires that the model be called for each individual, i.e., as many times as the population size.

(iv) *Selection*. Random pairs of individuals are subject to tournament, that is, mutual comparison of their fitnesses [43]. Tournament winners are promoted for recombination.

(v) *Recombination (mating)*. The one-point crossover operator [42] is applied to the couples of individuals that are selected for recombination (parents). One-point crossover works on the chromosomes (binary encodings) of the individuals. The resulting chromosomes (children) are inserted to the population replacing their parents and they are decoded to produce their corresponding real parameter vector.

(vi) *Mutation*. A small part of the population is randomly mutated, i.e., random bits of the chromosomes change value.

(vii) Steps (iii)–(vii) are repeated for a fixed number of generations or until acceptably fit individual has been produced.

The randomized nature of the genetic algorithm enables it to avoid local extrema of the parameter space and converge towards the optimum or a near-optimum solution. It should be noted, though, that this feature does not guarantee convergence to the global optimum. This behavior is common to all multimodal optimization techniques and not a specific genetic algorithm characteristic.

The implementation of the genetic algorithm that was described above is not the only one possible. There are a number of design decisions and parameters that influence the operation, efficiency, and speed of the genetic algorithm. The present implementation is classical, though. Its characteristics are summarized in Table 2.

Application Examples

The model's predictive ability is going to be demonstrated in a number of typical applications. The first step is to tune the model for a specific catalyst configuration in typical driving cycle test and the estimate the kinetic parameters of the model. Successful tuning in this phase implies that (i) the model incorporates the appropriate degrees of freedom in order to match the measurement, (ii) the tuning methodology is able to tackle the parameter estimation optimization problem successfully, and (iii) experimental data are in a certain level of accuracy and has been processed through a quality assurance procedure [44].

First, a MVEG test is considered, (European test cycle). A three-way catalytic with a 2.4-l volume, two beds, 400 cpsi, 6.5-mil wall thickness, underfloor converter with 50 g/ft^3 Pt:Rh 7:1 precious metal loading is installed on a passenger car with 2-l engine displacement. The measured catalyst's performance on this car is presented in Fig. 1, by means of the measured instantaneous CO, HC, and NO_x emissions at converter inlet and exit, over the 1180-sec duration of the cycle.

Obviously, the specific converter attains a significant overall efficiency: The emissions at catalyst's exit are diminished after the cold start phase. However, the emissions standards themselves are quite low: Thus the model should not only accurately predict catalyst light-off, but it should also be capable of matching the catalyst's breakthrough during accelerations, decelerations and especially in the extra-urban, high-speed part of the cycle.

In order to match this catalyst's behavior, the model was tuned using the genetic algorithm. The measured emissions during the full NEDC were employed as a reference period for parameter estimation ($\tau=1180$ s in Eq. (19)). CPU time of the order of 48 h was required for the computation of 135 generations (100 individuals each) on a Pentium IV 2.4-GHz PC. However, if one needs faster execution time, a part of the cycle containing the cold start and some hot operation could equally do with just one-third of the time.

The tuning process resulted to the kinetics parameters of Table 3. The evolution of the most important kinetics parameters values of the individuals as determined by the genetic algorithm during the 135 generations is presented in Fig. 2. It may be observed that the genetic algorithm converges to specific values for these parameters. This behavior is not observed for all kinetics parameters, and this is taken into account for improvements in the kinetics scheme [22]. The computed results which are produced when the model is fed with the frequency factors determined by the 135th generation of the genetic algorithm, are summarized in the form of cumulative CO, HC, and NO_x emissions at catalyst's exit, compared to the corresponding measured curves in Fig. 3. The error in the prediction of cumulative emissions does not generally exceed 5% during the cycle for any species.

Also, it is useful to mention that although the specific genetic algorithm matures after about 120 generations, the convergence is clear even from the 20th generation: This means that we could compute good kinetics parameters even with 8 h CPU time. Thus the genetic algorithm approach can no more be considered as forbidding due to excessive computation time. For comparison purposes, it should be mentioned that the tuning process is the most critical part of the modeling job, and it could take several working days from experienced engineers. Moreover, its result was not guaranteed. With the new developments, whenever the genetic algorithm fails to converge, is an indication that the qual-

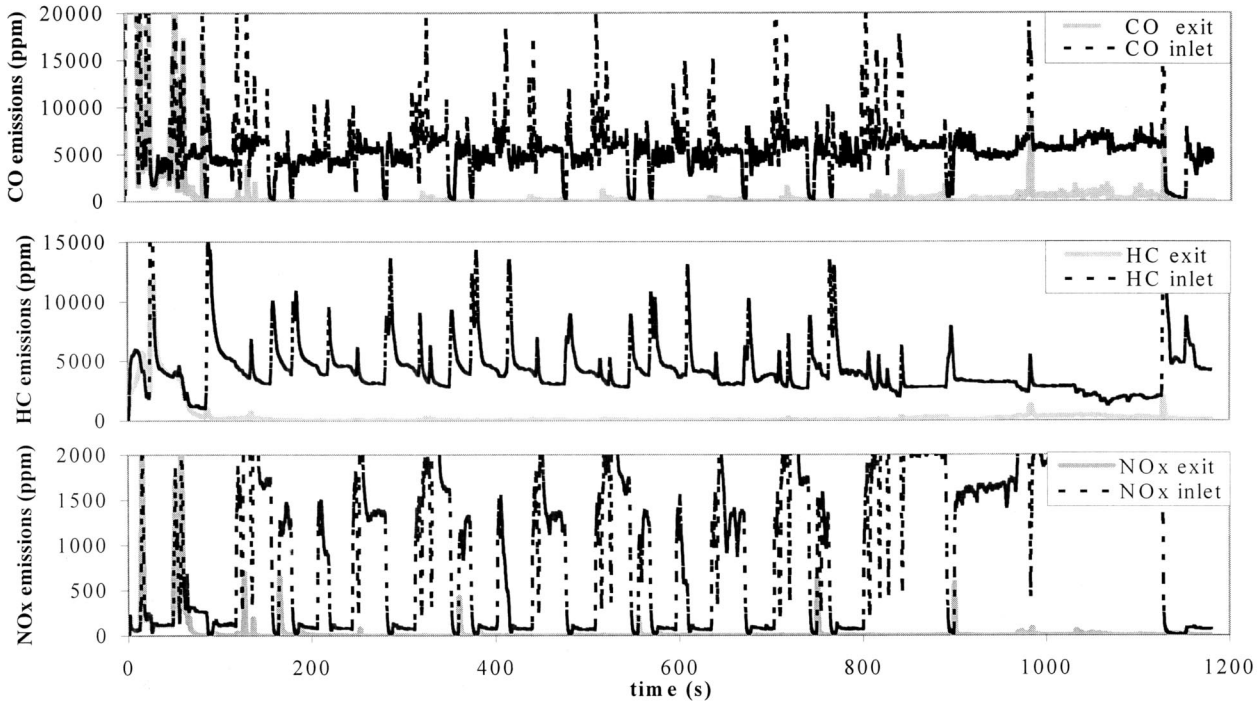

Fig. 1 Measured instantaneous CO, HC, and NO_x emissions at converter inlet and exit, over the 1180-sec duration of the cycle: 2-l-engined passenger car equipped with a 2.4-l underfloor converter with 50-g/ft^3 Pt:Rh catalyst

ity of the test data employed in the tuning process is questionable. Thus the tuning effort with the specific data is stopped and the quality assurance team must examine and possibly reject the test data [44].

In addition, computed and measured temperatures at the converter's exit are compared in Fig. 4. Apparently, the model is capable of matching the catalyst's behavior with a remarkable accuracy, allowing the performance of design optimization studies.

Since one of the objectives of this paper is to quantify the attainable accuracy, we proceed to a more detailed comparison of model predictions and measurements in the form of instantaneous CO, HC, and NO_x emissions. Prediction of instantaneous emissions over the full extent of a real legislative cycle is a significant challenge to any catalytic converter model.

Figure 5 presents the computed and measured instantaneous CO emissions at converter inlet and exit during the first 600 sec of NEDC: Apparently, the model successfully matches light-off behavior of the catalyst, as well as subsequent breakthrough during acceleration. The role of oxygen storage and release reactions in matching the CO breakthough behavior is better assessed by including in the graph the computed degree of filling of the total washcoat's oxygen storage capacity. (See, for example, the small breakthroughs, which are of the order of 200 ppm, with maximum peaks of the order of 1000 ppm, that are accurately matched by the computation).

Table 3 Kinetics parameters tuned to the Pt:Rh catalyst

	Reaction	A	E
1	$CO+1/2O_2 \rightarrow CO_2$	$2.000E+20$	90,000
2	$H_2+1/2O_2 \rightarrow H_2O$	$2.000E+19$	90,000
3, 4	$C_\alpha H_\beta+(\alpha+0.25\beta)O_2 \rightarrow \alpha CO_2+0.5\beta H_2O$	$1.800E+20$	95,000
		$2.710E+19$	120,000
	NO reduction		
5	$2CO+2NO \rightarrow 2CO_2+N_2$	$3.403E+09$	90,000
	Oxygen storage		
6	$2CeO_2+CO \rightarrow Ce_2O_3+CO_2$	$7.832E+09$	85,000
7, 8	$C_\alpha H_\beta+(2\alpha+\beta)CeO_2 \rightarrow$	$1.283E+10$	85,000
	$\rightarrow(\alpha+0.5\beta)Ce_2O_3+\alpha CO+0.5\beta H_2O$	$3.631E+13$	85,000
9	$Ce_2O_3+1/2O_2 \rightarrow 2CeO_2$	$2.553E+09$	90,000
10	$Ce_2O_3+NO \rightarrow 2CeO_2+1/2N_2$	$4.118E+10$	90,000

A comparison of computed and measured CO emissions for the cycle part from 600 to 1180 s is given in Fig. 6. In the extra-urban part of the cycle, the efficiency of the converter is reduced due to high flowrates. Again, the breakthroughs are observed when the oxygen stored in the washcoat is gradually depleted. The prediction of the model is remarkably good, especially when the order of magnitude of the breakthroughs is considered. This successful prediction indicates that the oxygen storage reactions that are implemented in the model are capable of modeling the phenomenon with high accuracy. An exception to this good behavior is observed only in the interval between 930 and 980 sec. Here there exists room for further improvement of the storage submodel and reaction scheme.

Figures 7 and 8 present the computed and measured instantaneous NO_x emissions at converter inlet and exit during the two halves of the NEDC: Apparently, the model successfully matches light-off behavior of the catalyst, as well as subsequent NO_x breakthrough behavior during accelerations. Oxygen storage is critical also here. The prediction accuracy is remarkable when one notes that the breakthroughs are of the order of a few ppm. A weak point of the model is spotted in the comparison of computed and measured behavior between 980 and 1100 sec. Again, this is the subject for future improvements in the oxygen storage submodel.

The situation appears equally good in Figs. 9 and 10 where the computed and measured instantaneous HC emissions at converter inlet and exit during the first 600 s and the rest of NEDC are given. The connection between HC breakthroughs and oxygen storage phenomena in the washcoat is apparent also in this case. The model results are of comparable quality as the previous figures, since the model predicts the events (HC breakthroughs) of the extra-urban part of the cycle, not only qualitatively, but also quantitatively, in a certain extent. HC light-off behavior is also

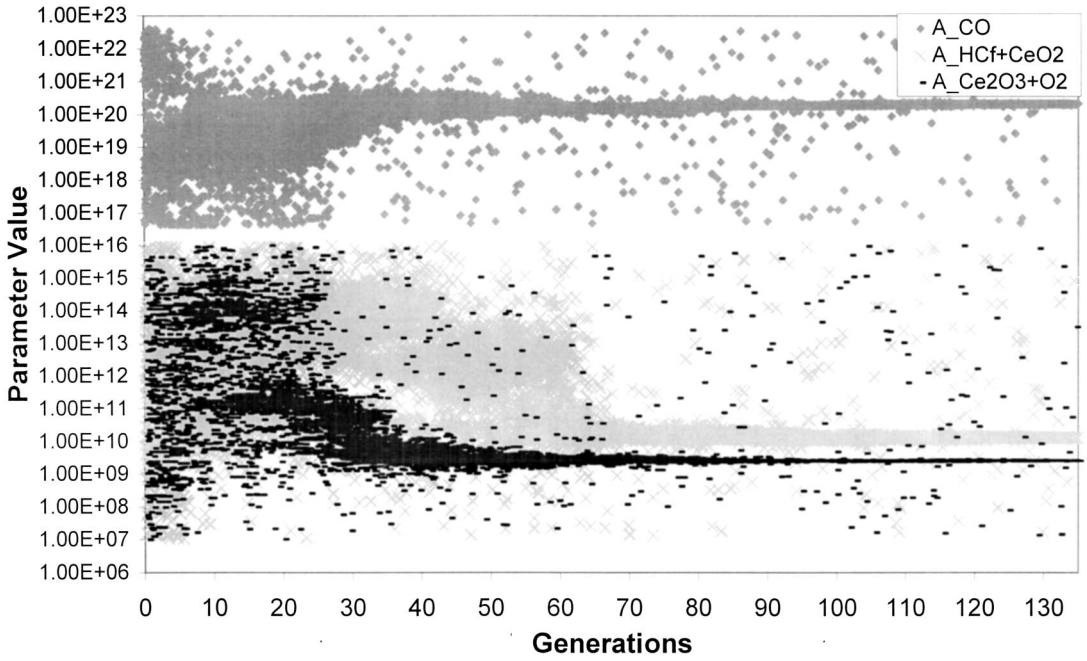

Fig. 2 Evolution of the values of three selected kinetics parameters in the 100 individuals of the population during 135 generations. The convergence to the final values is apparent even from the 40th generation.

matched with a very good accuracy, taking into account the complexity of the hydrocarbons composition that is modeled only by two representative components.

The overall performance of the specific model prediction's can be quantitatively assessed by means of evaluating the performance measure which is defined in Eqs. (15) and (16). The performance measure takes the value: $F' = 0.959$.

The above results indicate that the model formulation has the capability to match typical measurements of a three-way catalytic converter, and that the tuning methodology may be used successfully to fit the model to the measured data. Another important finding is that the model is capable of predicting the catalyst's performance outside the region where it has been tuned. That is, if we tested carrying out the tuning process based only on the first

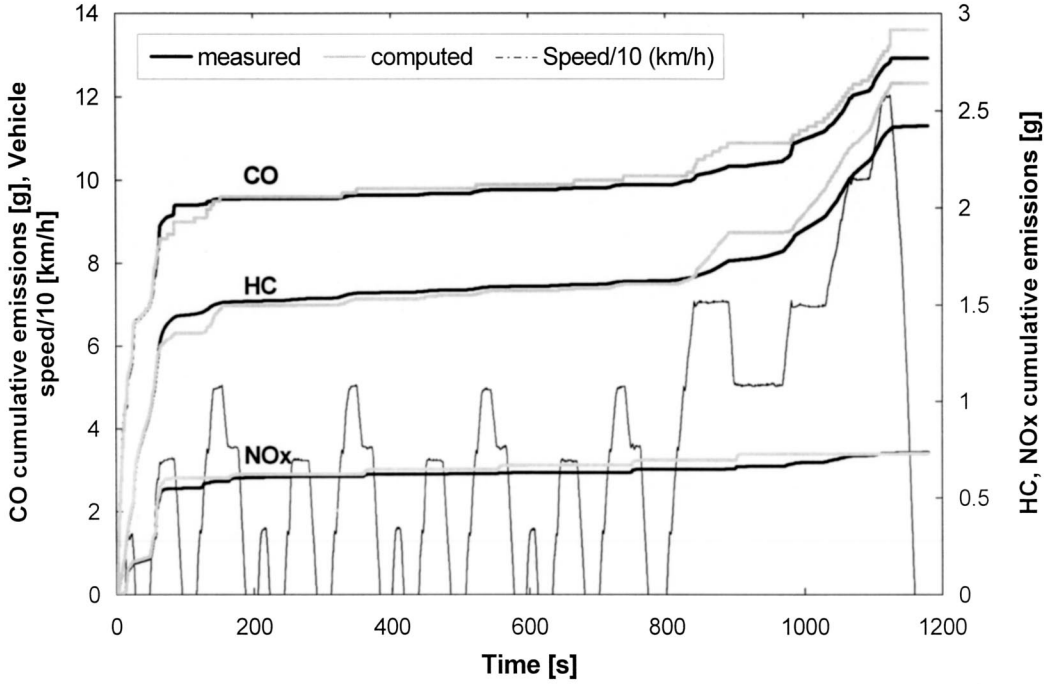

Fig. 3 Computed and measured cumulative CO, HC, and NO_x emissions at converter exit during NEDC: 2-l-engined passenger car equipped with a 2.4-l underfloor converter with 50-g/ft^3 Pt:Rh catalyst

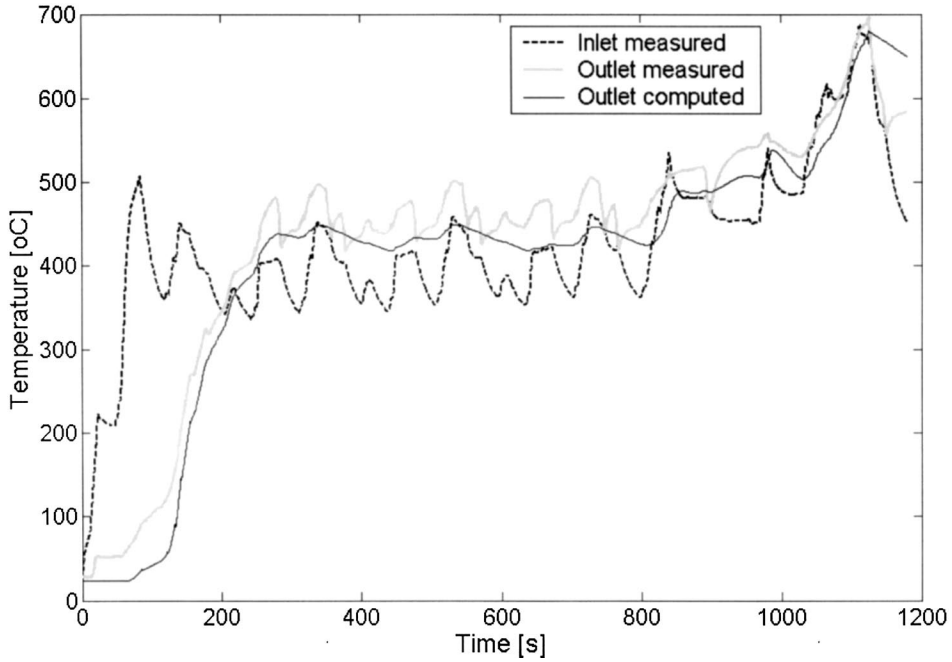

Fig. 4 Measured converter inlet temperatures, computed, and measured converter exit temperatures during NEDC: 2-l-engined passenger car equipped with a 2.4-l underfloor converter with 50-g/ft^3 Pt:Rh catalyst

400 s (see above discussion on genetic algorithm tuning), and the model demonstrated an equally satisfactory predictive ability for the catalyst performance throughout the full NEDC cycle.

Additional evidence is provided below about the model's ability to predict the operating behavior of a different catalytic converter configuration. This is achieved by using the model to predict the behavior of an alternative configuration of a three-way catalytic converter with no further kinetic parameter adjustments.

Therefore, as a next step in the assessment of the model's accuracy and predictive ability, the model is employed in the prediction of the performance of an alternative underfloor converter of the same washcoat type, which is $\frac{1}{4}$ the size of the original one.

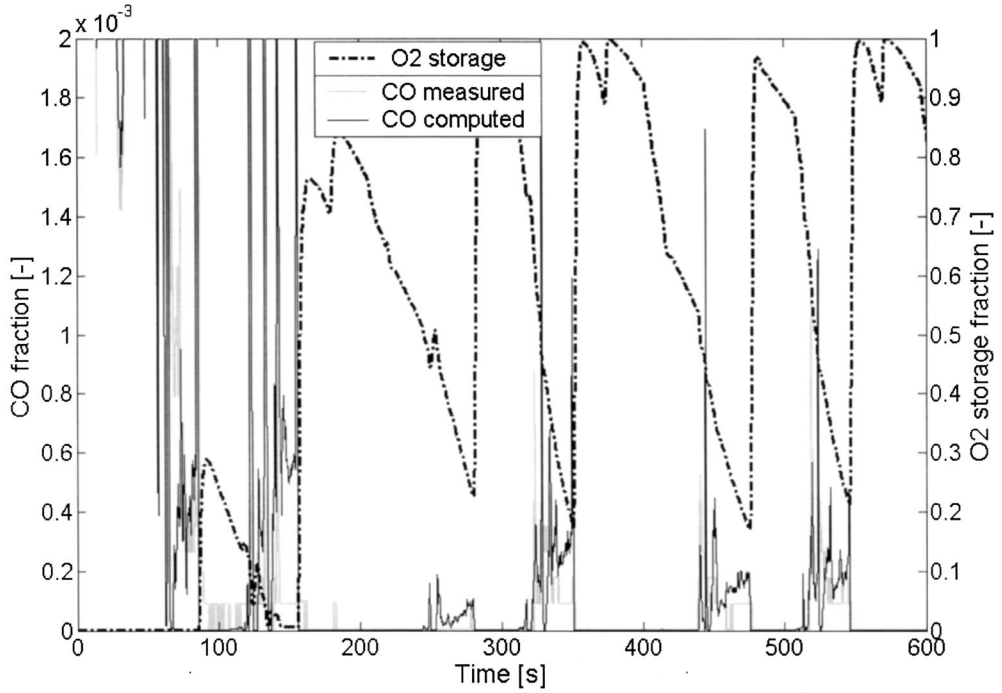

Fig. 5 Computed and measured instantaneous CO emissions at converter inlet and exit during the first 600 sec of NEDC: 2-l-engined passenger car equipped with a 2.4-l underfloor converter with 50-g/ft^3 Pt:Rh catalyst

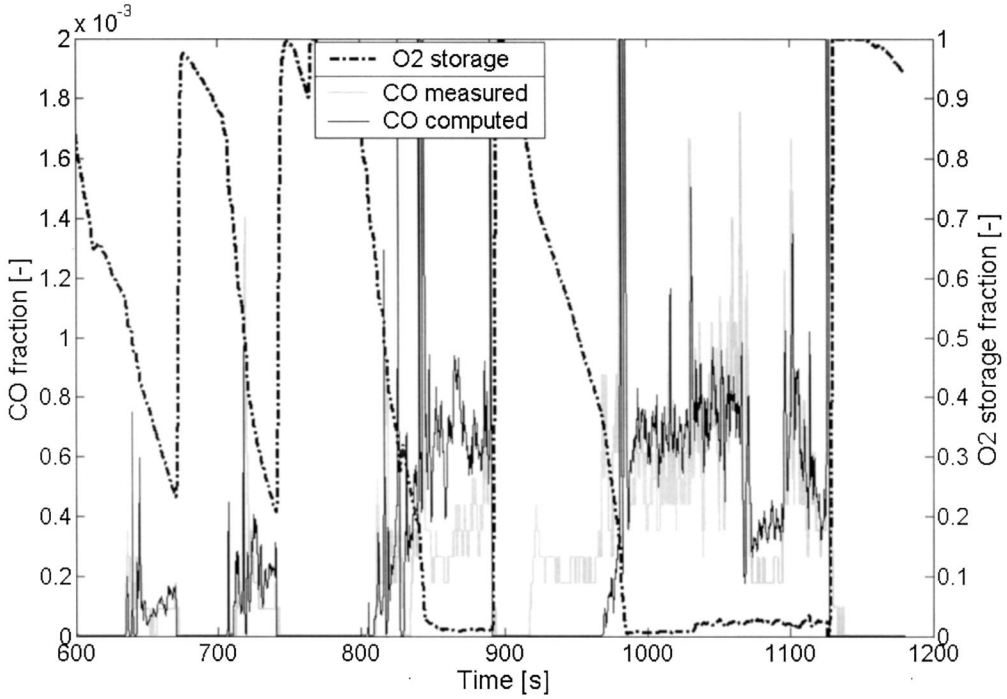

Fig. 6 Computed and measured instantaneous CO emissions at converter inlet and exit during the second half of the NEDC (600–1180 sec of NEDC): 2-l-engined passenger car equipped with a 2.4-l underfloor converter with 50-g/ft^3 Pt:Rh catalyst

Since the same catalyst formulation and precious metal loading is employed, modeling of this case is performed using the same kinetics parameters of Table 3 which where estimated for the original converter. Only the external dimensions of the converter are changed to the ones of the reduced size converter and no further tuning of the kinetic parameters is performed. The results of the model are then compared to the measured results for this converter in Fig. 11, in the form of cumulative CO, HC, and NO_x emissions. Apparently, the model is capable of predicting the significant change in all three pollutants emissions that is caused by

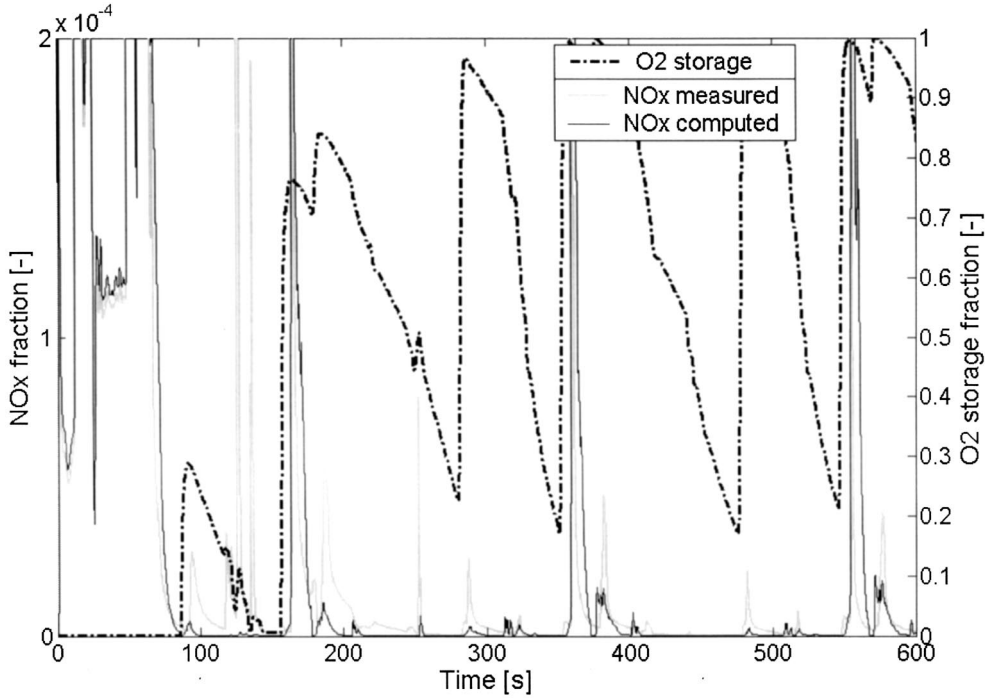

Fig. 7 Computed and measured instantaneous NO_x emissions at converter inlet and exit during the first 600 sec of NEDC: 2-l-engined passenger car equipped with a 2.4-l underfloor converter with 50-g/ft^3 Pt:Rh catalyst

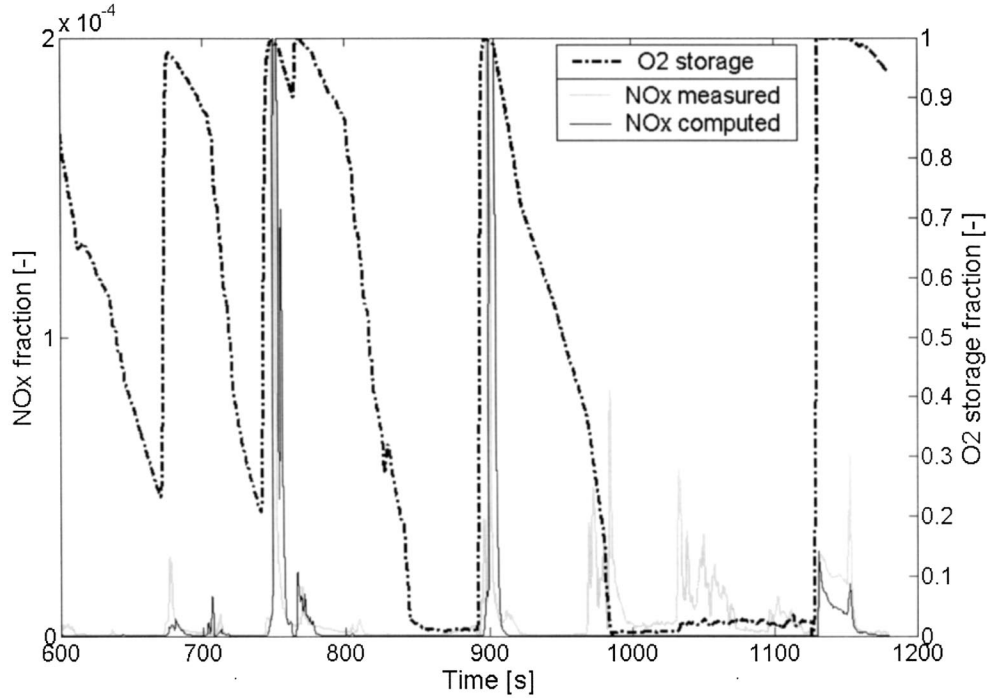

Fig. 8 Computed and measured instantaneous NO_x emissions at converter inlet and exit during the second half of NEDC: 2-l-engined passenger car equipped with a 2.4-l underfloor converter with 50-g/ft^3 Pt:Rh catalyst

the reduction of the converter's volume, without changes in its kinetic parameters. The performance measure now takes the value: $F' = 0.921$, which indicates a sufficiently accurate prediction of measured performance.

A better insight on the model's performance, also in association with oxygen storage and release behavior, can be made, for example, by a comparison of computed and measured instantaneous HC emissions at the converter's exit, during the full cycle (Fig.

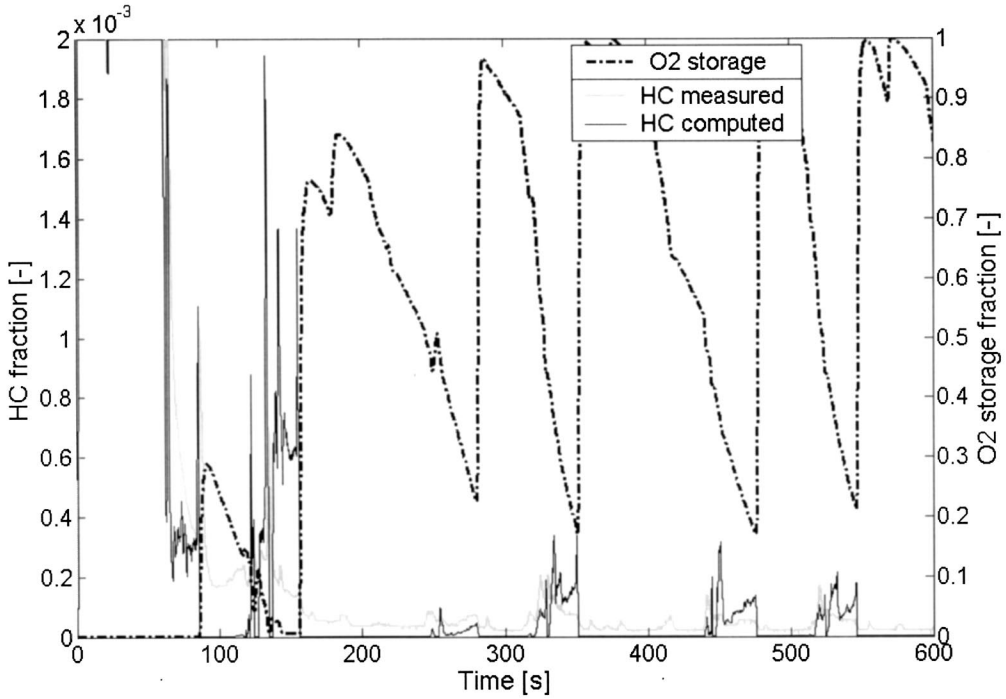

Fig. 9 Computed and measured instantaneous HC emissions at converter inlet and exit during the first 600 sec of NEDC: 2-l-engined passenger car equipped with a 2.4-l underfloor converter with 50-g/ft^3 Pt:Rh catalyst

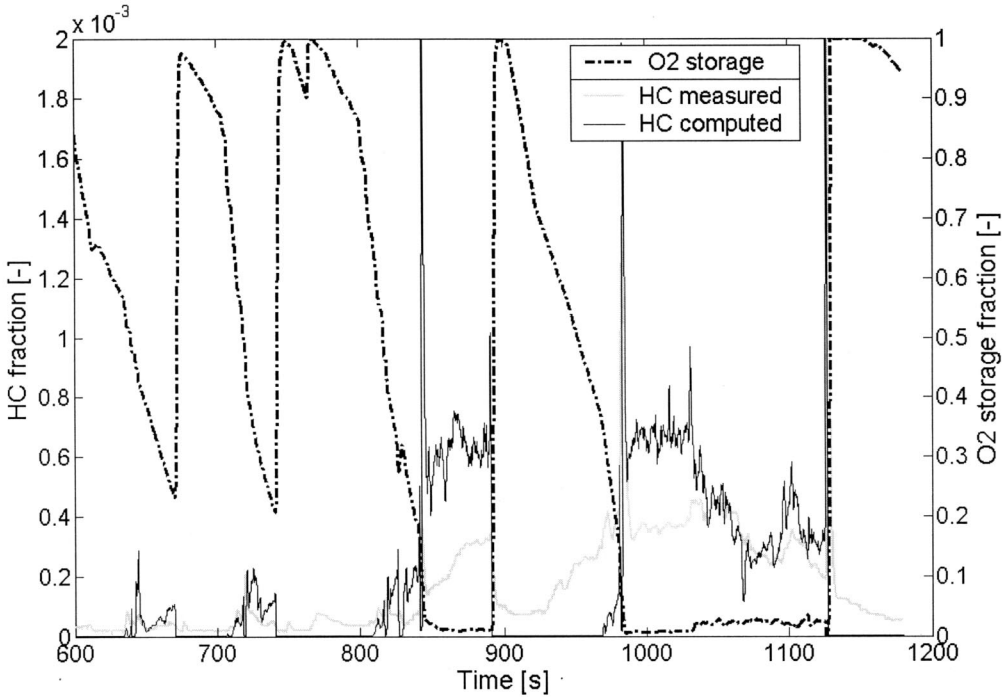

Fig. 10 Computed and measured instantaneous HC emissions at converter inlet and exit during the second half of NEDC: 2-l-engined passenger car equipped with a 2.4-l underfloor converter with 50-g/ft^3 Pt:Rh catalyst

12). Here, the model demonstrates the capacity of taking into account the change in total oxygen storage capacity, to accurately predict the effect of size reduction. The same good behavior is demonstrated with CO in Fig. 13, and NO_x (not shown here).

As a next step, we check the model's predictive ability with a different catalyst type, namely, a Pd:Rh 14:1, 150 gr/ft^3, 0.8-l volume converter, which is now fitted in a close-coupled position on a 2.2-l engined car. Again, the converter is a standard 400-cpsi,

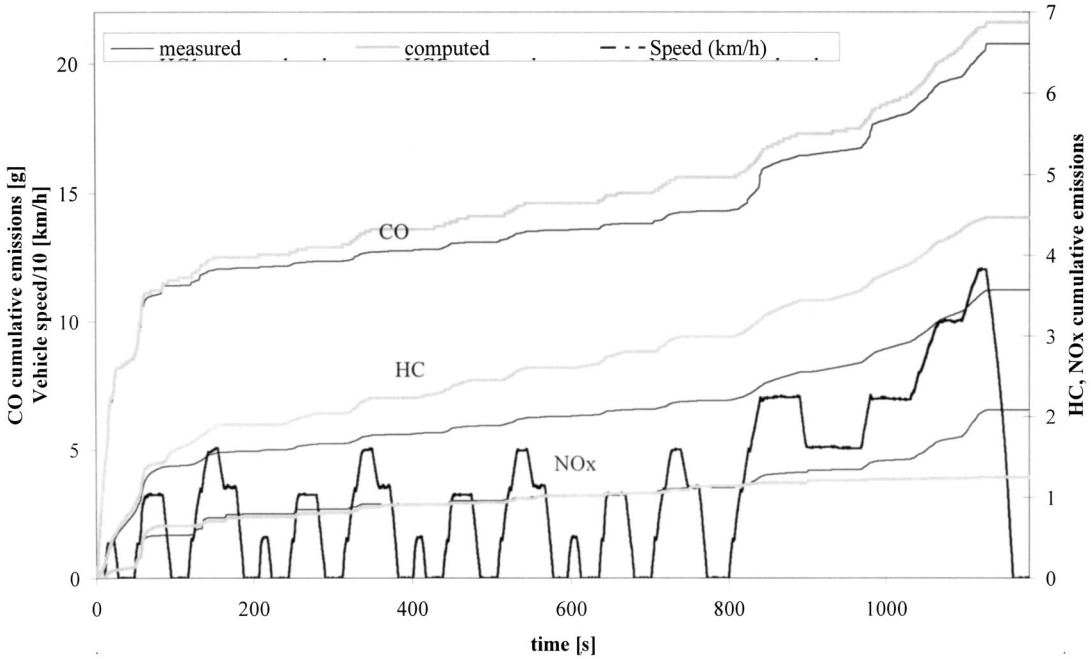

Fig. 11 Computed (based on the kinetics parameters values of Table 1) and measured cumulative CO, HC, and NO_x emissions at converter exit during NEDC. 2-l-engined passenger car equipped with a 0.6-l underfloor converter with 50-g/ft^3 Pt:Rh catalyst. Apparently, the model is capable of predicting the significant difference in CO, HC, and NO_x emissions at the exit of the reduced-size converter.

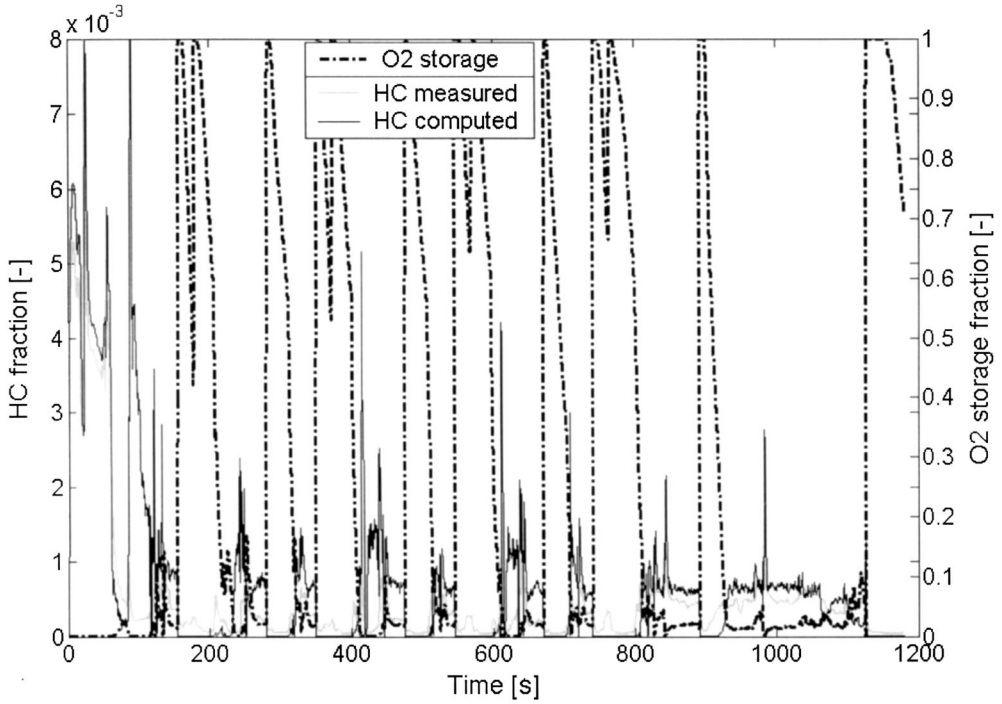

Fig. 12 Computed (based on the kinetics parameters values of Table 1) and measured instantaneous HC emissions at converter exit during NEDC: 2-l-engined passenger car equipped with a 0.6-l underfloor converter with 50-g/ft^3 Pt:Rh catalyst. Apparently, the model is capable of predicting with good accuracy the characteristic HC breakthrough with the reduced-size converter during the high-speed part of NEDC.

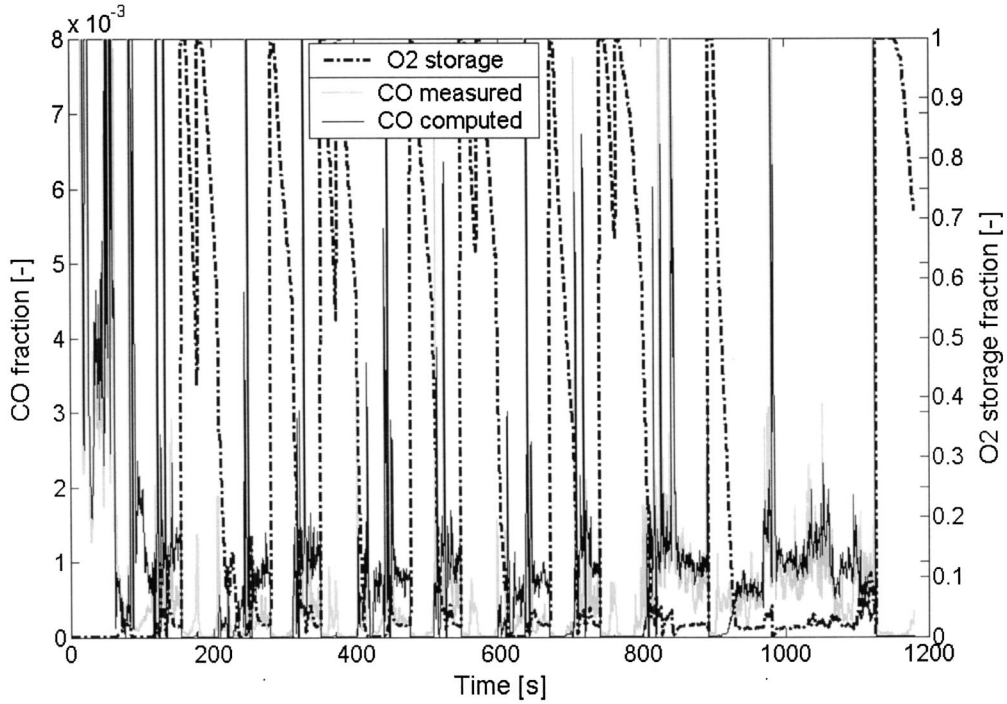

Fig. 13 Computed (based on the kinetics parameters values of Table 1) and measured instantaneous CO emissions at converter exit during NEDC: 2-l-engined passenger car equipped with a 0.6-l underfloor converter with 50-g/ft^3 Pt:Rh catalyst

Table 4 Kinetics parameters tuned to the Pd:Rh catalyst

	Reaction	*A*	*E*
1	$CO+1/2O_2 \rightarrow CO_2$	$1.10E+18$	90,000
2	$H_2+1/2O_2 \rightarrow H_2O$	$1.10E+18$	90,000
3, 4	$C_\alpha H_\beta+(\alpha+0.25\beta)O_2 \rightarrow \alpha CO_2+0.5\beta H_2O$	$2.00E+15$	70,000
		$1.00E+16$	105,000
	NO reduction		
5	$2CO+2NO \rightarrow 2CO_2+N_2$	$1.20E+13$	90,000
	Oxygen storage		
6	$2CeO_2+CO \rightarrow Ce_2O_3+CO_2$	$1.00E+09$	85,000
7, 8	$C_\alpha H_\beta+(2\alpha+\beta)CeO_2 \rightarrow$	$7.00E+09$	85,000
	$\rightarrow(\alpha+0.5\beta)Ce_2O_3+\alpha CO+0.5\beta H_2O$	$7.00E+09$	85,000
9	$Ce_2O_3+1/2O_2 \rightarrow 2CeO_2$	$1.00E+11$	90,000
10	$Ce_2O_3+NO \rightarrow 2CeO_2+1/2N_2$	$2.00E+11$	90,000

6.5-mil substrate. The test now is according to the U.S. FTP-75 procedure, which is considered as a more demanding test procedure for modeling catalytic converter behavior, because of the extensively transient nature of its driving cycle.

In this case, a new kinetic tuning is required, because we shift to a different type of catalyst and washcoat formulation. The genetic algorithm optimized the kinetic parameters of the model for the reference period of the first 600 s of the FTP cycle. This part boldly corresponds to the cold-start phase of the cycle. (This phase is followed by the transient phase (505–1369 s) and the hot-start phase (1369–1874 s), the latter starting after the engine is stopped for 10 min). The values of the kinetic parameters resulting from the tuning procedure are listed in Table 4.

The computed results are summarized in the form of cumulative CO, HC, and NO_x emissions at the catalyst's exit, compared to the corresponding measured curves in Fig. 14. The performance measure takes the value of $F'=0.955$. In addition, computed and measured temperatures at converter's exit are compared in Fig. 15. Apparently, also in this case, the model is capable of matching the catalyst's behavior with very good accuracy, allowing the performance of design optimization studies.

The model's accuracy can be assessed in more detail, by means of instantaneous emissions comparison. As an example, Fig. 16 presents the computed and measured instantaneous HC emissions at converter inlet and exit during the first 600 sec of FTP-75: Apparently, the model successfully matches light-off behavior of the catalyst, as well as subsequent breakthrough during the significant accelerations of FTP cycle. Again, the role of oxygen storage and release reactions in matching the HC breakthrough behavior is very well assessed by including in the graph, the computed degree of filling of the total washcoat's oxygen storage capacity.

The above indicative results can be considered to support a clear demonstration of the attainable accuracy and predictive ability of this category of models. Of course, these results have been achieved by continuous development and improvements of the specific model based on its extensive application in standard exhaust aftertreatment system design case studies during the last six years.

Moreover, the demonstrated model's capacity to predict the combined effect of the precious metal and Ceria kinetics on the transient converter's performance, allows us to support the complex optimization tasks of great interest to the emissions control engineer [45]. For example, a specific catalyst-washcoat design needs to be tailored to address specific converter's performance requirements, based on the raw emissions, exhaust temperature levels, and exhaust mass flowrate behavior of each different type of engine-vehicle-exhaust system combination.

Concluding Remarks

This paper aims to contribute towards a more clear definition of the state of the art in engineering design tools in automotive catalytic converter systems.

A model developed and continuously improved in the authors' lab, based on the experience from involvement in engineering design tasks during the last six years, is described in detail, in its current status of development, in comparison with other models existing in the literature, and employed in demonstration case studies with Pt:Rh and Pd:Rh catalysts.

A kinetic parameter estimation methodology that has been recently developed specifically to support this type of modeling is

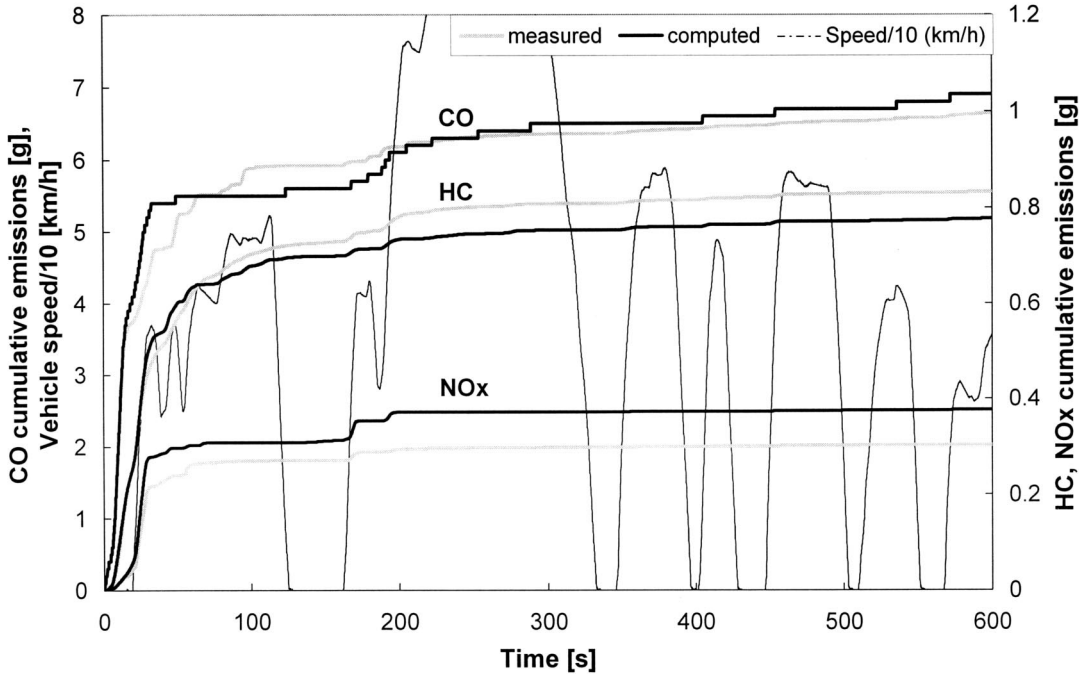

Fig. 14 Computed and measured cumulative CO, HC, and NO_x emissions at converter exit during FTP-75: 2.2-l-engined passenger car equipped with a 0.8-l close-coupled converter with 150-g/ft^3 Pd:Rh catalyst

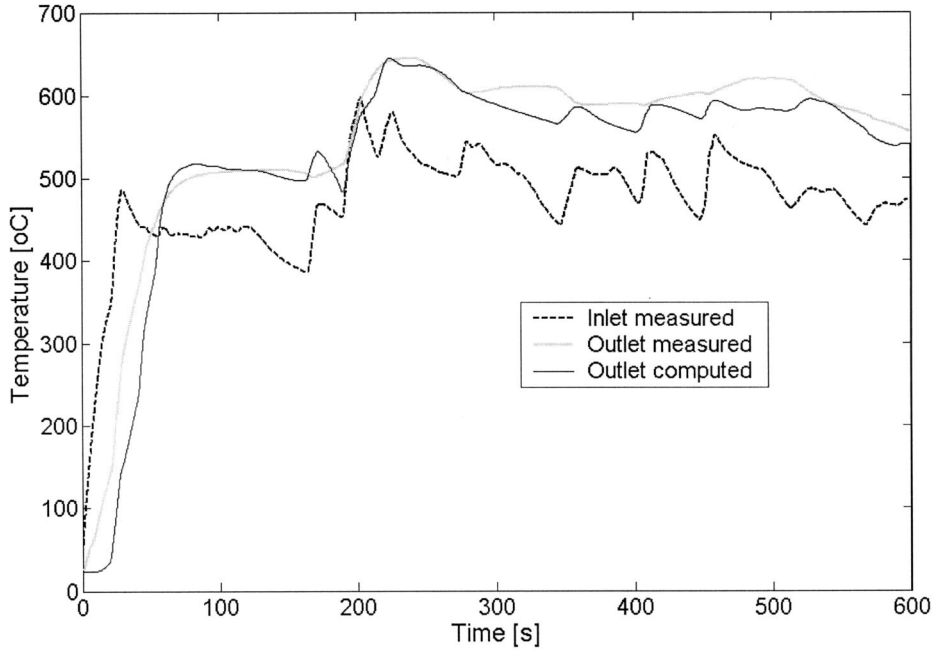

Fig. 15 Computed and measured converter exit temperatures during the first 600 sec of FTP-75 test cycle: 2.2-l-engined passenger car equipped with a 0.8-l close-coupled converter with 150-g/ft^3 Pd:Rh catalyst. Converter inlet temperature recording is also shown.

briefly presented and demonstrated in the case studies. This methodology is based on a combination of a genetic algorithm approach and a customized performance measure. The methodology proves quite successful in finding the parameters for the best fit of the model to the tuning data.

The model's predictions are compared to the respective experimental results, to enable an objective assessment of attainable accuracy. The comparison of measurements and computations is made in terms of cumulative CO, HC, and NO_x emissions at the converter exit, exhaust temperatures at the converter exit, as well

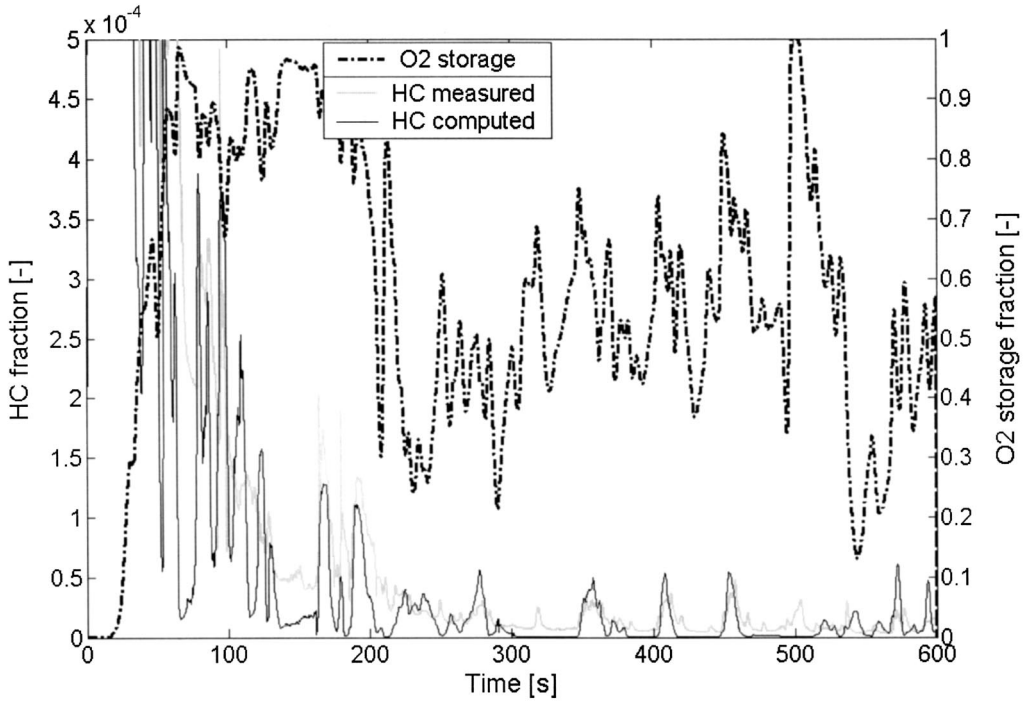

Fig. 16 Computed and measured instantaneous HC emissions at converter exit during the first 600 sec of FTP-75 test cycle: 2.2-l-engined passenger car equipped with a 0.8-l close-coupled converter with 150-g/ft^3 Pd:Rh catalyst

as instantaneous CO, HC, and NO_x emissions at the converter's exit, the latter being the most demanding task for a model.

In order to better quantify model accuracy in matching the experimental results, for the purpose of driving the genetic algorithm towards better solutions, a performance measure is developed and discussed in this paper. This performance measure, in addition to being essential in the parameter estimation methodology, may prove useful to assess the success of modeling exercises by this and other models of catalytic converters.

The overall demonstration is intended to show that the current state-of-the-art models of automotive catalytic converters provide an indispensable tool assisting the design of catalytic exhaust aftertreatment systems for ultra low emitting vehicles. This is succeeded due to the high accuracy attained by such models, despite their simplified kinetics scheme and their engineering approach with minimized degrees of freedom.

Nomenclature

$a_{j,k}$ = Stoichiometric coefficient of species j in reaction k
A = Pre-exponential factor of reaction rate expression (mol K/(m^3 s)
c = Species concentration (−)
c_p = Specific-heat capacity (J/(kg K))
e = Error between computeration and experiment (−)
E = i Activation energy of reaction rate expression (J)
ii Conversion efficiency (−)
f = Performance function (−)
F = Performance measure (−)
G = Inhibition term (Table 1) (K)
ΔH = Molar heat of reaction (J/mol)
h = Convection coefficient (W/(m^2 s))
k = Thermal conductivity (W/(m K))
k_m = Mass transfer coefficient (m/s)
K = Inhibition term (Table 1) (−)
ℓ = Genetic algorithm binary encoding resolution (−)
$\dot{m}$ = Exhaust gas mass flow rate (kg/s)
M = Molecular mass (kg/mol)
N_R = Number of reactions (−)
N_P = Number of tunable parameters (−)
Q_{amb} = Heat trasferred between converter and ambient air (J/(m^3 s))
r = Rate of reaction (mol/m^3 s)
R_g = Universal gas constant (8.314 J/(mol K))
R = Rate of species production/depletion per unit reactor volume (mol/(m^3 s))
S = Geometric surface area per unit reactor volume (m^2/m^3)
t = Time (s)
T = Temperature (K)
u_z = Exhaust gas velocity (m/s)
z = Distance from the monolith inlet (m)

Greek Letters

α = Number of carbon atoms in hydrocarbon molecule (−)
β = Number of hydrogen atoms in hydrocarbon molecule (−)
γ = Catalytic surface area per unit washcoat volume (m^2/m^3)
δ = Washcoat thickness (m)
ε = Emissivity factor (radiation) (−)
ϑ = Tunable parameters vector
ρ = Density (kg/m^3)
σ = Stefan–Boltzmann constant (W/(m^2 T^4))
τ = Reference time period for parameter estimation (s)
ψ = Fractional extent of the oxygen storage component (−)
Ψ_{cap} = Washcoat capacity of the oxygen storage component (mol/m^3)

Subscripts

amb = Ambient
g = Gas
i = Parameter index
j = Species index
k = Reaction index
mon = Monolith
n = Time index
in = Inlet
s = (i) Solid; (ii) solid–gas interface
z = Axial direction

References

[1] Farrauto, R. J., and Heck, R. M., 1999, "Catalytic Converters: State of the Art and Perspectives," Catal. Today, **51**, pp. 351–360.
[2] Koltsakis, G. C., and Stamatelos, A. M., 1997, "Catalytic Automotive Exhaust Aftertreatment," Prog. Energy Combust. Sci., **23**, pp. 1–37.
[3] Oh, S. H., and Cavendish, J. C., 1982, "Transients of Monolithic Catalytic Converters: Response to Step Changes in Feedstream Temperature as Related to Controlling Automobile Emissions," Ind. Eng. Chem. Prod. Res. Dev., **21**, pp. 29–37.
[4] Oh, S. H., and Cavendish, J. C., 1985, "Mathematical Modeling of Catalytic Converter Light-off—Part II: Model Verification by Engine-Dynamometer Experiments," AIChE J., **31**(6), pp. 935–942.
[5] Oh, S. H., and Cavendish, J. C., 1985, "Mathematical Modeling of Catalytic Converter Light-off—Part III: Prediction of Vehicle Exhaust Emissions and Parametric Analysis," AIChE J., **31**(6), pp. 943–949.
[6] Tischer, S., Correa, C., and Deutshmann, O., 2001, "Transient Three-Dimensional Simulation of a Catalytic Combustion Monolith Using Detailed Models for Heterogeneous and Homogeneous Reactions and Transport Phenomena," Catal. Today, **69**, pp. 57–62.
[7] Pontikakis, G., and Stamatelos, A., 2001, "Mathematical Modeling of Catalytic Exhaust Systems for EURO-3 and EURO-4 Emissions Standards," Proc. Inst. Mech. Eng., Part D (J. Automob. Eng.), **215**, pp. 1005–1015.
[8] Young, L. C., and Finlayson, B. A., 1976, "Mathematical Models of the Monolithic Catalytic Converter: Part I. Development of Model and Application of Orthogonal Collocation," AIChE J., **22**(2), pp. 331–343.
[9] Siemund, S., Leclerc, J. P., Schweich, D., Prigent, M., and Castagna, F., 1996, "Three-Way Monolithic Converter: Simulations Versus Experiments," Chem. Eng. Sci., **51**(15), pp. 3709–3720.
[10] Koltsakis, G. C., Konstantinidis, P. A., and Stamatelos, A. M., 1997, "Development and Application Range of Mathematical Models for Automotive 3-Way Catalytic Converters," Appl. Catal., B, **12**(2-3), pp. 161–191.
[11] Chen, D. K. S., Bisset, E. J., Oh, S. H., and Van Ostrom, D. L., 1988, "A Three-Dimensional Model for the Analysis of Transient Thermal and Conversion Characteristics of Monolithic Catalytic Converters," SAE paper 880282.
[12] Montreuil, C. N., Williams, S. C., and Adamczyk, A. A., 1992, "Modeling Current Generation Catalytic Converters: Laboratory Experiments and Kinetic Parameter Optimization—Steady State Kinetics," SAE paper 920096.
[13] Dubien, C., Schweich, D., Mabilon, G., Martin, B., and Prigent, M., 1998, "Three-Way Catalytic Converter Modeling: Fast and Slow Oxidizing Hydrocarbons, Inhibiting Species and Steam-Reforming Reaction," Chem. Eng. Sci., **53**(3), pp. 471–481.
[14] Heck, R. H., Wei, J., and Katzer, J. R., 1976, "Mathematical Modeling of Monolithic Catalysts," AIChE J., **22**(3), pp. 477–484.
[15] Shamim, T., Shen, H., Sengupta, S., Son, S., and Adamczyk, A. A., 2002, "A Comprehensive Model to Predict Three-Way Catalytic Converter Performance," J. Eng. Gas Turbines Power, **124**(2), pp. 421–428.
[16] Konstantinidis, P. A., Koltsakis, G. C., and Stamatelos, A. M., 1997, "Computer-Aided Assessment and Optimization of Catalyst Fast Light-off Techniques," Proc. Inst. Mech. Eng., Part D (J. Automob. Eng.), **211**, pp. 21–37.
[17] Konstantinidis, P. A., Koltsakis, G. C., and Stamatelos, A. M., 1998, "The Role of CAE in the Design Optimization of Automotive Exhaust Aftertreatment Systems," Proc. Inst. Mech. Eng., Part D (J. Automob. Eng.), **212**, pp. 1–18.
[18] Baba, N., Ohsawa, K., and Sugiura, S., 1996, "Analysis of Transient Thermal and Conversion Characteristics of Catalytic Converters During Warm-up," JSAE Review of Automative Engineering, **17**, pp. 273–279.
[19] Schmidt, J., Waltner, A., Loose, G., Hirschmann, A., Wirth, A., Mueller, W., Van den Tillaart, J. A. A., Mussmann, L., Lindner, D., Gieshoff, J., Umehara, K., Makino, M., Biehn, K. P., and Kunz, A., 1999, "The Impact of High Cell Density Ceramic Substrates and Washcoat Properties on the Catalytic Activity of Three Way Catalysts," SAE paper 1999-01-0272.

[20] Stamatelos, A. M., Koltsakis, G. C., and Kandylas, I. P., 1999, ''Computergestützte Entwurf von Abgasnachbehandlungsystemen. Teil I. Ottomotor,'' Motortech. Z., **MTZ 60**(2), pp. 116–124.
[21] LTTE-University of Thessaly: CATRAN Catalytic Converter Modeling Software, User's Guide, Version v4r2f. Volos, June 2003.
[22] Pontikakis, G. N., and Stamatelos, A. M., 2002, ''Catalytic Converter Modeling: Computer-Aided Parameter Estimation by use of Genetic Algorithms'' Proc. Inst. Mech. Eng., Part D: J. Automob. Eng., accepted for publication.
[23] Pontikakis, G., 2003, ''Modeling, Reaction Schemes and Kinetic Parameter Estimation in Automotive Catalytic Converters and Diesel Particulate Filters,'' Ph.D. thesis, Mechanical & Industrial Engineering Department, University of Thessaly, June 2003. http://www.mie.uth.gr/labs/ltte/pubs/PhD_G_Pont.pdf
[24] Zygourakis, K., and Aris, R., 1983, ''Multiple Oxidation Reactions and Diffusion in the Catalytic Layer of Monolith Reactors,'' Chem. Eng. Sci., **38**(5), pp. 733–744.
[25] Hoebink, J. H. B. J., van Gemert, R. A., van den Tillaart, J. A. A., and Marin, G. B., 2000, ''Competing Reactions in Three-Way Catalytic Converters: Modeling of the NO_x Conversion Maximum in the Light-off Curves Under Net Oxidizing Conditions,'' Chem. Eng. Sci., **55**(9), pp. 1573–1581.
[26] Keren, I., and Sheintuch, M., 2000, ''Modeling and Analysis of Spatiotemporal Oscillatory Patterns During CO Oxidation in the Catalytic Converter,'' Chem. Eng. Sci., **55**, pp. 1461–1475.
[27] Voltz, S. E., Morgan, C. R., Liederman, D., and Jacob, S. M., 1973, ''Kinetic Study of Carbon Monoxide and Propylene Oxidation on Platinum Catalysts,'' Ind. Eng. Chem. Prod. Res. Dev., **12**, pp. 294–301.
[28] Young, L. C., and Finlayson, B. A., 1976, ''Mathematical Models of the Monolithic Catalytic Converter: Part I. Development of Model and Application of Orthogonal Collocation,'' AIChE J., **22**(2), pp. 337–343.
[29] Hayes, R. E., and Kolaczkowski, S. T., 1994, ''Mass and Heat Transfer Effects in Catalytic Monolith Reactors,'' Chem. Eng. Sci., **46**(21), pp. 3587–3599.
[30] Tanaka, M., Tsujimoto, Y., Miyazaki, T., Warashina, M., and Wakamatsu, S., 2001, ''Pecularities of Volatile Hydrocarbons Emissions From Several Types of Vehicles in Japan,'' Chemosphere-Global Change Science, **3**(2), pp. 185–197.
[31] Pattas, K. N., Stamatelos, A. M., Pistikopoulos, P. K., Koltsakis, G. C., Konstantinidis, P. A., Volpi, E., and Leveroni, E., 1994, ''Transient Modeling of 3-Way Catalytic Converters,'' SAE paper 940934, SAE Trans., **103**, pp. 565–578.
[32] Koberstein, E., and Wannemacher, G., 1987, ''The A/F Window With Three-Way Catalysts. Kinetic and Surface Investigations,'' *CAPOC, International Congress on Catalysis and Automotive Pollution Control*, Brussels.
[33] Siemund, S., Leclerc, J. P., Schweich, D., Prigent, M., and Castagna, F., 1996, ''Three Way Monolithic Converter: Simulations Versus Experiments,'' Chem. Eng. Sci., **51**(15), pp. 3709–3720.
[34] Heck, R. H., Wei, J., and Katzer, J. R., 1976, ''Mathematical Modeling of Monolithic Catalysts,'' AIChE J., **22**(3), pp. 477–484.
[35] Zygourakis, K., 1989, ''Transient Operation of Monolith Catalytic Converters: A Two-Dimensional Reactor Model and the Effects of Radially Nonuniform Flow Distributions,'' Chem. Eng. Sci., **44**, pp. 2075–2086.
[36] Jahn, R., Snita, D., Kubicek, M., and Marek, M., 1997, ''3-D Modeling of Monolith Reactors,'' Catal. Today, **38**, pp. 39–46.
[37] Dubien, C., and Schweich, D., 1997, ''Three Way Catalytic Converter Modeling. Numerical Determination of Kinetic Data,'' in *CAPOC IV, Fourth International Congress on Catalysis and Automotive Pollution Control*, Brussels.
[38] Pontikakis, G. N., Papadimitriou, C., and Stamatelos, A. M., 2004, ''Kinetic Parameter Estimation by Standard Optimization Methods in Catalytic Converter Modeling,'' Chem. Eng. Commun., **91**, pp. 3–29.
[39] Glielmo, L., and Santini, S., 2001, ''A Two-Time-Scale Infinite Adsorption Model of Three-Way Catalytic Converters During the Warm-Up Phase,'' ASME J. Dyn. Syst., Meas., Control, **123**, pp. 62–70.
[40] Bates, D. M., and Watts, D. G., 1988, *Nonlinear Regression Analysis and its Applications*, Wiley, New York.
[41] Luenberger, D. G., 1989, *Linear and Nonlinear Programming*, Second Edition, Addison-Wesley, Reading, MA.
[42] Goldberg, D. E., 1989, *Genetic Algorithms in Search Optimization, and Machine Learning*, Addison-Wesley, Reading, MA.
[43] Emanuel Falkenauer, 1998, *Genetic Algorithms and Grouping Problems*, Wiley, New York.
[44] Konstantas, G., and Stamatelos, A., 2004, ''Quality Assurance of Exhaust Emissions Test Data,'' Proc. Inst. Mech. Eng., Part D: J. Automob. Eng., , **218**, pp. 901–914.
[45] Votsmeier, M., Bog, T., Lindner, D., Gieshoff, J., Lox, E. S., and Kreuzer, T., 2002, ''A System(atic) Approach Towards Low Precious Metal Three-Way Catalyst Application,'' SAE paper 2002-01-0345.

Journal of Engineering for Gas Turbines and Power

Book Review

Advanced Gas Turbine Cycles J. H. Horlock, Elsevier Science Ltd, Kidlington, Oxford, 2003.

REVIEWED BY WILLIAM W. BATHIE[1]

This book requires that the individual using the book be very familiar with the principles of thermodynamics. Most of the equations presented in the text are presented in final form with very little development. Abbreviations (such as CBTBTX, CICBTBTX, etc.) are used extensively in the text, requiring the reader to quickly develop an understanding of the meaning of the letters used in the abbreviations or constantly refer back to the text.

The book has many strengths. The author contrasts the thermal efficiency of a closed gas turbine cycle with the efficiency for an open cycle. It covers a wide range of configurations for gas turbine cycles from the basic cycle, improvements to the basic cycle, combined steam and gas turbine cycles, combined heat and power cycles, and novel cycles illustrating ways to control and/or remove CO_2 emissions. The author gives reasons why modifications help achieve higher cycle efficiencies, including figures (plots) that show trends as one or more variables are changed, but does not include numerical calculations to justify these trends. The text includes a good discussion on why turbine cooling is used and another on the change in stagnation temperature and pressure through an open cooled blade row. Excellent references are included for those who want additional details and/or detailed numerical calculations on the many cycles discussed in this text. A brief discussion on how electricity is priced is included in the appendix.

The text has several weaknesses. Many of the equations are not developed in the book, but are given only in final form. This requires that the reader be very familiar with the source and limitations of the equations. Figures extensively use abbreviations. One must either be very familiar with what these symbols represent or constantly refer back to the text material that identifies them. The text lacks numerical calculations. The reader must refer to listed references for more details or rely exclusively on the figures included with the book to observe trends that occur as one or more variables are changed.

Individuals wanting an overview of the various cycles will find this book useful. Practicing engineers that want an in-depth analysis of these cycles will find other combined cycle, gas turbine cycle, or power plant engineering books more useful.

[1]Professor Emeritus, Iowa State University, Ames, Iowa.

